Studies in Electrical Machines & Wind Turbines associated with developing Reliable Power Generation

PETER JOHN TAVNER

STUDIES IN ELECTRICAL MACHINES & WIND TURBINES ASSOCIATED WITH DEVELOPING RELIABLE POWER GENERATION

by

Peter John TAVNER

Publications submitted for the degree of
Doctor of Science

Energy Group
School of Engineering and
Computing Sciences
Durham University
United Kingdom
February 2012

STUDIES IN ELECTRICAL MACHINES & WIND TURBINES

ASSOCIATED WITH

DEVELOPING RELIABLE POWER GENERATION BY DR P J TAVNER

SUBMISSION FOR THE DEGREE OF DOCTOR OF SCIENCE

Dr P J Tavner has been Professor of New & Renewable Energy in the School of Engineering, Durham University since 2003, having previously followed a career in academia and in the electrical engineering industry in research, development and manufacturing.

He is a Fellow of the Institution of Engineering and Technology, a Senior Member of the Institute of Electrical & Electronic Engineers and has been Head of the School of Engineering and Computing in Durham.

The publications listed in date order at the end of this document, all after Tavner's PhD awarded in 1978, are offered for the Degree of Doctor of Science in Durham University and have been selected from Tavner's full publication list. No part of the material offered has previously been submitted by Tavner for a degree in this or any other University. For the joint works submitted the proportions of them contributed by Tavner are estimated as set out below.

The publications were selected to represent the range and relevance of Tavner's work to the application of electrical engineering science in practical aspects of power generation. Their details are as follows:

Tavner's early research work [1] [2] used fundamental electromagnetic theory to identify magnetic field sources at the ends of the stator cores of large electrical generators. This work was the basis of Tavner's idea to use fundamental analysis to identify the root causes of incipient failure, which could then be monitored to give advance warning of large generator failure modes. More practical work followed to assess the influence of circulating currents in cores [3], which were seen as a significant root cause of generator failure. At this time Tavner worked in the Electrical Supply Industry applying this fundamental work to the condition monitoring of large plant to prolong life. In particular this work was applied to 500 and 660 MW turbogenerators in operation at that time and to the present day. This led to a seminal publication on the condition monitoring of large electrical machines [4] and the 1st edition of a book entitled "Condition Monitoring of Electrical Machines".

The was followed by work to study the rate of rise of temperature in induction motor rotor bars [5], a pressing problem for motors in hazardous gas environments. Tavner helped supervise the work and provided the industrial confirmation of the research results. Further fundamental analysis followed [6], to discover the true propagation behaviour of discharge currents in machine windings and their coupling between conductors, an

important step in locating electrical discharge sites, identified as another significant root cause of generator failure. The paper was awarded the Institution Premium of the Institution of Electrical Engineers in 1988.

After a period when Tavner held the Technical, Engineering and Group Technical Director positions in three related large UK and International electrical engineering companies, he returned to investigating fundamental electromagnetic issues associated with emerging electrical machine geometries [7], concentrating on the cross-magnetisation of magnetic structures in machines.

The need for renewable energy sources led Tavner to investigate machines being used for generation from the wind, particularly the unconventional Brushless Doubly Fed Induction Generator (BDFIG) [8], which is affected by cross-magnetisation, and the conventional Doubly Fed Induction Generator (DFIG) [11]. He initiated both research activities and provided in the publications here vital practical knowledge on the electro-magnetics, design and construction of those machines, guiding the work towards the real operational problems faced by them.

The former work has led to the establishment of a Cambridge University spin-out company, Wind Technologies, of which Tavner is a Non-Executive Director, developing the BDFIG for wind power application. Wind Technologies have now installed a 20 kW wind turbine, the first in the world operating with the BDFIG machine.

The later work on the DFIG [11] considered and provided a solution for one of the most important recent electrical problems for >1.5 MW wind turbines, that is the ability of the DFIG generator to ride-through voltage transients caused by grid operation.

In publication [9] he studied stator core failures in large generators, drawing together existing knowledge and developing new research on the root causes of these faults to show how they initiate and grow, applying the ideas and techniques developed in earlier papers [1][2][3][4] & [5] and concluding the studies on 500 and 660MW turbogenerator failures.

Concerns about the cost-effectiveness of renewable energy sources led Tavner to consider the reliability and root causes of failure of wind turbines [10], [14] and their condition monitoring [13], [15] to mitigate the effects of incipient failure. The most recent invited publication [16] is a review of wind turbine reliability performance in the UK Round 1 offshore wind farms.

He has recently been invited to update work initiated in the 1980s, by publishing the latest review of rotating machine condition monitoring [12] and has published, with a wider group of co-authors, a 2nd Edition of the earlier book “Condition Monitoring of Rotating Electrical Machines”.

These documents constitute a continuum of original work in fundamental and applied electrical science, spanning 30 years, deployed on real industrial problems, making a significant contribution to conventional and renewable energy power generation.

This is the basis of a claim of high distinction, constituting an original and substantial contribution to engineering science.

Papers presented for the DSc

[1] Tavner, P J, Hammond, P & Penman, J 1978. Contribution to the study of leakage fields at the ends of rotating electrical machines. IEE Proceedings-B Electric Power Applications 125(12): 1339-1349. PJT contribution 60%.

[2] Tavner, P J, Penman, J, Stoll, R L, Lorch, H. O. 1978. Influence of winding design on axial flux in laminated-stator cores. IEE Proceedings-B Electric Power Applications 125(10): 948-956. PJT contribution 60%

[3] Tavner, P. J. & Penman, J 1983. Currents flowing in the stator-core frames of large electrical machines. IEE Proceedings-C Generation Transmission and Distribution 130(6): 273-277. PJT contribution 70%.

[4] Tavner, P J, Gaydon, B G & Ward, D M 1986. Monitoring generators and large motors. IEE Proceedings-B Electric Power Applications 133(3): 169-180. PJT contribution 50%.

[5] Siyambalapitiya, D.J.T., McLaren, P.G., Tavner, P J. 1988. Transient thermal characteristics of induction machine rotor cage, IEEE Trans Energy Conversion, 3(4): 849-854. PJT contribution 30%.

[6] Tavner, P. J. & Jackson, R. J. 1988. Coupling of discharge currents between conductors of electrical machines owing to a laminated steel core. IEE Proceedings-B Electric Power Applications 135(6): 295-307, awarded Institution Premium of the IEE. PJT contribution 80%.

[7] Tavner, P. J. 2004. Cross-magnetisation effects in electrical machines. IEE Proceedings Electrical Power Applications 151(3): 249-259.

[8] Roberts, P. C., McMahon, R. A., Tavner, P. J. , Maciejowski, J. M. & Flack, T. J. 2005. Equivalent circuit for the brushless doubly fed machine (BDFM) including parameter estimation and experimental verification. IEE Proceedings, Electric Power Applications 152(4): 933-942. PJT contribution 30%.

[9] Tavner, P. J. & Anderson, A. F. 2005. Core faults in large generators. IEE Proceedings Electric Power Applications 152(6): 1427-1439. PJT contribution 80%.

[10] Tavner, P J, Xiang, J & Spinato, F. 2006. Reliability analysis for wind turbines. Wind Energy 10(1): 1-18. PJT contribution 70%

[11] Xiang, D, Ran, L, Tavner, P J & Yang, S. 2006. Control of a doubly fed induction generator in a wind turbine during grid fault ride-through. IEEE Trans Energy Conversion 21(3): 652-662. PJT contribution 25%.

[12] Tavner, P.J. 2008. Review of condition monitoring of rotating electrical machines, IET Electrical Power Applications, 2(4): 215–247, invited paper.

[13] Yang, W, Tavner, P. J. & Wilkinson, M R. 2008. Condition monitoring and fault diagnosis of a wind turbine synchronous generator drive train, IET Renewable Power Generation, 3(1): 1–11. PJT Contribution 40%

[14] Spinato, F., Tavner, P.J., van Bussel, G. J. W., Koutoulakos, E. 2009. Reliability of wind turbine subassemblies, IET Renewable Power Generation, 3(4): 1–15.PJT contribution 40%.

[15] Yang, W, Tavner, P.J, Crabtree, C J, Wilkinson, M R. 2010. Cost-effective condition monitoring for wind turbines, IEEE Trans Industrial Electronics, 57(1): 263-271. PJT contribution 40%.

[16] Feng, Y, Tavner, P. J, Long, H. 2010. Early experiences with UK round 1 offshore wind farms, Proceedings of ICE - Energy, 163(4), pages 167 –181 , ISSN: 1751-4223, E-ISSN: 1751-4231, invited Paper. PJT contribution 45%.

Co-authors:

Spinato and Wilkinson were Research Students at Durham University supervised by Tavner.

Roberts and Siyambalapitiya were Research Students at Cambridge University industrially supervised by Tavner.

Xiang, D was a Research Associate at Durham University co-supervised by Tavner.

Feng, Yang and Xiang J were Research Associates at Durham University supervised by Tavner.

McLaren, McMahon and Ran are academic colleagues of Tavner at Cambridge, Cambridge and Durham respectively.

Proceedings of the Institution of Civil Engineers
Energy 163
November 2010 Issue EN4
Pages 167–181
doi: 10.1680/ener.2010.163.4.167

Paper 900036
Received 08/09/2009
Accepted 10/02/2010

Keywords:
renewable energy/reviews/management

Y. Feng
Post-doctoral Research Associate, New & Renewable Energy Group, School of Engineering and Computing Sciences, Durham University, Durham, UK

P. J. Tavner
Professor of New & Renewable Energy Group, Energy Group, School of Engineering and Computing Sciences, Durham University, Durham, UK

H. Long
Lecturer in Mechanics Group, School of Engineering and Computing Sciences, Durham University, Durham, UK

ice
Institution of Civil Engineers

Early experiences with UK round 1 offshore wind farms

Y. Feng BBA, PhD, P. J. Tavner MA, PhD, Eur Ing, CEng, FIET, SMIEEE and H. Long MSc, PhD, CEng, MIMechE, MIET, FMEA

The UK government plans that offshore wind power should play a major part in meeting the UK's renewable energy and carbon emission targets by 2020. The pioneer UK round 1 offshore wind farm projects, based on sites let in 2001, were supported by the UK Department of Trade and Industry's 'Offshore wind capital grants scheme'. Round 2 offshore sites were let in 2003 and the successful bidders for round 3 offshore sites were announced in January 2010; therefore the published reports from round 1 could provide valuable information on offshore experiences for the operation of later rounds. This paper reviews the performances of those UK round 1 offshore wind farms during their early operation based on published reports from the 'Offshore wind capital grants scheme' available for the period 2004–2007 and early operational issues. UK round 1 offshore wind farms have achieved an average cost of energy of £69 per MWh, in line with expectations, but at 80·3% the average availability fell short of expectations. The availability of UK round 1 offshore wind farms has been shown to decrease with increasing wind speed therefore it is recommended that improvements of availability at wind speeds of 7–14 m/s will be needed to meet more ambitious economic targets.

1. INTRODUCTION

The UK is facing twin challenges of climate change and security of energy supply. To meet these challenges the UK government is developing a strategy of having a diverse mix of low-carbon energy sources, in which renewable sources will play a vital part. A component of that strategy was the development of round 1 offshore wind farms from 2001, as presented in Figure 1 and Table 1.

In March 2007, the European Union (EU) Council of Ministers agreed that renewable energy should meet at least 20% of EU energy demand by 2020. In December 2008, the UK agreed to a legally binding target for 15% of energy production from renewable sources by 2020, increasing from 1·5% in 2006 (DECC, 2009a, p. 4). Offshore wind power is intended to play an important part in meeting these UK renewable energy targets, improving energy security and reducing carbon emission by 2020.

The consultative document published by the Department for Business, Enterprise and Regulatory Reform (BERR) in June 2008 showed that offshore wind power could contribute up to 19% of the UK renewable energy target by 2020 (BERR, 2008, p. 8). In June 2009, the Department of Energy and Climate Change (DECC) announced a new plan for 25 GW of new offshore wind capacity, on top of existing plans for 8 GW (DECC, 2009a, p. 2). In January 2010, the UK's Crown Estate has announced the successful bidders for the round 3 which is anticipated to take the development of at least 25 GW offshore wind capacity.

The UK has a rich offshore wind resource and the deployment of large-scale offshore wind power could have some advantages. Offshore wind speeds are higher, turbulence is less and offshore wind turbines should expect a larger energy capture than equivalent onshore machines. The noise impact of offshore wind farms is less than onshore and their visual impact is perceived to be less. However, there are concerns about offshore wind in the UK owing to the lack of operating experience on large-scale offshore wind farms and the possible risks of energy capture owing to low reliability and availability, in view of the difficulties of accessing offshore turbines for maintenance. In 2001 the 'Offshore wind capital grants scheme' was launched by the Department of Trade and Industry (DTI) to encourage the deployment of large-scale offshore wind farms. Five projects with a total capacity of 390 MW of round 1 offshore wind farms, supported by the scheme, are now fully operational, including the UK's first major offshore wind farms North Hoyle (Carter, 2007), Scroby Sands, Kentish Flats, Barrow and Burbo Bank. Figure 2 presents a view of Scroby Sands offshore wind farm from the beach, demonstrating that these sites are all close inshore. These projects were designed to provide valuable experience for the upcoming larger offshore wind projects in rounds 2 and 3. From 2005, the annual operational reports of round 1 offshore wind farms have been published by DTI, subsequently BERR (DTI and BERR, 2004–2007).

Operational performance is critical to the economics of a wind farm. This is because the operation and maintenance (O&M) costs constitute a sizable share of the annual cost of a wind farm, and turbine downtime, owing to repair or maintenance, causes an annual energy production loss. This paper analyses early operational data from the available reports of round 1 offshore wind farms, placing them in context alongside the published performance of onshore wind farms in Europe and their own early operational issues.

The paper is organised as follows: Section 2 explains the terminologies used. Section 3 describes the background of

Figure 1. UK round 1 offshore wind farms (produced by Design & Imaging Unit, Durham University)

recent onshore wind turbine operational studies, based on public and commercial databases. Section 4 records the operational issues experienced at each of round 1 offshore wind farms. Section 5 presents economic and operational analyses based on the round 1 reports and previous experience; it then goes on to explain the observed performance and proposes suggestions for future improvement in Section 6. Section 7 draws conclusions.

2. TERMINOLOGY

Cost of energy (COE) is commonly used to evaluate the economic performance of different wind farms. This methodology was adopted in a joint report (IEA *et al.*, 2005, p. 173) by the IEA (International Energy Agency), the European OECD (Organisation for Economic Cooperation and Development) and US NEA (Nuclear Energy Agency), referred to

Location	Status	Capacity: MW	Period: reported year	Turbine					Water depth: m	Distance from wind farm centre to shore: km	Operator
				No.	Maker	Type	Rating: MW	Swept area: m			
North Hoyle	Operational (July 2004)	60	3	30	Vestas	V80	2	5027	7–11	9·2	RWE npower Renewables
Scroby Sands	Operational (Jan 2005)	60	3	30	Vestas	V80	2	5027	5–10	3·6	E.on UK Renewables
Kentish Flats	Operational (Jan 2006)	90	2	30	Vestas	V90	3	6362	5	9·8	Vattenfall
Barrow	Operational (July 2006)	90	1	30	Vestas	V90	3	6362	15–20	12·8	Centrica/ DONG Energy
Burbo Bank	Operational (Oct 2007)	90		25	Siemens	SWT-3·6-107	3·6	9000	2–8	8	DONG Energy
Rhyl Flats	Partial operational (July 2009)	90		25	Siemens	SWT-3·6-107	3·6	9000	6·5–12·5	10·7	RWE npower Renewables
Lynn/Inner Dowsing	Installed (July 2008)	194		54	Siemens	SWT-3·6-107	3·6	9000	5–10/ 18·6–26	6·9/6·2	Centrica Renewable Energy
Gunfleet Sands I	Under construction	108		30	Siemens	SWT-3·6-107	3·6	9000	0·5–10	7·4	DONG Energy
Robin Rigg	Under construction	180		60	Vestas	V90	3	6362	0–20	11·5	E.on Climate & Renewables UK

* See http://www.bwea.com/offshore/round1.html, accessed August 2009
† See http://www.4coffshore.com/windfarms, accessed August 2009

Table 1. Operational round 1 offshore wind farm sites in the UK*†

in this paper as the 'IEA 2005 report'. It compares the cost of different electricity production options. A simplified calculation equation is adopted in the US to calculate the COE (£/MWh) for a wind turbine system (Walford, 2006)

$$\text{COE} = \frac{\text{ICC} \times \text{FCR} + \text{O\&M cost}}{\text{E}} \quad (1)$$

where ICC is initial capital cost (£), FCR is annual fixed charge rate (%), E is annual energy production (kWh), O&M cost is annual operation and maintenance cost (£). The result of this approach is the same as that of levelised electricity generation cost used in the IEA 2005 report (p. 174), where the parameter

Figure 2. Scroby Sands offshore wind farm seen from the beach (see http://en.wikipedia.org/wiki/Scroby_Sands_wind_farm, attributed to Anke Hueper, Germany)

FCR is a function of the discount rate r used in the IEA 2005 report, as follows

$$\text{FCR} = \frac{r}{[1-(1+r)^{-n}]} \quad (2)$$

where $r \neq 0$.

The discount rate r is the sum of inflation and real interest rates. If inflation is ignored, the discount rate equals the interest rate. For the special case of a discount rate $r = 0$, unlikely in the real world, FCR will be ICC divided by the economic lifetime of the wind farm in years, currently estimated at $n = 20$ years.

It is essential to clarify the definition of availability. Since 2007, an International Electrotechnical Commission working group has been working to produce a standard to define availability. Until that standard is published, there is no internationally agreed definition of availability (Harman *et al.*, 2008). However, two availability definitions have been generally adopted in the reports (DTI and BERR, 2004–2007) and are summarised below.

(*a*) Technical availability, also known as system availability (Harman *et al.*, 2008), is the percentage of time that an individual wind turbine/wind farm is available to generate electricity expressed as a percentage of the theoretical maximum.
(*b*) Commercial availability, also known as turbine availability (Harman *et al.*, 2008), is the focus of commercial contracts between wind farm owners and wind turbine manufacturers

to assess the operational performance of a wind farm project. Some commercial contracts may exclude downtime for agreed items, such as requested stops, scheduled repair time, grid faults and severe weather, when wind turbines cannot operate normally.

For the rest of the paper, the term 'availability' refers to the technical or system availability, as defined above. It lends itself to comparison from project to project (Harman *et al.,* 2008). From the above definitions, it follows that technical or system availability will always be lower than the turbine or commercial availability because there is more alleviation of downtime for the latter.

Capacity factor and specific energy yield are two commonly used terms describing the productivity of a wind turbine or wind farm. Capacity factor is defined as the percentage of the actual annual energy production E (kWh) over the rated annual energy production from a wind turbine or wind farm (Hau, 2006, p. 530)

$$\text{Capacity factor} = \frac{E}{\text{rated power} \times 8760} \times 100\% \quad (3)$$

Specific energy yield (kWh/m^2/year) is defined as the annual energy production of a wind turbine normalised to the swept rotor area (m^2) of the turbine

$$\text{Specific energy yield} = \frac{E}{\text{swept rotor area}} \quad (4)$$

The ratio of rated power over swept rotor area is a fixed value for a type of wind turbine

$$\text{Ratio}_{\text{rs}} = \frac{\text{rated power}}{\text{swept rotor area}} \quad (5)$$

or

$$\text{Ratio}_{\text{rs}} = \frac{\text{specific energy yield}}{\text{capacity factor} \times 8760} \quad (6)$$

For a specific type of wind turbine, the specific energy yield is proportional to the capacity factor

$$\text{Specific energy yield} = \text{ratio}_{\text{rs}} \times \text{capacity factor} \times 8760 \quad (7)$$

Therefore, the operational performance factor of a wind turbine or wind farm can be defined as the percentage of the achieved capacity factor (or specific energy yield) over the expected capacity factor (or expected specific energy yield)

$$\text{Performance factor} = \frac{\text{achieved capacity factor}}{\text{expected capacity factor}} \quad (8)$$

or

$$\text{Performance factor} = \frac{\text{achieved specific energy yield}}{\text{expected specific energy yield}} \quad (9)$$

3. BACKGROUND

Quantitative reliability studies of onshore wind turbine operation have been carried out recently (Harman *et al.,* 2008; Spinato *et al.,* 2009; Tavner *et al.,* 2006). The objectives of these studies were to extract information from existing commercial or public databases to understand wind turbine reliability from a statistical point of view and provide a benchmark for future analysis.

Harman *et al.* (2008) shed light on the availability by considering a commercial database representing turbines of 14 000 MW operating in onshore wind farms, approximately 15% of the total worldwide installed capacity. The work focused on the annual availability risks of wind farms. The results showed that the mean average annual availability of onshore wind farms over their economic lifetime, that is 20 years, was approximately 97%. The probability of a wind farm annual availability being less than 80% is low at 1%. The availability rises from 93% in the first quarter of first year operation to over 96% after the end of the second year. The availability, studied from the 10 min average SCADA data, remains relatively constant for wind speeds between 7 and 14 m/s and it is in this range that the majority of energy is delivered. However, the availability reduces at wind speeds above 14 m/s and at low wind speeds below 7 m/s. At high winds above 14 m/s, high load faults may be more common causing a reduction in availability; while at low winds below 7 m/s, downtime may be associated with non-urgent maintenance activities which have been scheduled for periods of low wind.

Commercial databases are not open to public scrutiny for confidentiality reasons. Tavner *et al.* (2006) published a comprehensive study of wind turbine reliability based on publicly available Windstats data investigated over 10 years of modern wind turbine operation, paying particular attention to 904 Danish and 4285 German turbines, representing about 15 000 MW and 46 500 turbine-years in total. The investigation focused on reliability because that depends intrinsically upon the turbine itself and should therefore be predictable. The study analysed in detail how turbine design, configuration, time and weather affected reliability. This research was later extended (Spinato *et al.,* 2009) to a study of the reliability of wind turbine subassemblies, which paid particular attention to 1740 turbines in Germany representing about 1500 MW and 21 200 turbine-years.

Operational data in the public domain from relatively new offshore projects are rare compared to data collected from onshore projects developed from the 1980s to date. The operational reports published under the 'Offshore wind capital grants scheme' (DTI and BERR, 2004–2007) have provided an opportunity to learn about offshore wind turbine experience through quantitative study and comparison with the accumulated onshore data. Table 2 shows the population information, including the relative size and significance of the data in this paper in relation to the studies already completed.

4. SITES AND OPERATIONAL ISSUES

Four offshore wind farms have reported under the government's 'Offshore wind capital grants scheme'

(*a*) North Hoyle (July 2004–June 2007)
(*b*) Scroby Sands (January 2005–December 2007)

	Turbines	MW	Turbine years	Onshore/offshore
Harman *et al.* (2008)	Not available	~14 000	Not available	Onshore
Tavner *et al.* (2006)	~5000	~15 000	~46 500	Onshore
Spinato *et al.* (2009)	~1740	~1 500	~21 200	Onshore
This paper	120	300	270	Offshore

Table 2. The population information of wind turbine reliability studies

(*c*) Kentish Flats (January 2006–December 2007)
(*d*) Barrow (July 2006–June 2007).

These reports represent data from turbines of 300 MW and 270 turbine-years. Figure 3 shows the monthly data from these wind farms, including availability, capacity factor and wind speed to provide an overall impression of performance. Figure 3 shows that the mean wind speed conditions at the four sites are similar and that the capacity factors and availabilities of the wind farms, particularly during the winters of 2004/5 and 2006/7, were also similar during relatively windy conditions (Figure 3).

The following sections record the operational issues experienced at each of these four sites concerning unplanned work affecting availability. The reader can consider that most of these issues represent teething problems during early operation and have a bearing on the results in Section 5.

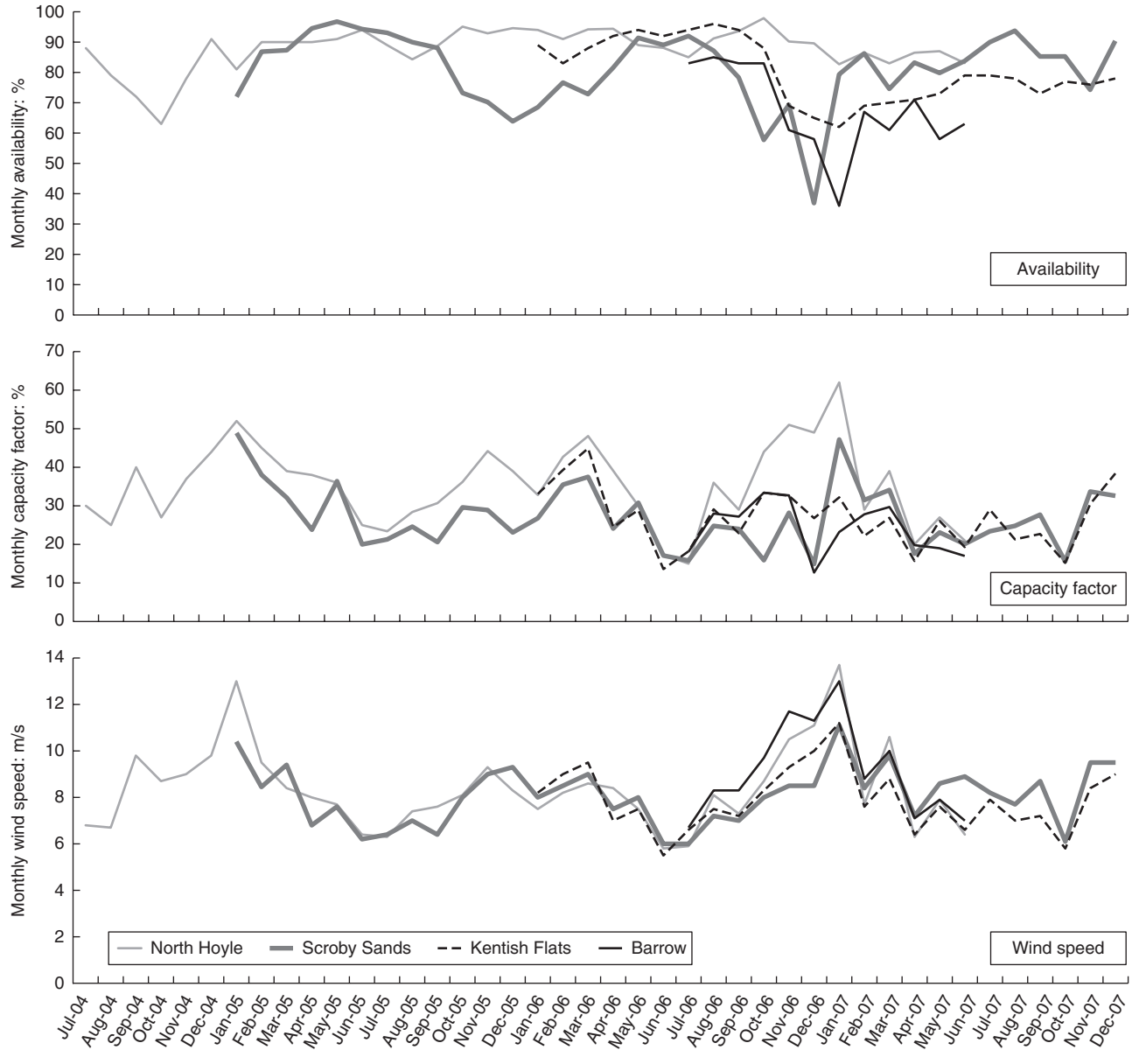

Figure 3. Monthly data of UK offshore wind farm (July 2004–December 2007)

4.1. Scroby Sands

In 2005 there was substantial unplanned work attributed to minor commissioning issues, corrected by remote turbine resets, local turbine resets or minor maintenance work, mostly resolved within a day. A smaller number of unplanned works involved larger-scale plant problems with more serious implications, the primary cause being gearbox bearings.

In 2005 27 generator side intermediate speed shaft bearings and 12 high-speed shaft bearings were replaced. A number of reasons for the gearbox bearing damage were identified related to the bearing designs.

In 2005 four generators were replaced with generators of alternative design.

In 2006 unplanned work involved three outboard intermediate speed shaft gearbox bearings, nine high-speed shaft gearbox bearings and eight generator failures. Generating capacity was also significantly reduced for 2 months when one of the three transition joints in the cable to the beach failed.

In 2007 problems experienced with the generators were resolved by replacing all original generators with a generator of proven design. The gearbox bearing issue was managed in the short term by proactive replacement of the outboard intermediate speed bearings; in addition 12 high-speed shaft bearings were identified as worn during routine internal inspections and proactively replaced before failure. Three gearboxes were also identified as requiring replacement. Capacity was also affected by a transition joint failure in another cable to the beach; commissioning tests also identified a fault in the sub-sea portion of the cable, for which replacement was planned for spring 2008.

4.2. North Hoyle

In 2004–2005 unplanned work involved a high-voltage cable fault, generator faults associated with cable connections and SCADA (supervisory control and data acquisition) electrical faults.

In 2006 the following issues arose

(*a*) two generator bearing faults
(*b*) six gearbox faults
(*c*) an unplanned grid outage
(*d*) preparation and return of turbines to service further extended downtime
(*e*) downtime owing to routine maintenance and difficulties in the means of access to the turbines.

In 2007 the following issues arose

(*a*) four gearbox bearing faults and chipped teeth resulting in gearbox replacements delayed by the lack of a suitable maintenance vessel
(*b*) two generator rotor cable faults
(*c*) two circuit breaker failures
(*d*) one cracked hub strut
(*e*) one turbine outage for yaw motor failures
(*f*) an unplanned grid outage
(*g*) again downtime owing to difficulties in the means of access.

4.3. Kentish Flats

In 2006 there was substantial initial unplanned work attributed to minor commissioning issues corrected by remote turbine resets, local turbine resets or minor maintenance work. Other unplanned work involved larger-scale plant problems and included

(*a*) main gearbox
(*b*) generator bearings
(*c*) generator rotor cable connections from the slipring unit
(*d*) pitch system.

The generator bearing and rotor cable problems were prolonged as the generator sub-supplier undertook the repairs to avoid jeopardising the warranty.

The first main gearbox damage was detected in late 2006 and an intensive endoscope campaign revealed that 12 gearboxes required exchange. In 2007 all 30 gearboxes were exchanged owing to incipient bearing failures in the planetary gear. The exchange programme was scattered over the year, and due to waiting time and the lack of a crane ship, the outages were longer than the repair time. About half of the generators were refurbished owing to

(*a*) damage on internal generator rotor cable connections
(*b*) shaft tolerances
(*c*) grounding of bearings to avoid current passage.

Other unplanned tasks included

(*a*) pitch system repair
(*b*) blade repair on one turbine due to crane impact during gearbox exchange.

4.4 Barrow

In 2006–2007 unplanned work on the turbines was substantial although some issues were minor, solved by a local reset or minor work to the turbine. Other larger issues were

(*a*) generator bearings failed and replaced with a new type
(*b*) generator rotor cables replaced with a new type
(*c*) pitch systems modified.

Owing to gearbox problems seen on other turbines of the same type an inspection process commenced in 2007 showing a few gearboxes beginning to show similar problems. It was decided proactively to replace gearboxes before failure and this started in July 2007 completing in October 2007.

5. RESULTS

5.1. Capacity factor and availability

Table 3 shows the average operational performance of the four offshore wind farms for 2004–2007. The figures are calculated using the data published in the reports and the annual averages are weighted taking account of the number of reporting year for each wind farm.

The comparison that can be made between the four offshore wind farms and for the period reported is as follows.

(*a*) Barrow has a low availability of 67·4%, low capacity factor of 24·1% with higher average wind speed, much of which may be attributable to the generator, gearbox and pitch system issues recoded above, bearing in mind that only one year's performance has been reported.
(*b*) Scroby Sands and Kentish Flats are similar with availabilities of ~80%, capacity factors of ~27% and annual average wind speeds of ~8 m/s.

	Turbine type	Annual average wind speed: m/s	Specific energy yield: kWh/m/year	Capacity factor: %	Performance factor: %	Availability: %
Barrow	V90	9·15	996	24·1	68·9	67·4
North Hoyle	V80	8·36	1220	35·0	100·0	87·7
Scroby Sands	V80	8·08	943	27·1	77·4	81·0
Kentish Flats	V90	7·88	1146	27·7	79·1	80·4
Annual average				29·5		80·2

Table 3. The operational performance of four UK round 1 offshore wind farms

(*c*) North Hoyle has the highest availability of 87·7% and capacity factor of 35% despite the operational experiences recorded above.

The annual average availability for UK round 1 offshore wind farm for the reported period is low at only 80·2%, lower than the availability reported by Harman *et al.* (2008) achieved by onshore wind farms at 97% and lower than a typical EU established offshore wind farm, Middelgrunden, calculated at 93·3% based on data provided by Larsen *et al.* (2005). However, these data from UK round 1 wind farms were collected during periods of early operation.

The annual average capacity factor for reporting UK round 1 offshore wind farms is 29·5%, higher than the average value of 27·3% reported in 2007 for UK onshore wind farms (DECC, 2009b) but lower than the expected 35·0% estimated from EU offshore wind farms. The latter being based on Horns Rev, Denmark 33%, Nysted, Denmark 40% (IEA, 2005), Samsø, Denmark 38% (Samsø Offshore Wind Farms, 2009), Egmond aan Zee, Netherlands 35% (Noordzee Wind, 2008) and Middelgrunden, Denmark 27% (Svenson and Larsen, 2008) as summarised in Figure 4.

The ratio of rated power over swept rotor area $Ratio_{rs}$ is 398 W/m^2 for a V80 turbine and 472 W/m^2 for a V90 turbine. From Equation 7, the expected specific energy yields for these two types of turbine are quite different, even though the capacity factors expected from them, based on European experience, should be the same at 35%. The expected specific energy yield for a V80 is calculated to be 1220 kWh/m^2/year and for a V90 turbine 1446 kWh/m^2/year. For the wind farms with the same type of turbine, the specific energy yield varies with the availability as shown in Table 3. For example, the specific energy yield of North Hoyle is greater than that of Scroby Sands owing to higher capacity factor and availability.

To compare wind farms with different types of turbine, the performance factor defined in Equations 8 and 9 is suggested. Although the absolute value of the specific energy yield of Scroby Sands (943 kWh/m^2/year) is much lower than that of Kentish Flats (1146 kWh/m^2/year), the performance factor of Scroby Sands is at 77·4% which is very close to that of Kentish Flats at 79·1%. The performance factors for North Hoyle and Barrow are 100% and 68·9% respectively.

5.2. Cost of energy

Table 4 shows the COE, capital cost, O&M cost, percentage of O&M cost over COE of the four UK round 1 reporting offshore wind farms. The figures are calculated using the data published in the reports at a discount rate of 10%. In the absence of other information the discount rate adopted throughout the paper will be 10%, close to the FCR of 11·85% used by US NREL (National Renewable Energy Laboratory) in some studies (Fingersh *et al.*, 2009). The COE average and O&M cost average are weighted taking account of the number of reporting year for each wind farm.

The discount rate has a big impact on the COE estimation. Analysis of the sensitivity of offshore wind COE to the discount

	COE: £/MWh	Capital cost: £/kW	O&M cost: £/kWh	O&M cost: £/MWh
Barrow	86	1367	10	12
North Hoyle	67	1350	15	22
Scroby Sands	67	1113	11	16
Kentish Flats	67	1167	11	16
Average	69	1249	12	18

Table 4. The economics of four UK round 1 offshore wind farms (calculated at a discount rate 10%)

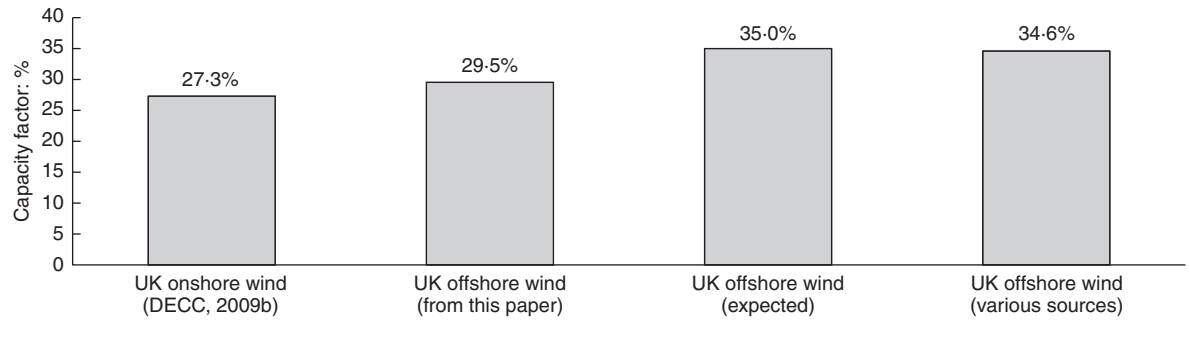

Figure 4. The capacity factors of UK and EU offshore wind farms

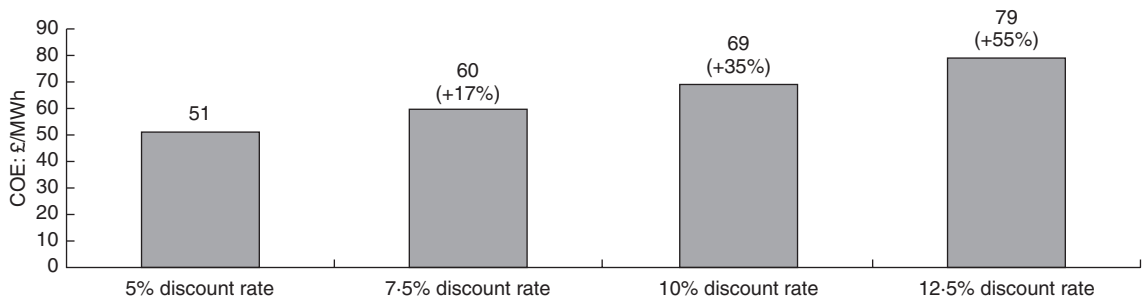

Figure 5. The sensitivity analysis of the COE of UK round 1 offshore wind farms

rate risk is shown in Figure 5. When the discount rate increases by 1%, the COE increases by ~£3·60 per MWh, or ~7%.

To provide a benchmark comparison of wind turbine COE performance we estimate the COE for coal- and gas-fired plants with carbon capture storage systems (CCS) by adopting the median values reported by DTI in 2006 (DTI, 2006), where approximately the COE for coal with CCS was £45 per MWh and for gas with CCS was £56 per MWh, in which the assumption of discount rate at 10%, median prices for coal of £25/t, for gas of 37p/therm and for carbon dioxide €36/t were made.

Note that DECC and BERR regularly update their fuel and carbon dioxide price assumptions. In May 2009, the latest communication, the assumed price in 2015 for coal was £48/t, with a GB pound £: US dollar $ exchange rate of 1 : 1.65 in 2009, and for gas 63p/therm, predicted for moderate global energy demand (DECC, 2009c). These price assumptions are almost double those cited by DTI in 2006.

Therefore, the COE estimations adopted here for fossil-fired plant are likely to increase dramatically in the future. The latest price assumption for carbon dioxide made by BERR in April 2009 was €34/t, close to the figure cited by DTI in 2006.

Krohn *et al.* (2009) have suggested a risk-based model for comparing the power generating cost of different technologies by taking into account the fuel and carbon price risk. Fuel and carbon prices are highly unpredictable and have added extra risk cost to the basic estimation of the COE for coal and gas, whereas for wind power the fuel is free and is classified in cost estimation as a low-risk fuel. Based on the estimation made for the EU, the historic fuel price has been assumed, a 'no-cost 40-year fuel purchase' contract and a proportional fuel risk cost added to the basic COE estimation of coal-fired or gas-fired plant for UK.

For the COE of coal with CCS, the historic fuel risk and 'no-cost 40-year fuel purchase' will each increase the basic estimation by 108% and 65% respectively. For the COE of gas with CCS, the historic fuel risk and no-cost contract will each increase the basic estimation by 85% and 65%, respectively.

A comparison between the COE of the two fossil fuel options above, the current COE for onshore wind farms given by E.ON at mean £47 per MWh in the report to House of Commons (2006) and the average COE results from the four reporting UK offshore wind farms are shown in Figure 6 together with their sensitivity to the fuel risk. The figure shows the strategic economic advantage for onshore and offshore wind energy, in that the COE remains unchanged because the technology carries no fuel price risk.

A comparison is made in Figure 7 between the COE of the reporting UK offshore wind farms and EU wind farms based on the discount rate at 10%. The average COE for several Danish offshore wind farms (Krohn *et al.*, 2009, p. 67); – that is, Middelgrunden, Horns Rev I, Samsø and Nysted – is calculated at £104 per MWh with discount rate 10% using a GB pound £: Euro € exchange rate of 1 : 1·5 for year 2006. The COE of EU onshore is £80 per MWh for a coastal site at discount rate 10% (Krohn *et al.*, 2009, p. 60). As shown in Figure 7, the COE of UK or EU offshore wind farm is generally higher than that of onshore wind farm by £22–24 per MWh.

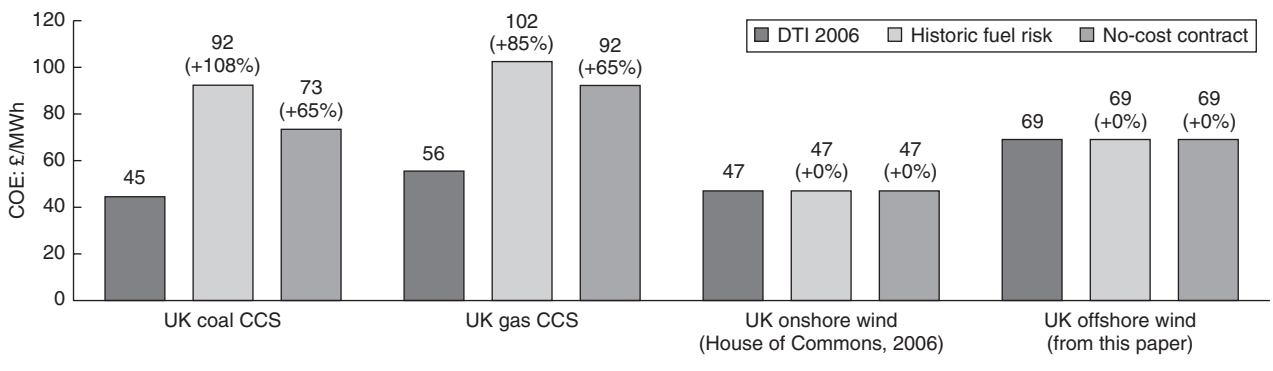

Figure 6. COE for four electricity generation technologies

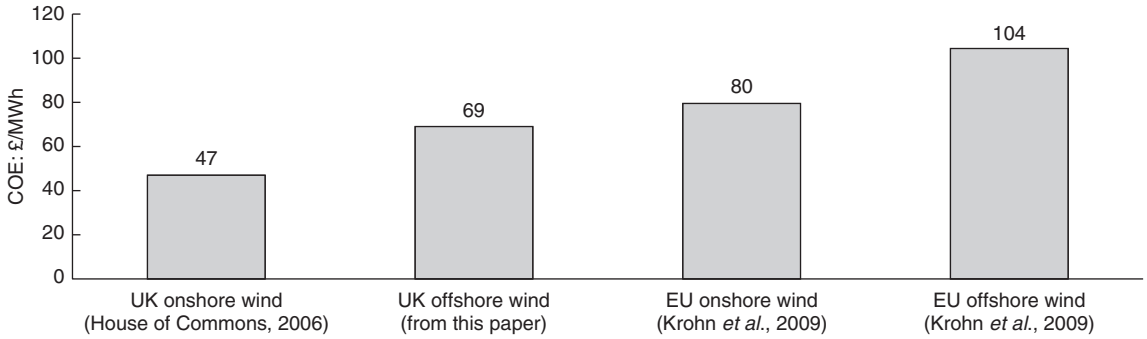

Figure 7. The COE of UK and EU wind generated power

5.3. O&M costs

Table 4 shows the average O&M cost as a percentage of COE for an offshore wind farm in the UK. The average O&M cost of UK round 1 offshore wind farms is calculated from this paper to be £12 per MWh. For the UK offshore wind farms, annual O&M cost includes land rental, electricity charges, site maintenance and service fees, insurance, management fees and miscellaneous charges (Greig, 2004). A comparison of the percentage of O&M and fuel costs in the COE is given in Figure 8.

The cost percentages related to UK coal and gas, onshore wind technologies are estimated based on the data published by PB Power in 2006. Offshore wind power is a capital-intensive technology but the fuel is free. The variable costs of wind farm are much lower than those of the conventional fossil fuel-fired technologies in which as much as 37–73% of the COE is related to the fuel and O&M costs. The percentage O&M cost of UK offshore wind farms, at 18%, is higher than that of UK onshore wind, at 12%, but is not as high as the premium for offshore wind O&M costs which is suggested by some early models, accounting the percentage O&M cost as 25–30% or two to three times onshore O&M costs (Marsh, 2007). A reason for this disparity may be that some EU authors have included the revenue losses owing to maintenance downtime. However, this would double-count revenue losses which, when the calculation is per MWh, should have already been factored into the annual energy production *E*. It should be noted that the optimisation of offshore O&M strategies aims at minimising both the O&M and revenue loss costs. Occasionally, some authors might have quoted the COE values rather than O&M costs. The COE of EU offshore wind farms is 2·2 times of that of the UK onshore costs, as shown in Figure 7.

The components of O&M costs in Europe, which are similar to those in the UK, also do not include the revenue losses (Krohn *et al.*, 2009). The O&M cost of Middelgrunden offshore wind farm, established in 2000, was reported as approximately €16 per MWh (Svenson *et al.*, 2008). The O&M cost percentage of Middelgrunden at 24% is higher than for the reporting UK offshore wind farms at 18%, but this contained an unexpected transformer-related cost. If the transformer-related cost was excluded, the O&M percentage of COE for Middelgrunden would be 18%, the same as the UK offshore.

5.4. Interaction between capital and O&M costs, capacity factor, availability

Table 4 shows the capital costs at North Hoyle and Barrow were higher, owing to increased construction costs associated with further distance offshore and deeper water. The capital cost of Barrow was the highest while the O&M cost was the lowest. The capital and O&M costs of North Hoyle were both high. The capital and O&M costs of Scroby Sand and Kentish Flats were both lower than North Hoyle.

The data from Tables 2 and 3 show when the O&M cost was higher the availability and capacity factor were higher. When the capital cost was high, the wind farm itself must work harder to achieve a low COE for an acceptable payback time. The only way that a wind farm can improve its capacity factor is through the higher availability since there is little control over wind speeds. The outcomes of this effort are shown in North Hoyle

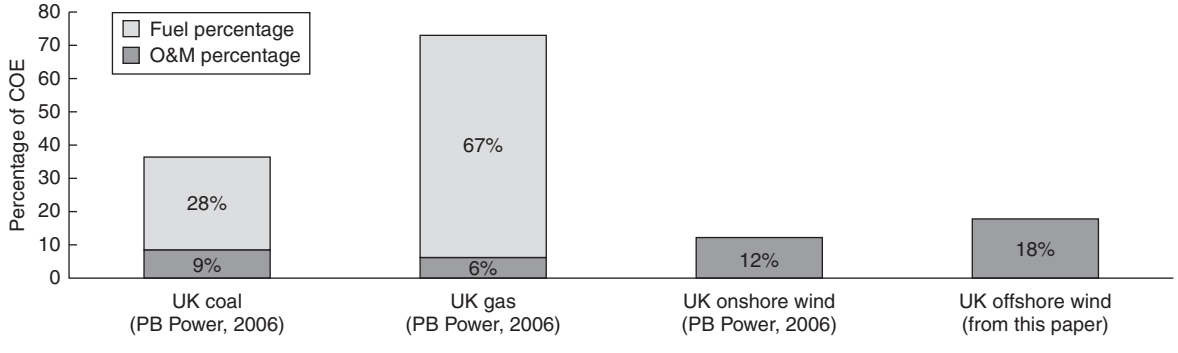

Figure 8. The O&M and fuel cost percentage in COE for four electricity generation technologies

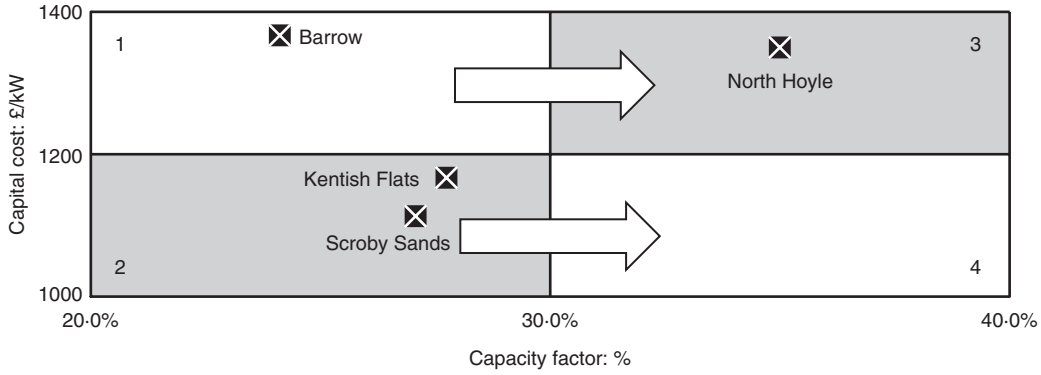

Figure 9. Improving the capacity factor can help the offshore wind farms to reduce COE

where the availability and capacity factor have been improved to 87·7% and 35·0%, respectively. Therefore, despite a relative high capital cost at North Hoyle, the COE has been kept down to approximately £67/MWh, the same level as Scroby Sands and Kentish Flats.

Figure 9 shows the relative position of capital cost and capacity factor for the different UK round 1 offshore wind farms. Barrow locates in region 1 which represents its high capital cost and low capacity factor and is attributable to the operational issues identified above. This is reflected in its high COE at approximately £86/MWh. Kentish Flats and Scroby Sands locate in region 2 which represents their lower capital cost and capacity factor. They both have great potential to reduce their COE by improving their capacity factor. North Hoyle locates in region 3 which represents high capital cost and capacity factor.

All three wind farms have COE at approximately £67/MWh. Region 4 would be the best option for economic performance, representing a low capital cost and a high capacity factor. Kentish Flats and Scroby Sands have the opportunity to enter region 4, while Barrow could enter region 3.

Figure 10 shows the monthly capacity factor against availability for four wind farms. Note that the bottom-left light-grey region shows a 'bad region' where monthly capacity factors are lower than 35% and availability is less than 70% regardless of wind speed. For availability more than 70%, the capacity factors achieved range from 10% up to 65%. This is attributed to wind speed influencing the capacity factor. The upper-right region shows a 'good region' of monthly performance in which availability is greater than 80% and capacity factors are greater than 20%.

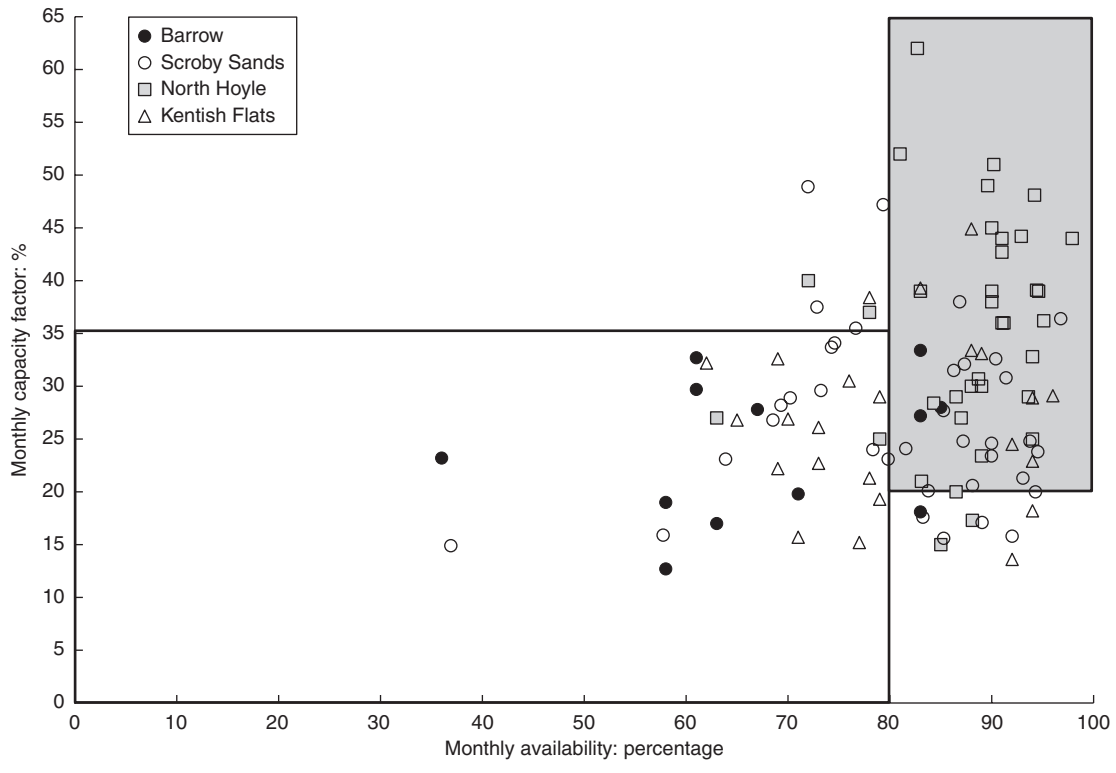

Figure 10. Monthly capacity factor against availability for the offshore wind farms, each point representing 1 month's operational data

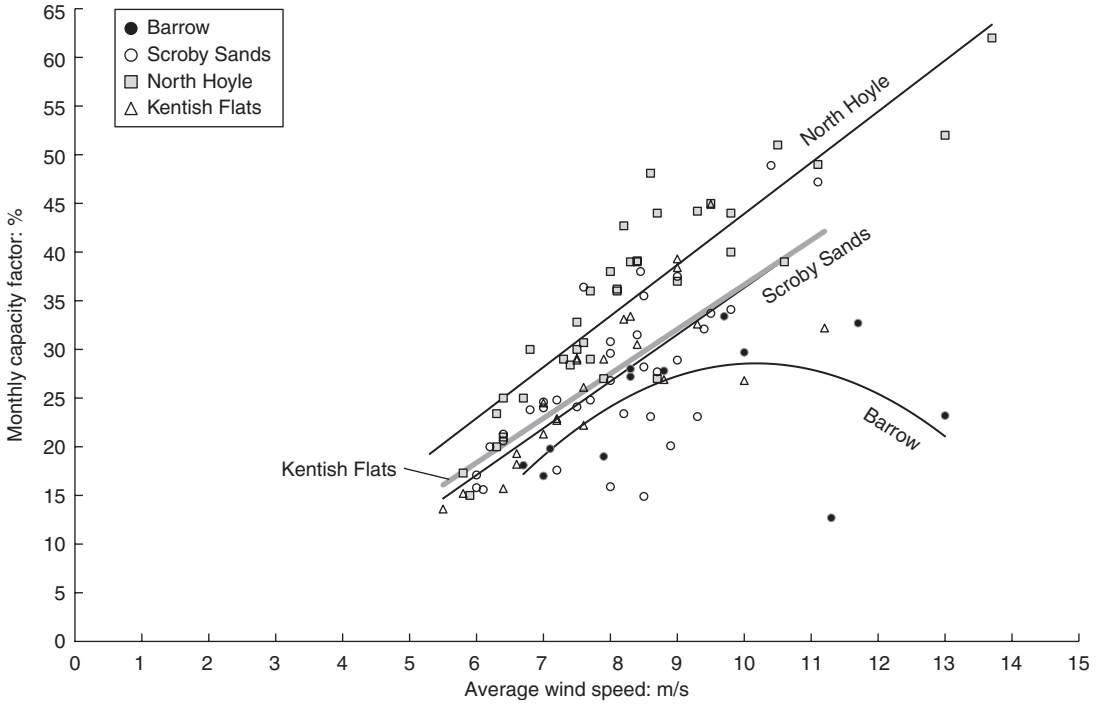

Figure 11. Monthly capacity factor against wind speed for the offshore wind farms

5.5. Influence of wind speed on performance

It has been shown in Section 5.4 that capacity factor and capital cost are the driving factors for the economic performance of UK offshore wind farms. Despite a mean annual wind speed over 9·15 m/s at Barrow, the wind farm's economic performance has not been as strong as might be expected. Possibly this has been the result of the pitch systems issues raised above and the data here record only the first year of operation.

Figure 11 shows that higher average wind speed usually brings a higher monthly capacity factor, except at Barrow which follows a non-linear trend. Wind speed does not affect the performance at Barrow positively, instead the capacity factor goes down as wind speed rises. For the same wind speed, the capacity factor of North Hoyle can usually reach a higher value than at other wind farms.

Figures 12 to 15 show the availability against wind speed on a monthly basis for the four wind farms, in which the larger circles represent higher capacity factors and vice versa. It can be seen that high capacity factors are all gathered around wind speeds 7–14 m/s, in line with the result of capacity factor shown in Figure 11. The monthly wind speed range 7–14 m/s delivers the majority of energy for UK round 1 offshore wind farms. For example, the highest monthly capacity factor achieved at North Hoyle in January 2007 was 62%, with a mean wind speed of 13·7 m/s and an availability of 82·7%.

The availabilities of UK round 1 offshore wind farms tend to decrease with increasing wind speed. These are illustrated by Figures 12–15, although some of the early problems reported above may be a cause; however, this trend confirms that reported in a much larger survey (Harman *et al.*, 2008). The

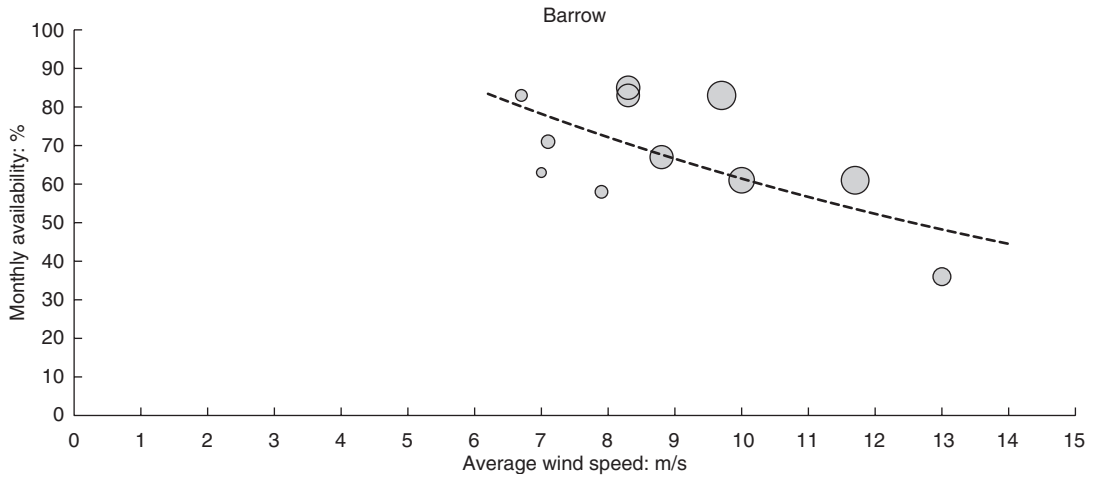

Figure 12. Monthly availability against wind speed for Barrow offshore wind farm (each circle representing 1 month's operational data; circle radius is proportionate to capacity factor)

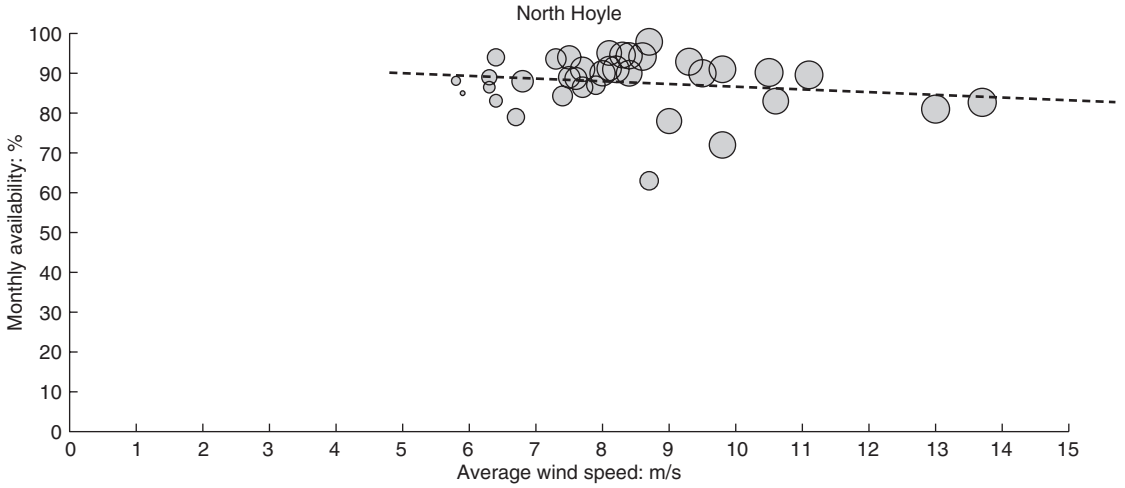

Figure 13. Monthly availability against wind speed for North Hoyle offshore wind farm (each circle representing 1 month's operational data; circle radius is proportionate to capacity factor)

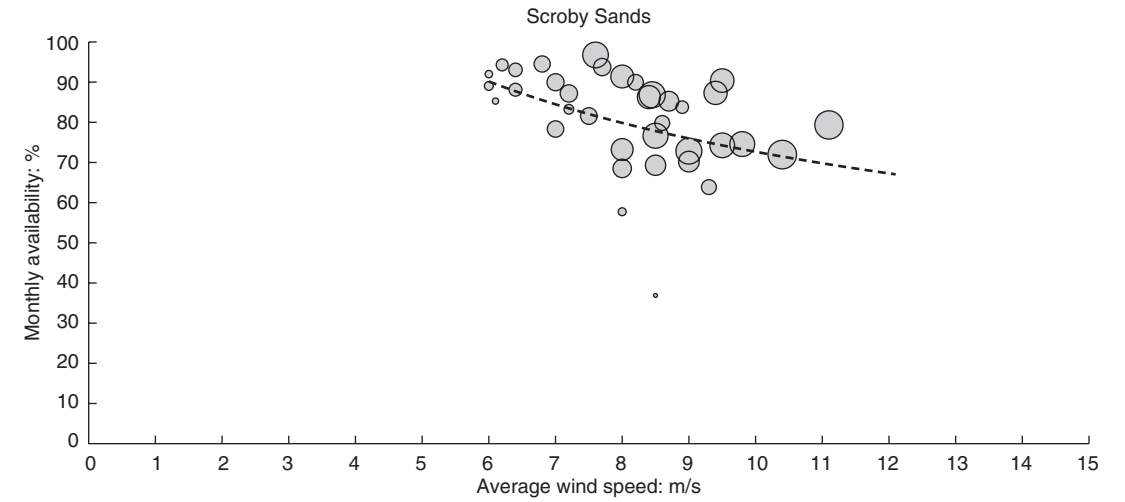

Figure 14. Monthly availability against wind speed for Scroby Sands offshore wind farm (each circle representing 1 month's operational data; circle radius is proportionate to capacity factor)

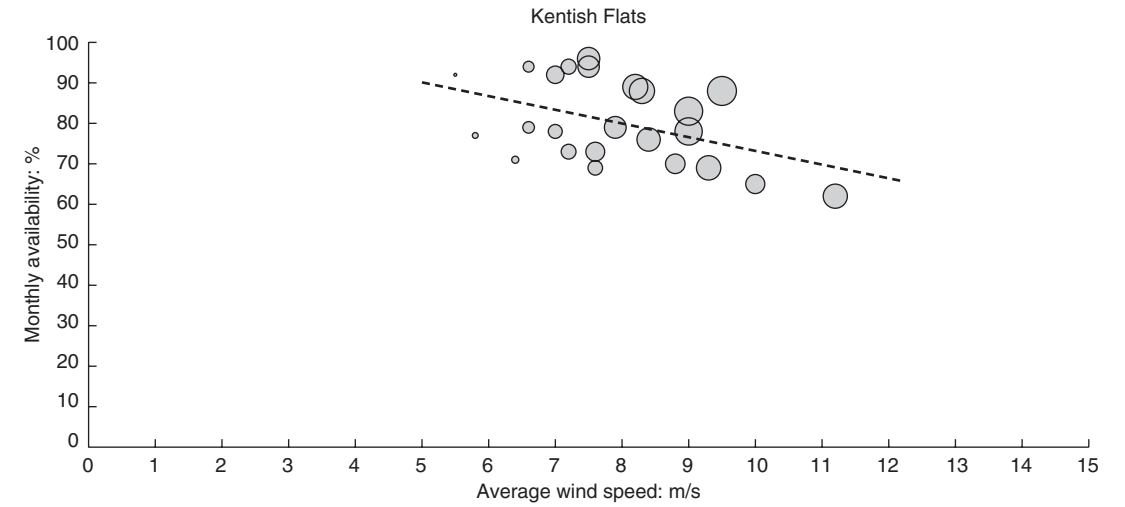

Figure 15. Monthly availability against wind speed for Kentish Flats offshore wind farm (each circle representing 1 month's operational data; circle radius is proportionate to capacity factor)

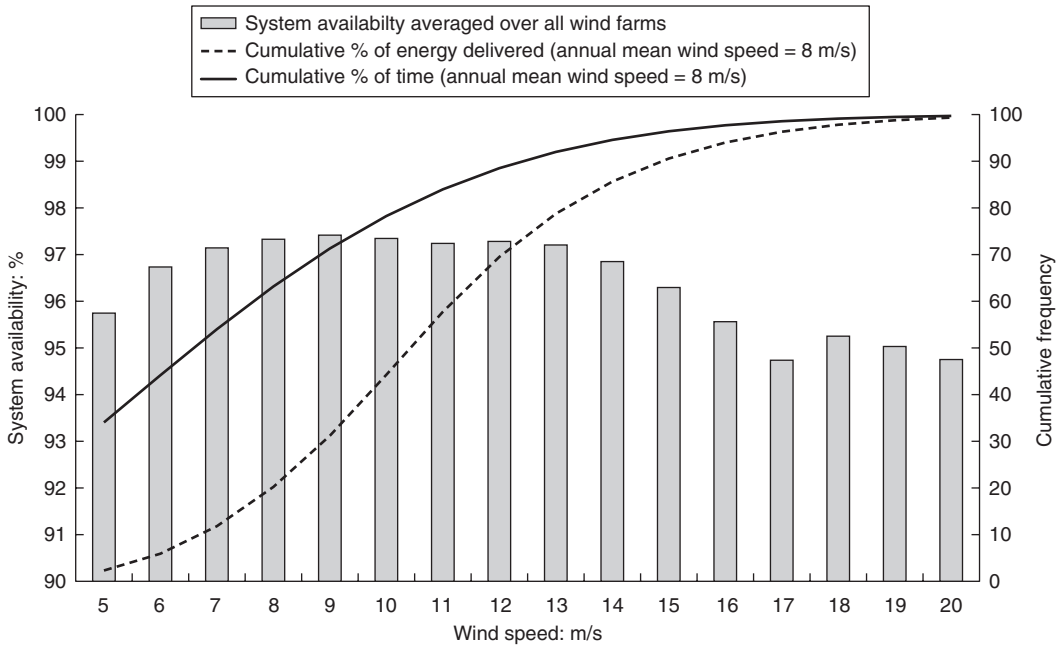

Figure 16. Worldwide onshore availability against wind speed (Harman *et al.* 2008, courtesy of the original authors for assistance to reproduce the figure)

trend line of Barrow is the steepest, while North Hoyle is the flattest. The trend lines of Scroby Sands and Kentish Flats are similar but steeper than North Hoyle. The gradient of the availability trend line is apparently correlated with the capacity factor trend line shown in Figure 11. In other words, the smaller the gradient of the availability trend line against wind speeds, the better the operational performance of offshore wind farms. The decreasing trends as shown above are much more severe than those that can be estimated from worldwide onshore wind farms, as shown in Figure 16 (Harman *et al.*, 2008). The 10-min average SCADA data show the onshore availabilities vary only from 94·5% to 97·5%, although they also tend to decrease at high wind speeds.

6. DISCUSSION

Two government reports (DTI, 2006; House of Commons, 2006) estimated that the COE for UK offshore wind generation would be £55–90/MWh (at discount rate 10%) and £55–84/MWh respectively. Based on published reports from the 'Offshore wind capital grants scheme' during the period 2004–2007, the economic performance of round 1 offshore wind farms with a COE of £69/MWh at discount rate 10% lies within those expectations, despite the early operational difficulties reported in Section 4.

The annual average capacity factor of round 1 offshore wind farms to date has been 29·5% and the annual average availability 80·2%. Onshore experience confirms that availability can improve after teething problems have been resolved in the first few years' operation (Harman *et al.*, 2008). Can offshore availability also be improved with time? The answer must be yes but the data period for 'Offshore wind capital grants scheme' reports was limited to 3 years in the early part of operation, so future data will need to be studied to find a definitive answer.

Although annual average availabilities were low, the wind farms still achieved an average capacity factor of 29·5%, greater than onshore UK wind farms with an average availability of 97%, because onshore wind speeds are lower than offshore. From this point of view, UK offshore wind farms, with higher wind speeds, have the potential to improve their capacity factors as can be seen from Figure 11. On the other hand, rich wind resources pose new challenges for the operation of offshore wind farms. The average availability achieved by these UK offshore wind farms is only at the level of Danish onshore wind turbines in the early 1980s. This might be because for the wind farms reported the wind turbines being used were originally designed for onshore rather than offshore use therefore may not have been sufficiently modified to meet the challenging offshore environment.

The results show that despite a good COE the reported UK round 1 offshore wind farms lost substantial annual energy production due to low availability; this is clear in Figure 3. The early economic performance of the reported UK round 1 offshore wind farms depends strongly on the availability. In one case, Barrow, an offshore wind farm with good wind resource, did not achieve strong economic performance during the reporting period because of low availability, although there were extenuating operational difficulties which will have caused this.

If project capital costs increase, a strategy that may have to be adopted by some wind farm operators to improve offshore economics, as appears to have been done at North Hoyle, is to encourage more proactive O&M, raising O&M costs but increasing energy yield. This will mitigate high capital costs by improving annual energy production.

The results also show that the availability of reported UK offshore wind farms tends to decrease at monthly wind speeds 7–14 m/s while the majority of energy is delivered in this speed range. For onshore wind farms, the causes of this availability

reduction could be severe climate issues causing systematic turbine faults due to excessive loads, which wind sector managers will try to minimise by operational management. For the UK offshore wind farms, the early operational issues are likely the causes of the availability reduction. Therefore, it is important to solve these operational problems and improve availability at wind speeds 7–14 m/s to raise the overall economic performance.

Given poorer accessibility for maintenance offshore, it is essential to improve the intrinsic reliability of offshore wind turbines, needing close collaboration between turbine manufacturers, wind farm operators and research institutes. To this end, future research for wind energy in UK could be

(*a*) to develop a generic methodology for reliability data collection and analysis
(*b*) to establish a reliability benchmark of wind turbine subassemblies
(*c*) to understand the failure modes and failure mechanisms of different wind turbine subassemblies
(*d*) to develop a guideline for wind turbine manufacturers to conduct the reliability centred maintenance (RCM)
(*e*) to develop an advanced health monitoring system for wind turbines
(*f*) to develop cost-effective condition monitoring methods for wind turbine.

7. CONCLUSIONS

(*a*) At an approximate cost of energy (COE) of £69 per MWh during the period 2004–2007 the reporting UK round 1 offshore wind farms have an economic performance within the expectations of the government reports prior to these investments, despite the early operational problems at these wind farms.
(*b*) The annual average capacity factor for reporting UK round 1 offshore wind farms during their early period of operation is 29·5%, greater than the current 27·3% average for onshore UK wind farms but less than that achieved by other European established offshore wind farms.
(*c*) The greatest cause of loss of energy for reporting UK round 1 offshore wind farms is low technical or system availability. The annual average technical availability for reporting UK round 1 offshore wind farms is 80·2%, much less than the average availability of 97% achieved by onshore wind farms in the UK or the availability at 93·3% achieved by an established EU offshore wind farm, Middelgrunden. It is likely that these low availabilities are a direct result of the early operational issues at these wind farms.
(*d*) The annual average O&M cost as a percentage of COE for reporting UK round 1 offshore wind farms is 18% and the O&M cost is approximately £12 per MWh. This percentage compares well with the value of 12% O&M costs for onshore wind in the UK and this is much less than the premium for O&M costs for offshore wind predicted in the industry.
(*e*) A strategy that could be adopted by wind farm operators to improve offshore economics would be to encourage more proactive O&M, raising O&M costs but increasing energy yield. This will mitigate high capital costs by improving annual energy production.
(*f*) The availability of reporting UK round 1 offshore wind farms tends to decrease with increasing wind speed, though North Hoyle is an exception to this.
(*g*) Improvements in the performance of these and other offshore wind farms should focus on improving the availability at wind speeds 7–14 m/s.
(*h*) UK offshore wind farms have great potential to extract more energy from the wind and achieve lower COEs, but their reliability and availability must be substantially improved. This could be achieved through intensive R&D activities by manufacturers and operators and a plan for such activities has been set out in the paper.

ACKNOWLEDGEMENTS

This work has been funded by the EU FP7 Project RELIAWIND 212966 with some assistance from the UK EPSRC Supergen Wind Programme EP/D034566/1. The authors would like to thank Ben Hendrik and Michael Wilkinson of GL Garrad Hassan & Partners Ltd, Dave Pearce of E.ON UK and anonymous reviewers for their valuable comments and discussion.

REFERENCES

BERR (Department for Business, Enterprise and Regulatory Reform) (2008) *UK Renewable Energy Strategy: Consultation Document*. BERR, London.

Carter JMF (2007) North Hoyle offshore wind farm: design and build. *Proceedings of the Institution of Civil Engineers, Energy* **160(EN1)**: 21–29, **doi:** 10.1680/ener.2007.160.1.21.

DECC (Department of Energy and Climate Change) (2009a) *A Prevailing Wind: Advancing UK Offshore Wind Deployment*. DECC, London.

DECC (2009b) *Digest of United Kingdom Energy Statistics*, a national statistics publication. DECC, London.

DECC (2009c) *Communication on DECC Fossil Fuel Price Assumptions*. DECC, London.

DTI (Department of Trade and Industry) (2006) *Energy Challenge: Energy Review Report 2006*. Presented to Parliament by the Secretary of State for Trade and Industry. DTI, London.

DTI and BERR (Department for Business Enterprise and Regulatory Reform) (2004–2009) Offshore wind capital grants scheme annual reports: Scroby Sands offshore wind farm 1st and 2nd annual report, January 2005–December 2006; Scroby Sands offshore wind farm 3rd annual report, January–December 2007; North Hoyle offshore wind farm 1st and 2nd annual report, July 2004–June 2006; North Hoyle offshore wind farm 3rd annual report, July 2006–June 2007; Kentish Flats offshore wind farm 1st annual report, January–December 2006; Kentish Flats offshore wind farm 2nd annual report, January–December 2007; Barrow Offshore wind farm 1st annual report, July 2006–June 2007.

Fingersh L, Hand M and Laxson A (2006) *Wind Turbine Design Cost and Scaling Model*. NREL, USA, Technical Report, NREL/TP-500-40566.

Greig E (2004) *Monitoring and Evaluation of Blyth Offshore Wind Farm: Projecting O&M Costs of UK Offshore Wind Farms Based on Experience at Blyth*. AMEC Wind, Knutsford, UK.

Harman K, Walker R and Wilkinson M (2008) Availability trends observed at operational wind farms. *Proceedings of European Wind Energy Conference 2008, Brussels*. Operations and Maintenance Session DT3.1.

Hau E (2006) *Wind Turbines: Fundamentals, Technologies, Application, Economics*, 2nd edn. Springer, Berlin and New York.

House of Commons (2006) *Keeping the Lights on Nuclear, Renewables and Climate Change*, Sixth report of session 2005–06, Vol. I. The Stationery Office Limited, London.

IEA (International Energy Agency) (2005) *Offshore Wind Experiences*. IEA, France.

IEA, OECD (European Organisation for Economic Co-operation and Development), NEA (US Nuclear Energy Agency) (2005) *Projected Costs of Generating Electricity*. OECD, France.

Krohn S, Morthorst P and Awerbuch S (eds) (2009) *Economics of Wind Energy*. European Wind Energy Association, Brussels.

Larsen J, Soerensen H, Christiansen E, Naef S and Vølund P (2005) Experiences from Middelgrunden 40 MW offshore wind farm. Copenhagen Offshore Wind Conference and Exhibition, 26–28 October.

Marsh G (2007) What price O&M? Operation and maintenance costs need to be factored into the project costs of offshore wind farms at an early stage. *Refocus* **8(3)**: 22, 24, 26–27.

Noordzee Wind (2008) *Operations Report 2007*. CE Ijmuiden, the Netherlands, Document No. OWEZ_R_000_20081023.

PB Power (2006) *Powering the Nation: A Review of Costs of Generating Electricity*. PB Power, Newcastle upon Tyne, UK.

Samsø Offshore Wind Farms (2009) See http://www.samsohavvind.dk/windfarm/ (accessed 1st August 2009).

Spinato F, Tavner PJ, van Bussel GJW and Koutoulakos E (2009) Reliability of wind turbine subassemblies. *IET Renewable Power Generation* **3(4)**: 1–15.

Svenson J and Larsen J (2008) Eight years O&M experience from Middelgrunden offshore wind farm. *Proceedings of European Wind Energy Conference 2008, Brussels*. Operations and Maintenance Session DT3.3.

Tavner PJ, Xiang JP and Spinato F (2006) Reliability analysis for wind turbines. *Wind Energy* **10(1)**: 1–18.

Walford CA (2006) *Wind Turbine Reliability Understanding and Minimizing Wind Turbine Operation and Maintenance Costs*. Sandia Labs, Albuquerque, USA, Report SAND 2006-1100.

Cost-Effective Condition Monitoring for Wind Turbines

Wenxian Yang, Peter J. Tavner, *Senior Member, IEEE*, Christopher J. Crabtree, and Michael Wilkinson

***Abstract*—Cost-effective wind turbine (WT) condition monitoring assumes more importance as turbine sizes increase and they are placed in more remote locations, for example, offshore. Conventional condition monitoring techniques, such as vibration, lubrication oil, and generator current signal analysis, require the deployment of a variety of sensors and computationally intensive analysis techniques. This paper describes a WT condition monitoring technique that uses the generator output power and rotational speed to derive a fault detection signal. The detection algorithm uses a continuous-wavelet-transform-based adaptive filter to track the energy in the prescribed time-varying fault-related frequency bands in the power signal. The central frequency of the filter is controlled by the generator speed, and the filter bandwidth is adapted to the speed fluctuation. Using this technique, fault features can be extracted, with low calculation times, from direct- or indirect-drive fixed- or variable-speed WTs. The proposed technique has been validated experimentally on a WT drive train test rig. A synchronous or induction generator was successively installed on the test rig, and both mechanical and electrical fault-like perturbations were successfully detected when applied to the test rig.**

***Index Terms*—Adaptive signal processing, condition monitoring, fault diagnosis, induction generators, signal processing, synchronous generators, time–frequency analysis, wavelet transforms, wind power generation.**

NOMENCLATURE

A	Estimated energy of the frequency component of interest.
$a_{\min}$, $a_{\max}$	Minimum and maximum wavelet scales considered by the adaptive bandpass filter.
a	Wavelet scale.
b	Wavelet time-shift parameter.
ε	Voltage or current transducer error.
e	Specific unbalance.
f_{rm}	Rotational frequency of the generator rotor.
f_{se}	Electrical supply frequency.
G	Balance quality grade.
I_i	Line currents.
m	Unbalanced mass.
$M_{\rm eq}$	Equivalent mass of the test rig rotor.
ω	Angular frequency of interest.
ω_c	Mean frequency of the prescribed frequency component during the time interval T.
$\omega_{\rm fg}$	Fluctuation of the generator rotational frequency.
ω_f	Fluctuation of the frequency of interest.
$\omega_{\rm upper}$, $\omega_{\rm lower}$	Upper and lower cutoff frequencies of the adaptive filter.
ω_0	Central angular frequency of the mother wavelet.
ω_{rm}	Angular rotational frequency of the generator rotor.
P	Three-phase total power output from the generator.
r	Effective radius of the equivalent unbalanced mass.
R_{AB}, R_{BC}, R_{CA}	Combined line-to-line resistances.
R_{AS}, R_{BS}, R_{CS}	Brush gear and slip ring resistances.
R_{AV}, R_{BV}, R_{CV}	Load bank resistances.
R_A, R_B, R_C	Generator rotor winding resistances.
δR	Electrical resistance imbalance.
s	Induction machine slip.
ψ	Mother wavelet function.
T	Sliding window averaging time interval.
t_0	Starting time moment of the sliding window.
U_e	Electrical asymmetry on the generator rotor.
U_m	Mechanical unbalance on the generator rotor.
V_i	Phase voltages.
x	Real-time signal.
η	Constant between $\omega_{\rm fg}$ and ω_f.

Manuscript received December 5, 2008; revised September 3, 2009. First published September 22, 2009; current version published December 11, 2009. This work was supported by the U.K. Engineering and Physical Sciences Research Council Supergen Wind Program EP/D034566/1.

W. Yang is with the New and Renewable Energy Centre, NE24 3AG Blyth, U.K.

P. J. Tavner is with the School of Engineering and Computing Sciences, Durham University, DH1 3LE Durham, U.K. (e-mail: Peter.Tavner@durham.ac.uk).

C. J. Crabtree is with Durham University, DH1 3LE Durham, U.K.

M. Wilkinson is with Garrad Hassan, BS2 0QD Bristol, U.K.

Color versions of one or more of the figures in this paper are available online at http://ieeexplore.ieee.org.

Digital Object Identifier 10.1109/TIE.2009.2032202

I. INTRODUCTION

OVER THE last 40 years, there has been an increased application of wind turbines (WTs) around the world, with growth in rating from 30 kW to $>$ 5 MW and, more recently, their application offshore [1]. To reduce the cost of energy from WTs, there is a pressing need to improve the WT availability and reduce the operational and maintenance (O&M)

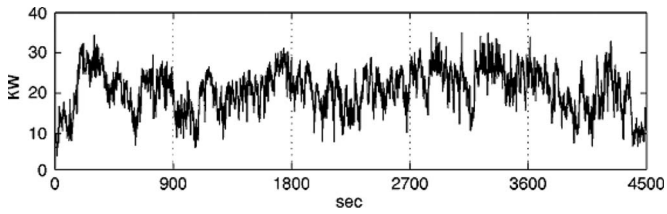

Fig. 1. Variation in power output from a 33-kW fixed-speed WT over five successive periods of 900 s, each showing the large variation in the signal due to wind turbulence (taken from [7]).

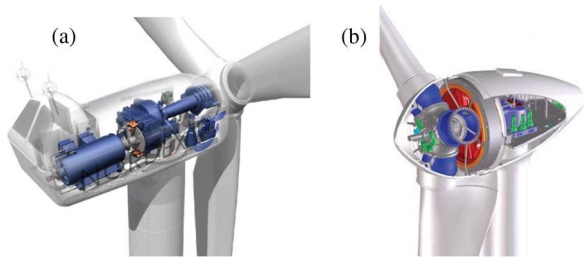

Fig. 2. Structures of real large WTs. (a) Geared. (b) Direct drive.

costs. Aside from developing more advanced machine designs [2] to improve the availability, an effective way to achieve this improvement would be to apply reliable and cost-effective condition monitoring [3], which is why this subject is attracting industrial and academic attention.

The wind industry currently uses condition monitoring systems (CMSs), such as vibration, temperature, lubrication oil, and generator current analysis, developed from other rotating machine power generation industries [4]–[6], where they have achieved success. However, despite their application in the wind industry [7], they have not yet proven their effectiveness due to the peculiarities of a WT, which has a slow speed and rapidly varying torque. Commercial WT CMSs mostly employ vibration-based techniques, which are sophisticated, and the sensors and cabling are costly. The technique is also not ideally suited to all WT types and faults. Lubrication oil analysis is becoming more popular for detecting gearbox tooth and bearing wear but cannot detect failures outside the gearbox. More advanced techniques, such as optical strain measurement, have been developed for monitoring WT blade integrity. However, these are expensive, and recent reliability surveys [8] have shown that WT electrical systems have a higher failure rate than the mechanical systems. For these reasons, an electrically based WT CMS would be beneficial and could be more comprehensive, simpler, and cheaper than other techniques. This paper will propose such a technique.

Instantaneous electric power measurement has been demonstrated on induction machines for detecting motor faults [9]. Three-phase total power monitoring has also been applied to WTs as a condition monitoring and fault diagnosis signal [10] but has not achieved commercial application. This research will be based entirely on the use of this signal and the generator speed for condition monitoring. Power output measurement was considered for condition monitoring in [7] and [10], but Fig. 1, taken from [7], shows how the WT power output signal experiences continuous and rapid variations during operation.

The work reported in this paper is an enhancement of the research described in [11], now including the following:

1) a more comprehensive description of the background technology and the state of the art of the proposed technique;
2) an improved mathematical presentation;
3) additional figures to enhance the description of the technique;
4) more substantial experimental results;
5) an amended conclusion.

The novelties of the proposed technique are summarized as follows:

1) a technique for WT condition monitoring based on measuring the generator total power signal rather than more conventional measurements validated by experiments on a test rig with a simple fault setup;
2) a new adaptive continuous-wavelet-transform (CWT)-based energy tracking method, reducing the calculation time for feature extraction when applied to lengthy signals, making possible less time-intensive WT condition monitoring;
3) the successful detection of two types of fault using this method has been demonstrated on two WT arrangements, including both electrical and mechanical faults;
4) the proposed method is more efficient for the detection of faults in variable-speed WTs than other more conventional techniques;
5) the technique used in this paper can be applied to any WT generator for tracking any characteristic, fault-related frequency component, so it is general and could be applied to detect a variety of faults depending on the choice of frequency selected.

Wavelet transforms have been successfully used in condition monitoring and diagnosis of rotating electrical machine faults [1], [12]–[14]. However, most used the discrete wavelet transform (DWT) rather than the CWT, although the latter is superior to the former in multiresolution signal analysis. However, the CWT involves more intensive convolution calculations than the DWT, making it more difficult to process lengthy online data, such as WT monitoring signals. Moreover, it is inconvenient to apply the traditional time–frequency–amplitude CWT image to machine condition monitoring, as was done in [15]. Wavelets have been proposed for WT condition monitoring [16], [17] but have not yet received commercial application.

II. Applying Generator Power Monitoring to WTs

A WT converts the kinetic energy of the wind into electrical energy, utilizing mechanical and electrical conversion, control, and transmission systems. The architectures of two commonly used large WTs are shown in Fig. 2.

The application of vibration, temperature, and lubrication oil techniques to monitoring WTs should improve their availability but, to date, is not being widely used for the following reasons:

1) lack of practical industry experience with condition monitoring in the wind environment;
2) difficulties collecting and interpreting the data, including the risk of false or missed alarms;

3) the fact that present techniques may not be suited to all types of WTs such as shown in Fig. 2;
4) the fact that developing reliable WT condition monitoring techniques requires complex and lengthy collaboration between WT operators and manufacturers in the field.

WT power flows are disturbed by both mechanical and electrical faults [16], [17]. To measure the WT shaft torque is costly and usually impractical for a real WT. In contrast, shaft speed and electrical power output are routinely monitored for WTs, but, to date, commercial CMSs do not use these signals.

In comparison with conventional stator current analysis, widely adopted for condition monitoring motors [4], [6], power monitoring could have the following disadvantages.

1) The error in the total power signal depends not only on the voltage and current transducer error ε but also on the measurement method. In the three-wattmeter method, the error will be 6ε, but, in the two-wattmeter method, the error is limited to 4ε, whereas the current signal error would be only ε. Therefore, the signal-to-noise ratio for basic analysis should be better for current than power analysis.

On the other hand, monitoring based on power analysis could have the following advantages.

1) The power signal is already available from the generator terminal voltage and current signals for the control of the WT and can conveniently be accessed.
2) Fewer cheaper transducers than accelerometers and oil debris probes are required for power monitoring.
3) Mechanical and electrical faults both disturb the generator power output, so power monitoring could detect both types of faults.
4) Single line current analysis contains the mains frequency carrier, whereas this is absent in the power signal. Therefore, the signal-to-noise ratio for faulty feature analysis should be better for power than current analysis, balancing the aforementioned transducer error effect.
5) In the power signal, the fault-related frequency sidebands, around the mains frequency, are folded down around dc, limiting the bandwidth needed to monitor the signal.

An example of the current, voltage, and power signals measured under faulty conditions on an induction generator, fitted to the test rig described in the following, is shown in Fig. 3, where the signals were collected when a periodic rotor electrical asymmetry was applied in the presence of serious noise due to power system imbalance.

The fault in Fig. 3 was applied at the time intervals of 20–40 s and 60–80 s and was absent in the other time intervals. It can be seen that the amplitudes of both the current–time and voltage–time waveforms gave no indication of abnormal conditions, whereas the total three-phase power signal P changes significantly during the abnormality due to the presence of $2f_{se}$ and $2sf_{se}$ components. The total power $P(t)$ was calculated using

$$P(t) = \sum_{i=1}^{3} I_i(t) \cdot V_i(t). \tag{1}$$

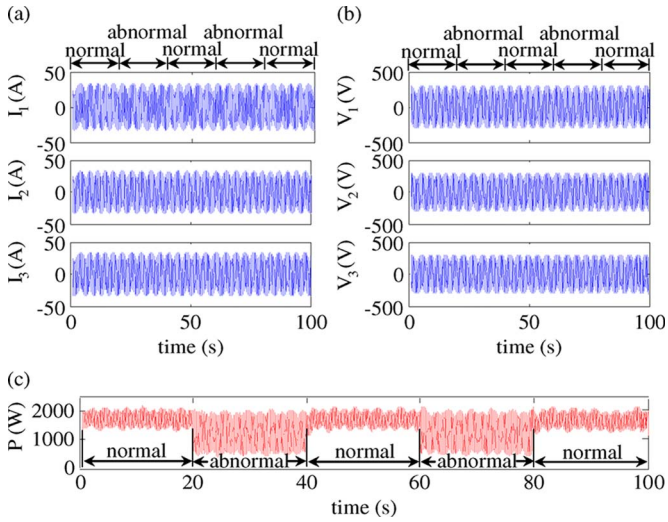

Fig. 3. Comparison of current, voltage, and total power signal in the presence of a rotor asymmetry fault. (a) Line currents. (b) Phase voltages. (c) Total power.

III. Design of Wavelet-Based Adaptive Filter

In this paper, a CWT-based adaptive filter has been designed to track the energy in the power signal in the prescribed fault-related frequency bands rather than at all frequencies of the monitoring signal. In this way, the wavelet calculation can significantly be reduced, and the results can be displayed graphically rather than as a screen dump image, making the technique attractive for online application. Details of the technique are described as follows.

The CWT of a real-time signal $x(t)$ can be defined as

$$\text{CWT}(b,a) = \frac{1}{\sqrt{|a|}} \int_{-\infty}^{\infty} x(t)\psi^* \left(\frac{t-b}{a}\right) dt \tag{2}$$

where the asterisk "$*$" indicates the complex conjugate.

Traditionally, the wavelet function $\psi(t)$ is dilated or compressed by changing the scale parameter a so that all signal components ranging from frequency 0 to half the sampling frequency can be projected onto an appropriate time-scale map, as shown in Fig. 4. The bottom figure shows the time waveform of a sample signal of increasing frequency being inspected; the top figure shows the wavelet coefficients of this signal obtained at different wavelet scales and times.

Many of the calculations shown in Fig. 4 are unnecessary for WT condition monitoring because the fault-related frequencies are few in number and the energy extracted at nonfault-related frequencies is not helpful to assess the machine condition.

Therefore, an adaptive CWT-based filter has been designed, which only extracts energy at known fault frequencies, while frequencies unrelated to the fault are left unprocessed. The calculation time for the new technique will be much shorter than that for a conventional CWT applied to a broad bandwidth signal. Therefore, the proposed CWT-based energy tracking technique should prove more efficient for online processing of WT monitoring signals than conventional CWT processing.

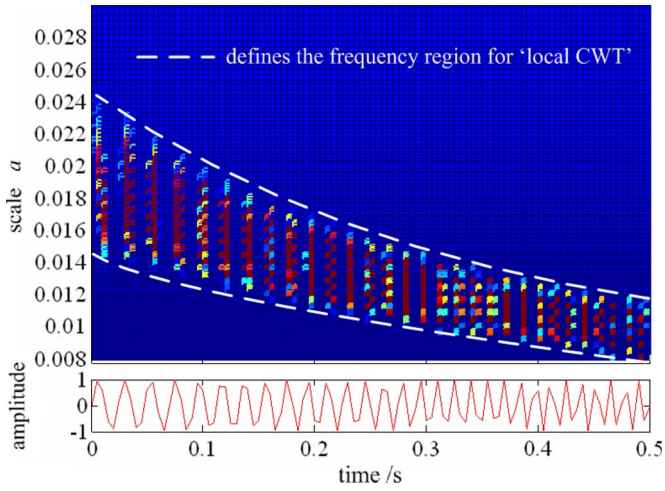

Fig. 4. Illustrative example of the conventional CWT.

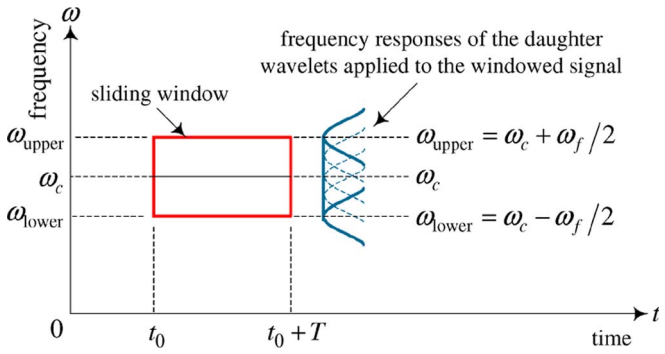

Fig. 5. Two-dimensional sliding window.

A time–frequency sliding window has been designed for this task, as shown in Fig. 5. Its central frequency ω_c is the mean frequency during the time interval T of the prescribed fault-related frequency band. The upper and lower cutoff frequencies ω_{upper} and ω_{lower} are adapted to the fluctuation of the generator rotational speed ω_{fg} in that interval, i.e.,

$$\begin{cases} \omega_{\text{upper}} = \omega_c + \omega_f/2 \\ \omega_{\text{lower}} = \omega_c - \omega_f/2 \\ \omega_f = \eta\omega_{\text{fg}}. \end{cases} \tag{3}$$

From Fig. 4, it is noticed that ω_f could also be a time-varying parameter, intrinsically dependent on the turbulence of the wind. Experience has shown that onshore wind turbulence varies between 12% and 20%, whereas offshore turbulence approximates to ∼6%.

The relationship between any prescribed frequency ω and its corresponding wavelet scale a is

$$a = \frac{\omega_0}{\omega}. \tag{4}$$

With the aid of (3) and (4), the range of the wavelet scales for conducting bandpass filtering can be determined by

$$a \in [a_{\min} \quad a_{\max}] \tag{5}$$

$$\begin{cases} a_{\min} = \frac{\omega_0}{\omega_{\text{upper}}} \\ a_{\max} = \frac{\omega_0}{\omega_{\text{lower}}}. \end{cases} \tag{6}$$

TABLE I
COMPUTATIONAL EFFICIENCY COMPARISON BETWEEN CWT, DWT, AND PROPOSED APPROACH

Method	Time cost	Operation manner	Accuracy
CWT	18.91s	All frequencies between zero and half sampling frequency are calculated.	Good
DWT	0.31s	Interested frequency band is determined in a rigid dyadic step way.	Not good
Energy tracking	0.16s	Interested frequency band is determined intelligently.	As good as CWT

Subsequently, by performing the CWT locally in the scale range defined by (5), a matrix of wavelet coefficients is obtained

$$\text{CWT}_{\text{local}}(b,a) = \frac{1}{\sqrt{|a|}} \int_{-\infty}^{\infty} x(t)\psi^*\left(\frac{t-b}{a}\right) dt. \tag{7}$$

The energy A of the frequency component of interest in the time interval T is estimated by

$$A(t_0 + T/2) = \max\left(|\text{CWT}_{\text{local}}(b,a)|\right) \quad \begin{cases} a \in [a_{\min} \quad a_{\max}] \\ b \in [t_0 \quad t_0 + T]. \end{cases} \tag{8}$$

The sliding window is moved forward along the signal; the maximum and minimum wavelet scales in (5) being redefined within each time interval according to the generator rotational speed ω_{fg}. Then, using the aforementioned technique, the energy A in the fault-related frequency band is calculated in each time interval using (7) and (8). These calculations are repeated until the whole signal has been processed. Finally, a curve of the energy variation in the fault-related frequency band is obtained, and changes in the running condition of the WT can be assessed.

This task could have been accomplished using a series of conventional bandpass filters set up to cover the expected speed range of the turbine. However, such an analysis would not have the advantages of the CWT in processing nonstationary signals shown in Fig. 1 and [18].

To verify the computational efficiency of the proposed technique compared to the traditional CWT and DWT, a calculation was performed to extract the 50-Hz energy component from 1 s of line current signal, sampled at a frequency of 2 kHz. The time taken by each approach is listed in Table I. The calculations were done in a computer with 1.4 GHz of Intel Pentium processor and 512 MB of RAM.

From Table I, it can be concluded that the proposed energy tracking technique is the most computationally efficient of the three approaches.

IV. WT CONDITION MONITORING BY POWER SIGNAL ANALYSIS

In view of the proposed advantages of generator power signal analysis for detecting both mechanical and electrical faults in a variety of designs of WT drive train, it has been applied in this paper, in combination with the energy tracking method described previously, to develop a new WT condition monitoring technique.

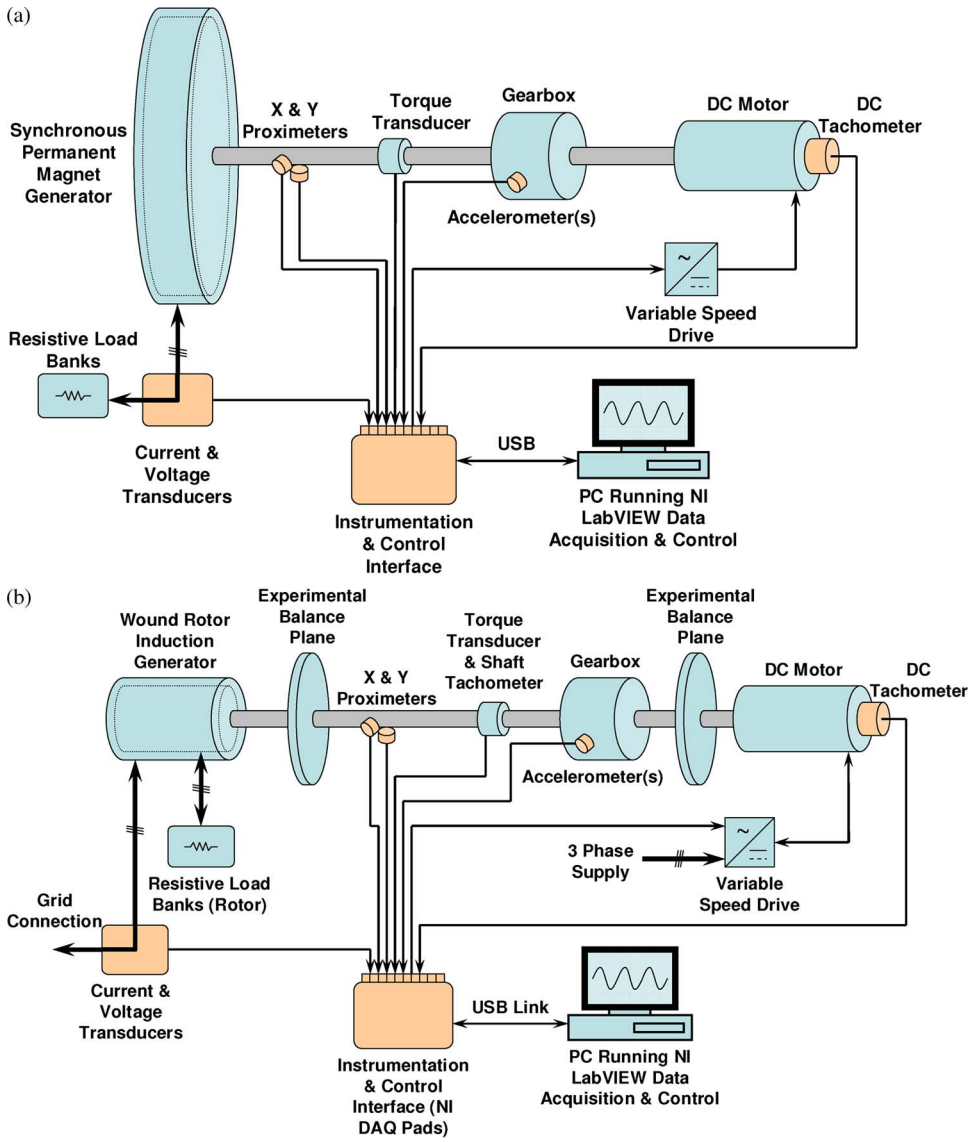

Fig. 6. Schematic diagrams of the WT drive train test rig. (a) With permanent-magnet synchronous generator installed. (b) With induction generator installed.

A. WT Drive Train Test Rig

One of the difficulties in gaining practical industry experience of condition monitoring on real WTs is the lack of collaboration needed with WT operators and manufacturers, due to data confidentiality, particularly when faults are present. This can be avoided by gaining condition monitoring experience using a controllable experimental test rig to which defined faults can be applied. Therefore, the technique proposed in this paper has been validated experimentally on a WT drive train test rig designed to investigate condition monitoring signals in the laboratory. This test rig was described in detail in [16] and was equipped first with a permanent-magnet synchronous generator and, subsequently, with an induction generator, both as shown in Fig. 6.

The synchronous generator [Fig. 6(a)], such as might be used in a direct-drive WT, was rated for the experiment at 10 kW, three-phase 54-pole permanent-magnet machine with a rectified output feeding a resistive load bank.

The induction generator [Fig. 6(b)], such as might be used in a geared-drive WT, was rated for the experiment at 30 kW, three-phase four-pole wound-rotor machine, with the rotor circuit coupled via slip rings to a three-phase resistive load bank, so that rotor electrical imbalance could be applied, and the generator stator fed the three-phase mains.

The test rig comprises a 54-kW dc variable-speed motor and a two-stage gearbox, instrumented and controlled using LabVIEW. In the experiments, a variety of wind speed inputs could be applied to the test rig via the dc motor, the speed of which is controlled by an external model incorporating the properties of natural wind at a variety of speeds and turbulences and the mechanical behavior of a 2-MW WT operating under closed-loop conditions. Relevant signals were collected from the terminals of the generator and the drive train when subjected to this driving speed.

A number of electrical and mechanical drive train faults could be applied to the test rig. Because they are not necessarily

precise replicas of WT faults, they have been called "fault-like perturbations" but contain similarities with faults on real WTs.

In this paper, to verify the efficacy of the proposed condition monitoring technique for WTs, two "faultlike perturbations" were applied to two different generator configurations as follows.

1) In the first configuration, with the synchronous generator representing a direct-drive WT, the "faultlike perturbation" applied was mechanically unbalanced on the generator rotor, representing the effect of a mechanical unbalance fault on the WT generator drive train.
2) In the second configuration, with the slip-ring induction generator representing a geared-drive WT, the "fault-like perturbation" applied was electrically asymmetric on the generator rotor, representing the effect of a rotor winding fault, brush imbalance, or air gap eccentricity in the WT generator.

Details of both experimental arrangements are described as follows.

B. Mechanical Unbalance Fault Simulated on Rotor of Synchronous Generator

The mechanical unbalance fault was simulated by attaching a 1-kg mass to the generator rotor with an equivalent rotating mass of 290.7 kg, which is ∼0.3%. This represents a balance quality grade of G 7.8 (7.8 mm/s), within the limit of G 16 (16 mm/s) prescribed in ISO1940-1:2003 for a low-speed propeller shaft, applicable to a direct-drive WT shaft. The details of this estimation are given in Appendix A. The peak-to-peak measured displacement of the generator shaft changed a little before and after the placement of the unbalanced mass, varying in the range 90–140 μm. The equivalent vibration velocity would have been 0.13–0.21 mm/s, with the generator running at the maximum rotational speed of 28 r/min well within the 0.71-mm/s limit that is acceptable for machines $\leq$ 15 kW prescribed in ISO2372:1974.

When the synchronous generator ran at varying speed representing the wind driving situation, the speed, torque, and total power were measured using a sampling frequency of 1 kHz, and the "fault-like perturbation" was periodically applied to the rotor. The time waveforms of the signals before and after the application are shown in Fig. 7(a).

From Fig. 7(a), it can be seen that, in the presence of the mass unbalance fault, the driving shaft torque signal gave a response at the shaft rotational frequency f_{rm}, as expected, fluctuating by 8% range due to the combined effects of mass unbalance fault and wind driving turbulence, which can be compared to fluctuating by 4% due to the wind driving turbulence alone. By contrast, the generator power showed only a slight change in the presence of the fault. In this case, the fault-related frequency is f_{rm}, and the CWT-based energy tracking technique was applied to extract energy at this frequency, as shown in Fig. 7(b). This provided a clear indication of the presence or absence of the mechanical unbalance fault despite the fact that the shaft speed was varying continuously throughout the experiment and the effect could not be observed in the unprocessed total power signal shown in Fig. 7(a).

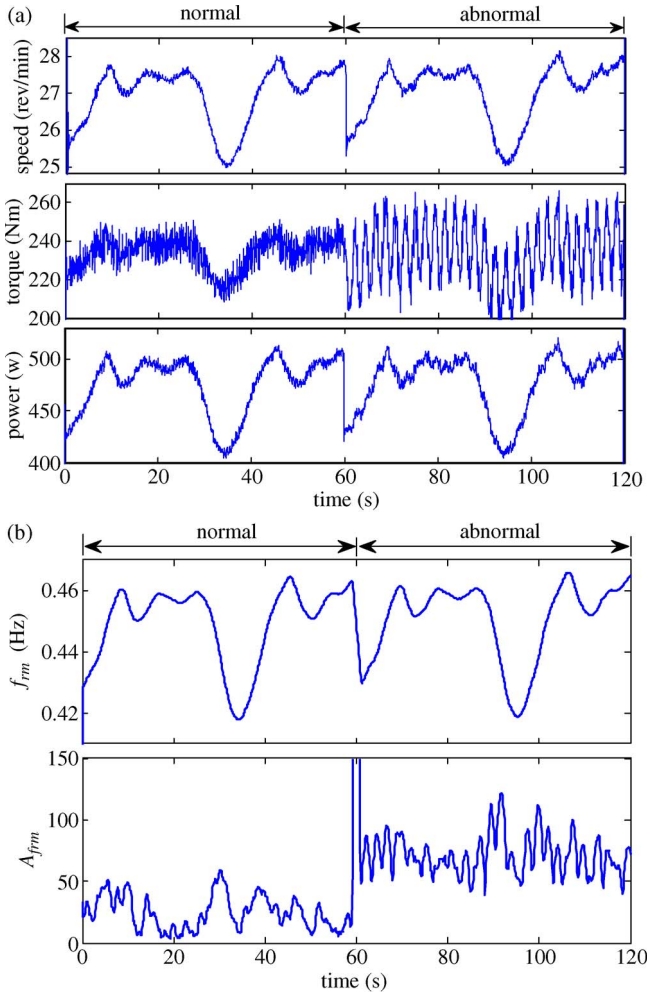

Fig. 7. Mass unbalance fault applied to a synchronous generator rotor on the WT test rig, representing a direct-drive WT. (a) Signals when a mass unbalance fault was simulated on a synchronous generator rotor. (b) Detecting a mass unbalance fault from the power signal.

TABLE II
PARAMETERS USED FOR CALCULATION RESULTS IN FIG. 7

ω_c	ω_f	T
ω_{rm}	$0.03\,\omega_{rm}$	$0.2s$

It can be seen from Fig. 7(b) that a 0.3% or G 7.8 unbalance fault was easily detectable. This shows that the proposed technique has the potential to detect an incipient mechanical unbalance fault of 0.3% or G 7.8 on a direct-drive WT. The parameters used for this calculation are given in Table II.

C. Electrical Asymmetry on Rotor of Induction Generator

The electrical asymmetry was simulated on the induction generator by adjusting the phase resistances in the load bank externally connected to the rotor. Two levels of rotor asymmetry were applied to investigate the effect of an incipient fault. These were an electrical asymmetry of $U_e = 4.7\%$ and, then, a larger asymmetry of 9.2%. The details of the rotor circuit and the estimation of asymmetry are described in Appendix B and in Table IV.

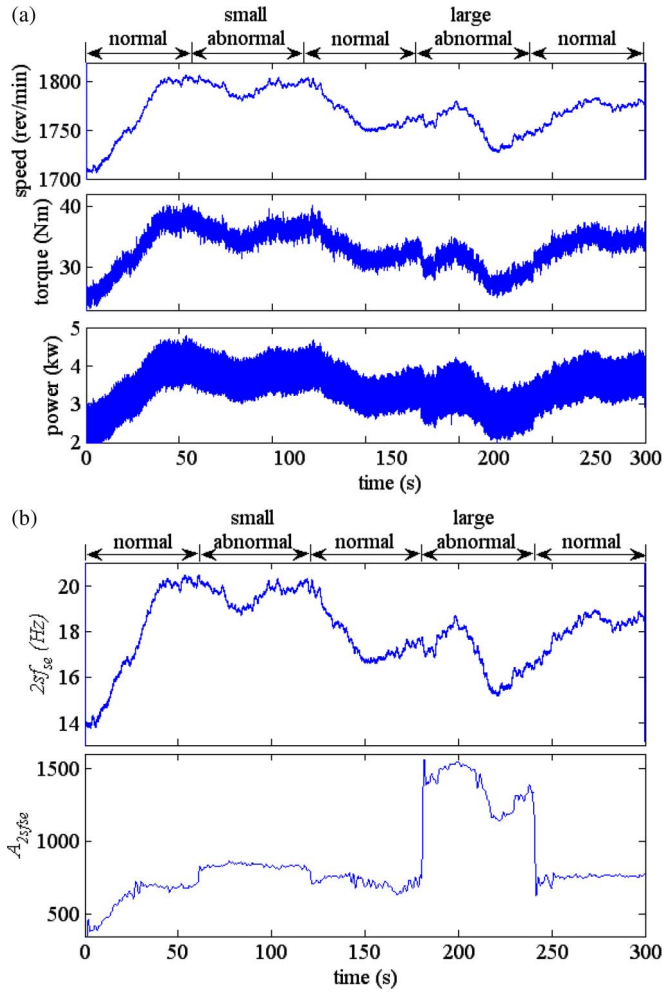

Fig. 8. Electrical asymmetry applied to an induction generator rotor on the test rig, representing a geared-drive WT. (a) Signals when an electrical asymmetry fault was simulated on an induction generator rotor. (b) Detecting an electrical asymmetry fault from the power signal.

As in the mechanical unbalance experiment, the rotational speed, mechanical drive shaft torque, and generator total power signals were measured when the "faultlike perturbation" was periodically applied to the rotor. A smaller fault was applied in the period 60–120 s and a larger fault between 180 and 240 s, with the rotor circuits being balanced in the periods 0–60 s, 120–180 s, and 240–300 s. The time waveforms of the signals collected in this experiment are shown in Fig. 8(a), and it can be seen that, due to the effect of the varying generator speed, the fault symptom cannot be observed clearly from either the generator shaft torque or total power.

When the rotor phase resistances are imbalanced, the generator current, voltage, and power are modulated twice by the slip frequency as the rotor asymmetry moves through the air gap magnetic field twice for every pole pair cycle [4]. Therefore, in this case, the fault-related frequency is $2sf_{se}$, and the CWT-based energy tracking technique was applied to extract the energy at that frequency, as shown in Fig. 8(b).

From Fig. 8(b), it can be seen that the smaller, 4.7%, fault was not clear although it is still visible, so the condition monitoring algorithm had limited detectability in this case. This lack of detectability was due to the residual imbalances present in the rotor windings, brush gear, and connections, as well as the negative influence of the timely varying generator rotational speed which partially hid the faulty feature. However, the larger 9.2% fault was clearly visible in the figure and, therefore, readily detectable despite the fact that the $2sf_{se}$ frequency signal was varying during the experimental processes.

This shows that the proposed technique has the potential to detect an incipient 9.2% electrical asymmetry fault on a geared-drive WT generator. The parameters used for this calculation are given in Table III.

TABLE III
PARAMETERS USED FOR CALCULATION RESULTS IN FIG. 8

ω_c	ω_f	T
$2sf_{se}$	$0.4sf_{se}$	$0.12s$

V. CONCLUSION

To improve the WT availability and reduce the O&M costs, a new WT condition monitoring technique has been proposed. From this research, the following conclusions can be reached.

1) In comparison with the conventional vibration, temperature measurement, and lubrication oil analysis, the technique proposed shows the following potential advantages:
   a) reduced capital cost;
   b) ability to detect both electrical and mechanical faults;
   c) applicable to both geared and direct-drive WTs.
2) The proposed CWT-based energy tracking method not only reduces the calculation needed to extract features from lengthy online data but also provides a feasible condition monitoring approach that is applicable to WTs operating at either fixed or variable speed.
3) Experiments have shown that the proposed technique is capable of detecting both mechanical and electrical faults in WT drive trains of different types.
4) The technique is a feasible way to establish a simple, cheap, but potentially global cost-effective CMS for a WT.

The technique now needs to be applied to the power signals obtained from real WTs during real mechanical and electrical faults to determine the detectability of the algorithm and its ability to detect incipient faults in both cases.

Further work will also be needed to establish the ability of this technique for a wider range of faults and for a variable-speed WT under closed-loop control.

APPENDIX A
GENERATOR ROTOR MECHANICAL UNBALANCE

Based on BS ISO1940-1:2003, the balance quality grade G may be calculated by

$$G = e \cdot 2\pi f_{rm} \tag{A1}$$

where

$$e = mr/M_{\text{eq}} \tag{A2}$$

$$U_m = (m/M_{\text{eq}}) \times 100. \tag{A3}$$

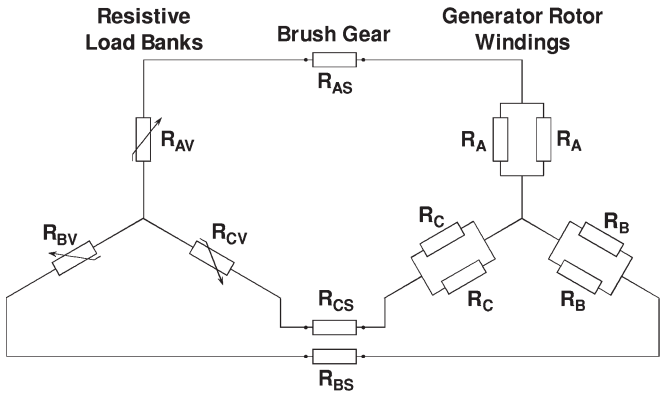

Fig. 9. Rotor circuit diagram, including a resistive load bank.

TABLE IV
ELECTRICAL ASYMMETRY APPLIED TO TEST RIG IN FIG. 8

Time (s)	Description	U_e (%)
0 – 60s	Balanced	0.0
60 – 120s	Low asymmetry	4.7
120 – 180s	Balanced	0.0
180 – 240s	High asymmetry	9.2
240 – 300s	Balanced	0.0

For the test rig shown in Fig. 6(a), the unbalance mass $m = 1.0$ kg, the effective radius $r = 865$ mm, and the equivalent rotating mass of the test rig $M_{\text{eq}} = 290.7$ kg. The average rotational speed of the generator rotor is 25 r/min. This gives a balance quality grade and mechanical unbalance for Fig. 7 of G 7.8 ($G = 7.8$ mm/s) and $U_m = 0.3\%$, respectively.

APPENDIX B
GENERATOR ROTOR ELECTRICAL ASYMMETRY

The details of the generator rotor circuit shown in Fig. 6(b) taking into account the external resistive load bank are shown in Fig. 9.

The balanced circuit resistances were given by

$$\begin{cases} R_{AB} = R_{AV} + R_{BV} + R_{AS} + R_{BS} + (R_A + R_B)/2 \\ R_{BC} = R_{BV} + R_{CV} + R_{BS} + R_{CS} + (R_B + R_C)/2 \\ R_{CA} = R_{CV} + R_{AV} + R_{CS} + R_{AS} + (R_C + R_A)/2. \end{cases} \tag{B1}$$

The circuits are balanced, giving

$$R_{AB} = R_{BC} = R_{CA} = \overline{R} = 7.60\ \Omega \tag{B2}$$

where $\overline{R} = (R_{AB} + R_{BC} + R_{CA})/3$.

Then, the electrical imbalance can be estimated through calculating the residual circuit resistance δR, i.e.,

$$\delta R = |R_{AB}e^{i\theta_1} + R_{BC}e^{i\theta_2} + R_{CA}e^{i\theta_3}| \tag{B3}$$

where $i = \sqrt{-1}$, $\theta_1 = 0$, $\theta_2 = 2\pi/3$, and $\theta_3 = 4\pi/3$.

The percentage fault can be described by

$$U_e = (\delta R/\overline{R}) \times 100. \tag{B4}$$

The larger the value of U_e, the more serious the electrical asymmetry. The electrical asymmetries applied in Fig. 8 are listed in Table IV.

ACKNOWLEDGMENT

The authors would like to thank the New and Renewable Energy Centre, Blyth, for the assistance for the original provision of the test rig.

REFERENCES

[1] J. F. Manwell, A. L. Rogers, and J. G. McGowan, "Status of offshore wind energy in the United States," in *Proc. IEEE Power Eng. Soc. Summer Meeting*, Jul. 15–19, 2001, vol. 1, pp. 10–13.
[2] H. Polinder, F. F. A. van der Pijl, G. J. de Vilder, and P. J. Tavner, "Comparison of direct-drive and geared generator concepts for wind turbines," *IEEE Trans. Energy Convers.*, vol. 21, no. 3, pp. 725–733, Sep. 2006.
[3] J. Nilsson and L. Bertling, "Maintenance management of wind power systems using condition monitoring systems—Life cycle cost analysis for two case studies," *IEEE Trans. Energy Convers.*, vol. 22, no. 1, pp. 223–229, Mar. 2007.
[4] P. J. Tavner, "Review of condition monitoring of rotating electrical machines," *IET Elect. Power Appl.*, vol. 2, no. 4, pp. 215–247, Jul. 2008.
[5] D. Casadei, F. Filippetti, A. Yazidi, C. Rossi, and G. A. Capolino, "Diagnostic technique based on rotor modulating signals signature analysis for doubly fed induction machines in wind generator systems," in *Conf. Rec. IEEE IAS Annu. Meeting*, Oct. 8–12, 2006, vol. 3, pp. 1525–1532.
[6] A. Bellini, F. Filippetti, C. Tassoni, and G. A. Capolino, "Advances in diagnostic techniques for induction machines," *IEEE Trans. Ind. Electron.*, vol. 55, no. 12, pp. 4109–4126, Dec. 2008.
[7] P. Caselitz and J. Giebhardt, "Rotor condition monitoring for improved operational safety of offshore wind energy converters," *Trans. ASME, J. Sol. Energy Eng.*, vol. 127, no. 2, pp. 253–261, May 2005.
[8] F. Spinato, P. J. Tavner, G. J. W. van Bussel, and E. Koutoulakos, "Reliability of wind turbine subassemblies," *IET Renew. Power Gener.*, vol. 3, no. 4, pp. 1–15, 2009.
[9] S. F. Legowski, A. H. M. Sadrul Ula, and A. M. Trzynadlowski, "Instantaneous power as a medium for the signature analysis of induction motors," *IEEE Trans. Ind. Appl.*, vol. 32, no. 4, pp. 904–909, Jul./Aug. 1996.
[10] W. Q. Jeffries, J. A. Chambers, and D. G. Infield, "Experience with bicoherence of electrical power for condition monitoring of wind turbine blades," *Proc. Inst. Elect. Eng.—Vis. Image Signal Process.*, vol. 145, no. 3, pp. 141–148, Jun. 1998.
[11] W. Yang, P. J. Tavner, C. J. Crabtree, and M. Wilkinson, "Research on a simple, cheap but globally effective condition monitoring technique for wind turbines," presented at the XVIII Int. Conf. Electrical Machines (ICEM), Vilamoura, Portugal, Sep. 2008, Paper ID 1053.
[12] J. Cusido, L. Romeral, J. A. Ortega, J. A. Rosero, and A. E. Garcia, "Fault detection in induction machines using power spectral density in wavelet decomposition," *IEEE Trans. Ind. Electron.*, vol. 55, no. 2, pp. 633–643, Feb. 2008.
[13] A. Ordaz-Moreno, R. de Jesus Romero-Troncoso, J. A. Vite-Frias, J. R. Rivera-Gillen, and A. Garcia-Perez, "Automatic online diagnosis algorithm for broken-bar detection on induction motors based on discrete wavelet transform for FPGA implementation," *IEEE Trans. Ind. Electron.*, vol. 55, no. 5, pp. 2193–2202, May 2008.
[14] M. Riera-Guasp, J. A. Antonino-Daviu, M. Pineda-Sanchez, R. Puche-Panadero, and J. Perez-Cruz, "A general approach for the transient detection of slip-dependent fault components based on the discrete wavelet transform," *IEEE Trans. Ind. Electron.*, vol. 55, no. 12, pp. 4167–4180, Dec. 2008.
[15] S. S. Tsai, C. T. Hsieh, and S. J. Huang, "Enhancement of damage-detection of wind turbine blades via CWT-based approaches," *IEEE Trans. Energy Convers.*, vol. 21, no. 3, pp. 776–781, Sep. 2006.
[16] W. Yang, P. J. Tavner, and M. Wilkinson, "Condition monitoring and fault diagnosis of a wind turbine synchronous generator drive train," *IET Renew. Power Gener.*, vol. 3, no. 1, pp. 1–11, Mar. 2009.
[17] E. Wiggelinkhuizen, T. Verbruggen, H. Braam, L. Rademakers, J. Xiang, and S. Watson, "Assessment of condition monitoring techniques for offshore wind farms," *Trans. ASME, J. Sol. Energy Eng.*, vol. 130, no. 3, pp. 1–9, Aug. 2008.
[18] S. K. Lee, "An acoustic decay measurement based on time–frequency analysis using wavelet transform," *J. Sound Vib.*, vol. 252, no. 1, pp. 141–153, Apr. 2002.

Wenxian Yang received the Ph.D. degree in mechanical engineering from Xi'an Jiaotong University, Xi'an, China, in 1999. He completed his postdoctoral research in Northwestern Polytechnical University, Xi'an, in 2001.

He was with the City University of Hong Kong, Kowloon, Hong Kong; Nottingham Trent University, Nottingham, U.K.; Cranfield University, Cranfield, U.K.; and Durham University, Durham, U.K. He is currently a Technical Specialist with the New and Renewable Energy Centre, Blyth, U.K. He has worked in the areas of new and renewable energy, signal processing, machine condition monitoring and fault diagnosis, nondestructive testing and nondestructive evaluation, and artificial intelligence in both industry and academia.

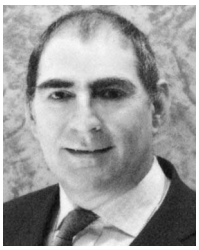

Peter J. Tavner (SM'08) received the M.A. degree from Cambridge University, Cambridge, U.K., in 1969 and the Ph.D. degree from Southampton University, Southampton, U.K., in 1978.

He held research and technical positions in the industry, including being a Group Technical Director with FKI Energy Technology, Loughborough, U.K. He is currently a Professor of new and renewable energy and the Head of the School of Engineering and Computing Sciences, Durham University, Durham, U.K. His research interest includes machines for renewable energy, condition monitoring, and reliability.

Dr. Tavner was the recipient of the Institution Premium of the Institution of Electrical Engineers, U.K.

Christopher J. Crabtree received the M.Eng. degree in engineering from Durham University, Durham, U.K., in 2007, having studied new and renewable energy as an electrical engineer, where he is currently working toward the Ph.D. degree in condition monitoring of offshore wind turbines.

His research interests include the development of condition monitoring techniques using industrial data and a test rig.

Michael Wilkinson received the M.Sc. degree in electromagnetic sensing from Durham University, Durham, U.K., in 2003 and the Eng.D. degree with a thesis on condition monitoring for offshore wind turbines from Newcastle University, Newcastle upon Tyne, U.K., in 2007, in a collaborative project with Durham University and FKI Energy Technology.

In 2007, he joined Garrad Hassan, Bristol, U.K., as part of the operational projects team, where he has been monitoring wind farms worldwide on behalf of owners. His research interests include condition monitoring and reliability of wind turbines.

Published in IET Renewable Power Generation
Received on 29th January 2008
Revised on 26th September 2008
doi: 10.1049/iet-rpg:20080060

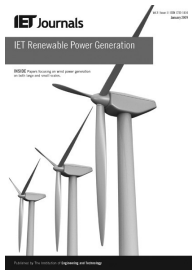

ISSN 1752-1416

Reliability of wind turbine subassemblies

F. Spinato[1] *P.J. Tavner*[1] *G.J.W. van Bussel*[2] *E. Koutoulakos*[2]

[1]*New & Renewable Energy Group, School of Engineering, Durham University, UK*
[2]*Wind Energy Research Group, Delft University of Technology, Delft, The Netherlands*
E-mail: peter.tavner@durham.ac.uk

Abstract: We have investigated the reliability of more than 6000 modern onshore wind turbines and their subassemblies in Denmark and Germany over 11 years and particularly changes in reliability of generators, gearboxes and converters in a subset of 650 turbines in Schleswig Holstein, Germany. We first start by considering the average failure rate of turbine populations and then the average failure rates of wind turbine subassemblies. This analysis yields some surprising results about which subassemblies are the most unreliable. Then we proceed to consider the failure intensity function variation with time for wind turbines in one of these populations, using the Power Law Process, of three subassemblies; generator, gearbox and converter. This analysis shows that wind turbine gearboxes seem to be achieving reliabilities similar to gearboxes outside the wind industry. However, wind turbine generators and converters are both achieving reliabilities considerably below that of other industries but the reliability of these subassemblies improves with time. The paper also considers different wind turbine concepts. Then we conclude by proposing that offshore wind turbines should be subject to more rigorous reliability improvement measures, such as more thorough subassembly testing, to eliminate early failures. The early focus should be on converters and generators.

Nomenclature

β	shape parameter in the power law function
$\lambda(t)$	failure intensity with respect to time for a repairable system
λ	failure rate, in the useful life period where shape parameter $\beta = 1$ and λ is constant
ρ	scale parameter in the power law function
i	integer counting intervals
l_i	time lost because of failures during interval i
I	total number of intervals in survey
k	integer counting subassemblies
K	total number of subassemblies in a turbine
$\mu(t)$	rate of occurrences of failure
n_i	number of failures during interval i
n_i,k	number of failures in subassembly k during interval i
N_i	number of turbines in population at interval i
$N(t)$	cumulative number of failures after operational or calendar time t
$P(t)$	probability of failure at time t
P	overall period for which data were collected
T_i	length of reporting interval, which varies according to month, h
t_i	time to ith failure
CF	capacity factor
LWK	LWK survey in Schleswig Holstein, Germany
MTTF	mean time to failure
MTBF	mean time between failures, MTBF = (MTTF + MTTR)
MTTR	mean time to repair
NHPP	non-homogeneous Poisson process
O&M	operation and maintenance
PLP	power law process
SCADA	supervisory control and data acquisition system
WSDK	Windstats survey in Denmark
WSD	Windstats survey in Germany
WT	wind turbine

1 Introduction

The reliability of large modern onshore wind turbines (WT) is improving but it is necessary for the wind industry to have a clear understanding of the factors which drive reliability if it is to face the economic challenges of offshore installations, where the wind energy harvest is greater but the conditions are more inclement. In these circumstances it will be necessary to increase reliability further, because access to those WTs will be more limited.

An earlier paper [1] has shown that a failure rate of 1–3 failures per turbine per year is common onshore, whereas a failure rate of 0.5 failure per turbine per year is likely to be necessary offshore, where planned maintenance visits need to be kept at or below 1 per year.

This paper will consider the reliability, or more precisely the unreliability, or failure intensity function, $\lambda(t)$, of WTs rather than the wider issue of availability and capacity factor (CF). This is because reliability depends primarily on WT construction and is intrinsically predictable. Whereas availability, yearly production and CF depend not only on reliability but also more strongly on wind conditions and the consequences of faults, which in turn depend on turbine location, access logistics and maintenance regime, not primarily to the WT construction.

The paper carries forward analysis previously made by the authors [1] and [2] on data collected from publicly available European databases of WT failures, paying particular attention to some of the most vital subassemblies in the WT, namely the gearbox, generator and power electronic converter. The foundation of that analysis had been the application of recognised reliability analysis methods on WT data collected over a period of 11 years, from Windstats surveys in Denmark and Germany [3], termed in this paper WSDK and WSD, respectively. This has been supplemented by work on a population of WTs of known model and design installed in Schleswig Holstein in Germany, contained in a survey [4] performed by the LandWirtschaftsKammer, termed in this paper LWK.

These analyses will show striking differences between the reliability characteristics of the selected subassemblies, gearboxes, generators and converters over the period. Some of the results can be related to experience with such subassemblies outside the wind industry.

Considerable interest has also been shown in the industry about differences in cost and performance achieved by different WT architectures, see for example [5], but reliability information was lacking. The analysis in this paper sheds light on this and identifies specific reliability behaviours of selected subassemblies, where work could be done to improve overall WT.

2 Wind turbine construction and reliability

2.1 Concepts and configurations

As the technology of modern WTs has matured the construction has become standardised around the three-bladed, upwind, variable speed concept. But within this concept there are different architectures and Fig. 1 shows two, as follows:

- Geared WTs with a gearbox, a high-speed asynchronous generator and a partially rated converter (DFIG) (Fig. 1*a*).

- Direct Drive WTs with no gearbox but a specialised direct drive, low-speed synchronous generator and fully rated converter (Fig. 1*b*).

The anticipated benefit of the geared concept is that it uses a more standardised, high-speed generator and a partially rated converter, thereby saving cost as shown in [5].

An anticipated benefit of the direct drive concept is that by avoiding the use of the gearbox it should prove to be more reliable but there are other potential benefits, for example lower losses in low wind.

There are also a number of control configurations which need consideration and these are listed in Appendix 2, Table 3.

This paper will investigate the reliability of a number of these turbine concepts where a concept means the sum of the WT architecture and control configuration.

2.2 Subassemblies

To understand WT reliability we need to break down the WT into more detail than Figs. 1*a* and 1*b* using the following nomenclature:

- System, the whole WT;

- Subsystems of the WT, such as the drive train, consisting of rotor hub, shaft, bearing, gearbox, couplings and generator.

- Subassemblies of subsystems, such as the gearbox;

This paper focuses on the subassemblies recorded in the surveys WSDK, WSD and LWK. The terminology used by the surveys was not consistent and it has been necessary to aggregate subassemblies as shown in an Appendix 2, Table 4.

2.3 Populations and operating experience

WSD, WSDK and LWK data, [3] and [4], were collected by operators on hand-written or computer-written report sheets,

doi: 10.1049/iet-rpg:20080060

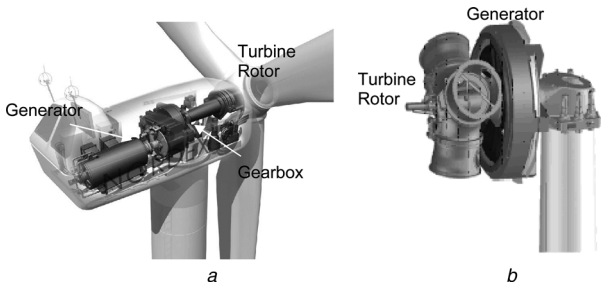

Figure 1 *The main subassemblies of WT*

a Construction of the nacelle of a Geared WT showing the main subassemblies
b Construction of the nacelle of a Direct Drive WT showing the main subassemblies

rather than generated automatically, and the data have some limitations, as follows:

1. They gather the failures in a given period for each turbine and subassembly within the population without giving details of failure modes.

2. The periods of data collection differ for each population as follows; WSDK monthly; WSD quarterly; LWK annually. These periods have affected the results presented, as explained in Section 9, Appendix 1.

3. There are other differences between the populations:

• WSDK is a large mixed population decreasing in WT numbers (2345–851 over the period), with turbines of average age of >14 years, mostly of stall-regulated configuration. Their technology is consolidated as confirmed by their failure intensities, approaching a constant average failure rate. The failures of individual turbine models cannot be distinguished in this data.

• WSD is a larger mixed population growing in number (1295–4285 over the period) and includes larger turbines, with an average age of <3 years, including a variety of turbine models with different control configurations but their failure intensities are also approaching a constant value, although at a faster rate than WSDK. The failures of individual turbine models again cannot be distinguished in this data.

• LWK is a smaller, segregated, more static population in number (158–643 over period) and includes larger turbines of average age up to 15 years, with fixed and variable speed configurations, both with geared and a significant number with the direct drive concept. The failures of individual turbine models can be distinguished in this data.

2.4 Industrial reliability data for subassemblies

Some WT subassemblies, such as the rotor and pitch control, are specialised for the wind power application. But some, such as the gearbox, generator and converter can be found in similar form, albeit in different sizes and designs, in other power conversion machinery. The usefulness to the industry of reliability figures presented in this paper is enhanced by comparing them to values from other industries, as tabulated in Table 1.

3 Reliability analysis assuming constant failure rate

The unreliability of repairable systems, can modelled in terms of failure intensity by the bathtub curve [10], which represents the three different phases of a population life, as shown in Fig. 2. In turn, each phase of the bathtub curve can be modelled by a failure intensity function as shown in Fig. 3. This paper is based on the concept of a bathtub curve for a repairable system and its mathematical formulation, the Power Law process (PLP).

The PLP is a special case of a Poisson process with a failure intensity function

$$\lambda(t) = \rho\beta t^{\beta-1} \tag{1}$$

β determines the trend of the curve is dimensionless and called the shape parameter. ρ is a scale parameter which has the units per year^{-1}. $\lambda(t)$ has units in this paper of failures per item per year or per year^{-1}, where an item can be a WT or a subassembly.

For $\beta < 1$ or $\beta > 1$ the curve shows, respectively, a downward or upward trend. When $\beta = 1$ the intensity function of the PLP is equal to ρ, the process represents the bottom of the bathtub curve, called the intrinsic failures phase and λ is described as the average failure rate.

Elements of the reliability theory used to analyse the failure data in this paper are summarised in Section 9, Appendix 1 and [11].

Table 1 Reliability of generators, gearboxes and converters taken from industrial experience

Subassembly	Failure rate, failures per item per year	MTBF, h	Source
generator	0.0315–0.0707	123 900–278 000	Tavner [6] and IEEE Gold Book [7]
gearbox	0.155	56 500	Knowles [8]
converter	0.045–0.2	43 800–195 000	Spinato [9]

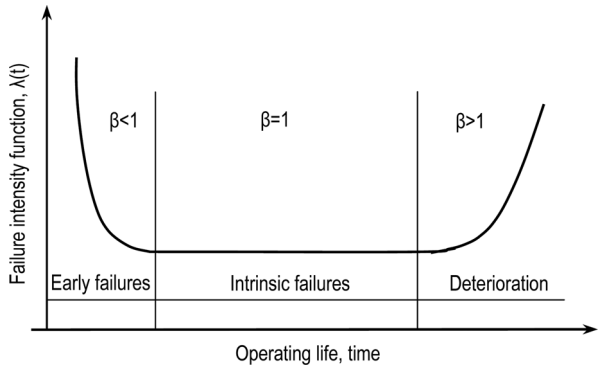

Figure 2 *The 'bathtub curve' for the intensity function showing how the reliability varies throughout the life of repairable machinery*

Previous work by the authors of [1] and [2] concentrated on the average WT failure rate, assuming the systems were at the bottom of the bathtub Fig. 2. This showed for WSD, WSDK, Fig. 4*a*, the overall trend in WT failure intensities against calendar time since the days of the early expansion of wind power in California in the early 1980s. The results of the LWK survey have been added to Fig. 4*a* with the measured failure rates from other mature power generation sources, largely extracted from IEEE sources [7], showing that WT reliability is becoming better than some other generation sources, notably diesel generator sets. However, this graph needs to be treated with caution for the following reasons:

• The WT data is taken from mixed and changing WT populations. Because the ratings of newly introduced WTs are increasing and their failure rates are generally rising, the averaging implicit in the HPP process tends to underestimate the failure rates of these newer, larger, more complex WTs, at least during the early failures period.

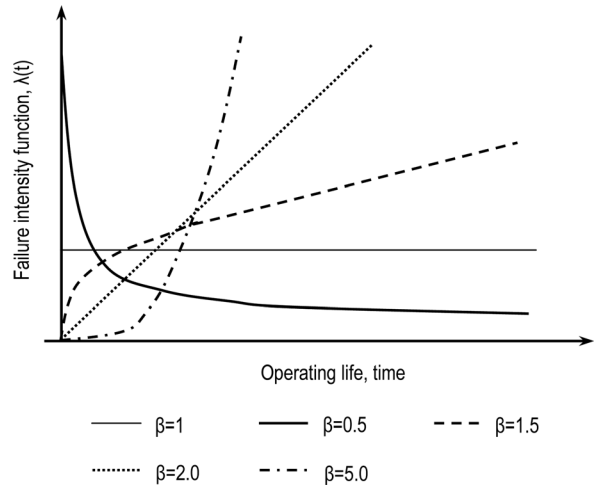

Figure 3 *The power law function showing how the failure intensity changes with the shape parameter β*

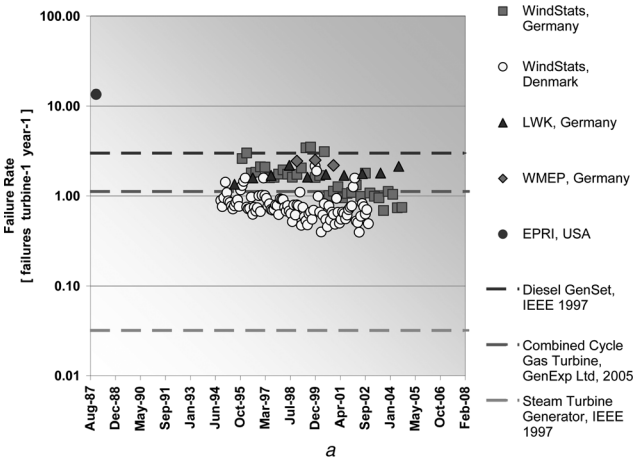

a

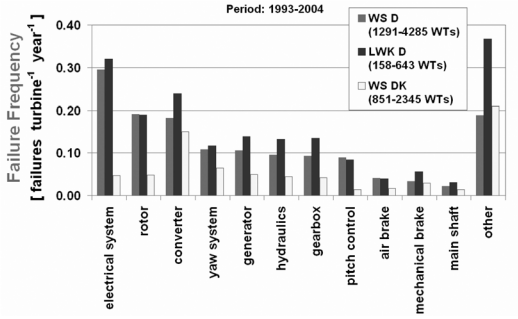

b

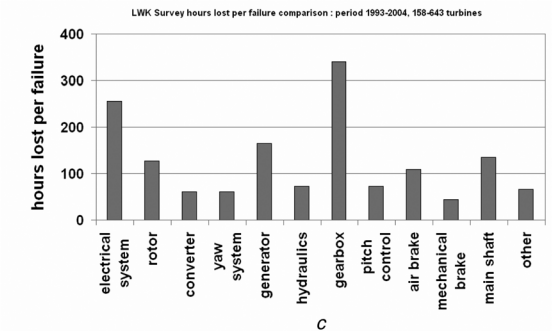

c

Figure 4 *Results from surveys assuming a constant failure rate and the HPP model*

a Summary of WT failure intensities from various sources over 15 years and >10 000 turbines [1]
b Distribution of failure intensities between subassemblies in WTs from the WSD, WSDK and LWK surveys, averaged over 11 years and >6000 turbines
c Distribution of downtime between major subassemblies in WTs from the LWK survey, averaged over 11 years and >2000 turbines

• Other mature power generation source failure data came from historic surveys of limited size, which do not represent the reliability improvement to be studied in this paper but which is also inherent in those sources.

The relative unreliability of WT subassemblies can also be extracted from the WSD, WSDK and LWK data as shown in Fig. 4*b*, where the assumed constant failure rates of 12 major turbine subassemblies, listed in Appendix 2, Table 4, have been compared. The LWK population has a higher consistency in terms of technology throughout the period,

doi: 10.1049/iet-rpg:20080060

as it is an installed fleet that has remained relatively unchanged. However, the LWK population is much smaller than the WSD and WSDK populations. Fig. 4*b* reveals interesting information:

1. Overall failure rates in Danish turbines are lower than German turbines, as seen in Fig. 4*a*. This was attributed in [1] to the greater age, smaller size and simpler technology of the Danish turbines resulting in a higher overall reliability.

2. Fig. 4*b* shows that the failure rates of subassemblies in the two German populations, WSD and LWK, are remarkably similar and have more in common with one another than with the WSDK data. This consistency supports the validity of the two German surveys despite their different sizes.

3. The results of Fig. 4*b* show that the subassemblies with the highest failure rates are, in descending order of significance:

- Electrical system
- Rotor (i.e. blades and hub)
- Converter (i.e. electrical control, electronics, inverter)
- Generator
- Hydraulics
- Gearbox

Similar results have been reported from Sweden [12] and from a different survey in Germany, WMEP [13].

The failure rates obtained for WT subassemblies will also be compared in this paper with those obtained from industry in Table 1.

Fig. 4*b* considers failure rate only and not failure severity. However, LWK data records the downtime or MTTR of different subassembly failures and this is shown in Fig. 4*c*, presented in the same order as Fig. 4*b*. Here the effects of electrical system, generator and gearbox failures are more apparent, in particular the dominance of the gearbox MTTR. It is suggested that this is the main reason for the industry's focus on gearbox failures. Similar results have also been obtained in Sweden [12].

4 Reliability analysis of turbine concepts

4.1 General

4.1.1 Comparison of turbine concepts: The paper now considers the failure rates of individual subassemblies most at risk. The LWK data allows turbine models to be grouped according to size and concept. Fig. 5 summarises the failure rates over 11 years for 12 WT models in the LWK population, as listed in Appendix 2, Table 3. This shows the general trend of failure rate rising with turbine rating, reaffirming a conclusion of [1].

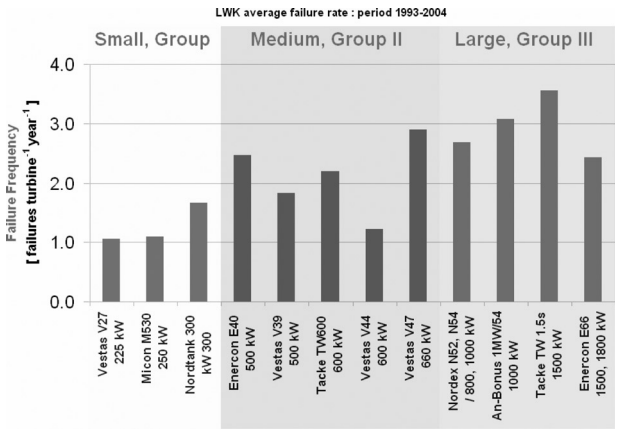

Figure 5 *Distribution of failure intensities between different turbine models, sorted by turbine size*

The next analysis repeats the approach of Fig. 4*b*, comparing subassembly failure rates for selected LWK turbine models, concentrating on subassemblies in the drive train. This is shown in Fig. 6, which is segregated by turbine concept and control configuration, see the third column of Appendix 2, Table 3. The figure shows the relationship between failure rates of blades, pitch mechanism, gearbox and generator as turbine concepts and control configurations change.

With fixed speed, stall-regulated turbines a significant number of failures are concentrated in the blades and gearbox. With the introduction of variable speed, pitch-regulated machines the pitch mechanism now appears as a failure mode, as expected. However, the introduction of the pitch mechanism reduces the blade and generator failure rates, see Fig. 6*a* for smaller WTs. This is confirmed for larger WTs in Fig. 6*b* where blade, generator and gearbox failure rates reduce, with the exception of the E40, direct drive WT, where the generator failure rate is high. This will be discussed in Section 4.2.2. The reduction in blade failures is even more noticeable with the larger E66 direct drive WT in Fig. 6*c*.

In other words the technological advance of variable speed and pitch control not only confers energy extraction and noise reduction improvements but also, despite introducing another failure mode, can improve the turbine reliability with time.

4.2 Reliability of subassemblies

4.2.1 General: The failure data collected exhibits a variation with time, and can be represented by a Non-homogeneous Poisson process (NHPP) see Section 9.4. The paper will now use reliability growth analysis, based on

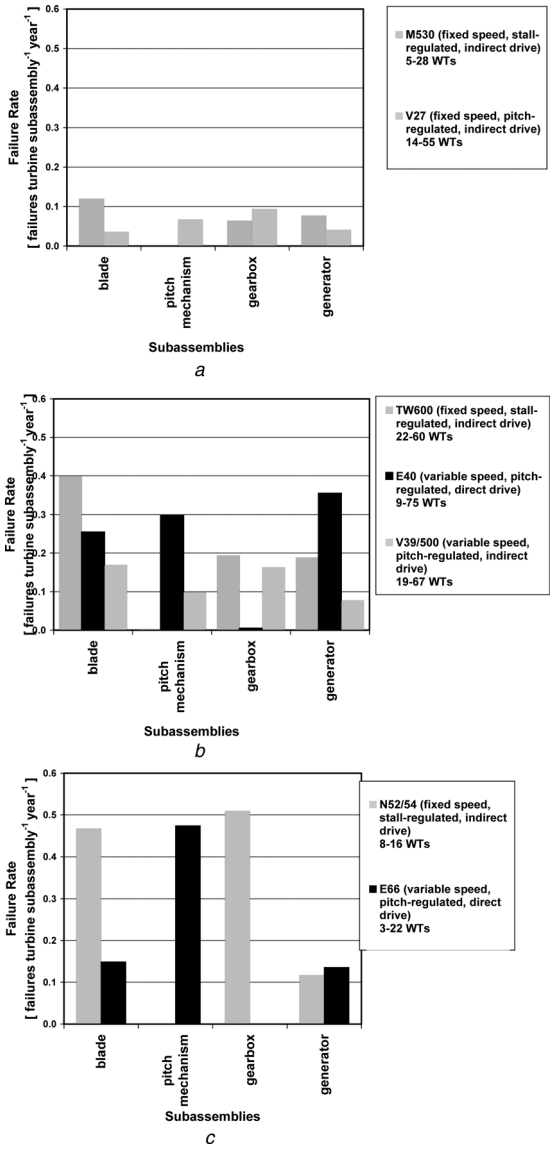

Figure 6 *Distribution of failure intensities as in the graphs but focussing solely on the blades, pitch mechanism, gearbox and generator*

a LWK, Group I 300 kW fixed speed, geared turbines with pitch-regulated or stall-regulated control
b LWK, Group II 600 kW Fixed speed, geared, stall-regulated, or limited variable speed pitch-regulated turbines or variable speed direct drive pitch regulated turbines
c Group III 1 MW Variable speed geared, pitch-regulated, turbines or variable speed direct drive, pitch-regulated turbines
The stall regulated turbines are shown to the left the variable speed, pitch-regulated turbines are shown to the right

the PLP representation, a specific case of the NHPP, to analyse reliability time trends from the LWK population of WTs concentrating on three subassemblies identified above:

- Generator
- Gearbox
- Converter (i.e. electrical control, electronics, inverter)

These subassemblies have been chosen because they are crucial to the operation of the WT and central to the debate about turbine concept, in particular whether to employ direct drive or geared WTs [14].

The method of presentation is to plot the intensity function obtained from the LWK data against total time on test (TTT) of the subassembly, see Section 9.6. Plotted failure intensity points have been aggregated to comply with requirements for valid numbers of failures in an interval and the Crow-AMSAA model, as described in the Section 9, Appendix 1. On each graph the failure rate of that subassembly in other industries taken from Table 1 is also shown, together with a time cursor to demonstrate the span in years of the data, as described in Section 9.6.

For these subassemblies the PLP interpolation of data presented has been tested against two statistical criteria:

- goodness-of-fit
- null hypothesis of no reliability growth.

Only results complying with those criteria have been presented. Subassemblies from specific WT models are selected here but the conclusions drawn below may be generalised to other WTs in the LWK population.

4.2.2 Generators: Fig. 7 shows the reliability of a number of LWK generators showing that failure intensities are generally falling, that is a PLP with $\beta < 1$, reflecting that reliability is improving.

Industrial generator reliability data, given in Table 1, is superimposed on the graphs and Fig. 8 shows that both direct and geared drive WT generator reliabilities are not as good as these at the start of life. However, the demonstrated reliabilities, as defined in Fig. 10, achieved by all except the E40 generator shows a good result when compared with the industrial failure rate.

The failure intensities for both direct drive generators are higher than the failure intensities of their geared drive competitors. However, it is clear that the E66 generator is a considerable improvement on the E40 generator. Important questions are raised by these results as follows:

- Why is there such a large disparity between the reliabilities of direct and geared drive generators at the start of operational life?
- Why do the failure intensities of three generators improve with time?
- Why cannot the wind industry achieve, at the start of operational life, the respectable demonstrated reliabilities ultimately achieved?

doi: 10.1049/iet-rpg:20080060

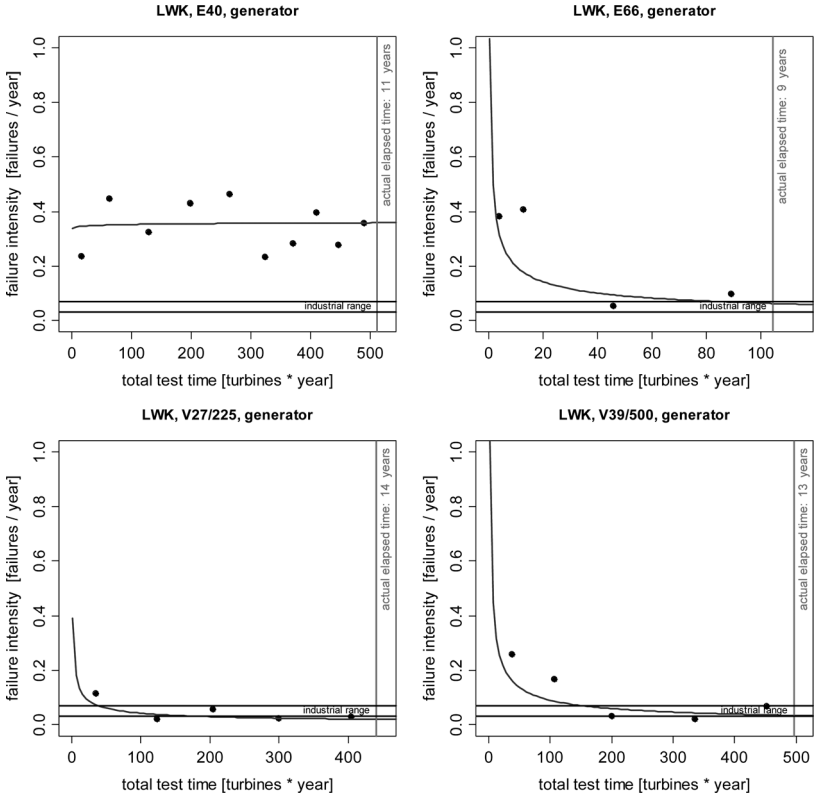

Figure 7 *Variation between the failure intensities of generator subassemblies, in the LWK population of German WTs, using the PLP model*

The upper two are low-speed direct drive generators whereas the lower two are high-speed geared drive generators

These questions suggest, from this limited extract from LWK data, that generators deserve reliability attention from manufacturers and operators if we are to achieve higher WT reliability and will be discussed in Section 5.

4.2.3 Gearboxes: Fig. 8 gives the results for the reliability of a number of LWK gearboxes, which each show a remarkably similar form with rising failure intensities, which is a PLP with β from 1.2–1.8, see Fig. 3.

This suggests that WT gearboxes are of a mature technology and that the machines are operating in the deterioration phase of the bathtub curve. Therefore substantial improvements in designed reliability for these gearboxes are unlikely.

The reliability data for industrial gearboxes, given in Table 1, is an average from a number of sources and has been superimposed on the graphs. It shows that, from this limited extract from LWK data, reliabilities being obtained by these wind industry gearboxes are comparable with those obtained by other industries, apart from the Nordex 52/54 WT data.

4.2.4 Converters: The converter is a complex subassembly with a large number of components. There is difficulty in recording failures for converter subassemblies as operators may be unable to assign a turbine failure unequivocally to the converter because the subassembly is complex. This is in contrast to the generator or gearbox where this is usually straightforward. This means that we must be cautious in considering recorded converter failures. To overcome this we have aggregated the failures from inverter and electronics in the LWK survey, see Table 4, and the data has been plotted for specific turbines with the generic subassembly name, converter.

Fig. 9 gives reliability results for three LWK converters. For two cases, the Enercon E40 and TW 1500, the results are similar to the generators, in that failure intensities are falling, that is a PLP with $\beta < 1$, reflecting reliability improvement. However in the case of the Enercon E66 and E40 converters the failure intensities improve with time but are nearly flat with $\beta <= 1$. Industrial converter failure rate data in Table 1 range between 0.045 and 0.2 failure per subassembly per year. The lower limit arises from a specific analysis of relatively small converters [9] but such a low value of failure rate cannot be applicable to the larger converters in WTs, therefore an upper limit of 0.2 failure per subassembly per year is proposed. Important questions raised by these results are as follows:

- Why do the failure intensities of converters improve with time?

- Why are the failure intensities considerably higher than values given for converters in normal industrial use?

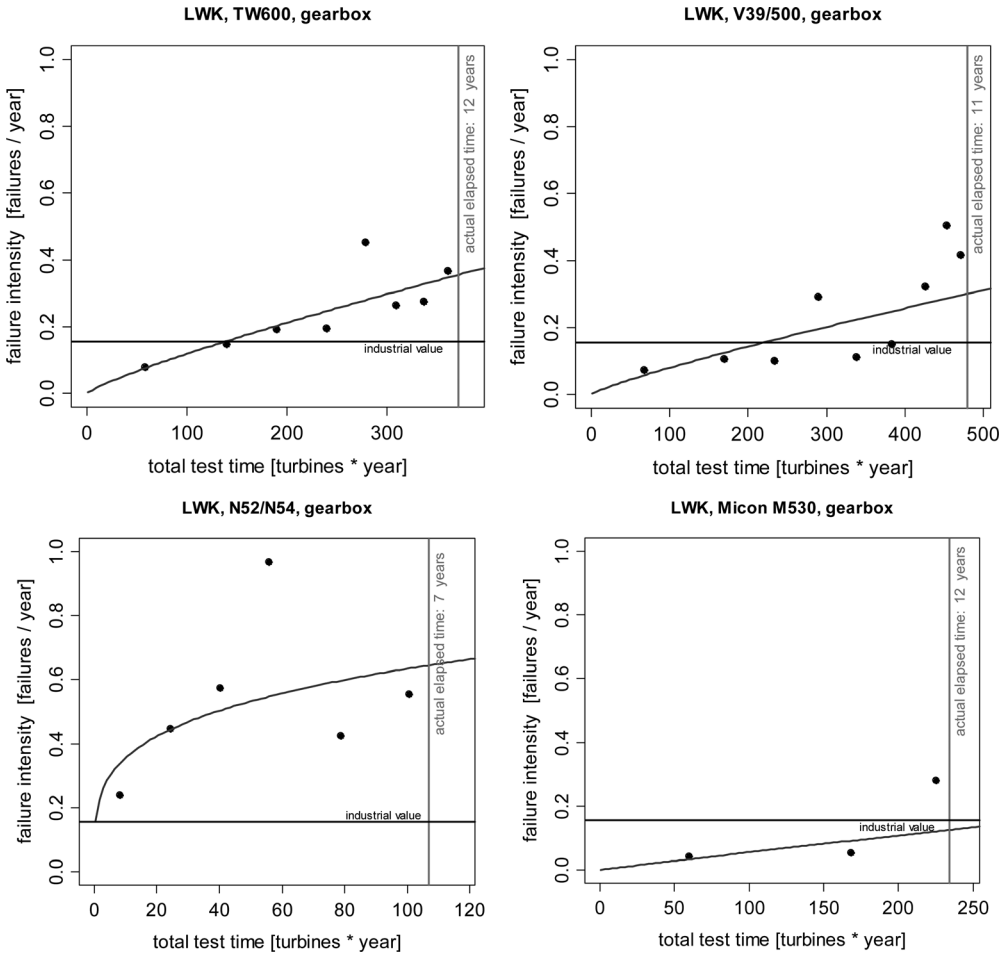

Figure 8 *Variation between the failure intensities of gearbox subassemblies, using the PLP model, in the LWK population of German WTs*

These suggest, from this limited extract from LWK data, that converters deserve reliability attention from manufacturers and operators if we are to achieve higher WT reliability and will be discussed in Section 5.

5 Discussion

5.1 Methods to improve reliability

5.1.1 Reliability results and future turbines: The results presented above have all been obtained on existing WTs of historic design of size ranging from 200 kW to 2 MW. To what extent can these data be used to predict the reliability performance of new designs of WT of much larger size, say 3–5 MW?

Reliability analysis is of necessity backward looking and rarely produces data which is younger than 5 years, however, its great advantage is that data is numerical and comparable.

It is proposed that the WT failure rates shown in Fig. 4*a* can be used as a datum against which future designs should be measured. For example while an average failure rate of 1 failure per turbine per year could be acceptable onshore, it is unlikely to be acceptable offshore where access may be limited to one visit a year.

The WT subassembly failure rates can also be used as a datum for comparison between different concepts and different designs, however, they must also be considered against the MTTR, as the gearbox data has shown.

Reliability improvement analysis will be useful for WT and subassembly manufacturers to define where design and testing effort can be deployed to improve future reliability.

5.1.2 Design: One simple approach to improve reliability, taken by Enercon, has been to remove the gearbox and use a direct drive configuration. Enercon also adopted an all-electric approach, avoiding the use of hydraulics for pitch or yaw control.

Taking up the comparison between direct and geared drive WTs, raised by Polinder *et al.* [5], this paper and an earlier reference [15] have shown that:

1. From Fig. 5 direct drive WTs do not necessarily have better reliability than geared drive WTs. In Fig. 5 the

doi: 10.1049/iet-rpg:20080060

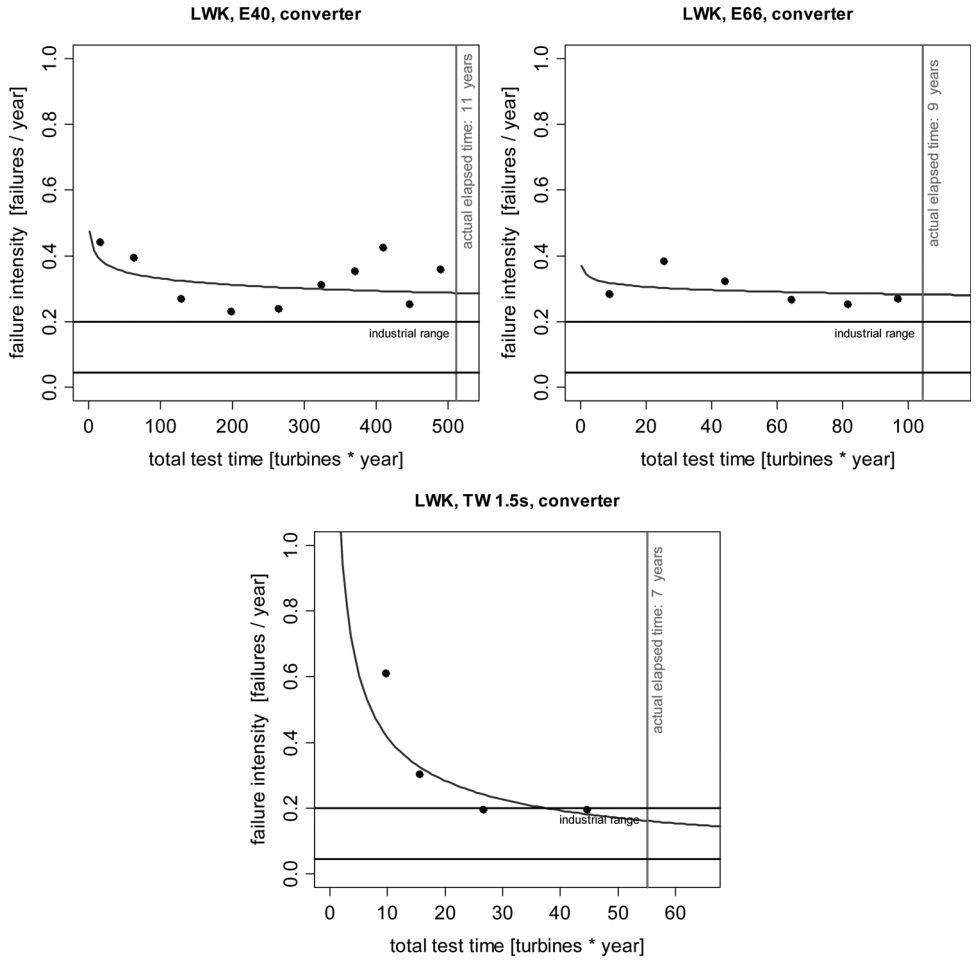

Figure 9 *Variation between the failure intensities of converter subassembly, using the PLP model, in the LWK population of German WTs*

The upper two are for fully rated converters applied to low-speed direct drive generators, whereas the lower one is a partially rated converter applied to a high-speed geared drive generator

direct drive E40 has a higher failure rate than its geared drive partners of the same size, whereas the direct drive E66 has a lower failure rate than its partners, although the E66 data is rather limited in number of WTs.

2. From Fig. 6 and reference [15] the aggregate failure rates of generators and converters in direct drive WTs are generally greater than the aggregate failure rate of gearboxes, generators and converters in geared WTs. Therefore the price paid by direct drive WTs for the reduction of failure rate by the elimination of the gearbox is a substantial increase in failure rate of electrical-related subassemblies.

3. On the other hand from Fig. 4*c* it can be seen that the MTTR of electronic subassemblies is lower than the MTTR of gearboxes suggesting that an all-electric direct drive WT may ultimately have an intrinsically higher availability than a geared drive WT.

4. From Figs. 6*b* and 6*c* the failure intensities of larger direct drive generators are up to double that of the geared drive generators of similar size. The following explanation is offered. The direct drive machines in this paper are wound-rotor, synchronous generators with high pole pair number, incorporating a large number of rotor and stator coils. Whereas the geared drive machines are four or six switchable pole, high-slip, induction generators or double-fed, induction generators, with far fewer coils. It is suggested that the disparity in failure intensities is because of:

- The much larger number of coils in the direct drive machine. The failure rate could be improved by replacing field coils by permanent magnets, but this would introduce other, reactive control issues.

- The larger diameter of the direct drive generator making it difficult to seal the more numerous coils from the environment, exposing coil insulation to damage because of the air contaminants and environmental humidity.

- Insufficient standardization in the manufacture of the large direct drive machines, as a consequence of smaller production runs, compared to the more common doubly fed induction generator.

From a general consideration of direct drive or geared concept WTs the following arises from this work associated with the design:

- The reliability of these WT generators, from Fig. 7, is worse during early operational life than that achieved by generators in other industries.

- From Fig. 8 the reliability of these WT gearboxes are seen to be that of a mature technology, constant or slightly deteriorating with time. The reliabilities are comparable with those obtained by gearboxes in other industries. Therefore substantial improvements in the designed reliability of these gearboxes are unlikely in the future, although design improvements in gearboxes for newer, larger designs of WTs are being actively pursued and it appears that maybe a greater onus is being placed on wind turbine gearbox reliability by the stochastically varying torque to which it is subjected

- From Fig. 9 the reliability of these WT converters is considerably worse throughout their operation than achieved by converters in other industries.

- From the observations above improvements in generator and converter reliability design will be crucial to improving the reliability of both direct drive and geared concept WTs.

5.1.3 Subassembly testing: Testing of these subassemblies, particularly converters and generators, can also achieve higher WT reliability at the start of operational life by eliminating early failures.

A suggestion is that for offshore WTs nacelles could be tested complete, at full or varying load, at elevated temperature, to accelerate the occurrence of early failures.

This is a standard practice in the electrical machine and gearbox industry where prolonged heat runs at elevated temperatures are done as type tests on new products. These type tests are then repeated on individual machines from batch sizes specified for example by IEC Standards 60034 and 61852.

It is also a standard practice, in the volume production of low-rating power converters, <100 kW, to routinely age test key converter subassemblies and then carry out extended load tests on assembled converters from batch sizes specified for example by IEC Standard 60700 to identify generic weaknesses before despatch.

5.1.4 Operation and maintenance and condition monitoring: The improving reliability of generators and converters in Figs. 7 and 9 indicates that operations and maintenance (O&M) activities are already having a reliability effect.

Condition monitoring measures machine performance indicating the need for remedial action when performance deteriorates. The wind industry has been very successful in applying Supervisory Control and Data Acquisition (SCADA) systems to WTs and most wind farms now have a SCADA system providing data to remote control rooms. However, agreement has not yet been reached on condition monitoring the large quantities of data generated to indicate incipient failures. O&M methods need to use this information to predict failure and thereby schedule maintenance, although work is currently going on in this area [16, 17]. If the design and testing suggestions above are heeded and the condition monitoring technique is resolved the O & M approach will require:

- Maintenance based on the measured condition of the WT so that failures of vital subassemblies like the generator, gearbox and converter can be pre-empted.

- The provision of adequate spares to reduce downtime when maintenance on the basis of condition takes place.

6 Conclusions and recommendations

The paper has investigated the reliability of more than 6000 WTs in Denmark and Germany over 11 years and particularly the changes in reliability of generators, gearboxes and converters in a subset of 650 of these WTs in Schleswig Holstein, Germany. The paper has demonstrated the following:

1. The subassemblies with the highest failure rates are, in descending order of significance:

- Electrical system
- Rotor (i.e. blades and hub)
- Converter (i.e. electrical control, electronics, inverter)
- Generator
- Hydraulics
- Gearbox

2. Larger WTs have a lower reliability than smaller WTs.

3. Results are supported by other surveys in Sweden and Germany.

4. Technological advances in WT variable- speed and pitch-control have conferred reliability improvements with time.

5. Direct drive WTs are not necessarily more reliable than geared WTs. Aggregate failure intensities of generators and

doi: 10.1049/iet-rpg:20080060

converters in direct drive WTs are greater than the aggregate failure rate of gearboxes, generators and converters in geared WTs. Therefore the elimination of a gearbox has resulted in a substantial increase in the failure rate of electrical-related subassemblies. However, it has been shown that the downtime of electrical-related subassemblies is lower than the downtime of gearboxes suggesting that an all-electric, direct drive WT may ultimately have an intrinsically higher availability than a geared drive WT.

6. WT gearboxes are a mature technology with a constant or slightly deteriorating reliability with time. Therefore substantial improvements in the designed reliability of existing gearboxes are unlikely in the future. The reliabilities of WT gearboxes are comparable with those obtained by similar size gearboxes in other industries and do not have the highest failure rate compared to other WT subassemblies. However, the results do show that the gearbox exhibits the highest downtime. This rather than the failure rate is the real reason for the industry's focus on the gearbox.

7. WT direct drive and geared drive generators in these surveys exhibit higher failure rates during the initial phases of operation than generators in other industries.

8. The failure intensities of larger direct drive generators in these surveys are up to double that of the geared drive generators. This disparity may be because of the much larger number of coils used in the direct drive machine, the larger diameter of the machine and the fact that it is not a standard machine produced in large numbers. The failure rate of the direct drive generator could be improved by replacing the field coils by permanent magnets.

9. The power electronic converters of direct and geared drive WTs exhibit higher failure intensities throughout their operation than converters in other industries.

10. For offshore WTs it is recommend that their subassemblies should be tested more thoroughly than at present, particularly converters and generators, to eliminate early failures. A suggestion is that WT nacelles could be tested complete, at full or varying load, at elevated temperature, to accelerate early failures during test so that they enter service with an improved reliability.

7 Acknowledgments

The authors are grateful to Bill Grainger formerly of AMEC Wind Energy and now of Clipper Wind who suggested some of the ideas which initiated this work. They have also received helpful comments and encouragement from the New & Renewable Energy Centre at Blyth, Northumberland, the Centre of Renewable Energy Systems Technology, Loughborough University and Dr Polinder at TU Delft. The work on reliability was funded by an EPSRC CASE Award, 'Towards a Zero Maintenance Wind Turbine', GR/P03636/01. The work also contributes towards the EPSRC-funded Supergen Wind Energy Technologies Consortium, EP/D034566/1, in which Durham and Loughborough Universities and AMEC Wind Energy are partners.

8 References

[1] TAVNER P.J., XIANG J., SPINATO F.: 'Reliability analysis for WTs', *Wind Energy*, 2007, **10**, pp. 1–18

[2] VAN BUSSEL G.J.W., ZAAIJER M.B.: 'Estimation of turbine reliability figures within the DOWEC project'. DOWEC Report, 2003, **10048**, (4), ECN, The Netherlands

[3] Windstats (WS): www.windstats.com

[4] Landwirtschaftskammer (LWK). Schleswig-Holstein, Germany: http://www.lwksh.de/cms/index.php?id=1743

[5] POLINDER H., VAN DER PIJL F.F.A., DE VILDER G.J., TAVNER P.J.: 'Comparison of direct-drive and geared generator concepts for WTs', *IEEE Trans. Energy Conversion*, 2006, **EC-21**, (3), pp. 725–733

[6] TAVNER P.J.: 'Review of condition monitoring of electrical rotating machines', *IET Proc., Electrical Power Appl.*, 2008, **2**, (4), pp. 215–247

[7] IEEE, Gold Book: 'Recommended practice for design of reliable industrial and commercial power systems' (IEEE Press, Piscataway, 1990)

[8] KNOWLES M.: 'Failure modes and effects analysis for a large wind turbine'. MEng Project Report, Durham University, 2006

[9] SPINATO F.: 'The Reliability of Wind Turbines'. PhD thesis, Durham University, 2008

[10] RIGDON S.E., BASU A.P.: 'Statistical methods for the reliability of repairable systems' (John Wiley & Sons, New York, 2000)

[11] GOLDBERG H.: 'Extending the limits of reliability theory' (John Wiley & Sons, New York, 1981)

[12] RIBRANT J., BERTLING L.M.: 'Survey of failures in wind power systems with focus on Swedish wind power plants during 1997–2005', *IEEE Trans. Energy Conversion*, 2007, **EC22**, (1), pp. 167–173

[13] HAHN B., DURSTEWITZ M., ROHRIG K.: 'Reliability of wind turbines, experiences of 15 years with 1,500 WTs, in 'Wind Energy' (Springer, Berlin, 2007), ISBN 10 3-540-33865-9

[14] TAVNER P.J., SPINATO F., VAN BUSSEL G.J.W., KOUTOULAKOS E.: 'Reliability of different wind turbine concepts with relevance to offshore application'. European Wind Energy Conf., EWEC2008, Brussels, 2008

[15] TAVNER P.J., VAN BUSSEL G.J.W., SPINATO F.: 'Machine and converter reliabilities in WTs'. IEE International Conf. PEMD, Dublin, 2006

[16] CASELITZ P., GIEBHARDT J.: 'Rotor condition monitoring for improved operational safety of offshore wind energy converters', *ASME Trans. J. Solar Energy Eng.*, 2005, **127**, pp. 253–261

[17] YANG W., TAVNER P.J., WILKINSON M.R.: 'Condition monitoring and fault diagnosis of a wind turbine synchronous generator drive train', *IET Proc. Renewable Power Generation*, 2008, **2**, (3), pp. 1–11

[18] MIL-HDBK-189: 'Reliability Growth Management'. Department of Defense, Washington, 1981

9 Appendix 1: relevant reliability theory

9.1 General

To track changes of reliability with time during the different operational phases of a product, reliability growth models have been developed [18] most notably using the Crow-AMSAA model. The same model can be applied on failure data collected from the field to investigate whether product reliability stays constant, or shows an improvement or deterioration with time.

9.2 Basic definitions

Reliability of a subassembly is the probability that it will perform its required function under stated conditions for a specified period of time. The unreliability is related to the failure intensity function, $\lambda(t)$, defined below.

Failure is the inability of a subassembly to perform its required function under defined conditions; the item is then in a failed state, in contrast to an operational or working state.

A non-repairable system is one which is discarded after a failure. Examples of non-repairable systems are small batteries or light bulbs.

A repairable system is one that, when a failure occurs, can be restored into operational condition after any action of repair, other than replacement of the entire system. Examples of repairable systems are WTs, car engines, electrical generators and computers.

Repair actions can be an addition of a new part, exchange of parts, removal of a damaged part, changes or adjustment to settings, software update, lubrication or cleaning.

9.3 Point processes

A point process is a stochastic model describing the occurrence of discrete events in time or space. In reliability analysis, failures of repairable systems can be described with point processes in the calendar time domain, for example hourly, quarterly or annually, or using an operational variable, like kilometres driven or number of flying hours.

A random variable $N(t)$ that represents for example the number of failure events in the interval $[0, t]$ is called the *counting random variable*. Subsequently the number of events in the interval $(a, b]$ will be

$$\mathrm{N(a, b]} = \mathrm{N(b)} - \mathrm{N(a)} \tag{2}$$

The *Point Process Mean Function* $\Lambda(t)$ is the expected number of failures, E, in the interval throughout time t

$$\Lambda(t) = E[N(t)] \tag{3}$$

The *Rate of Occurrences of Failure* $\mu(t)$ is the rate of change of expected number of failures

$$\mu(t) = \frac{\mathrm{d}}{\mathrm{d}t}\Lambda(t) \tag{4}$$

The *Intensity function* $\lambda(t)$ is the limit of the probability, P, of having one or more failures in a small interval divided by the length of the interval.

$$\lambda(t) = \lim_{\Delta t \to 0} \frac{P(N(t, t + \Delta t]) \geq 1}{\Delta t} \tag{5}$$

If the probability of simultaneous failures is zero, which occur only where the mean function $\Lambda(t)$ is not discontinuous, then

$$\lambda(t) = \mu(t) \tag{6}$$

9.4 Non-homogeneous Poisson process (NHPP)

Assuming minimal repair, that is the failed subassembly is brought back to the same condition it was just before the failure, the NHPP can be used to describe changes in reliability of repairable systems [10]. A counting process $N(t)$, that is the cumulative number of failures after operational or calendar time t, is a Poisson process if:

1. $N(0) = 0$

2. For any $a < b \leq c < d$, the random variables $N(a,b]$ and $N(c,d]$ are independent. This is known as the independent increment property.

doi: 10.1049/iet-rpg:20080060

Table 2 Values of β for different failure intensities

Value of β	Failure intensity	Reason	Model type
$\beta < 1$	decreasing with time	design improvements/alterations on field	NHPP
$\beta = 1$	constant with time $\lambda(t) = \rho$	no major design modifications – Wear and tear not apparent yet	HPP
$\beta > 1$	increasing with time	normal deterioration of materials/accumulated stresses	NHPP

3. There is a function λ (*intensity function*) such that

$$\lambda(t) = \frac{\lim}{\Delta t \to 0} \frac{P(N(t, t + \Delta t]) = 1}{\Delta t} \tag{7}$$

Note that if λ is constant then the process is homogeneous Poisson process (HPP).

4. Simultaneous failures are not possible

$$\frac{\lim}{\Delta t \to 0} \frac{P(N(t, t + \Delta t]) \geq 2}{\Delta t} = 0 \tag{8}$$

The main property of NHPP is that the number of failures *N(a,b]* in the interval $(a,b]$ is a random variable having a Poisson distribution with mean.

$$\Lambda(a, b] = E[N(a, b]] = \int_a^b \lambda(t)\mathrm{d}t \tag{9}$$

9.5 Power Law process

An NHPP is called a power law process (PLP) if the cumulative number of failures through time t, $N(t)$ is given by

$$N(t) = \rho t^{\beta} \tag{10}$$

Therefore, the expected number of failures for a specific time interval $[t_1,t_2]$

$$N[t_1, t_2] = N(t_2) - N(t_1) = \rho(t_2^{\beta} - t_1^{\beta}) \tag{11}$$

Its intensity function is then:

$$\lambda(t) = \frac{\mathrm{d}N(t)}{\mathrm{d}t} = \rho\beta t^{\beta-1} \tag{12}$$

One of the advantages of using the PLP model for repairable systems is that its intensity function (12) is flexible enough to represent separately the three different phases of the bathtub curve, see Fig. 2, based on the value of the shape parameter β, as described in Table 2.

9.6 Total time on test

The variable t that appears in the various equations of the Crow-AMSAA model [18] represents the time to a point process but it differs from calendar time, as reported in the failures tables of WSDK, WSD and LWK. Reliability growth, as well as other reliability analysis, is normally carried out on the basis of specific tests made on subassemblies under investigation. For a repairable system the test is stopped after a failure or a planned inspection and the number of running hours elapsed since the previous failure are recorded. After a number of failures have been accumulated, failure data are interpolated with a mathematical model, like the Crow-AMSAA, to verify the achieved reliability or, using the terminology of the military standard, the 'demonstrated reliability'. The independent variable t of the plot is the cumulative quantity called the Total time on test (TTT) that is the integral of the number of running hours of the entire population for the observed period. In this way the hours of inactivity are not included in the evaluation of the TTT.

Using TTT rather than calendar time presents advantages and disadvantages and the meaning of TTT, for WT failure data, must be clarified. First, it is in the nature of reliability engineering to deal with running hours rather then calendar time. This distinguishes a reliability analysis from an availability analysis. In this case the age of many electromechanical systems can be measured with the number of cycles completed or the total running hours and often this differs substantially from the calendar age. Nevertheless, the calendar time plays an important role in reliability studies where chemical–physical properties deteriorate with time, for example the insulating property of a dielectric. For data sets like LWK, WSD or WSDK the TTT in a certain interval i, $\Delta\mathrm{TTT}_i$ is calculated by multiplying the number of WTs, N_i, by the number of hours in the interval, h_i. The recorded total hours lost from WT production, l_i, in that interval are then subtracted, when this information is available. In these surveys this data included only out of service time, rather than time when the WT was unable to operate for lack of wind.

The aggregated TTT up to an arbitrary time cell k, t_k, is then

$$t_k = \sum_{i=1}^{k} \Delta\mathrm{TTT}_i \; = \sum_{i=1}^{k} N_i * h_i - l_i \tag{13}$$

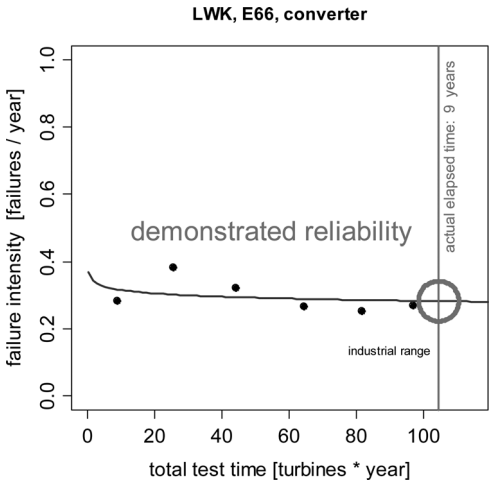

Figure 10 *Graph showing the presentation of failure intensity information in this paper using the total time on test, TTT, showing demonstrated reliability for a subassembly showing early failures*

To calculate the TTT for LWK data, three considerations are necessary.

• For each time interval the WTs in the survey are considered representative of the entire of population. Therefore the sample reliability for each time interval is assumed to represent the reliability of the entire population. This hypothesis is necessary to overcome one of the major deficiencies of the data, the variable number of WTs in each time interval. In reality any reliability improvement or deterioration spreads throughout the population with a certain rate, indicated by the shape parameter β, as long as sample WTs are assumed randomly chosen from the entire population and the usage of each WT in the population is similar.

• Using TTT has the effect of stretching the curve on the abscissa. Since TTT depends on the number of turbines considered it has no absolute meaning, as calendar time would have. The abscissa t has significance only for the WT population being examined, however, by showing the cursor at the right of Fig. 10, calendar time can be inferred.

• As the intensity function interpolates data on TTT rather than calendar time, the fit produced is intrinsically weighted by the number of turbines in each period. A larger number of WTs results in a larger TTT interval and the fit constraint is stronger. When TTT is used rather than calendar time the abscissa stretches to a longer interval for more WTs surveyed and the scale parameter increases. In cases of early or constant failures the most important result is the demonstrated reliability, as shown in Fig. 10.

10 Appendix 2: WT configurations and subassemblies

The following Tables 3 and 4 detail the configuration and subassemblies of the WTs considered in this paper, including the nomenclature used in the surveys considered.

Table 3 Turbine control configurations considered in the paper

Speed control	Pitch control	Power control	WT models considered in the paper
fixed speed/Dual speed	none	passive stall regulation geared drive train with asynchronous generator	NEG Micon M530 TW600
fixed speed	yes, pitch to stall	active stall regulation geared drive train with asynchronous generator	Vestas V27 Nordex N52/54
limited variable speed	yes	geared drive train with asynchronous generator control using variable rotor resistance	Vestas V39
variable speed	yes	geared drive train with slip ring asynchronous generator control using a partly rated converter	Tacke TW1500, Bonus 1MW/54
variable speed	yes	direct drive with synchronous generator control using a fully rated converter	E40, E66

doi: 10.1049/iet-rpg:20080060

Table 4 Terminology used for WT subassemblies in the paper

This paper	WSD	WSDK	LWK
rotor	rotor	blades, hub	blades
air brake	air brake	air brake	rotor brake
mechanical brake	mechanical brake	mechanical brake	brake
main shaft	main shaft, bearings	axle/bearing, coupling	shaft/bearings
gearbox	gearbox	gearbox	gearbox
generator	generator	generator	generator
yaw system	yaw system	yaw system	yaw system
converter	electrical control	electrical control	electronics, inverter
hydraulics	hydraulics	hydraulics	hydraulics
electrical system	electrical system	grid	electrics
pitch control	pitch adjustment	mechanical control	pitch mechanism
other	anemometry, sensors, other	other	anemometry, sensors, other

doi: 10.1049/iet-rpg:20080060

Published in IET Renewable Power Generation
Received on 22nd January 2008
Revised on 11th April 2008
doi: 10.1049/iet-rpg:20080006

ISSN 1752-1416

Condition monitoring and fault diagnosis of a wind turbine synchronous generator drive train

W. Yang[1,2] *P.J. Tavner*[1] *M.R. Wilkinson*[3]

[1]*New and Renewable Energy Group, School of Engineering, Durham University, Durham DH1 3LE, UK*
[2]*Institute of Vibration Engineering, Northwestern Polytechnical University, Xi'an 710072, People's Republic of China*
[3]*Garrad Hassan and Partners Ltd, St Vincent Works, Bristol BS2 0QD, UK*
E-mail: peter.tavner@durham.ac.uk

Abstract: Some large grid connected wind turbines use a low-speed synchronous generator, directly coupled to the turbine, and a fully rated converter to transform power from the turbine to mains electricity. The condition monitoring and diagnosis of mechanical and electrical faults in such a machine are considered, bearing in mind that it has a slow variable speed and is subject to the stochastic, aerodynamic effects of the wind. The application of wavelet transforms is investigated in the light of the disadvantages of spectral analysis in processing signals subject to such stochastic effects. The technique can be used to monitor generator electrical and drive train mechanical faults. It is validated experimentally on a wind turbine condition monitoring test rig using a three-phase, permanent-magnet, slow-speed, synchronous generator, driven by a motor controlled by a model representing the aerodynamic forces from a wind turbine. The possibility of detecting mechanical and electrical faults in wind turbines by electrical signal and particularly power analysis is heralded.

1 Introduction

Wind power, with an average annual increase approaching 32% is, over the last 10 years [1], the world's fastest growing renewable energy source. Today, the largest wind turbines (2–5 MW) are becoming established as economically viable alternatives to traditional fossil-fuelled power generation. In some countries, such as Denmark, Germany and Spain, wind turbines have become a key part of the national power networks [2]. The reliability of these machines therefore has an influence on the performance of the electrical power system, although there is not always agreement about the benefits [3]. This heightens the need to improve reliability and the development of wind turbine condition monitoring and fault diagnosis can assist this. In particular, wind turbines are prone to failure from the fluctuating load and extreme environmental conditions to which they are subjected.

Some large wind turbines use a low-speed synchronous generator, directly coupled to the turbine, and a fully rated converter to transform power from the turbine to grid connected mains electricity. This paper considers the condition monitoring and diagnosis of mechanical and electrical faults in such a machine, bearing in mind that it has a slow variable speed, subject to the stochastic aerodynamic effects of the wind.

Condition monitoring technology has been developed in electric power production, aerospace, marine propulsion and process industries and is being applied to wind turbines. An example is the application of supervisory control and data acquisition systems (SCADA) to many wind farms, although most SCADA systems do not incorporate any condition monitoring and wind turbine condition monitoring has not yet developed its full potential. To advance the development, researchers and engineers have developed techniques specific to wind turbines, as reviewed in [4]. Among these techniques improved signal processing has considerable potential because of its convenience and low per unit cost. To date, the majority of wind turbine condition monitoring techniques use Fourier transforms (FT), [4–6], which have

limited success dealing with non-stationary signals. Larger wind turbines are driven at variable speed; both electrical and mechanical signals from wind turbines are non-stationary in the time and frequency domains, and so more advanced signal analysis should be used. The wavelet transform (WT) is applicable here because of its capability to analyse non-stationary signals and success demonstrated in other industrial applications [7, 8].

In this paper, the application of WTs to condition monitoring and fault diagnosis is investigated for a wind turbine subject to varying torque from the wind resource. At this stage, no consideration is given to the effect that a varying grid system would also have on the condition monitoring signals, as that will be the subject of later investigation.

Both the discrete wavelet transforms (DWT) and the continuous wavelet transforms (CWT) are employed in this work.

The DWT is used for noise cancellation, as drive train signals from wind turbines are noise rich and this noise can be difficult to remove using conventional filters with fixed cut-off frequencies. The CWT is then used for feature extraction.

The use of the WT for condition monitoring and fault diagnosis in wind turbines will be demonstrated by a series of experiments on a wind turbine condition monitoring test rig with a synchronous generator.

The remaining parts of the paper are organised as follows. In Section 2, a new criterion for monitoring the running condition of the wind turbine with a synchronous generator is proposed. In Sections 3.2 and 3.3, drive train mechanical and generator electrical faults are diagnosed with the aid of the CWT. In Section 3.4, the possibility of detecting drive train mechanical faults by electrical signal analysis is investigated. In Section 4 conclusions are given.

2 Condition monitoring synchronous generator

2.1 Condition monitoring criterion

When a synchronous machine is operated as a generator, the prime mover drives the generator at synchronous speed, ω_s, as shown in Fig. 1. In steady state, the mechanical torque T_{pm} of the prime mover balances with the electromagnetic torque T_{em} produced by the generator and the electro-mechanical loss torque T_{loss}, that is

$$T_{pm} = T_{em} + T_{loss} \tag{1}$$

For a well designed, large synchronous generator, with an efficiency in excess of 96%, the loss torque T_{loss} will be small

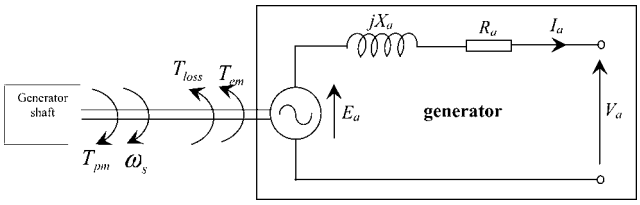

Figure 1 *Synchronous machine operated as a generator*

and can be neglected. Accordingly, (1) can be rewritten as

$$T_{pm} \simeq T_{em} \tag{2}$$

The electromagnetic torque produced by a three-phase non-salient pole synchronous machine is [9]

$$T_{em} = 3\frac{|\bar{E}_a \times \bar{V}_a|}{\omega_s X_a} = 3\frac{E_a V_a}{\omega_s X_a}\sin\ \delta \tag{3}$$

where $\bar{E}_a$ refers to the phasor per-phase induced emf in the winding, $\bar{V}_a$ the phasor per-phase terminal voltage, X_a the synchronous reactance and δ the load angle between $\bar{V}_a$ and $\bar{E}_a$. From Fig. 1, the circuit equation can be derived as

$$\bar{V}_a = \bar{E}_a - (jX_a + R_a)\bar{I}_a \tag{4}$$

where $\bar{I}_a$ is the phase current. As the winding resistance R_a in large synchronous generators is much smaller than the synchronous reactance X_a, (4) can be approximately expressed as

$$\bar{V}_a \simeq \bar{E}_a - jX_a\bar{I}_a \tag{5}$$

Substituting (5) into (3), gives

$$\begin{aligned} T_{em} &= 3\frac{|\bar{E}_a \times (\bar{E}_a - jX_a\bar{I}_a)|}{\omega_s X_a} \\ &= 3\frac{E_a \cdot |(\bar{E}_a - jX_a\bar{I}_a)|}{\omega_s X_a}\sin\ \delta \end{aligned} \tag{6}$$

For a phase winding with N turns in series, the induced emf from Faraday's law is

$$E_a = -Nk_w\frac{d\phi}{dt} \tag{7}$$

where k_w is the winding factor, which includes the distribution and pitch factors; $\phi = \hat{\phi}\sin(\omega_{se}t)$ is the flux per pole of a round rotor revolving at angular velocity ω_s,where ω_{se} refers to the electrical supply frequency and $\omega_s = \omega_{se}/p$ where p is the number of pole pairs. As the flux revolves, the emf in the phase winding can be expressed as

$$E_a = -Nk_w\omega_{se}\hat{\phi}\cos(\omega_{se}t) \tag{8}$$

doi: 10.1049/iet-rpg:20080006

and

$$E_a \cdot \left|\left(\bar{E}_a - jX_a\bar{I}_a\right)\right| \propto E_a^2 = N^2 k_w^2 \omega_{se}^2 \hat{\phi}^2 \cos^2(\omega_{se}t) \quad (9)$$

Further substitution of (9) into (6), gives

$$T_{em}(t) \propto 3\frac{N^2 k_w^2 \omega_{se}^2 \hat{\phi}^2 \cos^2(\omega_{se}t)}{\omega_s X_a} \sin\delta$$
$$= 3\frac{N^2 k_w^2 \omega_s \hat{\phi}^2 \cos^2(\omega_{se}t)}{p^2 X_a} \sin\delta \quad (10)$$

when load, δ, and flux, ϕ, are constant, then

$$T_{em} \propto \frac{\omega_s}{X_a} \quad (11)$$

In steady-state conditions T_{pm} is approximately balanced with T_{em} ; see (2), then

$$T_{pm} \propto \frac{\omega_s}{X_a} \quad (12)$$

This is why the mechanical torque T_{pm} can be regarded as a valid indicator of the running condition of synchronous machines. However, as large wind turbines operate at variable rotational speed, the effects of mechanical/electrical faults in T_{pm} are hidden and difficult to distinguish. Therefore to remove the effect of the variable speed, a condition monitoring criterion C is proposed

$$C = \frac{T_{pm}}{\omega_r} \quad (13)$$

where $\omega_r = \ell\omega_s$ refers to the rotational speed of the shaft, ℓ a positive constant representing the gear ratio of a gearbox if fitted. All drive train mechanical faults of the wind turbine, for example in the shaft or gearbox, will have a response in C, and owing to $C \propto 1/X_a$ all electrical faults, for example stator and rotor winding faults, will also have response in C. The criterion C is therefore versatile for machine condition monitoring and can be used to monitor drive train mechanical and generator electrical faults.

2.2 Test rig

The proposed criterion was demonstrated by experiments performed on a wind turbine condition monitoring test rig with a synchronous generator, shown in Fig. 2 [9]. The test rig comprised a 50 kW DC drive motor for speed control, a two-stage gearbox and a three-phase generator. The synchronous generator used was slightly unusual, being a permanent magnet machine, the small-scale prototype of a lightweight synchronous machine originally designed for application on large direct-drive wind turbines [10]. The machine had 84 coils on the stator and 108 permanent magnets on the rotor and the output of each coil was rectified, then coupled to a DC bus and fed to a resistance load bank. The load was therefore fixed and did not represent the variable condition of an infinite bus. However, the machine had advantages in that it was a synchronous machine that allowed easy application of electrical and mechanical faults.

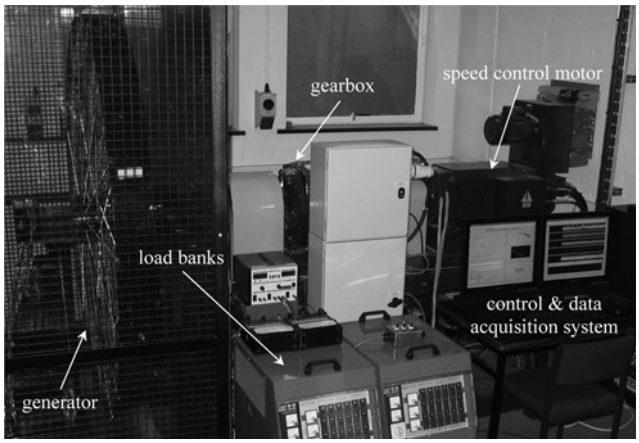

Figure 2 *Test rig of the wind turbine with a synchronous generator*

The system was instrumented using LabVIEW such that a variety of wind speed inputs could be applied and the relevant signals could be collected from the drive train and terminals of the generator. In the experiments, the speed of the DC motor was controlled by an external model, in which the properties of both natural wind and the turbine rotor aerodynamic behaviour were incorporated [11]. Both the generator electrical and wind turbine mechanical faults could be simulated on the test rig. A number of transducers had been fitted to the rig to measure the shaft rotational speed, torque, vibration and the load DC current and voltage of the generator, as illustrated in Fig. 3.

Shorted-coil faults in the stator winding could be applied to the generator with the aid of remote relays, installed on the stator, to enable either one or more coils to be shorted or connected normally; the arrangement is shown in Fig. 4.

2.3 Validity of the criterion

The effectiveness of criterion C in monitoring the running condition of the wind turbine generator is demonstrated in Fig. 5, by measuring the torque-speed characteristic of the generator at half load and full-load before and after the three coils were shorted. The results from the half-load test with and without faults are compared in Fig. 5.

From Fig. 5, it is confirmed that for a direct-drive wind turbine synchronous generator:

i. there is a linear positive proportional relationship between mechanical torque T_{pm} and shaft speed ω_s and the relationship depicted in (12) is correct;

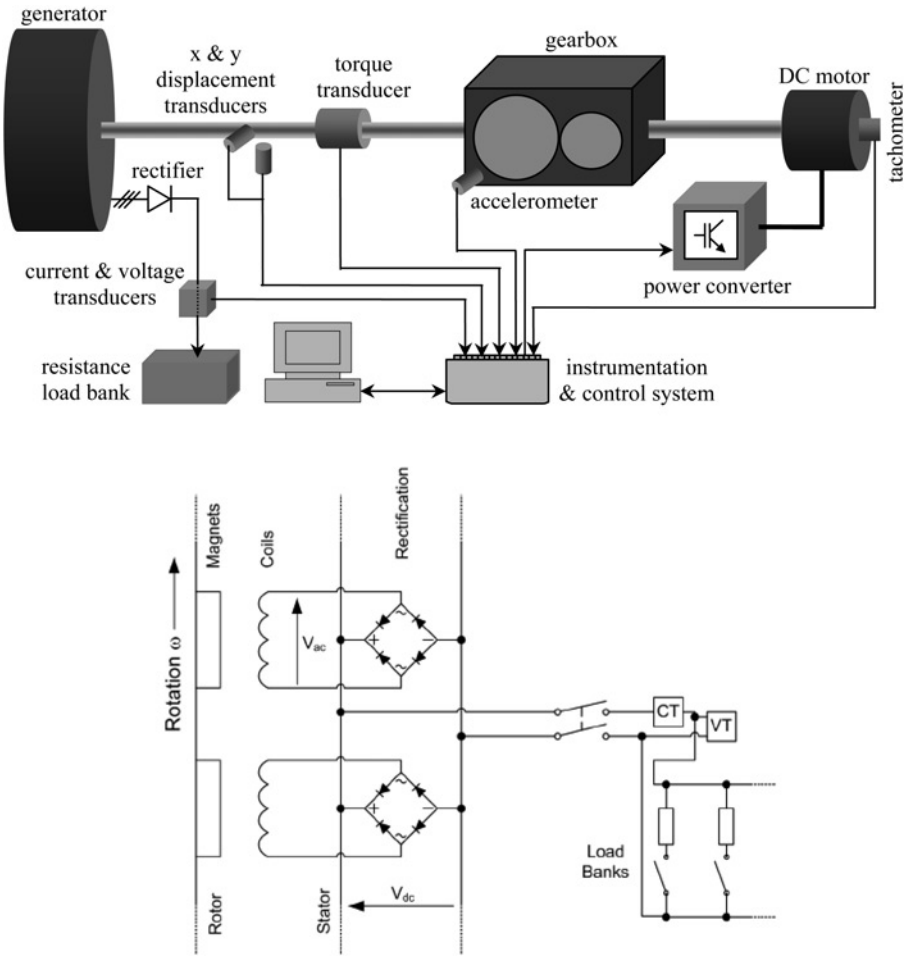

Figure 3 *Locations of the transducers fitted to the test rig and circuit arrangement of the synchronous generator*

ii. the criterion C is sensitive for monitoring changes in wind turbine running condition.

The transient load and dynamic torque conditions experienced by a wind turbine indicate that T_{pm} is not always balanced with T_{em} and transient changes in T_{loss} must also be taken into account. However, observation of the torque-speed characteristic under transient conditions shows that the quantity C can still be considered a valid condition monitoring criterion, a full transient analysis being beyond the scope of this paper.

Further experiments will reveal that criterion C is also effective in detecting the presence of drive train mechanical faults.

2.4 Experiments demonstrating use of the criterion

In the first experiments, the generator was partially loaded with an aerodynamic load, representing a real wind driving condition, over a long period of 900 s and three stator coils were successively shorted and unshorted by operating the remote relays. The corresponding shaft rotational speed and torque signals were monitored at a data rate of 1 kHz as shown in Fig. 5. The shaft speed was derived from a DC tachometer, which had significant intrinsic noise, and was converted to the generator speed using the gear ratio. In Fig. 6, the upper subplot shows the converted generator shaft speed; the lower subplot shows the torque.

2.5 Wavelet theory

From Fig. 6, the variations because of wind driving are clearly visible and the noise originating from various sources is present in both speed and torque signals, regardless of generator condition. This significantly increases the difficulty of condition monitoring the wind turbine. To reduce the noise WTs were employed. Two basic approaches are possible to reduce noise, the first based on the singularity information analysis with wavelets [12] and the second on thresholding wavelet coefficients [13]; the second was adopted in this work, in view of its much simpler computational algorithm. Wavelets are families of functions obtained by the dilation and translation of a mother wavelet $\psi(t)$. The daughter wavelets $\psi_{a,b}(t)$ at scale a and translation b may be expressed mathematically as

$$\psi_{a,b}(t) = \frac{1}{\sqrt{a}}\psi\left(\frac{t-b}{a}\right) \tag{14}$$

doi: 10.1049/iet-rpg:20080006

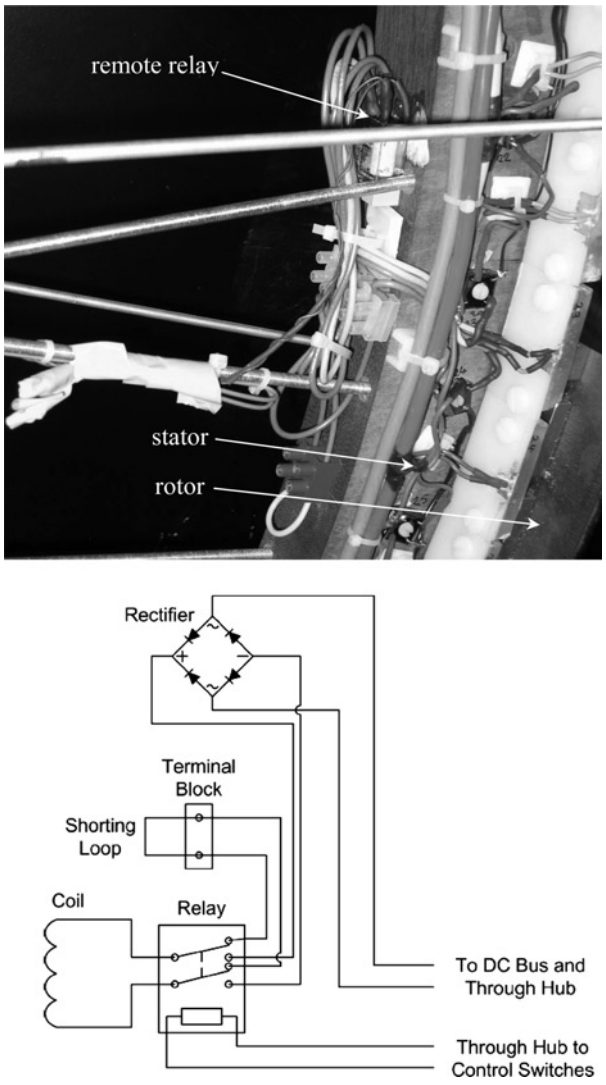

Figure 4 *Remote relay for simulating short-coil fault and circuit arrangement*

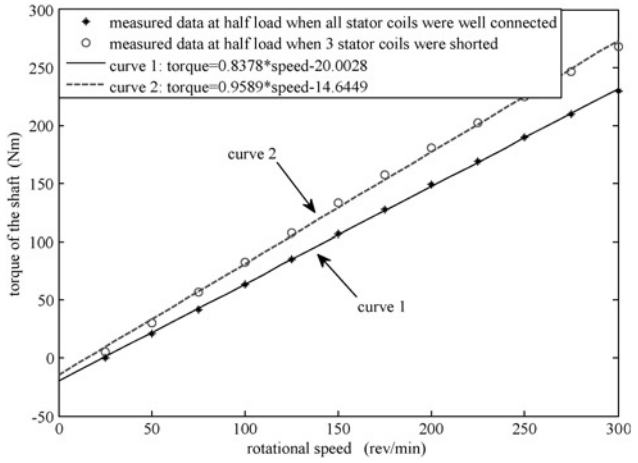

Figure 5 *Generator torque-speed curves before and after the coils were shorted*

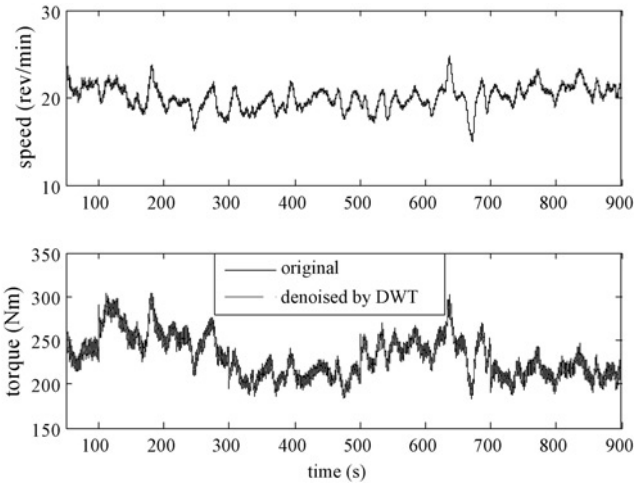

Figure 6 *Shaft rotational speed and mechanical torque signals*

The CWT of a signal $x(t)$ is implemented by the following equation

$$\mathrm{CWT}_{a,b}(t) = \int_{-\infty}^{\infty} x(t)\psi_{a,b}(t)\,\mathrm{d}t \tag{15}$$

Wavelet-based noise reduction is accomplished by using the DWTs. The dyadic DWT is a special form of the CWT with dilation $a = 2^j$ and translation $b = 2^j n$, that is

$$\mathrm{DWT}_{j,n}(t) = \mathrm{CWT}_{2^j,2^j n}(t) = \frac{1}{\sqrt{2^j}}\int_{-\infty}^{\infty} x(t)\psi\left(\frac{t}{2^j} - n\right)\mathrm{d}t, \quad (j, n \in Z) \tag{16}$$

The practical calculation of the DWT is conducted through a digital filter tree combined with decimation blocks [12], as shown in Fig. 7.

In the figure, $g(t)$ is a low-pass filter and $h(t)$ is a high-pass filter. At each level of the filter tree, the input is decomposed into two frequency bands; the high-frequency band shows the 'details' and the low-frequency band the 'smoothed approximations' of the input signal. Finally, the signal $x(t)$ is expressed in the following discrete form

$$x(t) = \sum_{n=-\infty}^{\infty} a_{0,n}(t)g_{0,n}(t) + \sum_{j=0}^{\infty}\sum_{n=-\infty}^{\infty} d_{j,n}(t)h_{j,n}(t) \tag{17}$$

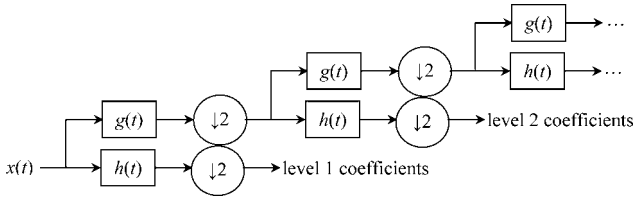

Figure 7 *DWT of the signal x(t)*

where

$$\begin{cases} a_{0,n}(t) = \int_{-\infty}^{\infty} x(t) g_{0,n}(t)\,\mathrm{d}t \\ d_{j,n}(t) = \int_{-\infty}^{\infty} x(t) h_{j,n}(t)\,\mathrm{d}t \end{cases} \tag{18}$$

with

$$\begin{cases} g_{j,n}(t) = 2^{j/2} g(2^j t - n) \\ h_{j,n}(t) = 2^{j/2} h(2^j t - n) \end{cases}, \quad (j \in Z^+, n \in Z) \tag{19}$$

After applying the thresholding technique, the reconstructed de-noised signal, $\hat{x}(t)$ can be obtained by using the same pyramidal scheme as that used for the DWT. In practice, two thresholding approaches are possible. They are

i. Hard thresholding

$$\hat{d}_{j,n}(t) = \begin{cases} d_{j,n}(t) & \text{if} \quad \left|d_{j,n}(t)\right| > \theta \\ 0 & \text{if} \quad \left|d_{j,n}(t)\right| \le \theta \end{cases} \tag{20}$$

ii. Soft thresholding

$$\hat{d}_{j,n}(t) = \begin{cases} d_{j,n}(t) - \theta & \text{if} \quad d_{j,n}(t) > \theta \\ 0 & \text{if} \quad \left|d_{j,n}(t)\right| \le \theta \\ d_{j,n}(t) + \theta & \text{if} \quad d_{j,n}(t) < \theta \end{cases} \tag{21}$$

In the equations, $\hat{d}_{j,n}(t)$ are the thresholded values of $d_{j,n}(t)$. The threshold θ can be estimated as follows [13]

$$\theta = \sigma\sqrt{2\,\log(L)} \tag{22}$$

Where σ is an estimate of the noise level, L the number of wavelet coefficients in the current level. Then, the de-noised signal $\hat{x}(t)$ may be constructed by using the following equation

$$\hat{x}(t) = \sum_{n=-\infty}^{\infty} \hat{a}_{0,n}(t) g_{0,n}(t) + \sum_{j=0}^{\infty} \sum_{n=-\infty}^{\infty} \hat{d}_{j,n}(t) h_{j,n}(t) \tag{23}$$

The calculation of $\hat{a}_{0,n}(t)$ is similar to that of $\hat{d}_{j,n}(t)$. The hard thresholding approach is computationally simpler, but the use of a fixed threshold value inevitably leads to discontinuities in the de-noised signal. By contrast, soft thresholding solves the problem by using a variable threshold; for this reason, it was used so that the smoothness of the de-noised signal could be guaranteed. The noise cancellation operation may be fulfilled using the MATLAB functions 'wavedec.m' and 'waverec.m', the former for multilevel wavelet decomposition and the latter for multilevel wavelet reconstruction. The de-noised torque signal, obtained using Daubechies mother wavelet 'db16', is also shown in Fig. 6, where the noise in the original signals has been dramatically removed. As 'db16' is a well defined mother wavelet and its coefficients can be accessed by running MATLAB function 'WFILTERS.m', its detailed description is not repeated here. The criterion C is then calculated by using the de-noised signals and the results are shown in Fig. 8, in which C derived from the original signals are also shown for comparison. The signal in Fig. 8 reduces with time because of the rising temperature of the generator windings during the test, which increases the generator winding resistance.

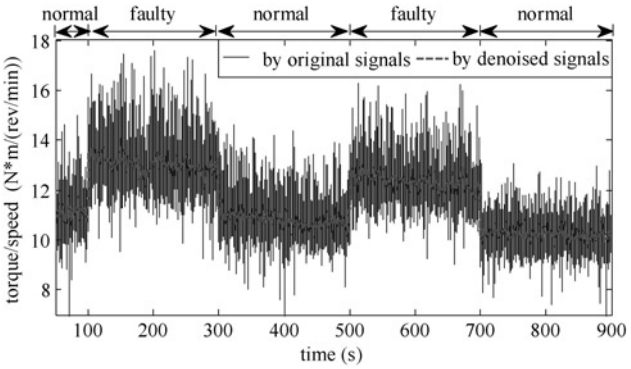

Figure 8 *Monitoring results using criterion C*

From Fig. 8, it is found that when the three coils are shorted, the criterion C gives increased sensitivity, which is explicable through (12) and (13) that the shorted coils reduce the generator synchronous reactance X_a, which therefore results in a larger mechanical torque T_{pm} during the fault to achieve the same shaft rotational speed ω_r. The comparison of the results shown in Figs. 5 and 8 show that the criterion C becomes more sensitive to changes in machine condition when the generator is fully loaded.

3 Wind turbine diagnosis with criterion and wavelets

3.1 General

The stochastic variations in the time domain signals in Fig. 6 make it difficult to extract their features using conventional spectral analysis techniques, such as the fast FT (FFT) and power spectral density (PSD). Although the FFT, the PSD and other techniques based upon them, for example the short-time FT and FFT-based bispectrum/bicoherence, are widely used in the literature[5, 6, 9], the CWT is different from these conventional techniques, distinguished by its multiple resolution in both time and frequency domains and its powerful capability to analyse non-stationary signals. These properties indicate that the CWT is ideal for dealing with condition monitoring and fault diagnosis problems in wind turbine signals. In the following sections, the potential capability of the CWT to diagnose wind turbine faults is investigated. This work will be of importance for improving the reliability of wind turbines; however, the penalty with wavelet techniques is the greatly increased computational effort required.

doi: 10.1049/iet-rpg:20080006

3.2 Diagnosis of generator electrical fault

The CWT is first used to investigate generator electrical faults. When three coils are shorted simultaneously to simulate a winding fault, asymmetry is introduced in the magnetic field, see Section 2.1.

As shown in Fig. 9, the three coils are distributed at equal 37° angular intervals. In the experiment, the generator was partially loaded over a shorter period of 50 s and the three stator coils were successively shorted and unshorted by controlling the remote relays. The corresponding generator speed, current, voltage and power signals were then monitored at 1 kHz over the shorter period again, to limit the computational burden when carrying out the wavelet analysis, as shown in Fig. 10.

According to [14], the characteristic frequencies $k\omega_{se}(k = 1, 3, \ldots)$ will be present in the phase current signal when a stator winding fault occurs in a synchronous machine, where ω_{se} refers to the electrical supply frequency. For the synchronous machine shown in Fig. 2

$$\omega_{se} = p\omega_s \tag{24}$$

$2p = 108$, the number of magnets installed on the rotor of the generator.

When the three coils are shorted, low-frequency amplitude modulation is introduced into the electrical signals. The modulating fault frequency ω_f can be estimated by the following equation

$$\omega_f = k \cdot \frac{M.\alpha}{360^\circ} \cdot \omega_{se}, \quad k = 2, 4, \ldots \tag{25}$$

where $\alpha = 37^\circ$ is the circumferential angle between the coils being shorted and $M = 3$ is the number of coils being shorted; note that $\alpha = 360^\circ$ when $M = 84$. From (25), the characteristic shorted coil fault frequency, when $k = 1$, is

$$\omega_f = k \cdot \frac{M \cdot \alpha}{360^\circ} \cdot p.\omega_s = \frac{3 \times 37^\circ}{360^\circ} \times 108 \times \omega_s = 33.3\omega_s \tag{26}$$

From the speed signal, Fig. 10, the characteristic fault frequency is estimated, that is, $\omega_f = 33.3\omega_s = 33.3 \times 0.3 \simeq 10\,\text{KHz}$.

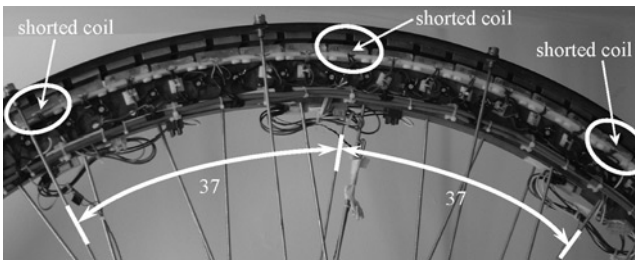

Figure 9 *Three coils being shorted*

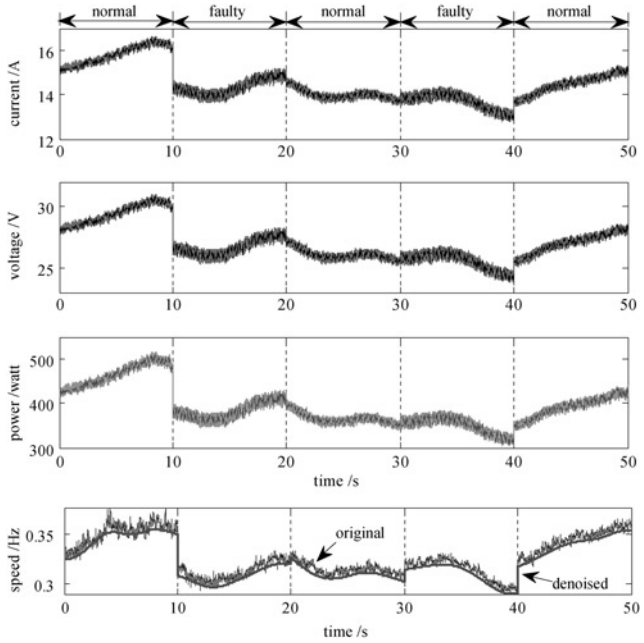

Figure 10 *Generator speed and electrical signals when stator coils were successively shorted*

From this, the electrical signals shown in Fig. 10 are analysed using the CWT and the results are shown in Fig. 11.

From Fig. 11*a*, it is clearly seen that when the coils are shorted, a characteristic frequency component does appear at 10 Hz in the time-frequency map of the current signal; and when the short is removed, the characteristic frequency component disappears. Therefore the observed phenomenon matches the theoretical prediction. Thus, it can be said that the feature characterising the stator-winding fault of the generator has been correctly identified from the current signal using the CWT.

The same fault-related characteristic frequency component also observed from the CWT results for power shown in Fig. 11*b*. This latter experiment demonstrates that the CWT of the current or power can diagnose electrical faults in the wind turbine synchronous generator, even though the electrical signals are harmonic-rich information because of the variable speed and stochastic aerodynamic load.

It is necessary to note that in Fig. 11, the frequency components appearing at about 25 and 33 Hz account for the slotting frequencies introduced, respectively, by the 84 coils installed on the generator stator and the 108 magnets on the generator rotor, that is, $M\omega_s = 84 \times 0.3 \simeq 25(\text{Hz})$ and $p\omega_s = 108 \times 0.3 \simeq 33(\text{Hz})$.

3.3 Diagnosis of drive train mechanical fault

The CWT is next used to investigate mechanical faults in the drive train of the test rig. Our test rig drive train incorporated

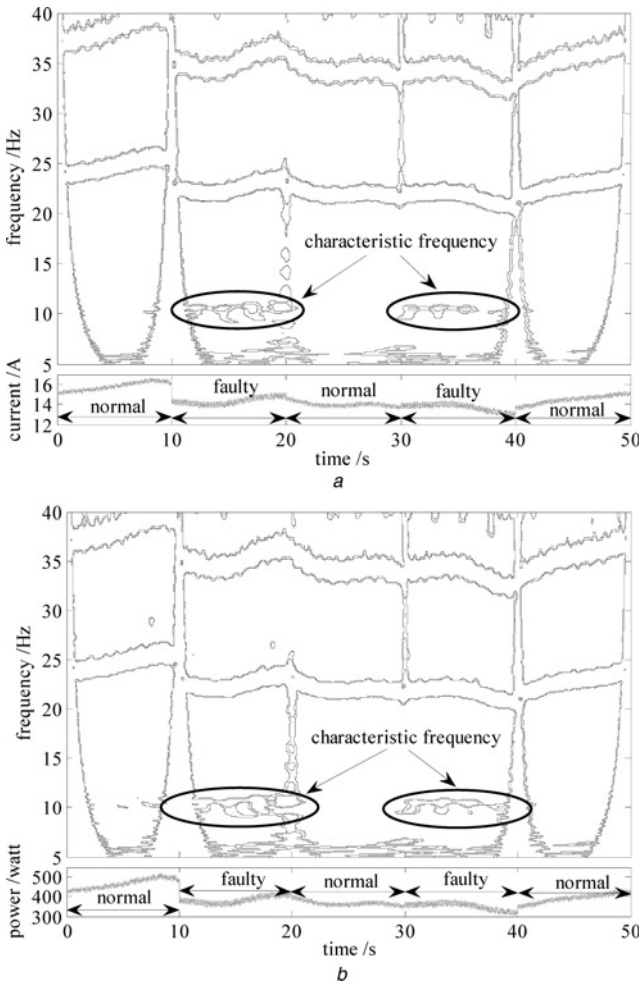

Figure 11 *CWTs of the electrical signals*

a CWT of the current signal
b CWT of the power signal

a gearbox, to allow it to be driven by a high-speed DC motor, although a full-size wind turbine direct drive synchronous generator drive train would not. However, we can use our test rig gearbox as an exemplar for developing techniques for detecting mechanical faults occuring in the wind turbine drive trains. When the generator coils were connected and shorted periodically, the vibration of the drive train gearbox was also monitored. The time response of the acceleration signal with the corresponding current signal of the generator and the generator shaft rotational speed signal are shown in Fig. 12. In the experiment, the generator was partially loaded for an even shorter period of 5 s and the three stator coils were successively shorted and unshorted by controlling the remote relays. This was necessary because of the increased sampling rate needed for the accelerometer, 5 kHz, and to limit the computational burden when carrying out the wavelet analysis. The acceleration signal shown in Fig. 12 is analysed by using the CWT and the results are shown in Fig. 13.

Fig. 13 discloses that a low-frequency amplitude modulation is present in the acceleration signal, regardless of the connection

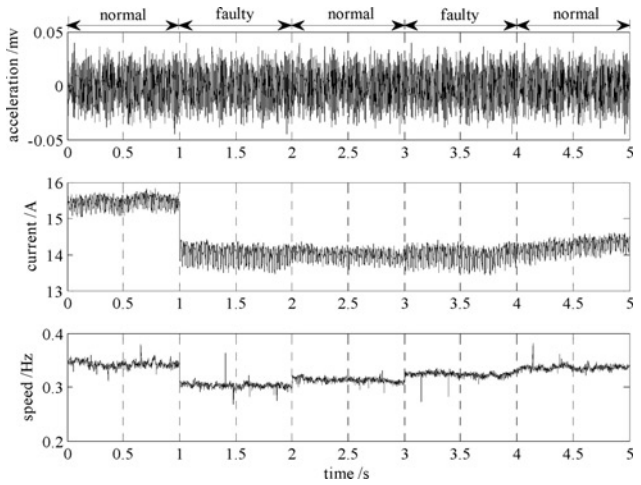

Figure 12 *Acceleration signal of the drive train gearbox*

state of the stator coils. The frequency period of the modulating signal is ~0.25 s in the first second and then 0.3 s in the following 4 s. As the modulation is independent of the coil connection state, it cannot originate from the electrical fault but must be caused by a mechanical fault. To discover its root cause, the mechanical structure of the drive train gearbox, shown in Fig. 14, is investigated.

The transmission path of the gearbox is as follows

$$\text{input (DC motor)} \rightarrow \left(\frac{Z_1}{Z_2}\right) \rightarrow \left(\frac{Z_3}{Z_4}\right) \rightarrow \text{output (generator)}$$

therefore

$$\omega_s = \omega_r \cdot \frac{Z_1}{Z_2} \cdot \frac{Z_3}{Z_4} \tag{27}$$

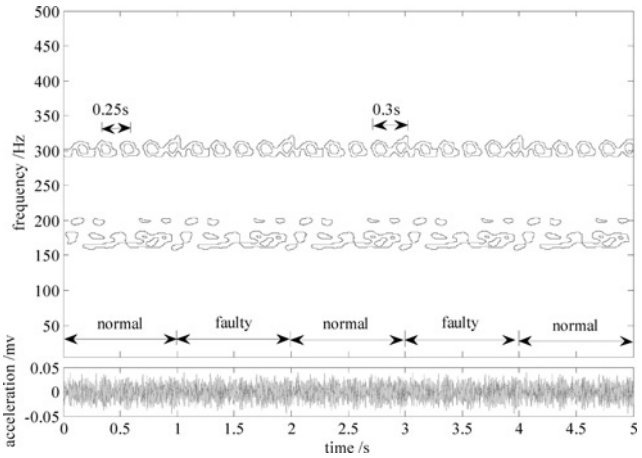

Figure 13 *CWT of the gearbox acceleration signal*

doi: 10.1049/iet-rpg:20080006

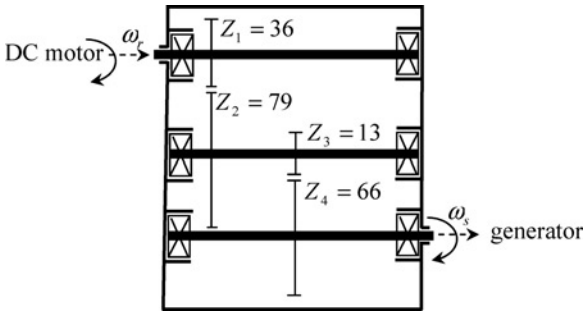

Figure 14 *Diagram of the gearbox used in the drive train of the wind turbine*

According to the speed signal in Fig. 12 and using (27), the gear Z_1 rotational frequency should be

$$\omega_r = \omega_s \cdot \frac{Z_2}{Z_1} \cdot \frac{Z_4}{Z_3} = (0.3 \sim 0.35) \times \frac{79}{36} \times \frac{66}{13} = 3.3 \sim 3.9(Hz) \quad (28)$$

that indicates a rotational cycle of 0.26–0.3 s, which matches the period of the modulation present in Fig. 13. According to the gearbox diagnosis experience [15], this phenomenon suggests that the modulation probably originates from an eccentricity fault in gear Z_1. This is confirmed by the presence of the typical characteristic gear-eccentricity fault frequency $n\omega_m + m\omega_r$ in the time-frequency map shown in Fig. 13, where, $n, m \in Z^+$, and ω_m represents the mesh frequency of the gear being investigated. In other words, an eccentricity fault in gear Z_1 is confirmed by the presence of the characteristic frequency 300 Hz, obtained when $n = 2$ and $m = 3$.

This experiment demonstrates that the CWT of the accelerometer signal can play a vital role in diagnosing drive train mechanical faults in wind turbines.

3.4 Diagnosis of mechanical fault by electrical analysis

The application of a torque transducer to a wind turbine would be prohibitively expensive, however, its global monitoring capability is attractive, but the analysis of electrical terminal signals, such as current and power, would be a viable alternative. These signals, particularly current, have been shown [14, 16] to be effective for the condition monitoring and diagnosis of electrical and mechanical faults in electrical machinery. However, research on their effectiveness for diagnosing mechanical faults in machinery connected to an electric machine demonstrates that they work [16] but are not proven in the practical environment and not yet applied to wind turbines.

It is easy to understand that mechanical drive train faults will lead to abnormal changes of torque T_{pm}, although according to (2) and (10), once T_{pm} changes, the phase current I_a of the generator will respond accordingly. Moreover, because of the linear relationship between T_{pm} and I_a, the characteristic frequency of a mechanical fault will also be present in the current signal. Thus, in theory, a drive train mechanical fault can be detected by investigating the generator current. In the following section, this prediction will be verified by analysing the current signal shown in Fig. 12 with the aid of a CWT and the results are shown in Fig. 15.

From Fig. 15*a*, it is shown that the amplitude-modulation phenomenon presented in Fig. 13 is observed in the CWT map of the current signal, as predicted above. Moreover, the characteristic frequency 300 Hz also appears, regardless of the connection state of the coils. These phenomena confirm the effectiveness of using the time-frequency characteristics of generator electrical signals to detect mechanical faults.

However, the power signal has been shown in [14, 17] to be a more generic condition monitoring signal than current

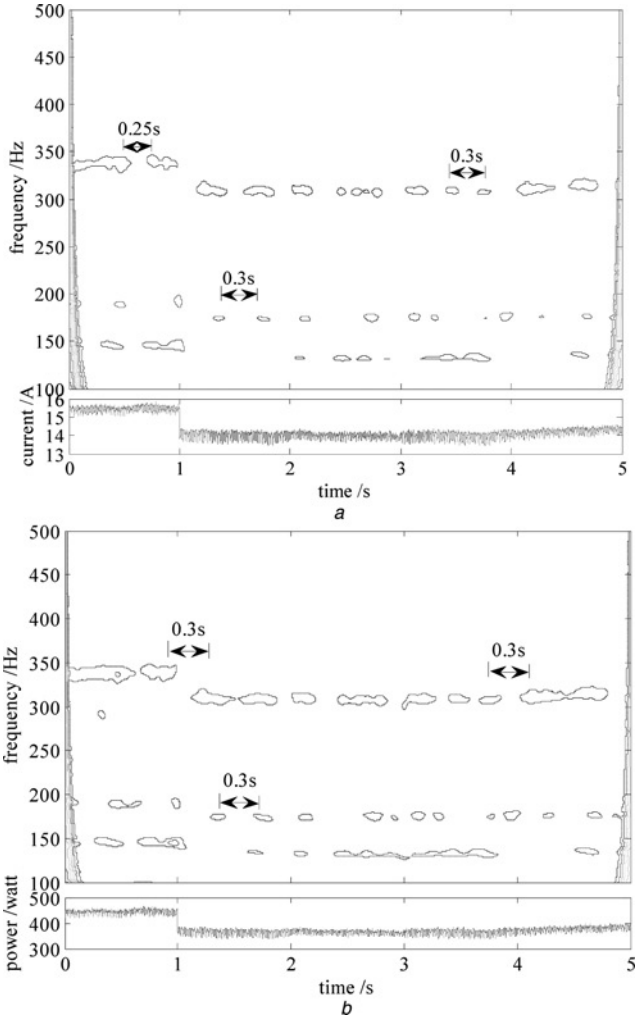

Figure 15 *CWT maps of the electrical signals*

a Current signal
b Power signal

and is already monitored in the wind turbine for energy production purposes. The CWT map in Fig. 15*b* shows the amplitude-modulation phenomenon presented in Fig. 13.

The experimental results of Fig. 15 suggest that the CWT is a promising tool for accomplishing this task but it is computationally intensive.

4 Conclusions

The application of WTs to the condition monitoring and fault diagnosis of a synchronous wind turbine generator drive train has been investigated. Wind turbine signals contain harmonic-rich, instantaneous information because of the variable, stochastic aerodynamic forces on the machine. The effectiveness of the proposed approach has been validated by both theoretical analysis and experimental results from a test rig on signals subject to these stochastic variations. The following conclusions have been reached.

- The condition monitoring criterion proposed, based on the torque-speed characteristic of the synchronous machine, was tested on the wind turbine condition monitoring test rig and was shown to be effective for detecting electrical faults in a direct drive generator wind turbine drive train.

- The criterion overcomes the stochastic effects of the highly variable signals in the assessment of wind turbine condition.

- The use of DWT reduced the noise in the highly variable shaft torque and speed signals, and enhanced the effectiveness of the proposed condition monitoring criterion.

- The CWT can extract time-frequency features correctly from the highly variable wind turbine signals.

- The experiment proves that it is also feasible to detect drive train mechanical faults by analysing electrical signals from the generator and, in particular, the power signal has been shown to be valid. This will be simpler and cheaper to obtain from a wind turbine generator than torque, vibration or proximeter measurements.

- The remaining problem will be how to analyse the power signal correctly using a valid signal processing technique. The work presented in this paper suggests that the CWT is a promising and effective technique for this purpose. Therefore the WT will play a role in solving the condition monitoring and fault diagnosis problems in wind turbines.

- The condition monitoring test rig has been demonstrated to be an effective way of testing condition monitoring algorithms.

5 Acknowledgments

Wenxian Yang was funded by the EPSRC Supergen Wind Energy Technologies Consortium, EP/D034566/1.

Michael Wilkinson was funded under the EPSRC Engineering Doctorate Scheme, GR/R99737/01, on Power Electronics Machines and Drives at Newcastle University but supervised at Durham University.

The Wind Turbine Condition Monitoring Test Rig was funded by the New and Renewable Energy Centre (NaREC), Blyth, Northumberland for which support the authors are grateful.

The authors are grateful for the advice and collaboration of, Drs Simon Watson and Xiang Jianping of Loughborough University.

Durham and Loughborough Universities, Garrad Hassan and NaREC are partners in the Supergen Wind Energy Technologies Consortium funded by the EPSRC.

6 References

[1] CLARK T.J., BAUER R.F., RASMUSSEN J.R.: 'Wind power comes of age', *Orbit*, 2004, Second Quarter, pp. 20–27

[2] TAVNER P.J., XIANG J., SPINATO F.: 'Reliability analysis for wind turbines', *Wind Energy*, 2007, **10**, pp. 1–18

[3] E.ON NETZ: 'Wind report 2004'. Technical Report, 2004

[4] HAMEED Z., HONG Y.S., CHO Y.M., AHN S.H., SONG C.K.: 'Condition monitoring and fault detection of wind turbines and related algorithms: a review', *Renew. Sustain. Energy Rev.*, 2007 (Accepted for publication)

[5] CASELITZ P., GIEBHARDT J.: 'Rotor condition monitoring for improved operational safety of offshore wind energy converters', *ASME Trans. J. Solar Energy Eng.*, 2005, **127**, pp. 253–261

[6] JEFFRIES W.Q., CHAMBERS J.A., INFIELD D.G.: 'Experience with bicoherence of electrical power for condition monitoring of wind turbine blades', *IEE Proc., Vis. Image Signal Process.*, 1998, **45**, (3), pp. 141–148

[7] YANG W.X., TSE P.W.: 'An advanced strategy for detecting impulses in mechanical signals', *Trans. ASME J. Vib. Acoust.*, 2005, **127**, (3), pp. 280–284

[8] TSE P.W., YANG W.X., TAM H.Y.: 'Machine fault diagnosis through an effective exact wavelet analysis', *J. Sound Vib.*, 2004, **277**, pp. 1005–1024

doi: 10.1049/iet-rpg:20080006

[9] SARMA M.S.: 'Synchronous machines, their theory, stability, and excitation systems' (Gordon and Breach Science Publisher, New York, 1979)

[10] SPOONER E., GORDON P., BUMBY J.R., FRENCH C.D.: 'Lightweight ironless-stator PM generators for direct-drive wind turbines', *IEE Proc. Electr. Power Appl.*, 2005, **152**, (1), pp. 17–26

[11] WILKINSON M.R., SPINATO F., TAVNER P.J.: 'Condition monitoring of generators & other subassemblies in wind turbine drive trains'. IEEE Int Conf SDEMPED, Cracow, September 2007

[12] MALLAT S., HWANG W.L.: 'Singularity detection and processing with wavelets', *IEEE Trans. Inf. Theory*, 1992, **38**, pp. 617–643

[13] DONOHO L.D.: 'De-noising by soft-thresholding', *IEEE Trans. Inf. Theory*, 1995, **41**, pp. 613–627

[14] TAVNER P.: 'Review of condition monitoring of rotating electrical machines', *IET Electr. Power Appl.*, 2008, **2**, (4), pp. 215–247

[15] FAN X.F., ZUO M.J.: 'Fault diagnosis of machines based on D-S evidence theory. Part 2: application of the improved D-S evidence theory in gearbox fault diagnosis', *Pattern Recognit. Lett.*, 2006, **27**, pp. 377–385

[16] RAN L., YACAMINI R., SMITH K.S.: 'Torsional vibrations in electrical induction motor drives during start up', *Trans. ASME J. Vib. Acoust.*, 1996, **118**, (2), pp. 242–251

[17] TRZYNADLOWSKI A.M., LEGOWSKI S.F., GHASSEMZADEH M.: 'Diagnostics of mechanical abnormalities in induction motors using instantaneous electric power', *IEEE Trans. Energy Convers.*, 1999, **14**, (4), pp. 1417–1423

Published in IET Electric Power Applications
Received on 23rd June 2007
Revised on 13th November 2007
doi: 10.1049/iet-epa:20070280

ISSN 1751-8660

Review of condition monitoring of rotating electrical machines

P.J. Tavner

School of Engineering, Durham University, South Road, Durham, DH1 3LE, UK
E-mail: peter.tavner@durham.ac.uk

Abstract: Condition monitoring of rotating electrical machinery has received intense research interest for more than 30 years. However, electrical machinery has been considered reliable and the application of fast-acting digital electrical protection has rather reduced the attention operators pay to the equipment. The area based upon current literature and the author's experience is reviewed. There are three restrictions: only on-line techniques for rotating machines are dealt with; specific problems of variable speed drives are not dealt with, except in passing; conventional rather than emerging brushless, reluctance and permanent magnet machines of unusual topology are concentrated upon. The art of condition monitoring is minimalist, to take minimum measurements from a machine necessary to extract a diagnosis, so that a condition can be rapidly inferred, giving a clear indication of incipient failure modes. The current state of the art is reviewed in the following ways: survey developments in condition monitoring of machines, mechanically and electrically, over the last 30 years; put that work in context alongside the known failure mechanisms; review those developments which have proved successful and identify areas of research which require attention in the future to advance the subject.

Nomenclature

$b_{n,2}\ (t)$	nth harmonic of airgap flux density in rotor frame, Tesla
$\hat{B}_{n,\ 2}$	peak nth harmonic of airgap flux density in rotor frame, Tesla
d_b	rolling element diameter, mm
D_b	rolling element pitch, mm
F	factor relating to bearing geometry
$f_{1\ \text{or}\ 2}(t)$	stator or rotor side instantaneous MMF, ampere turns
f_{se}	stator side electrical frequency, Hz
f_{rm}	mechanical rotational frequency, Hz
$I_{1\ \text{or}\ 2}$	stator or rotor side winding current, amperes
$\hat{I}_{mq}$	peak mth harmonic of current in qth phase, amperes
k_{e}	eccentricity order, 0 for static eccentricity, 1, 2, 3 … for dynamic eccentricity
k	integer stator winding MMF space harmonic number, 1, 3, 5, 7…
ℓ	integer stator time or rotor winding fault harmonic number
M	integer current harmonic number
$N_{1\ \text{or}\ 2}$	integer stator or rotor side winding turns
N_{r}	integer rotor slot number
N	shaft rotational speed, rev/min
n	integer voltage harmonic number, 0, 1, 2, 3….
n_{b}	integer number of rolling elements in bearing
P	integer pole pair number
$p(t)$	instantaneous power measured at stator terminals, Watts
q	integer phase number
R	shock pulse meter reading
s	asynchronous machine rotor speed slip, 0–1
t	time, s
$\hat{V}_{nq}$	peak nth harmonic of voltage in qth phase, Volts

ϕ	rolling element contact angle with races, degrees
ϕ_{nq}	phase angle between $\hat{I}_{nq}$ and $\hat{V}_{nq}$, degrees
θ 1 or 2	angular displacement on rotor or stator, degrees
ω_{se}	stator side electrical angular frequency, rad/s
ω_{sm}	stator side mechanical vibration angular frequency, rad/s
$\omega_{rm} = 2\pi N/60$	mechanical rotational angular frequency, rad/s
$\omega_{rm} = \omega_{se}/p$	for a synchronous machine, rad/s
$\omega_{rm} = (1-s)\,\omega_{se}/p$	for an asynchronous machine, rad/s
$\theta_{\ell k}$	$\ell\ \omega_{se}\ t + (q-1)\ (2\pi\ k/3)$ relation between winding angular displacement, degrees

1 Introduction

This paper reviews condition monitoring methods for rotating electrical machines based on the literature of the past 30 years and the author's experience. It covers the failure modes and reliability of electrical machines and the application of electrical, mechanical and other techniques to condition monitoring to improve that reliability. The paper takes a holistic view of the subject and describes the methods in relation to the structure of machines and their usefulness. Therefore it is suitable for practitioners and researchers.

The art of condition monitoring should be minimalist, to take the minimum measurements necessary and by analysis extract a detection and diagnosis of the machine. A condition can then be inferred, in minimum time, giving a clear indication of incipient failure modes.

The paper deals with this concept logically in four sections:

1. Considering previous survey publications on the subject.

2. Considering machine reliability from surveys made from 1975 to the present, identifying which parts of electrical machines make the greatest contribution to failure.

3. Giving an account of specific monitoring techniques, starting with thermal and chemical degradation methods, progressing to mechanical and electrical methods, considering first terminal conditions and finally discharge monitoring of electrical machine insulation systems.

4. Considering the application of artificial intelligence (AI) to condition the monitoring and use of condition-based maintenance (CBM) for the asset management of a plant.

The paper seeks to critically review the direction in which the monitoring of electrical machines is going, giving key references for each technique, but there is insufficient space to review each publication. However, in its conclusions, the paper identifies those areas which have proved fruitless and those which demonstrate success or future potential.

In particular, the author asks the reader to use the information in the paper to relate the potential future of individual condition monitoring methods to detecting real faults that occur in rotating electrical machines in service.

2 Previous reviews

The paper has a comprehensive bibliography.

The first modern book on the subject was [1] followed by [2] and the most up to date is [3], aimed at winding and insulation problems. The journal literature on condition monitoring of electrical machines is growing rapidly, although not necessarily in directions most useful to industry. There are a number of general survey papers of condition monitoring techniques for machines of which the most relevant are [4], describing large machines; [5], giving a guide to machine trouble-shooting; [6], dealing with induction machine and drives; [7], looking at electrical equipment in general and [8], the most recent review, dealing with monitoring and diagnostics.

3 Reliability

3.1 Failure sequence and effect on monitoring

It is useful to put condition monitoring in context alongside the known machine failures. The sequence from operation to failure for a specific failure mode in a typical component, such as, for example, the main shaft of a machine, is drawn in Fig. 1.

The duration of a failure sequence depends on the failure mode, operation and ambient condition of the machine. Fig. 2 demonstrates the timeline for such a process, described by a normal distribution. Fig. 2*a* shows the

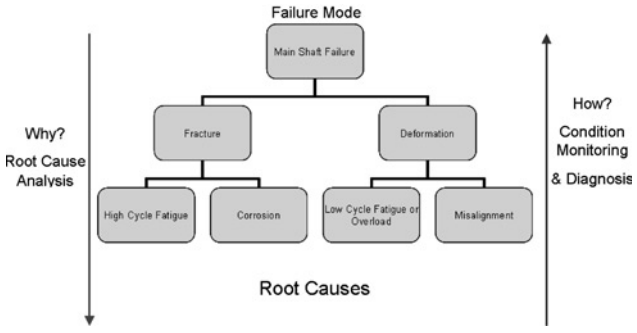

Figure 1 *Cause and effect diagram, relationship between failure sequence and root cause analysis. Example: failure by fracture of a main shaft initiated by corrosion cracking or overload*

doi: 10.1049/iet-epa:20070280

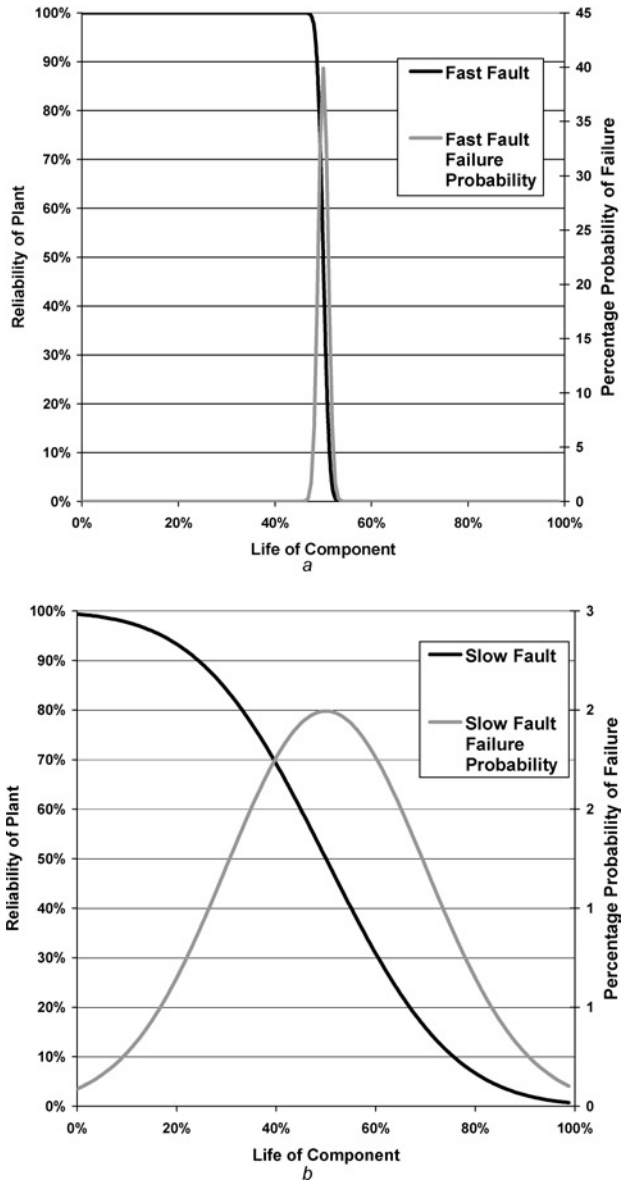

Figure 2 *Timeline for such a process, described by a normal distribution*

a Failure sequence, fast speed fault
b Failure sequence, slow speed fault

rapid progression of a fast fault from a reliable to unreliable operation at, for example, the 50% life point. Fig. 2*b* repeats the sequence for a slow speed fault. This process is at the heart of condition monitoring. If a failure sequence is rapid, as in Fig. 2*a*, effective condition monitoring is impossible and this is the situation for electrical faults detected by protection, where the period of action may be only seconds or cycles. However, if the failure sequence is days, weeks or months, like the slow fault in Fig. 2*b*, then condition monitoring has the potential to provide early warning of impending failure. Therefore condition monitoring must concentrate on root causes and failure modes that exhibit a slow failure sequence.

3.2 Typical machine root causes and failure modes

It is important to distinguish between root causes, which initiate the failure sequence and can be detected by condition monitoring, and the failure mode, which terminates it. After a failure, operators are used to trace the sequence back from the failure mode to the root cause, in the process called root cause analysis, to determine the true cause of failure, as shown by the left arrow in Fig. 1. On the other hand, the designer of a condition monitoring system must keep in mind the need to predict the reverse of that process, tracing how a failure develops.

The most common root causes and failure modes in rotating electrical machines, defined by [9–12] are set out in Table 1. It is surprising how few root causes and failure modes there are and it should be noted that they are generic.

3.3 Reliability surveys

Reliability is notoriously difficult to establish but information on mean time between failures (MTBF) is available from surveys, mostly conducted in the USA under the auspices of the IEEE, including [9–16]. Information about the life of electrical machines has also come to light from recent experience in the defence and wind industries, [17, 18]. MTBF can be deceptive, representing the prospective life of the machine, assuming it has a constant failure rate, as shown in the constant failure rate region of the bathtub curve, Fig. 3. One could consider that there would be a 50% probability of failure before the MTBF and 50% probability of failure afterwards. Table 2 extracts data from the surveys of electrical machines above, giving MTBFs and failure rates for a range of machines, showing a remarkable degree of consistency with MTBFs ranging from 18 to 33 years for a large steam turbogenerator at the top end. It should be noted that larger surveys are dominated by induction motors because of the ubiquity of that machine. Table 2 also gives an idea of the significance of each survey by noting the number of machines surveyed and the number of failures recorded.

The distribution of failures within the machine is also important because it can guide the condition monitoring applied. The data in Table 3 comes from the same surveys and they show a consistent trend in failure areas in the descending order of importance:

- Bearings
- Stator related
- Rotor related

The distribution, in particular the relative weighting of stator to rotor winding failures, is affected by size, voltage and type of machine.

Table 1 Root causes and failure modes in electrical machines

Root causes	Failure modes
defective design or manufacture; material or component; installation; maintenance or operation	Electrical: core insulation failure; stator winding or insulation failure; rotor winding or insulation failure; brushgear failure; slip ring failure; commutator failure; electrical trip Mechanical: Bearing failure; rotor mechanical integrity failure; stator mechanical integrity failure
ambient conditions	
overspeed	
overload	
low cycle fatigue or shock load	
high cycle fatigue or excessive vibration	
component failure	
excessive temperature: in windings in bearings	
excessive dielectric stress: steady or transient	
debris, dirt or corrosion	

For example small, low-voltage induction machines, exemplified by the first two columns of Table 3, are dominated by bearing failure modes, as low-voltage windings experience very few faults. Smaller machine bearings are usually rolling elements and their reliability depends heavily on the standard of maintenance. Induction machines show a much lower proportion of rotor or squirrel cage faults compared with stator winding faults, because of the ruggedness of cage construction.

Larger, high-voltage machines, exemplified by the next three columns of Table 3, receive a higher proportion of stator winding failure modes because of dielectric stress and vibration, as these may be high-voltage windings. Large machine bearings are usually of a sleeve construction, with constant lubrication and are more reliable than smaller machine bearings. Thus, in larger machines, stator winding and bearing faults can be of similar significance.

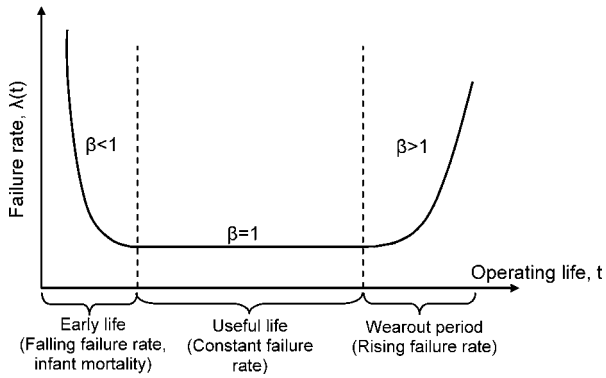

Figure 3 *Aggregate hazard function or failure rate for a population of components forming a piece of machinery, known as the bath-tub curve*

3.4 Relation to literature

An aspect of this analysis is the attention being paid to different failure modes in the literature. The author used the search engine IEEEXplore to consider IEEE and IEE Journal papers in the period 1980 to date searching the metadata under the following headings:

- Broken bars in induction motor rotor cages, 35 papers
- Discharge activity in MV and HV stator windings in motors and generators, nine papers
- Stator winding faults excluding discharge activity in motors and generators, 19 papers
- Bearing faults in electrical machines, 17 papers.

The spread of these 80 papers is shown alongside the relevant failure areas in Table 3. It shows that more publishing effort in electrical journals has gone into the study of the least prevalent rotor faults than into the more prevalent bearing faults, although the balance of the literature on stator faults appears about right. Induction motor rotor cage faults can be detected through perturbations of the airgap magnetic field, described later in the paper. The study of the effects of eccentricity in induction motors, the most numerous of machines, which also can be a guide to bearing failure, can also be elicited from the literature which has recorded 36 papers on this subject since 1980.

4 Temperature monitoring

4.1 Introduction

Limits to the rating of electrical machines are set by the maximum permissible temperature for insulation.

doi: 10.1049/iet-epa:20070280

Table 2 List of typical measured failure rates and MTBFS for electrical machines obtained from the literature

Machine type	No of machines in survey	Machine years in survey	No of failures in survey	Failure rate, failures/machine/yr	MTBF, hrs	Source of data
Large steam turbogenerators	Not known	762	24	0.0315	2 73 750	Dickinson, 1974 [10] also IEEE Gold Book [9]
Motors greater than 75 kW generally MV and HV induction motors	6312	41 614	1474	0.0354	2 47 312	Albrecht, 1986 [13]
Wind turbine generators <2 MW	643	5173	710	0.0400	2 19 000	Tavner, van Bussel, Spinato, 2006 [18]
Induction motors 601-15000 V	Not known	4229	171	0.0404	2 16 831	Dickinson, 1974 [10] also IEEE Gold Book [9]
Motors greater than 11 kW generally MV & HV induction motors	2596	25 622	1637	0.0639	1 37 109	Thorsen, 1995 [15]
Motors greater than 150 kW generally MV & HV induction motors	1141	5085	360	0.0707	1 23 735	O'Donnell, 1985 [12] also IEEE Gold Book [9]

Table 3 Distribution of failed subassemblies in electrical machines obtained from the literature

Subassemblies	Predicted by an OEM through FMEA techniques, 1995-7 [*]	MOD survey, tavner, 1999 [17]	IEEE large motor survey, 1985, O'Donnell, 1985 [15]	Motors in Utility Applications, Albrecht, 1986 [16]	Motor Survey Offshore and Petrochemical, Thorsen, 1995 [11]	Proportion of 80 Journal Papers published in IEEE and IEE on these subject areas over the past 26 years
types of machines	small to medium LV motors and generators <150 kW, generally squirrel cage induction motors	small LV motors and generators < 750 kW, generally squirrel cage induction motors	motors greater than 150 kW generally MV and HV induction motors	motors greater than 75 kW generally MV & HV induction motors	motors greater than 11 kW generally MV & HV induction motors	all machines
bearings	75%	95%	41%	41%	42%	21%
stator related	9%	2%	37%	36%	13%	35%
rotor related	6%	1%	10%	9%	8%	44%
other	10%	2%	12%	14%	38%	—

[*] Private communication from Laurence, Scott & Electromotors Ltd

doi: 10.1049/iet-epa:20070280

Measurement of temperature is therefore important in the monitoring of electrical machines and there are three approaches:

1. measure local point temperatures using embedded temperature detectors (ETD);

2. use thermal images, fed with suitable variables, to monitor the temperature of the perceived hottest spot in the machine;

3. measure distributed temperatures of the machine or bulk temperatures of the coolant fluid.

These demonstrate the fundamental difficulty of temperature monitoring; the conflict between easily made point measurements, which give only local information, and bulk measurements that are more difficult and run the risk of overlooking local hot-spots.

4.2 Local measurement

This can be done using thermocouples, resistance temperature detectors (RTD) or ETDs. To monitor the active part, they are usually embedded in the stator winding, stator core or bearings. The choice of location requires careful consideration during specification. For example, temperature detectors embedded in the stator winding need to be located close to its hottest part, which may be in the slot or end-winding portions. For a machine with asymmetrical cooling, they should be located at the hottest end of the machine. Fig. 4 gives guidance on the location of ETDs. The weakness of these methods is that ETDs and RTDs are metallic devices and cannot be located in the hottest position on the winding copper, because they need electrical isolation. Devices have to be embedded in the insulation, and as a result the measured temperature will be a proportion of the copper temperature. It would be desirable to develop temperature monitoring devices that can be affixed to a high-voltage winding and given electrical isolation. Such methods have been developed using fibre-optic techniques. A particular design, using the dependence of the polarisation of light on the temperature of a material, is described by [19].

Temperature measurements described so far have been on the stator. However, many machines are rotor-critical, particularly large induction motors under stall conditions and there may be no apparent deterioration after one or two stalls, but should this repeatedly occur, there will be a weakening of rotor bars and/or end rings resulting in premature failure. A device has been described [20] for monitoring eight thermocouples, multiplexing the signal on the rotor, then optically coupling to the stator and decoding in a digital signal processor (DSP).

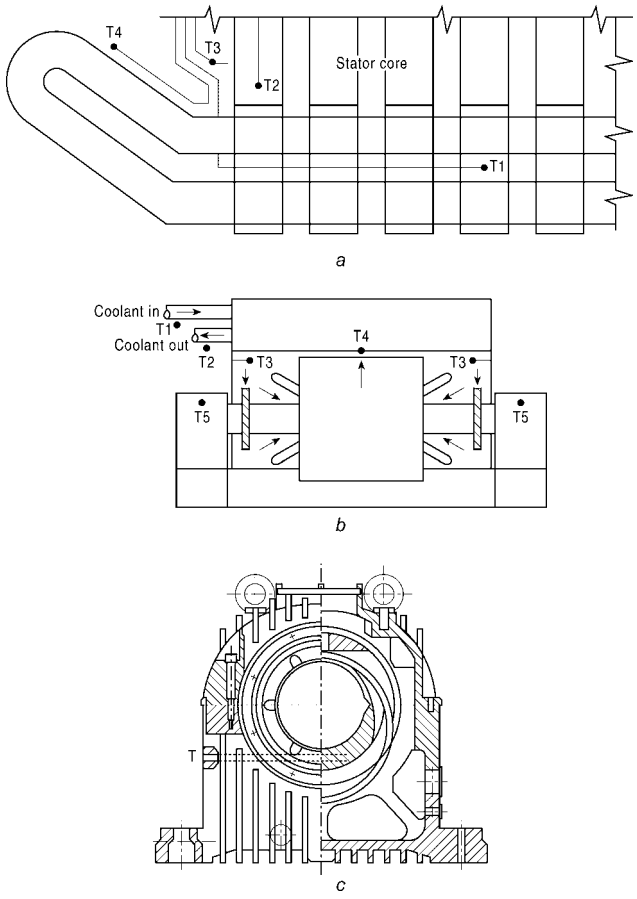

Figure 4 *Location of temperature detectors in electrical machines*

a Embedded between conductors in the slot portion (T1)
Embedded in core pack laminations (T2)
Mounted on potentially hot components such as pressure plates (T3)
Embedded on conductors in the end winding portion (T4)
b Water or air inlet to the heat exchanger (T1)
Water or air outlet from the heat exchanger (T2)
Re-entry air to the machine from the heat exchange (T3)
Exhaust air from the machine to the heat exchanger (T4)
Bearing temperatures (T5)
c Bearing temperature (T)

4.3 Hot-spot measurement and thermal images

Local temperature measurements give the operator confidence, but the detectors may not be at the hottest point. This problem has been recognised in power transformers because of difficulties in obtaining embedded winding temperatures, in the presence of thick EHV insulation, so hot-spot images are used. Thermal images have not received wide application on rotating electrical machines, although they have deserved to. The availability of a thermal image hot-spot temperature of a machine could be used for monitoring and protection, as proposed in [21–23] whereby a technique was proposed for small totally enclosed fan-cooled (TEFC) induction motors where a thermal model of the machine was configured in a DSP, fed with ambient air temperature and stator winding

doi: 10.1049/iet-epa:20070280

current signals. The model predicted temperatures at a variety of key points, the stator core, winding slot and end-windings. Fig. 5 shows a comparison of results from two machines going through severe duty cycles and it can be seen that the results are extremely good.

4.4 Bulk measurement

In the active part of the machine, there is still a need for bulk indications of thermal state, even when hot-spot locations and temperatures are surmised from thermal images. This can be found from the measurement of the internal and external coolant temperature rises, obtained from thermocouples located as shown in Fig. 4. An increase in temperature rise clearly shows that a machine is overloaded

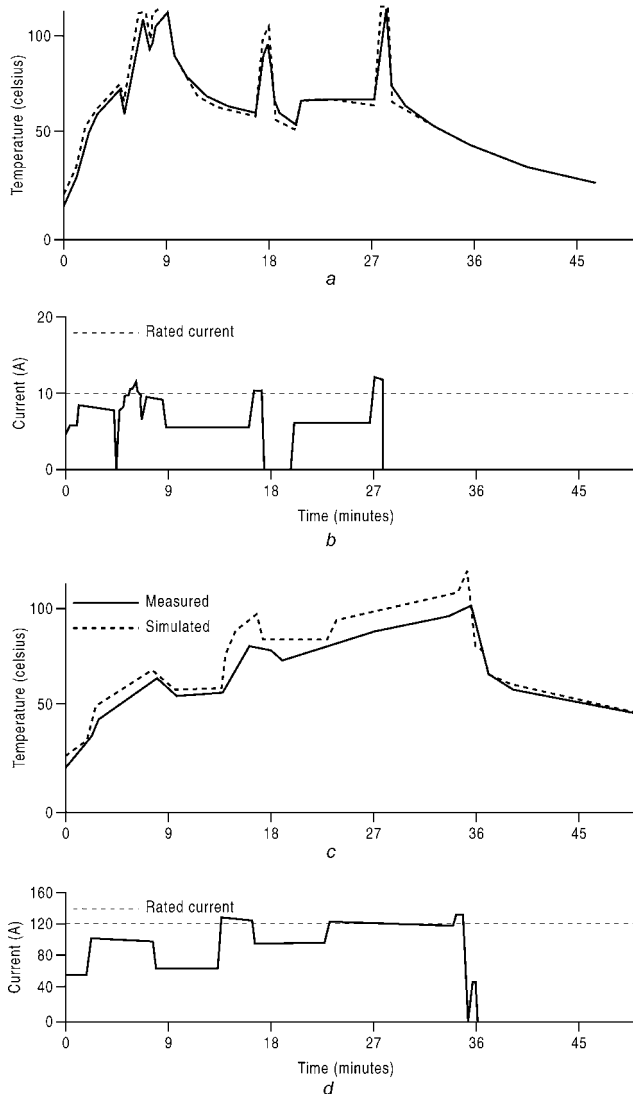

Figure 5 *Comparison between measurements and the predictions of a thermal image of an electrical machine Taken from [23]*

a Comparison for 5.5 kW induction motor
b Duty cycle for *a*
c Comparison for 7.5 kW induction motor
d Duty cycle for *c*

or coolant circuits are not performing. However, the method is insensitive to localised overheating. Therefore effort has been devoted, alternatively to the thermal image, to devising methods for single temperatures to be obtained from devices embedded in the bulk of the machine. Lengths of the signal cable using heat-sensitive semi-conducting material as insulation have been proposed, but most effort has been devoted to the use of optical fibres. Various methods have been described, including point measurements on high-voltage components, using optical fibres for isolation [24]. However, they also describe how a continuously-sensitive fibre could be embedded in the machine, adjacent to the high-voltage copper, using its temperature-sensitive properties to detect localised overheating anywhere in the winding and yet provide a single indication.

5 Chemical and wear monitoring

5.1 Insulation degradation detection

Thermal degradation as a failure mode is determined by insulation materials that are complex organic materials, which when degraded by heat or electrical action, produce a large number of gaseous, liquid and solid products. Insulation materials are natural or synthetic organic polymers and their thermal degradation is complex. As the temperature rises above its permitted value, circa 160°C, volatiles used as solvents in manufacture start to be driven off as gases. Then, heavier compounds in the resin reach their boiling point and the gases produced are heavier hydrocarbons, such as ethylene. As the temperature rises above 180°C, chemical decomposition of the resin starts. A supersaturated vapour of the heavier hydrocarbon decomposition products forms in the cooling gas close to the hot insulation. Rapid condensation of that vapour occurs as the cooling gas leaves the hot area, producing condensation nuclei that continue to grow until they reach a stable droplet size. The materials given off depend not only on the insulation material but also on the machine's cooling gas. The insulation binder material, wood, paper, mica or glass fibre, can usually withstand much higher temperatures, but when 400°C is reached, they start to degrade and char, releasing gases such as carbon monoxide and dioxide, drawing oxygen from the air or from the degradation of the complex hydrocarbon in the resin. Pyrolysing activity therefore gives rise to a wide range of gases, liquid droplets and solid particles, which together form the smoke being driven off from the insulation.

Electrical discharge activity, within or adjacent to the insulation system, also degrades the insulation, releasing particulate and gaseous products. The very high temperature associated with sparking breaks down the insulation hydrocarbon compounds to form acetylene. It also breaks down the oxygen in the cooling gas, if it is air, to give ozone. Furthermore, continuous discharge activity gradually carbonises and erodes the insulating material to

produce, on a smaller scale, the degradation products that result from more widespread overheating.

Insulation degradation can be monitored chemically by detecting the presence of particulate matter in the coolant gas or by detecting gases, like carbon monoxide, ozone, or more complex hydrocarbon gases, like ethylene and acetylene.

5.1.1 Particulate detection-core monitors: Detecting the smoke given off from degrading insulation is the simplest technique, since proprietary smoke detectors already exist using ion chambers to detect smoke particles. As the cooling gas of the machine enters the ion chamber, it is ionised by a weak radioactive source. The gas then flows through an electrode system carrying a polarising voltage. Free charges in the gas are collected on the electrode and flow through an external electrometer amplifier, which produces an output proportional to the ion current. When heavy smoke particles enter the chamber, their greater mass implies a lower mobility compared with gas molecules and, thus, the ion current reduces. Therefore the smoke is detected by a reduction in the amplifier output voltage. An ion chamber was designed to detect the products of heated insulation and this was applied to a large turbogenerator [25]. The primary impetus for this work was the need to provide early warning of core faults in large turbogenerators referred to in [4]. The lifetime of pyrolysed particles in the closed hydrogen cooling circuit of a large generator is 15–30 min after which the particulates are deposited onto the exposed surfaces of the machine. A single instance of insulation overheating should lead to a reduction of the core monitor ion current for this period of time. Fig. 6 shows typical core monitor responses. The sensitivity of the device depends upon the ion chamber design, but experimental figures for the monitor described in [25] show that it will produce a response ranging from 85%–95% of full scale deflection when 100 cm^2 of lamination insulation is pyrolised, depending on the material. However, the monitor has practical difficulties:

1. the output fluctuates with cooling gas pressure and temperature;

2. it responds to oil mist that may be present in the circuit of any hydrogen-cooled machine because of faulty hydrogen seals [26];

3. it is non-specific; that is, it cannot distinguish between the materials being overheated.

Items (1) and (2) affect the background signal from the monitor, which any signal because of damaging overheating must exceed. Fig. 7*c* shows a typical core monitor trace from a machine affected by oil mist. Item (3) affects the attitude of a machine operator to an alarm from the core monitor, since there will be less confidence in the monitor if it does not reveal the part of the machine where the detection originated.

A more advanced monitor, described in [27], overcame problems (i) and (ii) by using two identical ion chambers in series in the gas flow, with an intermediate particulate filter between them. The monitor displays the difference between the ion currents in the two chambers and, thereby, eliminates fluctuations because of pressure and temperature. It was suggested that oil mist is only produced by overheating and, thus, that its detection may be useful. The use of heated ion chambers was not initially encouraged, however, the current thinking is that heated ion chambers are essential for reliable detection. However, the oil mist content in a machine varies widely and can be high, in which case there can be frequent false alarms and, thus, the use of a heated ion chamber gives an advantage. To vapourise an oil mist, the ion chamber temperature must be raised above 120°C. The monitor described in [27] had heated ion chambers and the authors' experience, using these set to 120°C, was that they gave an adequate protection against spurious oil mist indication but that they also reduced the number of droplets produced by overheating, causing a loss of sensitivity quantified in [28] at 120°C as 20%,

The author is not aware of the core monitor being used on air-cooled machines, or machines without a closed cooling circuit, although, apart from the short time constant of the indication from the monitor, there seems to be no reason why it could not be used for these applications. Experience has shown that the core monitor cannot be relied upon, on its own, to give incontrovertible evidence of an incipient fault. It is a valuable device that does detect pyrolised insulation, but its indications need to be considered alongside those of other monitoring devices. The core monitor needs to be complemented by off-line techniques analysing the particulates causing the detection.

5.1.2 Particulate detection-chemical analysis: Authors advocated taking particulate material samples when a core monitor indicates an alarm [25]. To collect a detectable amount of particulate matter within a short time, it is necessary to have a very large gas flowrate through the filter by venting the pressurised casing of the machine through the filter to the atmosphere. However, there is no agreement about the method of analysis, because the pyrolysis products contain large numbers of organic compounds and the resultant chromatograms are difficult to interpret, [29] and Fig. 7. An alternative is to reduce the chemical information by using less sensitive techniques one of which makes use of the fact that many organic materials fluoresce when irradiated with ultra-violet light. The resultant UV spectrum is less complex than a chromatogram. Despite the techniques described here, there is, as yet, no conclusive way to identify material collected on a core monitor filter. A way out was sought by inserting tagging compounds in the machine, which when overheated give off materials with easily identifiable chemical compositions. This technique was used in the US in [25].

doi: 10.1049/iet-epa:20070280

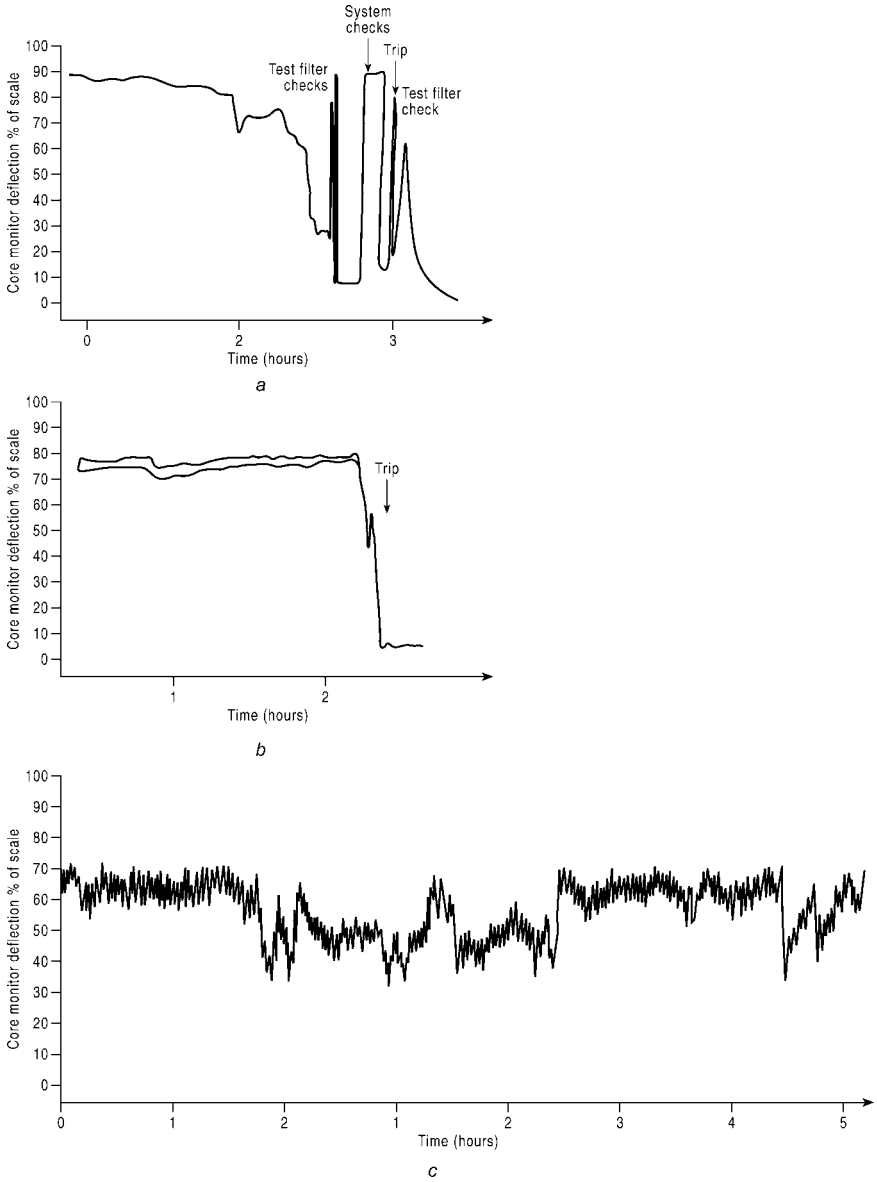

Figure 6 *Typical core monitor responses*

a Machine with overheating conductor bar
b Machine with a core fault
c Machine with no overheating but oil contamination

5.1.3 Gas detection: The advantage of on-line gas analysis is that, because of the long residence times of overheating gases, earlier warning may be obtained of machine damage. The disadvantages are the complexity of the analysis and the difficulty of translating it into an electrical signal. Based on [30] a continuous monitor was devised for hydrogen-cooled generators, using a flame ionisation detector (FID) to measure the total organic content in the hydrogen. This detector is used for the detection of organic species and the generator cooling gas is introduced into a hydrogen/air flame, which forms part of a circuit that normally presents high resistance. When organic species are introduced, carbon ions are formed and the flame resistance decreases linearly with the amount of organic compound introduced. The device is sensitive and can detect increases as small as 0.2 parts per million by volume (vpm) of methane (CH_4) equivalent. Its sensitivity is reduced by the presence of background levels of organic compounds that can be 10–50 vpm with a variability of $\pm 20\%$. However, one advantage over the core monitor is that it shows the trend of any increase.

An alternative to the FID detector is the photo ionisation detector, which contains an ultraviolet lamp that ionises the gas stream flowing past it. A potential is applied across electrodes in the detector and the conductivity is measured as in the FID, as shown in Fig. 8 alongside the core monitor indication. The device detects heavier hydrocarbon compounds in the gas stream and it has been shown that a fault on a large generator, involving 2 g of organic material

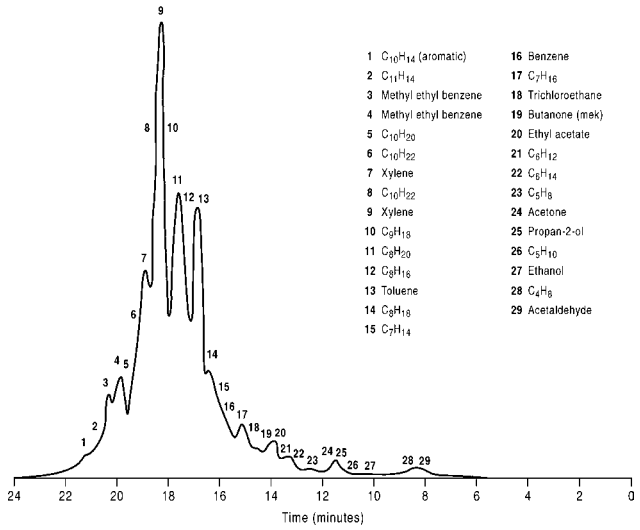

Figure 7 *Gas chromatogram of generator hydrogen impurities extracted from a Tenax GC precolumn taken from [29]*

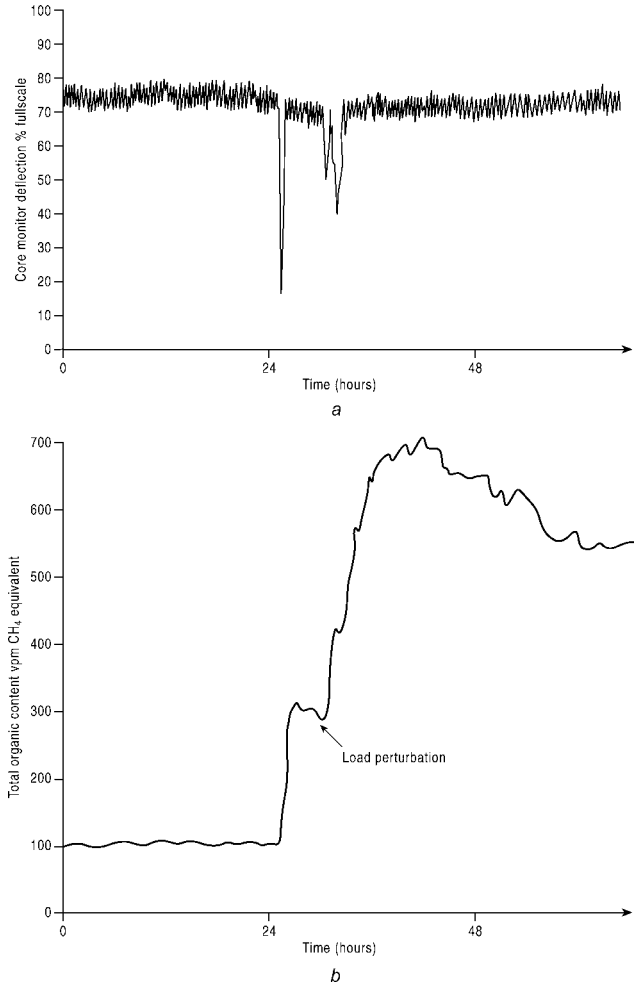

Figure 8 *Comparison of the traces from continuous gas monitoring with response of a core monitor on a 500 MW turbogenerator following an incident*

a Core monitor response
b Continuous gas response

overheating, produced a 1–2 vpm deflection against background levels of 7–10 vpm.

Recent work [31–33] has reverted to detecting the gases from faults using the more complex quadrupole mass-spectrometer.

On air-cooled machines overheating incidents produce a large volume of carbon monoxide and dioxide as well as light hydrocarbon gases. An instrument to detect overheating by measuring the carbon monoxide concentration was described in [4] containing a pump that drew air from sampled motors, to a commercial infra-red analyser measuring the carbon monoxide content. The air in a sealed motor enclosure should recirculate with a long residence time but leaks reduce this, diluting the carbon monoxide. However, the analyser detected carbon monoxide concentrations of less than 1 vpm. Calculations showed that 180 g of insulation heated to 300°C will introduce a 1.5 vpm rise in carbon monoxide concentration in the cooling air. Therefore the analyser had sufficient sensitivity to detect motor winding overheating.

5.2 Oil degradation detection

Smaller electrical machine shafts are supported on rolling element bearings lubricated with grease and bearing faults could not be detected by the above techniques. High-speed machines above 300 kW and low-speed machines above about 50 kW use oil-lubricated rolling element bearings and larger sizes need sleeve bearings with a continuous oil supply. An author [34] suggested that continuous monitoring of the oil supply provides early warning of problems. The chemical detection of oil degradation has been effective for transformers, where oil is used for insulation and cooling and is sealed within the transformer enclosure.

5.3 Wear debris detection

The normal failure mode of rolling element bearings is fatigue cracking of elements or raceways, although fretting, scuffing and abrasion also generate debris. For white-metalled sleeve bearings failures are not usually progressive. Debris is released in short bursts, when bearings are transiently overloaded or oil-films momentarily rupture. Substantial damage can be tolerated while the bearing is copiously fed with cool lubricating oil. Nevertheless fatigue failure, white-metal surface cavitation and lubrication system corrosion, can be diagnosed from lubricating oil analysis. Incipient failure will also lead to local heating and degradation of the lubrication oil at the wear site. A particular electrical machine problem is current flow, caused by magnetically induced shaft voltages, through bearings and oil films, as summarised in [35], which pit the bearing surface, producing metallic debris and degrading the lubrication oil. Two approaches that could be used to detect these failure activities are:

doi: 10.1049/iet-epa:20070280

- detection of oil degradation products
- detection of bearing degradation products in the oil.

5.3.1 Ferromagnetic techniques: Rolling element bearing failure modes produce metal fragments up to a millimetre in size. An on-line device [36] can be inserted into the bearing oil line that counts the number of ferromagnetic particles in the oil flow. A pair of screened oils surround the oil line and form two arms of an AC bridge circuit. Magnetic or conducting particles entrained in the flow cause unbalance in the bridge. The phase of the unbalance enables discrimination between ferromagnetic and conducting particles. System sensitivity varies according to particle shape but can be adjusted to record particles from 0.2–2 mm dia, in oil flow velocity of 1–12 m/s. The device has been used on jet aircraft, where performance in a high temperature, pressure and vibration environment has been proved. There is no record of this device being used on an electrical machine.

The instrumented oil drain plug is another device giving a signal proportional to; the amount of debris deposited, the rate of accumulation of debris and the temperature of the oil. The device can detect masses of ferromagnetic debris attracted to the pole pieces ranging from 10 to 600 mg with a resolution of 10 mg in an oil flow velocity of 0.1–0.5 m/s.

5.3.2 Other techniques: Ferromagnetic techniques are appropriate for rolling element bearings but not for the white-metalled sleeve bearings. An author [37] investigated this problem on a number of 60 MW turbogenerators, correlating the results with plant condition. The detection process was based on the presence of white-metal in the machine bearings containing 85% tin. The results showed that by determining the tin-to-iron ratio in the debris an operator can identify bearing damage; Fig. 9. It has been investigated [37] how the oil system could be monitored to provide early warning of bearing damage and X-ray fluorescence detection considered to measure oil electrical properties but this was prohibitively expensive.

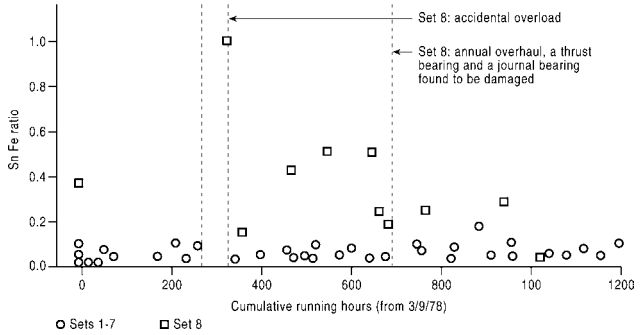

Figure 9 *Ratio of tin to iron in the oil filter deposits from eight 60 MW turbogenerator sets Taken from [37]*

6 Mechanical vibration monitoring

6.1 Introduction

The electrical machine support structure forms a complex electromechanical system subjected to excitation by the airgap electromagnetic field and torque spectrum, at natural and other frequencies. These may cause high cycle fatigue ending in machine failure or make the machine emit acoustic noise. The principal, interrelated excitation sources are:

- stator core response to attractive forces developed between rotor and stator;
- dynamic behaviour of the rotor in the bearings as the machine rotates;
- response of the shaft bearings and foundations, to vibrations transmitted from the rotor;
- response of the stator end-windings to the electromagnetic forces on the structure.

6.2 Stator core response

Changes in stator core, frame and winding vibrations because of machine faults can be calculated from the airgap flux density using numerical techniques, as described in the literature. A qualitative assessment can be made using less accurate methods. Many authors examined the sources of airgap unbalanced magnetic pull (UMP) and their effect on vibration identifying the role of static eccentricity [38] in the production of UMP. The calculation of harmonics in the flux wave because of rotor eccentricity was shown using a conformal transformation to re-centre the rotor [39] and a review of UMP was given in [40]. The simplest method of calculating the flux wave form is to multiply the magnetomotive force (MMF) distribution because of winding currents, by the permeance of the airgap, [41] suggested this had limited accuracy, but [42] applied the technique successfully, accommodating geometrical and winding effects and later [43] used an analytical permeance wave method to deduce harmonic equivalent circuits to predict rotor torques. Various authors subsequently applied this method, incorporating finite element solutions, for intractable three-dimensional effects. With these techniques, it has been possible to analyse the effects of winding faults and rotor eccentricity on airgap flux density and UMP.

6.3 Stator end-winding response

End winding structures have high compliance and nonlinear damping, because of frictional contact between adjacent conductors. Compliance may be reduced by bracing, as in large turbogenerators or induction machines with onerous starting duties. Stator end-winding motion is excited by three mechanisms:

• seismic excitation of the coils by the ovalising displacements of the stator core;

• seismic excitation by motion of the machine on its foundation;

• electromagnetic forces between the coils, because of the currents flowing in them.

These forces have been considered in [44] but the dynamics are complex, because of the geometry, the distributed nature of the applied forces and the nonlinear response coefficients. Resultant displacements are at twice the electrical supply frequency, ω_{se}, and complete analysis is needed to determine mode shapes, as described in [45]. Mobility tests on the structure can be used to determine modal response more simply. Utilities have installed triaxial accelerometers on large turbogenerators' end-winding structures to monitor the vibration amplitudes, particularly close to the excitation frequency, $2\omega_{se}$, to confirm that the end-windings have not slackened, but these measurements produce a mass of data and require expert opinion for analysis and interpretation. On smaller induction motors, displacements are not large, but they do require prediction and measurement as described, respectively, in [46, 47].

6.4 Rotor response

The rotor responds to:

• Transverse excitation, because of self-weight, mechanical unbalance, shaft whirling, dynamic/static UMP because of eccentricity or a combination of all four.

• Torsional excitation, because of prime mover drive or electromagnetic torques.

The transverse response depends on rotor rigidity. Short rigid rotors may be considered a single mass acting at the bearings. The degree of residual unbalance is denoted by the quantity $G = e\omega_{rm}$ and the permissible limits are provided by international standard ISO 1940-1:2003. For electrical machinery, the quality grade is towards the lower end, $G = 2.5$ for machines of all sizes and $G = 1.0$ for special requirements. Large two-pole turbogenerators have long, slender, flexible rotors operating at higher speeds, and therefore the rigid rotor approach is inadequate and unbalanced distribution must be considered. Rotor shaft mode shapes depend upon bearing stiffnesses. For most electrical machines, the bearings may be considered to be hard, but [48] has shown that on large machines, foundation flexibility will influence transverse vibration behaviour.

6.5 Torsional response

Torsional behaviour of large rotating electrical machine systems is also complex. Forced torsional oscillation of the rotor of a turbogenerator is possible because of its great length and small radius, and these will depend upon disruptions that occur in the connected mechanical or electrical system. Electrical system disturbances are particularly important since they excite torsional responses, which limit the fatigue life of the shaft, [49].

6.6 Bearing response

Rotor vibration is transmitted to the stator via the airgap magnetic field and the bearings in parallel. Therefore bearing responses must be considered alongside the rotor system. Rotor-forcing vibrations will cause motion of the rotor relative to the bearing and absolute vibration of the bearing housing. These need to be considered for both rolling element bearings and oil-lubricated sleeve bearings.

6.6.1 Rolling element bearings: A schematic view of a rolling element bearing is shown in Fig. 10*a*. Rolling element bearing failure is the most common failure mode associated with smaller machines. Because of their construction,

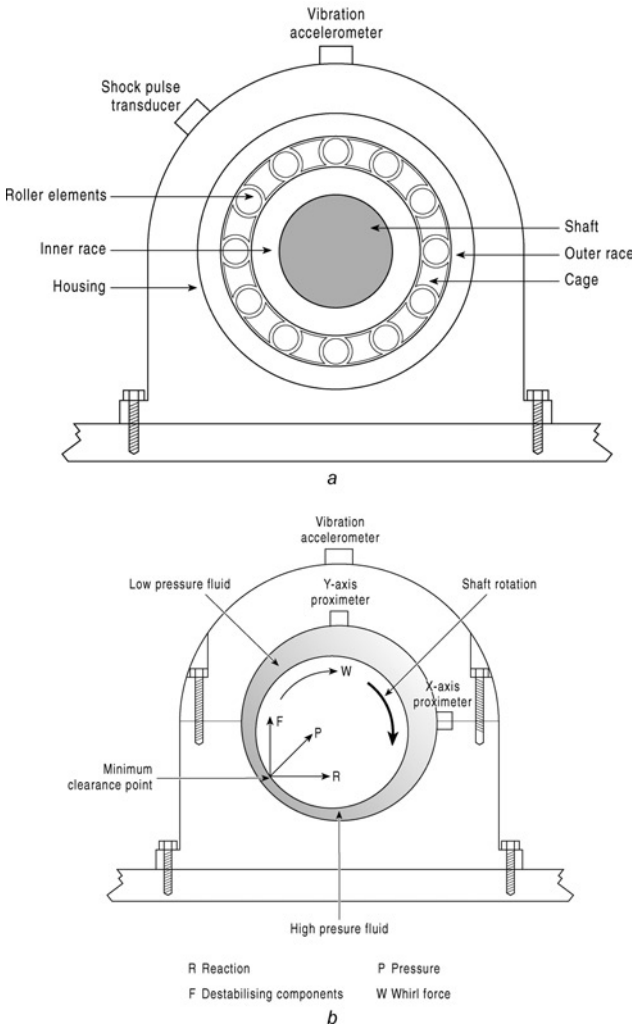

Figure 10 *Rolling element and sleeve bearings*

a Rolling element bearing assembly
b Forces acting upon a shaft in a sleeve bearing

doi: 10.1049/iet-epa:20070280

rolling element bearings generate precise, identifiable frequencies. Since the oil or grease film is very thin, the relative motion between the housing and shaft is small and it is possible to detect faults using stator side vibrations, ω_{sm}, with an accelerometer mounted directly on the bearing housing. Characteristic frequencies of rolling element bearings depend on the geometrical size of the various elements and are given in Table 4. When the damage is small, the magnitudes of these components may be lost in background noise, but because of their precise nature, they can be used for monitoring bearing degradation.

6.6.2 Sleeve bearings: In a sleeve bearing, the shaft is supported by a fluid film pumped, by the motion of the shaft, at high pressure into the space between the bearing liner and shaft, Fig. 10*b*. Because of the oil film compliance and limited flexibility of the bearing, vibrations measured at the bearing housing will be small. This points to the use of shaft proximeters, but they will only be useful at lower frequencies. Higher frequencies, multiples of the rotational frequency, are best measured with an accelerometer on the bearing housing, but they will be attenuated by the oil film. In sleeve bearings, the onset of instability in the oil film causes an oil whirl and a subsequent oil whip. The oil film is circulating at a speed of approximately half the shaft speed, but because of the pressure difference on either side of the minimum clearance point, the shaft precesses at just below the half-speed described by (1)

$$\omega_{sm} = (0.43 \text{ to } 0.48)\omega_{rm} \quad (1)$$

6.7 Monitoring techniques

Mechanical and electrical faults excite the machine structure in different ways, for example:

- Mechanical faults, including self-weight defects, mechanical unbalance and shaft whirl, excite transverse motion in the machine frame, detectable by transverse vibration sensors.

- Dynamic or static electromagnetic UMP because of eccentricity, which may be caused by bearing wear, also excites transverse motion in the machine frame, again detectable by transverse vibration sensors.

- Electrical faults in stator or rotor windings excite torsional motion in the shaft detectable in the torque signal but not necessarily by vibration sensors, unless it is coupled to the transverse motion by asymmetries in the machine frame.

Faults can be identified by more than one technique. Vibration can be detected by accelerometers and velocimeters mounted on bearings, or proximeters mounted adjacent to bearings. Accelerometers are more appropriate to higher frequencies, whereas velocimeters and proximeters to lower frequencies.

6.7.1 Overall transverse vibration monitoring: This is the simplest but least effective form of monitoring. The measurement is the rms value of the vibration acceleration or velocity on the stator side measured over a bandwidth of 0.01–1 kHz or 0.01–10 kHz. The technique

Table 4 Vibration standard VDI 2056

Vibration velocity, mm/s rms	Vibration velocity, dB, ref 10^{-6} mm/s	Group K	Group M	Group G
45	153	not permissible	not permissible 20 dB (x10)	not permissible
28	149			
18	145			
11.2	141			just tolerable
7.1	137		just tolerable	
4.5	133	just tolerable		allowable
2.8	129		allowable	
1.8	125	allowable		good large machines with rigid and heavy foundations whose natural frequency exceeds machine speed
1.12	121		good medium machines 15–75 kWor up to 300 kW on special foundations	
0.71	117	good small machines up to 15 kW		
0.45	119			
0.28	109			
0.18	105			

doi: 10.1049/iet-epa:20070280

has found favour because considerable experience has been built up over the years to relate vibration levels to machinery failure modes. This has resulted in the publication of recommended vibration standards for running machinery, which do not give diagnostic information, but indicate the machinery health at a given vibration level. An example is the German Vibration Standard VDI 2056, illustrated for electrical machines in Table 4, the up-to-date standard is ISO 10816-1:1995. These criteria are based on machine rating and support systems, and utilise a 0.01–1 kHz bandwidth. The standard recommends that when the vibration changes by >8 dB, care must be exercised, and when the change >20 dB, action must follow. Group K signifies a smaller, quiet running plant, Group M is medium-sized plant and Group G is the larger, noisier plant and shows that electrical machines uncoupled from their prime mover or driven plant, are low-noise, low-vibration machines.

The strength of this method is the simplicity of the instrumentation applied to the machine stator, and it is common in many installations. The sensitivity of the technique is low, particularly when a fault is at an early stage, and the diagnostic information is low.

6.7.2 Spectral transverse vibration monitoring: This is the most widely used modern vibration diagnostic. Various levels of spectral analysis are used from the overall level down to the narrow bandwidth constant frequency presentation. The spectrum is split into discrete bands, so that when the frequency is scaled logarithmically, the bands are of equal width. Narrow band spectra allow the operator to trend machine condition more effectively. This requires an initial baseline spectrum and subsequent spectra are compared with it. The use of digitally derived spectra means that the results of comparisons can be computed quickly, since the spectra reduce to a simple sequence of numbers at discrete frequencies. In this way, criteria such as VDI 2056 can be applied for each frequency band. The basis of this technique is illustrated in Fig. 11, where the baseline is set at the maximum vibration expected and the operational envelope, at which trips are initiated, is set above this. To identify unsatisfactory performance and pinpoint specific problems, discrete frequencies are examined. Induction motors, in particular, require a high-frequency resolution since the speed of rotation, close to the synchronous speed, derived from the electrical supply frequency, modulates the vibration signal producing sidebands spaced at $2s\omega_{se}$ around harmonics of the supply frequency. The application of vibration monitoring to fault diagnosis in large turbogenerators was described by [50], computer analysis techniques applied off-line to vibration data collected on-line are described in [51], and the effect of the foundation response to machine excitation is given in [48]. More up-to-date signal processing techniques have been used on induction motor vibration analysis in [52, 53].

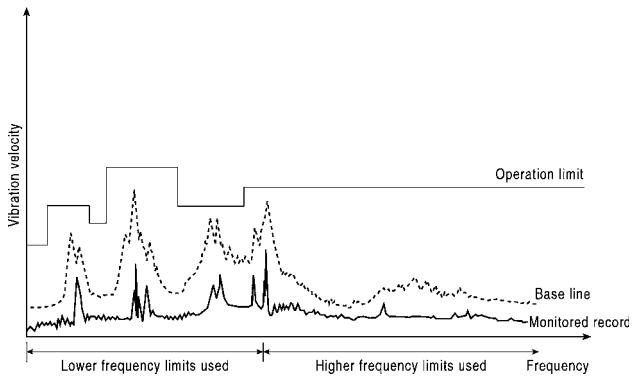

Figure 11 *Operational envelope around a vibration spectral response*

6.7.3 Specific spectral transverse vibration monitoring: UMP can excite stator side vibration components at one, two and four times the supply frequency. Dynamic unbalance and coupling misalignment also produce this effect [40, 54, 55]. The latter reference suggests that even orders of the fundamental frequency occur in the frame vibration spectrum because of inter-turn winding faults on the stator. The principal slot harmonics were also used in [54–56] as an indicator of eccentric running. These references use the transverse mechanical angular frequency, ω_{sm}, measured on the stator frame, excited by radial forces, given in [2] and others as

$$\omega_{sm} = \omega_{se}\left[(nN_r \pm k_e)\frac{(1-s)}{p} \pm k\right] \quad (2)$$

Using the techniques above, the frame vibration can be used to monitor a variety of fault conditions, particularly in induction machines. Caution must be exercised, however, because vibration transmitted from an adjacent or coupled plant may excite natural modes of the machine, whereas a forcing component from a fault within the machine may be sufficiently different from any natural frequency to produce only a slight response.

It was suggested in [40] that, on a machine supplied at $f_{se} = 50$ Hz, vibration at or near 50, 100 and 200 Hz is indicative of eccentricity, but the picture is confused because other anomalies also manifest themselves by the production of such frequencies, for example, misalignment and dynamic unbalance. It has been shown [52] that on a machine supplied at $f_{se} = 50$ Hz, the stator frame vibration exhibits 100, 200 and 300 Hz components because of inter-turn winding faults or supply unbalance, including single phasing. They also show higher order harmonics in the stator frame vibration, because of eccentricity, as derived from (2). To summarise the dominant frequencies for a given fault [56, 57] carried out a theoretical review of the relationships that exist between electrical winding parameters and the mechanical vibration of AC machine elements under normal and faulted operating conditions. Table 5 has been compiled to distil the information to be found in these various references.

doi: 10.1049/iet-epa:20070280

Table 5 Mechanical frequency components related to specific machine faults

		Rotational angular frequency of the rotor, ω_m, rad/s	Transverse vibration angular frequency on the stator, ω_{sm}, rad/s	comments
Mechanical Faults	Oil whirl and whip in sleeve bearings	—	ω_{sm}= (0.43 to 0.48)ω_{rm}	equation (1). Pressure-fed lubricated bearings only.
	damage in rolling element bearings	—	$\omega_{sm} = \frac{n_b}{2}.\omega_{rm}.\left(1 - \frac{d_b}{D_b}\cos\phi\right)$ $\omega_{sm} = \frac{n_b}{2}.\omega_{rm}.\left(1 + \frac{d_b}{D_b}\cos\phi\right)$ $\omega_{sm} = \frac{D_b}{2d_b}.\omega_{rm}.\left(1 - \left(\frac{d_b}{D_b}\right)^2\cos^2\phi\right)$ $\omega_{sm} = \frac{1}{2}.\omega_{rm}.\left(1 - \frac{d_b}{D_b}\cos\phi\right)$	common source of vibration.Also frequencies in the range 2–60 kHz due to element resonance.Rolling element bearing faults can also be diagnosed by Shock pulse method.
	static misalignment of rotor shaft in a synchronous machine	$\omega_{rm} = \omega_{se}/p$	$\omega_{sm} = 2p\omega_{rm}$	causes static eccentricity.
	unbalanced mass on rotor of a synchronous machine		$\omega_{sm} = \omega_{rm}$	very common.Unbalance causes dynamic eccentricity of the rotor, see below.
	dynamic eccentricity in a synchronous machine		$\omega_{sm} = \omega_{rm}$	dynamic eccentricity causes UMP in an electrical machine.
	dynamic displacement of shaft in bearing housing in a synchronous machine		$\omega_{sm} = \omega_{rm}$, $2\omega_{rm}$ ...	causes dynamic eccentricity. generates a clipped time waveform, due to shaft motion being limited by bearing constraint, therefore produces a high number of harmonics.
	general expression for static and dynamic eccentricity in an induction machine	ω_{rm} = (1 − s)nω_{se}/p	$\omega_{sm} = \omega_{rm}\left[\left(nN_r \pm k_e\right)(1-s) \pm pk\right]$	Equation (2). Sidebands at plus or minus slip frequency may occur and components due to UMP, see above.
	commutator faults in DC machine	−	ω_{sm}= 2pk$_c\omega_{rm}$ for lap wound ω_{sm} = 2 k$_c\omega_{rm}$ for wave wound	unbalanced rotor components also generated.

Continued

doi: 10.1049/iet-epa:20070280

Table 5 *Continued*

		Rotational angular frequency of the rotor, ω_m, rad/s	Transverse vibration angular frequency on the stator, ω_{sm}, rad/s	comments
Electrical Faults	broken rotor bar in an induction machine	$\omega_{rm} \pm \frac{2ns\omega_{se}}{p}$	$\omega_{sm} = \left(\omega_{rm} \pm \frac{2ns\omega_{se}}{p}\right)$	difficult to detect because of small amplitude. Current, speed or leakage field have better detection levels
	stator winding faults induction and synchronous machines	—	$\omega_{sm} = p\omega_{rm}, 2p\omega_{rm}, 4p\omega_{rm} \ldots$	problems can be identified as of electrical origin by removing supply and identifying change.Cannot differentiate winding fault types on vibration alone, current monitoring also necessary.

6.7.4 Torsional vibration monitoring: The direct approach would be to mount strain gauges on the shaft, together with telemetry but this is not appropriate for long-term use. An indirect method, outlined in [49], compares the angular displacement of the non-drive end of the turbine shaft with the non-drive end of the generator exciter. The airgap torque produced by the machine is calculated directly from the terminal electrical quantities.

Monitoring torsional vibration can also detect induction motor faults. The speed of an induction motor driving an ideal load should be constant. Perturbations in load and faults within the rotor circuit of the machine will cause the speed to fluctuate. If the rotor is defective, the speed fluctuation will occur at twice the slip frequency. This is because the normally torque-producing slip frequency currents that flow in the rotor winding are unable to flow through the defective part. The speed fluctuations complement the twice slip frequency current fluctuation described in Section 2. A defective induction machine with a rotor of infinite inertia will have twice slip frequency current fluctuations and no speed variation, whereas a low-inertia rotor will exhibit twice slip frequency speed fluctuations but no current fluctuation. This method was reported in [4] and more recent work has been done in [58] in a method described as instantaneous angular speed (IAS) analysis.

6.7.5 Shock pulse monitoring: The shock pulse method is used exclusively for rolling element bearings, which deteriorate at the moving surfaces, developing small pits or imperfections. The interaction between such surfaces generates mechanical stress waves, or shock pulses, in the bearing material, propagating into the structure of the machine. These shock pulses are at ultrasonic frequencies and can be detected by piezoelectric transducers with a resonant frequency characteristic tuned to the expected frequency of the pulses, around 32 kHz. The condition of the bearing is assessed by defining a quantity known as the shock pulse value (SPV), defined as

$$\text{SPV} = \frac{R}{N^2F^2} \tag{3}$$

Low values in (3) indicate bearings in good condition. The development of rolling element bearing monitoring including vibration, acoustic and shock pulse methods is described in [59, 60]. Classification of motor bearing faults in [61] illustrates the unpredictable and broad-band nature of the effects produced. The quantitative evaluation of bearings using the shock pulse method remains difficult.

7 Electrical current, flux and power monitoring

7.1 Generator and motor stator faults

7.1.1 Stator winding: The most significant technique in this area is on-line discharge detection described in Section 8.

7.1.2 Stator current: This work, mostly concerned with motors, is connected with that described in Section 6, which considered rotor eccentricity, but is now extended to stator winding faults. The work is closely associated with the detection of rotor winding faults described later. Theoretical work, verified by laboratory experiments, was started in [62] which concentrated primarily on detecting stator winding faults. The method was then applied in industrial applications [55, 63] but with the intent also to detect eccentricity indicating machine bearing deterioration.

doi: 10.1049/iet-epa:20070280

7.1.3 Brushgear fault detection: Brushgear in machines requires regular maintenance if a minimum level of sparking is to be maintained. Poor performance can be detected by measuring brush or brush-holder temperatures but a more direct method detects the radio frequency energy generated by sparking, as described in [69]. They used a dipole antenna connected to an RF amplifier with a bandwidth from 10–100 MHz, the output of which was rectified and the electronics measured the area under RF power pulses that enter the amplifier as a result of brush-sparking activity.

7.2 Generator rotor faults

The rotors of large turbogenerators have high mechanical, thermal and electrical stresses, and consequently they are prone to faults developing over long periods. The rotor is inaccessible for signals during running and this, with the high value of the turbogenerator plant, has meant that generator rotor monitoring has become sophisticated. Some of the techniques described below are also applicable to smaller machines, but have yet to become fully accepted.

7.2.1 Earth leakage faults on-line: A single earth leakage fault on a generator rotor winding is not serious in itself, because the earth leakage current is limited by the leakage resistance of the excitation and, thus, it cannot cause any damage. However, if two well separated earth faults occur, then large currents can flow, leading to damage of the winding, insulation and rotor forging. The aim of a rotor earth fault detector is to apply a DC bias voltage to the rotor winding and monitor the current flowing to the rotor body via an alarm relay. If an alarm occurs, many utilities consider that the machine should be shut down for investigation. However, operational pressures are such that this is often not possible, and it is necessary to continue running the unit. The next step is to monitor the earth leakage current and manually trip the unit if there is any increase, indicative of a second earth fault.

An alternative method is to use a potentiometer fed to earth via a sensitive relay in a bridge circuit. As the earth fault location alters or a second fault occurs, the bridge unbalances and an indication occurs on the relay. The problem is that the second earth fault may arise close to the location of the first fault and the resultant change in earth leakage current may not be large. A more sensitive indicator of the onset of a second earth fault is the resistance of the winding to earth, measured from either terminal.

7.2.2 Turn-to-turn faults on-line: Airgap search coils: Turn-to-turn faults in a generator rotor winding may lead to local overheating and eventually to rotor earth faults. In addition, the shorting of turns causes unequal rotor heating, leading to bending and UMP, which together cause increased vibration as described in [65]. Such faults can be detected off-line, but a way of detecting them on-line was first described in [66] using a stationary search coil, with a diameter less than the rotor tooth-width, fixed to the stator in the airgap, which detects either the radial or circumferential magnetic flux component.

Fig. 12 shows typical waveforms obtained from such a radial search coil in a two-pole generator operating on load. When a shorted turn occurs, the MMF distribution is disturbed, causing low-order even harmonics or an asymmetry in the flux, and the slot ripple harmonics are disrupted. These changes were used in [66] to determine the number and location of shorted turns by measuring the peak heights of the ripple from stored oscilloscope waveforms, recorded under open and short circuit test conditions.

Since that time, many large steam turbine-driven generators have been fitted with airgap search coils, experience has been obtained and detection techniques refined to deal with the different types and locations of search coils, to detect shorted turns under off- and on-load conditions. New digital techniques have been developed to:

- Give an initial indication of inter-turn faults.
- Allow off-line analysis of downloaded waveforms.

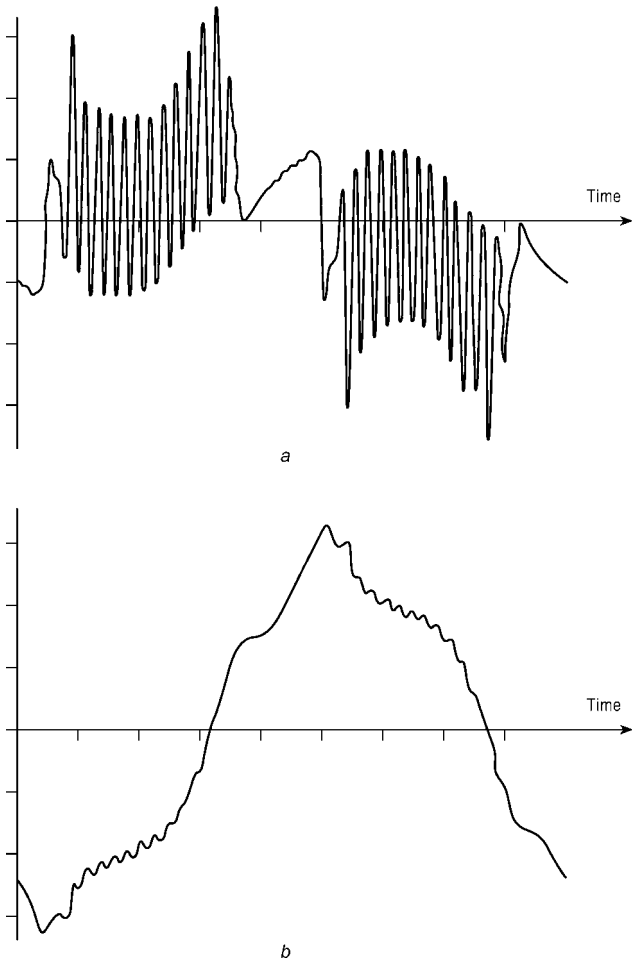

Figure 12 *Typical voltage and flux waveforms obtained from a generator airgap search coil*

- Positively identify and locate the faults.

Circulating current: An alternative way of monitoring shorted turns uses the stator winding itself as the search coil. The principle of this technique, suggested in [66], has been developed and fitted to generators in the UK. This technique makes use of the fact that in large two-pole generators, each phase of the stator winding parallels two half-phase windings. Any asymmetry in the rotor MMF will induce a counter-MMF in the stator winding with twice the fundamental frequency, which will circulate between the half-phases. The presence of shorted turns is detected by measuring those even harmonics. The size of the currents depends upon the severity of the shorted turns. This approach has been developed, with supporting analysis, in [67]. The currents are detected using air-cored Rogowski coils wrapped around the winding. An advantage of this technique, when compared with airgap search coils, is that the current transducers can be installed without removing the rotor. A disadvantage is that it does not give information on the location turn. Neither the airgap nor Rogowski coil method appears to have been applied to multi-pole hydro-type generators or even four-pole turbine-type machines.

7.3 Motor rotor faults

7.3.1 Airgap search coils: The rotors of other electrical machines can be highly stressed, although perhaps not to the same degree as turbogenerators. The work on airgap search coils has been applied to smaller machines in [69] but for measuring torque rather than machine faults. This technique was applied to induction motors [70] using a distributed coil on the stator. The technique of using a stator search coil has not been widely used on motors, but it is possible to use the stator winding itself as a search coil in a manner similar to the method described for generators above. Recently [71, 72] detected rotor defects from voltages induced in the stator winding when the motor stator is disconnected; however, this technique is strictly outside the scope of the paper because it is off-line.

7.3.2 Stator current: Any rotor fault in an induction motor will cause a characteristic swing in the supply ammeter reading. Careful measurement of the stator current will therefore enable such a fault to be monitored. The current drawn by an ideal motor should have a single component of supply frequency. Changes in load will modulate the amplitude of the current to produce sidebands. Faults in the rotor circuit will generate a sideband below the supply frequency that is displaced from it by twice the slip frequency. This effect was described in the references of [4] and the literature [73] shows that the resultant stator MMF wave is given by

$$f_1(t) = \frac{N_2 I_2}{2}\{\cos((3-2s)\omega_{se}t - 3p\theta_1) - \cos((1-2s)\omega_{se}t - p\theta_1)\} \quad (4)$$

The first component of MMF in (4) induces zero sequence EMFs in the three-phase stator winding, because it contains $3\omega_{se}t$ and $3\theta_1$, and gives rise to no current contribution from the supply. The second component of MMF, however, induces a proper three-phase set of currents at the normal supply frequency but contains a component, or sideband, $2s\omega_{se}$ below that frequency. This is the twice slip frequency modulation of the supply current, seen as the swing on the ammeter reading. Such a cyclic variation in the current reacts on the rotor to produce a twice slip frequency torque variation that, if the rotor does not have an infinitely high inertia, gives rise to the $2sp\omega_{rm}$ variation in speed or $2s\omega_{se}$ variation in mechanical vibration, that can also be used for fault detection as described in Section 6. The speed effect reduces the lower sideband, $(1-2s)\ \omega_{se}$, current swing and produces an upper sideband at $(1+2s)\omega_{se}$, enhanced by modulation of the third harmonic flux in the stator, and it can be shown that other sidebands at $(1 \pm 2ns)\ \omega_{se}$ are also found. The ratio of the lower sideband amplitude to the main supply frequency component gives a straightforward indication of the extent of rotor damage, as described in [74]. The supply current can be monitored easily, without interfering with the machine, by fitting a clip-on current transformer (CT) around the supply cable or the cable of the protection CT. Figs. 13*a* and 13*b* taken from [63] shows the power spectral density for the current from two induction machines, Fig. 13*b* with a rotor fault of fractured cage bars, shown by spectral components at a slip frequency of 0.0.719 Hz for $n = 1$ and a slip, s, of 1.4%, with sidebands described by $(1 \pm 2ns)f_{se}$. Because the current measuring technique looks into the motor from the terminals, it is also possible to see beyond the electrical circuits and detect faults on the mechanical load train, such as worn gear teeth, which the motor is driving. Fig. 13*a* shows a wider frequency range of the current spectrum from an induction motor driving through a gearbox, with no $(1-2s)$ component indicating rotor damage, but other sidebands because of the damaged gearbox. Detection is more difficult when the motor speed varies rhythmically because of the driven load, such as a belt or mill drive, or if the frequency variation is significant; for example, on a small power system. This technique has stimulated a surge in the literature as analysts have sought to describe the precise conditions under which faults can be detected; examples include [75–77], the last making a comparison between current, vibration and acoustic methods of detection.

7.3.3 Rotor current: The rotor circuits of wound rotor motors are poorly protected. Faults in brazed joints and slip-ring connections sometimes cause severe damage because they are not detected promptly. Overheating of rotors can also be caused by a current imbalance in the external resistors connected to the slip rings. The low frequency of these currents makes measurements with conventional CTs inaccurate. Faults of these types were part of the development of the proprietary leakage flux technique described later, [78]. However, low-frequency

doi: 10.1049/iet-epa:20070280

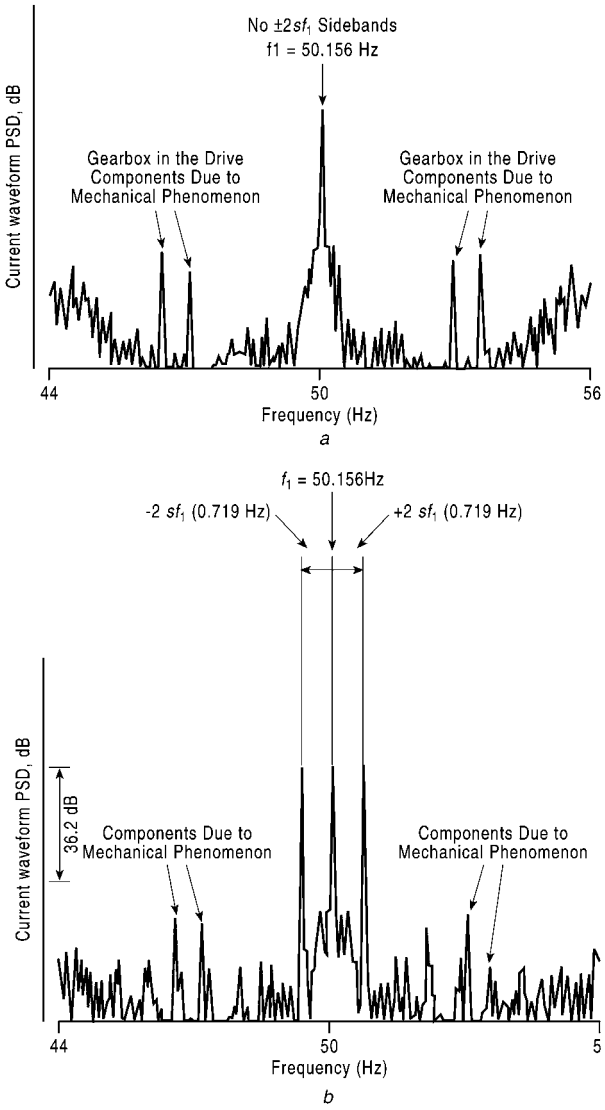

Figure 13 *Supply current spectra from induction motors (MCSA) with faults in the drive train*

Taken from [63] © IEEE (2001)
a Current from an induction motor with broken bars
b Current from an induction motor driving through a damaged gearbox

currents can be measured accurately by Rogowski coils. These have been used to monitor the rotor resistance currents in variable speed wound rotor motors where the signals are integrated to give a voltage proportional to the rotor current.

7.4 Comprehensive methods

Electrical techniques have much in common and there would be an advantage to devising a single technique capable of detecting all electrical faults on the rotor or stator. Authors advocated this generalised approach for induction machines [79–81] and one has applied that technique to three-phase synchronous generators, [82]. Four generalised techniques are summarised below.

7.4.1 Shaft flux: Shaft, or axial leakage flux, occurs in all electrical machines because of construction asymmetry. It is the cause of homopolar fluxes in the machine shaft that can lead to shaft voltages described later. This asymmetry leads to a net axial or shaft flux. Faults, such as winding short circuits, voltage imbalance and broken rotor bars, disrupt the internal symmetry of the machine resulting in a change in axial leakage flux. The production of such fluxes in squirrel cage induction motors was studied in [81] with particular emphasis on the changes occurring because of static eccentricity. It was shown in [83] that it is possible to detect the loss of a supply phase through axial flux monitoring. It was shown in [84] that discrimination could be achieved between a variety of fault conditions by processing the axial flux signal and in [78, 85] a protection device based on this principle was developed. The technique examines changes in the spectral components of the airgap flux in the rotor frame given by

$$b_{n,2}(t) = \hat{B}_{n,2} \cos\left[\left(1 \pm (1-s)\frac{n}{p}\right)\omega_{se}t \pm n\theta_2\right] \quad (5)$$

The flux harmonics in (5) induce currents in rotor circuits, which because of electromagnetic asymmetries appear as components in the axial flux, summarised in Table 6. Fig. 14 illustrates comparable results from a small four-pole squirrel cage induction machine using the technique. Only the spectral components below 500 Hz are shown and the spectral amplitude is linear to emphasise the differences. Faults, such as inter-turn short circuits, broken rotor bars or negative-phase sequence in the supply, are visible in the spectra and have been identified. This technique is embryonic requiring spectral analysis of the signal from a search coil wound concentrically with the shaft of a machine. The most recent paper has adopted a frequency domain technique, [86]. The method is non-invasive and a single sensor can be used for a variety of fault types. However, it is complex and relatively untested.

7.4.2 Stator current: Section 7.3.2 has shown that monitoring stator current is a viable condition monitoring technique, which has become known as motor current spectral analysis (MCSA). The ability to look beyond the electrical machine to the mechanically driven load, Fig. 13*a*, has been exploited for a variable speed drive downhole pump in [87, 88] where wavelet analysis was used to deal with the non-stationary behaviour of the signal from this variable speed machine.

There is now extensive literature on the current analysis method in [89, 90], in which the fundamental magnetic field effects on the airgap was investigated; [91, 92] give a good account of the present state of the art; [93] describes a method appropriate to variable speed drives and [94] describes an analytical approach. Table 7 summarises the angular frequency components that can be detected in the stator current and their relation to machine faults.

Table 6 Axial flux angular frequency components related to specific induction machine assymmetries (5), taken from [2]

	space harmonic of the stator winding MMF			
	$k = 1$	$k = 3$	$k = 5$	$k = 7$
	angular frequency components, rad/s			
Stator asymmetry	$s\omega_{se}$, $(2 - s)\omega_{se}$	$(3s - 2)\omega_{se}$, $(4 - 3s)\omega_{se}$	$(5s - 4)\omega_{se}$, $(6 - 5s)\omega_{se}$	$(7s - 6)\omega_{se}$, $(8 - 7s)\ \omega_{se}$
Rotor asymmetry	$s\omega_{se}$, $(2s - 1)\omega_{se}$	$(3 - 2s)\omega_{se}$, $(4s - 3)\omega_{se}$	$(5 - 4s)\omega_{se}$, $(6s - 5)\omega_{se}$	$(7 - 6s)\omega_{se}$, $(8s - 7)\omega_{se}$

7.4.3 Power: Recent work in [95] has shown that the terminal power spectrum may be an effective monitor of machine health, simplifying the complexities of the stator current and axial flux spectra. This was pioneered in [96], in which it was shown that the equations reduce to

$$p_1(t) = \sum_{n=1}^{\infty}\sum_{m=1}^{\infty}\left\{\begin{array}{l} \dfrac{\hat{V}_n\hat{I}_{+m}}{2}\left[\cos\left(\theta_{(m-n)(m-n)} + \phi_{+m}\right)\right. \\ \left. -\cos\left(\theta_{(m+n)(m+n)} + \phi_{+m}\right)\right] \\ +\dfrac{\hat{V}_n\hat{I}_{-m}}{2}\left[\cos\left(\theta_{-(m-n)(m-n)} + \phi_{-m}\right)\right. \\ \left. -\cos\left(\theta_{-(m+n)(m+n)} + \phi_{-m}\right)\right] \\ +\dfrac{\hat{V}_n\hat{I}_{0\,m}}{2}\left[\cos\left(\theta_{(m-n)-n} + \phi_{0\,m}\right)\right. \\ \left. -\cos\left(\theta_{(m+n)\,n} + \phi_{0\,m}\right)\right] \end{array}\right\} \tag{6}$$

From (6), when $m = n$, a DC contribution is made to the power in each phase. For harmonic components of power, however, because of the presence of the phase factor, $(q - 1)2\pi/3$, a contribution to the power only occurs when $(m - n)$ or $(m + n)$ are multiples of three, or are triplens. These contributions will be at + or $-(m - n)\omega_{se}t$ or + or $-(m + n)\ \omega_{se}t$, depending on whether the positive or negative sequence currents are contributing to the power. From inspection of the last term in (6), it can be seen that there will be no zero sequence contribution to the ripple in instantaneous power. This is because for all values of n, the term in $(q - 1)2\pi/3$ in θ ensures that the summation over three phases always comes to zero. An application of these equations to power condition monitoring of an electrical machine could be a three-phase induction motor with a broken cage. We already know from Table 6 that at a fundamental supply voltage angular frequency of ω_{se}, the fundamental supply current will contain components at (1 $\pm$ 2s) ω_{se}. Therefore for the 1st and (1−2s)th harmonics of voltage

$$\begin{aligned} -(m - n)\omega_{se} &= 2s\omega_{se} \\ (m + n)\omega_{se} &= 2(1 - s)\omega_{se} \end{aligned} \tag{7}$$

Thus, the power spectrum because of the fundamental supply voltage will contain components at $2s\omega_{se}$ and $2(1-s)\omega_{se}$. An example simulated in [95], is shown in Fig. 15, for a six-pole induction motor with a damaged rotor fed at $f_{se} = 60$ Hz with a very large slip at this operating condition of 15.8%, and therefore the sidebands on the current spectrum because of damage are at 41 and 79 Hz, above and below the 60 Hz fundamental, whereas on the power spectrum the damage sideband is positioned at 19 Hz.

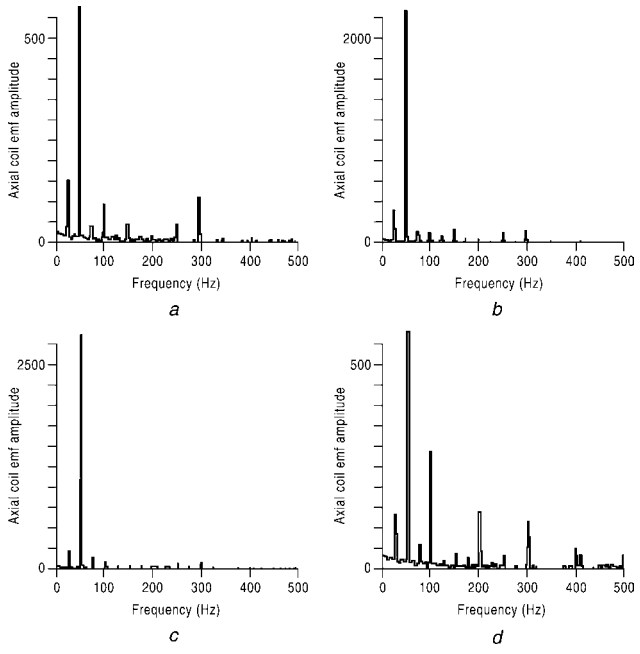

Figure 14 *Typical spectra taken at identical gains from an axial flux search coil fitted to an experimental motor*

a Good rotor, no faults, no load
b Broken rotor bar, no other faults
c Goof rotor, large shorted turn 1 amp, no load
d Good rotor, small negative phase sequence, no load

7.4.4 Shaft voltage or current: Many electrical power utilities have attempted to monitor voltages induced along the shafts of electrical machines in the hope that they may be an indicator of core or winding degradation, because they give rise to large shaft currents. Brushes would normally be placed at either end of the machine to embrace the complete shaft flux circuit. A full report on the mechanisms for the production of shaft voltages and currents and the faults they may indicate was given in [35], and proposed a shaft voltage monitor. A more up-to-date version was proposed in [97]. The author's experience, however, is that shaft voltage is not a useful parameter for monitoring. The voltage is difficult to measure

doi: 10.1049/iet-epa:20070280

Table 7 Electrical angular frequency components related to specific electrical machine faults

		Angular frequency components, rad/s		
		Current	Flux	Power
Mechanical faults	oil whirl and whip in sleeve bearings	$(0.43–0.48)\omega_{se}/p$	—	$\omega_{se}\left[1+\frac{0.43-0.48}{p}\right]$
	unbalanced mass on rotor of a synchronous machine	ω_{se}/p	—	$\omega_{se}\left[1+\frac{1}{p}\right]$
	dynamic eccentricity in a synchronous machine	$2\omega_{se}/p$	—	$\omega_{se}\left[1+\frac{2}{p}\right]$
	dynamic displacement of shaft in bearing housing of a synchronous machine	$\omega_{se}/p, 2\omega_{se}/p \ldots$	—	$\omega_{se}\left[1+\frac{1}{p}+\frac{2}{p}+\cdots\right]$
	static misalignment of rotor shaft in a synchronous machine	$\omega_{se}/p, 2\omega_{se}/p, 3\omega_{se}/p \ldots$	—	$\omega_{se}\left[1+\frac{1}{p}+\frac{2}{p}+\cdots\right]$
	static and dynamic eccentricity in induction machine	$\omega_{se}\left[\left(nN_r \pm k_e\right)\frac{(1-s)}{p} \pm k\right]$	$\omega_{se}\left[k_e\frac{(1-s)}{p} \pm k\right]$	$\omega_{se}\left[1+k_e\frac{(1-s)}{p} \pm k\right]$
Electrical faults	broken rotor bar in induction machine	$(1 \pm 2ns)\omega_{se}/p$	$s\omega_{se} \ldots$ $(2s-1)\omega_{se} \ldots$	$2ns\omega_{se}/p$ $2n(1-s)\omega_{se}/p$
	stator winding faults in a synchronous machine	$\omega_{se}, 2\omega_{se}, 4\omega_{se} \ldots$	ω_{se}	$\omega_{se}, 3\omega_{se}$
	stator winding faults in an induction machine		$s\omega_{se} \ldots$ $(2-s)\omega_{se} \ldots$	—

continuously, and the damage to the machine needs to be substantial before a significant variation in shaft voltage occurs.

8 Electrical discharge monitoring

8.1 Introduction

Discharges in high-voltage machine insulation system also cause terminal voltage perturbations, which can be analysed to detect them. This technique has received attention because the insulation system lies at the heart of the machine and deterioration is slow and, thus, it should be a good target for condition monitoring. Discharge behaviour is complex and can be categorised in the ascending order of energy and damage as:

- Corona discharge
- Partial discharge (PD)
- Spark discharge
- Arc discharge

A wellmade insulation system will exhibit corona discharge on the surface of the insulation at AC voltages above 4 kV rms to ground. If there are voids inside the body of the insulation system, those voids will also exhibit PD. This activity worsens progressively depending on the quality of the insulation, the local strength of the field and the mechanical and electrical conditions to which the insulation is subjected. Certain parts of high-voltage winding

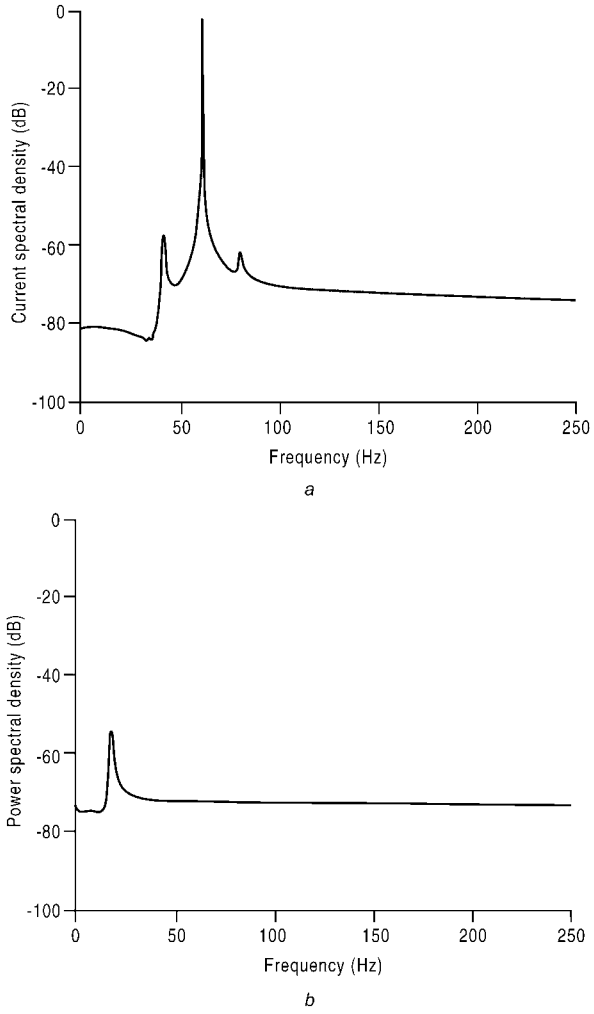

Figure 15 *Spectra from a simulation of an induction motor with broken rotor bars*

The upper curve shows the current spectrum with the typical fault sidebandsThe lower graph shows the power spectrum with the fault sideband shifted down to DC
Taken from [96] © IEEE (1999)
a Current spectrum with typical fault sidebands
b Power spectrum with fault sideband shifted down to DC

insulation systems are particularly vulnerable to discharge activity:

- Stator slot wall, where PD activity erodes and damages the main wall.

- Slot emergence, where coils emerge from the earth protection of the slot and insulation is exposed to surface discharge activity.

- End-winding surfaces, subjected to damaging discharge activity at the phase separation regions, when the surface is wet, dirty or both.

Electrical discharge activity is an early indicator of many electrical faults and the activity is related to insulation remnant life. Discharge activity detection could therefore give valuable warning of failure and provide information about the remnant life. Electrical discharges are transitory, low-energy disturbances that radiate electromagnetic, acoustic and thermal energy. That conducted energy causes perturbations to the voltage and current waveforms at the terminals. The earliest applications of PD detection were to isolated insulation components, such as high-voltage bushings or EHV cable stop joints, in [98], where the insulation under inspection is close to the coupling circuit and energised solely at the cable-phase voltage. After successful application to stop joints, the method was applied to HV turbine and hydrogenerator windings. However, an electrical machine winding represents a more complex insulation system than a stop joint.

8.2 Discharge detection techniques

8.2.1 RF coupling method: The earliest work, summarised in [99], was developed by Westinghouse in the USA to detect on-line, subconductor arcing in the stator windings of large steam turbogenerators, by measuring perturbations in the winding current. Arcing activity produces broad-band electromagnetic energy, some of which propagates into the neutral connection of the star-connected winding. Emery used a ferrite-cored radio frequency current transformer (RFCT) wrapped around the neutral to couple this activity that was detected using a radio interference field intensity (RIFI) metre. The neutral cable is a good measurement location because it has a low potential to ground and because arcing at any generator location causes RF current to flow into the neutral. The RFCT had a frequency response from 30 Hz to 30 MHz and the RIFI meter had a narrow bandwidth of ~10 kHz centred at 1 MHz. The centre frequency is tuned to resonances in the winding that the arcing activity excites; the meter measures the average peak energy received by the instrument and the RFCT and RIFI metre were proprietary items. Westinghouse developed a specialised RF monitor based on this technique described in [99], which also proved, with further details in [100, 101], the detection of subconductor arcing and sparking in the generator. However, the change in signal level, when arcing occurs, was not dramatic. An increase of less than 50% of the unfaulted indication was typical, making an alarm level setting for such a monitor difficult.

This technique was applied in [102] to steam and water turbogenerators in American Electric Power. This used broader bandwidth quasi-peak RIFI instruments connected to the neutral RFCT and analysed the signal in the frequency and time domains, showing evidence of slot discharge activity on hydroelectric machines and other forms of unexpected corona activity.

A similar, cheaper technique was devised in the UK, known as an earth loop transient monitor [98], applied to the generator and motor stator winding insulation using a Rogowski coil [103], wrapped around the neutral cable. The frequency response of the Rogowski coil is broad, but the

doi: 10.1049/iet-epa:20070280

detector had a narrow bandwidth of ~15 kHz centred at 1 MHz calibrated in picocoulombs and measured the average peak energy. Care must be taken in the calibration because energy is propagated to the instrument from different insulation discharge sites simultaneously. A theoretical model for the propagation of energy from the discharge to the neutral was provided in [104] and has shown how this depends critically on the winding configuration and size of the stator core.

8.2.2 Capacitive coupling method: An alternative technique was described in [105] and applied to hydroelectric generators in Canada aimed at detecting the slot discharge activity with which these high-voltage, air-cooled windings are afflicted. Connection to the winding is made through coupling capacitors at the machine line terminals and discharge pulses are coupled to a specialised pulse height analyser, of bandwidth 80 MHz, sufficient to capture PD pulses with rise-times of 1 to 10 ns. Initially the capacitors were connected to the machine during an outage, but [106] describes how the capacitors could be permanently built into the phase rings of the machine, so that the measurements can be made without service interruption. These permanent couplers also ensure that the discharge activity from the electrical supply system, to which the machine is connected, is rejected. The analysis of discharges is carried out at intervals during the life of the machine rather than continuously on-line.

8.2.3 Broad-band RF method: All the techniques described operate at low RF frequencies (1–80 MHz) and detect the electromagnetic energy propagated along the winding to the neutral or line end connections. In a healthy machine, there will be a background of corona and PD activity that varies from machine to machine and with time. It has been shown that serious PD, sparking or arcing, has faster rise-times than the background corona and PD activity, and therefore produce a much higher bandwidth of electromagnetic energy, up to 350 MHz. If this energy is detected, at as high a frequency as possible, the ratio of damaging discharge signal to background noise is increased. Frequencies >4 MHz do not propagate from the discharge site along the winding, as with the lower frequency techniques, but by radiation from the winding. This radiation can be detected by an RF aerial located inside the enclosure of the machine or outside, close to an aperture in it, using a technique similar to that proposed in [64]. A monitor for detecting damaging discharge activity in a turbogenerator stator winding by this method was described in [4] based on using an aerial with a band-pass filter tuned above the cut-off frequency of background activity (~350 MHz), avoiding interference from nearby radio or radar stations. The received signal cannot be related directly to discharge magnitudes in picocoulombs and all timing information about the discharge was lost. The higher signal-to-noise potential of broad-band RF techniques at frequencies (100 MHz–1 GHz) has been investigated most recently in [107], and there could be a potential for discharge site location by the use of a directional aerial, but the dimensions of the aerial, diameter 0.6–6 m, at these frequencies would be impracticable. Therefore despite the potential of broad-band RF techniques, their lack of location ability means that these techniques have now largely been superseded.

8.2.4 Insulation remnant life: Besides identifying specific faults, PD measurement can also determine the remnant life of insulation systems, and this has occupied the literature, [3, 108]. The process requires complex multi-parameter measurements of insulation resistance, polarisation index, capacitance, dissipation factor tip-up, PD magnitude and discharge inception voltage as well as on-line PD activity and is an elusive and difficult interpretation.

8.3 Detection problems

Lower frequency (1–80 MHz) propagation along the conductor permits the location of the discharge site by the time-of-flight measurement. However, reflections at winding discontinuities make the identification of pulses difficult. Low-frequency RFCTs produced an output and discharge activity could be calibrated in picocoulombs because the response could be related directly to the amplitude of the discharge calibration pulse. The Rogowski coil was easier to fit than the RFCT but suffered from low sensitivity and is now little used. Other PD detectors have been investigated, including the portable Tennessee Valley Authority (TVA) probe and discharge locator (DL), [109], and the stator slot coupler, [110], which can be mounted above the stator conductor in the slot beneath the wedge. These detectors enable operators off-line to locate discharge activity. More recently, PD measurement has been made using the standardised capacitive coupler, a robust power engineering component of capacitance C that can be calibrated in Q_m, the discharge value in millivolts across the coupler, where $Q_m = Q/C$, where Q is the discharge value. In all detection systems, it is necessary to shield the desired PD activity signal from external noise, either because of PD activity in the connections and switchgear of the electrical machine, sparking in brushgear or harmonic activity because of nearby power electronics. Noise and calibration issues are dealt with in [104, 110–113]. A fundamental problem for PD detection systems is that activity on identical windings of different machines exhibit large variations in background activity because of variations in ambient conditions, small changes in the insulation homogeneity and noise.

8.4 Modern discharge detection techniques

Modern on-line discharge detection methods for rotating electrical machines have developed from the work described above and can now be divided into two techniques:

- The hydrogenerator partial discharge analyser (PDA), based on Section 8.1 Fig. 16*a* and [114].

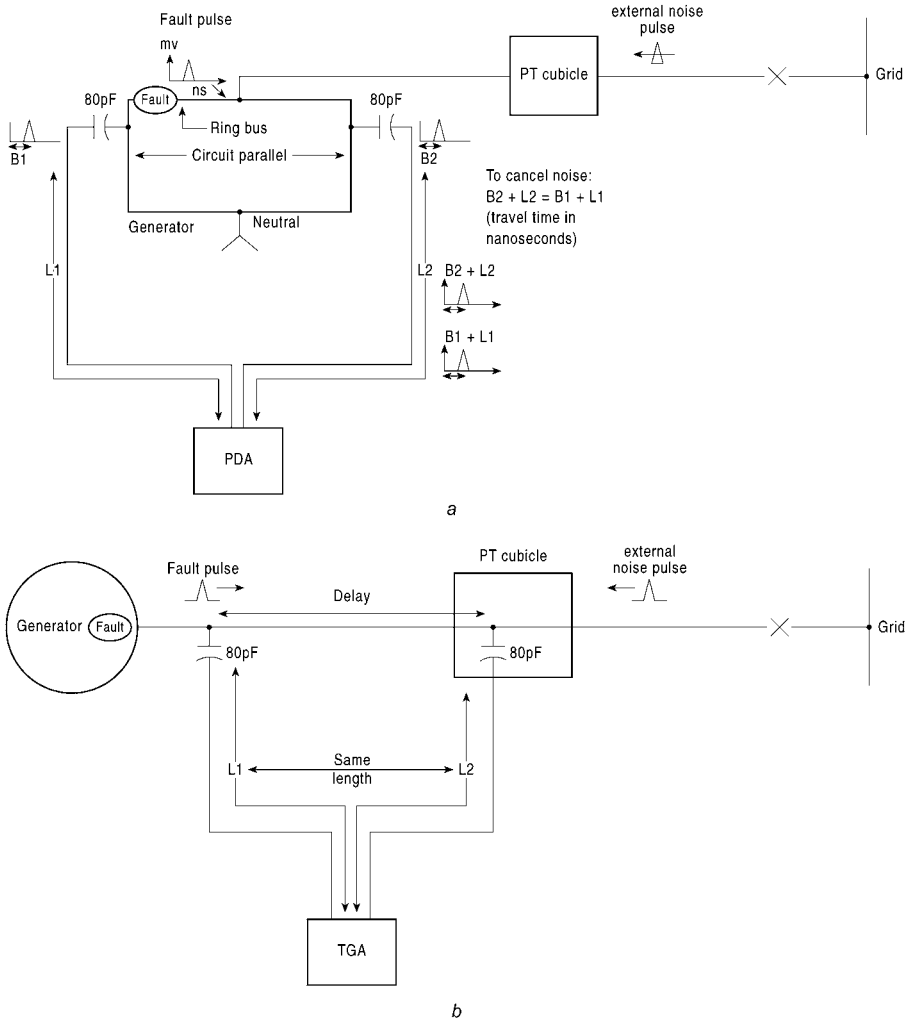

Figure 16 *Hydrogenerator and turbogenerator partial discharge detection schemes*

a Diagram of the coupler connections and electronics for the PDA
b Diagram of the connections and electronics for the TGA
Taken from [3] © IEEE(2004)

• The motor or turbogenerator analyser, based on Sections 0 and 0, which adopts a variant of the PDA to improve the signal-to-noise ratio of PD detection on windings of the types found in motors and turbogenerators, Fig. 16*a*. Experience with this technique is described in [115].

An IEEE standard has also now been devised [116] to standardise the measurement of PD on rotating machines. Work is continuing on PD detection methods, including work on lower voltages, 4 kV, motors in [117], larger machines in [118] and an example of an insulation monitoring system that detects insulation leakage currents by measuring machine terminal voltages on an induction motor in [119].

9 AI techniques

9.1 Introduction

Condition monitoring has to establish a map between input signals and machine condition output and the tables shown in the paper provide a basis for such a map. Considerable effort has been made to develop AI for electrical machines to establish such maps and play the role currently performed by engineers. Expert systems, fuzzy logic and artificial neural networks (ANN) have been used by machine manufacturers and utilities.

9.2 Expert systems

Knowledge can be presented in a number of ways to a computer system. Fig. 17 shows the general architecture of a rule-based expert system. An expert system was developed for monitoring stator insulation in turbogenerators in [120]. It can be seen that several interacting factors, including vibration, overheating and moisture contamination, are involved in the degradation process and insulation failure can occur in different parts of the winding.

PD signals are high-frequency spikes, in the 100 MHz range, which can be confused with noise and can be

doi: 10.1049/iet-epa:20070280

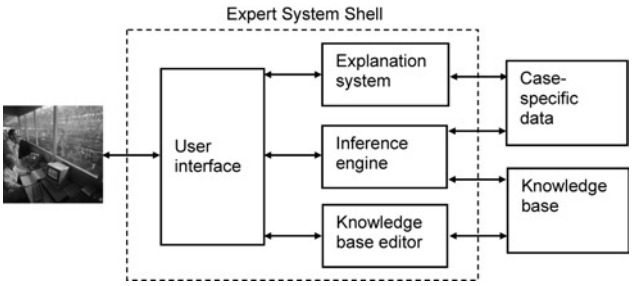

Figure 17 *Expert system architecture*

monitored as described in Section 8. Expert knowledge is important to improve the reliability of the PD measurement data. Given the reliability of the acquired PD data, conclusions can only be drawn based on trend analysis, comparison with other generators, maintenance records, earlier off-line test results, present operating point, vibration and temperature measurement, visual inspection and fleet experience. Such aspects are taken into account using human expert knowledge, represented in rules, as it is hard to establish algorithmic solutions for such problems. An expert system to monitor turbogenerators, including PD activity, has been described in [121] and Fig. 18 shows the architecture of an appropriate system including stator and rotor winding data. Interactions between different modules are taken into account and these modules may overlap in their functionalities.

9.3 Fuzzy logic

Condition monitoring signatures could lead to the conclusion that signal interpretation can always be unambiguous, but it is not so. The condition of the machine being monitored can be described in a linguistic manner, for example, machine condition is not necessarily 'good' or 'bad', but falls into an intermediate range. Fuzzy logic is particularly suitable in such circumstances, where condition monitoring input signals can be associated with certain membership functions. A membership function allows quantities, such as a negative sequence current or temperature, to be associated with a linguistic variable with a degree of confidence. Differently shaped membership

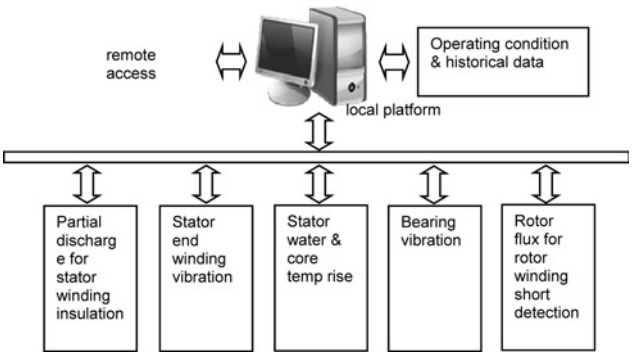

Figure 18 *Configuration of a modular expert system for a large turbogenerator*

functions can be chosen for different applications. Construction of the membership functions requires insight into the physical meaning of the signals, and the linguistic variables to be used. Practical experience and experiments in the laboratory or industrial environment are the only way to gain such insight; hard work cannot be bypassed, as illustrated in [122]. However, fuzzy logic does provide a powerful tool for information representation and processing. The power of fuzzy logic is more evident in the operation and inference stages of the process, which derive new results that then provide progressively more precise information about the actual condition of the machine. An early fuzzy diagnostic system for a linear induction motor drive has been described in [123]. There are similarities between expert and fuzzy logic systems, in that they are both knowledge-based. The added feature of a fuzzy logic diagnostic system is in the representation of knowledge as membership functions and the fuzzy inference methodology.

9.4 Artificial neural networks

The attractive feature of ANN for condition monitoring is their ability to represent complex, nonlinear relationships and to self-learn the pattern recognition of those relationships. Monitoring broken rotor bars in cage induction motors, for example, requires correlating between current components, other signals and fault severity. However, a quantitative relationship is complex and factors such as operating point, load and machine electromagnetic asymmetries have effects on the relationship. These factors are difficult to take into account in an analytical way. A neural network can be trained to represent the desired target relationship. In this approach, the electrical machine is treated as a black box with input and output signals used to train the network. The signals are chosen to be those most relevant to the condition monitoring task, requiring expert knowledge of the machine. Time domain signals are pre-processed by a fast Fourier transform and these components and their derivatives are inputs to the neural network; [124] adopted this approach for condition monitoring machines using the axial flux method.

9.4.1 Supervised learning: Of all neural network structures, the multi-layered perceptron (MLP), trained using the back-propagation algorithm, is the most widely used. MLP training can be viewed as a gradient descent technique and therefore possesses a high degree of credibility, although the local minimum problem needs to be dealt with in the training process. An MLP network has been developed in [125] to detect broken rotor bar faults in induction motors.

9.4.2 Unsupervised learning: A neural network can also learn unsupervised, [126]. Unsupervised learning is a simpler but more protracted approach to the identification of abnormal operation. The system proceeds through the learning stage without the provision of input of data classifications, whereas the connection weight adaptation of

the MLP is driven by that knowledge. However, the possibility of training a network on a dataset, without labelled inputs, offers practical advantages. However, interpretation of the outputs and the use for fault classification requires detailed knowledge of the training dataset. Nevertheless, unsupervised networks require less training iterations as they do not require exact optimisation.

10 Discussion

10.1 Mechanical and chemical methods

Temperature detection has been successfully used and is an excellent global indicator of electrical machine deterioration. The technique has been neglected of late because of the growth of newer, superficially more attractive methods. However, temperature measurement still deserves application, especially coupled with more modern techniques of detection, analysis and modelling.

Vibration and shock pulse methods have been used extensively in the field and have proved themselves to be effective, particularly for monitoring bearing deterioration.

Chemical and wear monitoring methods have also demonstrated themselves to be effective, but the equipment has tended to be expensive in the past and interpretation has been difficult. Reductions in cost and improvements in computer analysis will reduce these limitations.

Motor speed has been analysed to detect rotor electrical faults, but it has not been widely used by operators.

10.2 Comprehensive electrical methods

Sections 2 and 9 show that electrical techniques have much in common and provide a comprehensive condition monitoring for the machine. There would be advantages in devising a single electrical technique capable of detecting all electrical faults, on rotor or stator, and this approach was recommended in [1, 2] and more recently in [79–82]. The four general techniques in the order of importance are:

- Power
- Stator current
- Shaft flux
- Electrical discharge activity
- Shaft voltage or current

Shaft voltage or current is not considered useful for continuous monitoring.

Discharge monitoring with a PDA has shown itself to be the most problematic electrical method of condition monitoring. It addresses insulation; it can detect global effects, including remanent life, and it does have a long Failure Sequence from Root Cause to Failure Mode. However, the proportion of failures because of insulation is now less than a third. Furthermore, the method is open to interpretation when applied to distributed, multi-path, multi-connection, variably stressed, electrical machine insulation systems. Its greatest impact has been on hydrogenerator applications where a specific Failure Mode is searched for in known locations.

Shaft flux and stator current have both been shown to be non-invasive methods, shaft flux using a single additional sensor; stator current can use existing sensors, but both require broad bandwidth and complex spectral interpretation. Current monitoring has been used extensively in the field as MCSA and has proved itself to be effective, whereas shaft flux monitoring has not.

Power monitoring is the most comprehensive means of encompassing all electrical terminal measurements for condition monitoring purposes using existing sensors and requiring less bandwidth and less complex spectral interpretation. It is yet to prove itself effective in operational application.

10.3 Effects of variable speed operation

Variable speed converters are being applied in increasing numbers to electrical machines. The key problems that may arise in condition monitoring variable speed machines are:

- If the speed of the drive remains constant for substantial periods of time, then spectral analysis of flux, voltage, current, power or vibration can still be done provided the results are interpreted for the speed and base frequency when the measurements are made.

- If the speed varies significantly, then non-stationary techniques, such as short time interval spectrograms, wavelets or Wigner-Ville techniques, dependent on the rate of change of speed, need to be used.

- If speed varies under control loop action, then the frequency content of the monitoring signals will be affected by the controller bandwidth, as described in [127]. In this case, it is possible for the drive controller to suppress fault harmonics in the terminal quantities. However, [127] has shown that it is still possible to extract condition monitoring information from signals derived within the controller.

- When supplied from a variable speed drive, all terminal quantities of the electrical machine will be polluted by drive harmonics, and filtering will be essential for obtaining a good signal-to-noise ratio.

A condition monitoring system for variable speed induction motors using the power line as the

doi: 10.1049/iet-epa:20070280

communication channel was demonstrated in [128]. This is a brave attempt to achieve universal monitoring and the author has wisely concentrated on monitoring the winding temperature.

10.4 Multi-parameter monitoring, AI and CBM

Electrical techniques have proven to be powerful tools for monitoring electrical machines, offering a comprehensive condition monitoring signal. The difficulties are broad signal bandwidth, complexity of the spectral analysis, the interpretation of their content and the low signal-to-noise ratio of the resultant signal when a fault is present. This situation is exacerbated on variable speed drives where individual fault frequencies may need to be tracked with the drive speed. AI techniques are potentially valuable for electrical machine condition monitoring because the underlying physics, as shown in this paper, is rich in fundamental rules, and these could be exploited by expert systems to mitigate the difficulties above. However, the development of AI for electrical machine condition monitoring is still in its infancy and has neither yet been widely proven nor accepted.

Experience shows that other global indicators of machine health, such as temperature, chemical degradation or vibration give clear signals which can be used alongside electrical signals to improve detection. This approach was recommended in [1, 4], in what was described as multi-parameter monitoring. An example is shown in Fig. 8 where indications from two independent parameters on the same machine, in this case a core monitor signal and a gas signal, gave confirmatory results. This type of correlation in condition monitoring gives enormous confidence to operators in condition monitoring signals.

Multi-parameter monitoring can still be considered a minimalist approach since the minimum effective number of signals should be compared to achieve the necessary detection.

AI techniques can be used with multi-parameter signals to improve the signal-to-noise ratio and, thus, AI and multi-parameter methods should play a major role in future machine condition monitoring.

The era of CBM, life cycle costing (LCC) and Asset Management is new, and the only published results relevant to rotating electrical machines are in [120, 121, 129]. It is clear from experience with another electrical plant, [130], that the techniques could be applicable to rotating electrical machines, particularly in large installations. The monitoring techniques of greatest significance for condition assessment are likely to be those of global significance to the machine such as:

- Winding and coolant temperature rise;
- Rotor dynamics and bearing condition via power, current, speed and vibration measurement;
- PD monitoring for high-voltage windings.

The most effective techniques in the future will consider:

- Failure modes and the root causes of failure in machines;
- Adopt AI techniques, based upon the tables of physical rules exemplified in the paper;
- Relate monitoring signals with one another in a multi-parameter approach.

11 Conclusions

- Temperature detection has repeatedly been shown to be an effective global monitoring technique for electrical machines, using simple sensors and narrow bandwidth (<1 Hz) low data rate signals but has been neglected as a monitoring method. It should be employed more widely, making use of temperature rise, temperature imaging and modelling techniques and modern sensor technology such as fibre optics.
- Motor speed has been analysed using IAS to detect rotor electrical faults but has not been widely used by operators.
- Chemical and wear analysis have been demonstrated to be effective global monitoring techniques for electrical machines which can produce narrow bandwidth (<1 Hz) signals, but the cost of the equipment and the quantity of data generated by chemical analysis currently confine their application to only the largest machines.
- The availability of high-quality, digitally sampled, mechanical vibration and electrical terminal data from electrical machines opens the possibility for more comprehensive monitoring of the machine and a prime mover for driven machine combinations. However, these signals generally require broad bandwidth (>50 kHz) and a high data rate for adequate analysis.
- Vibration monitoring and shock pulse analysis are non-invasive but use a number of specialised sensors and broad bandwidth with complex analysis. The precise selection and location of sensors is very important. However, because of its wide application in other rotating machines, vibration analysis has established itself as a reliable and widely accepted technique for electrical machines, and so has shock pulse analysis for rolling element bearings.
- Comprehensive monitoring of an electrical machine can be achieved by measuring shaft flux, current, power and electrical discharge activity. These are broad bandwidth (generally >50 kHz) signals requiring complex analysis. Shaft flux, current and power signals are capable of

detecting faults in both the electrical and mechanical parts of a drive train.

• Shaft flux monitoring is non-invasive and uses a single sensor, but it is complex to analyse and untested in the field.

• Current monitoring is also non-invasive, but uses existing sensors and has established itself as MCSA, a reliable and widely accepted technique for machine monitoring.

• Power monitoring is also non-invasive, uses existing sensors but requires less bandwidth ($<$10 kHz) and less complex spectral interpretation to detect faults, but it is not yet widely accepted and, thus, it deserves investigation for future development.

• Electrical discharge activity requires special sensors, wide bandwidth ($>$100 kHz) and very complex analysis for fault detection and can only be recommended where a specific high-voltage failure mode is being searched for in a known location on a large machine.

• Shaft voltage or current is an ineffective condition monitoring technique for electrical machines.

• The comprehensive analysis of condition monitoring signals must take into account the inter-relationship between electrical and mechanical signals.

• AI techniques applied to electrical machine drives will be successful if they exploit comprehensive signals and the fundamental physical rules included in the paper. AI techniques should also use multi-parameter monitoring to raise the signal-to-noise ratio and increase operator confidence in condition monitoring interpretation.

• CBM, LCC and Asset Management techniques applied to electrical machine drives will be successful if they exploit these multi-parameter and AI techniques and are likely to increase in importance in the future.

• Future condition monitoring of electrical machines must be oriented more closely towards the detection of identified machine failure root causes, including bearing faults. Future research on condition monitoring of electrical machines should reflect the above and concentrate more on proving the effectiveness of new techniques on operating plant.

12 Acknowledgments

The author acknowledges help he has received from colleagues in condition monitoring, Dr Li Ran and Prof J Penman. He has also been assisted by Dr. J. R. Bumby and his students at Durham, Michael Wilkinson, Fabio Spinato and Mark Knowles. The volume of reference material in machine condition monitoring is enormous, and the author has selected references to reflect the spread of work which has been done. He acknowledges the work of all those authors but also of the many others, whose works are too numerous to be included in this review.

13 References

[1] TAVNER P.J., PENMAN J.: 'Condition monitoring of electrical machines' (Research Studies Press and John Wiley & Sons, Letchworth, UK, 1987)

[2] VAS P.: 'Parameter estimation, condition monitoring and diagnosis of electrical machines' (Clarendon Press, Oxford, 1996)

[3] STONE G.C., BOULTER E.A., CULBERT I., DHIRANI H.: 'Electrical insulation for rotating machines, design, evaluation, aging, testing and repair' (Wiley-IEEE Press, New York, 2004)

[4] TAVNER P.J., GAYDON B.G., WARD D.M.: 'Monitoring generators and large motors', *IEE Proc. B, Electr. Power Appl.*, 1986, **133**, (3), pp. 169–180

[5] FINLEY W.R., BURKE R.R.: 'Troubleshooting motor problems', *IEEE Trans. Ind. Appl.*, 1994, **30**, (5), pp. 1383–1397

[6] SINGH G.K., AL KAZZAZ S.A.S.: 'Induction machine drive condition monitoring and diagnostic research – a survey', *Electr. Power Syst. Res.*, 2003, **64**, (2), pp. 145–158

[7] HAN Y., SONG Y.H.: 'Condition monitoring techniques for electrical equipment – a literature survey', *IEEE Trans. Power Deliv.*, 2003, **18**, (1), pp. 4–13

[8] NANDI S., TOLIYAT H.A., LI X.: 'Condition monitoring and fault diagnosis of electrical motors – a review', *IEEE Trans. Energy Convers.*, 2005, **20**, (4), pp. 719–729

[9] IEEE : 'Gold Book: 'Recommended practice for design of reliable industrial and commercial power systems' (IEEE Press, Piscataway, 1990)

[10] DICKINSON W.H.: 'IEEE reliability working group, report on reliability of electric plant. Part I, II and III', *IEEE Trans. Ind. Appl.*, 1974, **10**, pp. 201–252

[11] EVANS D.L.: 'IEEE reliability working group, report on problems with hydrogenerator thermoset stator windings. Part I, II and III', *IEEE Trans. Power Appl. Syst.*, 1981, **100**, pp. 3284–3303

[12] O'DONNELL P.: 'IEEE reliability working group, report of large motor reliability survey of industrial and commercial installations. Part I, II and III', *IEEE Trans. Ind. Appl.*, 1985, **21**, pp. 853–872

[13] ALBRECHT P.F., MCCOY R.M., OWEN E.L., SHARMA D.K.: 'Assessment of the reliability of motors in utility

doi: 10.1049/iet-epa:20070280

applications-updated', *IEEE Trans. Energy Convers.*, 1986, **1**, pp. 39–46

[14] BONNETT A.H., SOUKUP G.C.: 'Cause and analysis of stator and rotor failures in three-phase squirrel-cage induction motors', *IEEE Trans. Ind. Appl.*, 1992, **28**, (4), pp. 921–937

[15] THORSEN O.V., DALVA M.: 'A survey of faults on induction motors in offshore oil industry, petrochemical industry, gas terminals and oil refineries', *IEEE Trans. Ind. Appl.*, 1995, **31**, (5), pp. 1186–1196

[16] THORSEN O.V., DALVA M.: 'Failure identification and analysis for high-voltage induction motors in the petrochemical industry', *IEEE Trans. Ind. Appl.*, 1999, **35**, (4), pp. 810–818

[17] TAVNER P.J., HASSON J.P.: 'Predicting the design life of high integrity rotating electrical machines'. 9th IEE Int. Conf. Electrical Machines and Drives (EMD), Canterbury, 1999 (IEE)

[18] TAVNER P.J., VAN BUSSEL G.J.W., SPINATO F.: 'Machine and converter reliabilities in wind turbines'. 3rd IET Int. Conf. Power Electronics Machines and Drives (PEMD), Dublin, 2006 (IET)

[19] ROGERS A.J.: 'Distributed optical-fibre sensing', *Meas. Sci. Technol.*, 1999, **10**, (8), pp. R75–R99)

[20] SIYAMBALAPITIYA D.J.T., MCLAREN P.G., TAVNER P.J.: 'Transient thermal characteristics of induction machine rotor cage', *IEEE Trans. Energy Convers.*, 1988, **3**, (4), pp. 849–854

[21] ZOCHOLL S.E.: 'Motor analysis and thermal protection', *IEEE Trans. Power Deliv.*, 1990, **5**, (3), pp. 1275–1280

[22] MILANFAR P., LANG J.H.: 'Monitoring the thermal condition of permanent-magnet synchronous motors', *IEEE Trans. Aerosp. Electron. Syst.*, 1996, **32**, (4), pp. 1421–1429

[23] MELLOR P.H., ROBERTS D., TURNER D.R.: 'Lumped parameter thermal model for electrical machines of TEFC design', *IEE Proc. B, Electr. Power Appl.*, 1991, **138**, (5), pp. 205–218

[24] BRANDT G.B., GOTTLIEB M.: 'Fiber optic temperature sensors using optical fibers', Abstracts of Papers of the American Chemical Society, September 1982, Vol. 184, p. 64

[25] CARSON C.C., BARTON S.C., ECHEVERRIA F.S.: 'Immediate warning of local overheating in electrical machines by the detection of pyrolysis products', *IEEE Trans. Power Appl. Syst.*, 1973, **92**, pp. 533–542

[26] CARSON C.C., BARTON S.C., GILL R.S.: 'The occurrence and control of interference from oil-mist in the detection of overheating in a generator', *IEEE Trans. Power Appl. Syst.*, 1978, **57**, (5), pp. 1590–1514

[27] RYDER D.M., WOOD J.W., GALLAGHER P.L.: 'The detection and identification of overheated insulation in turbo-generators', *IEEE Trans. Power Appl. Syst.*, 1979, **98**, (7), pp. 333–336

[28] BRAUN J.M., BROWN G.: 'Operational performance of generator condition monitors: comparison of heated and unheated ion chambers', *IEEE Trans. Energy Convers.*, 1990, **5**, (2), pp. 344–349

[29] DEAR D.J.A., DILLON A.F., FREEDMAN A.N.: 'Determination of organic compounds in the hydrogen used for cooling large electricity generators', *J. Chromatogr.*, 1977, **137**, pp. 315–322

[30] KELLEY J.K., AULD J.W., HERTER V.J., HUTCHINSON K.A., RUGENSTEIN W.A.: 'Early detection and diagnosis of overheating problems in turbine generators by instrumental chemical analysis', *IEEE Trans. Power Appl. Syst.*, 1976, **95**, (3), pp. 879–886

[31] SORITA T., MINAMI S., ADACHI H., TAKASHIMA N., NUMATA S.: 'The detection of degraded materials in turbine generators by chemical analysis', Proc. Int. Symp. Electrical Insulating Materials, 1998

[32] SORITA T., MINAMI S., FUJIMOTO T., TAKASHIMA N., NAKAMURA K.: 'On-line detection of overheating material in turbine generators using chemical analysis'. Annual Conf. Electrical Insulation and Dielectric Phenomena, 1999

[33] SORITA T., ENMANJI K., KATO K., TAKASHIMA M., NAKAMURA K.: 'A novel on-line method and equipment to detect local problems in turbine generators'. Annual Conf. Electrical Insulation and Dielectric Phenomena, 2000

[34] BOWEN R., SCOTT D., SIEFERT W., WESTCOTT V.C.: 'Ferrography', *Tribol. Int.*, 1976, **9**, (3), pp. 109–115

[35] VERMA S.P., GIRGIS R.S.: 'Shaft potentials and currents in large turbogenerators', Report for the Canadian Electrical Association Report, 1981

[36] WHITTINGTON H.W., FLYNN B.W., *ET AL.*: 'An on-line wear debris monitor', *Meas. Sci. Technol.*, 1992, pp. 656–661

[37] LLOYD O., COX A.F.: 'Monitoring debris in turbine generator oil', *Wear*, 1981, **71**, pp. 79–91

[38] BINNS K.J., DYE M.: 'Identification of principal factors affecting unbalanced magnetic pull in cage induction motors', *IEE Proc. B*, 1973, **120**, pp. 349–354

[39] SWANN S.A.: 'Effect of rotor eccentricity on the magnetic field of a non-salient pole machine', *IEE Proc.*, 1963, **110**, pp. 903–915

[40] RAI R.B.: 'Airgap eccentricity in induction motors', ERA Report 1174–1188, 1974

[41] BINNS K.J.: 'Cogging torques in induction machines', *IEE Proc.*, 1968, **115**, pp. 1783–1790

[42] LIM C.Y.: 'Characteristics of reluctance motors', *IEEE Trans. Power Appar. Syst.*, 1951, **70**, (Pt. II), pp. 1971–1978

[43] WILLIAMSON S., SMITH A.C.: 'Field analysis for rotating induction machines and its relationship to the equivalent circuit method', *IEE Proc. B*, 1980, **127**, (2), pp. 83–90

[44] BRANDL P.: 'Forces on the end windings of AC machines', *Brown Boveri Rev.*, 1980, **2**, pp. 128–134

[45] OHTAGURO M., YAGIUCHI K., YAMAGUCHI H.: 'Mechanical behaviour of stator endwindings', *IEEE Trans. Power Appl. Syst.*, 1980, **99**, (3), pp. 1181–1185

[46] WILLIAMSON S., ELLIS M.R.E.: 'Influence of rotor currents on end-winding forces in cage motor', *IEE Proc. B, Electr. Power Appl.*, 1988, **135**, (6), pp. 371–379

[47] CAMPBELL J.J., CLARK P.E., MCSHANE I.E., WAKELEY K.: 'Strains on motor endwindings', *Trans. IEEE Ind. Appl.*, 1984, **20**, (1), pp. 37–44

[48] SMART M.G., FRISWELL M.I., LEES A.W.: 'Estimating turbogenerator foundation parameters: model selection and regularization', *Proc. R. Soc. A, Math. Phys. Eng. Sci.*, 2000, **456**, (1999), pp. 1583–1607

[49] WALKER D.N., ADAMS S.L., PLACEK R.J.: 'Torsional vibration and fatigue of turbine-generator shafts', *IEEE Trans. Power Appar. Syst.*, 1981, **100**, (11), pp. 4373–4380

[50] MAYES I.W.: 'Use of neutral networks for online vibration monitoring', *Proc. Inst. Mech. Eng. A, J. Power Energy*, 1994, **208**, (A4), pp. 267–274

[51] HERBERT R.G.: 'Computer techniques applied to the routine analysis of rundown vibration data for condition monitoring of turbine-alternators', *Br. J. Non-Destr. Test.*, 1986, **28**, (6), pp. 371–375

[52] AL KAZZAZ S.A.S., SINGH G.K.: 'Experimental investigations on induction machine condition monitoring and fault diagnosis using digital signal processing techniques', *Electr. Power Syst. Res.*, 2003, **65**, (3), pp. 197–221

[53] SINGH G.K., AL KAZZAZ S.A.S.: 'Vibration signal analysis using wavelet transform for isolation and identification of electrical faults in induction machine', *Electr. Power Syst. Res.*, 2004, **68**, (1), pp. 119–136

[54] DORRELL D.G., THOMSON W.T., ROACH S.: 'Analysis of airgap flux, current and vibration signals as a function of the combination of static and dynamic airgap eccentricity in 3-phase induction motors', *IEEE Trans. Ind. Appl.*, 1997, **33**, (1), pp. 24–34

[55] THOMSON W.T., BARBOUR A.: 'On line current monitoring and application of a finite element method to predict the level of static air gap eccentricity in three phase induction motors', *IEEE Trans. Energy Convers.*, 1998, **13**, (4), pp. 347–357

[56] NANDI S., BHARADWAJ R.M., TOLIYAT H.A.: 'Performance analysis of a three-phase induction motor under mixed eccentricity condition', *IEEE Trans. Energy Convers.*, 2002, **17**, (3), pp. 392–399

[57] TRUTT F.C., SOTTILE J., KOHLER J.L.: 'Detection of AC machine winding deterioration using electrically excited vibrations', *IEEE Trans. Ind. Appl.*, 2001, **37**, (1), pp. 10–14

[58] BEN SASI A.Y., GU F., LI Y., BALL A.D.: 'A validated model for the prediction of rotor bar failure in squirrel-cage motors using instantaneous angular speed', *J. Mech. Syst. Signal Process.*, 2006, **20**, pp. 1572–1589

[59] TANDON N., NAKRA B.C.: 'Comparison of vibration and acoustic measurement techniques for the condition monitoring of rolling element bearings', *Tribol. Int.*, 1992, **25**, (3), pp. 205–212

[60] TANDON N., YADAVA G.S., RAMAKRISHNA K.M.: 'A comparison of some condition monitoring techniques for the detection of defect in induction motor ball bearings', *Mech. Syst. Signal Process.*, 2007, **21**, (1), pp. 244–256

[61] STACK J.R., HABETLER T.G., HARLEY R.G.: 'Fault classification and fault signature production for rolling element bearings in electric machines', *IEEE Trans. Ind. Appl.*, 2004, **40**, (3), pp. 735–739

[62] PENMAN J., SEDDING H.G., LLOYD B.A., FINK W.T.: 'Detection and location of interturn short circuits in the stator windings of operating motors', *IEEE Trans. Energy Convers.*, 1994, **9**, (4), pp. 652–658

[63] THOMSON W.T., FENGER M.: 'Current signature analysis to detect induction motor faults', *IEEE Ind. Appl. Mag.*, 2001, **7**, (4), pp. 26–34

[64] MICHIGUCHI Y., TONISAKA S., IZUMI S., WATANABE T., MIYASHITA I.: 'Development of a collector ring monitor for sparking detection on generators', *IEEE Trans. Power Appl. Syst.*, 1983, **102**, (4), pp. 928–933

[65] KHUDABASHEV K.A.: 'Effect of turn short-circuits in a turbo generator rotor on its state of vibration', *Elektr. Stn.*, 1961, (7), pp. 40–45

[66] ALBRIGHT D.R.: 'Inter-turn short circuit detector for turbine generator rotor windings', *IEEE Trans. Power Appl. Syst.*, 1971, **50**, pp. 478–483

doi: 10.1049/iet-epa:20070280

[67] KRYUKHIN S.S.: 'A new principle for synchronous machine protection from rotor winding inter-turn and double earth faults', *Elect. Technol. USSR*, 1972, (2), pp. 47–59

[68] POYHONEN S., NEGREA M., JOVER P., ARKKIO A., HYOTYNIEMI H.: 'Numerical magnetic field analysis and signal processing for fault diagnostics of electrical machines', *COMPEL, Int. J. Comput. Math. Electr. Electron. Eng.*, 2003, **22**, (4), pp. 969–981

[69] KAMERBEEK E.M.H.: 'Torque measurements on induction motors using Hall generators or measuring windings', *Philips Tech. Rev.*, 1974, **34**, (7), pp. 152–162

[70] SEINSCH H.O.: 'Detection and diagnosis of abnormal operating conditions and/or faults in rotating electrical machines', Schorch Berichte, 1986)

[71] MILIMONFARED J., KELK H.M., NANDI S., MINASSIANS A.D., TOLIYAT H.A.: 'A novel approach for broken-rotor-bar detection in cage induction motors', *IEEE Trans. Ind. Appl.*, 1999, **35**, (5), pp. 1000–1006

[72] NANDI S., TOLIYAT H.A.: 'Frequency-domain-based technique to detect stator interturn faults in induction machines using stator-induced voltages after switch-off', *IEEE Trans. Ind. Appl.*, 2002, **38**, (1), pp. 101–109

[73] HARGIS C.: 'Steady-state analysis of 3-phase cage motors with rotor-bar and end-ring faults', *IEE Proc. B, Electr. Power Appl.*, 1983, **130**, (3), pp. 225–225

[74] JUFER M., ABDULAZIZ M.: 'Influence d'une rupture de barre ou d'un anneau sur les characteristiques externes d'un moteur asynchrone a cage'. Bulletin SEV/VSE, Switzerland'1978, **69**, (17)

[75] PENMAN J., STAVROU A.: 'Broken rotor bars: their effect on the transient performance of induction machines', *IEE Proc. B, Electr. Power Appl.*, 1996, **143**, (6), pp. 449–457

[76] MENACER A., NAT-SAID M.S., *ET AL*.: 'Stator current analysis of incipient fault into induction machine rotor bars', *J. Electr. Eng.*, 2004, **4**, (2)

[77] LI W.D., MECHEFSKE C.K.: 'Detection of induction motor faults: a comparison of stator current, vibration and acoustic methods', *J. Vib. Control*, 2006, **12**, (2), pp. 165–188

[78] RICKSON C.D.: 'Protecting motors from overload due to asymmetrical fault conditions', *Electr. Rev.*, 1983, pp. 778–780

[79] TRUTT F.C., SOTTILE J., KOHLER J.L.: 'Online condition monitoring of induction motors', *IEEE Trans. Ind. Appl.*, 2002, **38**, (6), pp. 1627–1632

[80] KOHLER J.L., SOTTILE J., *ET AL*.: 'Condition monitoring of stator windings in induction motors. I. Experimental investigation of the effective negative-sequence impedance detector', *IEEE Trans. Ind. Appl.*, 2002, **38**, (5), pp. 1447–1453

[81] KOHLER J.L., SOTTILE J., TRUTT F.C.: 'Condition monitoring of stator windings in induction motors. II. Experimental investigation of voltage mismatch detectors', *IEEE Trans. Ind. Appl.*, 2002, **38**, (5), pp. 1454–1459

[82] SOTTILE J., TRUTT F.C., LEEDY A.W.: 'Condition monitoring of brushless three-phase synchronous generators with stator winding or rotor circuit deterioration', *IEEE Trans. Ind. Appl.*, 2006, **42**, (5), pp. 1209–1215

[83] JORDAN H., KOVACS K., *ET AL*.: 'Messungen des schlupfes von asynchronmaschinen mit einer spule', *Elektrotech. Z.*, 1965, **86**, pp. 294–296

[84] ERLICKI M.S., PORAT Y., ALEXANDROVITZ A.: 'Leakage field changes of an induction motor as indication of non-symmetric supply', *IEEE Trans. Gen. Appl.*, 1971, **7**, (6), pp. 713–717

[85] PENMAN J., HADWICK G., STRONACH A.F.: 'Protection strategy against faults in electrical machines'. Int. Conf. Developments in Power System Protection, London, 1980, (IEE)

[86] HENAO H., DEMIAN C., CAPOLINO G.A.: 'A frequency-domain detection of stator winding faults in induction machines using an external flux sensor', *IEEE Trans. Ind. Appl.*, 2003, **39**, (5), pp. 1272–1279

[87] YACAMINI R., SMITH K.S., RAN L.: 'Monitoring torsional vibrations of electromechanical systems using stator currents', *Trans. ASME. J. Vib. Acoust.*, 1998, **120**, pp. 72–79

[88] RAN L., YACAMINI R., SMITH K.S.: 'Torsional vibrations in electrical induction motor drives during start up', *Trans. ASME. J. Vib. Acous.*, 1996, **118**, (2), pp. 242–251

[89] JOKSIMOVIC G.M., PENMAN J.: 'The detection of inter-turn short circuits in the stator windings of operating motors', *IEEE Trans. Ind. Electron.*, 2000, **47**, (5), pp. 1078–1084

[90] STAVROU A., SEDDING H.G., PENMAN J.: 'Current monitoring for detecting inter-turn short circuits in induction motors', *IEEE Trans. Energy Convers.*, 2001, **16**, (1), pp. 32–37

[91] BELLINI A., FILIPPETTI F., FRANCESCHINI G., TOSSONI C., KLIMAN G.B.: 'Quantitative evaluation of induction motor broken bars by means of electrical signature analysis', *IEEE Trans. Ind. Appl.*, 2001, **37**, (5), pp. 1248–1255

[92] BELLINI A., FILIPPETTI F., *ET AL*.: 'On-field experience with online diagnosis of large induction motors cage failures

using MCSA', *IEEE Trans. Ind. Appl.*, 2002, **38**, (4), pp. 1045–1053

[93] MIRAFZAL B., DEMERDASH N.A.O.: 'On innovative methods of induction motor interturn and broken-bar fault diagnostics', *IEEE Trans. Ind. Appl.*, 2006, **42**, (2), pp. 405–414

[94] HENAO H., RAZIK H., CAPOLINO G.A.: 'Analytical approach of the stator current frequency harmonics computation for detection of induction machine rotor faults', *IEEE Trans. Ind. Appl.*, 2005, **41**, (3), pp. 801–807

[95] TRZYNADLOWSKI A.M., GHASSEMZADEH M., LEGOWSKI S.F.: 'Diagnostics of mechanical abnormalities in induction motors using instantaneous electric power', *IEEE Trans. Energy Convers.*, 1999, **14**, (4), pp. 1417–1423

[96] HUNTER D.J., TAVNER P.J., WARD D.M., BENARAGAMA D.S.: 'Measurements of the harmonic components of the instantaneous electrical power delivered at the terminals of a 500 MW turbogenerator'. 3rd Int. Conf. Sources and Effects of Power System Disturbances, London, 1982, (IEE)

[97] NIPPES P.I.: 'Early warning of developing problems in rotating machinery as provided by monitoring shaft voltages and grounding currents', *IEEE Trans. Energy Convers.*, 2004, **19**, (2), pp. 340–345

[98] WILSON A., NYE A.E.T., HOPGOOD D.J.: 'On line detection of partial discharges in HV plant'. 4th BEAMA Int. Electrical Insulation Conf., Brighton, UK, BEAMA, 1982

[99] HARROLD R.T., EMERY F.T., MURPHY F.J., DRINKUT S.A.: 'Radio frequency sensing of incipient arcing faults within large turbine generators', *IEEE Trans. Power Appl. Syst.*, 1979, **98**, (4), pp. 1167–1173

[100] EMERY F.T., LENDERKING B.N., COUCH R.D.: 'Turbine- generator on-line diagnostics using RF monitoring', *IEEE Trans. Power Appl. Syst.*, 1981, **100**, (12), pp. 4974–4982

[101] HARROLD R.T., EMERY F.T.: 'Radio frequency diagnostic monitoring of electrical machines', *IEEE Electr. Insul. Mag.*, 1986, **2**, (2), pp. 18–24

[102] TIMPERLEY J.E.: 'Incipient fault detection through neutral RF monitoring of large rotating machines', *IEEE Trans. Power Appl. Syst.*, 1983, **102**, (3), pp. 693–698

[103] WARD D.A., EXON J.L.T.: 'Using Rogowski coils for transient current measurements', *Eng. Sci. Educ. J.*, 1993, **2**, (3), pp. 105–113

[104] GEARY R., KEMP I.J., WILSON A., WOOD J.W.: 'Towards improved calibration in the measurement of partial discharges in rotating machinery'. Int. Conf. Electrical Insulation, IEEE, Toronto, 1990

[105] KURTZ M., STONE G.C.: 'In-service partial discharge testing of generator insulation', *IEEE Trans. Electr. Insul.*, 1979, **14**, (2), pp. 94–100

[106] KURTZ M., STONE G.C., FREEMAN D., MULHALL V.R., LONSETH P.: 'Diagnostic testing of generator insulation without service interruption', *CIGRE*, 1980

[107] STONE G.C., SEDDING H.G., FUJIMOTO N., BRAUN J.M.: 'Practical implementation of ultrawideband partial discharge detectors', *IEEE Trans. Electr. Insul.*, 1992, **27**, (1), pp. 70–81

[108] STONE G.C., SEDDING H.G., LLOYD B.A., GUPTA B.K.: 'The ability of diagnostic tests to estimate the remaining life of stator insulation', *IEEE Trans. Energy Conversion.*, 1988, **3**, (4), pp. 833–841

[109] SEDDING H.G., STONE G.C.: 'A discharge locating probe for rotating machines', *IEEE Electr. Insul. Mag.*, 1989, **5**, (5), pp. 14–17

[110] SEDDING H.G., CAMPBELL S.R., STONE G.C., KLEMPNER G.S.: 'A new sensor for detecting partial discharges in operating turbine generators', *IEEE Trans. Energy Convers.*, 1991, **6**, (4), pp. 700–706

[111] WOOD J.W., SEDDING H.G., HOGG W.K., KEMP I.J., ZHU H.: 'Partial discharges in HV machines; initial considerations for a PD specification', *IEE Proc., A, Sci Meas. Technol.*, 1993, **140**, (5), pp. 409–416

[112] CAMPBELL S.R., STONE G.C., SEDDING H.G., KLEMPNER G.S., MCDERMID W., BUSSEY R.G.: 'Practical on-line partial discharge tests for turbine generators and motors', *IEEE Trans. Energy Convers.*, 1994, **9**, (2), pp. 281–287

[113] KEMP I.J., ZHU H., SEDDING H.G., WOOD J.W., HOGG W.K.: 'Towards a new partial discharge calibration strategy based on the transfer function of machine stator windings', *IEE Proc. A, Sci. Meas. Technol.*, 1996, **143**, (1), pp. 57–62

[114] LYLES J.F., GOODEVE T.E.: 'Using diagnostic technology for identifying generator winding needs', *Hydro Rev.*, 1993, pp. 58–67

[115] STONE G.C., SEDDING H.G., COSTELLO M.J.: 'Application of partial discharge testing to motor and generator stator winding maintenance', *IEEE Trans. Ind. Appl.*, 1996, **32**, (2), pp. 459–464

[116] IEEE1434-2000 : 'IEEE Standard: Trial use guide to the measurements of partial discharges in rotating machines' (IEEE), 2000)

[117] TETRAULT S.M., STONE G.C., SEDDING H.G.: 'Monitoring partial discharges on 4 kV motor windings', *IEEE Trans. Ind. Appl.*, 1999, **35**, (3), pp. 682–688

doi: 10.1049/iet-epa:20070280

[118] KHEIRMAND A., LEIJON M., GUBANSKI S.M.: 'Advances in online monitoring and localization of partial discharges in large rotating machines', *IEEE Trans. Energy Convers.*, 2004, **19**, (1), pp. 53–59

[119] LEE S.B., YOUNSI K., KLIMAN G.B.: 'An online technique for monitoring the insulation condition of AC machine stator windings', *IEEE Trans. Energy Convers.*, 2005, **20**, (4), pp. 737–745

[120] STONE G.C., KAPLER J.: 'Condition-based maintenance for the electrical windings of large motors and generators'. IEEE Pulp and Paper Conf., Cincinnati, USA, 1997, pp. 57–63

[121] STEPHAN C.E., LAIRD T.: 'Condition based maintenance of turbine generators: what makes it real?'. IEEE Electric Machines and Drive Conf., Madison, Wisconsin, USA, 2003, vol. 2, pp. 895–899

[122] BENBOUZID M.E.H., NEJJARI H.: 'A simple fuzzy logic approach for induction motors stator condition monitoring'. IEEE Electric Machines and Drives Conf., MA, USA, 2001, pp. 634–639

[123] CALDARA S., NUCCIO S., GALLUZZO G.R., TRAPANESE M.: 'A fuzzy diagnostic system: application to linear induction motor drives'. IEEE Instrumentation and Measurement Technology Conf., Ottawa, Canada, 1997, vol. 1, pp. 257–262

[124] MURRAY A., PENMAN J.: 'Extracting useful higher order features for condition monitoring using artificial neural networks', *IEEE Trans. Signal Process.*, 1997, **45**, (11), pp. 2821–2828

[125] FILIPPETTI F., FRANCESCHINI G., TASSONI C.: 'Neural networks aided on-line diagnostics of induction motor rotor faults', *IEEE Trans. Ind. Appl.*, 1995, **31**, (4), pp. 892–899

[126] PENMAN J., YIN C.M.: 'Feasibility of using unsupervised learning, artificial neural networks for the condition monitoring of electrical machines', *IEE Proc. B, Electr. Power Appl.*, 1994, **141**, (6), pp. 317–322

[127] BELLINI A., FILIPPETTI F., FRANCESCHINI G., TASSONI C.: 'Closed-loop control impact on the diagnosis of induction motors faults', *IEEE Trans. Ind. Appl.*, 2000, **36**, (5), pp. 1318–1329

[128] CHEN S., ZHONG E., LIPO T.A.: 'A new approach to motor condition monitoring in induction motor drives', *IEEE Trans. Ind. Appl.*, 1994, **30**, (4), pp. 905–911

[129] KOHLER J.L., SOTTILE J., TRUTT F.C.: 'Condition based maintenance of electrical machines'. Proc. IEEE Industry Applications Conf., 34th IAS Annual Meeting, Phoenix, AZ, 1999, (IEEE)

[130] MORTON K.: 'Asset management in the electricity supply industry', *Pow. Eng. J.*, 1999, **13**, (5), pp. 233–240

Control of a Doubly Fed Induction Generator in a Wind Turbine During Grid Fault Ride-Through

Dawei Xiang, Li Ran, *Member, IEEE*, Peter J. Tavner, and Shunchang Yang

***Abstract*—This paper analyzes the ability of a doubly fed induction generator (DFIG) in a wind turbine to ride through a grid fault and the limitations to its performance. The fundamental difficulty for the DFIG in ride-through is the electromotive force (EMF) induced in the machine rotor during the fault, which depends on the dc and negative sequence components in the stator-flux linkage and the rotor speed. The investigation develops a control method to increase the probability of successful grid fault ride-through, given the current and voltage capabilities of the rotor-side converter. A time-domain computer simulation model is developed and laboratory experiments are conducted to verify the model and a control method is proposed. Case studies are then performed on a representatively sized system to define the feasibility regions of successful ride-through for different types of grid faults.**

***Index Terms*—Current control, doubly fed induction generator (DFIG), flux linkage, grid fault, power converter, safe operating area (SOA), wind energy.**

I. Introduction

THE doubly fed induction generator (DFIG) is a common configuration for large, variable-speed wind turbines that are connected to a grid [1]. On detecting a grid fault, the generator unit is usually disconnected to protect the vulnerable rotor-side converter. In the recent years, this has been achieved by applying a crowbar short circuit to the rotor slip ring terminals. This was accepted when wind power represented only an insignificant part of the generation in the system. As the penetration of wind power continues to increase, more wind turbines are required to remain connected during grid faults, i.e., to ride through the faults, and contribute to system stability after fault clearance [2]. For instance, the Grid Code of Scottish Power and Scottish Hydro-Electric [3] states that all wind turbines must remain connected in the event of any short circuit in the high-voltage transmission network. Grid codes in other parts of the world may be more stringent, demanding ride-through of faults at the generator terminal. For the reasons that will be discussed later, grid fault ride-through control is difficult for the DFIG and is a major challenge for wind turbine manufacturers.

Researchers are addressing the issue from several points of view. For instance, the study described in [4] suggests improving the generator terminal voltage during a grid fault using shunt reactive power compensation. Optimizing the parameters of the current control loops in the rotor-side converter is proposed in [5]. The use of the crowbar is evaluated in [6]. The inherent difficulty of ride-through control during a symmetrical grid fault is explained in [7].

It is usually thought that a fast semiconductor converter can limit the current fed to a grid fault immediately, a merit that is frequently attributed to HVDC systems [8], [9]. At first glance, it seems straightforward to apply the same principle to a DFIG, so that the rotor-side converter current could be constrained while the protection operates on impedance rather than overcurrent relays. However, in a DFIG wind turbine arrangement, the converter is on the rotor side of the generator. There are known cases where a DFIG rotor converter operated this way experienced over-voltages and failed to limit the fault current, leading to the destruction of the converter. This paper extends the initial study presented in [7] and proposes a new control approach without additional hardware but based on the insight gained from analysis and modeling backed up by experiment.

Section II of the paper reviews the generator model. The behavior of the DFIG system during a grid fault is analyzed. It is shown that the fault current depends on the internal state of the machine as well as the voltage applied on the rotor side. Section III derives the control algorithm in order to assist the system to ride through the grid fault, which takes into account the machine's internal state. Section IV verifies the proposed control method and validates the simulation model on a laboratory test rig. The validated model is used in Section V to evaluate the system performance with respect to the fault type and prefault condition. The operating region for successful ride-through for a typical 2-MW DFIG system is then defined for each fault type in terms of the severity of the fault and the prefault machine speed.

II. DFIG During Grid Fault

Fig. 1 is the block diagram of a DFIG wind turbine system. The generator has a three-phase wound rotor supplied, via slip rings, from a four-quadrant, pulse width modulation (PWM) converter with voltage of controllable amplitude and frequency. The generator can operate at variable speed, while the stator remains at a constant grid frequency. The machine usually operates in the vector-control mode orientated to the stator-flux linkage, which can be calculated as follows using the measured voltage and current [10]:

$$\psi_{sabc} = \int (u_{sabc} - R_s i_{sabc}) dt \tag{1}$$

where ψ_{sabc} is the space vector of the flux linkages of the three-phase stator windings. u_{sabc} and i_{sabc} are the corresponding

Manuscript received July 15, 2005. The work of D. Xiang was supported by a visiting scholarship from Chongqing University, Chongqing, China. Paper no. TEC-00246-2005.

D. Xiang and S. Yang are with the Department of Electrical Engineering, Chongqing University, Chongqing 400044, China. (e-mail: xdw_cqu@hotmail.com; shunchangyang@yahoo.com).

L. Ran and P. J. Tavner are with the School of Engineering, University of Durham, Durham DH1 3LE, U.K. (e-mail: li.ran@durham.ac.uk; Peter.Tavner@durham.ac.uk).

Digital Object Identifier 10.1109/TEC.2006.875783

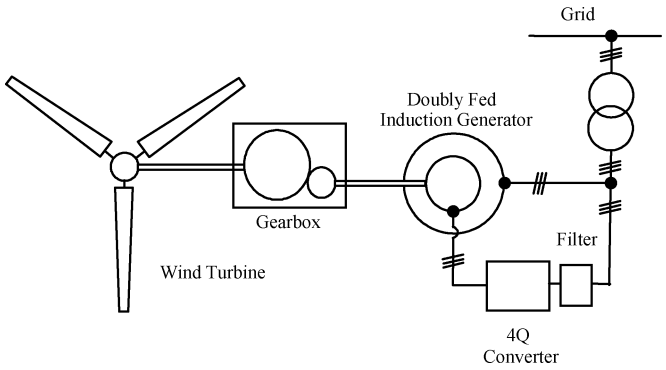

Fig. 1. Configuration of the DFIG wind turbine system.

voltage and current space vectors. The positive current directions are defined as feeding the generator. $R_{\rm s}$ is the stator resistance. Generally, "s" and "r" in subscript distinguish quantities or parameters on the stator or rotor side.

The stator- and rotor-flux linkages are related to the currents as

$$\psi_{sabc} = (L_{\rm ls} + L_{\rm m}) i_{sabc} + L_{\rm m} i_{rabc} \tag{2}$$

$$\psi_{rabc} = L_{\rm m} i_{sabc} + (L_{\rm lr} + L_{\rm m}) i_{rabc} \tag{3}$$

where $L_{\rm ls}$ and $L_{\rm lr}$ are the leakage inductances, and $L_{\rm m}$ is the magnetizing inductance. During normal operation, both the stator- and rotor-flux linkages rotate at synchronous speed with respect to the stator.

In the rotor reference frame, the voltage equation of the rotor windings is

$$u_{rabc} = R_r i_{rabc} + \frac{d\psi_{rabc}}{dt}. \tag{4}$$

The rotor-flux linkage can be expressed in terms of stator-flux linkage and rotor current according to (2) and (3) [10], [11].

$$\psi_{rabc} = \frac{L_{\rm m}}{L_{\rm s}} \psi_{sabc} + \frac{L_{\rm s} L_{\rm r} - L_{\rm m}^2}{L_{\rm s}} i_{rabc} \tag{5}$$

where $L_{\rm s} = L_{\rm ls} + L_{\rm m}$ and $L_{\rm r} = L_{\rm lr} + L_{\rm m}$. All the quantities are in per unit (p.u.).

The equivalent circuit of the DFIG machine viewed from the rotor side, corresponding to (4) and (5), is shown in Fig. 2. The rotor current is jointly decided by the injected rotor voltage and the induced electromotive force (EMF) or the derivative of the stator-flux linkage with respect to time. In normal operation, the space vector ψ_{sabc} rotates at slip speed $s\omega_0$, with respect to the rotor winding, where s is the slip and ω_0 is the synchronous speed. Therefore, ψ_{sabc}/dt is $js\omega_0\psi_{sabc}$. This is predominantly balanced by the rotor voltage of the same frequency and determines the voltage rating of the rotor-side converter, with some margin. Now consider a three-phase fault on the grid side, which brings the stator terminal voltage down to zero. In such an extreme case, the space vector of the stator-flux linkage ψ_{sabc}, will "freeze" and stop rotating with respect to the stator winding, as implied by (1). As a result, ψ_{sabc} rotates at speed $\omega_{\rm r}$ with respect to the rotor winding. The induced EMF, $d\psi_{sabc}$, will then become $j\omega_r\psi_{sabc}$, where ω_r is the rotor speed in p.u.

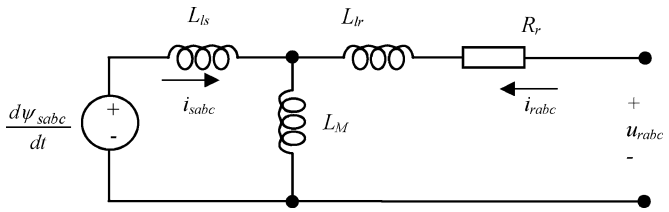

Fig. 2. Rotor-side equivalent circuit.

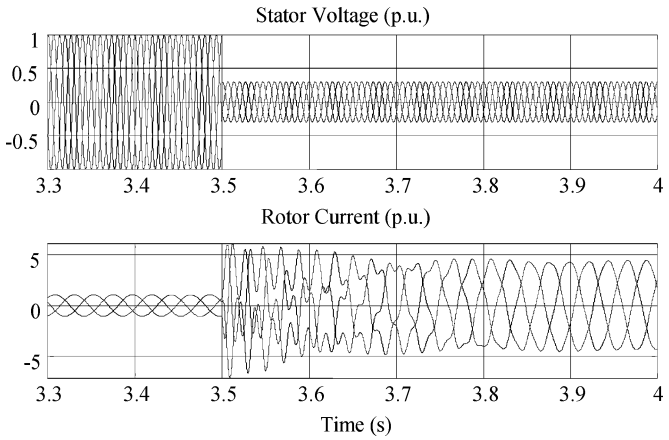

Fig. 3. Simulation results of a 2-MW DFIG during a grid fault.

a mismatch with the rotor supply voltage is introduced in terms of both amplitude and frequency. Current components at two frequencies, $s\omega_0$ and $\omega_r = (1-s)\omega_0$ are produced. Because the leakage inductance and rotor winding resistance are usually small, the rotor current, which is the superposition of the two components, is consequently large. With the effect of the stator resistance ψ_{sabc} will gradually decay, attenuating the transient fault current component at frequency ω_r; this is effectively the transient behavior of the rotor.

Note that the induced EMF viewed from the rotor can be relatively large during the fault because the rotor speed may be greater than the prefault slip speed. For instance, consider that the DFIG is initially running at the maximum speed, which is typically 30% above the synchronous speed [1]. The prefault slip is $s = -0.3$ p.u, while $\omega_r = (1-s)\omega_0 = 1.3\omega_0$ Correspondingly, the induced EMF increases by 333% in amplitude for the fault scenario described earlier, while the frequency also changes.

The analysis suggests that the difficulty of the rotor-side converter in constraining the current during a grid fault is associated with the induced EMF depending on the stator-flux linkage and speed. This is a major difference when compared with an inverter connected directly to a passive grid network. Fig. 3 shows the simulated fault current for a 2-MW DFIG system detailed in Appendix I. The machine initially operates with full load and is at 30% super synchronous speed. A three-phase grid fault brings the generator terminal voltage down to 0.3 p.u. The control implemented in the simulation model is the vector-control algorithm for terminal voltage regulation and the maximum active power tracking [12]. The rotor-side converter is represented

as controlled voltage sources. No additional action or control limit is included to constrain the fault current. It is observed that the rotor current increases from about 1.0 to 7.2 p.u. It is also evident that the current consists of components at different frequencies.

The analysis shows that a large rotor voltage would be required for the converter current to be constrained.

For an asymmetrical grid fault, a voltage component of negative phase sequence will appear at the generator terminal. This will cause a negative sequence component in the stator-flux linkage in addition to the dc component described earlier with respect to the stator. The rotor winding rotates with respect to the negative sequence flux component at speed $\omega_0 + \omega_r$. The corresponding EMF induced depends on the terminal voltage and the prefault machine speed. The consequence can also be explained using Fig. 2.

III. Control for Grid Fault Ride-Through

There are different interpretations to the requirements of grid fault ride-through. Ultimately, the DFIG is desired to act like a synchronous machine capable of providing fault current for protection relays and voltage support [6]. It is difficult to provide the current without increasing the converter rating. This study views the challenge of ride-through as constraining the fault current in the presence of change of the induced EMF in the machine. No additional hardware equipment, e.g., the crowbar, is to be used. In addition, the transient associated with the clearance after the fault is also to be dealt with, as the generator returns to the normal control.

The rotor-side converter usually employs the IGBT as the semiconductor switching device. Its continuous current rating is determined by the steady-state load, while the over load capability could be exploited during transient. In theory, the maximum current switched by the device can be the peak pulse rating, as long as the junction temperature reached in the IGBT is permissible and the V–I switching trajectory is within the safe operating area (SOA) [13]. The pulse current rating of an IGBT is typically 100% higher than the continuous current rating. Therefore, the control objective of this study is to constrain the instantaneous rotor current below 2.0 p.u., while the converter dc-link voltage is also maintained below the device's voltage rating. In practice, the PWM switching frequency could be temporarily reduced to prevent excessive switching losses due to increased device current and voltage during grid fault ride-through control.

A logical conclusion from the analysis in Section II is that during fault the voltage applied from the rotor converter to the rotor winding should be used to weaken the effect of the dc and negative sequence components in the stator-flux linkage. According to either (4) or Fig. 2, the effect is actually expressed through the corresponding flux components linking the rotor side. The total stator-flux linkage is dictated by the stator voltage. It is desirable to orient the rotor current such that it contains components that oppose the rotor flux linkage dc and negative sequence components. This is shown in Fig. 4, where subscripts "1," "2," and "0" indicate the positive, negative, and zero (dc) sequence components in the flux linkage or current space vectors, respectively. The converter voltage on the rotor side can be used for such an objective and the rotor current is to be kept to an acceptable limit. Whether this is achievable depends on how strongly the voltage can be applied, as compared to the internal induced EMF. The whole scenario is then dependent on the severity of the fault and the prefault condition of the DFIG system. This will be described later as the feasibility region for successful ride-through. The control approach adopted in this study aims to enlarge the feasibility region. Equation (5) can be approximated as follows:

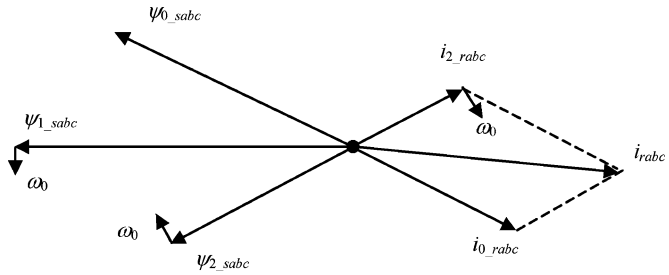

Fig. 4. Control of the rotor current.

$$\psi_{rabc} = \frac{L_{\rm m}}{L_{\rm s}}\psi_{sabc} + \frac{L_{\rm s}L_{\rm r} - L_{\rm m}^2}{L_{\rm s}} i_{rabc} \approx \psi_{sabc} + (L_{\rm sl} + L_{\rm lr}) i_{rabc}. \quad (6)$$

Equation (6) shows that the rotor current can be controlled to counter the undesired components in the stator-flux linkage. It should also be noticed that if the DFIG machine is designed with increased rotor or stator leakage inductance, it will increase the effectiveness of rotor current control and hence the ability to ride through grid faults. This is similar to the fact that a synchronous machine with increased winding leakage inductance may improve its transient behavior.

Fig. 5 shows the proposed controller including three parts: 1) stator-flux linkage estimation and decomposition; 2) calculation of rotor current reference; and 3) implementation of rotor current control. Fig. 6 shows the algorithm to decompose the stator-flux linkage vector into positive, negative, and zero sequence (dc) components. The stator voltage and current are used to calculate the total flux linkage as shown in (1). A second-order band-pass filter, whose gain and phase response are set as unity and zero degree, respectively, at the nominal stator frequency (50 Hz), is used to remove the dc component and the effect of switching harmonics. The output is ac including the positive and negative sequence components with respect to the stator winding. The dc component can therefore be calculated as follows:

$$\psi_{0\_sabc} = \psi_{sabc} - \psi_{ac\_sabc}. \quad (7)$$

It should be noted that in Fig. 6, the derivative operation has the effect of phase shifting the positive and negative sequence flux linkage components by $\pi/2$ and $-\pi/2$ (rad), respectively. The amplitude is not affected if all quantities are expressed in per

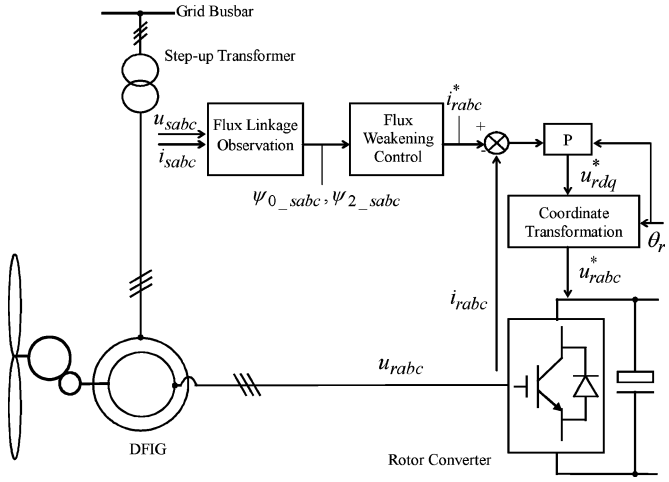

Fig. 5. Control block diagram.

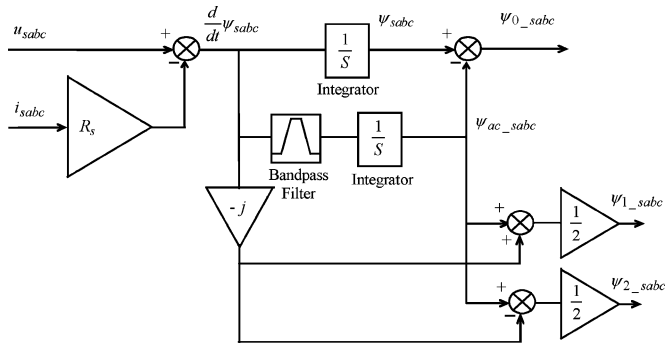

Fig. 6. Observation of components in stator-flux linkage.

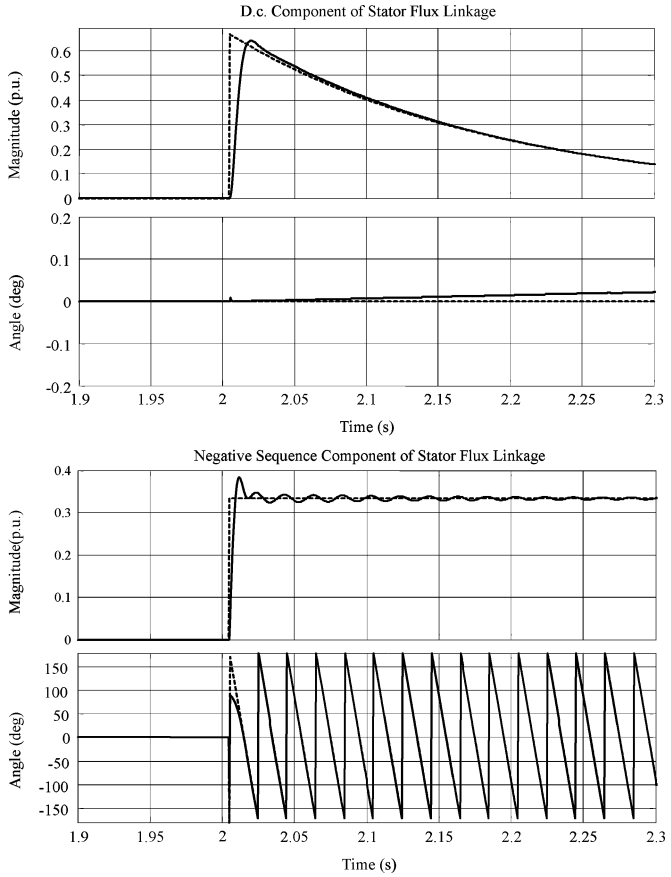

Fig. 7. Observation of components in stator-flux linkage—Test of algorithm using simulation.

unit and the system operates at the base or nominal frequency on the stator side. This is used to separate the positive and negative sequence components ψ_{1_sabc} and ψ_{2_sabc}

$$\begin{aligned}
&\frac{1}{2}\left[\psi_{ac_sabc} - (-j) \times \frac{d\psi_{sabc}}{dt}\right] \\
&\quad = \frac{1}{2}\left[(\psi_{1_sabc} + \psi_{2_sabc}) - (-j)\right. \\
&\qquad \left. \times \frac{d}{dt}(\psi_{0_sabc} + \psi_{1_sabc} + \psi_{2_sabc})\right] \\
&\quad = \frac{1}{2}[(\psi_{1_sabc} + \psi_{2_sabc}) \\
&\qquad - (-j) \times (j\psi_{1_sabc} - j\psi_{2_sabc})] \\
&\quad = \psi_{2_sabc} \qquad (8) \\
&\frac{1}{2}\left[\psi_{ac_sabc} + (-j) \times \frac{d\psi_{sabc}}{dt}\right] \\
&\quad = \frac{1}{2}\left[(\psi_{1_sabc} + \psi_{2_sabc}) + (-j)\right. \\
&\qquad \left. \times \frac{d}{dt}(\psi_{0_sabc} + \psi_{1_sabc} + \psi_{2_sabc})\right] \\
&\quad = \frac{1}{2}[(\psi_{1_sabc} + \psi_{2_sabc}) + (-j) \\
&\qquad \times (j\psi_{1_sabc} - j\psi_{2_sabc})] \\
&\quad = \psi_{1_sabc}. \qquad (9)
\end{aligned}$$

The proposed algorithm was demonstrated using simulation. A single-phase-to-ground fault on the stator side is simulated for the 2-MW DFIG system. Components in the stator-flux linkage, calculated using the above algorithm, are compared with those directly measured in the machine model. The comparison is shown in Fig. 7. The angles of the flux-linkage components are referenced to the magnetic axis of stator phase "a." Close agreement is observed with the estimation catching up the actual response in about a quarter of a 50 Hz cycle. This is because the derivative information has been taken into account in the flux-linkage observation algorithm. Control action can thus take place before the rotor current increases to an unacceptable level. Fast flux-linkage observation and rotor current response are essential to the proposed control method.

When the rotor current is used to cancel both the dc and the negative sequence components in the stator-flux linkage, it is necessary to coordinate the two aspects of the objective. The rotor current and voltage must always be within the SOA of the switching device. A series of simulations were performed to determine the appropriate sharing of the converter current

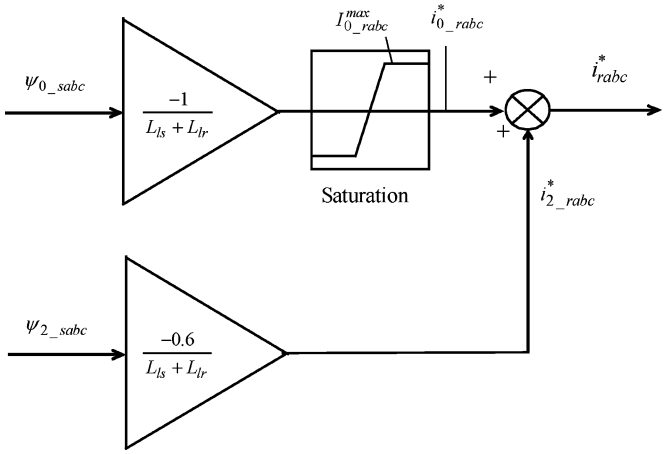

Fig. 8. Sharing of converter current capability.

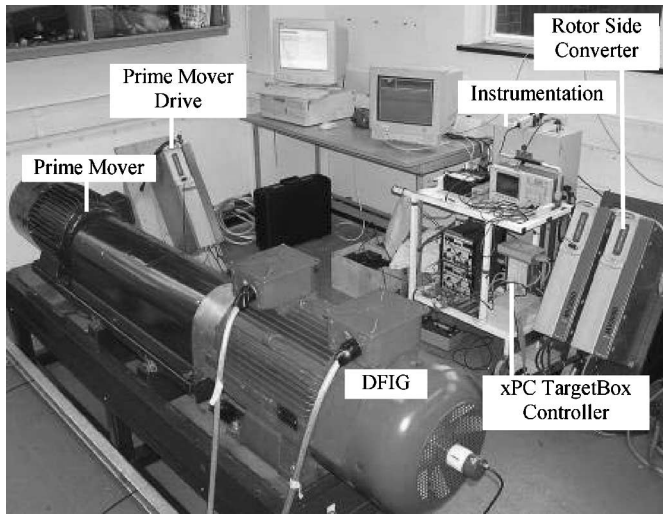

Fig. 9. Test rig setup.

capability. It was recommended to cancel 60% of the negative sequence component in the stator-flux linkage. For a typical DFIG system, this would be possible for all faults that could occur in the transmission network. The reminder of the current capability is used to deal with the dc component in the stator-flux linkage. Because the current components are at different frequencies, the maximum instantaneous current of the converter is the algebraic summation of the peak values, which must be less than 2.0 p.u. in this study. Fig. 8 shows the scheme of current capability sharing. The reference rotor current is consequently generated. The per unit limit of the dc current component is dynamically calculated depending on the negative sequence current compensation

$$I^{\max}_{0\_rabc} = 2.0 - \frac{0.6}{L_{\rm ls}+L_{\rm lr}}\left|\psi_{2\_sabc}\right|. \tag{10}$$

The implementation of the rotor current control is through a proportionalalgorithm in a stationary d–q reference frame fixed to the stator, as shown in Fig. 5. Coordinate transformation is necessary to determine the reference rotor phase voltages, taking into account the rotor angle.

IV. Experimental Verification

Fig. 9 shows the DFIG test rig set up to verify the proposed control method and the model used for full-scale system simulation. A 30-kW wound rotor machine is driven by a vector-controlled induction motor. Details of the test DFIG machine are given in Appendix III. The rotor windings of the DFIG are fed from a PWM inverter that is controlled by an xPC TargetBox real-time system. The stator and rotor currents, stator voltages and the rotor position of the DFIG machine are measured and the control algorithm described in Section III is implemented in Simulink, which generates the code to be downloaded into the xPC TargetBox. The fault occurrence is detected from a sudden change of the stator voltage, activating the fault ride-through control.

Fig. 10 shows the control response of the DFIG system during normal operation when subjected to sudden change of first real and then real and reactive power. The speed is fixed at 1950 r/min, corresponding to -0.3 p.u. slip for a four-pole machine.

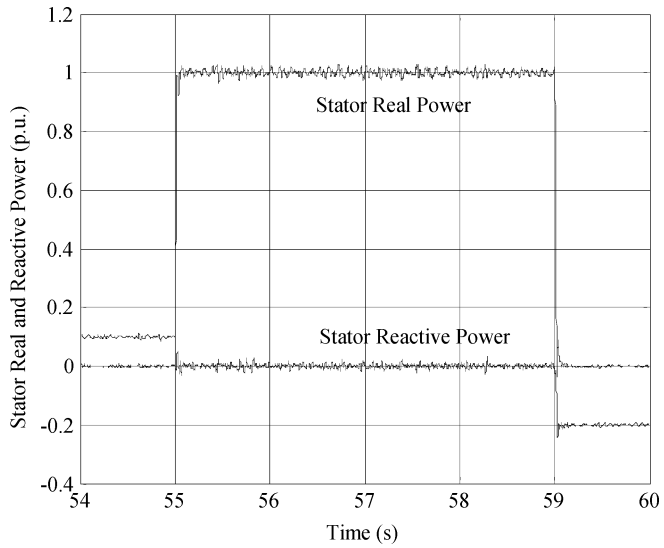

Fig. 10. Experimental results on a 30-kW DFIG control during normal operation.

The performance of fault ride-through control is verified with the DFIG initially operating with no load. The stator windings are initially open circuited and then a three-phase short-circuit fault is applied to the stator via a contactor. The unloaded machine is excited from the rotor side where the current determines the stator-flux linkage level. This is slightly different from the algorithm shown in (1) but a fault directly applied to the mains supply can be avoided. At the moment when the fault is applied to the stator, the stator-flux linkage is spontaneously trapped in the machine, giving rise to a dc component. The rotor windings then cut the trapped flux at the prefault speed, 1950 r/min in this experiment. The control objective is to constrain the rotor current in the presence of the induced EMF. The experiment setup is thus adequate to verify the proposed control method.

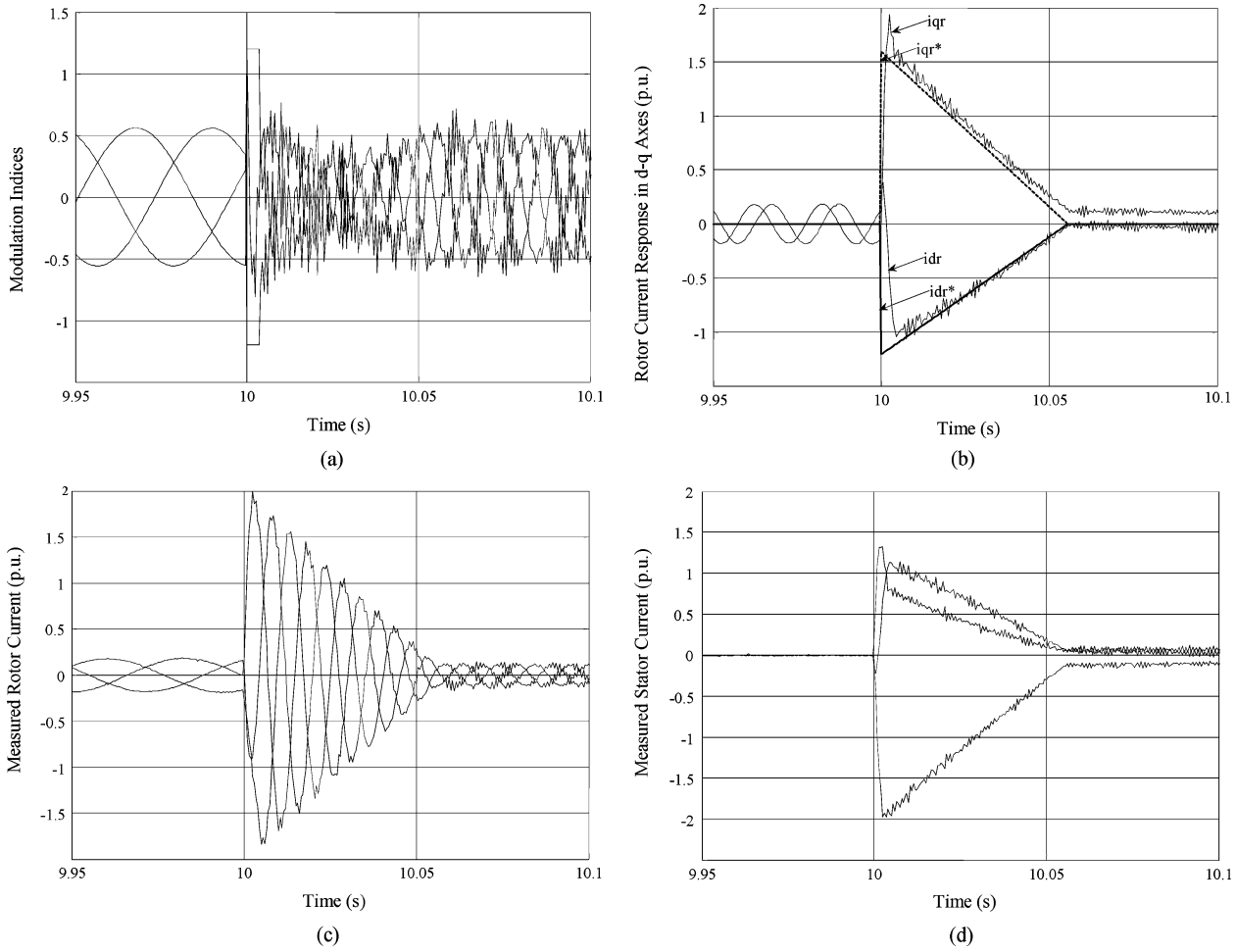

Fig. 11. Experimental results on a 30-kW DFIG with ride-through control.

Upon detecting the fault, the rotor current is controlled to oppose the dc component of the stator-flux linkage. The latter will decay due to the winding resistance. It can be shown that, without control action, it decays exponentially with the stator short-circuit time constant [14]

$$\tau_s' = \left[1 - \frac{L_{\rm m}^2}{(L_{\rm ls}' + L_{\rm m})(L_{\rm lr}' + L_{\rm m})}\right] \frac{L_{\rm ls}' + L_{\rm m}}{R_{\rm s}'} \qquad (11)$$

where $L_{\rm ls}'$ and $R_{\rm s}'$ include the contribution from the grid. The dc component of the stator-flux linkage decays more rapidly under control. In practice, the control gains should be enough for the flux to decay to nearly zero by the time when the fault is cleared. The compensating current component should decay correspondingly. In the experiment, the current decrease is represented in the control algorithm using a simple linear approximation.

Fig. 11 shows a set of experimental results where the decrease of the reference rotor current takes place in 55 ms. The initial compensation level is 2.0. p.u. in terms of the rotor current. The prefault rotor excitation level is set so that the stator voltage is initially 0.7 p.u. Fig. 11(a) shows the three-phase PWM modulation indices, which are to be compared with the triangular carrier between [-1, 1]. It is clear that overmodulation is required to increase the inverter output voltage while the dc link in this experiment is kept constant. Fig. 11(b) shows the response of the rotor current in the d–q reference frame where the d-axis coincides with stator phase "a" and the q-axis leads the d-axis by 90°. The small steady-state error is due to the proportional control and cross coupling between the two axes [15], which is not compensated in the study as the control is only for a short period of time. A small steady-state error is considered acceptable in this study. The three-phase rotor currents are also directly measured as shown in Fig. 11(c). While the envelope of the rotor current follows the desired profile, it is observed that the frequency changes from the prefault slip frequency (-0.3 p.u.) to a higher value (1.3 p.u.). Finally, Fig. 11(d) shows the measured response of the stator current. In this particular case, the stator current contains only the dc component during the fault.

Fig. 12 shows the simulation results corresponding to the experimental system, which indicates close agreement with the test although the fault occurs at a different phase angle on the waveforms. The experiment therefore verifies the simulation model, which can then be confidently used in full-scale system studies.

In both the experimental and the simulation results, the converter or rotor current is successfully constrained in 2.0 p.u. Note that the base voltage and current in Appendix III are purposely reduced as compared to the machine or converter rating to provide a safety margin. The rotor voltage also reaches the maximum that could be provided by the converter with

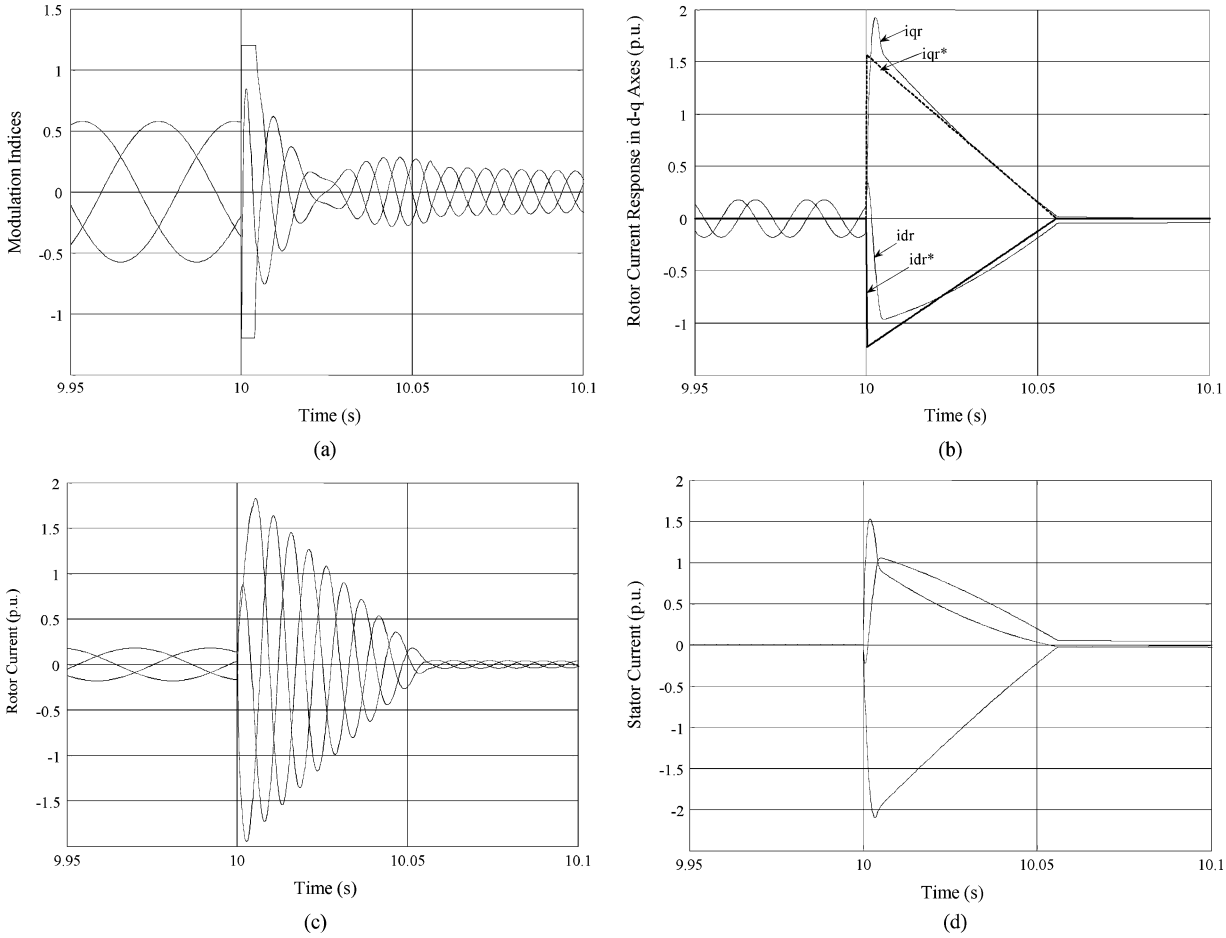

Fig. 12. Simulation results on a 30-kW DFIG with ride-through control.

overmodulation. Further experiments showed that for the same control setup, the current cannot be constrained if the prefault stator voltage is increased. This indicates that the success for the DFIG to ride through the fault depends on the dc component of the flux linkage trapped in the machine. As the prefault voltage increases, more flux is trapped increasing the induced EMF. The experimental results showing the effect of the prefault condition are summarized in Fig. 13.

V. Simulation Studies and Feasibility Regions

The verified model is used to simulate the ride-through control of the DFIG in different fault scenarios with a full-size machine. Fig. 14 shows a hypothetic network configuration of the 2-MW DFIG used in this study. The parameters of the step-up transformer and the double-circuit transmission network are given in Appendix II. From the generator point of view, the severity of the fault depends on the fault type and its distance from the generator terminal. Given the fault type, an index is defined to indicate the severity. The smaller is the K_{f}, the more severe is the fault.

$$K_{\mathrm{f}} = \frac{Z_2}{Z_2 + Z_3}. \tag{12}$$

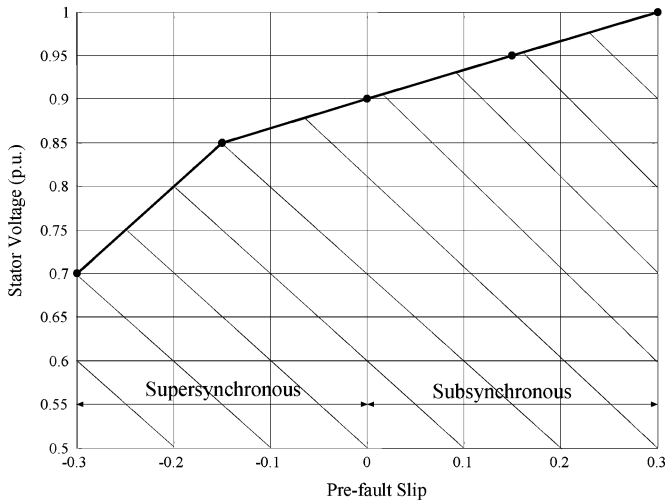

Fig. 13. Feasibility region (shaded) for ride-through control obtained from experiments.

A. Three-Phase Fault

Simulation is performed with $K_{\mathrm{f}} = 0.25$ and the results are shown in Fig. 15. The maximum slip is $s = \pm 0.3$ p.u. The

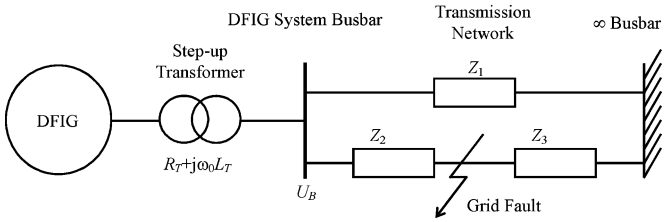

Fig. 14. Configuration of a simulated 2-MW DFIG system.

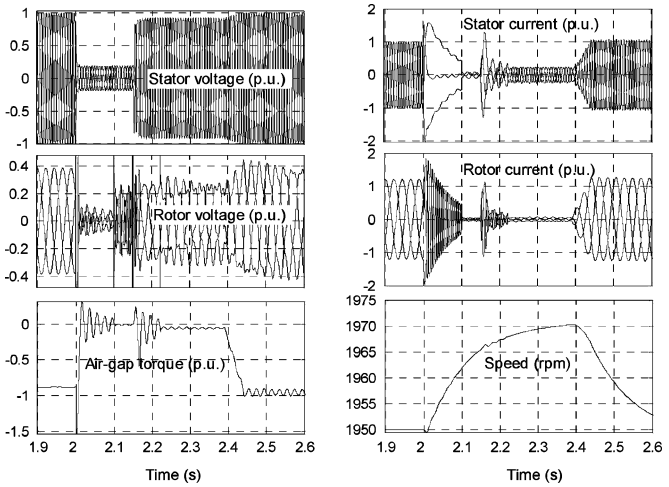

Fig. 15. Simulation results on a 2-MW DFIG for a three-phase fault.

rotor voltage, approximately $s\omega_0\psi_{rabc}$, is about 0.3 in the per unit system chosen in this study assuming 1.0 p.u. rotor flux linkage [16]. This means that the maximum rotor voltage will be around 0.43 p.u. with overmodulation [13].

The three-phase fault occurs at $t = 2$ s and it is assumed that the faulty transmission circuit is tripped after $t = 2.1$ s. The DFIG wind turbine initially runs at the nominal speed (1950 r/min) and the generator is almost fully loaded with a lagging power factor of 0.867. Fig. 15 shows that at the fault occurrence, the rotor current is constrained in 2.0 p.u. From $t = 2.1$ s, the reduced rotor current is forced to nearly zero, waiting for the fault to be cleared. As the dc component in the flux linkage would have reduced at this stage, it should be possible for the rotor converter to provide the voltage needed to null the current. At $t = 2.15$ s, the fault is cleared and the stator voltage recovers. The same concept of ride-through control is applied to the transient of fault clearance, which also introduces undesired components in the stator-flux linkage. From $t = 2.15$ s to $t = 2.25$ s, the rotor current is again controlled to weaken the dc component in the stator-flux linkage. It is controlled to zero after $t = 2.25$ s. At $t = 2.4$ s, the ride-through control is then disabled while the normal vector control is enabled. The air-gap torque is again developed.

Sensitivity studies were performed to investigate the factors that affect the ride-through control. The following changes in the prefault condition will make it more difficult to ride through the grid fault: 1) increase of machine speed and 2) increase of the reactive power generated by the DFIG on the stator side.

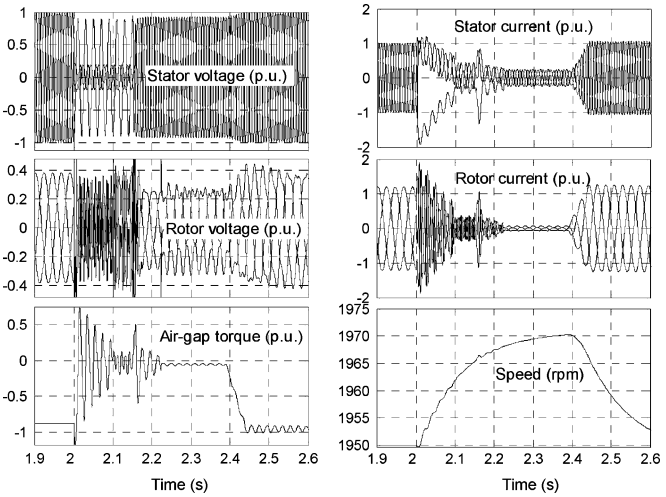

Fig. 16. Simulation results on a 2-MW DFIG for a phase–phase–ground fault.

This is consistent with the analysis on the mechanism of ride-through control since both of them increase the fault-induced EMF in the machine.

B. Phase–Phase–Ground Fault

Fig. 16 shows the simulation results with a phase–phase–ground fault in the network. Again, $K_{\rm f} = 0.25$. The prefault condition is the same as that given earlier.

Although the fault type is rare in practice, this case shows the features in an asymmetrical fault.

Compared with the previous case of symmetrical fault, the main difference is that a negative sequence component now exists in the stator-flux linkage during the transient. Part of the rotor current is utilized to cancel the effect of this component. However, as the cancellation is not complete, this leads to a new component induced in the rotor voltage, whose frequency is $2 - s$ p.u. As a result of the induced voltage, the maximum instantaneous value of the required rotor voltage may be higher than that used for the control. With interactions between the dc, positive-, and negative-sequence components in the flux linkages, the air-gap torque also has additional harmonic content not present previously.

In practice, an area of concern with an asymmetrical fault is the stabilization of the converter dc-link voltage. This was checked in simulation and it was found that the grid side converter could be controlled to avoid over current in the presence of unbalanced grid side voltage [17]. In general, with the proposed control of the rotor-side converter, the exchange of real power across the converter is also attenuated during the fault. The dc-link voltage can be readily stabilized for the fault scenario simulated.

C. Feasibility Region

Ride-through control is affected by many factors; the study identified that the most important ones are the prefault speed and the severity of the fault. The feasibility region for the DFIG to successfully ride through a grid fault is therefore investigated

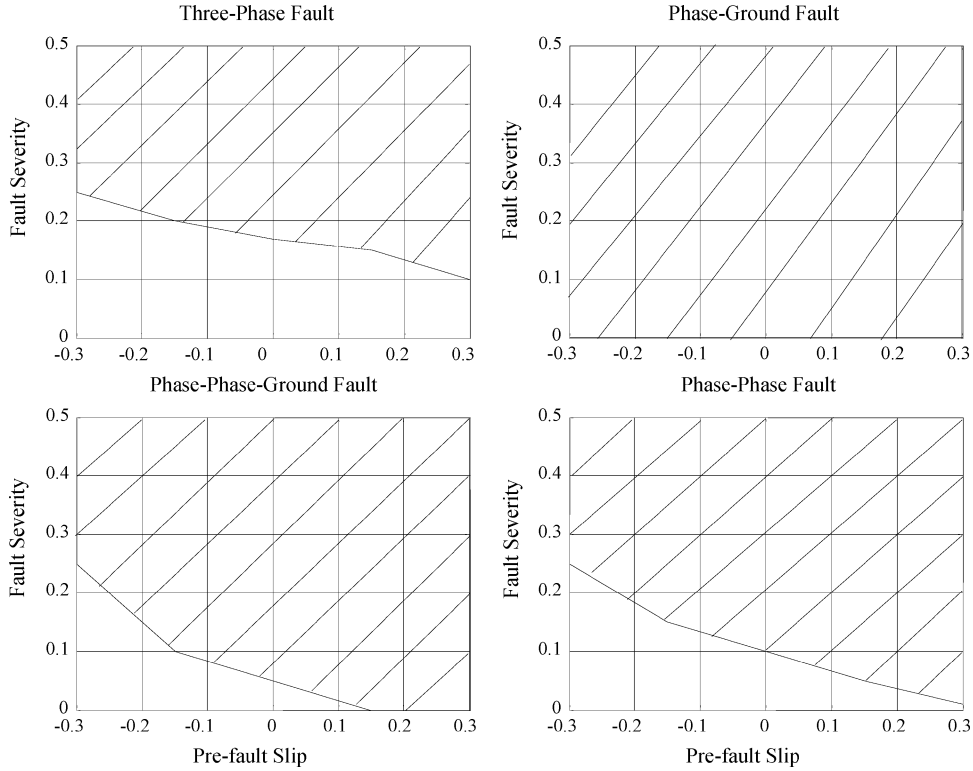

Fig. 17. Feasibility regions of grid fault ride-through (shaded) obtained from simulation.

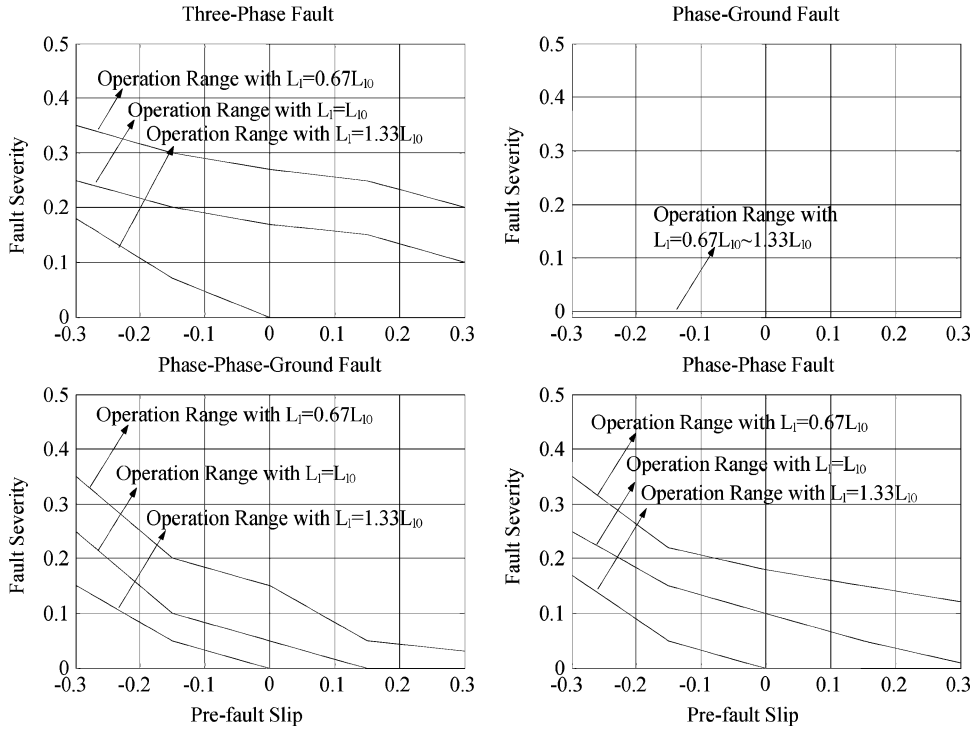

Fig. 18. Effect of machine leakage inductance on the feasibility region.

for each type of fault with respect to the prefault speed and K_{f}, to define the boundary that separates the situations that the DFIG can handle from those that it cannot and hence must be disconnected. The criterion is based on whether the rotor current can be constrained to 2.0 p.u. with a rotor voltage that is instantaneously lower than 0.43 p.u. as argued in Section V-A.

The feasibility regions identified are shown in Fig. 17. The slip covers the whole normal speed range, which is $\pm$ 30%

around the synchronous speed. The power factor on the stator side of the machine is fixed at 0.867 lagging. The total DFIG power changes with the speed and is shared between the stator and rotor circuits according to the slip [1]. In Fig. 17, any point in the shaded area means that the DFIG can ride through the grid fault in the corresponding condition. For any fault type, it is generally more difficult to ride through the fault of the same severity when the generator operates at a higher speed. When the generator operates at a speed 30% above the synchronous speed, i.e., -0.3 slip, it can ride through a symmetrical three-phase as long as the severity index is not less than 0.25 corresponding to the terminal voltage of about 0.3 p.u.

It is clear from Fig. 17 that the DFIG can ride through all single-phase-to-ground faults in the transmission network. This conclusion is however only valid for the specific system under study and the ride-through criterion described earlier. If the system configuration changes or the current and voltage capabilities of the converter are set differently, the feasibility regions for all fault types need to be revised.

As pointed out in the theoretical analysis in Section III, the DFIG ride-through control favors increased leakage inductance of the machine. Fig. 18 shows the feasibility regions as affected by total stator and rotor leakage inductance $L_{\rm l} = L_{\rm ls} + L_{\rm lr}$. Originally, $L_{\rm ls} = 0.1386$ p.u., $L_{\rm lr} = 0.1493$ p.u., and the total $L_{10} = 0.2879$ p.u. $L_{\rm ls}$ and $L_{\rm lr}$ are proportionally scaled to change the total leakage inductance. It is confirmed that increased leakage inductance indeed increases the feasibility regions. In practice, the stator and rotor leakage inductance can be increased by the choice of the slot depth, slot wedge, and the end winding arrangement [18]. An overall optimized solution should however be reached after also considering other effects, for example, the reactive power losses in the machine during normal operation.

VI. Conclusion

This paper analyzes the challenge for a DFIG wind turbine to ride through a grid fault. It has been shown that dc and negative sequence components are caused in the machine flux linkages, resulting in a large EMF induction in the rotor circuit. A new method is proposed to control the rotor-side converter so that the rotor current contains components to oppose the undesired components in the stator-flux linkage. Fast observation of the stator-flux linkage components is essential to the control, which effectively constrains the rotor current given the voltage capability of the converter. A test rig has been set up to verify the analysis and a control method has been proposed. Simulations based on a validated model provide the feasibility regions, in terms of fault severity and prefault speed, of successful ride-through control for a 2-MW DFIG connected to the grid through a double-circuit network. It is shown that the maximum turbine speed sets the most demanding scenario for ride-through control for all fault types. Increased machine leakage inductance is useful to the ride-through control method proposed.

The study clearly shows the ability for a DFIG wind turbine generator to ride through the grid fault and the limitations to that control objective. The study can be extended to evaluate the wind farm design, or to identify the situations where additional means of control and protection must be provided.

Appendix I

2-MW Machine Equivalent Circuit Parameters

Ratings: $S_{\rm n} = 2.0$ MW, $f_{\rm n} = 50$ Hz, $U_{\rm n} = 690$ V (line–line, rms), four pole
Winding connection (stator/rotor): Y–Y
Turns ratio: $N_{\rm s}/N_{\rm r} = 0.45$
Stator resistance: $R_{\rm s} = 0.00488$ p.u.
Stator leakage inductance: $L_{\rm ls} = 0.1386$ p.u.
Rotor resistance: $R_{\rm r} = 0.00549$ p.u.
Rotor leakage inductance: $L_{\rm lr} = 0.1493$ p.u.
Magnetizing inductance: $L_{\rm m} = 3.9527$ p.u.
$H = 3.5$ s
Base capacity: $S_{\rm b} = 2$ MVA
Base frequency: $f_{\rm b} = 50$ Hz
Base stator voltage (phase, peak value): $V_{\rm sb} = 563.4$ V
Base rotor voltage (phase, peak value): $V_{\rm rb} = 1252$ V
Proportional gain of current control: $K_{\rm p} = 1.6$

Appendix II

2-MW DFIG Transformer and Transmission Network Parameters

$S_{\rm n} = 2.5$ MW, $f_{\rm n} = 50$ Hz
Primary winding: 20 kV-Δ
Secondary winding: 690 V-Y0
Short-circuit impedance: $Z_{\rm T} = 0.0098 + j0.09241$ p.u.
Transmission line impedance: $Z_1 = Z_2 + Z_3 = 0.01 + j0.1$ p.u.
Base capacity: $S_{\rm b} = 2.5$ MVA

Appendix III

Test Rig DFIG Machine Parameters

Ratings: $S_{\rm n} = 30$ kW, $f_{\rm n} = 50$ Hz, $U_{\rm n} = 400$ V (line-line, rms), four pole
Winding connection (stator/rotor): Y–Y
Turns ratio: $N_{\rm s}/N_{\rm r} = 400/380$
Stator resistance: $R_{\rm s} = 0.0404$ p.u.
Stator leakage inductance: $L_{\rm ls} = 0.0673$ p.u.
Rotor resistance: $R_{\rm r} = 0.0315$ p.u.
Rotor leakage inductance: $L_{\rm lr} = 0.1152$ p.u.
Magnetizing inductance: $L_{\rm m} = 3.8997$ p.u.
Base capacity: $S_{\rm b} = 2.887$ kVA
Base frequency: $f_{\rm b} = 50$ Hz
Base stator voltage (phase, peak value): $V_{\rm sb} = 81.65$ V
Base rotor voltage (phase, peak value): $V_{\rm rb} = 77.57$ V
Proportional gain of current control: $K_{\rm p} = 1.6$
dc-link voltage: 48 V

Acknowledgment

The authors would like to acknowledge ALSTOM Power Conversion and FKI-DeWind for providing the test rig equipment. They would also like to thank several colleagues

for the help they provided during the study, particularly Dr. J. Bumby and Dr. P. Taylor of Durham University, Durham, U.K.; Dr. S. Finney of Heriot-Watt University, Edinburgh, U.K.; and Dr. X. Yuan of GE-Shanghai, Shanghai, China.

REFERENCES

[1] S. Muller, M. Deicke, and R. W. De Doncker, "Doubly fed induction generator systems for wind turbine," *IEEE Ind. Appl. Mag.*, vol. 8, no. 3, pp. 26–33, May–Jun. 2002.

[2] P. Fairley, "Steady as she blows," *IEEE Spectr.*, vol. 40, no. 8, pp. 35–39, Aug. 2003.

[3] J. L. Dallachy and I. Tait, "Guidance note for the connection of wind farms," 2.2.2, *SP Transmission and Distribution, Scottish Hydro-Electric*, 2002.

[4] O. Anaya-Lara and N. Jenkins, "Fault current contribution of DFIG wind turbines," presented at the IEE Conf. Reliability of Transmission and Distribution Networks, London, Feb. 2005.

[5] A. Petersson, L. Harnefors, and T. Thiringer, "Evaluation of current control methods for wind turbines using doubly-fed induction machines," *IEEE Trans. Power Electron.*, vol. 20, no. 1, pp. 227–235, Jan. 2005.

[6] G. Pannell, D. Atkinson, R. Kemsley, L. Holdsworth, P. Taylor, and O. Moja, "DFIG control performance under fault conditions for offshore wind applications," presented at the CIRED Conf., Turin, Italy, Jun. 2005.

[7] D. Xiang, L. Ran, P. J. Tavner, and J. R. Bumby, "Control of a doubly fed induction generator to ride through a grid fault," presented at the Int. Conf. Electric Machines (ICEM), Cracow, Poland, Sep. 2004.

[8] N. M. Kirby, L. Xu, M. Luckett, and W. Siepmann, "HVDC transmission for large offshore wind farms," *Power Eng. J.*, vol. 16, no. 3, pp. 135–141, Jun. 2002.

[9] U. Axelsson, A. Holm, C. Liljegren, K. Eriksson, and L. Weimers, "Gotland HVDC light transmission—world's first commercial small scale dc transmission," presented at the CIRED Conf., Nice, France, May 1999.

[10] P. C. Krause, *Analysis of Electrical Machinery*. Piscataway, NJ: IEEE Press, 1995, pp. 164–178.

[11] P. Vas, *Vector Control of AC Machines*. Oxford, U.K.: Oxford Univ. Press, 1990, pp. 39–40.

[12] R. Pena, J. Clare, and G. Asher, "Doubly fed induction generator using back-to-back converters and its application to variable-speed wind-energy generation," *IEE Proc.-Elect. Power Appl.*, vol. 143, no. 3, pp. 231–241, May 1996.

[13] N. Mohan, T. M. Undeland, and W. Robbins, *Power Electronics: Converters, Applications and Design*. New York: Wiley, 2003, pp. 626–637, 208–210.

[14] D. W. Novotny and T. A. Lipo, *Vector Control and Dynamics of AC Drives*. Oxford, U.K.: Oxford Univ. Press, 1996, p. 178.

[15] L. Ran and Y. Liao, "Sampling-induced resonance in an encoderless vector controlled induction motor drive," *IEEE Trans. Ind. Electron.*, vol. 51, no. 3, pp. 551–557, Jun. 2004.

[16] M. S. Vicatos and J. A. Tegopoulos, "Transient state analysis of a doubly-fed induction generator under three phase short circuit," *IEEE Trans. Energy Convers.*, vol. 6, no. 1, pp. 62–68, Mar. 1991.

[17] C. Hochgraf and R. H. Lasseter, "Statcom controls for operation with unbalanced voltages," *IEEE Trans. Power Del.*, vol. 13, no. 2, pp. 538–544, Apr. 1998.

[18] B. Charmers and A. C. Williamson, *A. C. Machines Electromagnetics and Design*. Chichester, U.K.: Wiley, 1991, pp. 52–55.

Dawei Xiang was born in Sichuan, China. He received the B.Eng. and M.Sc. degrees in electrical machinery and apparatus from the School of Electrical Engineering, Chongqing University, China, in 1999 and 2000, respectively.

He was an exchange student to the University of Electro-Communications, Tokyo, Japan, from October 1999 to September 2000. In 2004, he was a Visiting Scholar at Durham University, Durham, U.K. Currently, he is a Lecturer of electrical machinery and apparatus at the School of Electrical Engineering, Chongqing University. His research interests include the control of doubly fed electrical machines as used in renewable energy systems.

Li Ran (M'98) received the Ph.D. degree from Chongqing University, Chongqing, China, in 1989, in power systems engineering.

Currently, he is a Lecturer in electrical power and control at the School of Engineering, University of Durham, Durham, U.K. He participated in the commissioning of the Gezhouba-Shanghai HVDC system in China, in 1989. His research interests include application and control of power electronic technologies in power systems and renewable energy systems such as wave and wind energy converters.

Dr. Ran received the Stanley Gray Award—Offshore Technology, from the Institute of Marine Engineers, London, U.K., in 1999, for his study on interconnection of offshore oil rigs.

Peter J. Tavner received the M.A. degree in engineering sciences from Cambridge University, Cambridge, U.K., in 1969, and the Ph.D. degree from Southampton University, Southampton, U.K., in 1978.

Currently, he is a Professor of new and renewable energy at the School of Engineering, University of Durham, Durham, U.K. He has held a number of research and technical positions in the industry including those of the Technical Director of Laurence, Scott & Electromotors Ltd., Norfolk, U.K. and Brush Electrical Machines Ltd., Loughborough, U.K. He was also the Group Technical Director of FKI-DeWind Energy Technology, Loughborough, U.K. His research interests include electrical machines for the extraction of energy from renewable sources and their connection to electricity systems, electromagnetic analysis, the application of condition monitoring to electrical systems, and the use of converters with electrical machines.

Dr. Tavner is a receipient of the Institution Premium Award of the Institution of Electrical Engineers, U.K.

Shunchang Yang was born in Shanghai, China. He received the Graduation degree from the Electrical Engineering Department, Chongqing University, Chongqing, China, in 1960.

In 1960, he was an Assistant Lecturer at the Electrical Engineering Department. From 1985 to 1986, he was a Visiting Scholar at Tennessee University, Knoxville. Since 1988, he has been a Professor at Chongqing University. In 1991, he was at the Kiev Institute of Technology, Kiev, Ukraine and the All Soviet Union Institute of Electrical Engineering and Sciences, Moscow, Russia, in an international project entitled "Asynchronized Synchronous Machines and their Applications in Power Systems." His research interests include design and control of electrical machines of new topologies.

WIND ENERGY
Wind Energ. 2007; **10**:1–18
Published online 12 July 2006 in Wiley Interscience
(www.interscience.wiley.com) DOI: 10.1002/we.204

Reliability Analysis for Wind Turbines

P. J. Tavner*, New & Renewable Energy Group, School of Engineering, Durham University, Durham DH1 4RL, UK
J. Xiang, CREST, Loughborough University, Loughborough, UK
F. Spinato, New & Renewable Energy Group, School of Engineering, Durham University, Durham DH1 4RL, UK

Key words: wind turbine; reliability; electric network; homogeneous Poisson process; power law process

Modern wind turbines are complex aerodynamic, mechanical and electrical machines incorporating sophisticated control systems. Wind turbines have been erected in increasing numbers in Europe, the USA and elsewhere. In Europe, Germany and Denmark have played a particularly prominent part in developing the technology, and both countries have installed large numbers of turbines. This article is concerned with understanding the historic reliability of modern wind turbines. The prime objective of the work is to extract information from existing data so that the reliability of large wind turbines can be predicted, particularly when installed offshore in the future. The article uses data collected from the Windstats survey to analyse the reliability of wind turbine components from historic German and Danish data. Windstats data have characteristics common to practical reliability surveys; for example, the number of failures is collected for each interval but the number of turbines varies in each interval. In this article, the authors use reliability analysis methods which are not only applicable to wind turbines but relate to any repairable system. Particular care is taken to compare results from the two populations to consider the validity of the data. The main purpose of the article is to discuss the practical methods of predicting large-wind-turbine reliability using grouped survey data from Windstats and to show how turbine design, turbine configuration, time, weather and possibly maintenance can affect the extracted results.

Received 24 September 2005; Revised 17 May 2006; Accepted 17 May 2006

Introduction

An increasing number of wind turbines are being incorporated into European electrical networks. In some countries such as Denmark, Germany and Spain they are becoming a key part of networks and as such affect the overall system performance and reliability.[1]

The configuration, technology and size of wind turbines have been changing rapidly over the last few years, and larger turbines (≥2 MW) incorporating new technology are being installed onshore throughout Europe. There is potential for more wind turbines to be erected in remote and offshore locations, to achieve a greater wind energy harvest, where the access to turbines for maintenance will be restricted. This is heightening the need for accurate reliability predictions so that wind turbine availability and life can be predicted and reasonable predictions of wind energy harvest over the life of the turbines can be made.

This article concerns the reliability of wind turbines in Denmark and Germany, using data extracted from Windstats (www.windstats.com) over the past 10 years. Both populations include modern turbines, but the

*Correspondence to: P. J. Tavner, New & Renewable Energy Group, School of Engineering, Durham University, Durham DH1 4RL, UK
E-mail: peter.tavner@durham.ac.uk

German data include many larger wind turbines. One of the authors has previously shown, for electric motors,[2] that such data can be used to predict the reliability of future equipment. Reliability predictions for wind turbines will have an important bearing on the future development of wind power resources.

Windstats is a reliability survey which collects, organizes and groups failure data into periods of months or quarters. Therefore time to failure (TTF) information is not available. The data are collected from wind turbines, which, being both maintained and repaired, are typical repairable systems, for which failure times cannot in general be considered to be independent. Therefore the correct statistical model must be chosen.

This article analyses the failure rates derived from Windstats, considers problems that have arisen and provides evidence of how turbine failure rates are improving with time.

The article is organized to describe first the background to the reliability issue for wind turbines, then to describe the modelling methods available to analyse the data available, then to apply those methods to the collected data; finally, a discussion considers the various results, and conclusions are drawn.

Background

Windstats Data

Windstats is a commercial newsletter for the wind industry and records details of operation of wind turbines in many countries.

The overall period P investigated in this article was 10 years from October 1994 to September 2004. This period was restricted to ensure that the data being considered concerned modern designs of wind turbines. Data from two countries in particular have been analysed, Germany and Denmark, because the wind turbine populations reporting to Windstats from these two countries are large. The data give information about the items shown in Table I, including failures for the subassemblies which make up the turbines.

The German survey population includes up to 4500 turbines and the Danish survey population includes up to 2500 turbines, as will be shown below. The Windstats survey covers a fraction of the turbines installed in Germany and Denmark, which currently number approximately 20,000 and 6000 turbines respectively.

Windstats data are published quarterly, but the survey collects the number of failures occurring in the two turbine populations of successive Intervals of 1 month for Danish data and quarterly for German data.

The size of the population and the size of the interval are statistically important, since the larger the population and the larger the interval, the larger is the number of failures that are likely to occur in an interval. Over time the population is altering, as turbines are added or taken out of service, so the character of the population is changing. It would seem statistically that the German data are likely to give greater accuracy, since then represent a larger population and a longer interval and so are recording much larger numbers of failures per interval.

Table I. Data recorded in Windstats for the two populations

Information	Unit
Length of reporting interval i	Month or quarter
Number of intervals for which data were collected	I
Turbines reporting in a population	Number N_i per interval i
Turbines added and removed from the population	Number per interval
Total rating of all turbines in a population	kW
Energy produced by all turbines in a population in an interval	kWh
Failures in major subassemblies	Number $n_{i,k}$ per interval i per subassembly k (see Table II)
Time lost due to subassembly failures for all turbines N_i	Hours, T_s
Time lost due to non-subassembly failures for all turbines N_i	Hours, T_n
Time lost due to failures for which only hours recorded for all turbines N_i	Hours, T_h
Total time lost per interval for all turbines N_i	Hours, $T_t = T_s + T_n + T_h$

DOI: 10.1002/we

In fact, the Danish data show very low numbers of failures for some subassemblies in the most recent months of the survey. This may legitimately be the result of improving turbine failure rates, but it causes concern to the authors, because in some recording intervals the Danish data show zero failures for some turbine subassemblies, and this reduces the accuracy of those data.

Architecture of Wind Turbines

Within the survey populations there are many detailed variants, including:

- variations in turbine size from 100 kW up to 2.5 MW;
- variations in turbine blade aerodynamic and structural design;
- variations in mechanical architecture, including direct drive from the turbine to a low-speed generator or indirect drive with a gearbox and high-speed generator;
- variations in mechanical control for yaw;
- variations in mechanical control for speed, ranging from simple stall control, fixed speed turbines with induction generators to sophisticated pitch control, variable speed turbines with doubly fed induction or direct drive synchronous generators.

However, the vast majority of turbines covered by the survey will be of the Danish concept, i.e. a three-bladed, upwind turbine, mounted on a nacelle, on top of a cylindrical tower, such as shown in Figure 1.

One of the tasks of this article is to deduce some common facts from the failure data reported from this disparate range of turbines.

Figure 1. Typical Danish concept wind turbines as considered in this article (courtesy of GE Wind Power)

DOI: 10.1002/we

Wind Turbine Subassemblies

A wind turbine is made up of a number of key subassemblies, and Windstats provides failure information for each subassembly, as set out in Table II, for each interval. German and Danish data have slight variations in the name used for each subassembly, and there is no agreed descriptor for these subassemblies. In order to analyse the data in a common way, it has been necessary to group subassemblies as shown in Table II, which gives the subassembly name used in this article and that used by Windstats in each of the two national populations. The subdivision of faults by subassemblies cannot be taken to mean that the failure mode necessarily lies in the subassembly itself.

Modelling Wind Turbine Reliability

Machinery Life and Reliability, the HPP and PLP Models

The train of equipment at the heart of a modern wind turbine includes the key subassemblies shown in Table II. This article will use turbine and subassembly reliability results, plus a mathematical model, to interpret the data.

The subassemblies, and therefore the turbine, are repairable and the power law process (PLP) is commonly used in the reliability analysis of complex repairable equipment.[3,4] Its intensity function $\lambda(t)$ describes the failure rate of a piece of machinery, such as a wind turbine, and has the form

$$\lambda(t) = \frac{\beta}{\theta}\left(\frac{t}{\theta}\right)^{\beta-1} \tag{1}$$

β is a parameter which describes the shape of the intensity function; θ, the scale parameter, has dimensions of time, and $\theta > 0$ for $t \geq 0$.

Figure 2 shows a complete failure intensity curve, usually referred to as the bathtub curve, whose three regions are described by equation (1) using different values for the shape parameter β:

- early failures, $\beta < 1$;
- constant failure rate, $\beta = 1$;
- deterioration, $\beta > 1$.

When $\beta = 1$, equation (1) reduces to a constant and the process becomes a homogeneous Poisson process (HPP), a particular case of a Poisson process for which the times between failures (TBFs) are independent and

Table II. Wind turbine subassemblies in the two populations

Subassembly name used in this article	Subassembly name used in Germany	Subassembly name used in Denmark
Rotor blades	Rotor	Blades, hub
Air brake	Air brake	Air brakes
Mechanical brake	Mechanical brake	Mechanical brake
Main shaft	Main shaft	Main shaft, coupling
Gearbox	Gearbox	Gearbox
Generator	Generator	Generator
Yaw system	Yaw system	Yaw system
Electrical controls	Electrical controls	Electrical control
Hydraulics	Hydraulics	Hydraulic system
Grid or electrical system	Electrical system	Electrical control
Mechanical or pitch control system	Mechanical control	Pitch control
Other	Other, instrumentation, sensor, windvane	Other

DOI: 10.1002/we

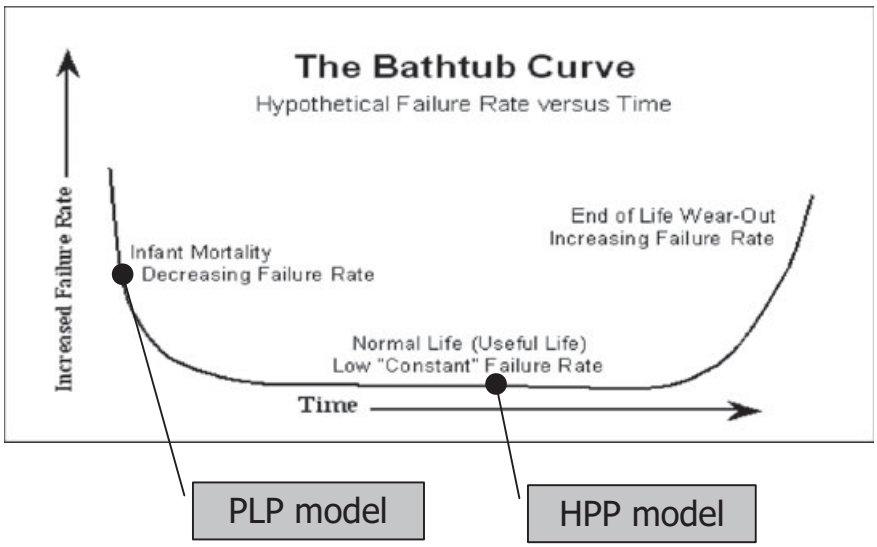

Figure 2. The intensity function of machinery

identically distributed (IID) exponential random variables. Thus θ becomes the mean time between failures (MTBF) of the turbine, and the maximum likelihood estimate (MLE) of θ is

$$\hat{\theta} = \frac{1}{\lambda} = \frac{\sum_{i=1}^{I} T_i}{\sum_{i=1}^{I} n_i} \tag{2}$$

The deterioration phase ($\beta > 1$) has not yet been encountered in wind turbines, probably owing to their relatively young age.[5] Furthermore, if the reliability of a wind turbine reduces dramatically, it will be taken out of service before the deterioration phase can be detected.

If we collect data from a large number of turbines, we can deduce an average failure rate at a given interval by assuming that every turbine in the population lies on the constant failure rate part of the bathtub curve, which can be modelled by the HPP. The failure rate λ_i, expressed as the number of failures per turbine per year, can then be obtained at the ith interval by dividing the total number of turbine failures in this interval, $n_i = \sum_{k=1}^{K} n_{i,k}$, by the number of turbines, N_i, in the population for the interval and by the length in hours of the interval, T_i. The yearly based failure rate is then obtained by correcting the figure by the number of hours in a year as follows:

$$\lambda_i = \frac{\sum_{k=1}^{K} n_{i,k}}{N_i T_i / 8760} \tag{3}$$

Using the same method, a failure rate $\lambda_{i,k}$ for the kth subassembly in the ith interval can been obtained from each population at each interval i:

$$\lambda_{i,k} = \frac{n_{i,k}}{N_i T_i / 8760} \tag{4}$$

DOI: 10.1002/we

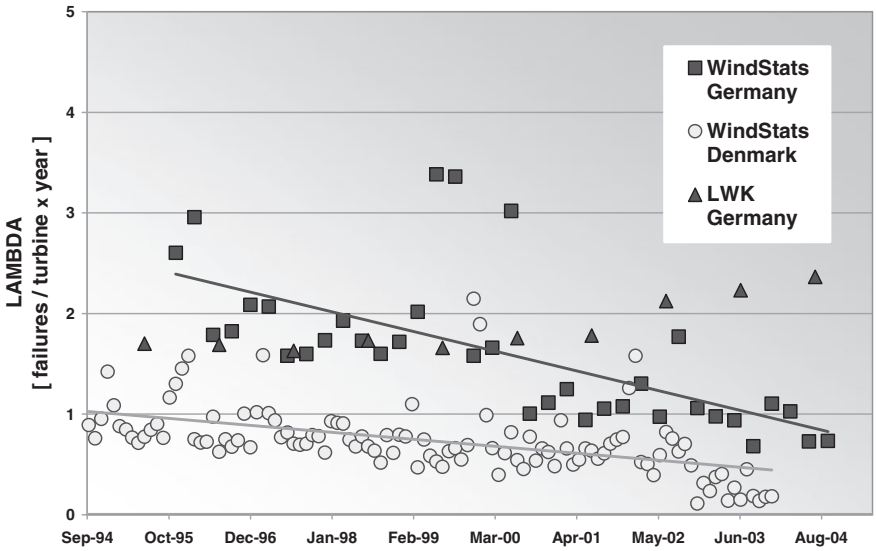

Figure 3. Turbine failure rates for two sets of data from turbines in Denmark and Germany using the HPP model

The average number of failures per turbine per year, λ, for the overall period $P = \sum_{i=1}^{I} T_i$ is given by

$$\lambda = \frac{\sum_{i=1}^{I}\sum_{k=1}^{K} n_{i,k}/N_i}{\sum_{i=1}^{I} T_i/8760} \tag{5}$$

The failure rates for an average turbine in the two national populations in each interval from 1994 to 2004, using equation (3), are shown in Figure 3.

The Homogeneous Poisson Process Model

Probability

The data obtained from Windstats over the 10 years have a variable population at each interval, a month for Danish and a quarter for German data. The data have been reorganized so that populations and failure rates are available for 40 successive quarters for both Denmark and Germany, as statistical analysis shows that there is no loss of information after reorganization.

In order to use the HPP model for probability predictions, it is necessary to consider a group of turbines in a given interval of a month/quarter as an independent population which varies in each subsequent month/quarter. If it is assumed that the times between failures are IID exponential random variables, then the HPP model[6,7] describes the probability $P(t)$ of having n failures through time t as

$$P(N(t) = n) = \frac{1}{n!}(\lambda t)^n e^{-\lambda i}, \quad n = 0,1,2,\ldots \tag{6}$$

where the failure rate λ is the intensity function of the Poisson process, and the probability $P(t)$ that the nth failure will occur before time t is defined by

$$P(t_n < t) = \int_0^t \frac{\lambda^n t^{n-1}}{\Gamma(n)} e^{-\lambda t} dt \tag{7}$$

DOI: 10.1002/we

Considering the turbines in each quarter as an independent population, according to the HPP model, the failure rate is $\lambda = 1/\theta$ with MTBF θ constant for each quarter, and, if we take the average failure number of all the turbines reported in each quarter to be the failure number of a single average turbine, the varying population has no effect on the analysis. The assumptions are justified because the turbines have similar subassemblies, even though the populations vary from quarter to quarter.

To evaluate the reliability of a wind turbine and its subassemblies, the probability of observing n or more failures in the interval (t_1, t_2) can be calculated as

$$P_n = P(N \geq n) = \sum_{n}^{\infty} P(N = n) \tag{8a}$$

$$\therefore P_n = \sum_{n}^{\infty} \frac{1}{n!} \lambda (t_2 - t_1)^n e^{-\lambda (t_2 - t_1)} \tag{8b}$$

$$P_n = 1 - P(N \leq n-1) = 1 - \sum_{0}^{n-1} \frac{1}{n!} \lambda (t_2 - t_1)^n e^{-\lambda (t_2 - t_1)} \tag{8c}$$

Variation in MTBF between Subassemblies

Since the data from Windstats are processed by analysing I identical repairable populations for each interval, it is necessary next to test whether all I populations have the same MTBF θ. For each of k subassemblies to have the same MTBF, the following hypothesis needs to be satisfied:

$$\mathrm{H}_0\text{: } \theta_{1,k} = \theta_{2,k} = \ldots = \theta_{I,k} \textit{ versus } \mathrm{H}_1\text{: } \theta_{1,k} \neq \theta_{2,k} \neq \ldots \neq \theta_{I,k}$$

The hypothesis-testing procedure is based on the likelihood ratio (LR) principle and the use of the chi-square approximation of the test statistic. The likelihood ratio LR_k is

$$\begin{aligned} LR_k &= \frac{\max_{H_0} L(\theta_{1,k}, \theta_{2,k}, \ldots, \theta_{I,k})}{\max L(\theta_{1,k}, \theta_{2,k}, \ldots, \theta_{I,k})} \\ &\equiv \frac{\max_{\theta} \theta^{-\Sigma_{i=1}^{I} n_{i,k}} e^{-\sum_{i=1}^{I} T_i/\theta}}{\max_{\theta_{1,k}, \theta_{2,k}, \ldots, \theta_{I,k}} \prod_{i=1}^{I} \theta_{i,k}^{-n_{i,k}} e^{T_i/\theta_{i,k}}} \\ &\equiv \frac{\hat{\theta}_k^{-\Sigma_{i=1}^{I} n_{i,k}} e^{\sum_{i=1}^{I} T_i/\hat{\theta}_k}}{\prod_{i=1}^{I} \tilde{\theta}_{i,k}^{-n_{i,k}} e^{T_i/\tilde{\theta}_{i,k}}} \\ &\equiv \frac{\prod_{i=1}^{I} \tilde{\theta}_{i,k}^{n_{i,k}}}{\hat{\theta}_k^{\Sigma_{i=1}^{I} n_{i,k}}} \end{aligned} \tag{9}$$

Where $\hat{\theta}_{i,k}$ is the value of $\theta_{i,k}$ which maximizes the denominator of the likelihood ratio, and $\hat{\theta}_k$ is the MLE of the expression in the numerator, i.e.

$$\tilde{\theta}_{i,k} = \frac{T_i}{n_{i,k}} \tag{10a}$$

$$\hat{\theta}_k = \frac{\sum_{i=1}^{I} T_i}{\sum_{i=1}^{I} n_{i,k}} \tag{10b}$$

DOI: 10.1002/we

Table III. Example of results from the likelihood ratio test (Danish data)

Subassembly	$\chi^2_{0,\kappa}$	H_0	Conclusion
Main shaft	0·0017	Accepted	Identical
Gearbox	0·0025	Accepted	Identical
Mechanical brake	0·0036	Accepted	Identical
Generator	0·0064	Accepted	Identical
Hydraulic system	0·0016	Accepted	Identical
Yaw system	0·0041	Accepted	Identical
Electrical control	0·0012	Accepted	Identical
Air brakes	0·0024	Accepted	Identical
Coupling	0·0021	Accepted	Identical

The likelihood ratio statistic

$$-2\ln LR_k = 2\sum_{i=1}^{I} n_{i,k} \ln \hat{\theta}_k - 2\sum_{i=1}^{I} n_i \ln \tilde{\theta}_{i,k} \tag{11}$$

is distributed approximately as a chi-square with $I - 1$ degrees of freedom.

Let $\chi^2_{0,\kappa} = -2\ln(\mathrm{LR}_k)$. Giving a specified value for the significance level α, we have $\chi^2_{\alpha,I-1}$ as the critical value. The test procedure calls for rejecting the null hypothesis H_0 when the value of this ratio $\chi^2_{0,\kappa}$ is large, say, whenever $\chi^2_{0,\kappa} > \chi^2_{\alpha,I-1}$. In other words a large value of $\chi^2_{0,\kappa}$ leads to a rejection of the null hypothesis. If the null hypothesis is not rejected, the θs are equal and the populations are identical in the sense that their MTBFs are the same. For a test with $\alpha = 0{\cdot}05$ we would reject the null hypothesis when $\chi^2_{0,\kappa} > \chi^2_{\alpha,I-1} = 18{\cdot}3$. For a test with $\alpha = 0{\cdot}10$, we would reject the null hypothesis when $\chi^2_{0,\kappa} > \chi^2_{\alpha,I-1} = 16{\cdot}0$.

Table III gives the calculated results for the Danish subassembly data of the likelihood ratio statistic with $\alpha = 0{\cdot}05$. It shows that it is reasonable to assume that the subassemblies in each quarter have the same MTBF.

Similar results were obtained for the German data.

The Power Law Process Model

The PLP model can be used to track the reliability improvement of a system and to predict the effectiveness of further design developments. The standard[4] provides a procedure for the determination of the parameters of the intensity function for data collected in grouped form, like the data from Windstats. A goodness of fit test is also provided. Data are referred to as 'grouped' when only the number of failures in each period is known and the information about the actual TTFs is missing. The method has been applied considering one wind turbine subjected to the average number of failures of the population in each period. If the intensity function is rewritten as

$$\lambda(t) = \rho\beta t^{\beta-1} \tag{12}$$

then the MLE for the shape parameter $\hat{\beta}$ is obtained by solving numerically the non-linear equation[8]

$$\sum_{i=1}^{I} n_i \left(\frac{t_i^{\hat{\beta}} \ln t_i - t_{i-1}^{\hat{\beta}} \ln t_{i-1}}{t_i^{\hat{\beta}} - t_{i-1}^{\hat{\beta}}} - \ln t_I \right) = 0 \tag{13}$$

in which, by definition,

$$t_0^{\hat{\beta}} = \ln t_0 = 0 \tag{14}$$

DOI: 10.1002/we

and the set $[t_{i-1}, t_i]$ defines the ith interval. The MLE for the scale parameter $\hat{\rho}$ is then

$$\hat{\rho} = \frac{\sum_{i=1}^{I} n_i}{t_I^{\hat{\beta}}} \tag{15}$$

The assumption of considering the reliability of the population of wind turbines improving according to a PLP can be tested with a goodness of fit test. The test is built starting from the expected number of failures in the ith interval, which is approximated by

$$e_i = \hat{\rho}\left(t_i^{\hat{\beta}} - t_i^{\hat{\beta}-1}\right) \tag{16}$$

Thus the statistic

$$x^2 = \sum_{i=1}^{I} \frac{(n_i - e_i)^2}{e_i} \tag{17}$$

is approximately distributed as a chi-square random variable with $I - 2$ degrees of freedom, for which the critical values can be found in the usual tables. The hypothesis is accepted if the statistic assumes values smaller than the critical value, which is calculated for the level of confidence, α, chosen.

Discussion

Interpretation from Data

Turbine Reliability, Failure Rate

The average failure rates for each interval plotted using equation (3) are shown in Figure 3 and are striking.

- Failure rates in both populations are falling with time.
- German failure rates are higher than Danish failure rates.
- Danish monthly failure rates exhibit some periodicity, which the authors ascribe to the effect of the weather.
- There are some significantly high failure rates in both populations, and some of these high failure rates in the two populations coincide in time.

The first two results have also been reached independently in a report from the Netherlands by DOWEC.[9] This work has previously been reported by the authors.[10,11]

Subassembly Reliability, HPP

Figure 4 shows the failure rate for each subassembly in the two national populations of turbines during the period 1994–2004 using equation (4), the HPP Model, sorting the failure rates in their order of significance for German turbines.

Comparing the failure rates of subassemblies between Denmark and Germany, it can be seen that, as expected from Figure 3, Danish failure rates are lower, but for some subassemblies the two populations have similar failure rates, e.g. on the main shaft and mechanical brake. This implies that Danish and German turbines, using the HPP model, could have similar reliability features, not surprisingly, since brakes and shafts produced in varying sizes for the same industry are likely to have similar failure rates in different populations. On the assumption that the turbine subassemblies conform to the HPP model, the MTBFs for the subassemblies can be given as in Table IV.

The principal contributors to the higher German failure rate are the electrical control or system subassemblies (grid or electrical system, yaw system and mechanical or pitch control system) rather than mechanical subassemblies such as the gearbox. This is consistent with the introduction of variable speed drive technology but is contrary to the received wisdom that gearboxes are a major cause of turbine failure.

DOI: 10.1002/we

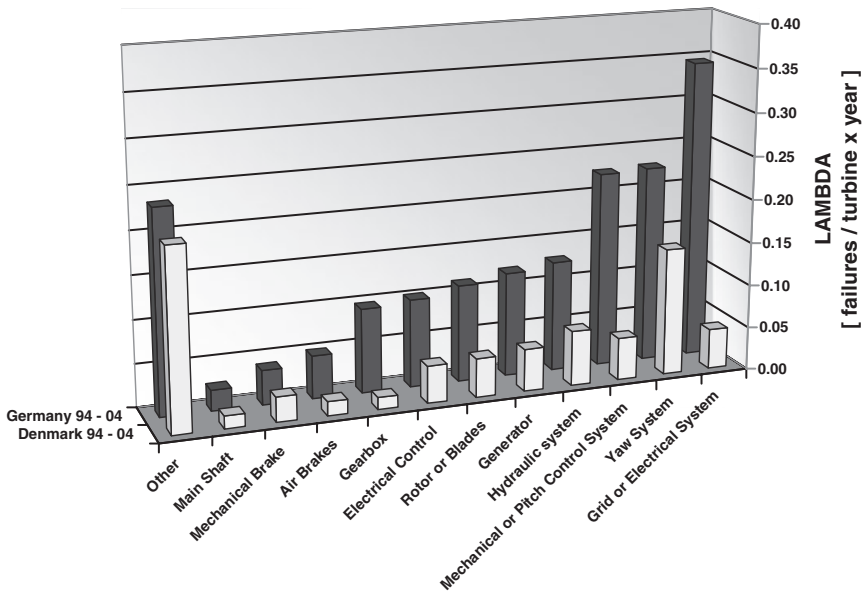

Figure 4. Variation in subassembly failure rates for the two populations in the overall period using the HPP model

Table IV. MTBFs of German and Danish turbine subassemblies calculated from Figure 4 assuming the HPP model

Subassembly	German turbine subassembly MTBF (h)	Danish turbine subassembly MTBF (h)
Rotor blades	39,297	252,033
Air brake	180,078	1,286,050
Mechanical brake	223,447	627,055
Main shaft	365,339	807,174
Gearbox	87,174	218,871
Generator	73,234	365,534
Yaw system	69,504	318,903
Electrical controls	39,205	175,561
Hydraulics	79,363	285,195
Grid or electrical system	25,708	450,643
Mechanical or pitch control system	90,472	1,236,712
Other	25,449	51,871

However, it must be understood that failure of a gearbox, or of a blade or generator for that matter, is likely to have a great impact on turbine availability owing to the extended mean time to repair (MTTR) necessary for its removal from a nacelle and replacement.

It should be noted that the distribution of subassembly failures shown in Figure 4 and their respective order will vary according to the span of years considered, but that the figure shown adequately summarizes the overall effect.

DOI: 10.1002/we

Comparison between German and Danish Turbine Populations

The failure rates in this article are an average over large populations of 900–4000 turbines, each of which population includes turbines of different technology and age, which may not necessarily lie on the flat part of the bathtub curve. Thus the HPP model implicit in Figures 3 and 4 needs to be used with caution. For example, newer turbines which are still in the early failure phase will have a rapidly falling failure rate, which will affect the averaging implicit in equation (3). However, this approach is recommended in Reference 3.

To select valid mathematical models, the data must be analysed further to determine the characteristics of the German and Danish populations. The Danish and German data have been investigated regarding the numbers and average sizes of turbines in each population, as presented in Figures 5 and 6. These figures show

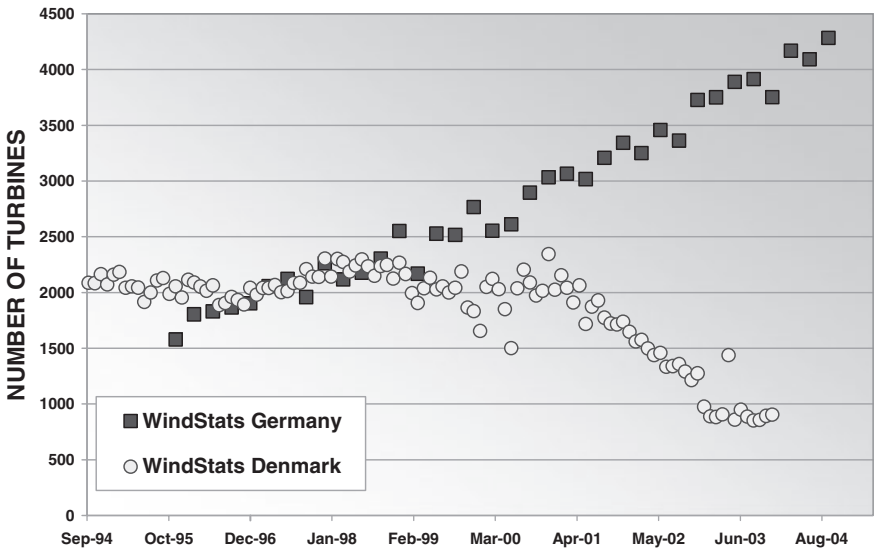

Figure 5. Numbers of turbines in the Danish and German populations

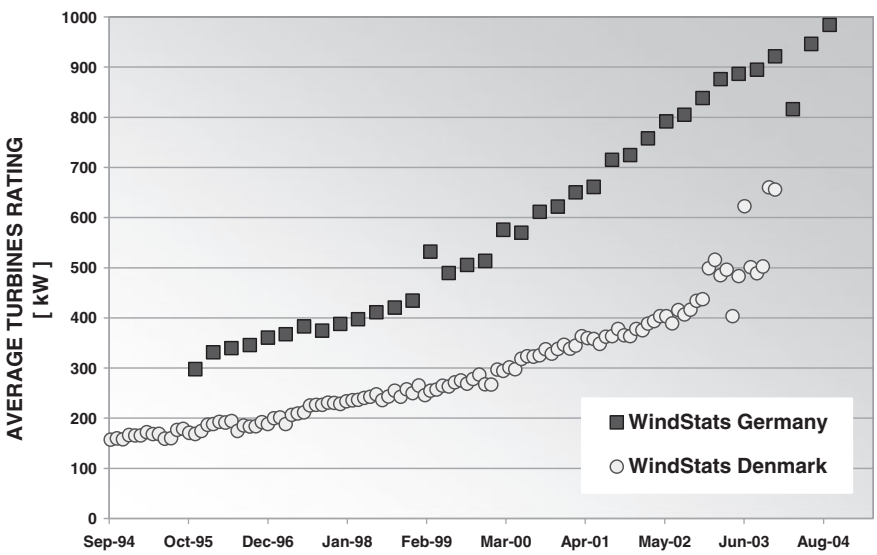

Figure 6. Sizes of turbines in the Danish and German populations

DOI: 10.1002/we

that the number of Danish turbines is decreasing but their rated size is half that of German turbines. This is consistent with the knowledge that Denmark started building large wind turbines before Germany but has had an installation moratorium, only replacing older, smaller turbines with newer, larger machines. The increase in German turbine numbers is a result of the growth in that market, which has been reported elsewhere.[1]

The implication of Figures 5 and 6 is that the Danish turbines in the survey are smaller and older than the German turbines and are likely to be largely stall-regulated, constant speed machines.

Predictions from Data

Reliability Growth Curve, PLP

'Modelling Wind Turbine Reliability' showed how to fit the reliability growth curve to the failure data using the PLP model.

Using the procedure in 'The Power Law Process Model', the German and Danish estimated reliability growth curves are given in Figure 7, while in Figure 8 the two curves are directly compared.

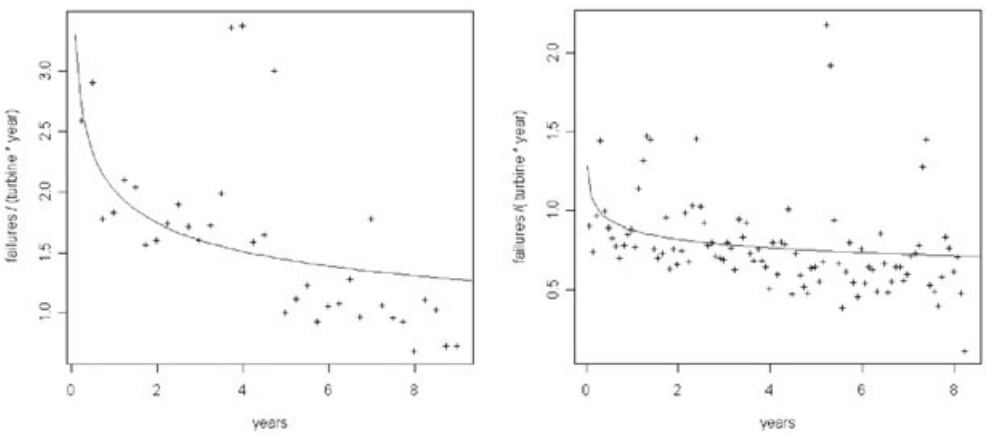

Figure 7. PLP model results, German on left and Danish on right

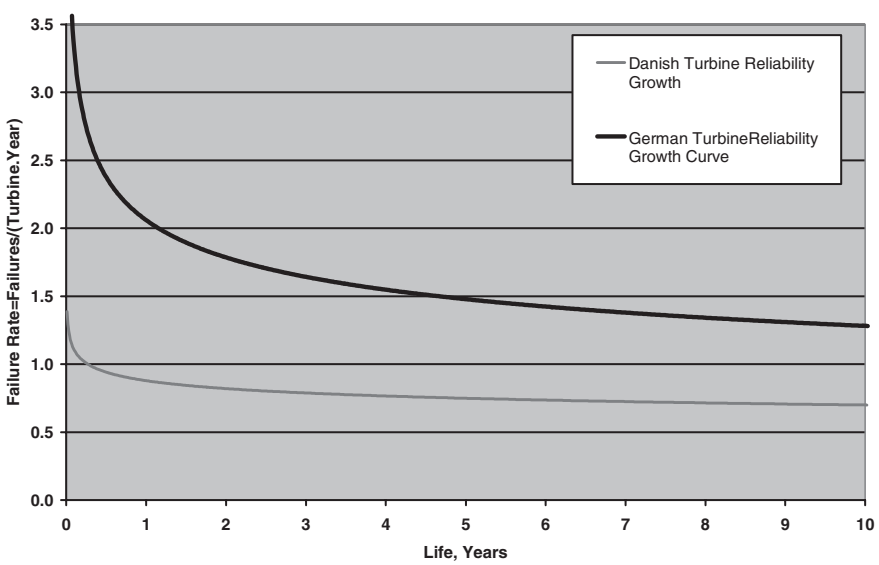

Figure 8. Calculated reliability growth curves using the method in 'The Power Law Process Model', confirming different history and trend for German and Danish populations

DOI: 10.1002/we

Table V. Parameters estimated with failure rate λ (failures per year); see equations (12)–(17)

	β	ρ	x^2	$\chi^2_{\alpha,I-2}$
German turbines	0·794	2·530	5·390	48·6
Danish turbines	0·901	0·975	0·906	121·0

The estimates for β and ρ from equations (12)–(17) for those are curves are given in Table V. This confirms that the shape parameters of the two curves are dissimilar, demonstrating a substantially different improvement history and current trend. Furthermore, the reciprocal value of the intensity function can be considered as the instantaneous MTBF, and the comparison of the two curves confirms the worse reliability for the German wind turbines. The value of the intensity function in the last interval may be interpreted as the constant failure rate that the system would have if the development phase was terminated.

The German turbines are newer than the Danish turbines, so a larger improvement in their reliability can be expected in the future. On the other hand, the reliability performance of the Danish wind turbines can hardly be improved owing to the maturity of their technology, attested by the shape of the intensity function.

These results are consistent with the data shown in Figures 5 and 6, concerning respectively the average number and the rating of the two populations of wind turbines, which might partially justify the results.

Failure Probability, HPP

'Modelling Wind Turbine Reliability' showed how the HPP model can be used to predict the probability of failure events. Here we will use that method to predict the probability of observing failures over the life of a turbine. Following equations (7) and (8), probabilities have been computed of observing, in periods of 1 and 25 years, the following numbers of failures, N:

- no failures, $P(N = 0)$;
- one or more failures $P(N \geq 1)$;
- two or more failures $P(N \geq 2)$.

Results are given in Figures 9(a) and 9(b) for the Danish turbines only, showing a negligible probability of subassembly failures in 1 year and a probability of very few failures after 25 years. This indicates that for these turbines a 1 year guarantee involves very little risk and a 25 year life looks reasonable.

Results for the German turbines are not displayed but do show that they deteriorate more rapidly than the Danish turbines on the basis of this model.

Maintenance and Lost Hours

It should be borne in mind that the predictions above were made using data from maintained turbines, maintenance operations were probably recorded in the survey as hours lost, and the data give no information on how much time was devoted to maintenance.

However, the survey does indicate, for the German population, the time lost on turbines in each interval (see Table I), and this has been plotted in Figure 10. The hours lost due to subassembly failures are reducing with time, but the total hours lost per turbine per quarter are steadily rising, although at *ca* 35 h per quarter they are not excessive. These data are informative, but the authors are unable at this time to separate the time lost due to failures from the time lost maintaining the turbine. This is of crucial importance to operators, since it is possible to achieve higher reliability by greater maintenance activity, but the ultimate goal of the industry would be to achieve higher reliability with decreased maintenance.

DOI: 10.1002/we

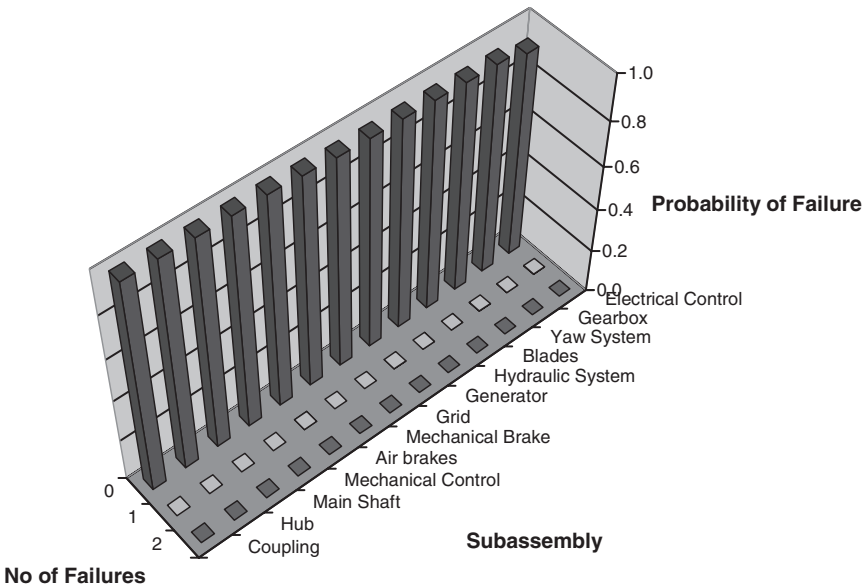

Figure 9(a). Prediction of failures in subassemblies of Danish turbines after 1 year

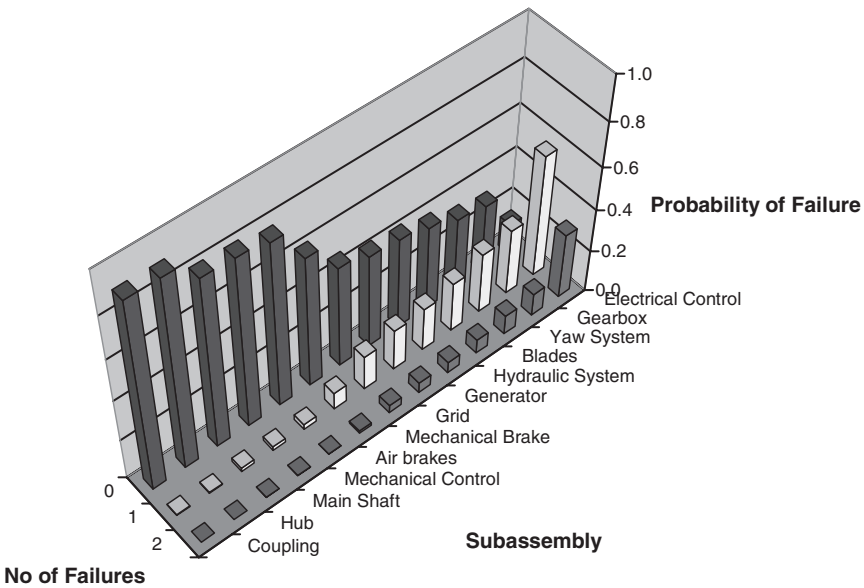

Figure 9(b). Prediction of failures in subassemblies of Danish turbines after 25 years

Historic Context of Turbine Reliability

The modern age for wind turbines has now extended over a number of decades, therefore the data collected by Windstats should be put into that historical context. Data are available from other sources, including from the USA (EPRI) and Germany (WMEP and LWK) in the DOWEC report.[9] The Windstats data and these extra data have been plotted in Figure 11, using equation (3), with a logarithmic failure rate scale to accommodate the wide variation observed. The EPRI results go back to US experience in California, where turbine failure

DOI: 10.1002/we

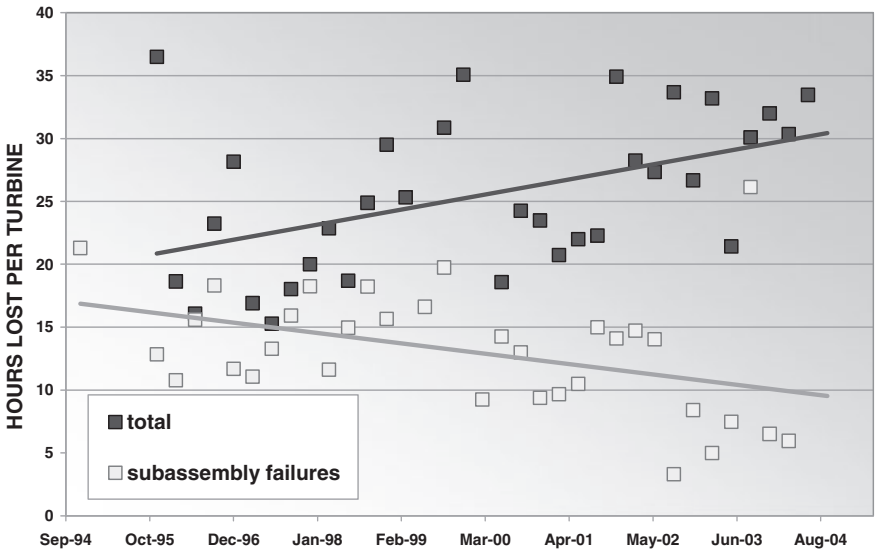

Figure 10. Hours lost per quarter due to failures and maintenance in German turbines

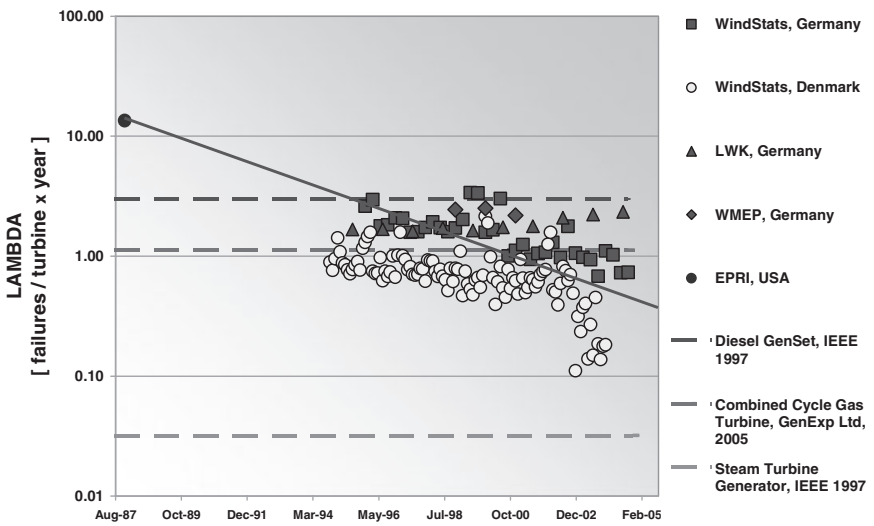

Figure 11. Average failure rates of German and Danish wind turbines in historical context and compared with failure rates of other power sources

rates were exceptionally high. The data from the other German surveys (WMEP and LWK) show similar figures to those given by Windstats, giving confidence in the validity of this information.

Figure 11 confirms the improving trend shown in this article and shows how much wind turbine reliability has improved over the past 16 years, particularly when placed alongside earlier US experience.

Figure 11 also compares wind turbine failure rates with those for diesel, combined cycle gas turbine (CCGT) and steam turbine generation, reported variously by the IEEE[12,13] and GenExp (personal communication).

The striking observation here is that wind turbines are now achieving better reliability than diesel generation, have a similar level to CCGT in the UK and could achieve similar reliability to steam turbine generation within the next 10 years. It is important to note that all these reliability figures are achieved by maintenance.

DOI: 10.1002/we

Further Work

The article has shown that a considerable amount of information useful to turbine manufacturers and operators can be extracted from reliability data. However, it is also clear that more information could be extracted if the data were more extensive and were organized in a way more tractable to reliability theory. In particular, the following aspects need to be considered in any future work:

- to expand the reliability database by considering turbine reliability data from other sources where there are large numbers of turbines, possibly in Germany, the Netherlands and Spain;
- to collect reliability data from offshore wind turbines.

Conclusions

This article has extracted average failure rates and reliability growth curves for maintained, onshore German and Danish wind turbines from Windstats failure data, using respectively the homogeneous Poisson process and the power law process. the article has demonstrated the following.

- There is a downward trend in failure rate in both German and Danish wind turbine populations, however, there is no indication of the effect which maintenance is having on this downward trend.
- The data show a higher failure rate for German turbines than for Danish turbines.
- The HPP model for turbine life has been demonstrated to be applicable for Danish turbines because of the higher average age of their long-serving, reliable turbine designs, which lie in the constant failure rate region of the bathtub curve.
- The PLP needs to be used for German turbines, because they have lower average age and the majority are in the early failure region of the bathtub curve.
- The calculated reliability growth curves for the German and Danish turbines are substantially different, implying that the technologies involved have dissimilar maturities. Nevertheless, the margin for further improvement for German wind turbines is large.
- German turbines have a higher average failure rate because they are newer. Many of these new turbines are large and incorporate variable speed technology.
- The introduction in Germany of larger turbines with more technological complexity is raising their average failure rate in the first few years of life, but the downward trend in failure rate is faster than in the Danish population. This suggests that the newer turbines are not potentially less reliable than their smaller predecessors, despite their increased complexity.
- The Windstats data show that the principal contributors to the higher German failure rate are electrical control or system subassemblies rather than mechanical subassemblies such as the gearbox. This is consistent with the introduction of variable speed drive technology. However, it is understood that the failure of a gearbox is likely to have a much greater impact on turbine availability owing to the extended MTTR compared with an electrical control failure.
- The analysis shows that the configuration of wind turbines affects reliability, but it does not show that eliminating gearboxes or variable speed technology will necessarily improve modern wind turbine reliability, which is improving anyway.
- Maintained, onshore wind turbines in Germany and Denmark have been demonstrated to have a better reliability than indicated by a US survey of diesel generating sets and are approaching the reliability indicated for UK combined cycle gas turbine generating sources. The trend in reliability improvement suggests that within the next 10 years they will approach the reliability indicated by a US survey of steam turbine generating sources.
- There appears to be a periodicity in the failure rates of Danish wind turbines, which the authors ascribe to the effect of the weather.
- If this work is to be applied to offshore wind turbines, some estimate must be made of the impact on the data in this article of onshore maintenance and the likely effect of changing that to planned maintenance for offshore turbines.

DOI: 10.1002/we

- It would be beneficial to devise a European code to standardize the recording of wind turbine reliability data, bearing in mind US experience in reliability surveys with electrical plant,[12,13] so that:
  - failure codes are harmonized between countries and concentrate on failure modes;
  - names and descriptions of subassemblies are harmonized between countries;
  - maintenance outages are recorded and differentiated from failures;
  - lost hours from turbines due to faults and maintenance are recorded in a standard way,
- It would be beneficial to consider the impact of weather on turbine reliability.

Acknowledgements

The authors would like to thank AMEC Wind Energy, Hexham for encouragement and information, Windstats for advice on the data presented in its studies, and the Technical University of Delft for helpful discussions.

Appendix: Nomenclature

α	statistical significance level
β	shape parameter from power law function
$\hat{\beta}$	MLE for shape parameter
Γ	gamma function
λ	average failure rate of a turbine
λ_i	average failure rate of a turbine, i.e. failures per turbine per year, in ith interval
$\lambda_{i,k}$	average failure rate for kth subassembly of a turbine, i.e. failures per subassembly per year, in ith interval
$\lambda(t)$	intensity function of Poisson process, equated to failure rate
θ	scale parameter of power law function
$\theta_{i,k}$	average MTBF in ith period for kth subassembly
$\hat{\theta}$	MLE for denominator of likelihood ratio
$\hat{\theta}$	MLE for numerator of likelihood ratio, MLE for θ in HPP
ρ	scale parameter of intensity function (alternative form)
$\hat{\rho}$	MLE for ρ
χ^2	chi-square distributed random variable
x^2	deviation statistic for chi-square test
e_i	expected number of failures in interval i for PLP goodness of fit
H_0	null hypothesis
i	integer counting intervals
I	total number of intervals in survey
k	integer counting subassemblies
K	total number of subassemblies in a turbine
n_i	number of failures during interval i
$n_{i,k}$	number of failures in subassembly k during interval i
N_i	number of turbines in population at interval i
P	overall period for which data were collected
$P(t_n < t)$	cumulative distribution function for nth failure
T_i	length of reporting interval, which varies according to month (h)
T_s	time lost due to subassembly failures (h)
T_n	time lost due to non-subassembly failures (h)
T_h	time lost due to failures for which only hours recorded (h)
T_t	total time lost, $T_t = T_s + T_n + T_h$ (h)

DOI: 10.1002/we

t_i	time to *i*th failure (h)
A	availability, A = MTBF/(MTBF + MTTR)
HPP	homogeneous Poisson process
IID	independent and identically distributed
LR	likelihood ratio
MLE	maximum likelihood estimate
MTBF	mean time between failures
MTTR	mean time to repair
PLP	power law process
TBF	time between failures
TTF	time to failure

References

1. E.ON Netz. Wind report 2004. *Technical Report*, 2004.
2. Tavner PJ. Predicting the design life of high integrity rotating electrical machines. *IEE 9th International EMD Conference*, Canterbury, 1999, pp 286–290.
3. Billinton R, Allan RN. *The Reliability of Engineering Systems* (2nd edn). Plenum: New York, NY, 1992.
4. *Reliability Growth Management (Military Handbook 189).* Department of Defense: Washington, DC, 1981.
5. ISET. Wind energy report, WMEP. *Technical Report*, 2004.
6. Pulcini G. A bounded intensity process for the reliability of repairable equipment. *Journal of Quality Technology* 2001; **33**: 480–492.
7. Rigdon SE, Basu AP. *Statistical Methods for the Reliability of Repairable Systems.* Wiley: New York, NY, 2000.
8. Buchanan JL, Turner PR. *Numerical Methods and Analysis.* McGraw-Hill: New York, NY, 1992.
9. DOWEC. Estimation of turbine reliability figures within the DOWEC project. *Report Nr 10048, Issue 4*, 2003.
10. Tavner PJ, Xiang J. Wind turbine reliability, how does it compare with other embedded generation sources. *IEE RTDN Conference*, London, 2005.
11. Tavner PJ, Xiang J, Spinato F. Improving the reliability of wind turbine generation and its impact on overall distribution network reliability. *IEE 18th International Conference on Electrical Distribution, CIRED*, Turin, 2005.
12. Report on reliability survey of industrial plants. Part I: Reliability of electrical equipment. In *IEEE Gold Book (IEEE Std 493–1997)*. IEEE: New York, NY, 1997; 201–223.
13. Reliability survey of 600–1800 kW diesel and gas turbine generating units. In *IEEE Gold Book (IEEE Std 493–1997)*. IEEE: New York, NY, 1997; 403–417.

DOI: 10.1002/we

Core faults in large generators

P.J. Tavner and A.F. Anderson

Abstract: A core fault is a failure in the laminated core of a large electrical machine. Such faults are relatively rare but when they occur, the value of the machine and its importance mean that the investigation of the failure assumes a high priority. On many occasions the details of such failures assume major commercial significance, therefore failure investigations have, of necessity, to be handled in a confidential manner, touching as they do on the design, manufacture, operation and insurance of large electrical plant. There has therefore been no published literature on core faults. However, the scientific principles of the mechanisms at work have been studied in considerable detail and papers published on those principles in the international literature. This paper brings together that literature and those scientific principles, giving details of the underlying design, constructional and operational factors which affect these faults. New evidence is presented of the underlying factors which allow core faults to initiate and grow. The paper will allow engineers to analyse such faults, draw rational conclusions on the causes for each occasion and devise suitable repair/rebuild strategies applicable to that situation.

List of symbols

B	flux density, Tesla
H	field strength, ampere-turns/m
J	current density, amperes/m^2
ℓ	length of the core fault cavity
L_ℓ	inductance of length ℓ of the core and frame circuit to Yoke Flux Linking
R_i	inner radius of the stator core
R_o	outer radius of the stator core
R_c	radius of core fault cavity in stator core
R_b	stator core radius at a background temperature of T_b
R_ℓ	resistance of length ℓ of the core and frame circuit to the Yoke Flux Linking
Z_ℓ	impedance of length of the core and frame circuit to the Yoke Flux Linking
ρ	resistivity of the coreplate material, S
σ	density of coreplate material, g/mm^3
T_i	melting point of core steel, °C
T_b	mean temperature of the core, °C
κ	radial heat transfer coefficient of laminated core steel, W/m°C
μ_o	magnetic constant
μ_r	relative permeability of a permeable material
δ	skin depth in permeable conducting material, mm
δ_o	skin depth in non-permeable conducting material, mm
γ	stacking factor of a laminated core
x	horizontal axis, in the plane of coreplates, m
y	horizontal axis, in the plane of coreplates, m
r	radial axis, in plane of coreplates, m
θ	circumferential axis, in plane of coreplates, radians
z	vertical axis, perpendicular to the plane of coreplates, m

IEE Proceedings online no. 20050102

doi:10.1049/ip-epa:20050102

Paper first received 26th March and in final revised form 23rd June 2005

P. Tavner is with the School of Engineering, Durham University, South Road, Durham, DH1 3LE, UK

A.F. Anderson is an Independent Electrical Engineering Consultant

E-mail: peter.tavner@durham.ac.uk

1 Introduction

1.1 What is a core fault?

Core faults can occur anywhere in the laminated steel core of large rotating electrical machines but are more common in the stator core. They can also occur in transformers but are more unusual, probably because the transformer has lower leakage fields and a more stable electrical, thermal and mechanical operating regime.

A core fault, Fig. 1*a*, initiates when coreplates are electrically connected together, either because of an insulation failure between them, or as a result of physically imposed short circuits, Fig. 1*b*, due to various causes including foreign bodies. These connections circulate additional currents in the core, coupling the main flux, leading to additional losses and heating, further weakening coreplate insulation and expanding the fault. The fault is then a zone in the core which is overheated, buckled and electrically interconnected. This can expand, melting material, leading to the catastrophic runaway of the fault and creating a cavity in the core continuing until the main conductor insulation is damaged and the machine is disconnected for an earth fault. Core faults generally occur some distance from the main conductors and final disconnection frequently occurs after irreparable damage has been done to the core and conductors. Core faults still remain an important issue, the authors have been involved in investigating such faults on modern machines during the past four years.

1.2 Core construction

Figure 2 is a photograph of a large stator core of a two-pole turbogenerator under construction, showing some of the

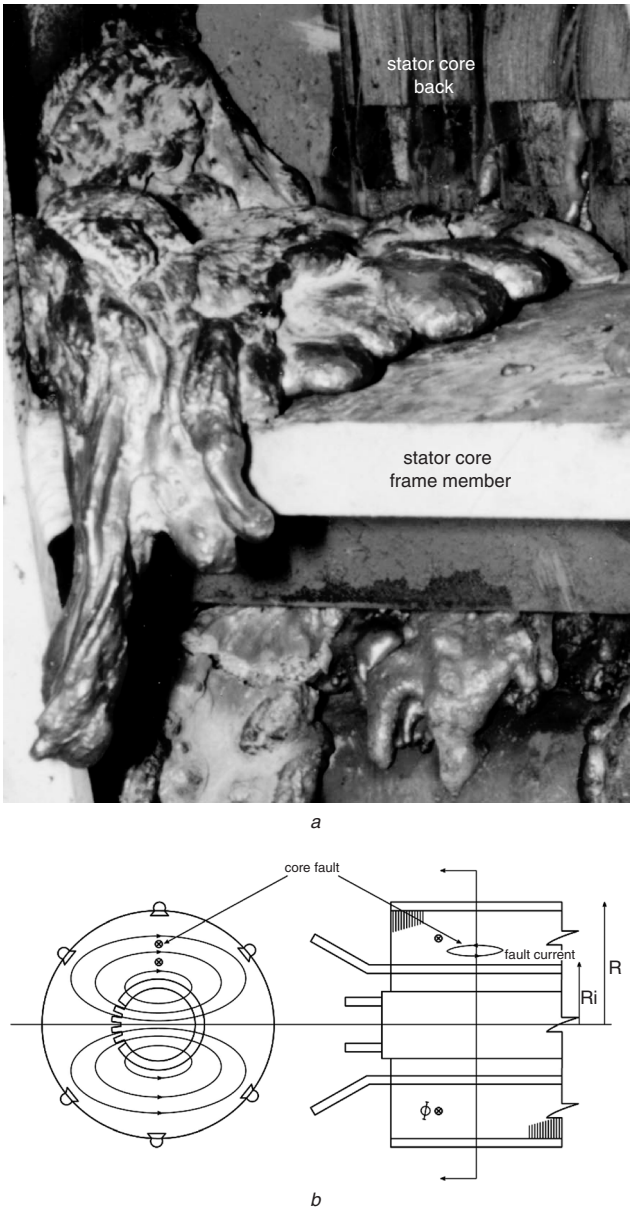

a

b

Fig. 1 *Laminated core with core fault*
a Example of damage to the end of a laminated core after a core fault, showing molten coreplate material running out over the stator core frame
b Laminated stator core showing origin and spread of a core fault

constructional features described below. Cores are constructed from sheets or coreplates of electrical steel, alloyed with silicon to lower losses and insulated to prevent conduction between them. A variety of proprietary insulations have been produced for coreplates including:

- Oxide layers on the steel, produced during the rolling and annealing process employed only on small machines, outside the scope of this paper.
- Layers of paper insulation, an old technique no longer in current use.
- Coatings of inorganic material rendered insulating by baking in the production process.
- Coatings of organic resin varnish cured during the production process.

The last method is almost exclusively used on large modern electrical machines. Coreplates are usually stamped from insulated steel strip and may be deburred after stamping, to

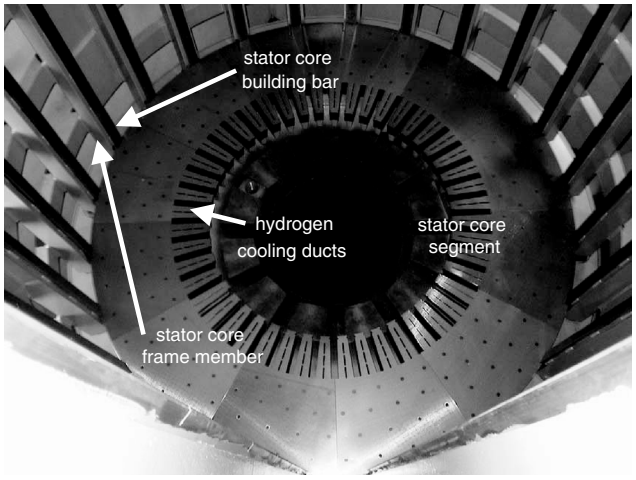

Fig. 2 *Laminated stator core of a 500 MW, 2 pole hydrogen-cooled turbogenerator under construction*
Clearly showing the segmental core construction, axial cooling ducts in the coreplate, keybars and stator frame

lower the risk of interlaminar conduction, sometimes they are reinsulated after deburring. For smaller (<8 MW) stator cores the coreplates can be complete circles or annuli but for larger machines, as in Fig. 2, they are always stamped in segments and the core is built up in brick wall fashion, with butt joints between each segment. Coreplates are also stamped with holes and slits to create axial cooling ducts, also visible in Fig. 2.

The core cooling medium may be air for smaller machines (<120 MW) or hydrogen particularly for larger two- or four-pole machines (>150 MW). Stator cores can be cooled by the axial flow of coolant gases but also by radial flow, in which case the core is divided into packets separated by the radial ducts for ventilation. These ducts are supported by radial spacer beams. Many axially-cooled large cores also have additional radial ducts near the core ends to assist the cooling of that high loss part of the core. Coreplates near the core end on large machines may receive multiple reinsulation coats after deburring.

Coreplates are keyed to frame bars or welded to frame sticks, providing support for the huge weight of the core and the necessary mechanism to resist the torque reaction from the air-gap magnetic field. Welded construction is used for smaller machines, with complete circular coreplates, but for segmental cores the coreplates always interlock with keybars attached to the inner bore of the stator frame. It is then the mechanical contact between the coreplate and these so-called keybars that provides the torque reaction. There are various technologies associated with keybars:

- They can be bolted or welded to the frame, as shown in Fig. 2.
- They can be manufactured of steel or a lower resistance material such as bronze.
- The keybars can be insulated from the coreplates or the frame to prevent the flow of current between core and frame but this insulation can be weakened by the torque reaction forces.
- In the case above one keybar can be provided with a conformable copper insert between the coreplate and the key, connected to earth. This is done to provide an earth connection for the core. In some cases these conformable copper straps are fitted to all keybars.
- Low resistance keybars of bronze or conformable copper are sometimes connected together at each core end,

forming a conducting cage surrounding the core, with the intention of reducing the leakage flux which can reach the core frame.

The stator frame formed by these sticks or keybars is either the main frame of the machine or, for larger machines, an inner frame housed in a larger outer casing, which in the case of hydrogen-cooled machines forms the coolant pressure vessel. For large two-pole machines the inner frame will be isolated from the outer by tuned springs, to reduce external noise due to the twice frequency excitation of the core.

The core is built up in an external frame, or for smaller machines in an internal mandrel. Mechanical pressure is applied to core packets successively by the use of axial hydraulic rams. This process continues until the full core length is reached, when the core is clamped between clamping plates, which finally are firmly attached to the keybars or sticks. A ring flux test can then be applied to confirm that the core can withstand the full magnetic flux without excessive overheating.

These processes are carried out in accordance with defined manufacturing procedures, which provide objective evidence of quality control, usually in the form of records of:

- Electrical steel origin, thickness and grade;
- Applied pressure;
- Core tightness;
- Personnel involved;
- Finally core ring flux withstand when the core is complete.

1.3 Published literature

Problems of overheating due to stray load losses were first recorded in the stator cores of rotating electrical machines at the end of the 19th century, when the technology of using insulated steel coreplates in the core of AC machines was becoming established. These problems generally arose because of inappropriate steel thickness or incorrect alloying content or poor insulation. The practice of using silicon steel alloys in coreplates of 0.5–1 mm thickness, insulated with interleaved sheets of paper was generally being applied after 1903, when the first patent for silicon alloying of electrical steel was taken out. It is not clear when and where core faults first occurred but it was certain that their cause was associated with stray losses, particularly towards the ends of the stator core.

The first analysis of stray losses in machines appeared in Germany in 1924 from Rudenberg [1]. Rockwood [2] in 1928 devised more methods for calculating stray loss and Laffoon [3] followed in 1929 as the USA wrestled with the introduction of larger AC generating units, feeding transmission lines of great length, where the effect of capacitive loading and underexcitation of the machine was beginning to be realised. Phear [4] in 1936 initiated a process of analysing the true MMF drop in the butt joints of stator cores, which were now so large they had to be constructed using coreplate segments. This started a thread that will run right through the study of core loss and failure.

Post-war, the hydrogen-cooling pioneered in the USA in the 1930 s started a rush to use the higher ratings, >100 MVA in other countries. In UK Richardson [5] demonstrated better methods of calculating stray loss on these larger machines. Estcourt *et al.* [6] wrote a seminal work in 1953 on machines in California experiencing elevated stator core end region temperatures because of underexcited operation. Winchester [7] in 1955 presented an analysis of the end region field of a turbogenerator using the electrolytic tank. This was the forerunner of many papers using numerical methods to compute the field. Mason [8] followed in 1959 with operational experience on UK turbogenerators. The first paper to describe explicitly the damage that can lead to a core fault was Oberretl [9] in 1963, although his work was about a short circuit generator used for switchgear testing.

By the early 1960s the construction of larger rating machines required more attention to design and manufacture. Walker, Rogers and Jackson [10] in 1964 studied the pressure in the laminated core. By 1970 when large 500–700 MVA machines were becoming common, Howe [11] searched for design methods to manage the end region leakage demonstrating the factors determining leakage flux on the surface and within the stator core. Stoll [12] also extended the work on butt joints. Vickers [13] in 1974 produced the most thorough review available of current and proposed turbogenerator construction methods.

Jacobs [14] in 1978 published the first 3D analysis of the end region field in a laminated stator core, although a number of manufacturers had demonstrated operational programs without publication. Subsequent work used newly available computer facilities to analyse stray fields in machines more carefully, predicting the unusual effects observed operationally in earlier work.

Renew [15] measured the influence of transient machine disturbances on end region field, because it had become clear that pole slipping could be a core fault initiator. Tavner [16] in 1978 continued trying to define design office rules to manage end region fields while Jackson [17] analysed the effect of leakage field and eddy currents on the voltages between coreplates and their possible contribution to the damage reported by Oberretl. Again this was thought to be a particularly important contributor to core fault initiation during transient operations. The discussion at a seminal meeting at the IEE in 1980 [18] summed up the concerns in UK at that time for external leakage field calculations under high temperature and transient fault conditions.

Work then moved into a more practical and applied phase as experience of a number of core faults on very large turbogenerators increased knowledge. Anderson [19] in 1980 reported a breakdown phenomenon, thought to arise in transient conditions and to be the initiator of a core fault. Anderson [20] measured the external leakage flux of a small machine and Platt [21] measured internal leakage flux and interlaminar voltages on a full size machine under similar conditions.

The emphasis now shifted to the coupling of the external leakage flux with the frame surrounding the core, because evidence had suggested that these components contributed to core faults. Tavner [22] offered a qualitative explanation of the phenomena and Hilliar [23] provided detailed measurements from a 500 MW turbogenerator showing that currents as high as 12 kA circulated in the frame at rated stator operating current but that these currents could be higher at lower rotor excitation. Bratoljic [24] in 1986 then used sophisticated 3D magnetic field analysis on a 360 MVA turbogenerator to predict the fields and currents surrounding a stator core, reaching values in excess of 16 kA, while Mecrow [25] in 1989 reported the application of similar 3D analysis to the field around and inside the stator core end region showing how the various design features of the machine affect the end region losses. This

completed the work of [14] but applied it for design purposes to practical turbogenerators.
By 1983 Sutton [26] had developed a low-voltage alternative to the core ring flux test for detecting incipient core faults in large machine cores. This paper reported a device developed by the CEGB and known as El CID, the Electromagnetic Core Imperfection Detector. The technique has become widely used by manufacturers and operators as a quality control check on laminated stator cores on completion of manufacture and in service.
Beckley in 2002 has traced in [27] the development of modern electrical steels, explaining the benefits of various insulation coatings and thicknesses on the performance of a stacked core and describes the action of a core fault. Finally in 2004 Mogi [28] has demonstrated a direct experimental method for measuring the rotational loss in a core with butt joints.

1.4 This paper

The published work has traced many, but not all the factors that can initiate a fault, but there have been only two papers, Oberretl [9] and Anderson [19], describing mechanisms occurring in real core faults. This is in part because of the commercial confidentiality surrounding failures and the sensitivity of the information involved but there is now adequate knowledge available in the public domain.
This paper attempts to rectify this omission by drawing the information together, presenting the results of new research and setting out the main causes and effects of core faults.

2 Design principles

The following quantities are important to the design of an electrical machine and there is a fundamental relationship between them:

- Electrical loading, axial linear current density at the air gap, in A/mm;
- Magnetic loading, air gap flux density, in Tesla;
- Mechanical loading, rotor peripheral velocity, in m/s;
- Thermal loading, temperature rise, in K.

Electrical design is a compromise between the electrical and magnetic loading, allowing the maximum transfer of power through electrical and mechanical components. The resultant design incurs losses in machine components impacting on the thermal loading, relieved by cooling in the radial or axial ducts at the thermally stressed areas. The

Table 1: Comparison of design parameters for large machines

Label	1	2	3	4	5	6	7	8	9
Type of Machine	Air cooled Induction Motor	Air cooled Induction Motor	Air cooled Turbogen-erator	H2-cooled Turbogen-erator	Air cooled Hydroge-nerator	H2O and H2-cooled Turbogen-erator	Air cooled Hydroge-nerator	Air cooled Hydroge-nerator	H2O and H2-cooled Turbogen-erator
Stator winding Cooling	Air Indirect	Air Indirect	Air Indirect	H2 Indirect	Air Indirect	H2O Direct	Air Indirect	H2O Direct	H2O Direct
Stator core Cooling	Air Direct	Air Direct	Air Direct	H2 Direct	Air Direct	H2 Direct	Air Direct	Air Direct	H2 Direct
Rotor Cooling	Air Direct	Air Direct	Air Direct	H2 Direct	Air Direct	H2 Direct	Air Direct	Air Direct	H2 Direct
S [MVA]	7.11	12.56	125	108.6	100	294.1	100	355.5	1111
P [MW]	6.14	10.75	100	92.3	91	250	90	320	1000
Poles	4	4	2	2	32	2	88	14	2
Rev/min	1790	1770	3000	3000	187.5	3600	68.2	428.6	3000
Core Length, mm	628	874	4450	2800	2500	3700	1280	2960	7200
Rotor Diameter, mm	742	988	890	924	6482	1034	12 968	4934	1200
Mechanical Loading, Rotor Peripheral Velocity [m/s]	69.5	91.6	139.8	145.1	63.6	194.9	46.3	110.7	188.5
U [kV]	6.8	13.8	11	13.8	15	15.75	15.75	22	24
Magnetic Loading, Air Gap Flux Density [Trms]	0.9	0.63	0.94	0.83	0.99	0.98	1.05	1.12	1
I [A]	604	538	6560	4543	3850	10 782	3666	9329	26 729
Power per unit Core Length [kW/mm]	9.8	12.3	22.5	33.0	36.4	67.6	70.3	108.1	138.9
Electric Loading, A [A/mm]	93.0	97.0	116.3	146.8	58.6	155.7	62.5	96.2	255.3
Current Density, h [A/mm2]	3.9	3.1	2.8	3.8	3.2	5.8	3.7	5.3	11.1

compromise achieved defines the rating of the machine in MVA.

Table 1 is a comparison of the loadings of nine large rotating electrical machines, with ratings from 7 to 1100 MVA, a range of over three decades. Figure 3 shows a graphical comparison of these machines in order of ascending power per unit core length kW/mm.

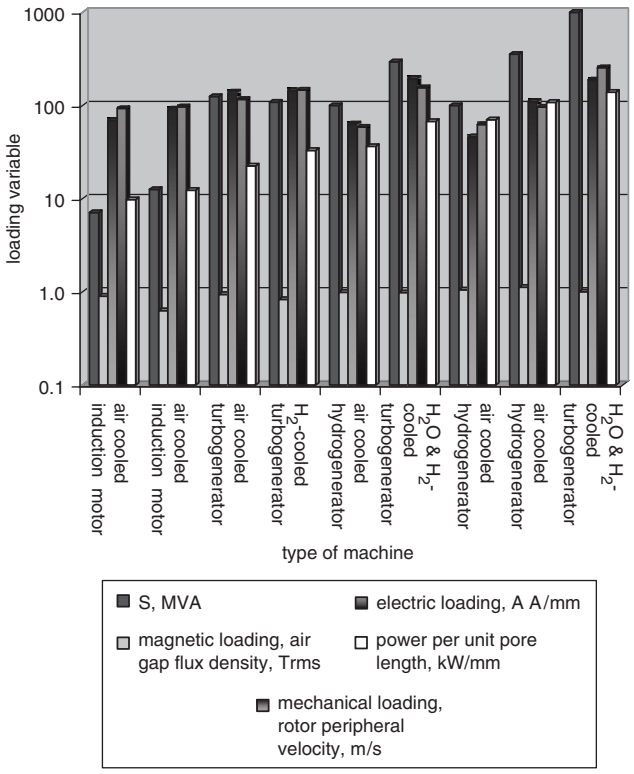

Fig. 3 *Variation of loading variables for different types of machine, see Table 1*

Core faults usually, but not always, occur in the stator and one can be forgiven for assuming that the only design factor of importance is the magnetic loading. But the saturation of electrical steels limits the variation of magnetic loading between machines of different size and design. The magnetic loadings in Table 1 extend from 0.81 to 1.12 Tesla a range of 139%. However, to study the effect of magnetic loading on a core fault consider Fig. 4*a*, which shows an overflux capability for a typical turbogenerator stator, where 1 pu corresponds to the rated air gap flux density. Typically a core can stand an overflux without core damage provided the application period is short. The curve shows that this manufacturer recommends that a 1.2 pu overflux can be sustained almost indefinitely. The curve also shows overflux test values specified in two international standards and it should be noted that the manufacturer's recommendation lies between those two standards, the IEC test offering the most arduous condition. Essentially any operation of a large machine that takes the magnetic loading above the recommended line in Fig. 6*a* could initiate a core fault. The magnetic loading, or air gap flux density, is defined by two dimensional magnetic analysis at the centre of the laminated core. But additional losses arise due to the segmented nature of the core and towards the core ends, where axial leakage flux drives up eddy currents, adding to the thermal loading [9, 11, 17]. Core faults do not usually originate in the centre of the machine core. Figure 4*b*, using results from [12, 28], shows how rapidly losses in a segmented core rise as magnetic loading increases.

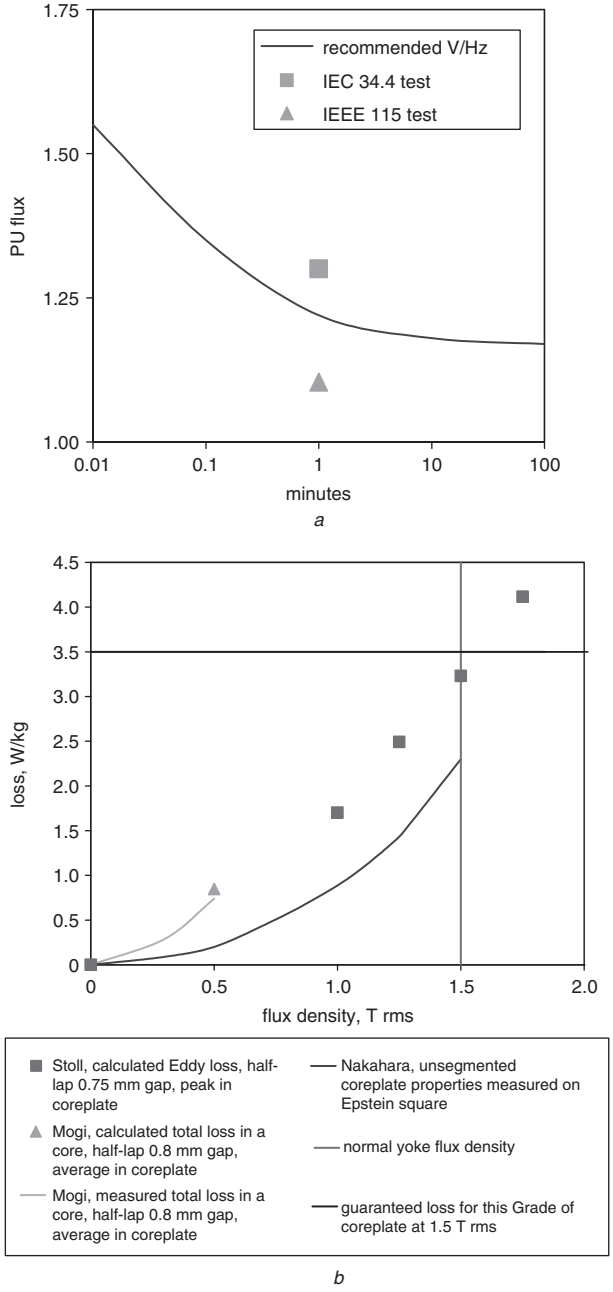

Fig. 4 *Stator core: Graph of overflux capability for a typical turbogenerator stator core*

a 1 pu flux represents a normal magnetic loading. The points show test values of overflux prescribed by IEC and IEEE

b Half-lap core losses for 350.50 coreplate showing from Mogi's measurements and predictions how losses increase sharply as flux density in the yoke increases

The mechanical loading in Table 1 extends from 46.3 to 194.9 m/s, a range of 420%. Leakage flux and consequent loss has an important influence on core loading. This is shown by [14, 25] to be related to the stator current and therefore the electric loading. Table 1 and Fig. 3 show a wide variation of electric loading from 58.6 to 255.3 A/mm, a range of 436%. It is interesting to note from Fig. 3 that the electrical and mechanical loadings of machines over the whole range are closely in step with one another. Electrical loading is affected by cooling, which allows conductors to carry higher currents, the most striking example being the largest machine, rated at 1000 MW, with an electric loading of 255.3 A/mm, achieved by directly water-cooled stator windings. The current density in the winding, at

11.1 A/mm^2, is over 50% higher than any other machine in Table 1. The measurements of [23] showed that the leakage flux at the core end of a practical machine increased in direct proportion to the stator current, thereby increasing the flow of stator frame currents.
Readers can conclude from Table 1, Fig. 3 and the above that:

- Loadings are not necessarily proportional to rating. Machines of low rating can have high electrical, mechanical or magnetic loadings and vice versa.
- Magnetic loading ranges are limited by saturation and probably do not indicate the propensity for a core fault to grow but operation of the machine above the curve in Fig. 4*a* is very likely to initiate a core fault and Fig. 4*b* shows how that could happen close to butt joints in a large core. Limiting the magnetic loading to 1 T will limit the risk of core fault but this limit may have to be exceeded in larger machines.
- Mechanical loading ranges are large and generally in step with electric loadings and do not affect core fault initiation or growth.
- Electric loading ranges are large, depending on cooling, and machines with higher electric loadings will have a greater propensity for core faults to grow, once initiated, and need to be designed to reduce this risk. Limiting the electric loading to 100 A/mm will limit the risk of core fault growth but again this limit has to be exceeded for larger machines. In such cases it is necessary pay attention to coreplate insulation quality and cooling intensity to reduce core fault risk.
- A critical factor in the propensity of a core to suffer from core faults could be power per unit Core Length, in kWmm. This will be discussed further.

3 Core fault theory and results

3.1 Fault process

There are two regimes for the core fault:

- Initiation.
- Growth.

These two processes do not necessarily follow one another immediately. In fact the authors have inspected stators where a core fault had initiated but remained dormant without expanding into an irreparable condition. Such a fault could remain dormant for days, weeks or even years, until conditions for growth are favourable.

3.2 Initiation

A core fault initiates when coreplates become electrically connected together by mechanical or electrical action caused by one or a combination of the following:

- Constructional defects
  - Burrs on the coreplate, [27].
  - Inadequate insulation of the coreplate.
  - Incorrect construction of the core.
  - Introduction of foreign bodies, particularly metallic, into the core during construction, shorting coreplates.
- Thermal factors
  - Local hot spot in the core.
  - Restricted cooling in one place in the core.
- Operational factors
  - Overfluxing incident.
  - Pole slipping or other severe transient operation of the generator.
  - Foreign bodies shorting coreplates, arising from within the machine due to wear and tear, introduced during operation.

3.3 Shape

The initiation zone of the core fault is a circular defect between coreplates, in the r–θ plane. The defect may be embedded in the core or at the core surface, in which case it will be part-circular. Figure 5*a* shows typical damage in a core fault at the heart of a core where:

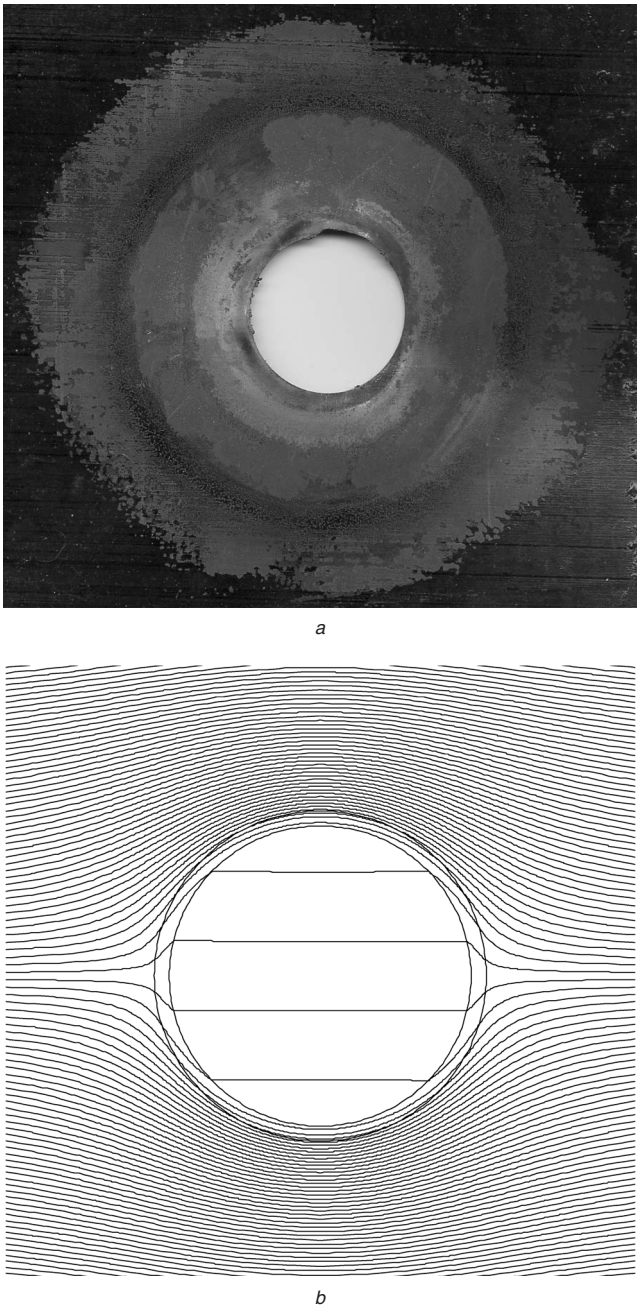

Fig. 5 *Core fault in turbogenerator*
a Photograph of a coreplate at the centre of a core fault in a 500 MW hydrogencooled turbogenerator
Note the 4 cm diameter cavity where melting has removed material, and the radial nature of the thermal damage to the coreplate insulation
b Flux plot generated using the MEGA FE package showing the field pattern surrounding a core fault developed by Mechanism I, Yoke Flux Diversion

- Each coreplate was in intimate electrical contact with its neighbour,
- Current could flow axially between coreplates,
- Current flow caused coreplates to overheat,
- Coreplate insulation had suffered thermal damage in a circular zone,
- Coreplates had buckled due to local thermal expansion,
- Coreplates had locally melted at the centre of the fault

This damage actually centred on a circular axial cooling duct and was believed to be initiated by debris in that duct. However, the heating and subsequent melting has enlarged the cavity exhibiting the circular form characteristic of most core faults. At the two axial tips of the fault cavity, see Fig. 6, the circulating current is concentrated. The fault expands axially until it meets an impenetrable barrier. The circular shape is dictated by effective cooling of the laminated core, which limits radial growth of the fault. There will be a high temperature at the centre of a fault but there is a substantial variation in temperature radially away from it. This is exemplified by the colour changes observed in the coreplate insulation around the fault shown in Fig. 5*a*. The high temperatures in a core fault can cause local melting of the coreplate, in which case the cylindrical defect becomes a cavity as in Fig. 5*a*. The initiation zone thus expands, radially and axially, to form a narrow ellipsoid cylinder-shaped defect, see Fig. 6. Core faults are rarely regularly shaped, however, they can be approximated to this ellipsoid model, allowing some analysis.

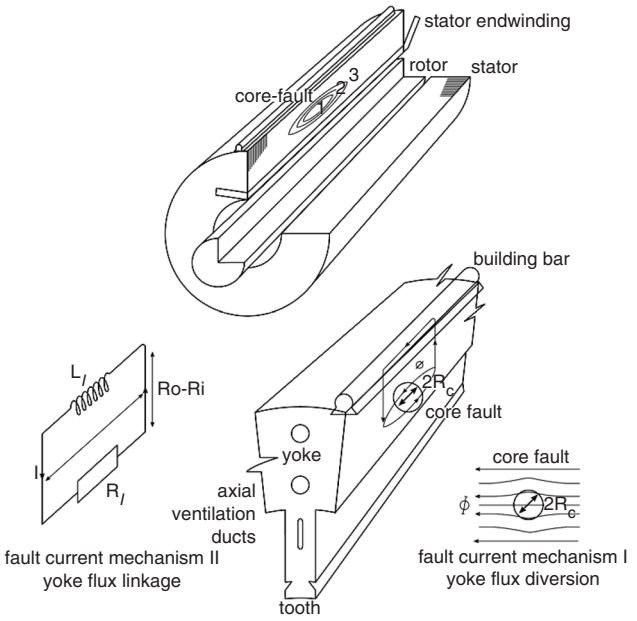

Fig. 6 *Section through a laminated core*
Showing extended core fault and Mechanisms I and II for the extension of the fault

3.4 Growth mechanisms

Once a core fault is initiated irreparable damage does not occur until the fault grows. Growth is a complex interplay of electromagnetic, thermal, material and constructional factors. There are two principal growth mechanisms for a core fault, as shown in Fig. 6, defined by the circulating current in the fault:

- Mechanism I or Yoke Flux Diversion at the site of the fault. Circulating current in the core fault itself opposes the main core flux, diverting it around the fault. The return current circuit is within the ellipsoid-shaped cavity itself. In this case the circulating current only links the flux crossing the core fault. A flux plot of a circular cavity with Mechanism I at work is shown in Fig. 5*b*.
- Mechanism II or Yoke Flux Linking between the core fault and the core frame. Current flows axially in the fault then radially from the fault through coreplates to the frame, flowing axially in the frame itself, see Fig. 6. In this case the circulating current links the main flux in the machine yoke.

The latter mechanism is the most powerful because it has the potential to develop a higher driving emf. The balance between the two mechanisms will be discussed in the Appendix.

A core fault grows in an axial direction, driven by the need for the fault to increase coupling with the main core yoke flux. Radial growth is limited by the effective cooling of the core. Axial growth is not limited by radial ventilation ducts, since conducting steel duct spacers bridge these ducts, allowing the fault current to pass across. There is evidence on some faults that the duct spacers focus the fault current, forcing it axially through the spacer at particularly favourable radial positions near the tooth root on coreplate butt-joints. Interestingly the use of spacers with insulating properties would limit the growth of core faults in machines with ducted cores. The authors have no knowledge of this approach in large machines. The spacer property of concern to the designer is mechanical strength and this would be expensive to achieve with insulating materials.

If the core is in contact with the core back, a tell-tale indicator of damage within the core will be arcing and sparking activity on the core back, most noticeably at the ends of core fault where the return fault current has bridged the contact between core and frame. At this point the contact may be good but will vary with torque reaction and load, opening and closing with each half cycle of the mains frequency, resulting in the arcing activity observed. The fault circuit is almost entirely in structural or electrical steel, the resistivity of which is high (30–55 μS).

In Mechanism I, in the local region round the surface of the ellipsoid cavity the skin effect could be fully developed and the currents inductance-limited as they circulate. The skin depth in the core fault will alter when melting occurs and the steel rises above the Curie Temperature, in which case skin depth increases, fault resistance falls and losses fall. In Mechanism II the skin effect is not necessarily fully-developed, therefore the fault current is generally resistance-limited.

In either case, Mechanisms I or II, the fault current has relatively little effect on the driving flux, like the resistance-limited circuit described by Stoll [31], and this is an important reason for the destructive power of a core fault, since, once initiated and growing, an increasing fault current does not significantly reduce the driving flux provided by the main excitation on the rotor of the machine. The fault current is in effect a single shorted turn, the main excitation remaining unaffected until the fault links a major proportion of the main flux.

The most serious damage a core could sustain would be if coreplates were shorted at the core bore, at the stator tooth tip or slot bottom for example, and the coreplates were in contact at the core back. This would permit the fault current to link the complete flux threading the core yoke on each cycle. Such surface defects are fairly common but in

the authors' experience rarely seem to develop into full core faults. Damaging core faults generally occur some way into the core, radially from the slot bottom.

3.5 Predicted results

The interplay of electromagnetic, thermal and constructional factors in a core fault cannot be fully described in mathematical terms, however, a limited analysis has been presented in the Appendix, to give an indication of the major factors at work. It should be noted that the power depends upon the length of the fault, as follows:

$$\begin{aligned} E(\ell) &= IZ(\ell) \\ \text{where } Z(\ell) &= R(\ell) + jX(\ell) \\ I &= \frac{E(\ell)}{Z(\ell)} \\ P &= I^2 R(\ell) \end{aligned} \tag{1}$$

Therefore it is satisfactory to consider only a 1 mm length of the core fault. In reality there will be effects at the ends of the core fault cavity where current is concentrated and specific resistances will rise but this is neglected in these calculations. The results from (7), (10) and (11), for 1 mm axial length of fault in a core with the details of Table 2, have been plotted out in Fig. 7 for core faults of varying radius, R_c, and the losses normalised to W/kg by assuming that the loss is distributed uniformly over the coreplate material inside R_c. This allows the loss density to be compared to the background core loss density predicted for the coreplate.

4 Discussion

4.1 General

The theory and results show the limits of the effects at work in a core fault but in real conditions these are modified by practical core conditions. The following discussion sets out these results with the other factors which can affect a fault, addressing detailed factors, which influence the initiation or growth of a core fault, not covered by the introduction and Appendices.

4.2 Results

The results show that in the core of a 500 MW turbogenerator carrying a flux of density 1.5 Trms, a fault of the size shown in Fig. 5*a*, 4 cm diameter, with each coreplate in intimate contact with its neighbour, would carry the following currents and losses:

- Mechanism I, Yoke Flux Diversion, could circulate 1004 Arms in the fault. This dissipates 33 kW/mm or 17 kW/kg in the core, less than a quarter of the power per unit Core Length for a machine of this size, see Table 1.
- Mechanism II, Yoke Flux Linking, could circulate 11541 Arms in the fault. This dissipates an enormous

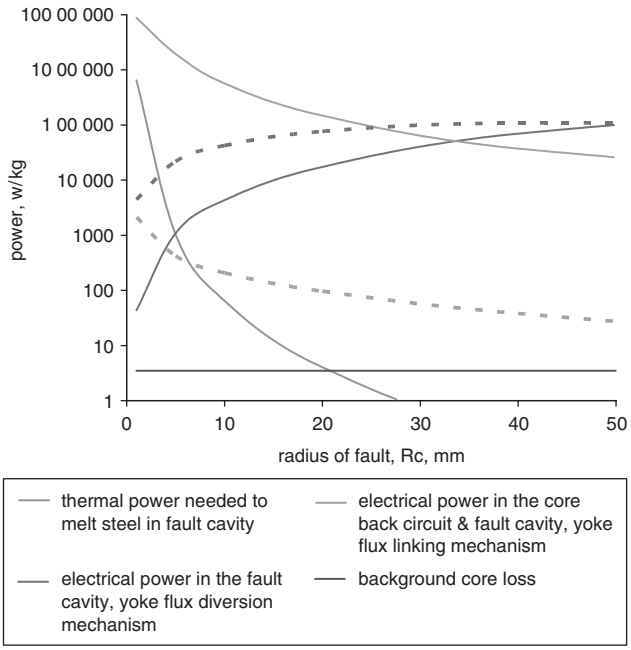

Fig. 7 *Variation of power in 1 mm of a core fault due to different driving mechanisms*
Calculated for a large turbogenerator core with details in Table 2. The dotted lines show changed power input when steel melts

Table 2: Values of parameters used in appendix

Parameter	Symbol	Value
Rating and Type of Machine	S	588 MVA, H2O and H2-cooled Turbogenerator
Core outer radius	R_o	139 cm
Slot bottom radius	R_i	82 cm
Frequency	f	50 Hz
Angular frequency	ω	314 rad/s
Flux density in the core back yoke, see Table 1 for the magnetic loading, which is the flux density in the air gap	B_{rms}	1.5 T rms
Radius of the core fault	R_c	Initiating at 1 mm and growing to 20 cm
Resistivity of the coreplate	ρ	51 μS
Permeability of the coreplate	μ_r	>300 as given by the B–H curve until the temperature exceeds the Curie point of 400°C, at that point it will fall to 1
Radial heat transfer coefficient of coreplate	κ	60 W/m°C
Density of the coreplate material	σ	7.86 g/mm^3
Skin depth in steel of permeability > 300	δ	0.94 mm
Skin depth in conducting material of permeability 1	δ_0	42.71 mm
Temperature of the core background	T_b	100°C
Temperature of coreplate at melting	T_i	1100°C

281 kW/mm or 148 kW/kg in the core, more than twice the power per unit Core Length for this size of machine. This amounts to more than 28 MW in a 10 cm long fault.

If these current values are compared with those measured or predicted in [23, 24] it can be concluded that a fault could circulate, within the core, currents of the same order as those circulated in the frame by the leakage field, outside the core, in normal operation.
Three important facts emerge from Fig. 7:

- The thermal model shows the power needed to melt coreplate material, when uniformly distributed over the ellipsoidal fault and this falls dramatically as the fault radius increases.
- The power input from the Mechanism I increases with fault radius but is relatively low at fault diameter below 1 cm. The power is insufficient to melt the core until the fault diameter is more than 1 cm. The power input goes up significantly when the fault melts.
- The power input from the Mechanism II is very large at small diameters and, although the power reduces as the fault diameter increases, it is more than sufficient to melt even the smallest fault.

In any core fault each of these three factors will play a greater or lesser part. However, it is very unusual for cores to fail in the catastrophic way described by the last point, suggesting that the Mechanism II is not normally effective. The authors have seen only one incident, exemplified by Fig. 1, where the catastrophic damage observed and the rapidity with which the faults grew, suggested that Yoke Flux Linking was the primary mechanism. A reason for Mechanism II being ineffective is likely to be the presence of high resistance contacts at the core back, dramatically reducing the currents flowing in that fault circuit. Indeed any core constructed with keybars insulated from the coreplates or the frame cannot develop Mechanism II unless that insulation is bridged. However, when the Mechanism II is operative the resultant core fault damage is large, fast and catastrophic.

4.3 Thermal factors

Since the 1920s engineers have known that the end region of the stator core has higher losses and consequentially a higher operating temperature varying with load power factor [3]. The authors have seen a number of core faults initiated in the core end region, close to butt joints near to core slot bottoms where flux densities are highest. This suggests that thermal factors are an important initiating mechanism. Losses have been shown to rise close to a butt joint [4, 12] and later work on electrical factors [17] has shown that planar eddy currents increase close to a butt joint at the slot bottom near a core end, exemplified by the calculated laminar eddy current patterns shown in Fig. 8 taken from [25]. This is emphasised by the results in Fig. 4*b*, taken from [12, 28], especially extrapolating the measured results of Mogi. Reference [29] has suggested that such elevated losses near butt joints could be due to local buckling in the core and high friction at the site due to vibration, although the authors have seen no examples of this in their experience on turbogenerators.

4.4 Electrical factors

4.4.1 General: In the UK a number of core faults on large turbogenerators were associated with transient faults close to the terminals of the affected machine. This lead to considerable investigation of the possibility that transient flux conditions could initiate core faults and [15] showed that pole slipping on a machine does give rise to substantial internal axial flux between coreplates, causing higher interlaminar voltages [17], which could lead to coreplate breakdown. The following is drawn from that experience.

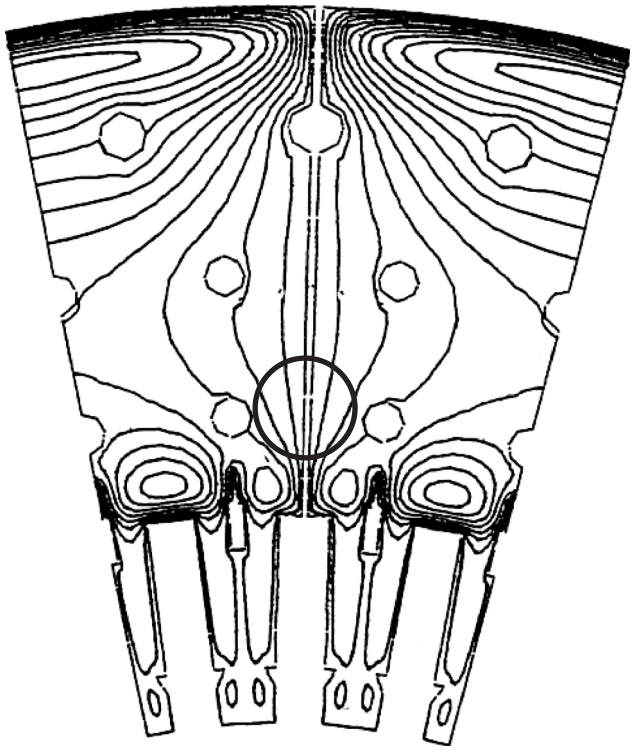

Fig. 8 *Plot of eddy currents in the plane of lamination segments at the quadrature axis*
Taken from Mecrow *et al.* The common site for core faults, at the junction between segments, near the slot bottom, is highlighted

4.4.2 Interlaminar voltages and breakdown: Coreplate insulation breakdown and spot welds between coreplates are observable after most core faults. They occur between coreplates, which prior to breakdown were seemingly well-insulated and it is striking that:

- The worst spot welds occur between coreplates with nominally the best insulation.
- Spot welds seem capable of penetrating a number of coreplates at one time.
- It has been shown experimentally on a sample ring core in keybars from a machine, that if current is passed between adjacent keybars, agitation of the keybars causes interlaminar breakdowns even on the opposite side of the core.

The core is behaving like a large parallel-plate capacitor, intermittently shorted by the keybars. At the site of the breakdown the insulation between coreplates is punctured and local melting takes place. Langmuir reported some of the features of arcs in hydrogen including the enhanced heat transfer produced by atomic disassociation [30]. Unusual interlaminar breakdowns have occurred in hydrogen, described in [19], where the breakdown arc has migrated some distance over the coreplate surface, driven by the

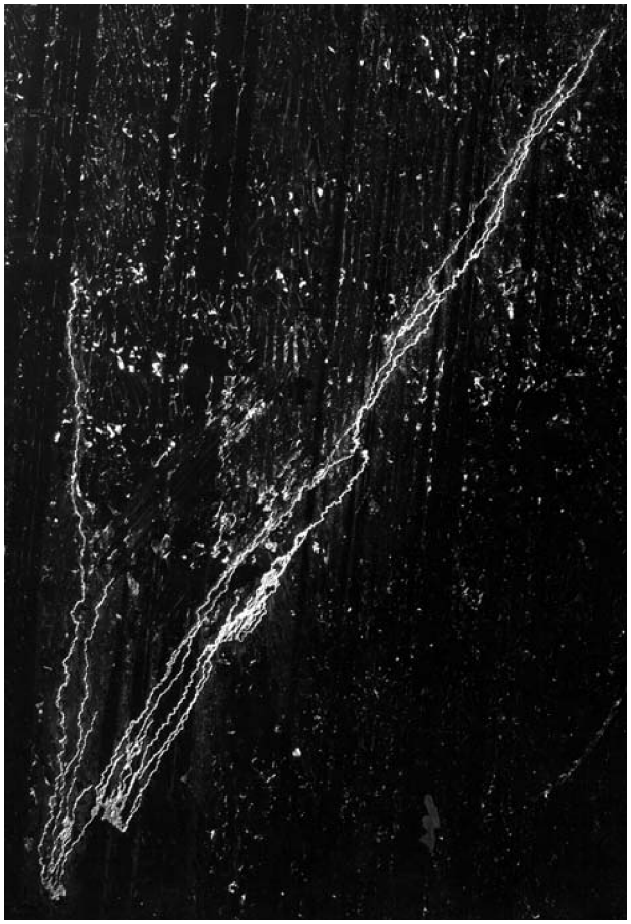

Fig. 9 *Photograph of a coreplate showing an unusual interlaminar breakdown in a large hydrogen-cooled turbogenerator subjected to a core fault, as described in [19]*

interlaminate fluxes in the machine, a photograph is shown in Fig. 9.

Industrial experience when surge testing transformers and electric motors has shown that the application of surge voltages to windings, to test interturn insulation, induces substantial surge voltages between coreplates. These surge voltages can be large enough to breakdown insulation, creating an electrical bond between coreplates. Both transformer and motor manufacturers have reported a rise in core losses after surge tests and this must be the result of these coreplate bonds. One motor manufacturer reported that the core losses reduced to the pre-surge test values, once the machine had been operating for some time, presumably as a result of thermal and vibration factors breaking the coreplate bonds formed during the surge test.

4.4.3 Frame currents: Considerable discussion has centred on the cause and route of core frame currents, as it was realised how large these can be on machines with a high electric loading [22–24]. A relationship was sought between the core back electrical activity observed after a core fault and the huge currents that are known to circulate in the frame during normal operation. To date no such relation has been made except that these currents do cause frame heating and may contribute to lowering the resistance between the coreback and frame.

4.5 Material factors

4.5.1 Cooling gasses: Large machines use air or hydrogen as a cooling gas, which may have a profound effect upon the growth of a core fault.

When carrying out postfault investigations it is noticeable that air-cooled machines show a much higher degree of carbonisation and fire damage than hydrogen-cooled machines, because of the presence of oxygen. Oxygen in cooling air oxidises any intermittent contacts made between coreplates or at the interface between the core and the keybars, reducing fault currents below predicted values.

In hydrogen-cooled machines monatomic hydrogen may have a role in the arcing processes of a core fault because when monatomic hydrogen reaches a coreplate surface recombination takes place dumping of energy into the coreplate. The effect on small interlaminar breakdowns is that dissociation takes energy out of the arc dissipating it into neighbouring surfaces without causing further damage [30]. It is likely that with energetic arcing in the confined space of an axial vent duct, monatomic hydrogen could be a vehicle for core fault growth. Progressive breakdown of interlaminar insulation may not be necessary to expand a core fault in a hydrogen-cooled machine, plasma containing monatomic hydrogen in a vent duct may do the job equally well. In addition a hydrogen-cooled machine does not oxidise coreplate and core back contact points so fault currents can reach predicted values.

4.5.2 Coreplate insulation: The quality of insulation has been considered important for coreplate integrity since the 1900s, indeed insulation tests are prescribed in the material specifications. However, Beckley has shown [27] that coreplate spacing is probably more important than insulation for minimising interlaminar loss. High quality coreplate insulation can concentrate the action of interlaminar voltages at the site of any insulation defect. The resultant powerful interlaminar arc does more damage than would be possible between coreplates of poorly insulated material, where interlaminar currents are diffuse and weak. However, in the latter case the background losses due to interlaminar currents are undoubtedly higher than would be the case with high quality insulation.

4.6 Further work

The discussion has shown that some features of core faults can be predicted. An important objective for turbogenerator operators on completion of plant outages is to confirm that the core is sound using Core Ring Flux Tests in the High Voltage or Low Voltage (El CiD) form.

A valuable piece of work, based on this paper, would be to use electromagnetic and thermal finite element techniques to predict the magnetic field and temperature at the bore of the turbogenerator core during the High Voltage and Low Voltage Tests, with circular defects of various sizes at positions as shown in Fig. 8.

5 Conclusions

- A core fault has the approximate shape of a cylindrical ellipsoid with its major axis perpendicular to the coreplate. Under extreme conditions melting of coreplate material occurs within the ellipsoid and a cavity is formed.
- A core fault may be initiated by:
  - Constructional defects in the core

- Thermal factors
- Electrical factors
- Operational factors, such as overfluxing, pole slipping or foreign bodies introduced during operation.

- A core fault may not grow immediately it is initiated and its growth is influenced by a complex interplay of electromagnetic, thermal, material and constructional factors, which may not be operative at the time of initiation.
- A core fault grows axially along its major axis. The radius of the cavity increases with length but this is not the main axis of growth because it is limited by core cooling.
- A core fault grows axially until the heating at the circumference of the cavity damages the main winding insulation, causing an earth fault of the machine and tripping, or the core fault extends to the core end.

- Three mechanisms have been identified which control fault growth:
  - Thermal cooling of the core limiting radial growth.
  - Mechanism I, Yoke Flux Diversion, which circulates current in the fault.
  - Mechanism II, Yoke Flux Linking, which circulates current between the fault and the core frame.

- Core faults tend not to grow unless the initiating defect is >1 cm in diameter.
- Yoke Flux Linking Mechanism II is the most powerful for growing a core fault but appears to be active in relatively few faults. It can be limited or eliminated by introducing a high resistance between the stator core and its frame.

- The currents flowing in a core fault can be as large as the current circulated in the core frame by the core leakage flux.
- The tendency of a laminated core to be subject to core faults can be reduced by:
  - Maintaining the highest quality in the construction of the core by:
    - Ensuring correct coreplate insulation quality and thickness.
    - Deburring individual coreplates.
    - Avoiding the introduction of foreign bodies, particularly metallic, into the core construction.
    - Applying uniform and adequate clamping pressure.
    - Carrying out recorded visual and electromagnetic/thermal inspection on completion of core build.
  - Insulating the core frame from the core can eliminate the effect of the Yoke Flux Linking Mechanism once a fault is initiated.
  - Lowering the magnetic loading below 1 T to reduce the effect of the Yoke Flux Diversion Mechanism, but this has to be consistent with other machine design requirements.
  - Lowering the electrical loading below 100 A/mm will reduce a risk of core faults, however, if this limit has to be exceeded for larger machines, for design reasons, it will be necessary pay closer attention to coreplate insulation quality and cooling intensity to reduce core fault risk.
  - Providing radial cooling ducts in the core with high-resistance/insulating duct spacers to resist the axial growth of the fault. This approach is as yet unknown in the industry and would involve expensive materials.
  - Ensuring that the machine is not operated at an excessive field or armature current and consequently core flux density and that it is not subjected to pole slipping.
- Early warning of core faults can be given by the use of core monitors, see [33].

6 Acknowledgments

The authors are grateful to R. Martin at Durham University for predicting the magnetic field around a core fault using the finite element package MEGA and to colleagues at Brush Turbine Generator Division in Loughborough, Ridderkirk and Plzeň for large machine design information.
Permission to publish Figs. 1*a*, 5*a*, and 9 has been given by Siemens Power Generation (UK), who emphasise that these photographs show core damage some 30 years old. Major faults on large machines are rare nowadays because of the improvements in design and constructional methods, described in the conclusions, and the widespread application of core monitors. The authors are grateful to Siemens for their permission to publish these photos.

7 References

1 Rudenberg, R.: 'Zusëtzliche Verluste In Synchronaschinen Uhd Ihre Messun', *Elektrotech. Zeitschrift.*, 1924, **59**, p. 37
2 Rockwood, G.H.: 'Calculation of stray losses', *AIEE Trans*, 1928, **47**, pp. 582–585
3 Laffoon, C.M., and Calvert, J.F.: 'Iron losses in turbine generators', *AIEE Trans.*, 1929, **48**, pp. 370–374
4 Phear, H.W., and Mallock, R.R.M.: 'The effect of the joints in the plates of a laminated iron core on the DC ampere-turns required for its magnetization', *J. IEE.*, 1936, **79**, p. 560
5 Richardson, P.: 'Stray losses in synchronous electrical machinery', *J. IEE*, 1945, **92**, (Pt. 2), pp. 291–304
6 Estcourt, V.F., Holley, C.H., Johnson, W.R., and Light, P.H.: 'Underexcited operation of large turbine generators on the Pacific Gas and Electric Co.'s system', *AIEE Trans.*, 1953, **72**, (Pt. iii), pp. 16–22
7 Winchester., R.L.: 'Stray losses in the armature end iron of large turbine generators', *AIEE Trans.*, 1955, **74**, (Pt. iii), pp. 381–397
8 Mason, T.H., Aylett, P.D., and Birch, F.H.: 'Turbogenerator performance under exceptional operating conditions', *Proc. IEE*, 1959, pp. 357–373
9 Oberretl, K.: 'Streufelder, Wirbelstromverluste, Erwarmungen, Krafte und Eisenbrand im Stirnraum von Turbogeneratoren', *Elektrotech. Maschin.*, 1963, **80**, pp. 539–550
10 Walker, J.H., Rogers, G.J., and Jackson, R.L.: 'Pressing and clamping laminated cores', *Proc. IEE*, March 1964, **111**, (3), pp. 565–577
11 Howe, D., and Hammond, P.: 'Examination of the axial flux in stator cores with particular reference to turbogenerators', *Proc. IEE*, 1976, **123**, (6), pp. 554–559
12 Stoll, R.L.: 'The effect of butt joints in large AC machine cores'. ICEM, Vienna, Sept. 1976
13 Vickers, V.J.: 'Recent trends in turbogenerators', *Proc. IEE*, 1974, **121**, (11R), pp. 1273–1306
14 Jacobs, D.A.H., Minors, R.H., Myerscough, C.J., Rollason, M.L.J., and Steel, J.G.: 'Calculation of losses in the end region of turbogenerators', *Proc. IEE*, 1977, **124**, (4), pp. 356–362
15 Renew, D.C., and Tavner, P.J.: 'Axial flux variation in a synchronous generator during pole slipping', *Proc. IEE*, 1978, **125**, (6), pp. 535–536
16 Tavner, P.J., Hammond, P., and Penman, J.: 'Contribution to the study of leakage fields at the ends of rotating electrical machines', *Proc. IEE*, 1978, **125**, pp. 339–349
17 Jackson, R.J.: 'Interlamination voltages in large turbogenerators', *Proc. IEE*, 1978, **125**, (11), pp. 1232–1238
18 Phemister, T.G., Smith, R., Hammond, P., Jackson, R.J., Tavner, P.J., Penman, J., Stoll, R.L., Lorch, H.O., and Howe, D.: 'Contributions to discussion on interlamination voltages in large turbine generators and influence of winding design on the axial flux in laminated stator cores and examination of flux distribution in segmented stator cores', *Proc. IEE*, 1980, **127**, (Pt C), p. 118
19 Anderson, A.F., and Guile, A.E.: 'An unusual type of interlaminar breakdown found in an electrical machine'. 6th Int. Conf. Gas Discharges and their Applications, Heriot-Watt University, 8–11 September 1980

20 Anderson, A.F., Bedford, T., and Craddock, A.F.: 'Transient leakage flux in small universal motors', *Proc. IEE*, 1981, **128**, (Pt B) (5), p. 254
21 Platt, R., Kerr, L.C., and Anderson, A.F.: 'Measuring flux and interlaminar voltage in turbine generator end regions'. IEE EMDA Conf., London , 13–15 July 1982, Conf. Pubn. 213, pp. 201–205
22 Tavner, P.J., and Penman, J.: 'Currents flowing in the stator-core of large electrical machines', *Proc. IEE*, 1983, **130**, (Pt C) (6), pp. 273–277
23 Hilliar, R.A., Jackson, R.J., Ward, D.A., and Bennett, R.B.: 'Measurements of the currents flowing in the stator frame of a 500 MW turbogenerator', *Proc. IEE*, Jan. 1986, **133**,(Pt C) (1), pp. 16–25
24 Bratoljic, T.: 'Currents induced in the inner stator frame of large turbogenerators by the end-zone field', *Trans. IEEE*, Dec. 1986, **EC-1**, (4), pp. 108–114
25 Mecrow, B., Jack, A.G., and Cross, S.: 'Electromagnetic design of turbogenerator stator end regions', *Proc. IEE*, Nov. 1989, **136**, (Pt C) (6), pp. 361–372
26 Sutton, J.: 'El CID:An easier way to test stator cores', *Electr. Rev.*, 1980, **207**, (1)
27 Beckley, P.: 'Electrical steels for rotating machines' (Peter Peregrinus, 2002)
28 Mogi, H., Kaido., C., Minematsu, E., Hanzawa, K., Nakahara, A., Takahashi, K., Ide, K., Kaneda, J., Hattori, K., and Watanabe, T.: 'Core losses in turbine generators: segment core evaluated by torque method'. Proc. 16th ICEM, Cracow, Poland, April 2004, pp. 13–14
29 Lehoczky, K.N.: 'Relationship between stator core buckling, core losses, vibration and local over-temperatures', *IEEE Trans. Eng. Convers.*, March 1988, **3**, (1), pp. 56–63
30 Langmuir, I.: 'Flames of atomic hydrogen', *Ind. Eng. Chem.*, 1927, **19**, (6, 667), pp. 141–158
31 Stoll, R.L.: 'The Analysis of eddy currents' (Clarendon Press, Oxford, 1974), p. 61
32 Moullin, E.B.: 'Principles of electromagnetism' (Oxford University press, 1955), p. 91
33 Tavner, P.J., Ward, D.A., and Gaydon, B.: 'Monitoring generators and large motors', *Proc. IEE*, 1986, **133**, (Pt B), pp. 169–180

8 Appendix theory

8.1 Parameters of core fault cavity

The core fault cavity to be investigated in this paper will be in a large, 500 MW, two-pole, hydrogen-cooled, turbogenerator and the parameters used are given in Table 2, they are identical to those used in [17] a machine between the rating of items 8 and 9 in Table 1. In the following sections the electromagnetic and thermal analytical factors are considered.

8.2 Electromagnetic factors

8.2.1 Mechanism I, yoke flux diversion: Consider the fault shown in Fig. 6, the intention is to calculate the current which could flow axially between coreplates around that fault under various conditions of fault size and skin depth of the currents concerned.

Currents will flow axially between connected coreplates at the surface of the fault driven by the pulsating circumferential component of the core back flux density, B, see Moullin [32]. Assume the fault is circular with a radius, R_c, and that the axial currents flow in the permeable core material. The degree of connection will depend upon the state of the fault, initially it may not be an intimate connection and the skin depth may not be fully developed. However, as the fault develops the coreplates will become intimately connected and eddy currents, limited in a skin-depth, δ, will flow axially between them. As the fault progresses the connection improves, the temperature rises, local core melting occurs and a cavity forms. In this case the coreplate temperature will rise above the Curie point and the skin depth, δ, will increase to the value for non-permeable material of the same conductivity, δ_0, and the resistance will reduce. Where:

$$\delta = \sqrt{\frac{2\rho}{\omega\mu_0\mu_r}} \tag{1}$$

$$\delta_0 = \sqrt{\frac{2\rho}{\omega\mu_0}} \tag{2}$$

Ref. [32] shows that the current density, J, must be distributed sinusoidally around the cavity to preserve a uniform flux density, $B' < B$, across the cavity. The relationship between the sinusoidally distributed current sheet around the cavity and the circumferential flux density, B, incident on the cavity is:

$$B_{rms} = \frac{\mu_0 J_{rms}\delta}{2}\sqrt{\left\{1+\frac{\delta_0^4}{R_c^2\delta^2}\right\}} \tag{3}$$

$$\therefore J_{rms} = \frac{2}{\delta}\left(\frac{B_{rms}}{\mu_0}\right)\frac{1}{\sqrt{\left\{1+\frac{\delta_0^4}{R_c^2\delta^2}\right\}}} \tag{4}$$

$$and\ I_{1rms} = 2\sqrt{2}R_c\left(\frac{B_{rms}}{\mu_0}\right)\frac{1}{\sqrt{\left\{1+\frac{\delta_0^4}{R_c^2\delta^2}\right\}}} \tag{5}$$

The power P_1 in the current flow, per unit length of the cavity can be calculated by integrating around the cavity giving:

$$P_1 = \frac{1}{2}\rho\pi^2 J_{rms}^2 R_c\delta \tag{6}$$

$$\therefore P_1 = 2\pi^2\rho\left(\frac{R_c}{\delta}\right)\left(\frac{B_{rms}}{\mu_0}\right)^2\frac{1}{\left\{1+\frac{\delta_0^4}{R_c^2\delta^2}\right\}}W/m \tag{7}$$

$$\therefore R_{1eff} = \frac{P_1}{I_{rms}^2} = \frac{\pi^2}{4\delta}\left(\frac{\rho}{R_c}\right)Ohms/m \tag{8}$$

8.2.2 Mechanism II, yoke flux linking: The fault current is not restricted to the cavity but also flows radially to the core frame and links the main yoke flux of the machine, as shown in Fig. 6. In which case the emf developed by the greater flux linked by the circuit will circulate a much larger fault current than calculated in the preceeding Section. This larger current will be superimposed on the current described above.

The fault current flows in a circuit with an impedance, Z_ℓ, consisting of an inductive reactance, L_ℓ, due to its self-inductance with the main core, in series with a resistance, R_ℓ, for the fault cavity, see Fig. 6. For the purposes of this analysis the resistance of the coreplate radial paths, the contact resistances at the core back and the resistance of the frame members are neglected:

$$Z_\ell = \sqrt{\left(R_\ell^2 + \omega^2 L_\ell^2\right)}$$

where the resistance R_2 is the axial resistance if the cavity

$$R_\ell = \frac{\rho\ell}{2\pi R_c\delta}$$

where the inductance L_ℓ, is the self inductance of the circuit shown in Fig. 3

$$L_\ell = \left(\frac{Ro - Ri}{Ro + Ri}\right)\frac{\ell\mu_o\mu_r}{\pi}$$

$$\therefore Z_\ell = \sqrt{\left\{\left(\frac{\rho\ell}{2\pi R_c\delta}\right)^2 + \left(\omega\left(\frac{Ro - Ri}{Ro + Ri}\right)\frac{\ell\mu_o\mu_r}{\pi}\right)^2\right\}}$$

$$Z_\ell = \frac{\rho\ell}{2\pi R_c\delta}\sqrt{\left\{1 + \left(\frac{4R_c}{\delta}\left(\frac{Ro - Ri}{Ro + Ri}\right)\right)^2\right\}}$$

Emf in the fault circuit:

$$E_{rms} = -N\frac{d\phi}{dt}, \quad \phi = -N\frac{d}{dt}(\ell(R_o - R_i)B_{rms}\cos\omega t),\ N = 1$$

$$E_{rms} = \ell(R_o - R_i)\omega B_{rms}\sin\omega t$$

$$I_{2rms} = \frac{E_{rms}}{Z_2} = \frac{\ell(R_o - R_i)\omega B_{rms}}{\frac{\rho\ell}{2\pi R_c\delta}\sqrt{\left\{1 + \left(\frac{4R_c}{\delta}\left(\frac{Ro - Ri}{Ro + Ri}\right)\right)^2\right\}}}$$

$$I_{2rms} = \frac{2\pi R_c\omega\delta(R_o - R_i)B_{rms}}{\rho\sqrt{\left\{1 + \left(\frac{4R_c}{\delta}\left(\frac{Ro - Ri}{Ro + Ri}\right)\right)^2\right\}}}$$

$$I_{2rms} = 4\pi\frac{R_c(R_o - R_i)}{\mu_r\delta}\left(\frac{B_{rms}}{\mu_0}\right) \times \frac{1}{\sqrt{\left\{1 + \left(\frac{4R_c}{\delta}\left(\frac{Ro - Ri}{Ro + Ri}\right)\right)^2\right\}}}$$

The power P_2 per unit length of the cavity will be:

$$P_2 = I_{2rms}^2 R_{2eff}$$

$$where\ R_{2eff} = \frac{\rho}{2\pi R_c\delta}\,Ohm/m$$

$$note\ R_{2eff} = \frac{2}{\pi^3}R_{1eff} \tag{9}$$

$$P_2 = \frac{\omega(R_o - R_i)B_{rms}^2}{\rho\delta\left\{1 + \left(\frac{4R_c}{\delta}\left(\frac{Ro - Ri}{Ro + Ri}\right)\right)^2\right\}}$$

$$\therefore P_2 = \frac{8\pi\rho}{\mu_r^2}\left(\frac{R_c(R_o - R_i)^2}{\delta^3}\right)\left(\frac{B_{rms}}{\mu_0}\right)^2 \times \frac{1}{\left\{1 + \left(\frac{4R_c}{\delta}\frac{(R_o - R_i)}{(R_o + R_i)}\right)^2\right\}}W/m \tag{10}$$

8.3 Thermal factors

As described in the text, core faults are generally circular in the core body and extend axially in the form of an ellipsoid. A simple thermal model of the fault can therefore assume circular symmetry. Heat transfer is radial, at the surface of the fault, R_c, the coreplate steel temperature has reached melting point temperature, T_i, and at some radial distance, R_b, from the fault the temperature is close to the mean temperature, T_b, of the core. Assuming that in the cylindrical region of the core fault:

- The power input in the fault is much greater than the background core loss,
- The power input is uniformly distributed over the fault region,
- The cooling effect of the core ventilation in the fault area is negligible,
- The radial heat transfer is that of the coreplate and is assumed constant at all temperatures.

Laplace's equation in two dimensions for heat transfer shows that with a volumetric power input, P, the surrounding temperature is as follows:

$$P = \frac{(T_i - T_b)4\kappa}{(R_b^2 - R_c^2)} \tag{11}$$

The distance, $(R_b - R_c)$, between the molten material, at the core fault radius, and the point of background temperature in the core is of crucial importance to understanding the growth of the fault.

Equivalent circuit for the brushless doubly fed machine (BDFM) including parameter estimation and experimental verification

P.C. Roberts, R.A. McMahon, P.J. Tavner, J.M. Maciejowski and T.J. Flack

Abstract: Experimental results from a frame size 180 brushless doubly fed (induction) machine (BDFM) fitted with four rotor designs are presented. The machine is intended for use as a variable speed generator, or drive. A per phase equivalent circuit for the machine has been developed and a method of obtaining parameters for the circuit is described. Expressions for the torque as a function of speed have been derived and predictions of machine performance in both self-cascaded and synchronous (doubly fed) modes have been verified experimentally. The work illustrates the link between rotor equivalent circuit parameters and machine performance and a comparison between rotor designs has been made.

List of symbols

X_1, X_2, X_r	indicating a stator 1, 2, or rotor quantity X
$\Re\{X\}$, $\Im\{X\}$	denotes real, imaginary part of complex X
$\angle(X)$	argument of complex X, i.e., arctan $\Im\{X\}/\Re\{X\}$
R, M, L, N	resistance, mutual, self inductance, turns ratio (real)
X'	indicates an apparent (referred) quantity
P	power quantity, or parameter value
V, I	complex voltage, current (symbols may represent real or complex numbers depending on the context)
p_1, p_2	stator winding pole pairs
ω_r	BDFM rotational shaft speed
s	slip
j	$\sqrt{-1}$
$\mathbb{B}$	$\left\{x : \begin{bmatrix} I \\ -I \end{bmatrix} x \leq \begin{bmatrix} 1 \\ \vdots \\ 1 \end{bmatrix}\right\}$, a hypercube around the origin

1 Introduction

The concept of incorporating two induction machines with airgap fields of different pole numbers in one frame to realise a self-cascaded machine can be attributed to Lydall [1]. Hunt [2, 3] also developed a machine using the same principle and showed that suitably designed stator and rotor windings could reduce copper losses significantly. Hunt's use of a single rotor winding coupling both airgap fields resulted in a more practical machine which was successful in suitable applications. These machines operated in the self-cascaded mode, that is with one stator winding fed from fixed frequency mains and the other shorted or connected to resistances.

The advent of sources of variable voltage and frequency from inverters offered the possibility of operation in a doubly fed mode, in which the shaft speed has a fixed relationship to the two excitation frequencies, as noted by Broadway and Burbridge [4], and subsequent work has focused on operation in this mode. Broadway and Burbridge further pointed out the attraction, from a manufacturing point of view, of a single-layer rotor winding made in a similar way to normal cage windings. This design, known as the 'nested-loop' design, was adopted and refined in the work of Wallace, Spée and others who studied BDFMs of this type extensively [5–10]. Williamson *et al.* consider a machine of this type in their papers on the generalised harmonic analysis of the BDFM [11, 12].

Current interest in the BDFM is primarily as a variable speed generator for wind turbines, although the benefits of the BDFM for variable speed drives have also been demonstrated [10]. The capital installation cost is lower, due to a fractional inverter power requirement. The advantage of brushless operation is particularly valuable for offshore wind turbine applications where maintenance costs are high.

The authors have constructed a frame size 180 machine which has been used to study control and measurement aspects of the BDFM [13–15]. The authors have more recently reported on the performance of alternative rotor configurations [16]. In this paper, a per-phase equivalent circuit for the BDFM is developed and a method of obtaining parameters from measured torque–speed characteristics is described. The equivalent circuit is shown to predict the performance of the BDFM and illustrates how the performance depends on the equivalent circuit parameters of the machine.

2 Introduction to BDFM operation

Details of the operation of the BDFM in synchronous mode, as shown in Fig. 1, have been given by various authors [8, 11]. Under synchronous conditions the shaft

IEE Proceedings online no. 20045106

doi:10.1049/ip-epa:20045106

Paper first received 28th July and in final revised form 8th November 2004. Originally published online: 16th June 2005

P.C. Roberts, R.A. McMahon, J.M. Maciejowski and T.J. Flack are with the Department of Engineering, University of Cambridge, Trumpington Street, Cambridge CB2 1PZ, UK

P.J. Tavner is with the School of Engineering, University of Durham, Durham DH1 3LE, UK

E-mail: pcr20@cam.ac.uk

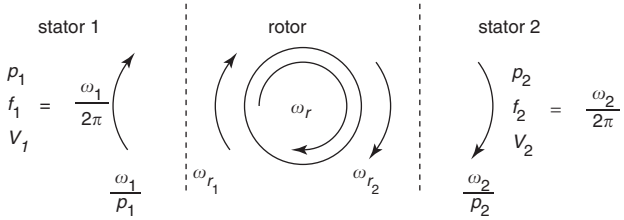

Fig. 1 *BDFM synchronous mode of operation*

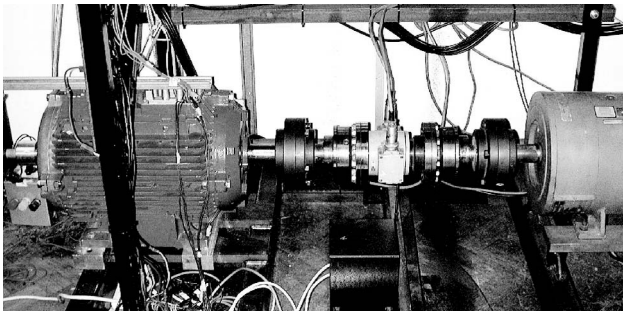

Fig. 2 *Prototype BDFM machine (left) on test rig with torque transducer and DC load machine (right)*

angular velocity is related to the supply frequencies by (1) (see [11]) and the frequency of rotor currents is later given by (5)

$$\omega_r = \frac{\omega_1 + \omega_2}{p_1 + p_2} \tag{1}$$

This leads to a definition of slips for the power and control windings in (2) and (3)

$$s_1 \triangleq \frac{\omega_1 - p_1\omega_r}{\omega_1} = \frac{\omega_{r_1}}{\omega_1} \tag{2}$$

$$s_2 \triangleq \frac{\omega_2 - p_2\omega_r}{\omega_2} = \frac{\omega_{r_2}}{\omega_2} \tag{3}$$

A further relationship is given in (4) for the so-called natural speed, that is the synchronous speed such that according to (1) the control winding is fed with DC

$$\omega_n = \frac{\omega_1}{p_1 + p_2} \tag{4}$$

The BDFM can also operate in the cascade mode, that is with the one winding shorted or connected to resistances. In the cascade mode the speed varies with load, but (1) and (5) still apply.

3 Machine design

Table 1 gives the physical data for the prototype machine used throughout this and the work described in [13–16]. The machine is shown in Fig. 2 on the experimental test rig. Four different rotors have been constructed [16]. Rotor 1 is of 'nested-loop' design and rotor 3 (shown in Fig. 3) is of a new double-layer design. Both rotors have been designed for BDFM action. Rotor 2 has 18 progressive loops and rotor 4 is a conventional cage rotor. Although these rotors do not show BDFM action, they are useful as benchmarks of performance. Details of the rotors are given in Table 1.

4 Experimental results

The aim of the experiments was to determine the torque speed characteristics of the BDFM with the different rotors to enable their performance to be compared and to provide data for the extraction of equivalent circuit parameters. Each rotor was tested in both simple induction and cascade mode. In the former case stator windings were energised in turn whilst the other was open circuit. In the latter case the nonenergised stator was short-circuited. The tests were all carried out at the same reduced supply voltage of 90 V_{rms} (phase), 50 Hz, to limit currents to acceptable values throughout the range of the test and to avoid saturating the iron circuit. The resulting airgap flux density was nominally 0.125 T rms for each pole number field.

The results are shown in Figs. 4–7 and illustrate a number of important features. All four rotors show some simple induction action, with rotor 4 being the strongest, because it was designed for that purpose. Rotors 1 and 3,

Table 1: Prototype machine data

Parameter		Value
Frame size		D180
Stator core length		190 mm
Stator slots		48
Stator winding 1	Poles	4
	coils per phase	16 (series connected)
	turns per coil	10
Stator winding 2	Poles	8
	coils per phase	16 (series connected)
	turns per coil	20
Effective airgap	0.5–0.6 mm depending on rotor	
Actual airgap	0.51–0.56 mm depending on rotor	
Rotor slots	36 for rotors 1–3 and 40 for rotor 4	
Rotor 1	Nested-loop design of Broadway/Burbridge [4], consisting of 6 'nests' of 3 concentric loops of pitch 5/36, 3/36 and 1/36 of rotor circumference. Each nest offset by 1/6 of circumference	
Rotor 2	Double layer winding of 18 successive single isolated turns each spanning 7/36 of the rotor circumference.	
Rotor 3	Novel double layer winding with 6 sets of 4 progressively wound groups of coils each coil spanning 1/6 of rotor circumference, each set of coils is offset 1/6 of circumference from next, for full details see [16]	
Rotor 4	Conventional squirrel cage rotor as designed for motor frame with Boucherot slot configuration	

Fig. 3 *Rotor 3: Prototype new double layer design*

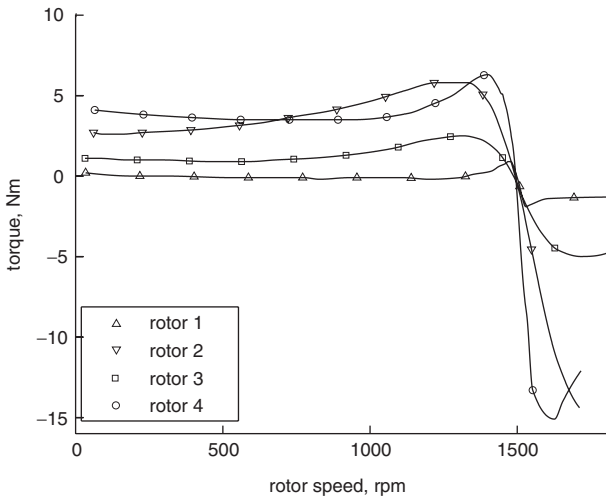

Fig. 4 *Measured torque–speed characteristic*
Four-pole stator supplied with 90 V_{rms}
Eight-pole stator open circuit (simple induction mode)

designed for BDFM action, show relatively low self-induction torques. In contrast, these rotors give strong torques in the cascade mode with the torque–speed characteristic passing through zero at the natural speed. Torques also fall to zero when the rotor is synchronous with field of the energised stator, i.e. at 1500 rpm when the four-pole winding is excited and at 750 rpm when the eight-pole field is excited. Rotors 2 and 4 do not produce torque in the cascade mode showing that negligible cross-coupling is taking place.

5 Equivalent circuit for the BDFM

The BDFM was conceived as two distinct induction machines in the same frame, intended for operation in the

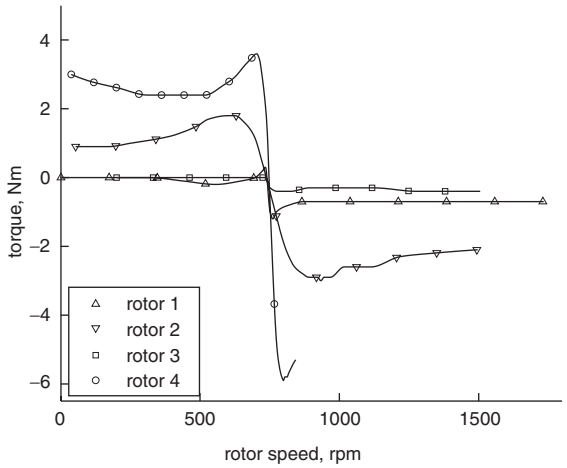

Fig. 5 *Measured torque–speed characteristic*
Eight-pole stator supplied with 90 V_{rms}
Four-pole stator open circuited (simple induction mode)

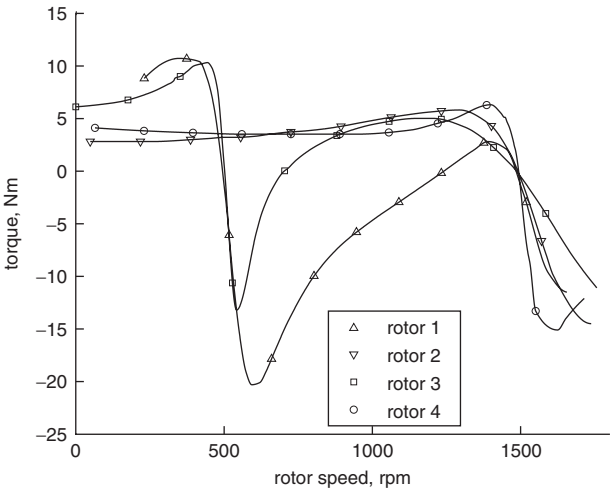

Fig. 6 *Measured torque–speed characteristic*
Four-pole stator supplied with 90 V_{rms}
Eight-pole stator open circuited (cascade induction mode)

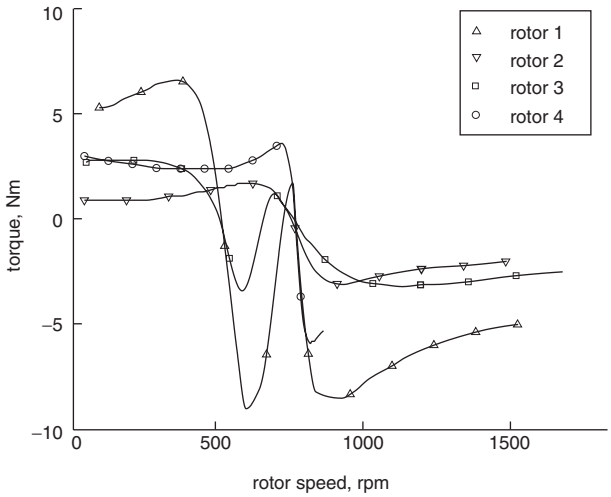

Fig. 7 *Measured torque–speed characteristic*
Eight-pole stator supplied with 90 V_{rms}
Four-pole stator short circuited (cascade induction mode)

self-cascaded mode [2]. Therefore it is possible to represent the BDFM as two connected induction machines and develop an equivalent circuit using the standard per-phase

model. Alternative approaches include the two-phase model proposed by Broadway and Burbridge [4] and models derived from considerations of a three winding transformer [8]. Gorti *et al.* use symmetrical component analysis applied to a coupled-circuit derived model [17]. A form of a single phase equivalent circuit has been presented, without derivation, by Liao [18].

Figure 8 shows the standard equivalent circuit for an induction motor with accessible rotor terminals, omitting iron losses. N is the effective turns ratio, L_m is the magnetising inductance of the fundamental space harmonic field, as the equivalent circuit can only represent coupling between rotor and stator for one field component, in this case the fundamental. However, the rotor and stator circuits must include series inductance terms which correspond to the additional series inductance due to any space harmonics created in the stator and rotor, respectively. These terms appear in series with leakage terms, i.e. terms which represent the flux which self-links without crossing the airgap. On the stator the term L_1 includes both these harmonic terms and leakage terms. On the rotor L_r represents these terms.

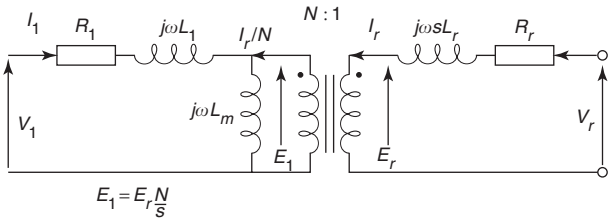

Fig. 8 *Induction machine per-phase equivalent circuit with rotor terminals*

If we now have two induction machines with different pole numbers, then we will have two induction motor equivalent circuits. These machines may share the same frame, and even the same iron circuit as the magnetic fields are of differing pole number (subject to conditions on the choice of pole number to avoid unbalanced magnetic pull [19]). If each 'machine' has a wound rotor of the appropriate pole number, then the equivalent circuit parameters of each 'machine' have the same interpretation as those of Fig. 8.

Notice that each equivalent circuit would, in general, have its own slip, s_1 and s_2, as previously defined in (2) and (3).

For an electrical machine to admit an equivalent circuit representation, the frequencies of the currents and voltages at the terminals must be equal. When the BDFM is operating in synchronous or cascade modes the rotor shaft speed and stator frequencies are related by (1), rearranging this gives

$$\begin{aligned}\omega_{r_1} &= \omega_1 - p_1\omega_r \\ &= -\omega_2 + p_2\omega_r = -\omega_{r_2}\end{aligned} \tag{5}$$

$$\Rightarrow s_1\omega_1 = -s_2\omega_2 \tag{6}$$

where ω_{r_1} and ω_{r_2} are the frequencies of the field in the rotor reference frame, hence the rotor frequencies in the referred circuit are equal in magnitude.

Suppose that we now connect the two rotors together, as shown in Fig. 9. From (6) it can be seen that $j\omega_2 s_2 L_{r_2} = -j\omega_{r_2} L_{r_2}$, which is equivalent to reversing the direction of current flow, hence the current direction through transformer 2 in Fig. 9 must be opposite to that

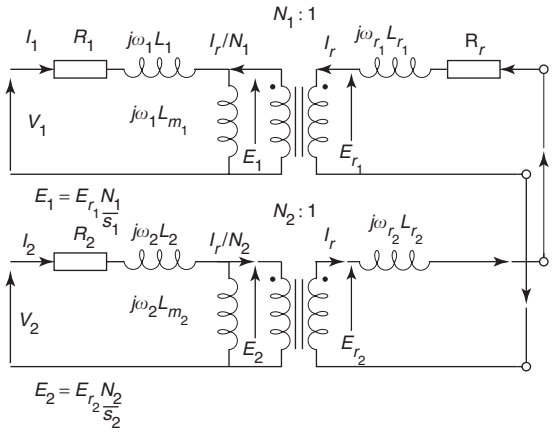

Fig. 9 *BDFM per-phase equivalent circuit*

of Fig. 8. Furthermore we may combine the rotor resistance into a single term, R_r.

This representation of the equivalent circuit is correct for any functioning BDFM irrespective of rotor design. When the BDFM has a specially designed rotor winding, as per [11], the rotor inductance may be understood as follows: as the machine only has one rotor it is more natural to represent the rotor by a single resistance and a single reactance. As L_m consists purely of spatial harmonic inductance corresponding to the stator pole number, L_r must contain all other harmonic components. Since any functional BDFM rotor links stator 1 and stator 2 pole number fields, the magnetising reactance for the stator 2 pole number field is contained within L_r, or more precisely

$$L_r = L_{r_1} + L_{r_2} + \frac{L_{m_2}}{N_2^2} \tag{7}$$

if the stator 1 winding is supplied or

$$L_r = L_{r_1} + L_{r_2} + \frac{L_{m_1}}{N_1^2} \tag{8}$$

if stator 2 winding is supplied.

It follows that in a BDFM rotor the spatial harmonic component of the self-inductance contains harmonic components of both stator 1 and stator 2 pole number fields.

It may be noted that this cannot be achieved with a standard squirrel cage rotor as the harmonic inductance of a cage rotor depends on the 'supplied' field pole number. For example if stator 1 is four-pole, then the cage rotor harmonic inductance only contains four-pole (and higher harmonic) components. As there are no even harmonics, there is no eight-pole component. Therefore, Fig. 9 is not appropriate for a cage rotor.

In Fig. 9, R_1 and R_2 are the resistances of the stator windings and R_r is the rotor resistance. $j\omega_1 L_1$ and $j\omega_2 L_2$ are the stator reactances and $j\omega_r L_r$ is the rotor reactance. The power winding is linked to the rotor by a transformer of turns ratio N_1 and the control winding is linked by a transformer of turns ratio N_2, as shown. The secondary voltages of the transformers are proportional to slip and the slips are, respectively, s_1 and s_2 for the power and control windings.

As for the conventional induction motor it is convenient to refer all quantities to the stator, as in Fig. 10 with values referred to stator 1. Alternatively, it is possible to transfer values to stator 2.

We can now find an expression for torque by considering how the conversion of electrical to mechanical energy is represented in the equivalent circuit. By applying the

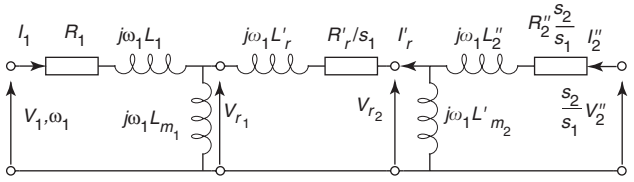

Fig. 10 *Referred per-phase equivalent circuit*

principle of power conservation to Fig. 10 we obtain

$$3\Re\{V_1 I_1^*\} + 3\frac{s_2}{s_1}\Re\{V_2'' I_2''\} = 3|I_1^2|R_1 + 3|I_1'^2|\frac{R_r'}{s_1} + 3|I_2''^2|R_2''\frac{s_2}{s_1} \quad (9)$$

$$3\Re\{V_1 I_1^*\} + 3\Re\{V_2'' I_2''^*\} = 3|I_1'^2|R_1 + 3|I_1'^2|R_r' + 3|I_2''^2|R_2'' + \omega_r T \quad (10)$$

where T is the torque generated by the machine, with positive values for motoring, and the '3's arise because Fig. 10 is a per-phase equivalent circuit.

From Fig. 10 we may define P_{r_1}, P_{r_2}, the power delivered at the rotor terminals from stator 1 and 2, respectively.

$$P_{r_1} \triangleq 3\Re\{V_{r_1} I_1^*\} = 3\Re\{V_1 I_1^*\} - 3|I_1^2|R_1 \quad (11)$$

$$P_{r_2} \triangleq 3\frac{s_1}{s_2}\Re\{V_{r_2} I_1''^*\} = 3\Re\{V_2'' I_2''^*\} - 3|I_2''^2|R_2'' \quad (12)$$

Subtracting (9) from (10) gives the fraction of power not dissipated in the rotor and stator resistances, i.e. the power which is converted to mechanical power.

$$3\Re\{V_2'' I_2''^*\}\left(1 - \frac{s_2}{s_1}\right) = 3|I_r'^2|R_r'\left(1 - \frac{1}{s_1}\right) + 3|I_2''^2|R_2'\left(1 - \frac{s_2}{s_1}\right) + \omega_r T \quad (13)$$

Rearranging, and substituting (12) for the I_2'' terms gives the torque as

$$T = \frac{P_{r_2}}{\omega_r}\left(1 - \frac{s_2}{s_1}\right) - \frac{3}{\omega_r}|I_r'^2|R_r'\left(1 - \frac{1}{s_1}\right) \quad (14)$$

Referring back to the definition of BDFM synchronous speed (1), and slips (2), (3), it is straightforward to see that the rotor speed, ω_r can be written in terms of a deviation from natural speed, as defined in (4).

$$\omega_r = \left(1 - \frac{s_1}{s_2}\right)\omega_n \quad (15)$$

Using (15), (2) and (12) the expression for the torque, (14), may be succinctly written as

$$T = -\frac{3\Re\{V_{r_2} I_2''^*\}}{\omega_n} + 3|I_r'^2|R_r'\frac{p_1}{\omega_1 s_1} \quad (16)$$

Under normal running conditions the power conversion is largely represented by the $3\Re\{V_{r_2} I_2''^*\}/\omega_n$ term in (16) as slips are generally not small. In contrast to the cage rotor induction motor, power conversion could be achieved even if the rotor resistance were zero, as is the case in induction machines where the rotor circuit is externally fed via slip rings. It is advantageous to reduce the rotor resistance, as far as is practical, to minimise losses.

6 Equivalent circuit parameter identification

The no-load and locked rotor tests are the classical way of determining parameters for the equivalent circuit of the conventional induction motor. In the case of the BDFM the no-load test can be applied in turn to each stator winding, with the other open circuit, to determine the magnetising reactance. As the self-induction torque of a BDFM is likely to be relatively small, an external drive may be needed to run the machine at synchronous speed but in any case this will improve the accuracy of the measurements. Stator resistances can be found through DC measurements. However, the locked rotor test cannot be used to determine the remaining parameters individually. For example, the two components L_r' and L_{m_2}'' cannot be separated. Although L_{m_2} may be determined using the synchronous test it is not possible to find the referred value, L_{m_2}'' as the turns ratio is not known.

Recognising that the equivalent circuit can predict the behaviour of the machine in both simple induction and cascade modes, we propose an alternative approach based on the extraction of parameters from measured torque–speed characteristics of the kind shown in Figs. 4–7. This approach has the advantage that a single frequency supply may be used to perform the tests. This is in contrast to the only previously published works on BDFM parameter extraction, [20, 21], where a method requiring operation at a range of different supply frequencies is proposed.

Nevertheless, not all the inductance terms in the equivalent circuit shown in Fig. 10 can be unambiguously determined. An alternative form of the equivalent circuit is shown in Fig. 11 for which all component values can be determined. A similar modification was proposed by Slemon in the case of parameter determination for the equivalent circuit for the standard induction motor [22]. For the circuit to be electrically equivalent to that of Fig. 10 the parameters, and turns ratios, will assume slightly different values, which can easily be calculated, see the Appendix (Section 11.2). However, in a BDFM the referred series rotor inductance is likely to be larger than the series stator inductance so differences in inductance values between the two circuits will be small. Direct measurements of rotor bar currents, for example using techniques described in [13], enable all parameters in Fig. 10 to be determined, but the relationship of these currents to those in the equivalent circuit must be known.

The parameter extraction is a nonlinear optimisation method, using a weighted sum of the squares of the errors between predicted values and those measured by experiment as a cost function. A significant advantage over previous

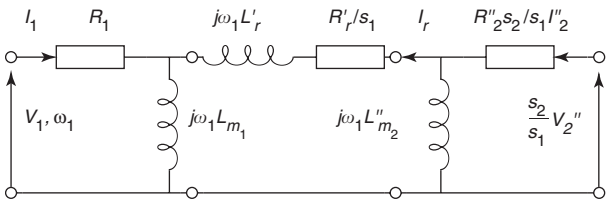

Fig. 11 *Simplified per-phase equivalent circuit*

methods is that the machine is being tested under conditions similar to those found in normal operation. The parameter extraction and optimisation methods are described in full in the Appendix (Section 11.1).

The method was applied to the data of the kind shown in Figs. 4–7. Each data set had between 10 and 15 data points. When solving the optimisation problem, in order to minimise the execution time of each random test point the mathematical functions governing the behaviour of the machine were simplified as far as possible using the

symbolic maths package, Maple, and then hard coded in a C function along with the random number generation code. This function was then called from Matlab. With this implementation it was possible, using a 2.8 GHz Pentium processor, to achieve 4×10^5 tests per second in cascade mode and slightly more in simple mode.

As an indication of the time taken to solve the optimisation to satisfactory accuracy, it took approximately 9×10^8 tests taking around 40 min to generate 10 candidate solutions of suitable accuracy for rotor 1. Tables 2–4 show the results of 2×10^{10} tests, along with the standard deviation taken over the best 20 results. The standard deviations are generally considerably smaller than the estimated parameter values, which indicates that the noise level in the measurements is sufficiently low to have confidence in the results. As an additional measure of effectiveness the algorithm returns the value of the minimised error which, if suitably normalised, gives a measure of fit 'quality'.

Parameters obtained from tests in the simple induction mode are given in Table 2 with the four-pole winding excited; the tests can be performed equally well by energising the 8-pole winding. The substantial values of the referred magnetising inductance ($L''_{m_2}\frac{N_2}{N_1}$) with rotors 1 and 3 reflect effective cross-coupling, and explain the high value of effective referred rotor inductance ($L'_r + L''_{m_2}$). In contrast rotor 2 shows very weak cross-coupling; rotor 4, the conventional cage rotor, shows no measurable cross-coupling, and the corresponding effective referred rotor inductances are correspondingly smaller. Therefore it is only possible to obtain meaningful parameters in the cascade mode for rotors 1 and 3 and these are given in Tables 3 and 4 for four-pole and eight-pole excitation, respectively. Similar values are obtained in both cases, and the values are reasonably consistent with the values found from simple induction mode tests.

Table 2: Simple induction mode extracted parameter values 4 pole winding

	R_1, Ω	R'_1, Ω	$L'_r + L''_{m_2}$, mH	L_{m_1}, mH	$L''_{m_2}(N_2/N_1)$, mH
Rotor 1: nested-loop rotor design					
Opt:	4.02	1.2	120	240	137
Std. dev.:	0.0243	0.00769	0.204	0.0507	0.00879
Rotor 2: 18 isolated loops rotor design					
Opt:	3.28	1.36	26.1	252	5.46
Std. dev.:	0.0548	0.00627	0.199	5.19	0.00855
Rotor 3: new double-layer rotor design					
Opt:	3.52	3.1	65.5	260	105
Std. dev.:	0.0384	0.0306	0.246	4.44	0.547
Rotor 4: standard cage rotor design					
Opt:	3.54	0.486	22.8	253	0
Std. dev.:	0.049	0.00705	0.202	17.7	0

Table 3: Cascade induction mode extracted parameter values 4 pole winding

	R_1, Ω	R'_r, Ω	L'_r, mH	L_{m_1}, mH	R''_2, Ω	L''_{m_2}, mH	N_1/N_2
Rotor 1: nested-loop rotor design							
Opt:	3.63	1.26	35.1	277	2.46	101	0.685
Std. dev.:	0.106	0.038	0.379	27.1	0.0628	3.83	0.0131
Rotor 3: new double-layer rotor design							
Opt:	3.6	2.92	27.4	299	0.716	40.8	0.408
Std. dev.:	0.125	0.0673	0.386	32.8	0.0197	1.55	0.00788

Table 4: Cascade induction mode extracted parameter values 8 pole winding

	R_1, Ω	R'_r, Ω	L'_r, mH	L_{m_1}, mH	R''_2, Ω	L''_{m_2}, mH	N_1/N_2
Rotor 1: nested-loop rotor design							
Opt:	5.79	2.82	72.9	288	7.25	391	1.41
Std. dev.:	0.213	0.0951	0.919	19.5	0.28	25.5	0.0447
Rotor 3: new double-layer rotor design							
Opt:	5.39	23.5	189	281	22.9	1640	2.51
Std. dev.:	0.391	0.377	1.27	5.52	0.487	39.4	0.0301

Manufacturer's data are available for rotors 2 and 4. Allowing for differences in airgap dimensions, inductance values are in the expected range. However, values of rotor resistance can be directly compared and the manufacturer gives 1.28 Ω and 0.46 Ω for rotors 2 and 4, respectively. The closeness of these values to those given in Table 2 confirm the effectiveness of this method of parameter determination.

In the extraction of the parameters, the solver aimed for a best fit of all parameters. Alternatively, certain parameters which can be accurately determined by independent means can be fixed. These include the sum of L_1 and L_m, which can be obtained from a synchronous or no-load test, and the stator winding resistances which can be obtained from DC measurements at working temperature, assuming that the skin effect can be ignored in the stator windings.

7 Results verification of predictions from the equivalent circuit

To demonstrate the use of the equivalent circuit, it has been used to predict the performance of the BDFM in both synchronous and cascade (asynchronous) modes. Figure 12 shows a torque–speed curve for rotor 3. The machine four-pole stator winding was supplied with a constant voltage and frequency supply at 90 V and 50 Hz. The machine eight-pole winding was short-circuited, hence the machine was operating in cascade induction mode. The Figure shows experimental points overlaid with a calculated torque–speed curve generated from the parameters listed in Table 3 using the equivalent circuit in Fig. 11. Negative torque denotes that the machine is acting as a generator. Close agreement between predicted and measured values is seen.

Figure 13 shows a synchronous torque envelope for rotor 3, with experimental data points overlaid. Again, the machine four-pole stator winding was supplied from a constant voltage and frequency supply at 90 V and 50 Hz. However, the machine eight-pole stator winding was fed with a variable voltage, variable frequency supply of f_2 Hz at $230 \times (f_2 = 50)$V. Again there is good agreement between theory and experiment. The dip in the torques near 500 rpm could have been overcome by applying a suitable voltage boost to the eight-pole stator winding at low excitation frequencies to maintain a constant voltage $|V_{r_2}|$.

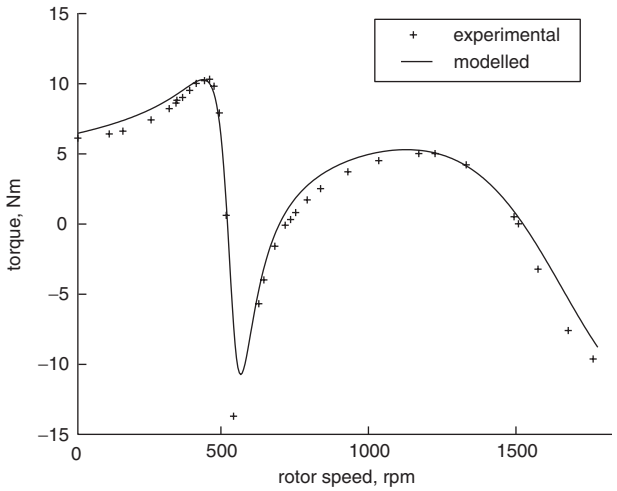

Fig. 12 *Experimental verification of the parameter extraction procedure: torque–speed plot for rotor 3*
Four-pole winding supplied with nominally 90 V (phase)
Eight-pole winding is short-circuited generated with parameters given in Table 3

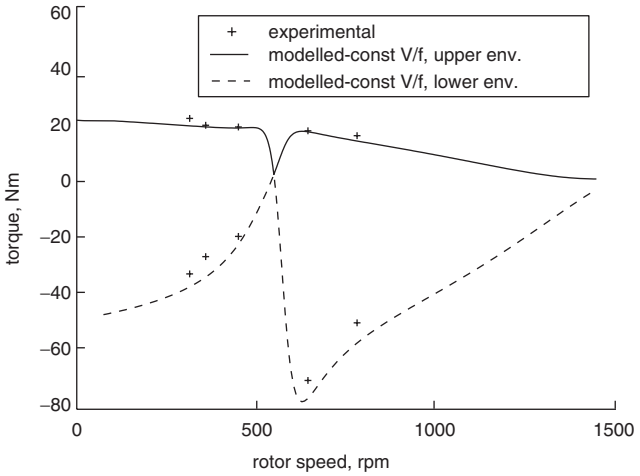

Fig. 13 *Experimental verification of the parameter extraction procedure. Synchronous torque envelope with varying rotor speed for rotor 3*
Four-pole winding supplied with nominally 90 V (phase)
Eight-pole winding is supplied with $2.56 \times 90\,(f_2/f_1)$ values given in Table 3

Figure 14 shows a synchronous torque envelope for rotor 1 with a higher voltage (220 V) applied to the four-pole stator winding. The eight-pole stator winding was supplied with a variable voltage, variable frequency supply of f_2 Hz at $220 \times (f_2/50)$V, with a voltage boost below $f_2 = 5$ Hz. However, there is still a dip in torque near 500 rpm, arising the change in sign of the voltage across the stator impedance. The torque envelope can be flattened by applying a voltage boost which is slightly asymmetrical about natural speed (500 rpm). The absence of measurements of generating torque above 100 Nm arises from limitations of the external drive.

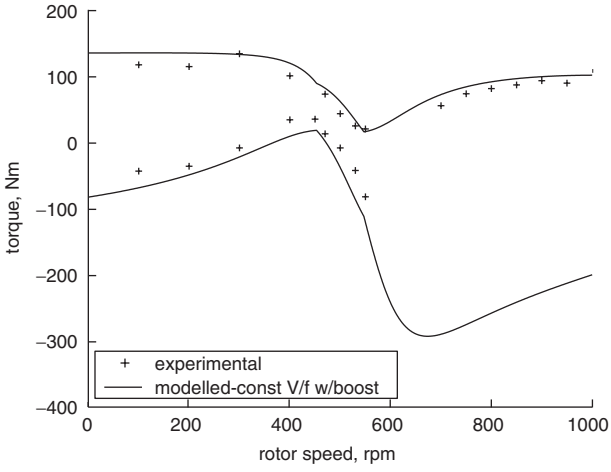

Fig. 14 *Experimental verification of the parameter extraction procedure. Maximum Synchronous torque envelope with varying rotor speed for rotor 1 (nested-loop design)*
Four-pole winding supplied with nominally 220 V (phase)
Eight-pole winding is supplied with constant V/f law with boost $V_8 = \max\{220\,|f_2/f_1|,\ 20.7\}$ parameters given in Table 3

8 Conclusions

We have presented experimental torque speed characteristics from a BDFM equipped with four rotor variants. A per-phase equivalent circuit valid for all modes of operation has been developed. The circuit parameters have precise physical meanings and torque equations have been derived.

With a simple modification the circuit reduces to a form for which all parameters can be obtained experimentally. A method of determining these parameters from measurements at machine terminals is presented. The equivalent circuit has been used to predict torque–speed characteristics in both synchronous and cascade modes and these predictions are in good agreement with measured values.

The performance of the rotors for a BDFM can be related to their equivalent circuit parameters. Although a full comparison is beyond the scope of this paper, we can note that the torque envelope depends strongly on the referred rotor resistance and reactance. A good rotor design will therefore involve making R'_r and L'_r as low as practical. Reducing L'_r is particularly challenging as harmonic inductance components are likely to be dominant. The harmonic elements are a consequence of the need to couple fields of different pole numbers and can only be minimised by careful rotor design.

The method of parameter estimation is geared to finding equivalent circuit values which give predictions that closely match the observed behaviour of the machine. We are currently looking at the effects of saturation on parameter values and whether accurate prediction of machine performance will remain possible. In addition, the method of parameter estimation can be used to find values for the equivalent circuit of the standard induction motor.

9 Acknowledgments

The authors wish to thank FKI Energy Technology, particularly its subsidiaries (Laurence, Scott & Electromotors Ltd. and Marelli Motori SpA) for their continued support, particularly for the provision of the prototype machine and fabrication of the rotors. Semikron UK Ltd. is thanked for supplying an inverter.

10 References

1 Siemens Brothers & Co. Ltd. and F. Lydall, British Patent 16839, July 1902
2 Hunt, L.J.: 'A new type of induction motor', *Inst. Electr. Eng. J.*, 1907, pp. 648–677
3 Hunt, L.J.: 'The 'cascade' induction motor', *Inst. Electr. Eng. J.*, 1914, pp. 406–434
4 Broadway, A.R.W., and Burbridge, L.: 'Self-cascaded machine: a low-speed motor or high frequency brushless alternator', *Proc. IEE.*, 1970, **117**, pp. 1277–1290
5 Wallace, A.K., Rochelle, P., and Spée, R.: 'Rotor modelling and development for brushless doubly-fed machines'. Conf. record of the Int. Conf. on Electrical machines, Cambridge, 1990, Vol. 1
6 Li, R., Wallace, A., and Spée, R.: 'Two-axis model development of cage-rotor brushless doubly-fed machines', *IEEE Trans. Energy Convers.*, 1991, **6**, (3), pp. 453–460
7 'Dynamic simulation of brushless doubly-fed machines', *IEEE Trans. Energy Convers.*, 1991, **6**, (3), pp. 445–452
8 Li, R., Spée, R., Wallace, A.K., and Alexander, G.C.: 'Synchronous drive performance of brushless doubly-fed motors', *IEEE Trans. Ind. Appl.*, 1994, **30**, (4), pp. 963–970
9 Boger, M., Wallace, A., Spee, R., and Li, R.: 'General pole number model of the brushless doubly-fed machine', *IEEE Trans. Ind. Appl.*, 1995, **31**, (5), pp. 1022–1028
10 Boger, M., Wallace, A., and Spée, R.: 'Investigation of appropriate pole number combinations for brushless doubly fed machines as applied to pump drives', *IEEE Trans. Ind. Appl.*, 1996, **31**, (5), pp. 1022–1028
11 Williamson, S., Ferreira, A.C., and Wallace, A.K.: 'Generalised theory of the brushless doubly-fed machine. part 1: Analysis', *IEE Proc. Electr. Power Appl.*, 1997, **144**, (2), pp. 111–122
12 Williamson, S., and Ferreira, A.C.: 'Generalised theory of the brushless doubly-fed machine. part 2: Model verification and performance', *IEE Proc. Electr. Power Appl.*, 1997, **144**, (2), pp. 123–129
13 Roberts, P.C., Abdi-Jalebi, E., McMahon, R.A., and Flack, T.J.: 'Real-time rotor bar current measurements using bluetooth technology for a brushless doubly-fed machine (BDFM)'. Int. Conf. Power electronics, machines and drives, 2004, Vol. 1, pp. 120–125
14 Abdi-Jalebi, E., Roberts, P.C., and McMahon, R.A.: 'Real-time rotor bar current measurement using a rogowski coil transmitted using wireless technology'. 18th Intl. Power systems conf, Iran, 2003, Vol. 5, pp. 1–9
15 Roberts, P.C., Flack, T.J., Maciejowski, J.M., and McMahon, R.A.: 'Two stabilising control strategies for the brushless doubly-fed machine (BDFM)'. Proc. Int. Conf. Power electronics, machines and drives, Bath, UK , 2002, pp. 341–346
16 Roberts, P.C., McMahon, R.A., Tavner, P.J., Maciejowski, J.M., Flack, T.J., and Wang, X.: 'Performance of rotors for the brushless doubly-fed (induction) machine (BDFM)'. Proc. 16th Int. Conf. Electrical machines, Cracow, Poland, 2004, pp. 450–455
17 Gorti, B.V., Alexander, G.C., and Spée, R.: 'Power balance considerations for brushless doubly-fed machines', *IEEE Trans. Energy Convers.*, 1996, **11**, (4), pp. 687–692
18 Liao, Y.: 'Design of a brushless doubly-fed induction motor for adjustable speed drive applications'. Proc. IEEE Ind. App. Soc. Annual Mtg, 1996, pp. 850–855
19 Creedy, F.: 'Some developments in multi-speed cascade induction motors', *Insti. Electri. Eng. J.*, 1920, pp. 511–537
20 Ramchandran, A., Alexander, G.C., and Spee, R.: 'Off-line parameter estimation for the doubly-fed machine'. Proc. Conf. on Industrial electronics, control, instrumentation, and automation, 1992, Vol. 3, pp. 1294–1298
21 Ramchandran, A., and Alexander, G.C.: 'Frequency-domain parameter estimations for the brushless doubly-fed machine'. Conf. Record of PCC 1993. Power Conversion Conference, Yokohama, 1993: IEEE, 1993, pp. 346–351
22 Slemon, G.R.: 'Modelling of induction machines for electric drives'. Conf. record of the IEEE Industry Applications Society Annual Meeting, 1989, Vol. 1, pp. 111–115
23 Zhigljavsky, A.A.: 'Theory of Global Random Search' (Kluwer, 1991)
24 Ho, Y.C., and Pepyne, D.L.: 'Simple explanation of the no-free-lunch theorem and its implications', *J. Optim. Theory Appl.*, 2002, **115**, (3), pp. 549–570
25 Matsumoto, M., and Nishimura, T.: 'Mersenne twister: A 623-dimensionally equidistributed uniform pseudorandom number generator', *ACM Trans. Model. Comput. Simul.*, 1998, **8**, (1), pp. 3–30
26 Tang, Z.B.: 'Adaptive partitioned search to global optimization', *IEEE Trans. Autom. Control.*, 1994, **39**, (11), pp. 2235–2244
27 Carlson, A.B.: 'Circuits: engineering concepts and analysis of linear electric circuits' (Wiley, New York, 1996)

11 Appendix

11.1 Parameter extraction optimisation method

11.1.1 General optimisation problem: The optimisation problem to be solved is a nonlinear least squares problem, and can be stated as

$$\text{Given } Y_i \in \mathbb{R}^k,\ P \in \mathbb{R}^n,\ U \in \mathbb{R}^{k\times m},\ F_i : P, U \mapsto \mathbb{R}^k,\ i \le l$$

$$\text{find } P : \min_{P \in W\mathbb{B}+P_0} \sum_{i=1}^{l} S_i \| Y_i - F_i(P,U) \|_2 \qquad (17)$$

where F_i is a function which estimates the ith measured output for a particular parameter vector, P. U is a matrix of input data points where each row is an individual data point. Y_i is a vector of the measured ith output data due to U. There are k input/output data pairs and m different measured outputs (i.e. U has k rows and m columns). S_i is a scalar weight applied to the ith output error. So there are n parameters, m inputs, k data points for each input and l outputs.

Furthermore, F_i is defined as

$$F_i(P,U) = \begin{bmatrix} f_i(P,u_1) \\ \vdots \\ f_i(P,u_k) \end{bmatrix} \quad U = \begin{bmatrix} u_1 \\ \vdots \\ u_k \end{bmatrix} \qquad (18)$$

where $f_i : P, u_j \mapsto \mathbb{R}^1$.

$W\mathbb{B} + P_0$ represents the set of possible parameter values which is chosen from a rectangular set (as $\mathbb{B}$ is a hypercube), centred on P_0 with corners at $P_0 \pm \text{diag}(W)$. Clearly the value of P that gives the minimum cost function value will, in general, not be unique. As stated this is a nonconvex optimisation problem, and therefore difficult to solve [23].

To solve this optimisation problem we use a simple (or crude) random search (also known as a Monte Carlo method). For practical and theoretical details of the algorithm see, for example, [23]. The principal advantage of a simple random search, for our purposes, is its strong resilience to measurement noise and modelling error while guaranteeing convergence to the global minimum. Furthermore, because it requires no gradient information there is no need for any a priori information about the particular cost function, and it can be shown that without any such information then a simple random search is as efficient as any other method, in reaching the global minimum [24]. The simplicity of the algorithm means that implementation is straightforward, and because the method does not depend on the cost function chosen, the algorithm can be applied to different cost functions without modification.

This search is performed across $W\mathbb{B}+P_0$ to find $Q=\{q_1,\cdots,q_N\}$ where $Q:\sum_{i=1}^{m}S_i\|Y_i-F_i(q,U)\|_2\leq\gamma$, where $\gamma>0$ is an acceptable value for the cost function to take. We generate guesses for candidate q_ks using the Mersenne twister [25], a fast uniform random number generator with a long repetition period. Having found Q we then find the, q_k corresponding to the minimum cost, $K_{\min}$. This q_k, called q_{opt} henceforth, is an estimate of the global minimiser and $K_{\min}$ is an estimation of the global minimum. Furthermore the standard deviation of Q gives an indication of how much confidence one should have in taking q_{opt} as the global minimum.

Although the efficiency could be increased by using a multistart [23] or probabilistic branch and bound algorithm (such as [26]), the additional complexity of the algorithm, and requirements to have some appreciation of the modelling error and noise, make these algorithm less appealing than they might first appear. Furthermore there is a trade-off between increased complexity in the algorithm against the decreased number of iterations required.

11.1.2 Application to BDFM: Notice that thus far it has not been necessary to specify what the measured outputs, Y are, or what the estimation functions F are.

We desire to choose the inputs and output such that they are easy to measure 'terminal' quantities. Therefore we are restricted to the stator voltages, currents, the torque and the rotor speed. Furthermore due to the substantial difficulty of trying to measure the phase difference between stator 1 and stator 2 quantities we restrict ourselves to magnitude measurements of stator 2 quantities.

In simple induction mode operation there are two inputs, three measured outputs, four parameters and N_s data points. The subscript simple/1 is used to indicate simple induction mode referred to stator 1. Y is chosen as follows:

$$Y_{\text{simple/l}_1}=\begin{bmatrix}T_1\\ \vdots\\ T_k\end{bmatrix}\quad Y_{\text{simple/l}_2}=\begin{bmatrix}\Re\{I_{1_1}\}\\ \vdots\\ \Re\{I_{1_k}\}\end{bmatrix}\tag{19}$$

$$Y_{\text{simple/l}_3}=\begin{bmatrix}\Im\{I_{1_1}\}\\ \vdots\\ \Im\{I_{1_k}\}\end{bmatrix}\quad U_{\text{simple/l}_2}=\begin{bmatrix}\omega_{r_1} & V_{1_1}\\ \vdots & \vdots\\ \omega_{r_k} & V_{1_k}\end{bmatrix}\tag{20}$$

$$P_{\text{simple/l}}=\begin{bmatrix}R_1\\ R'_r\\ L'_r+L''_{m_2}\\ L_{m_1}\end{bmatrix}\tag{21}$$

$F_{\text{simple/1}}$, can be derived from the referred equivalent circuit, Fig. 11, taking $I''_2=0$

$$T=f_{\text{simple/l}_1}(P_{\text{simple/1}},u_{\text{simple/1}})\tag{22}$$

$$\Re\{I_1\}=f_{\text{simple/l}_2}(P_{\text{simple/1}},u_{\text{simple/1}})\tag{23}$$

$$\Im\{I_1\}=f_{\text{simple/l}_3}(P_{\text{simple/1}},u_{\text{simple/1}})\tag{24}$$

If $U_{\text{simple/l}_1}$ is chosen so that the BDFM is exercised over a range of speeds such that the slip (2) varies substantially, say from 0 to 1.5, it can be shown from the equivalent circuit that each $f_{\text{simple/l}_1}$ depends strongly on each element of $P_{\text{simple/1}}$, therefore there is a unique $P_{\text{simple/1}}$ which solves the optimisation problem. However, due to the presence of measurement noise and modelling error this will not necessarily be the case. Solving this optimisation problem as outlined in Section 11.1.1 gives the parameters indicated in (21).

However, we have not used $|V_2|$ as one of the measurable outputs. It can be seen from Fig. 11, with $V''_2=V_2\frac{N_1}{N_2}$ (from Fig. 9)

$$|V_2|\frac{N_1}{N_2}=|I'_r\omega_1|L_{m_2}\tag{25}$$

and the ratio of the turns ratios, N_1/N_2 is unknown. Therefore all that can be achieved is the determination of $(N_2/N_1)L_{m_2}$. It is proposed therefore that, having determined the optimal parameter set, linear least-squares is used to determine $(N_2/N_1)L_{m_2}$

$$\frac{N_2}{N_1}L_{m_2}=A^T(A^TA)^{-1}\begin{bmatrix}|I'_{r_1}\omega_{1_1}|\\ \vdots\\ |I'_{r_k}\omega_{1_k}|\end{bmatrix},\quad A=\begin{bmatrix}|V_{2_1}|\\ \vdots\\ |V_{2_k}|\end{bmatrix}$$

and $\left|I'_{rj}\right|$ are calculated from Fig. 11 using the optimal parameter set.

In cascade induction mode operation there are two inputs, four measured outputs, six parameters and N_c data points. The subscript cascade/1 is used to indicate simple induction mode referred to stator 1. Y is chosen as follows:

$$Y_{\text{cascade/l}_1}=\begin{bmatrix}T_1\\ \vdots\\ T_k\end{bmatrix}\quad Y_{\text{cascade/l}_2}=\begin{bmatrix}\Re\{I_{1_1}\}\\ \vdots\\ \Re\{I_{1_k}\}\end{bmatrix}\tag{26}$$

$$Y_{\text{cascade/l}_3}=\begin{bmatrix}\Im\{I_{1_1}\}\\ \vdots\\ \Im\{I_{1_k}\}\end{bmatrix}\quad Y_{\text{cascade/l}_4}=\begin{bmatrix}|I_{2_1}|\\ \vdots\\ |I_{2_k}|\end{bmatrix}\tag{27}$$

$$U_{\text{cascade/1}}=\begin{bmatrix}\omega_{r_1} & V_{1_1}\\ \vdots & \vdots\\ \omega_{r_k} & V_{1_k}\end{bmatrix}\quad P_{\text{cascade/1}}=\begin{bmatrix}R_1\\ R'_r\\ L'_r\\ L'_{m1}\\ R''_2\\ \frac{N_1}{N_2}\end{bmatrix}\tag{28}$$

$F_{\text{simple/l}_1}$ can be derived from the referred equivalent circuit, Fig. 11, taking $V''_2=0$

$$T=f_{\text{simple/l}_1}(P_{\text{simple/1}},u_{\text{simple/1}})\tag{29}$$

$$\Re\{I_1\}=f_{\text{simple/l}_2}(P_{\text{simple/1}},u_{\text{simple/1}})\tag{30}$$

$$\Im\{I_1\} = f_{\text{simple/l}_3}(P_{\text{simple/1}}, u_{\text{simple/1}}) \quad (31)$$

$$|I_2| = f_{\text{simple/l}_4}(P_{\text{simple/1}}, u_{\text{simple/1}}) \quad (32)$$

As for the simple mode $U_{\text{cascade/l}_1}$ is chosen so that the BDFM is exercised over a range of speeds such that the slip (2) varies substantially, it can be shown from the equivalent circuit that each $f_{\text{cascade/l}_1}$ depends strongly on each element of $P_{\text{cascade/1}}$. However, $f_{\text{cascade/l}_i}$ also depends on L_2, and it is not possible to determine this from the measured outputs. Therefore the value extracted from the simple/2 is used, and is explicitly included in $f_{\text{cascade/l}_i}$. In these circumstances there is a unique $P_{\text{cascade/1}}$ which solves the optimisation problem, with the same caveat regarding noise and measurement error as in the simple mode procedure. Again the optimisation problem is solved as outlined in Section 11.1.1 giving the parameters indicated in (28).

Although the original problem (17) contained S_i, a weight, it is set to unity without exception for the applications described. The choice of weight can improve the algorithm by compensating for different scaling of the measured outputs, for example if $|V_2|$ had been included as a measured output then it would have been appropriate to scale down the effect of the error on this measurement as it is typically two orders of magnitude larger than the other measured outputs.

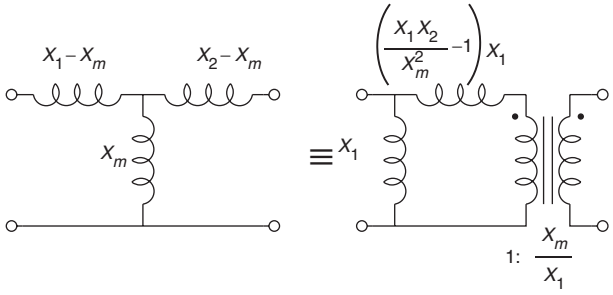

Fig. 15 *Equivalent forms of 'T' and 'Γ' networks*

11.2 Equivalent networks

Figure 15 shows equivalent forms of the 'T' and 'Γ' networks, details can be derived using, for example, [27].

Cross-magnetisation effects in electrical machines

P.J. Tavner

Abstract: Examples of cross-magnetisation effects in electrical machines are collated and the physical characteristics of the phenomena are reviewed qualitatively. New experimental results to clarify the phenomena are introduced. This subject has also been called a cross-axis, cross-magnetisation, cross-saturation, intersaturation or cross-reactance effect. Cross-magnetisation encompasses the magnetic behaviour of saturable machine materials when the vector of the main magnetomotive force (MMF) is applied in a direction that is not geometrically or analytically favoured in the magnetic structure of the machine. The phenomenon is important because it controls the magnetic behaviour of components that are closest to the highest field strengths in operating machines. A number of cases in electrical machines where this can occur are considered and conclusions drawn. These can be used to allow the cross-magnetisation effects from field calculations of electrical machines to be quantitatively represented and qualitatively explained, particularly for machines of unusual topology, in which key components are not subjected to a magnetic field in the preferred direction.

List of symbols

x	horizontal axis, in the plane of laminations, m
y	horizontal axis, in the plane of laminations, m
z	vertical axis, perpendicular to the plane of laminations, m
B	flux density, T
B_{direct}	flux density on the direct-axis, T
B_{cross}	flux density on the cross-axis, T
B_r	remanence of a permanent magnet, T
B_s	saturation flux density, T
H	magnetic field strength, AT/m
J	current density, A/m^2
K	constant associated with the characteristic of a permanent magnet
M	permanent magnetisation of a permanent magnet, AT/m
μ_0	permeability of free space
μ_r	relative permeability of a permeable material
γ	stacking factor of a laminated core

1 Introduction

This paper collates and reviews qualitatively a number of magnetic phenomena in electrical machines, known collectively as cross-magnetisation. The phenomena have also been called, by various authors, cross-axis, cross-saturation, intersaturation or cross-reactance effects. Considerable space is devoted in the paper to reviewing these earlier references to bring out the essential principles. The paper then builds on these principles, presenting additional experimental results that clarify the phenomenon of cross-magnetisation.

IEE Proceedings online no. 20040345

doi:10.1049/ip-epa:20040345

Paper first received 25th July 2003 and in revised form 26th November 2003. Originally published online: 16th March 2004

The author is with the School of Engineering, South Road, Durham DH1 3LE, UK

Cross-magnetisation is the behaviour of machine magnetic materials in which the main driving magnetomotive force (MMF) is not applied in the geometrically favoured direction of the magnetic component, so that there is some magnetisation of the component across the favoured direction. Figure 1 shows an ellipsoid of soft magnetic material placed in a field that does not act along its geometrically favoured direction, which, as a result, is not magnetised along its major axis. Cross-magnetisation has an important effect on the resultant field.

The study of cross-magnetisation effects has aroused controversy in the past among practising electrical engineers, who summarise the performance of machines using analytical models, which simplify the magnetic core and its behaviour. The source of this behaviour is the transfer of

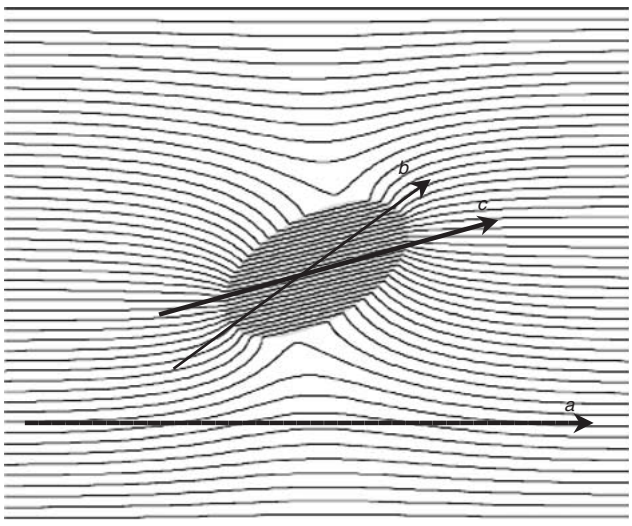

Fig. 1 *Magnetisation of a soft iron ellipsoid with the vector of the main DC MMF applied in a direction not geometrically or analytically favoured in the magnetic structure, i.e. it is not along the major axis of the ellipsoid*
a Applied MMF
b Major axis of ellipsoid
c Resultant field in ellipsoid

energy through the magnetic core of the machine under the action of the exciting currents: the MMF. That energy flow is constrained by the geometry of the core and modified by its magnetic properties. Since Faraday we have become accustomed to using magnetic flux to characterise that energy flow, and engineers subdivide that flux to suit physical models for the machine. However, we must remember that flux as such, and the engineer's subdivision of it, into lines and tubes, is a figment of our physical imagination. To analyse machines we have synthesised that flux into orthogonal components, to represent direct and quadrature magnetisation, and we have synthesised the phasors, representing the EMFs induced in coupled circuits, into inphase and quadrature components. The fluxes so synthesised do not always lie in a geometrically favoured direction with respect to the magnetic material of the machine and the non-linear behaviour of that material can lead to some unexpected results when the synthesised axes are considered in isolation.

What really matters is the geometry and magnetic properties of the machine core and its proximity to the associated current carrying conductors. This paper investigates the following phenomena:

(i) The behaviour of soft magnetic core materials in salient or non-salient machines, in which the main flux is divided between the direct and quadrature axes.

(ii) The behaviour of hard, permanent magnet materials in a machine under an MMF not aligned with the magnetised direction of that material.

(iii) The behaviour of laminated, soft, magnetic materials under the action of MMF components perpendicular to the plane of the lamination.

The paper concentrates on magnetostatic and therefore steady-state cross-magnetisation effects, but shows the influence of eddy currents, which can lead to transient cross-magnetisation effects when changing flux threads solid conducting magnetic components.

Finally the paper draws conclusions that can be used to allow the cross-magnetisation effects from field calculations of electrical machines to be quantitatively represented and qualitatively explained, particularly for machines of unusual topology.

2 Basic principles

2.1 Why is cross-magnetisation important?

Cross-magnetisation is not simply an unusual physical phenomenon of academic or historic interest but is important to modern machine applications because it concerns the behaviour of magnetic components closest to the highest field strengths in operating machines.

The development of machines in challenging applications is leading to higher loadings in unusual magnetic configurations, where the MMF cannot necessarily be aligned to principal component axes. This is clearly true in:

- permanent magnet machines for marine propulsion, such as the transverse flux machine
- synchronous reluctance machines with unusual rotor sections to promote reluctance behaviour used in high steady-state and transient torque applications
- linear machines applied for high force actuator applications.

Engineers represent the magnetic performance of machines by the use of models: equivalent circuits and analytically or numerically-solved flux plots. These models are representations and frequently give rise to unexpected results, because of the complexity of the field patterns, because components are being magnetised in unusual ways or because the model itself is limited. Underlying the model is the true field distribution in real machine components. This distribution is guided by the windings and geometry of the machine and also by the operation of the machine.

In the steady state, fluxes are stationary with respect to machine components and cross-magnetisation may be present due to geometrical effects, whereas in the transient conditions fluxes are altered by eddy currents where they thread conducting components, altering the cross-magnetisation. So steady-state and transient variants of cross-magnetisation can occur.

This paper does not develop a technique to be applied directly to machine models but describes cross-magnetisation in sufficient detail in different situations so that engineers can determine how best to apply their models to a particular machine arrangement. A clear physical understanding of the flux distribution is the way to resolve unexpected model results.

2.2 Sources of the magnetic field

The resultant field in a magnetic core body is affected by:

- the applied MMF
- the geometrical shape of the magnetic core
- the permeability function of the magnetic core
- the conductivity of the body.

However, in order to understand what is happening under an MMF that is not applied in the geometrically- or analytically-favoured direction, it is necessary to break these properties down into more physically understandable sources. The sources of magnetic field are important to synthesise its effect in the complex geometry of an electrical machine [1]. There are two types of source in the magnetic circuit: electric currents in conducting materials and magnetic sources in the iron. Mathematically there are three relationships:

$$\text{curl } H = J \tag{1}$$

$$\text{div } B = 0 \tag{2}$$

$$B = \mu_0 \mu_r H \tag{3}$$

The first is the statement that the MMF is equal to the ampere-turns, the second that magnetic flux is continuous and the third links the magnetising force to the flux density. Mathematically, any vector field is uniquely defined if its curl and divergence sources are specified. It is noted that the relationship of (3) can be taken either as a statement about the divergence of H or the curl of B, which determines the type of sources needed to represent the iron. It is important to the argument to regard the permeability μ_0, μ_r as a specification of magnetic sources rather than as a property of matter. Because it is easier to envisage divergence sources and to handle them mathematically, the permeability is chosen as a specification of divergence sources of H that are given the name magnetic polarity.

The two types of sources are, therefore, conduction currents and magnetic polarities, and the field under consideration is the H field, the magnetomotive force, MMF. Both types of sources can be either explicit or implicit. Explicit current sources are the assigned currents in the machine windings and implicit current sources are eddy currents induced in conducting parts, although in general in this paper they are not considered. Explicit polarity sources

are those due to permanent magnetism and the polarity of soft magnetic materials.

The magnetic field depends on both the strength and location of the sources. There is no difficulty about the explicit current sources in the windings, because both their strength and their position are determined. The problem of eddy currents is more difficult. However, because the energy associated with eddy currents has to diffuse into the material from the surface, the currents will be strongest near the surface and may, under certain circumstances, be regarded as current sheets. Moreover, in laminated cores, the dominant eddy currents flow in the plane of the laminations.

Magnetic polarity in iron arises from a dipole distribution throughout the volume of the magnetic core. The divergence of this dipole distribution determines the pole distribution. Inside the material, a divergence of the dipole distribution arises from a spatial variation of the permeability. The permeability variations within the material are generally small compared to the sharp variation at an iron/air interface. It is usually therefore a close approximation to assume that the polarity sources are confined to the surface of the iron. This is so in Fig. 1, where polarities developed on the surface of an ellipsoid, placed in an MMF at an angle to its major axis, act to drive the flux within the ellipsoid close to that axis. It is clear, however, that they are not entirely successful and the component exhibits a cross-magnetisation, which can be explained by the polarities developed on its surface. The surface polarities represent the shape effect of the magnetic body.

In a magnetic core that is saturated, the volumetric sources due to the spatial variation of the permeability can become important to the internal behaviour of the flux, and this is vital to a physical understanding of some cross-magnetisation effects in electrical machines. Therefore, the method of sources is not limited to an assumption of infinite permeability. In addition, laminated cores containing successive iron/air surfaces, will also exhibit considerable surface pole strength within the core and, when these are not matched on successive laminations, this represents a distributed volume pole strength. Similarly polarity will be associated with ducts, holes and embedded magnets in the material, which will be vital to the way in which a core responds to the applied MMF. This approach is described in [1].

The behaviour of sources can help to segregate the physical processes occurring in complex field situations in a rather better way than is possible simply by segregating fluxes along orthogonal axes.

3 Cross-magnetisation in electrical machines

3.1 Cross-magnetisation between direct and quadrature axes of circular structures

This phenomenon is the easiest to understand and yet has aroused the most controversy. It concerns the effect in AC cylindrical machines analysed along orthogonal direct and quadrature axes in the plane of any laminated structure, whereby the field on one axis affects the field on the other. In this case the body being magnetised is the main magnetic circuit of the machine, as shown in Fig. 2. That body is symmetrical in shape but may have saliency and non-uniform magnetic properties. The problem has been studied for both salient and non-salient cylindrical structures.

The electrical engineer finds it easiest to analyse the machine on orthogonal axes, assuming that they are therefore decoupled. But of course they are not, because the MMFs of the two axes occupy the same

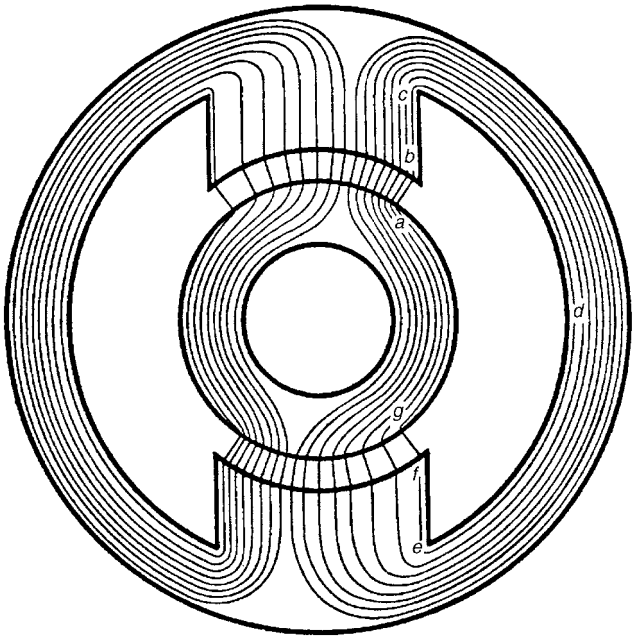

Fig. 2 *Magnetisation of a two-pole DC electrical machine, taken from Moullin [2], showing the effect of load or armature reaction*

magnetic body and those fields cannot be artificially separated and then linearly superposed without some loss of precision.

The main flux behaviour in an AC machine is no different from the flux distortion due to armature reaction on DC machines, described in careful detail by Moullin [2], who said that: 'it can never be exactly true that the fluxes due to two sets of (orthogonal) currents can be added when both sets of currents are active simultaneously'. Moullin demonstrated by test the cross-magnetisation phenomenon. The sources at work here are the rotor and stator currents and surface polarities, which would be clearly visible on a salient structure (see Fig. 2). But there are also volume polarities within the core owing to the variation of the permeability in the saturable parts.

Arguments first arose in the application of *d-q* analysis to cylindrical, non-salient, induction machines, when the prime objective was the accurate prediction of torques during transient operation. Brown, Kovacs and Vas [3] provided an analytical representation of the cross-magnetisation effect, citing the experimental experience of a number of workers of the phenomenon in these machines.

But Kovacs [4] repudiated the concept for a cylindrical machine with infinite permeance, stating that: 'Cross-magnetisation has no physical significance; it is an erroneous conclusion, obtained from otherwise correct mathematical formulation'. Kovacs concluded that such effects could only be caused by saliency. The statement above is correct for the assumptions that Kovacs prescribed. However, those assumptions, of cylindricality and infinite permeance, had excluded the possibility of the flux pattern being affected by rotor and stator teeth, with non-uniform surface polarities on their flanks, or by volume polarities within the core. However, these sources must occur in a practicable machine.

Later work by Vas Hallenius and Brown [5] established the reality of the phenomenon in a practicable, AC, induction motor and demonstrated it by measurements, remarkably similar to those described by Moullin [2]. Vas said: 'it has been shown that the phenomenon of cross-saturation exists in saturated smooth-air-gap machines and

it is similar to the phenomenon of the demagnetising effect of cross-magnetising armature reaction in DC machines'. Macdonald Reece and Turner [6] demonstrated the process for a cylindrical non-salient machine by finite-element solutions. Macdonald showed the effect of the magnetisation current on each of two orthogonal axes by synthesis of their associated flux plots. Figure 3*a* is the skewed flux plot of such a machine on load (compare with Fig. 2). Figure 3*b* shows the direct-axis flux plot using the permeabilities calculated from Fig. 3*a*, clearly showing cross-magnetisation. The source of the cross-magnetisation is primarily the non-uniform distribution of surface polarities on the flanks of teeth and volume polarities in the core due to permeability divergence. These flux plots dramatically demonstrate the effect of surface and volume polarities on the flux, when saturation changes the permeability. Macdonald said: 'Detailed examination of generator performance with the finite-element method has shown that under saturated conditions the windings on one axis produce flux on the other giving rise to cross-reactances'.

These principles are now accepted, and Levi and Levi [7, 8] have incorporated cross-saturation in synchronous and induction machines to obtain more accurate steady-state and transient torque predictions. For other geometries, such as the reluctance synchronous machine, new rotor shapes allow machines to develop higher torques, but the flux path needs to be shaped to obtain optimum performance.

El Serafi and Kar [9] have analysed the *d* and *q*-axis saturation of synchronous machines using a variety of methods including, in their Method 4, an equivalent permeability function. They do not explicitly refer to cross-magnetisation but the consequences of their use of an angular-dependent saturation function will inevitably result in cross-magnetisation effects, as described by Macdonald [6]. Kamper and Volschenk have shown [10] that the behaviour of the synthetically segregated fluxes interact in the same way as those in more conventional machines, saying that: 'Good agreement is reached between measured and calculated results, which confirms the effect (on these machines) of cross-magnetisation'. Kamper's results show the effect of the embedded sheets of surface polarity in the rotor body of this type of machine. Vagati, Pastorelli, Scapino and Franceschini [11] have also incorporated cross-magnetisation into a synchronous reluctance machine to obtain accurate torques under transient and overloaded servomotor operation, and Stumberger, Stumberger, Dolinar and Hamler [12] have applied similar techniques to a linear synchronous reluctance motor.

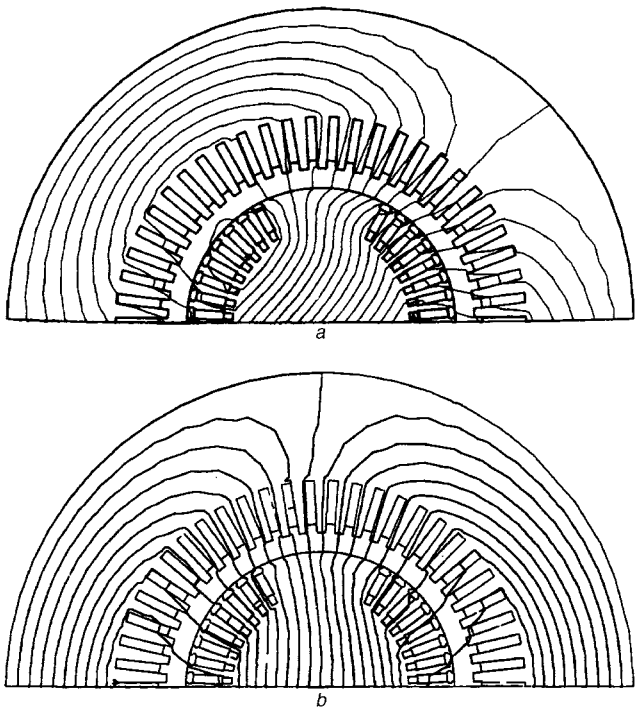

Fig. 3
a Magnetisation of a two-pole AC turbogenerator, taken from Macdonald [6], showing the effect of load or armature reaction. Compare with Fig. 2
b Effect of the permeability distribution of Fig. 3*a* on the direct-axis flux, taken from Macdonald [6]. The Figure clearly shows cross-magnetisation

3.2 Cross-magnetisation in permanent magnet structures

Permanent magnet materials are making a major contribution to the development of both large and small high-performance machines. They bring the potential of achieving higher flux densities, without the need for high currents and consequential losses, thereby achieving a higher power-to-weight ratio.

By the shaping of the permanent magnet materials, they also allow the flux path to be designed for maximum performance. However, permanent magnets are usually embedded into a soft magnetic material and there will always be points in the machine cycle when the magnetic field is not directed in the favoured direction of the permanent magnet. In this case, surface polarisation at the interfaces will create cross-magnetisation effects that will be important in determining the overall performance of the machine.

Binns Low and Jabbar [13] studied the effect of a permanent magnet sample in air subjected to an MMF at right angles to the permanent magnetisation in an arrangement shown in Fig. 4. Making detailed measurements both along and at right angles to the axis of magnetisation of the polymer-bonded rare-earth magnet material showed that even under a very large cross-magnetising field, of up to 180 kAT/m, the effect on the permanent magnet was surprisingly small. The authors then modelled the behaviour of the soft and hard magnetic materials for use in numerical calculations, using a permeability tensor, as follows:

$$\begin{vmatrix} B_x \\ B_y \end{vmatrix} = \begin{vmatrix} \mu_0\mu_x & (K_1 + K_2 B_{xi}/B_r) \\ 0 & \mu_0\mu_y \end{vmatrix} \begin{vmatrix} H_x \\ H_y \end{vmatrix} + \begin{vmatrix} M_x \\ M_y \end{vmatrix} \quad (4)$$

The equation shows in the first line the effect of cross-magnetisation between the x and y axes.

Binns' experiments showed that, for a polymer-bonded rare-earth magnet, $K_1 = 0.09\mu_0$ and $K_2 = -K_1$, and B_{xi}/B_r is the ratio of the flux density at the pole of a permanent magnet compared to the remanence, B_r, of the material. This varies with the aspect ratio of the magnet but, in the experimental example, was probably about 0.5. Therefore the cross-magnetisation term in the matrix above was of the order of $0.09 \times 0.5 = 0.045$, compared to a value of 1.1 for μ_x and μ_y. Therefore strong cross-magnetisation produced only a 4.5% reduction of the main magnetisation. This was verified in Binns' experiments when a cross-magnetising field of 180 kAT/m was applied to a permanent magnet with a polarisation of 0.55 T.

Binns then used the tensor in a numerical prediction of performance for a permanent magnet, which confirmed what a remarkably small effect cross-magnetisation had on the flux-form at the pole-face of the permanent magnet,

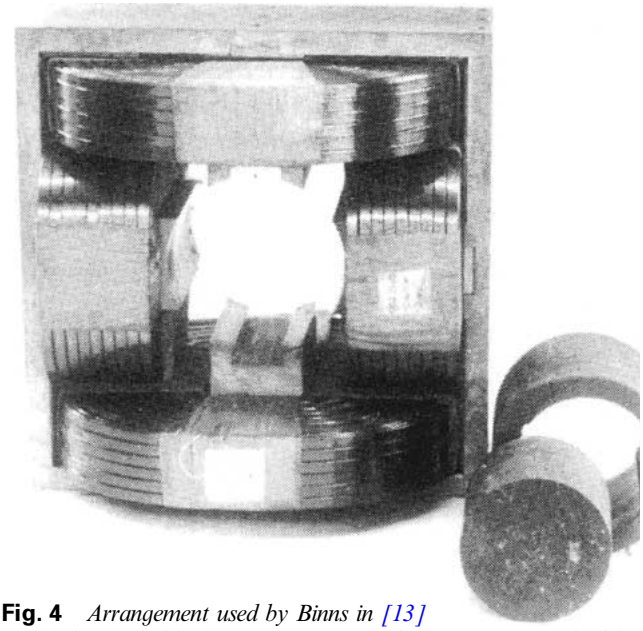

Fig. 4 *Arrangement used by Binns in [13]*
sample is a cylindrical permanent magnet being cross-magnetised by two coils. The cylindrical sample is shown extracted from the rig on the right hand side. A schematic of the arrangement is shown in Fig. 10*a*

implying that it is extremely difficult to divert the flux pattern of a strong permanent magnet. The reason for this is that the permanent magnets were air-cored and any attempt to cross-magnetise the magnet had to overcome the exceptionally strong surface polarities on the flanks of the magnet. Binns' experiment did not take account of effects on the magnet when embedded in soft magnetic material. We will return to this in a later experiment.

3.3 Cross-magnetisation in laminated structures

This problem arises wherever laminated cores are subjected to a flux normal to the plane of the laminations, for example in the core legs or magnetic shields of transformers and in the end regions of rotating electrical machines with laminated stator cores. The author first encountered cross-magnetisation in attempting to analyse the penetration of leakage flux into the annular core end-region of large rotating electrical machines, as discussed in [1] (see Fig. 5).

A detailed theoretical exposition of the problem with a numerical solution was made by Carpenter [14] and a numerical microstudy by Yagisawa, Takekoshi and Wada [15]. Figures 6 and 7 are taken from [14] and [15], respectively, and show a calculated pattern of flux penetration into a laminated core, including the effect of eddy currents.

Carpenter's theoretical approach in [14], shown in Fig. 6 reflects, some of the internal sources of the field. A helpful aspect is that Carpenter shows that the internal magnetic field of the laminated core can be represented by three, separate, superposable modes, related to the shape of the laminated body:

- Mode 1, satisfying Laplace's equation, representing the flux flowing through the laminations (see Fig. 6*b*). This is the magnetostatic flow of flux in the body and can be compared to later Fig. 8*b* and *c*.
- Mode 2, satisfying Poisson's equation, representing the flux constrained to the skin depth on the edge of the body (see Fig. 6*c*). This is the situation for flux penetration into a solid steel body, where flux is effectively excluded from the centre of the body.

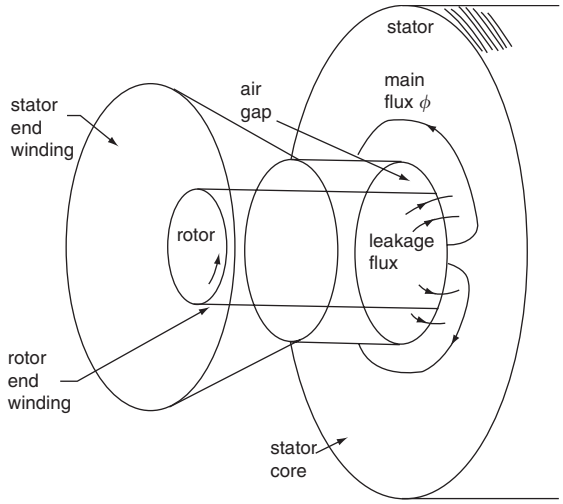

Fig. 5 *Main flux and leakage flux in the core end region of a rotating machine*

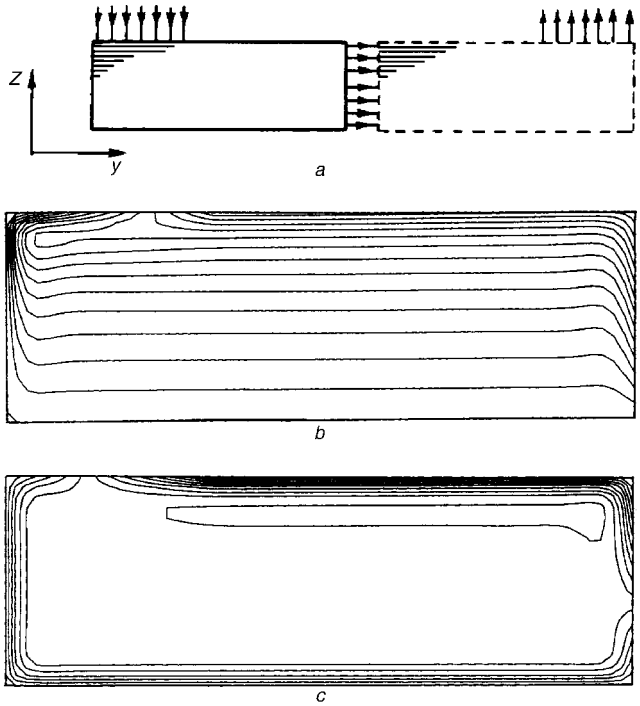

Fig. 6
a Geometrical arrangement for flux penetration into a laminated core. Taken from [14]
b Calculated plot of penetration of AC flux into the core
AC Flux, laminated steel, saturable material
Taken from [14], calculated using a T-omega method
c Calculated plot of penetration of AC flux into the core. AC flux, solid steel, saturable material. Taken from [14], calculated using a volume permeability

- Mode 3, representing the transfer of flux between Modes 1 and 2, also visible in Fig. 6*c*.

Carpenter's numerical representation, used the electric vector potential $\boldsymbol{T}$ ensuring that the eddy currents were constrained in the laminar planes of the laminar structure. However, it did not represent the effect of the surface polarities on the lamination flanks. The method was subsequently used to predict the penetration fields in a transformer core leg.

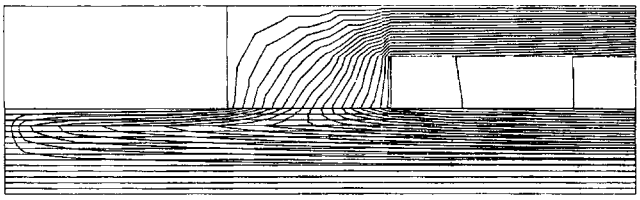

Fig. 7 *Calculated plot of penetration of AC flux into a laminated steel structure*
AC flux, laminated steel, saturable material
Taken from [15], calculated using a resultant axial permeability

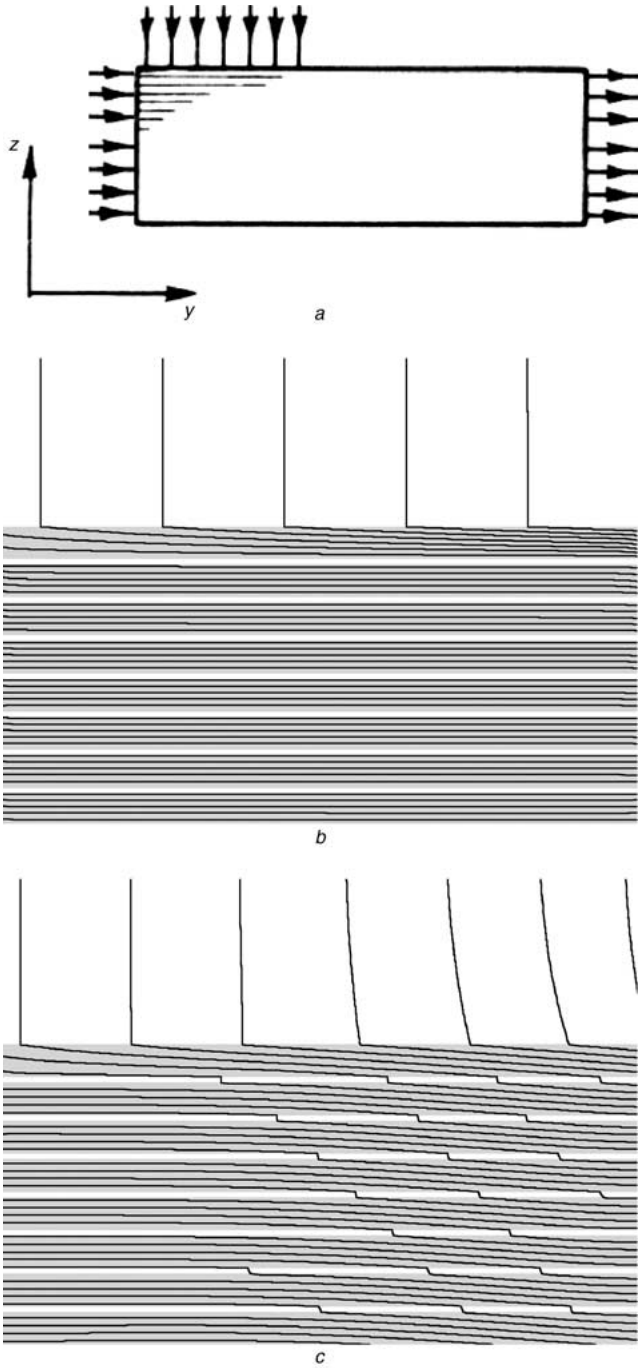

Fig. 8
a Geometrical arrangement for flux penetration into the end region of a rotating machine
b Leakage flux entering the end of the core. DC flux, laminated steel, linear material
c Leakage flux entering the end of the core. DC flux, laminated steel, saturable material. Note how the flux penetrates further in the saturable core

Yagisawa *et al.*'s approach [15], shown in Fig. 7, used a magnetic yoke to direct flux perpendicular to the laminations in a manner similar to that of Fig. 6*a* and a resultant axial permeability was used in his calculations. The flux penetration pattern appears similar to that of Carpenter [14].

The leakage flux penetration problem at the ends of rotating electrical machines, such as shown in Fig. 5, has been considered by authors using numerical techniques, including Jacobs, Minors, Myerscough, Rollason and Steel [16], Reece and Preston [17], and Mecrow, Jack and Cross [18]. These authors solved the problem in the ducted, laminated, end-region core of a turbogenerator by applying a resultant axial permeability, calculated by considering the reluctance of the composite axial path. Reference [16] used the following expression for the axial flux density, B_z, with the so-called axial permeability, μ_z:

$$B_z = \mu_0 \mu_z H_z \tag{5}$$

$$\mu_z = 1/(1 - \gamma + \gamma/\mu_r) \tag{6}$$

where $\cdot\gamma$ is the stacking factor of the laminated core. In using this expression special care was needed to define the permeability of the saturating lamination steel, because this has a large effect on the resultant axial permeability. It should be noted that this representation is a simplification. Hammond [19] says the use of the term 'axial permeability' is helpful but that: 'The surfaces of the laminations play a crucial role in deflecting flux from the axial into the radial and circumferential directions. It may be better therefore to talk of "axial reluctance" rather than "axial permeability".

To understand the situation it is helpful to study a flux plot for this type of penetration. Figure 8*a* shows the flux system in a laminated machine core end, such as shown on Fig. 5. Figure 8*b* shows the condition when the soft magnetic material has a constant permeability of about 1500, and Fig. 8*c* shows the effect, under the same excitation conditions, when a saturable material is used; the properties are those given later in the paper. These flux plots were obtained using a finite-element modelling package, MEGA, to solve the magnetostatic problem.

In Fig. 8*b* the magnetic core is carrying the heavy main flux of the machine in the plane of laminations but there is large leakage flux at the core-end, caused by the core-end itself and by end winding leakage flux. This creates a surface polarity source on the core-end, which is essential to support and drive the main flux around the core. The leakage flux is entering the core-end perpendicular to the plane of the lamination. As it joins the main flux, it is diverted into the plane of the lamination by the polarity sources on its flank but, because the leakage flux is significant there is a build-up of flux in the end lamination.

In the saturable example (Fig. 8*c*), the end lamination cannot carry this additional flux because it saturates. Leakage flux therefore has to penetrate deeper into the core, as can be seen by comparison of Figs. 8*b* and *c*. Saturation ensures that the flux is evenly distributed between successive laminations. This process develops surface polarities on the exit flank of each lamination and eddy current sources in the plane of the lamination, although these are not shown in Fig. 8 because it was a purely magnetostatic solution.

This dramatically demonstrates the effect of lamination surface polarities on the flux when saturation changes the permeability. If the MMF is strong enough it can also drive flux into the plane of the air gap between the laminations, creating surface polarities on the subsequent lamination, which do not match those on the preceding one. This is a consequence of saturation. Therefore those polarity sources

are unmatched and ultimately act as a volume polarity source. In summary:

- Surface polarities guide the leakage flux circumferentially into the lamination.
- Volume polarities are effectively created in the saturated region by the presence of flux in the airgap between laminations.
- Surface polarities on lamination flanks drive planar eddy currents within laminations generating losses.
- Losses decay axially the further the leakage flux penetrates into the core.
- Surface polarities and eddy currents adjust the axial penetration of the leakage flux into the laminated core.
- The consequence is that circumferential flux is uniformly distributed between the laminations, a well known experimental observation of saturated, laminated cores.
- These surface and volume polarities and eddy currents are the natural support mechanism for the main flux in a finite, laminated, core.

The importance of surface effects in large laminated cores was pointed out by Mecrow, Jack and Cross [18], observing that the presence of radial cooling ducts greatly increases the axial reluctance of the core and turns the axial leakage flux into the circumferential direction.

It is interesting to compare the flux plots from the different representations of laminated materials in Figs. 6, 7 and 8. Figures 6 and 7 represent a specific condition in which the total flux of the circuit is being injected at right angles to the plane of the laminated core, such as occurs in a magnetic shunt in a power transformer. Figure 8, however, represents the addition of a small but significant leakage to the main flux of the magnetic circuit, as occurs at the end of a rotating machine (Fig. 5). It is clear in this latter case that saturation has a significant effect on the penetration of the leakage flux, and therefore on the cross-magnetisation of laminations at a core end. To summarise, penetration is intimately affected by:

- The saturation in the plane of the laminations, as observed by Jacobs *et al.* [16].
- The stacking factor of the laminated core, as observed by Jacobs *et al.* [16] and Mecrow, Jack and Cross [18].
- The pattern of the planar eddy currents, as observed by Carpenter [14], who showed that penetration is affected by the continuity of the in-plane eddy currents at butt joints in the laminated core.

3.4 Cross-magnetisation at domain level

Early work on the magnetisation of laminated soft iron materials, for example by Dannatt [20], investigated the fact that eddy current losses in laminated materials are much higher than predicted from theory. Dannatt recorded in [20] that: 'Eddy-current losses at low frequency (25–50 Hz) … can only be explained on the basis of the existence of fluxes transverse to the direction of the applied MMF'. This is because the permeability and loss in single magnetic crystals are dependent on the direction of magnetisation in relation to the crystal axis, as one would expect from Fig. 1. In effect, because of the variable geometry and alignment of successive crystals in a lamination, the path of the flux is not consistently in line with the direction of the resultant magnetisation. This gives rise to effective micro-cross-fluxes, driving eddy currents in the plane of the laminations and increasing loss, another cross-magnetisation phenomenon.

4 Experimental investigation

4.1 Experimental arrangement

To investigate the effect of material properties on cross-magnetisation an experimental arrangement was prepared, which minimised shape and surface effects, as shown in Fig. 9. The experiments were conducted with direct current so the behaviour investigated was entirely magnetostatic, no eddy currents were involved, except during transients. It proved impractical, as Binns, Low and Jabbar reported [13], to magnetise a specimen of spherical shape. However, the author wanted to avoid the difficulties Binns experienced with a sample in air, so the sample was embedded in an iron circuit, as shown in Fig. 9. This enabled the sample to attain higher, saturable flux densities and eliminated exposed magnetic surfaces on the sides of the sample, the source of surface polarities. This is shown in Fig. 10, which compares the experimental arrangements of Binns and the present work.

The arrangement consists of two orthogonal, circular steel yokes, uniformly wound with toroidal magnetising coils that reached right to the polefaces, to minimise leakage flux. The yokes were constructed from magnetically soft, laminated, coreplate (Losil 1000) and each contained a 33mm air gap, whose faces were finished by grinding. The

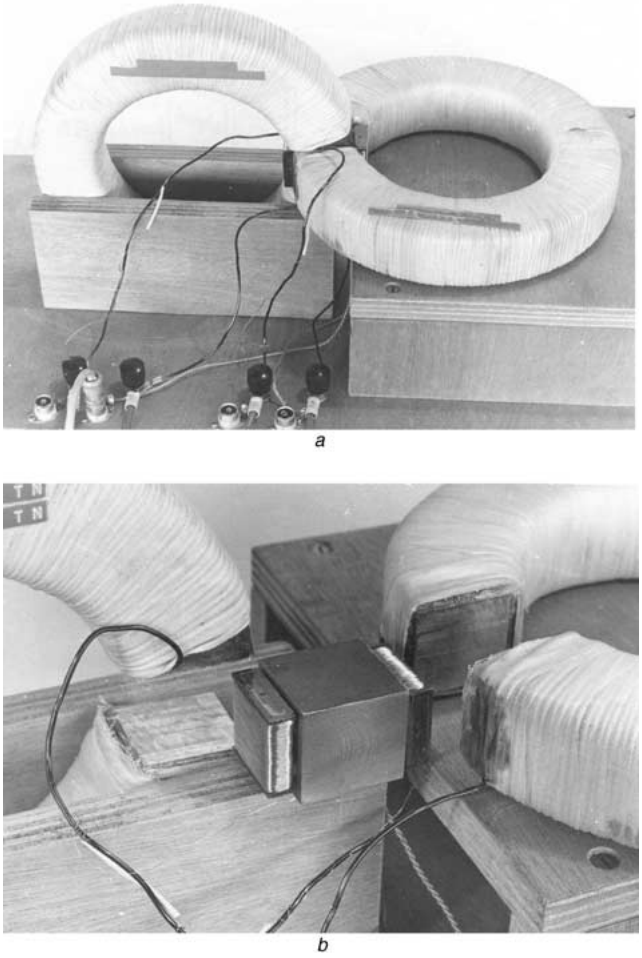

Fig. 9
a Arrangement of two intersecting orthogonal magnetising yokes
b Arrangement of a sample in two intersecting orthogonal magnetising yokes

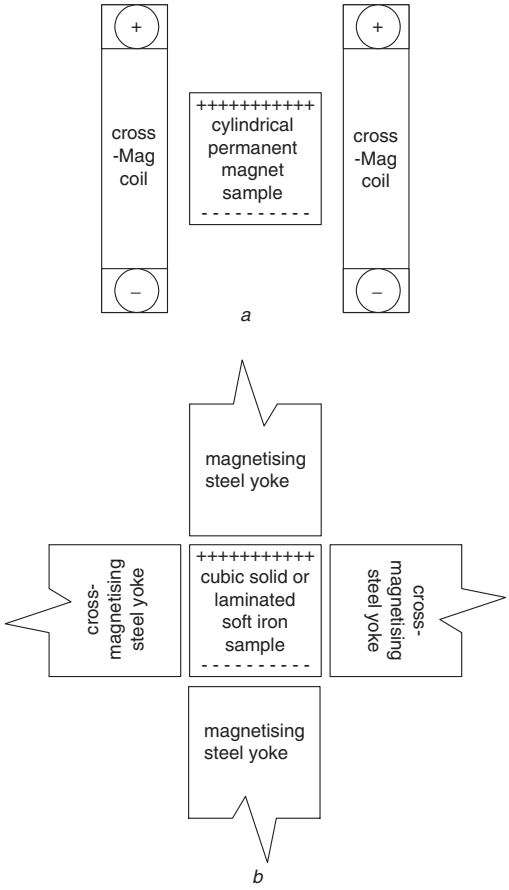

Fig. 10
a Arrangement used by Binns in [13]
Sample is a cylindrical permanent magnet beings cross magnetised by two coils
b Arrangement used in this paper. Sample is a solid or laminated soft iron cube being cross magnetised by two yokes, as shown in Fig. 9

two intersecting air gaps constituted a volume into which a ground cube sample of magnetic material can be inserted. Such a cubic sample can therefore be subjected to two powerful orthogonal magnetic fields, which can be adjusted independently.

Two samples were constructed for measurement. The first was milled from solid mild steel, the second was constructed from laminations of coreplate (Losil 450) cemented together. Both samples had all six surfaces ground to form accurate $33 \times 33 \times 33$ mm cubes so that, when the samples were inserted into the yokes, the resultant air gaps were minimised. The magnetic properties of the sample materials were measured as shown in Fig. 11.

The flux densities, B, in each of the two orthogonal yokes were measured using search coils wound on one pole of each yoke, close to the pole face to ensure that leakage flux was omitted from the measurement. The magnetic field strengths, H, in the samples could also be measured using multi-turn coils measuring the flux density in the air close to and tangential to the sample surfaces. These coils can clearly be seen in the photographs (Figs. 9*a* and *b*). The magnetising windings of the two yokes were supplied with up to 30A DC through separate reversing switches, and the DC supplies were completely independent. The maximum field that could be applied to the sample on each axis was about 170 kAT/m. This compares with the value of 180 kAT/m applied by Binns to his air-cored sample. In fact it was only necessary, on this iron-cored apparatus, to apply 8.5 kAT/m, on either axis, to drive the sample into saturation.

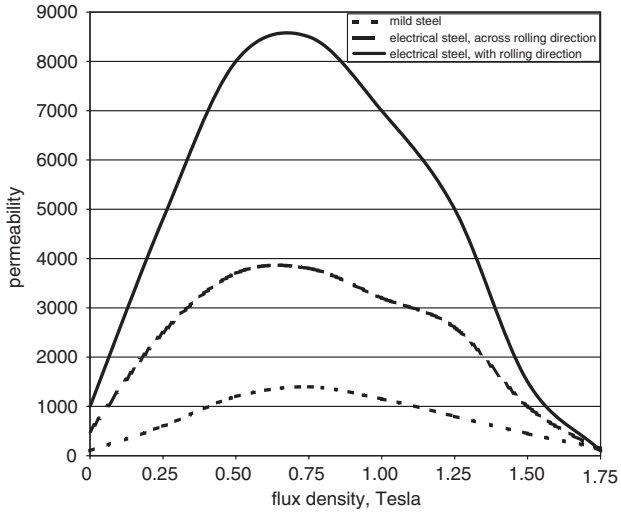

Fig. 11 *DC Magnetisation characterics of sample steels*

Measurements of the fluxes through the B-search coils were made using a Grassot flux meter. The H-search coils, however, had resistances of 900 Ω, which were too high for use with that meter, so a high input impedance electronic integrating flux meter was used for these measurements.

The measurement of B and H on each axis was made by recording the flux meter deflection, as the MMF applied to that axis was reversed. Thus the measurements represent points on a reversals curve. In taking these measurements it was important to check that, when the MMF was reversed on one yoke, there was no net change in the flux carried by the orthogonal yoke. This was done by measuring the output of the B-search coil on the orthogonal yoke, as the current was reversed. It is confirmed that no change in that orthogonal flux occurred. In the case of every measurement great care was taken to ensure that the sample was truly in the cyclic state and on the reversals curve before measurement. This was achieved by alternately reversing the magnetising current in each yoke a number of times before readings were taken.

4.2 Character of results

Detailed measurements were made on the rig using the solid and laminated samples. Figure 11 shows the DC magnetisation characteristics of the steels used in the two sample cubes, which were obtained separately by measurements on representative material in a solid ring for the mild steel and in an Epstein square for the laminated sample.

The most important results for this investigation concern the effect of the flux on one axis through the sample when a large field was applied orthogonally on the other axis. These results can best be displayed in the way shown in Fig. 12, particularly Fig. 12*b*, which shows plots of the changes in flux density, B_{direct}, on one axis of the sample, after being established initially at one level, while an increasing field is applied on the cross-axis. There are two distinct limiting characteristics of the graphs shown in Fig. 12*b*, depending on the magnetic properties of the sample. These are described as Class 1 and Class 2:

- Class 1: The material is magnetically linear as shown in Fig. 12*a*; the graph in Fig. 12*b* will consist of a straight line horizontal at the value of B_{direct} initially set up. Thus if a direct-axis flux density, B_{direct}, is set up at a value 1.5 T, as the cross-magnetising field is increased then that flux density 1.5 T will remain constant, but the flux density on the cross-axis will increase.

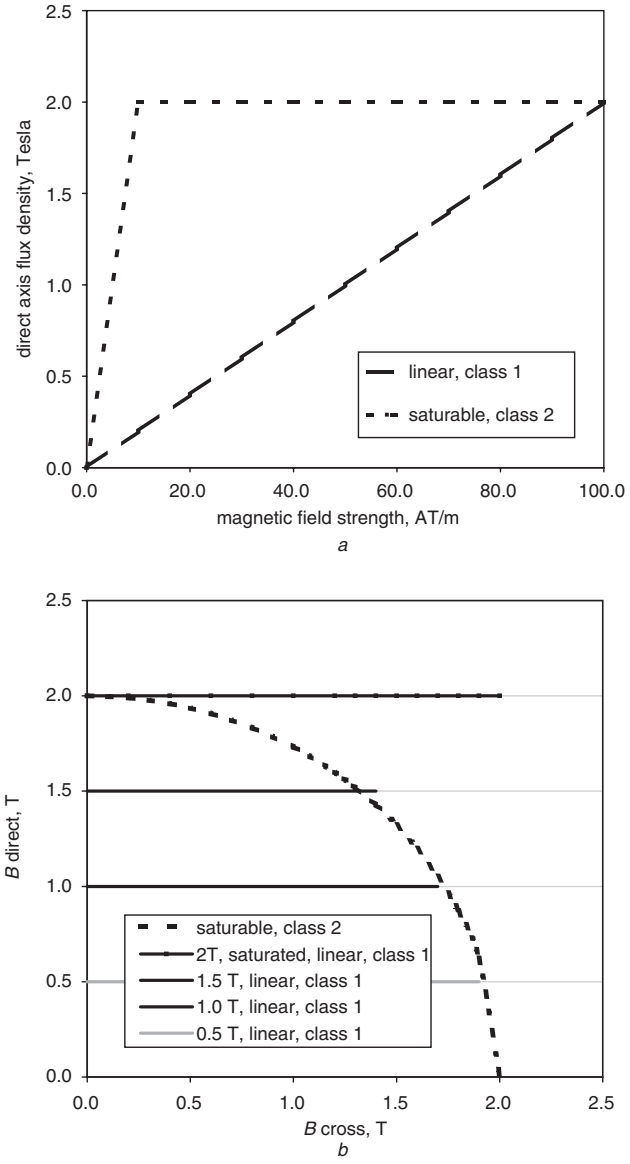

Fig. 12
a Idealised steel sample magnetisation characteristics
b Idealised cross-magnetising characteristics

• Class 2: The material is ideally saturable with a steep linear segment followed by a flat saturation characteristic, as shown in Fig. 12*a*. The resultant flux characteristic will consist of a horizontal segment at the initially set flux density, say 1.5 T, followed by a circle as the flux density reaches and is constrained to saturation, B_s, as shown in Fig. 12*b*.

A real magnetic sample will have properties that are intermediate between Class 1 and Class 2. Laminated materials will also have different properties in the plane of the laminations and perpendicular to them. If the material is non-linear the cross-magnetising characteristic will droop, as shown in Fig. 12*b*. When it is saturated the droop will tend towards a circle, again as shown in Fig. 12*b*, and the characteristic will alter at different flux density levels, showing least droop at the flux density at which the material permeability is lowest.

4.3 Results

The plots in Figs. 13 and 14 show the results of experiments on the solid mild steel and the laminated coreplate steel samples, respectively. For each sample two sets of curves are shown, the first curves with the direct-axis being the base flux direction, the second curves with the cross-axis being the base flux direction. Figures 13 and 14 should be compared with the limiting characteristics in Fig. 12*b*.

Consider first the isotropic mild steel sample (Figs. 13*a* and *b*). Because the material is isotropic the two sets of curves are near identical. The curves clearly show Class 2 drooping behaviour, the cross-magnetising effect of non-linearity. That droop is greatest at the mid flux density level around 1 T, which the permeability from the *B-H* curve is highest (Fig. 12). The droop diminishes, tending to Class 1 behaviour, as the flux density increases; when the material saturates, its permeability reduces and it becomes more linear.

Consider next the laminated coreplate steel sample (Figs. 14*a* and *b*). The two sets of curves do not map onto one another, because the material is anisotropic. They show cross-magnetising effects on both axes, but most notably, when the sample is magnetised on the direct-axis (Fig. 14*a*), the substantial droop, tending towards the Class 2 characteristic, demonstrates the non-linear behaviour of

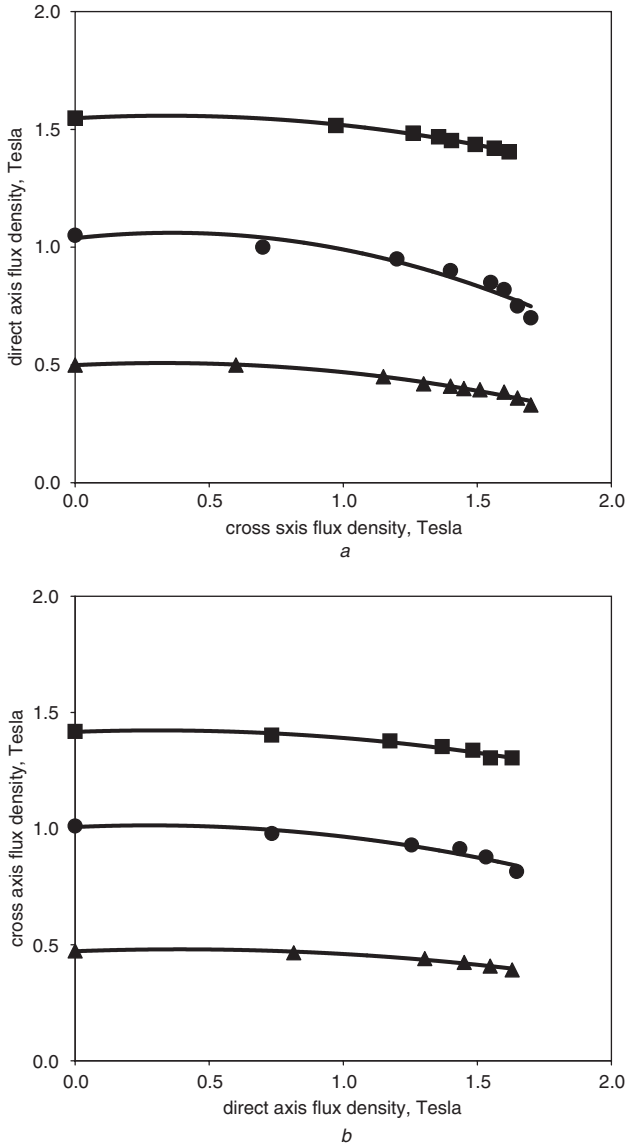

Fig. 13 *Cross-magnetisation characteristics on an isotropic mild steel sample*
a Field applied to the direct-axis
b Field applied to the cross-axis

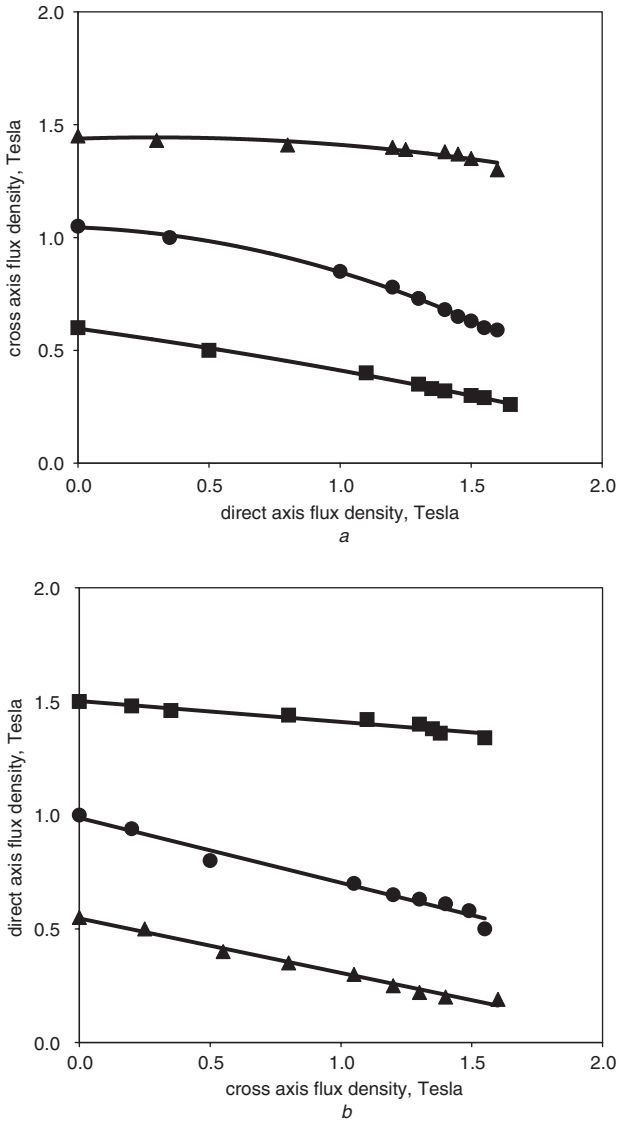

Fig. 14 *Cross-magnetisation characteristics on a laminated coreplate steel sample*
a Field applied to the direct axis
b Field applied to the cross axis

the material. This is clearly apparent at the base flux density of 1 T, and the shape of these curves is similar to those for the isotropic mild steel sample.

On the cross-axis (Fig. 14*b*), however, w here the main flux is being driven at right angles to the laminations, the material exhibits nearer Class 1 linear behaviour, as one would expect in an axis dominated by the interlaminar airgaps.

4.4 Explanation of results

An important observation in Fig. 14 is the small change in direct flux density that occurs when the cross-axis is magnetised. Consider the laminated sample magnetised in the direct axis in the plane of the laminations with 1.5 T (54 kAT/m field applied on that axis); a cross-magnetising flux density of 1.5 T (105 kAT/m applied on that axis) produced only a 15% reduction of the main flux. This echoes the result found by Binns (see Section 4.2) that it is difficult to reduce the flux density on the direct-axis by cross-magnetisation. But the difference in this case was that the samples were embedded in an iron circuit, so there were no exceptionally strong surface polarities on the flanks of the sample to oppose the cross-magnetisation. However, there were surface polarities on the flanks of the laminations confining the flux to the lamination.

In Fig. 14 at the lower flux density in the plane of the laminations of 1 T (21 kAT/m), a cross-magnetising flux density of 1.5 T (165 kAT/m) produced a much larger reduction of the main flux—50%. In this case the higher cross-magnetising MMF overwhelmed the low direct-axis MMF. But one is still left wondering how the direct-axis is still able to support a flux density of 0.5T in these conditions. The answers are:

- The surface polarities of the laminations preferentially maintain flux in that direction.
- The non-linearity of the steel requires only a small proportion of the MMF to maintain a significant flux density in the direct-axis even when the cross-axis is carrying a significant flux density.

The results show the effect of the material and its geometry on the cross-magnetisation characteristics, without the intervention of other sources at the external surfaces of the samples as the rig was designed to achieve.

5 Eddy currents

This paper has not considered the effects of eddy currents because of the difficulty of presenting clear explanations of the physical effects. However, it is clear from the work of Carpenter [14], Jacobs, Minors, Myerscough, Rollason and Steel [16] and Jackson [21] that eddy currents exert a profound effect on the distribution of flux inside a magnetic component. This is especially so when the applied field is inclined to the geometrically favoured axis of the component, such as in laminated bodies. Carpenter has shown that eddy current effects are best considered by subdividing the applied fields into modes that are aligned to the magnetic structure. The same approach was adopted by Tavner and Jackson [22], in a detailed study of the flux density in electrical machine laminations at high frequencies, at which high-frequency fluxes wrapped around the edges of the laminations carrying the main flux. Here it was clear that, at very high frequencies, up to 20 MHz, significant flux is carried in the skin depth on the flanks of core laminations at right angles to the main flux carried by them.

In a similar way, when a solid pole synchronous machine is subjected to transient loads the rotor angle changes with respect to the main flux, inducing transient frequency axial currents in the rotor pole face. These currents trap high-frequency flux in the surface of the rotor pole face flowing at right angles to the main DC flux carried by the pole.

However, it would be wrong to describe eddy current effects as overwhelming in cross-magnetisation, because cross-magnetisation is dominated by the flux entering and leaving the magnetic body and therefore by the boundary conditions on that body. So it is primarily a magnetostatic effect. The importance of eddy currents to cross-magnetisation is the change they effect when fluxes threading conducting parts change during operation. That is eddy currents affect the difference between steady-state and transient cross-magnetisation.

6 Conclusions

When an MMF is not applied in the geometrically favoured direction of a magnetically soft or hard component the resultant flux pattern can lead to unexpected results, especially when the magnetic behaviour is being synthesised along and at right angles to the favoured direction. The effects are unexpected in that magnetisation on one axis can

significantly affect the magnetisation on the other axis, a cross-magnetisation effect. This is not necessarily caused only by non-linearity of the magnetic material but also by the geometry of the magnetic components.

Shape and non-linear permeability play an important part in cross-magnetisation of cylindrical AC machines, because the air-gap surfaces are nominally cylindrically smooth. The source of the cross-magnetisation is:

- non-uniform distribution of surface polarities on the flanks of stator and rotor teeth
- volume polarities in the core due to permeability divergence.

The qualitative nature of this behaviour is similar to the flux distortion due to armature reaction seen in salient DC and AC electrical machines.

If permanent magnet materials are used with their side faces exposed to air, rather than embedded, the polarities on these exposed surfaces exercise a large effect in sustaining the flux through the magnet. It requires a very large cross-magnetising MMF to make a small change to the surface polarity on the magnet face. However, if the permanent magnet is embedded in soft magnetic material a modest cross-magnetising MMF can have a significant effect.

The difficulty of cross-magnetising shaped magnetic components has been clearly demonstrated in two sets of experiments:

- on a permanent magnet by Binns [13], in which the cause of the difficulty was the strength of surface polarities on the exposed faces of the magnet, as described above.
- on a laminated structure by this author, in which the cause of the difficulty was the successively polarised surfaces of the laminations and the consequential volume polarities.

A tensor representation of the behaviour of composite materials in two axes can be used, such as:

$$\begin{vmatrix} B_x \\ B_y \end{vmatrix} = \mu_0 \begin{vmatrix} \mu_x & \mu_{xy} \\ \mu_{yx} & \mu_y \end{vmatrix} \begin{vmatrix} H_x \\ H_y \end{vmatrix} + \begin{vmatrix} M_x \\ M_y \end{vmatrix}$$

where μ_{xy} represents cross-magnetisation behaviour. However, μ_{xy} can be a permeability based on a reluctivity calculation of the composite material, such as:

$$\mu_z = 1/(1 - \gamma + \gamma/\mu_r)$$

Experience has shown that use of these expressions in numerical calculations gives an indication of flux levels but cannot be relied on to provide detailed qualitative information on the flux patterns, because they ignore geometrical effects and particularly the effect of embedded laminar polarity and volume polarity sources.

The shortcomings of the above representation are particularly noticeable in laminated soft iron materials, in which the successively polarised surfaces of laminations, due to the normal MMF components, deflect the flux into the plane of the laminations and create consequential volume polarities, particularly when the laminations are heavily saturated. These volume polarities have a large influence on the penetration of flux from lamination to lamination.

Cross-magnetisation effects are controlled by the boundary conditions on the magnetic body and are therefore primarily magnetostatic. Eddy currents profoundly affect the flux threading the magnetic body if it is conducting and therefore affect the difference between steady-state and transient cross-magnetisation effects.

7 References

1 Tavner, P.J., Hammond, P., and Penman, J.: 'Contribution to the study of leakage fields at the ends of rotating electrical machines', *Proc. IEE*, 1978, **125**, pp. 339–349
2 Moullin, E.B.: 'Electromagnetic principles of the dynamo' (OUP, Oxford, UK, 1955), pp. 60–75
3 Brown, J.E., Kovacs, K.P., and Vas, P.: 'A method of including the effects of main flux path saturation in the generalised equations of ac machines', *IEEE Trans. Power Appar. Syst.*, 1983, **102**, (1), pp. 96–103
4 Kovacs, K.P.: 'On the theory of cylindrical rotor ac machines including main flux saturation', *IEEE Trans. Power Appar. Syst.*, 1984, **103**, (4), pp. 754–761
5 Vas, P., Hallenius, K.E., and Brown, J.E.: 'Cross-saturation in smooth-air-gap electrical machines', *IEEE Trans. Energy. Convers.*, 1986, **1**, (1), pp. 103–112
6 Macdonald, D.C., Reece, A.B.J., and Turner, P.J.: 'Turbine-generator steady-state reactances', *IEE Proc. C, Gener. Transm. Distrib.*, 1985, **132**, (3), pp. 101–108
7 Levi, E.: 'Impact of cross-saturation on accuracy of saturated induction machine models', *IEEE Trans. Energy Convers.*, 1997, **12**, (3), pp. 211–216
8 Levi, E., and Levi, V.A.: 'Impact of dynamic cross-saturation on accuracy of saturated synchronous machine model', *IEEE Trans. Energy Convers.*, 2000, **15**, (2), pp. 224–230
9 El Serafi, A., and Kar, N.C.: 'Methods for determining the *q*-axis saturation characteristics of salient-pole synchronous machines from measured *d*-axis characteristics', *IEEE Trans. Energy Convers.*, 2003, **18**, (1), pp. 80–86
10 Kamper, M.J., and Volschenk, A.F.: 'Effect of rotor dimensions on L_d and L_q inductances of reluctance synchronous machine with cageless flux barrier rotor', *IEE Proc. B, Electr. Power. Appl.*, 1994, **141**, (4), pp. 213–220
11 Vagati, A., Pastorelli, M., Scapino, F., and Franceschini, G.: 'Impact of cross-saturation in synchronous reluctance motors of the transverse laminated type', *IEEE Trans. Ind. Appl.*, 2000, **36**, (4), pp. 1039–1046
12 Stumberger, G., Stumberger, B., Dolinar, D., and Hamler, A.: 'Cross-magnetization effects of linear synchronous reluctance motor under load conditions', *IEEE Trans. Magn.*, 2001, **37**, (5), pp. 3658–3662
13 Binns, K.J., Low, T.S., and Jabbar, M.A.: 'Behaviour of a polymer-bonded rare earth magnet excitation in two directions at right angles', *IEE Proc., Electr. Power. Appl.*, 1983, **130**, pp. 25–32
14 Carpenter, C.J.: 'Theory of flux penetration into laminated iron and associated losses', *Proc. IEE*, 1977, **124**, (7), pp. 659–664
15 Yagisawa, T., Takekoshi, Y., and Wada, S.: 'Magnetic properties of laminated steel sheets for normal fluxes', *J. Magn. Magn. Mater.*, 1982, **26**, (1–3), pp. 340–342
16 Jacobs, D.A.H., Minors, R.H., Myerscough, C.J., Rollason, M.L.J., and Steel, J.G.: 'Calculation of losses in the end-region of turbogenerators', *Proc. IEE*, 1977, **124**, pp. 356–362
17 Reece, A.B.J., and Preston, T.W.: 'Finite element methods in electrical power engineering' (Oxford University Press, 2000), pp. 126–128
18 Mecrow, B., Jack, A.G., and Cross, S.: 'Electromagnetic design of turbogenerator stator end regions', *IEE Proc. C, Gener. Transm. Distrib.*, 1989, **136**, (6), pp. 361–372
19 Hammond, P.: 'Discussion on Reference 1', *IEE Proc. C. Gener. Transm. Distrib.*, 1980, **127**, (2), p. 118
20 Dannatt, C.: 'The variation of the magnetic properties of ferromagnetic laminae with frequency', *J. IEE*, 1936, **79**, pp. 667–680
21 Jackson, R.J.: 'Interlamination voltages in large turbogenerators', *Proc, IEE*, 1978, **125**, (11), pp. 1232–1238
22 Tavner, P.J., and Jackson, R.: 'Coupling of discharge currents between conductors of electrical machines owing to the laminated steel core', *IEE Proc. B, Electr. Power Appl.*, 1988, **135**, (6), pp. 295–307

Coupling of discharge currents between conductors of electrical machines owing to laminated steel core

P.J. Tavner, MA, PhD, CEng, FIEE
R.J. Jackson, MA

Indexing terms: Electrical machines, Power electronics, Electromagnetic theory

Abstract: Over the past few years, a number of techniques have evolved for detecting discharges in the insulation systems of electrical machines by measuring the discharge currents flowing at the machine terminals. The propagation of these currents through the winding, from the discharge site to the terminals, is influenced by the capacitive and inductive coupling between the conductors of the winding. The paper is concerned solely with the inductive component of that coupling, through the laminated steel stator core of the machine. It describes how this coupling makes a significant contribution to the equivalent circuit for the propagation of discharge currents containing frequencies from 20 kHz to 20 MHz.

List of symbols

a_n = arbitrary constant in the flux distribution calculation
B = magnetic flux density
b_n = arbitrary constant in the flux distribution calculation
c = velocity of light
c_n = arbitrary constant in the flux distribution calculation
f = frequency of excitation
f_n = Eigenfunction in the core steel
f'_n = Eigenfunction in the interlaminar gap
H = magnetic field strength
h = height of a stack of coreplate laminations
J = current density
j = complex number $= \sqrt{(-1)}$
L = self inductance of a coil
L = half thickness of coreplate lamination
l = core length
l = half the interlaminar gap
m = general expression for mutual inductance
M_e = mutual inductance between the coils coupled by the end winding
M_s = mutual inductance between two coils coupled by the laminated core
n = counts harmonics
R = radius of stator core back
r = radius of stator core bore
r, z, θ = cylindrical co-ordinate axes for the coupling coefficient calculation
X = half the radial core depth
X_n = a function in the coupling coefficient expression which depends upon the location of the conductors
x, y, z = rectangular co-ordinate axes for the flux distribution calculation
x = geometrical constant in the coupling coefficient calculation $= r/R$
Z_1 = primary leakage impedance of coupling coils
Z_2 = secondary leakage impedance of coupling coils
Z_n = mutual impedance of coupling coils
α = complex ratio $(1 + j)L/\delta$
α_n = is a complex constant
γ = stacking factor of the core
β = complex ratio X/Λ
ε_0 = primary electric constant
δ = skin depth $= \sqrt{(2\rho/\omega\mu_0\mu_r)}$
λ = pole pitch of a winding
Λ = penetration depth $= (-jc/\omega)\sqrt{[(1-\gamma)/(1-\gamma+\gamma\mu/\alpha)]}$
μ_0 = primary magnetic constant
$\bar{\mu}_e$ = complex effective relative permeability of the core
μ = relative permeability of the lamination steel
2ϕ = angular span of a conductor bar
ρ = resistivity of coreplate steel
ω = angular frequency
$\sum$ = coupling coefficient

Paper 6254B (P1/S3), first received 14th December 1987 and in revised form 27th May 1988

Dr. Tavner is with Laurence, Scott & Electromotors Ltd, P.O. Box 25, Kerrison Road, Norwich NR1 1JD, Norfolk, United Kingdom
Mr. Jackson is with GEC Turbine Generators Ltd, Stafford ST17 4LN, United Kingdom

1 Introduction

From the late 1960s to the late 1980s, a number of electrical techniques have been developed for the detection of discharges in the stator winding insulation of electrical machines [1–3]. These techniques depend upon detecting the currents induced by these discharges at the machine terminals (Fig. 1). To determine the relationship between the magnitude of a current at the terminals and the size of the discharge causing it, it is necessary to understand the propagation of these discharge current through the winding. This is determined by the equivalent circuit representation of the winding for the frequency components contained in the discharge current. Important parts of that equivalent circuit are the capacitive and inductive couplings between each conductor and its neighbours.

Although the contribution of capacitive coupling is reasonably well understood, the level of inductive coupling between conductors has been the subject of debate

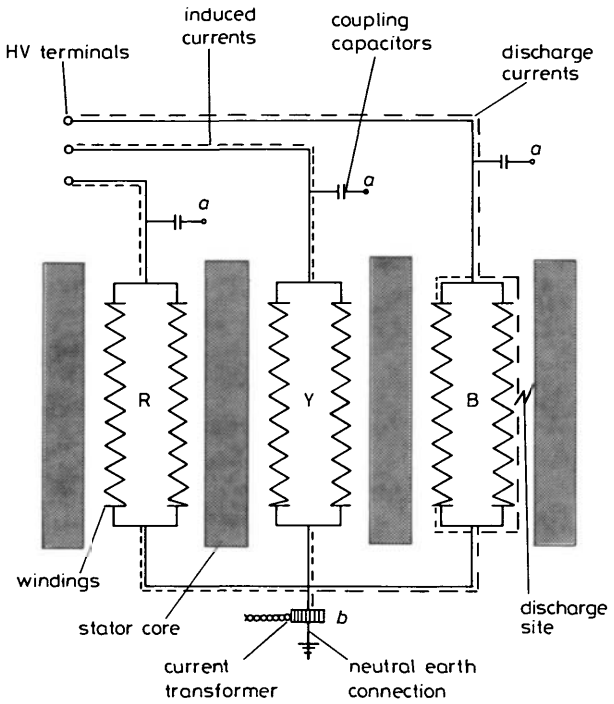

Fig. 1 *Schematic diagram of generator stator winding*
The diagram shows measurement of high frequency currents to detect discharge between stator winding and core

between those working in the area. In particular, agreement has not been reached about the effect of the laminated steel stator core in which the conductors are embedded. This paper is concerned solely with this effect. It investigates the different approaches of the various workers and clarifies by theoretical and experimental analysis the correct representation of that component of coupling.

2 Previous work

Previous work has considered two phenomena producing high frequency currents in machine windings. The first was concerned with the impact on the winding insulation of fast-fronted surges injected into the machine terminals during switching of the electrical distribution system. The second considered the detection of discharge pulses generated within the winding, and this is the topic that we are concerned with in this paper.

Surge and discharge pulses are different from one another in amplitude, rise time and duration, but as far as propagation is concerned the most important property is their spectral content, which is largely determined by their risetimes. Discharge pulses contain higher frequency components, at least at the site where they occur. However, although the frequency contents vary, modelling of pulse propagation generally relies on simple equivalent circuit representation of the machine windings.

Fig. 2 shows some of the equivalent circuits used to represent machine windings. In each case, a lumped parameter TEE or PI circuit represents each of the slot and endwinding portions of each turn of the winding. In Fig. 2*a* only the self inductance of the conductor and its capacitance to earth are considered. In Fig. 2*b* the effect of the coupling capacitance between turns is added while in Fig. 2*c* the coupling owing to mutual inductance is also considered. This mutual inductance is partly owing to the magnetic field surrounding the end windings M_e, and also to the magnetic field M_s in the core of the machine.

Generally, the inductive coupling owing to flux in the laminated core has been neglected in modelling pulse propagation in machine windings. For example, Rudenburg [4] stated that, '. . . the rapidly changing flux lines due to a travelling pulse cannot penetrate the boundary steel'. He therefore discounted any contribution to the propagation owing to coupling through the core. Heller and Veverka [5] stated that, '. . . the region of the wavefront is simultaneously the region of the fastest time variation . . . electric currents are therefore induced only in very thin film at the surface of the iron, while the rest of the iron is shielded by these eddy currents and is free of magnetic field'.

Wright *et al.* [6] used these results in their model for calculating the distribution of fast-fronted interturn voltages in a winding. In fact, they stated that, '. . . under the influence of high frequency excitation, the stator core iron behaves in a completely different manner to that when it is excited at power frequencies. Skin effect at high

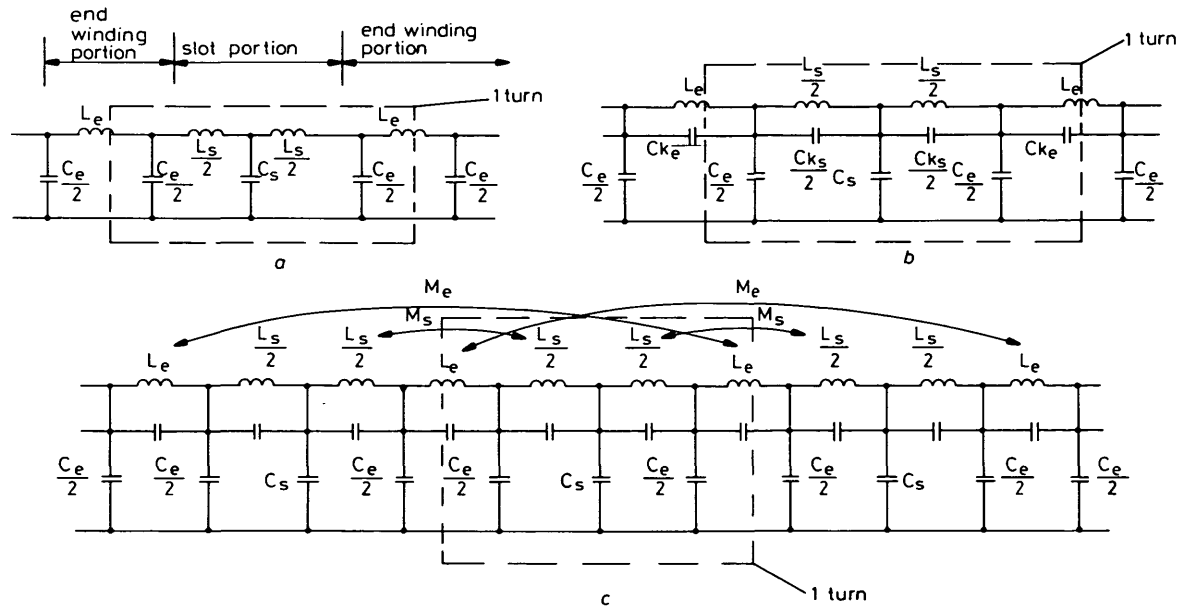

Fig. 2 *Equivalent circuit representation of machine windings*

frequencies, about 1 MHz, causes the iron enclosing a stator coil to act as a barrier to magnetic flux. The behaviour of the core iron under these circumstances is

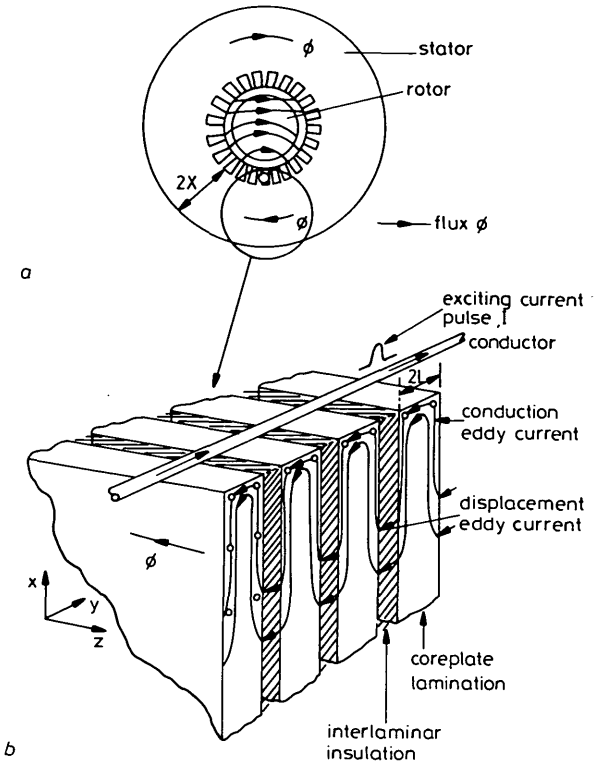

Fig. 3 *Distribution of magnetic flux in laminated core*
a Cross-section of an electrical machine
b Detail of a conductor alongside a laminated core

like that of an impenetrable earthed sheath'. These conclusions were drawn in these three references despite the fact that the core is laminated at right angles to the flow of any eddy currents which would act to screen the core.

McLaren *et al.* [7] dealt with a similar problem in calculating the voltage distribution in a winding subjected to rapid surges, but they addressed the problem by asking, '. . . how does a laminated structure support currents at right angles to the laminations?' They came, however, to the same conclusions as References 4–6 and said that, '. . . at high frequencies . . . the close capacitive coupling between laminations separated by a thin layer of insulation allows a low impedance path for axial currents. In the insulation itself, the current is a displacement current of equivalent effect to the conduction current in the iron laminations'.

Wilson *et al.* [1] described experimental measurements of pulse propagation in motor and turbo-generator stator windings. They concluded that at low frequencies, '. . . a discharge pulse will propagate through the stator winding as in a transmission line', but that at higher frequencies the capacitance and mutual inductance between coils of a motor or generator winding present a relatively low impedance path for currents flowing between the discharge site and instrumentation at the winding terminals.

This previous work therefore raises two interesting questions: Does the laminated stator core contribute to the coupling of surge or discharge pulses between conductors in an electrical machine, and if it does, on what frequency components of these pulses is it effective? To answer these questions, it is necessary to find theoretical and experimental answers to the following more detailed questions:

(*a*) At frequencies above the power frequency, how is flux distributed in the individual laminations of a laminated stator core excited from its bore?

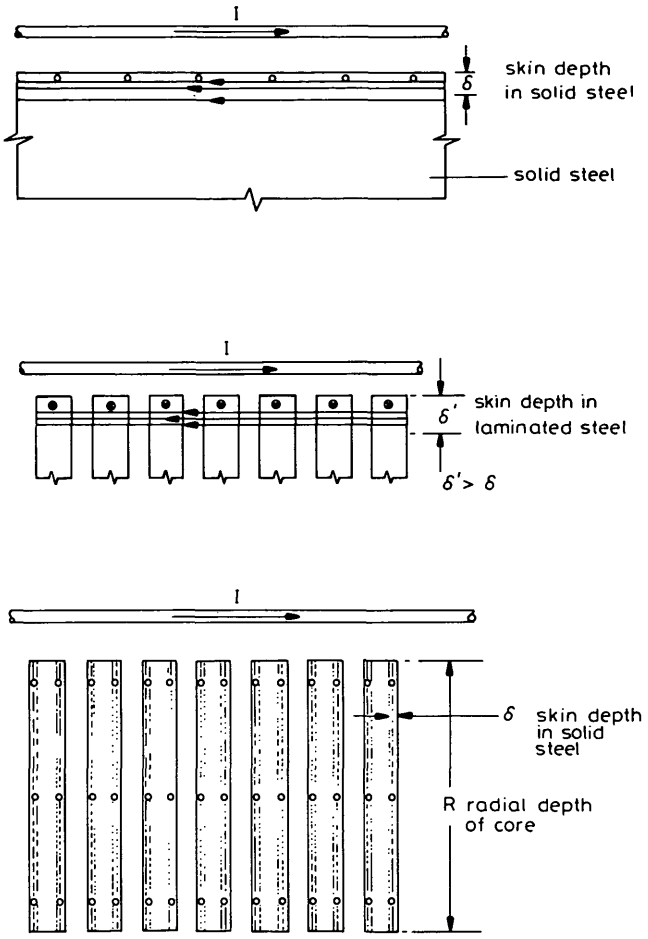

Fig. 4 *Distribution of magnetic flux in laminated steel*
Different theories:
a Rudenburg; Heller & Veverka
b Wright, Yang & McLeay; McLaren & Oraee
c Suggested distribution

(*b*) How does the effective permeability of a laminated core vary with frequency?

(*c*) How does the coupling coefficient between conductors embedded in such a core vary with frequency?

(*d*) At what frequency does a laminated core become effectively an impenetrable flux screen?

3 Theoretical work

When a current flows in a conductor embedded in a core slot (Fig. 3*a*) it will produce a circulating flux around the conductor and will establish a ring flux, Φ in the stator core, depending on the geometry and material properties of that core and the pulsation frequency of the flux. The degree of penetration into the core depends upon the eddy current pattern in the laminations. In this work, the effect of the earthed screen around high voltage conductor bars is not considered as it will not affect the distribution of flux within the core laminations.

Fig. 3*b* shows the flux pattern in the laminations due to a single conductor excitation. It is this pattern which is at the root of the differences expressed in the previous work and Fig. 4 summarises these. Fig. 4*a* shows the approach of Rudenberg [4] and Heller *et al.* [5] who quite simply assume that the core behaves as solid steel.

Fig. 4*b* shows the approach of Wright *et al.* [6] and McLaren *et al.* [7] who assume that the screening eddy currents flow axially through the laminated core, across the interlaminar gap. They perhaps assume that the skin depth of such currents may be greater than it would be in a solid iron core, increased by the additional impedance due to the flow of displacement current through the interlaminar gap. Fig. 4*c* shows what is perhaps a more accurate representation in which the flux penetrates between the laminations and is carried on their flanks, limited only by the skin depth of the flux in the lamination steel.

3.1 Penetration of high frequency fields

The problem of high frequency flux penetration into a laminated core has been considered, in a different context, by Bondi and Mukherji [8]. They were concerned with the loss induced in the laminated pole shoe of a DC machine by the pulsating flux of the tooth ripple of the armature as it passes the pole shoe. They considered the case of a laminated core subject to a sinusoidal current sheet, the tooth flux ripple, moving parallel to the plane of the laminations (Fig. 5).

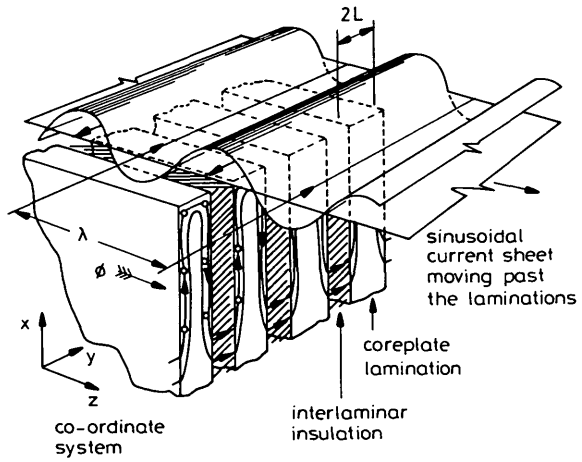

Fig. 5 *Excitation arrangement for analysis of tooth ripple* [8]

Although the analysis of Bondi and Mukherji is complex, it is possible to extract certain salient features. The co-ordinates of the analysis are shown in Figs. 5 and 6. The magnetic field H and current density J within the laminate can have components on all three axes. Bondi and Mukherji decompose the field into three modes which were superposed to represent the total field in a linear magnetic material. The form of these modal fields is shown in Fig. 6 for a single lamination.

In deriving expressions for the modal fields it was assumed that the interlaminar insulation was of negligible thickness and infinite resistance and that the effect of displacement currents could be neglected. Under these conditions, the flux distribution parallel to the plane of the laminations is described by the following expressions:

$$\text{Mode } a\ H_y = -\frac{2\pi j}{\lambda} \sum_{n\ odd} \frac{a_n \cos(n\pi y/2L)}{(n\pi/2l)^2 + ((1+j)/\delta)^2} \times \exp\left\{-x\left\{\left(\frac{2\pi}{\lambda}\right)^2 + \left(\frac{n\pi}{2l}\right)^2 + \left(\frac{1+j}{\delta}\right)^2\right\}^{1/2} + j\left(\omega t - \frac{2\pi z}{\lambda}\right)\right\} \quad (1)$$

$$\text{Mode } b\ H_y = \frac{2\pi}{\lambda} \times \sum_{m\ even} \frac{b_n \frac{m}{2}\left\{\left(\frac{2\pi}{\lambda}\right)^2 + \left(\frac{m\pi}{2L}\right)^2 + \left(\frac{1+j}{\delta}\right)^2\right\} \cos\left(\frac{m\pi y}{2L}\right)}{(m\pi/2L)^2 + ((1+j)/\delta)^2} \times \exp\left\{-x\left\{\left(\frac{2\pi}{\lambda}\right)^2 + \left(\frac{m\pi}{2l}\right)^2 + \left(\frac{1+j}{\delta}\right)^2\right\}^{1/2} + j\left(\omega t - \frac{2\pi z}{\lambda}\right)\right\} \quad (2)$$

$$\text{Mode } c\ H_y = -\frac{2\pi}{\lambda} c_\lambda \cosh((1+j)y/\delta) \times \exp\left\{-\frac{2\pi x}{\lambda} + j\left(\omega t - \frac{2\pi z}{\lambda}\right)\right\} \quad (3)$$

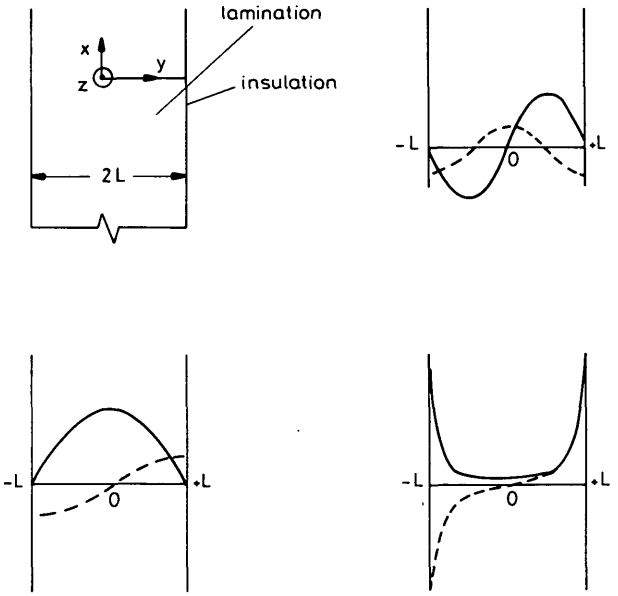

Fig. 6 *Modes of flux distribution in single lamination* [8]
a $H_y = 0$ for $n = 0$
—— H_z, H_x, J_y
- - - - J_z, J_x
b $J_y = 0$ for $m = 1$
—— H_y, J_z, J_x
- - - - H_z, H_x
c $J_y = 0, H_y = 0$
—— H_z, H_x
- - - - J_z, J_x

The importance of these expressions is the way in which they decay with radial depth into the laminated core, that is, along the x-axis. It can be seen from the expressions for modes *a* and *b* that the decay of the fields depends upon the term

$$\exp\left\{-x\left\{\left(\frac{2\pi}{\lambda}\right)^2 + \left(\frac{m\pi}{2L}\right)^2 + \left(\frac{1+j}{\delta}\right)^2\right\}^{1/2}\right\} \quad (4)$$

which, since $\delta \ll L \ll \lambda$ at high frequencies (>20 kHz) will reduce effectively to $\exp(-(1+j)x/\delta)$. The decay of field on the x-axis for those modes is therefore controlled by the skin depth. This is the manner of decay to which Rudenberg [4], Heller *et al.* [5] are referring. However, the decay of the mode *c* field depends on the term

$$\exp\left(-\frac{2\pi x}{\lambda}\right) \quad (5)$$

and hence on the pitch of the exciting field which is very much greater than the skin depth at frequencies above the power frequency. In the axial direction y this field decays rapidly within the lamination controlled by the skin depth, δ. It is this mode of flux distribution, on the flanks of the laminations, which is implied in Fig. 4c.

The resultant flux distribution owing to these three modes is shown in Fig. 7a. It is the mode c flux, penetrating deep between the laminations, which gives rise to the high tooth ripple losses observed in the laminated pole shoes of DC machines which Bondi and Mukherji were investigating.

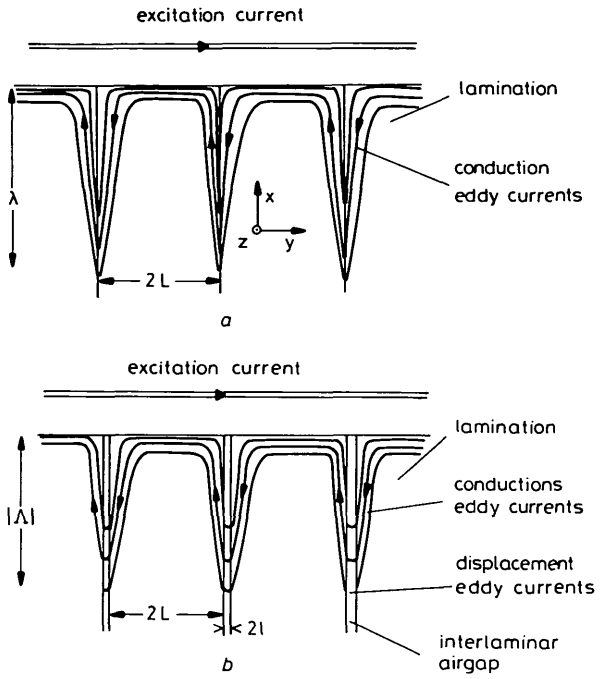

Fig. 7 *Penetration of high frequency magnetic flux into laminated core*
a The effect of neglecting displacement currents when the penetration is equal to the pitch of the excitation winding
b The effect of interlaminar displacement currents at high frequencies when the penetration depth is less than the pitch of the winding

3.2 Effect of displacement currents

There is less information in the literature on the effect of displacement currents between laminations in controlling the penetration of flux into laminated steel cores. This has therefore been considered in detail in Appendix 10.

The analysis presented in Appendix 10 models the flux distribution in a core excited by a ring winding with currents flowing axially along the bore and returning along the core back (see Fig. 16). It is shown that at sufficiently high frequencies, the penetration of flux between the laminations is controlled not by the pitch λ of the exciting winding as it is in Bondi's work, but by a penetration depth $|\Lambda|$ ($1/a$, in eqn. 35), where Λ is a complex quantity:

$$\Lambda = -\frac{jc}{\omega}\sqrt{\left\{\frac{(1-\gamma)}{(1-\gamma)+\mu\gamma/\alpha}\right\}} \tag{6}$$

where $\alpha = (1+j)L/\delta$

where c is the speed of light, γ the stacking factor of the laminate, ω the angular frequency, L the half thickness of the laminations and δ the skin depth in the steel.

As would be expected, this penetration depth decreases with increasing stacking factor and frequency. At high frequencies, it will be less than the pitch of the excitation winding and will thus limit the penetration of flux into the stator core (see Fig. 7).

In assuming that flux was excluded from the stator core by axial currents flowing as displacement currents in the insulation McLaren *et al.* [7] implied that this penetration depth $|\Lambda|$ was small compared to the dimensions of the stator core. However, it is shown in Appendix 8 that for practical laminates, with core steel of relative permeability $\mu < 1000$, the penetration depth $|\Lambda|$ is greater than half the radial depth of the largest electric machine core at frequencies up to 20 MHz. The flux distribution shown in Fig. 4c may therefore be considered representative when modelling the propagation of discharge currents up to this limiting frequency.

3.3 Effective permeability of the core

Both the previously mentioned treatments consider the response of the core to a sinusoidal excitation current. In practice, a discharge pulse will contain currents at all frequencies up to a limit determined by the rise time. It is necessary, therefore, to derive the effective permeability of the core as a function of frequency to determine the level of inductive coupling between conductors as a function of measurement frequency.

The mean effective permeability $\bar{\mu}_e$ of a laminate alone carrying eddy-current-limited flux on its flanks has been calculated by Stoll [9] and can be presented as

$$\bar{\mu}_e = \mu_0 \mu \tanh(\alpha)/\alpha \tag{7}$$

When the stacking factor γ of the laminate is taken into account, this expression yields an effective relative permeability of

$$\bar{\mu}_e = (1-\gamma) + \gamma\mu\mu_0 \tanh(\alpha)/\alpha \tag{8}$$

If the effect of the displacement currents described in Section 3.2 is also considered, then the effective relative permeability may be approximated to

$$\bar{\mu}_e = \{(1-\gamma) + \gamma\mu\mu_0 \tanh(\alpha)/\alpha\} \times \{\tanh(\beta)/\beta\} \tag{9}$$

where

$$\beta = \frac{X}{\Lambda}$$

and $2X$ is the radial depth of the core (Appendix 10, eqn. 36).

In eqn. 9, the terms contained in the former pair of braces account for the magnetostatic effects of the gaps between laminations and the effects of eddy currents which constrain the magnetic flux to a skin depth on the surface of the laminations. The term between the latter pair of braces accounts for the restriction on radial penetration of flux into the stator core owing to displacement currents flowing in the interlaminar gap. At frequencies up to 20 MHz, this term is effectively unity.

Eqn. 9 is used throughout this paper. It should be noted that in practice hysteresis as well as eddy currents contribute to the suppression of flux within a lamination, but no attempt has been made in this paper to represent this effect.

3.4 Coupling coefficient

It is clear from the flux distribution model of the preceeding Sections that even at high frequencies the core carries a significant amount of flux and will therefore contribute to the coupling of discharge pulses between conductors. The extent of this contribution is considered below.

The mutual inductance between conductor bars due to flux penetrating the stator core may be represented by the expression

$$m(\theta) = k\bar{\mu}_e \mu_0 l/2\pi \tag{10}$$

where l is the core length and k is a factor accounting for the conductor dimensions and angular spacing (θ). Thus, in practice the inductances between conductor bars of the stator winding depend on

(*a*) the effective permeability of the core at the measurement frequency

(*b*) the geometry of the core, in particular its length and radial depth

(*c*) the relative positions of the conductors.

An upper bound on the magnitude of the factor k may be obtained by neglecting the effects of the stator teeth and the rotor forging. Such an arrangement has been considered by Hammond [10] and is shown in Fig. 8*a*. Following his analysis, the mutual inductance between two single turn windings with return currents flowing through conductors at the core back is given by

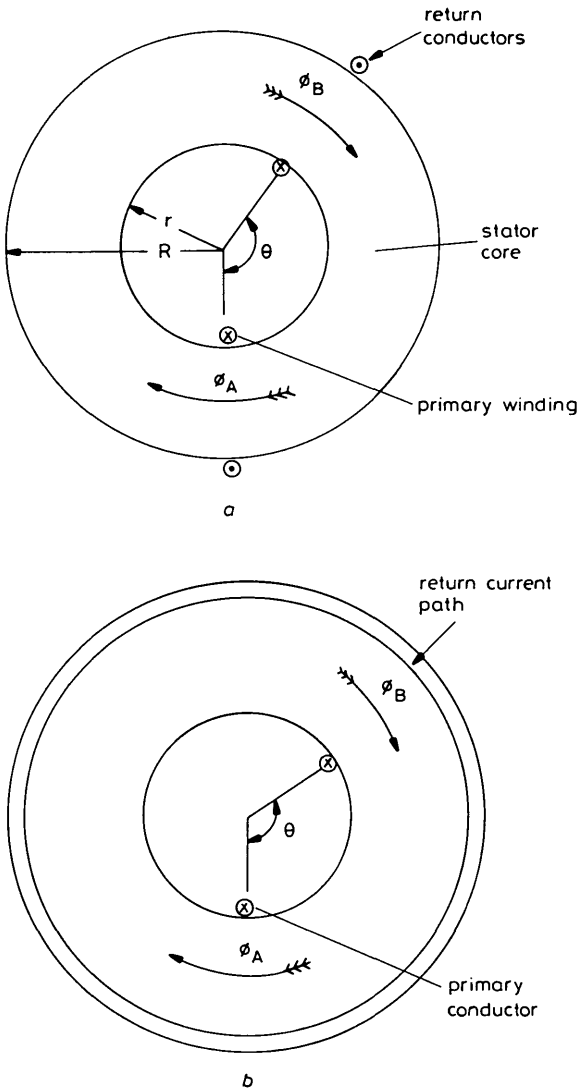

Fig. 8 *Coupling around laminated steel core for various conductor arrangements*

a Coupling with return path in a single conductor at the core back, gramme ring arrangement

b Coupling with the return currents in a uniform conducting sheet at the core back

$$k = -\ln(x) + \sum_n X_n \cos(n\theta) \tag{11}$$

where for Fig. 8*a*

$$X_n = \frac{4 \sin(n\phi)(1 - x^n) \cos(n\theta)}{n^2\phi((\bar{\mu}_e + 1) - (\bar{\mu}_e - 1)x^n)} \tag{12}$$

with $x = r/R$ and 2ϕ is the angular span of the conductor bar.

The above expression may be used to determine the coupling coefficient between windings, defined as the ratio of the flux linking the secondary and primary circuits, that is, the ratio of the mutual to self inductance:

$$\sum(\theta) = \frac{-\ln(x) + \sum_n X_n \cos(n\theta)}{-\ln(x) + \sum_n X_n} \tag{13}$$

In practice, discharge currents will return in various axial components of the core frame. Thus, the return conductors tend towards a uniform conducting sheet screening the radial field at the core back (Fig. 8*b*). In this case, the coupling coefficient is determined using the expression

$$X_n = \frac{4 \sin(n\phi)(1 - x^n) \cos(n\theta)}{n^2\phi((\bar{\mu}_e + 1)/x^n - (\bar{\mu}_e - 1)x^n)} \tag{14}$$

The above expressions may be used to determine the coupling coefficient between conductors. These results may then be compared with measurements to determine whether the model used and in particular the representation of the flux distribution in the stator core is adequate.

4 Experimental work

4.1 Experimental arrangement

The purpose of the experimental work was to measure, on practical cores, the effective permeability and coupling coefficient for the arrangement shown in Fig. 8*a*, over a range of frequencies. Two different cores were used with parameters shown in Table 1.

Table 1: Details of cores used in experimental investigations

Parameter	Core A	Core B
Material	Losil 1000	Ferrosil 187
Lamination thickness, mm	0.50 mm	0.35 mm
Coreplate resistivity, $\mu\Omega$m	0.24 $\mu\Omega$m	0.36 $\mu\Omega$m
Core inner radius, mm	69 mm	110.5 mm
Core outer radius, mm	104.5 mm	220.5 mm
Axial length of core, mm	52 mm	200 mm
Stacking factor	0.85	0.8
Effective relative permeability of the core at low frequencies	360	320

The cores were wound with two coils spaced 180° apart as shown in Fig. 9*a* which were connected to a Hewlett-Packard 4192A, LF impedance analyser using the circuit shown in Fig. 9*b*. The relays were controlled using a minicomputer, allowing measurement of any two components of the TEE equivalent circuit. The mutual and self inductance of each coil was then found by elimination.

Measurements were made over the frequency range 60 Hz to 10 MHz. For the purposes of the analysis it was assumed that the impedances were linear. This was considered acceptable in view of the very small amplitude of currents used in the experiment, intended to model the small currents produced by discharges. However, care was taken to ensure that the measurements were all made with a constant value of ampere-turns applied to the cores, to ensure similar magnetic conditions for each measurement.

4.2 Results

The effective permeability of the cores was determined from the measured mutual inductance using eqn. 10.

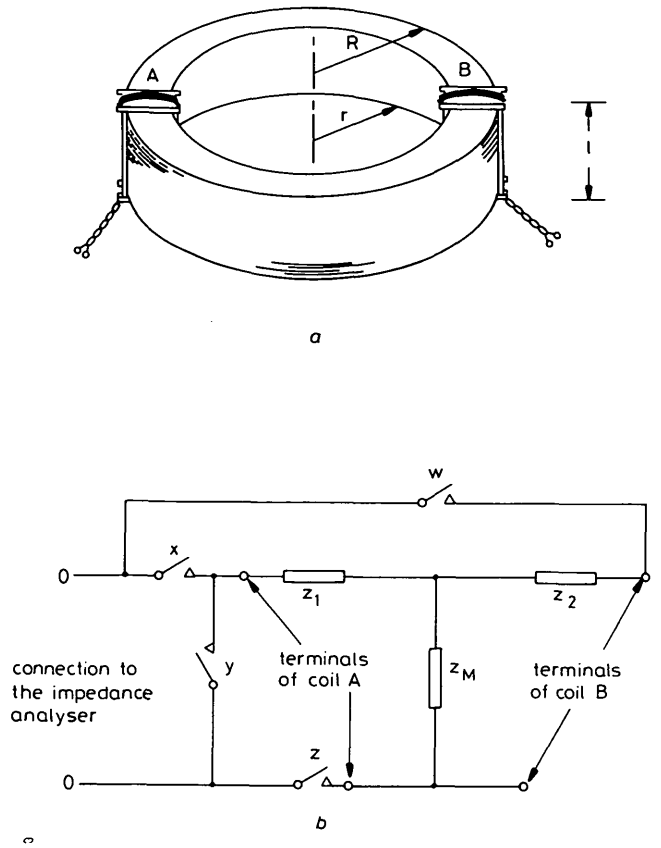

Fig. 9 *Arrangement of laminated cores and coils for measurements*
a Laminated core and coils
b Equivalent circuit representation of the coils and the impedance analyser

Results are shown in Fig. 10 together with the theoretical permeability calculated from eqn. 9, assuming the measured level of low frequency permeability. Both cores show the expected roll-off in permeability at frequencies above 1 kHz. Core A, which has the thicker laminations, shows a more rapid reduction in permeability than predicted from the analysis, falling to unity at 1 MHz. Core B, however, showed an effective permeability greater than unity at frequencies up to 10 MHz.

The measured reactances were also used to determine the coupling coefficients between windings. The results are shown in Fig. 11 together with

(*a*) the coupling coefficients for an infinite core:

$$\sum = m(\pi)/m(0) \tag{15}$$

(*b*) corrected coefficients including the effects of the self inductance m_0 associated with the radial section of winding at the core end:

$$\sum = m(\pi)/(m(0) + m_e) \tag{16}$$

where m_0 was adjusted to agree with the measured coupling coefficient at low frequencies.

The measured coupling coefficients show the expected roll-off at frequencies around 10 kHz, but the reduction at high frequencies is less severe than for the permeability curves in Fig. 10. Core A still shows significant coupling at frequencies up to 1 MHz and the measured coefficient for core B is comparable with the corrected theoretical value.

The graphs also show the calculated air cored coupling coefficient for coils of the size used on the cores. When the measured coupling coefficient falls below this predicted air cored value then the permeable core can be considered to have ceased contributing to the coupling.

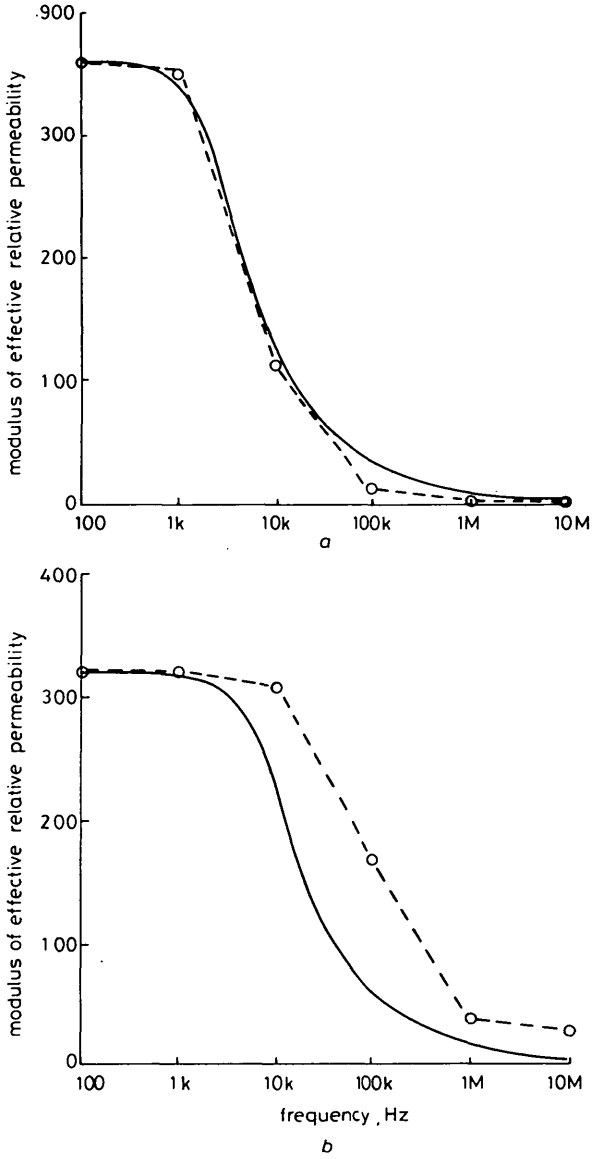

Fig. 10 *Variation of effective permeability of laminated steel cores with frequency*
a Core A *b* Core B
——— calculated from eqn. 9
--O-- measured on model cores

The significance of these results, and in particular the difference between measured and calculated values, is considered in Section 6.

5 Effect of core coupling on pulse propagation

It is beyond the scope of this paper to present a detailed model of pulse propagation in machine windings. However, it is worthwhile considering in general terms how the coupling between windings predicted by Section 3 and demonstrated experimentally in Section 4 may account for certain phenomena identified by experimental studies of pulse propagation in generator stator windings.

5.1 Coupling coefficient for a practical machine

To determine the effects of the finite core permeability on the propagation of discharge currents it is necessary first to evaluate the coupling coefficient for a core of practical

dimensions. To this end, the coupling coefficient has been calculated for a large turbine generator core with the laminate properties of core B in Table 1. Results are

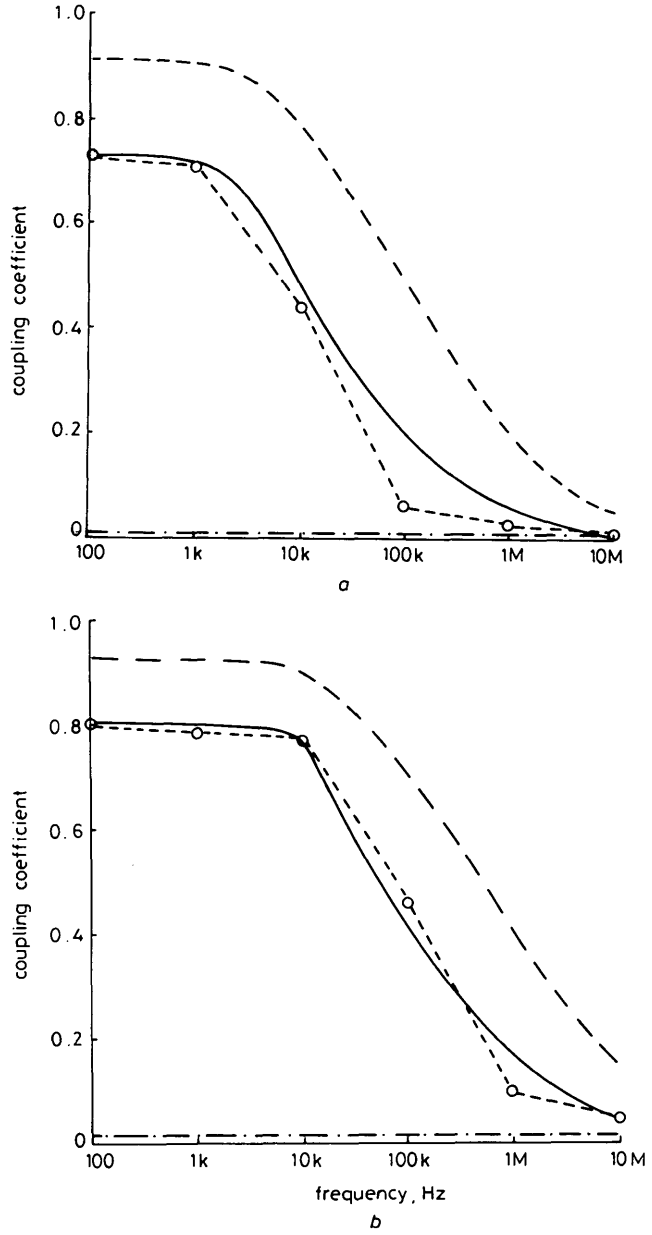

Fig. 11 *Variation of coupling coefficient across laminated steel cores with frequency*

a Core A *b* Core B
---- calculated from an ideal core
——— calculation including endwinding inductance
--O-- measured on model cores
—·—· air cored coupling for an effective permeability $\mu = 1$

shown in Fig. 12 for the experimental circuit of Fig. 8*a*, with the return currents flowing in a single conductor at the core back, and for the limiting case in which the currents return through a uniform conducting sheet at the core back (see Fig. 8*b*). In practice, the coupling coefficient would be expected to fall somewhere between these two extreme values.

Whilst the increase in core dimensions reduces the coupling coefficient predicted for the experimental circuit (Fig. 8*a*), the effect of the more even distribution of currents in the limiting circuit is to reduce the self inductance of the primary winding. Consequently, the coupling coefficients predicted for a large turbine generator ($\sum = 0.25$ to 0.85 at 1 MHz) are comparable with those predicted for the model cores (Fig. 11).

5.2 Modes of pulse propagation

Wilson *et al.* [1] identified two principal modes of pulse propagation for discharge pulses in generator stator

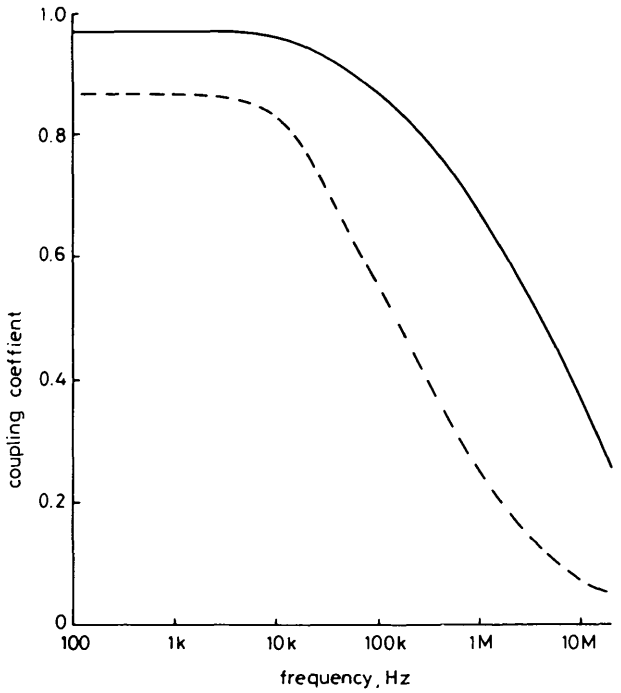

Fig. 12 *Calculated variation of coupling coefficient across large turbogenerator stator core*

---- with localised conductors at the core back
——— with a uniform conducting sheet at the core back

windings. At lower frequencies (10 kHz to 1 MHz) discharge pulses appear to propagate along the winding as in a transmission line. This series-mode propagation gives rise to a slow current pulse at the winding terminals with a transit time dependent on the wave velocity and the distance to the discharge site along the winding.

At higher frequencies (1 MHz to 17 MHz) a significant proportion of the measured current was produced by inductive and capacitive coupling between windings. This resulted in a fast current pulse at the winding terminals with an initial transit time almost independent of the location of the discharge site. This phenomena was referred to by Binder [13] as parallel-mode propagation.

5.3 Effect of core coupling

The penetration of the high frequency fields into the core is expected to have two principal effects on the propagation of discharge currents in generator stator windings.

(*a*) It increases the self inductance of the windings above the level expected if the core were to act as an earthed screen and hence reduces the wave velocity for series-mode propagation.

(*b*) It increases the mutual inductance between conductor bars, and hence increases the proportion of current propagating in parallel-mode at high measurement frequencies.

The effect of mutual coupling on pulse propagation may be seen by considering the simple model of the stator shown in Fig. 13. Here the stator winding is represented by just two conductor bars, a line end bar and a neutral bar, and it is assumed that the current pulse propagating in series-mode is severely attenuated along the length of the stator core. This allows the injected pulse to establish a circumferential flux at the terminal end of the core

which links the neutral bar inducing a current in the neutral earth connection.

It is shown in Appendix 11 that for this simplified representation of the core, the magnitude of current induced

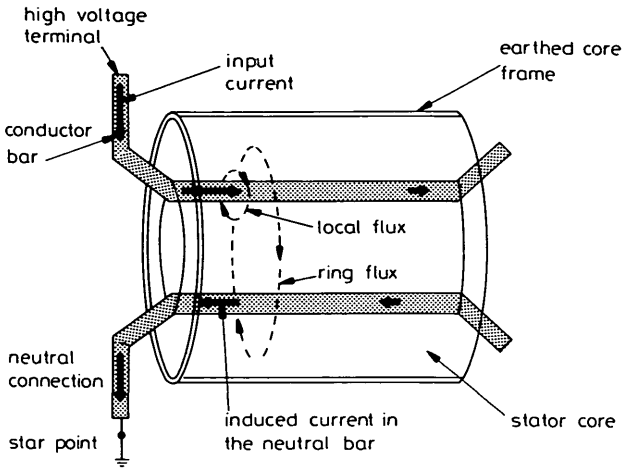

Fig. 13 *Simplified representation of generator showing effects of inductive coupling on propagation of high frequency currents in stator winding*

in the neutral earthing connection is simply related to the coupling coefficient between the circuits formed by the two conductor bars. Specifically, the ratio of the induced earth current to the current injected into the line end winding is $\frac{1}{2}\sum$ where $\sum$ is the coupling coefficient defined in Section 3.4.

It should be stressed that Fig. 13 represents a highly artificial model of the stator winding that may only be considered at all representative at high measurement frequencies when the series mode pulse is attenuated rapidly with distance along the core. At lower frequencies, currents reflected at the far end of the core will produce an opposing ring flux, and hence reduce the mutual coupling between sections of the stator winding. Having said this, the model does show how the finite permeability of the core could promote parallel mode propagation at high measurement frequencies producing a fast pulse of the same order as half the coupling coefficient shown in Fig. 12.

6 Discussion

Previous analyses of the propagation of surge and discharge currents in machine windings [4–7] have assumed that the laminated steel core supporting the stator winding could be represented by an impenetrable earthed screen (Figs. 4*a* and *b*). It is suggested here that this is not a valid representation of the core and that the distribution of magnetic flux in the core is more accurately represented by Fig. 4*c*. This shows that although the flux is constrained to the gaps between laminations and a skin depth on their flanks it penetrates deep into the stator core.

It has been suggested [6 and 7] that at high frequencies the magnetic flux will be excluded from the stator core by axial eddy currents flowing as displacement currents between laminations (Fig. 4*b*). However, the analysis presented in Appendix 10 shows that for practical coreplate (with $\mu < 1000$) the displacement currents will not significantly reduce the effective permeability of the largest generator stator cores at frequencies up to 20 MHz.

6.1 Effective permeability

The model of flux penetration shown in Section 3 has been used to derive an expression for the effective permeability of a laminated core as a function of frequency (eqn. 9). This indicates that although the effective permeability falls with frequency, there is still an appreciable component of magnetic flux linking a practical large core at frequencies up to 20 MHz.

Comparison of the calculated permeability with measurements on two model cores showed that the measured permeability was generally lower than the predicted value at high frequencies. Having said this, both cores showed an effective relative permeability that was greater than unity at frequencies up to 1 MHz.

It is possible that the discrepancy between the predicted and measured values results from the effect of hysteresis within the core steel at high frequencies. This would account for the reduction in permeability and the variation in high frequency permeability between two cores of different magnetic materials.

6.2 Coupling coefficient

Comparison of the predicted coupling coefficient with measured values showed that whilst the measured values were somewhat lower there was still significant coupling between the test windings at a frequency of 1 MHz ($\sum = 0.03$ for Core A and $\sum = 0.1$ for Core B).

In the practical situation, the coupling coefficient gives a measure of the mutual inductance between conductor bars relative to the bar self inductance. Generally, this depends not only on the effective permeability but also the stator dimensions. However, it is shown that significant coupling ($\sum = 0.25$ to 0.65 at 1 MHz) may be expected for a large turbine generator core suggesting that the finite permeability of the core will influence the propagation of discharge pulses in practical machines.

Generally, the results obtained on the model cores support the theoretical model of flux penetration in laminated cores proposed in Section 3 with the qualification that the present model is likely to overestimate the coupling coefficient between components of the stator winding.

6.3 Pulse propagation

Section 5.3 considered in general terms how the finite permeability of the core might affect the propagation of discharge pulses in the stator winding. The first and most direct effect is to increase the self inductance of conductor bars embedded in slots in the stator core, and hence reduce the velocity of series mode propagation depending on the measurement frequency.

There is some experimental evidence to support this proposition. Wilson *et al.* [1] measured a velocity of 69 m/μs for pulses with a central frequency of approximately 2 MHz compared to an expected velocity of some 150 m/μs if the core acts as an earthed screen. Also Binder [13] measured a velocity of 10 m/μs for series mode propagation at a central frequency of some 200 kHz. McLaren* carried out propagation experiments on machine coils embedded in both a solid and a laminated steel core. His result shows in Fig. 14, that the presence of a laminated core reduces the propagation velocity of the measured surge below the level measured on a solid steel core.

It was also shown in Section 5.2 that inductive coupling through the stator core could account in part for the

* McLaren, P.G. (private communication)

observed fast current pulse measured at the winding terminals. A highly simplified analysis in Section 9 suggests that the magnitude of the fast pulse relative to the

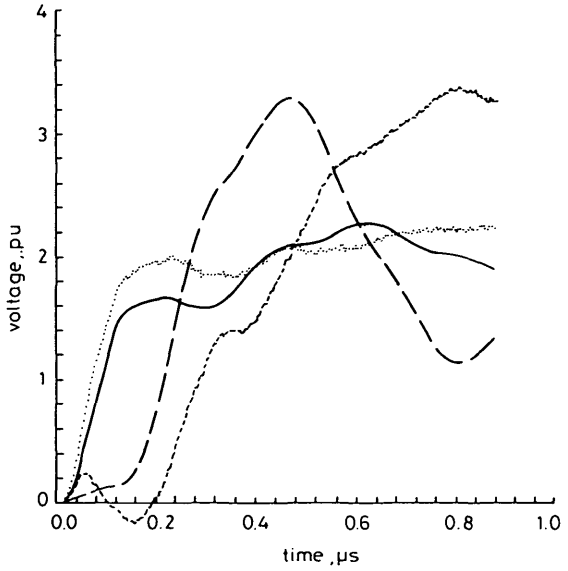

Fig. 14 *Effect of nature of core on propagation of surges through 10-turn machine coil*

——— coil 1, ground
— — coil 10, ground
} solid steel core as ground

····· coil 1, ground
- - - - coil 10, ground
} laminated steel core as ground

current injected at the discharge site will be of the same order as half the coupling coefficient defined in Section 3. Again there is some experimental evidence to support this suggestion. Figure 15, reproduced from Wilson *et al.*

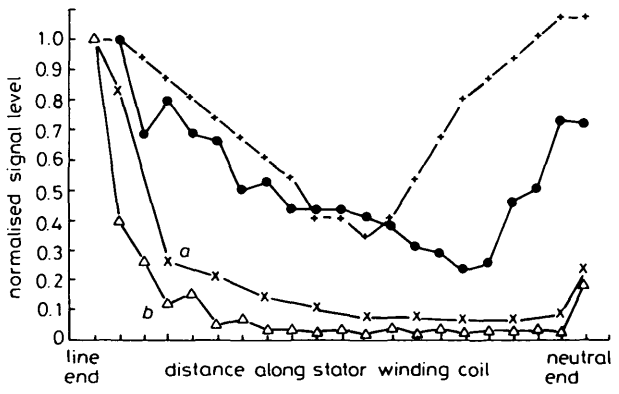

Fig. 15 *Variation of current measured at line-end terminal for current pulses injected on-to stator winding of 500 MW turbo-generator, from Wilson et al. [1]*

a Upper frequency limit = 1 MHz
b Upper frequency limit = 17 MHz
—+— 20–100 kHz
—●— 20–300 kHz
—×— 20K–1 MHz
—△— 0–17 MHz

[1] shows the relative magnitude of the current induced at the winding terminals for current pulses injected at various points along the stator winding of a large generator. At higher measurement frequencies, the measured current falls rapidly with distance of the current source into the winding due to the rapid attenuation of the series mode currents. However, the reduction is not truely exponential. Instead there remains a residual current almost independent of fault location associated with the fast pulse propagating in parallel-mode. The residual current of some 8% at an upper frequency limit of 1 MHz would correspond to a coupling coefficient of 0.016 and the level of 3% for a limit of 17 MHz to $\simeq 0.07$. These are of the same order as the coupling coefficients predicted for a large generator stator core in Fig. 12.

To summarise, there is evidence from experimental studies of pulse propagation in generator stator windings to support the proposition that the penetration of the magnetic flux into laminated cores has a significant effect on the propagation of discharge currents within the frequency range 20 kHz to 20 MHz.

There are many other contributors to the coupling between conductors besides the inductive effect of the core and these conclusions should not be taken to imply that the core coupling is the most important, but that it is significant.

7 Conclusions

A model of the distribution of magnetic flux in a laminated core excited by high frequency alternating currents is presented. It includes the effect of displacement currents flowing normally between laminations. This model may be simplified to give the following expression for the effective relative permeability of a laminated steel core:

$$\bar{\mu}_e = \{(1-\gamma) + \gamma\mu\mu_0 \tanh(\alpha)/\alpha\} \times \{\tanh(\beta)/\beta\}$$

where $\alpha = (1+j)L/\delta$ and $\beta = X/\Lambda$.

It is shown in Appendix 10 that for an ideal laminate, in which the permeability of the core steel is independent of frequency, the penetration depth at high frequencies is given by

$$\Lambda = -\frac{jc}{\omega}\sqrt{\left(\frac{(1-\gamma)}{(1-\gamma)+\mu\gamma/\alpha}\right)}$$

This model shows that for the frequencies contained in discharge and surge pulses it is not correct to say that the laminated steel stator cores of motors or generators act as impenetrable earthed screens. The model also shows that the penetration of flux into the core depends not only on the frequencies contained in the pulse but also on the stacking factor and radial depth of the core.

The stator cores of generators and large motors, made up of laminations of 0.35 mm or 0.5 mm thickness, make a significant contribution to coupling between conductors embedded in them up at frequencies up to 20 MHz. The cores do not act as impenetrable earthed screens at frequencies below at least a frequency of 20 MHz.

The effect of the laminated core on the propagation of discharge pulses is to reduce the velocity for series-mode propagation and to increase the amplitude of the currents propagating in the parallel-mode so that their per unit amplitude is of the same order as half the coupling coefficient of the core.

8 Acknowledgments

The authors would like to thank Mr. C.P. Burke who, together with Dr. B.G. Gaydon, devised the experimental arrangement described in Section 4, and carried out many of the experiments. This work was carried out largely at CEGB Laboratories. The paper is published with the permission of the Central Electricity Generating Board and the Directors of Laurence, Scott & Electromotors Ltd.

9 References

1 WILSON, A., JACKSON, R.J., and WANG, N.: 'Discharge detection techniques for stator windings', *IEE Proc. B*, 1985, **132**, (5), pp. 234–244
2 EMERY, F.T., LENDERKING, B.N., and COUCH, R.D.: 'Turbine-generator on-line diagnostics using RF monitoring', *IEEE Trans. Power Appl. & Syst.*, 1981, **PAS-100**, (12), pp. 4974–4982
3 MALIK, A.K., COOK, R.F., and TAVNER, P.J.: 'The detection of discharges in alternators using wideband radio frequency techniques'. Proc. 2nd Int. Conf. on Electrical Machines, Design and Application, IEE, London, 1985, Publication 254
4 RUDENBERG, R.: 'Electrical shock waves in power systems' (Harvard University Press, 1968), pp. 157–158
5 HELLER, B., and VEVERKA, A.: 'Surge phenomena in electrical machines' (Iliffe Books Ltd., London, 1968), p. 369
6 WRIGHT, M.T., YANG, S.J., and McLEAY, K.: 'General theory of fast-fronted interturn voltage distribution in electrical machine windings', *IEE Proc. B*, 1983, **130**, (4), pp. 245–256
7 McLAREN, P.G., and ORAEE, H.: 'Multiconductor transmission line model for the line-end coil of large AC machines', *ibid.*, 1985, **132**, (3), pp. 149–156
8 BONDI, H., and MUKHERJI, K.C.: 'An analysis of tooth-ripple phenomena in smooth laminated pole shoes', *IEE Proc.*, Monograph 225S, 1957, pp. 347–356
9 STOLL, R.L.: 'Analysis of eddy currents' (Clarendon Press, 1974), p. 15
10 HAMMOND, P.: 'Leakage flux and surface polarity in iron ring stampings', *IEE Proc. C*, 1955, **102**, pp. 1348–147
11 WAGNER, C.L., and SMITH, H.M.: 'Analysis of transient recovery voltage rating concepts', *IEEE Trans. Power Appl. & Syst.*, 1984, **PAS-103**, (11), pp. 3345–3363
12 BARTNIKAS, R., and McMAHON, E.J.: 'Engineering dielectrics, Vol. 1, Corona measurements and interpretation' (ASTM, Philadelphia, 1979)
13 BINDER, E.: 'Techniques of partial discharge measurements for stator windings of generators'. CIGRE Symposium, Vienna, 1987

10 Appendix

This Section describes the calculation of the effective permeability of a slab of laminate excited by high frequency currents on the slab surfaces flowing normally to the plane of the laminations (Fig. 16). This represents approximately the conditions arising when a generator stator core is excited by a ring winding with currents flowing axially along the bore and returning along the core back.

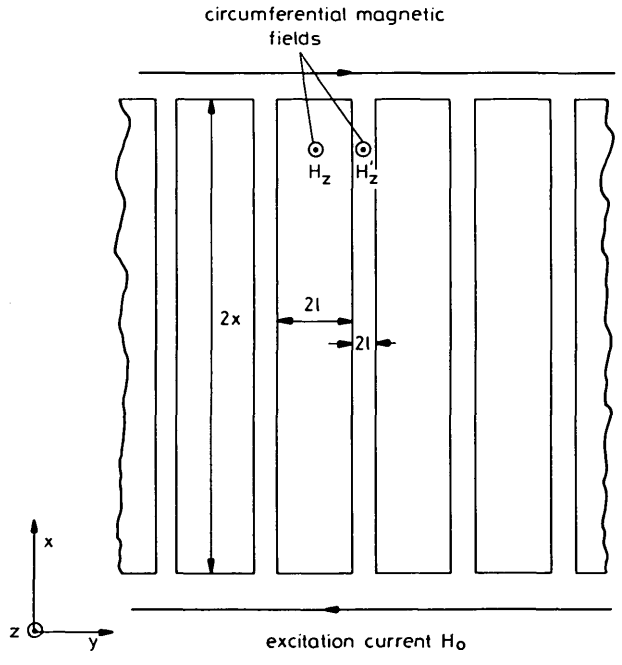

Fig. 16 *Notation and dimensions used for analysis of magnetic flux penetration*

10.1 Field equations and boundary conditions

The problem may be solved analytically in terms of the magnetic field H in the core steel and H' in the gap between laminations. Using the notation shown in Fig. 16, the symmetry of the problem dictates that components of magnetic field parallel to the plane of the laminations are zero, and the axial fields H_z and H'_z are symmetric about the origins which are at the midpoint of the lamination and gap respectively.

Within the core steel displacement currents are zero; thus, at an angular frequency, the magnetic field H_z satisfies the equation.

$$\frac{d^2H_z}{dx^2} + \frac{d^2H_z}{dy^2} = \frac{2j}{\delta} H_z \tag{17}$$

where $\delta = \sqrt{(2\rho/\omega\mu\mu_0)}$ and the components of electric field are given by

$$E_x = \rho \frac{dH_z}{dy} \quad \text{and} \quad E_y = \rho \frac{dH_z}{dx} \tag{18}$$

within the gap between laminations where currents are zero, thus the magnetic field H'_z satisfies the equation:

$$\frac{dH'_z}{dx^2} + \frac{d^2H'_z}{dy^2} = \frac{\omega^2}{c^2} H'_2 \tag{19}$$

in which $c = 1/\sqrt{(\varepsilon_0 \mu_0)}$ and the components of electric field are given by

$$E'_x = \frac{1}{j\omega\varepsilon_0} \frac{dH'_z}{dy} \quad E'_y = -\frac{1}{j\omega\varepsilon_0} \frac{dH'_z}{dx} \tag{20}$$

the electric fields and magnetic fields are continuous across the boundary between the core steel and the gap. Thus, for all values of x:

$$E_x)_l = E'_x)_{-l} \quad H_z)_l = H'_z)_{-l} \tag{21}$$

10.2 The exact solution

The field equations (eqns. 17 and 19) and the boundary value equations of eqn. 21 are satisfied by the expressions

$$H_z = \sum_n \alpha_n f_n \quad \text{and} \quad H'_z = \sum_n \alpha_n f'_n \tag{22}$$

where α_n is a constant and f_n and f'_n represent the Eigenfunctions in the core steel and the airgap, respectively,

$$f_n = c_n \sin(c_n l) \cos(b_n y) \frac{\cosh(a_n x)}{\cosh(a_n)} \tag{23}$$

and

$$f'_n = -j\omega\varepsilon_0 \rho b_n \sin(b_n L) \cos(c_n y) \frac{\cosh(a_n x)}{\cosh(a_n X)} \tag{24}$$

with

$$b_n = \sqrt{(a_n^2 - 2j/\delta^2)} \quad \text{and} \quad c_n = \sqrt{(a_n^2 + \omega^2/c^2)} \tag{25}$$

and a_n satisfying the Eigenvalue equation

$$(2jc^2/\mu\delta^2\omega^2)c_n \tan(c_n l) = b_n \tan(b_n l) \tag{26}$$

since the Eigenfunctions are orthogonal the constants, α_n may be determined from the magnetic field H_0 at the surface of the laminate ($x = X$) using the expression

$$\alpha_n = \frac{1}{k_n} \left\{ \left(\int_{-L}^{L} H_0 f_n \right) dy + \left(\int_{-l}^{l} H_0 f'_n \right) dy \right\} \tag{27}$$

where

$$k_n = c_n^2 \sin^2 (c_n l) \cos^2 (b_n L) x \times \left\{ L \operatorname{cosec}^2 (b_n l) + \frac{\tan (b_n L)}{b_n} + l \operatorname{cosec}^2 (c_n l) + \frac{\tan (c_n l)}{c_n} \right\} \quad (28)$$

Considering the simplest practical case in which the surface magnetic field is uniform and equal to H_0, the constants are given by

$$\alpha_n = \frac{2H_0}{k} c_n \sin (c_n l) \cos (b_n l) \times \left\{ \frac{\tan (b_n l)}{b_n} + \frac{\tan (a_n l)}{a_n} \right\} \quad (29)$$

To summarise, the magnetic field within a slab of laminate, of depth $2X$, excited by a uniform sinusoidal magnetic field at the surface of the laminate is given by

$$H_z = \sum_n \alpha_n f_n \quad \text{within the steel } (-L < y < L) \quad (30)$$

and

$$H'_z = \sum_n \alpha_n f'_n \quad \text{within the airgap } (-l < y < l) \quad (31)$$

where the Eigenfunctions f_n and f'_n are given by eqns. 23 and 24, and the constants n by eqn. 29.

10.3 Effective permeability

The effective permeability of the laminate, $\bar{\mu}_e$ may be defined as the mean value of the magnetic flux linking the laminate normalised to the product of the surface magnetic field and the cross-sectional area of the slab. Hence,

$$\bar{\mu}_e = \frac{\mu_0}{4(L + l)X} \times \int_{-X}^{X} \left\{ \int_{-L}^{L} \mu H_z \, dy + \int_{-l}^{l} H'_z \, dy \right\} dx \quad (32)$$

substituting for H_z and H'_z this yields

$$\bar{\mu}_e = \sum \frac{2 \tanh (a_n X)}{(L + l) a_n X} \times \left\{ \frac{(\mu \tan (b_n L)/b_n + \tan (c_n l)/c_n) \times (\tan (b_n L)/b_n + \tan (c_n l)/c_n)}{L \operatorname{cosec}^2 (b_n L) + \tan (b_n L)/b_n + L \operatorname{cosec} (c_n l) + \tan (c_n l)/c_n} \right\} \quad (33)$$

10.4 Approximate solutions

Although the above analysis gives exact expressions for the magnetic field within the laminate and its effective permeability, these are unwieldy and give little insight into the problem. The mode of penetration of high frequency magnetic fields into the laminate may be seen more clearly by considering approximate expressions for the Eigenfunctions and effective permeability, which are valid for practical laminates over the frequency range 0.01 to 100 MHz.

If the Eigenfunctions are ordered such that $|a_n| < |a_{n+1}|$, there exists one solution of the Eigenfunction equation for which $R_e(a_n) > 1$ and $|a_n| \ll 1/\delta$. This lowest order Eigenvalue, $|a_1|$, may be calculated approximately using the following simplifying assumptions;

(*a*) For a practical laminate, the thickness of the laminations $2L$ is much greater than the skin depth measured at high frequencies.

(*b*) At frequencies below 100 MHz, the penetration depth $1/a_1$ is much greater than the airgap width and than the wavelength c/ω.

Using the above approximations, the Eigenvalue equation reduces to

$$a_1^2 c^2/\omega^2 + 1 = -(1 - j)\mu\delta/2l \quad (34)$$

which has the meaningful solution

$$a_1 = \frac{j\omega}{c} \sqrt{\left(1 + (1 - j)\frac{\mu\delta}{2l}\right)} \quad (35)$$

This exponent determines the depth of penetration of the magnetic field into the laminate. In this mode, the magnetic flux is constrained to the gaps between laminations and to their side surfaces as shown in Fig. 7*b*.

Applying the same approximations to eqn. 33 for the effective permeability of the laminate, this reduces to

$$\bar{\mu}_e = \left\{ \frac{\mu \tan ((1 - j)L/\delta)(\delta/(1 - j) + l)}{(L + l)} \right\} \tanh (\beta)/\beta \quad (36)$$

where $\beta = X/\Lambda$ and Λ is the penetration depth between the laminations $1/a_1$.

The expression between the former pair of braces gives the effective permeability of a shallow section of laminate and the latter term determines the variation of effective permeability with core depth and frequency.

10.5 Example

The effect of displacement currents on the penetration of flux into a laminated core depends on the core dimensions and the electrical properties of the laminations. Generally, the lower the skin depth at high frequencies the smaller the penetration depth Λ.

Fig. 17 shows the variation of the penetration depth, Λ, with frequency for a core of representative dimensions

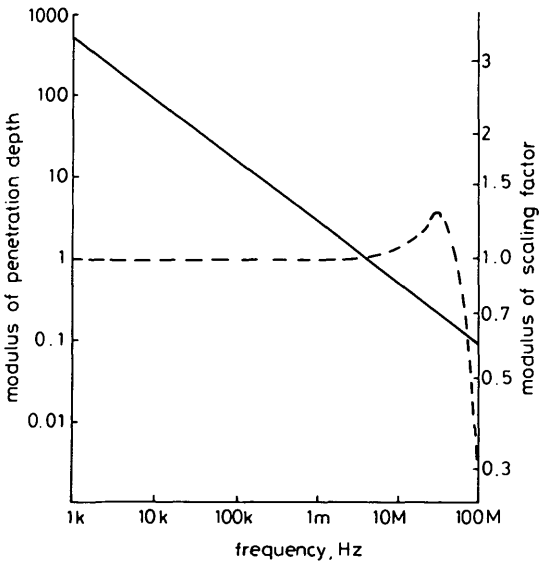

Fig. 17 *Variation with frequency of parameters governing penetration of magnetic flux into laminated core*

$L = 0.175$ mm, $l = 0.0175$ mm, $X = 0.25$ m, $\rho = 0.2$ μΩm, $\mu = 1000$

——— penetration depth

- - - - scaling factor

for a core steel of low resistivity (0.2 μΩm) and high relative permeability ($\mu = 1000$). It can be seen that even for these relatively extreme values, the penetration depth is

significantly greater than the dimensions of the largest generator cores ($X = 0.25$ m) for frequencies up to 10 MHz.

Also shown in Fig. 17 is the variation of the term determining the variation of effective permeability with frequency for a core depth $2X = 0.5$ m. This shows that the displacement currents do not materially reduce the effective permeability of the core below a frequency of some 20 MHz.

11 Appendix

This Section describes the calculation of the currents induced by a discharge pulse injected at the line end terminals of a generator stator winding. It refers to the simple model of a generator shown in Fig. 13, in which the stator winding is represented by just two conductor bars and the stator core is effectively of infinite length. That is to say, currents propagating along the bars are so severely attenuated along the length of the core that the currents in subsequent bars of the winding may be neglected.

The currents in the line end bar I_1 and neutral bar I_2 satisfy the equations

$$\frac{d^2I_1}{dx^2} = -\omega^2 LCI_1 - \omega^2 MCI_2 \tag{37}$$

$$\frac{d^2I_2}{dx^2} = -\omega^2 MCI_1 - \omega^2 LCI_2 \tag{38}$$

and

$$\frac{dI}{dx} = -C\frac{dV}{dt} \tag{39}$$

where V is the conductor bar voltage, L is the self inductance, and M is the mutual inductance. C is the capacitance to earth, ω the measurement frequency, and x the distance along the core.

The currents also satisfy the boundary conditions at the terminals ($x = 0$) of

$$I_1(0) = I_0 \cos(\omega t) \tag{40}$$

and

$$V_2(0) = 0$$

The above conditions are satisfied by the solution

$$I_1 = I_0(\cos(\omega t - K_1 x) + (K_1/K_2) \times \cos(\omega t - K_2 x))/(1 + K_1/K_2) \tag{41}$$

$$I_2 = I_0(\cos(\omega t - K_1 x) - (K_1/K_2) \times \cos(\omega t - K_2 x))/(1 + K_1/K_2)$$

where $K_1 = \omega\sqrt{((L + M)C)}$ and $K_2 = \omega\sqrt{((L - M)C)}$.

Hence the normalised current induced in the neutral earthing connection:

$$I_2(0)/I_0 = (1 - K_1/K_2)/(1 + K_1/K_2) \tag{42}$$

substituting for K_1 and K_2, this yields:

$$I_2(0)/I_0 = \frac{\sqrt{(L - M)} - \sqrt{(L + M)}}{\sqrt{(L - M)} + \sqrt{(L + M)}} \tag{43}$$

At high frequencies when the coupling coefficient $\sum = M/L$ is much less than unity the above expressions reduce to

$$I_2(0)/I_0 = -\frac{1}{2}\sum \quad \text{for } \sum \ll 1 \tag{44}$$

Thus, the ratio of the current measured in the neutral earthing cable to the injected current is $\frac{1}{2}\sum$ for the simple model of a generator shown in Fig. 13.

TRANSIENT THERMAL CHARACTERISTICS OF INDUCTION MACHINE ROTOR CAGE

D.J.T. Siyambalapitiya, Student Member, IEEE
and
P.G. McLaren, Member, IEEE

Cambridge University Engineering Department
Trumpington Street
Cambridge
United Kingdom CB2 1PZ.

P.J. Tavner

Laurence, Scott and Electromotors Ltd.
P.O. Box No. 25
Kerrington Road
Norwich
United Kingdom NR1 1JD.

Key Words:- Induction machines, Finite element analysis, Thermal analysis

Abstract- Thermal analysis of an induction machine cage rotor during stall conditions forms an important part of design calculations. The study of rotor circuit thermal behaviour is also useful to identify causes of failure in large cage rotor induction machines. The paper presents a 3-dimensional finite element based electrical-thermal analysis of the bar and end ring area of a large rotor to examine its thermal characteristics during a stall. Details of temperature variations at key locations in the bar and end ring are provided. The calculations are compared with experimental results and the advantages and limitations of the solution technique for rotor analysis are discussed.

INTRODUCTION

Induction machine cage rotor thermal analysis has been a subject of interest for machine designers in their efforts to improve machine reliability and in rotor design optimisations. Being the most widely used type of large industrial machine, the cage rotor induction machine thermal aspects have been studied especially in the cases of stall, long run-up time, overloading and frequent starting. Rotor temperatures measured during a series of tests on a 350-hp machine and the possible failure mechanisms of the rotor under excessive heat dissipation are reported in [1]. More recently, rotor temperature information about small and medium sized cage rotor machines has become useful in the design of inverter driven variable speed machines. The protection systems of large machines also require the rotor thermal information for the time-delay setting of overcurrent relays in conventional protection systems.

Rosenberry[2] used an equivalent thermal network of the rotor for transient thermal analysis of a cast aluminium cage rotor during stall conditions. The lumped thermal elements of such equivalent networks provided a general view of the rotor temperatures according to the level of discretization employed. The finite element analysis (FE) method and the presently available computer programs enable detailed rotor thermal analysis of a variety of small and large rotor areas, according to the preferred level of discretization and the conditions to be examined. The implementation of the finite element method for thermal analysis of a turbogenerator rotor and its use for the study of the effects of stator unbalanced operation is reported in [3].

88 WM 025-9 A paper recommended and approved tby the IEEE Rotating Machinery Committee of the IEEE Power Engineering Society for presentation at the IEEE/PES 1988 Winter Meeting, New York, New York, January 31 - February 5, 1988. Manuscript submitted August 28, 1987; made available for printing December 11, 1987.

Griffith et al.[4] used the finite element method to calculate the temperature distribution across a rotor bar of a large machine during several operating conditions including stall and run-up periods. A combined magnetic-electric-thermal model was used and the heat transfer between the bar/end ring model and the rotor iron were included in the analysis. Iron saturation over the top of the bar was also included in the magnetic-electric component of the analysis. It was reported that the maximum temperature during the stall condition occurs on the bar upper surface at a location within the slot close to its joint with the end ring. The effect of the coolant passages on the temperature distribution was highlighted. The measured temperatures agreed within 10°C of the calculated values at the end of a 26s stall at full stator voltage. Maximum temperatures during run-up could be calculated to agree with in 20°C of the measured values. Williamson and Lloyd [7] describe an equivalent electrical circuit method of calculating the temperature rise in a stalled cage but particularly highlighting the effect of stator winding space harmonics on the bars.

This paper describes a 3 dimensional finite element electrical-thermal analysis of the cage rotor of a 1600-kW machine intended for applications in potentially explosive environments. In such machines, the rotor surface temperatures during stall are of considerable concern to the designers. The analysis presented here is restricted to the stall condition at full rated voltage. It was intended to use a finite element discretization and implementation with minimum complexity and computing resources. The finite element model formulation, material thermal constants and the considered heat transfer mechanisms are described. Bar and end ring current distributions are assigned using standard design calculations.

The time variation of temperature at several key locations on the rotor circuits is given along with the measurements. Comparisons are made with the measurements made on the test machine and with the results of design calulations using thermal equivalent networks. The analysis is extended to a further period after de-energization and the heat flow patterns during this period are given.

FINITE ELEMENT IMPLEMENTATION

The 3-dimensional electric field due to current flows in the bar and end ring agrees with the equation,

$$\frac{\partial}{\partial x}\left(\frac{1}{\rho_x}\frac{\partial V}{\partial x}\right) + \frac{\partial}{\partial y}\left(\frac{1}{\rho_y}\frac{\partial V}{\partial y}\right) + \frac{\partial}{\partial z}\left(\frac{1}{\rho_z}\frac{\partial V}{\partial z}\right) = 0 \qquad (1)$$

where, V = rms voltage
ρ = electrical resistivity of material.
x,y and z are the coordinate directions.

The solution to (1) can be used to calculate the rate of heat generation $\dot{Q}$ due to current flows in the bar and end ring regions. $\dot{Q}$ is then used in the 3-dimensional transient thermal equation,

$$\frac{\partial}{\partial x}(k_x \frac{\partial T}{\partial x}) + \frac{\partial}{\partial y}(k_y \frac{\partial T}{\partial y}) + \frac{\partial}{\partial z}(k_z \frac{\partial T}{\partial z}) = DC \frac{\partial T}{\partial t} - \dot{Q} \qquad (2)$$

where, T = temperature
k = thermal conductivity
D = material density
C = material specific heat
$\dot{Q}$ = internal heat generation rate
t = time

Coefficients of both equations (1) and (2) can be temperature dependent material properties. The combined solution begins with the solution of (1) at ambient temperature conditions. The copper losses are then calculated and are used in (2) to obtain the temperature profile. In a multi-step solution, this result can again be used in (1) with the modification of temperature dependent constants based on the latest temperature solution. Temperature dependent coefficients of equation (2) are calculated based on its solution in the previous time step.

HEAT BALANCE AND THERMAL CONSTANTS

The heat generation and transfer mechanism in a cage rotor under stall conditions can be summarised as follows:-

Sources:-

i) Rotor bar I^2R losses in the slot area.
ii) I^2R losses in the bar over-hang and the end rings.
iii) Iron losses in the laminations.

Transfer:-

i) Convective transfer to air gap region, the surrounding air and internal air flow paths.
ii) Convective transfer from the surface of shaft.
iii) Heat transfer between the stator and the rotor.

The bar and end ring I^2R heating is the principal contributor to the heating of the rotor during stall conditions. Heat transfer between the stator and the rotor can occur only through the air gap or by radiation. Both are negligible at the usually encountered machine temperatures under stall conditions of short (typically 10s) duration. Thus the analysis assumes that the air gap provides complete thermal insulation between the stator and the rotor, which is also the standard practice in conventional thermal analysis of rotors [5]. The conduction heat transfer from the bar to the rotor steel is also neglected.

Eddy current and hysteresis losses are substantial during stall because of mains frequency fluxes. The thermal resistances between the slot and the bar is large and the contribution to bar temperature variation by iron losses is negligible compared with those from bar currents. Therefore for the present analysis, iron losses are also neglected.

STALLED ROTOR SIMULATION

The finite element technique was used for rotor electrical-thermal simulation of a stall condition in a 1600-kW cage rotor machine. The relevant specifications of the rotor are given in the appendix. Manufacturer's specifications for the machine were for an application in a potentially explosive environment in which the temperatures of the exposed areas needed to be accurately calculated and experimentally verified.

The rotor has no coolant passages in the radial direction and thus the symmetry of the bar/end ring model could be fully utilised to reduce the magnitude of the problem. Rotor bars are embedded in tunnel shaped slots which completely cover the bar. The shape of the rotor slots is not significant as no substantial heat transfer occurs between the bar and the slot for stall conditions of short duration. Rotor bars are brazed into the slotted end ring as shown in figure 1. The end ring is surrounded by a retaining ring which also can be excluded from the model in studies of short duration.

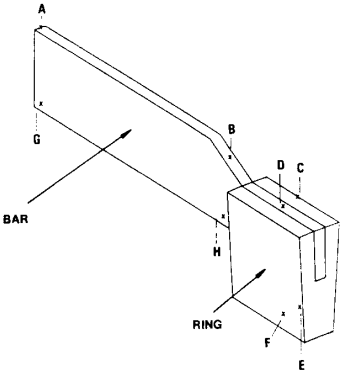

Fig.1. Details of bar/end ring joint area of the 1600-kW machine. Locations A-H are used to identify results in figures 6,7 and 10.

Finite element model and solution

The largest concentration of current and subsequent temperatures are expected to occur in the bar/end ring joint region. The finite element model, shown in figure 2, includes a quarter-length of a rotor bar and a sector of the end ring centred on the joint. Previous studies with a model including a half-length rotor bar indicated that the current distribution on the bar within the slot maintains a similar temperature distribution throughout the bar in the slot region away from the overhang. The complete finite element model uses 831 nodes forming 530 elements. However, the actual analysis uses a reduced model of 551 nodes and 323 elements, using the symmetry of the complete model in figure 2 about the bar centre plane. Heat flows are nearly 2-dimensional (axial and radial directions in terms of rotor coordinates) in the bar within the slot away from the overhang region and thus a coarse mesh was selected in the direction of the width of the bar.

All the elements have the electrical-thermal capability and the equations (1) and (2) are solved in a two-step process. In the transient simulation which uses a number of time steps, the solution to equation (1) within a time step is used to calculate the heat input term of equation (2) for the thermal solution in the next time step. For this reason, small time steps were selected at the beginning of the stall. The initial time step was 40ms and was increased to 3.5s toward the end of the 10s simulation period, thus minimising the number of steps and computing time. The results shown subsequently for a 10s stall simulation used 12 time steps.

Electrical inputs

It is assumed that the degree of heating around the cage is uniform, although the stator winding harmonics can affect this as described in [7].

Bar currents in the slot region: The current distribution on the rotor bar within the slot during stall is uneven due to leakage inductance

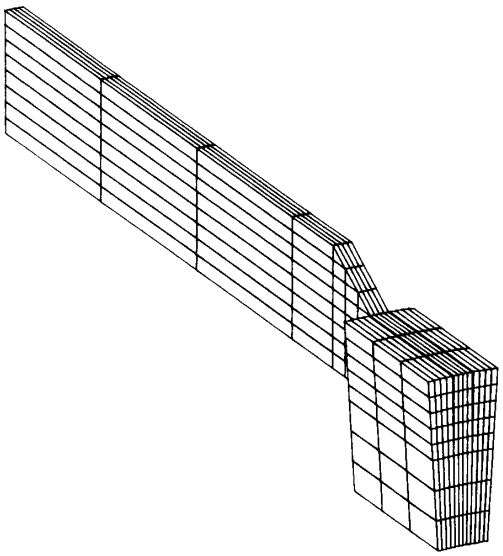

Fig.2. The 831-node, 530-element model of bar quarter-length and end ring segment. See the appendix for the dimensions of the modelled region.

considerations. The current density at a height of x from the bar bottom surface is expressed by [6],

$$\underline{J}_x = \frac{(1+j)I}{W\delta} \cdot \frac{\cosh[(1+j)(x/\delta)]}{\sinh[(1+j)(D/\delta)]} \qquad (3)$$

where, I = total rms current
D,W= bar dimensions as given in figure 3
and δ = skin depth, given by

$$\delta = \sqrt{\frac{2\rho}{\mu_0\omega}}$$

where, ρ = electrical resistivity of material
μ_0 = permeability of free space
and ω = angular frequency of currents

Thus, the density at a height of x is,

$$|\underline{J}_x| = \frac{\sqrt{2}I}{W\delta}\sqrt{\frac{\cosh(2x/\delta)+\cos(2x/\delta)}{\cosh(2D/\delta)-\cos(2D/\delta)}} \qquad (4)$$

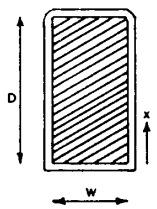

D = 40 mm
W = 12.5 mm
ρ = 2.51 x 10^{-8} Ohm m at 20°C

Fig.3. Bar dimensions

and currents were assigned to the elements of the bar within the slots accordingly.

Bar overhang and end ring: The current distributions in the bar overhang and the end ring are largely determined by the magnetic field due to their own currents and their proximity to the stator and rotor. For the purpose of this study, a uniform distribution of current is assigned to these regions of the model, but the effective resistivity of the material is adjusted to the ac resistivity ρ_{ac}, given by,

$$\rho_{ac} = \rho_{dc} \cdot \frac{DW}{\delta(D^2+W^2)} \left\{ W \cdot \frac{\sinh(2D/\delta)+\sin(2D/\delta)}{\cosh(2D/\delta)+\cos(2D/\delta)} + D \cdot \frac{\sinh(2W/\delta)+\sin(2W/\delta)}{\cosh(2W/\delta)+\cos(2W/\delta)} \right\} \qquad (5)$$

where ρ_{dc} is the dc resistivity of the material. Both the bar and the ring are made of chrome-copper alloy.

The initial current density on the ring is about 24 A/mm² resulting in an initial rate of rise of temperature of about 22°C/s. The corresponding values for the bar top surface are 35 A/mm² and 32°C/s. The temperature coefficient of resistivity of the bar and ring material is about 3.5×10^{-3} K^{-1}, which represents a 3.5% increase in resistivity for a 10°C rise. At constant stator applied emf, the increased rotor resistance reduces the current flows on the bars and the rings as the stall progresses. The electrical inputs to the FE model are in terms of currents obtained from design calculations using material resistivities at ambient temperatures. If the currents are maintained fixed at these initial values and if the temperature variation of resistivity is only accounted for in the heat input calculations, the results of the thermal analysis is likely to indicate inaccurate estimates for temperatures during the latter stages of the stall. The expected reduction in rotor bar currents under constant air gap emf is shown in figure 4. The reduction is due to the temperature increase in resistance while leakage reactance remains constant. As such, at constant emf, the rotor currents reduce with temperature and the copper losses on the cage rise at a rate much lower than the rate of rise of resistivity. The electrical-thermal analysis used in this paper, works on a constant current basis but the resistivity variation with temperature is adjusted such that the heat dissipation inputs to the thermal solution will be in accordance with the variation in figure 4.

Thermal properties

Isotropic, temperature independent thermal properties were assigned to the entire model. These values were,

thermal conductivity, k = 335 W/m.K
material density, D = 8900 kg/m^3
and, specific heat, C = 377 J/kg.k

Simulation results and measurements

Figure 5 shows the isotherms on the bar centre plane and the ring after 10s into the stall condition. The top surface of the ring reaches a temperature of 200°C. The temperature differential between the top and the bottom of the bar reaches 45°C at less than the quarter rotor length position from the slot end. Isotherms in the bar overhang region indicate that large heat flows occur from the ring to the bar through the joint. The temperatures on the ring end

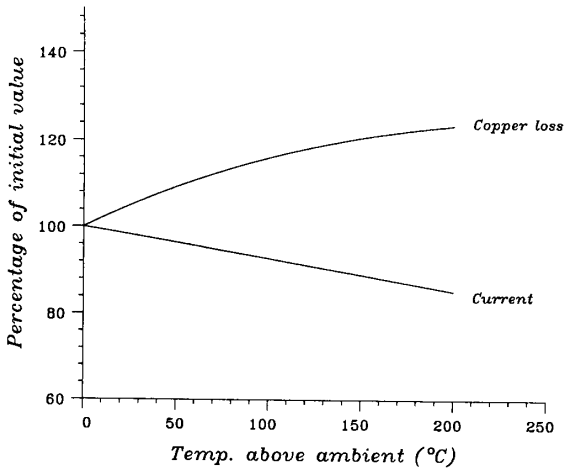

Fig.4. Rotor current and loss variation due to increased temperatures.

surface on the outer side of the cage are shown in figure 6.

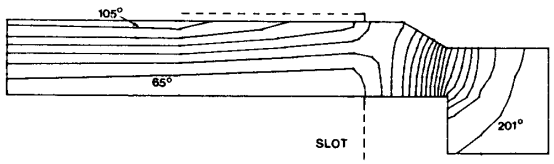

Fig.5. FE calculation of temperature rise on the bar mid-plane at 10s during stall. Contours are 8°C apart.

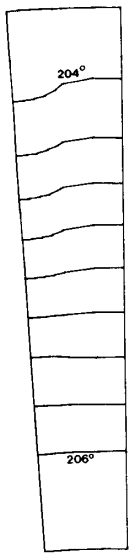

Fig.6. FE calculation of temperature rise on the ring outer surface at 10s. Only the left hand side part of the ring segment is shown.

The experimental results shown on figure 7 for the bar and end ring were obtained using thermocouples and conventional instrumentation during a stall test in the factory test bed under constant stator applied emf. The design calculations are based on a 4-element discretization of the bar region and thermal equivalent circuit analysis.

Figure 8 shows the FE calculated temperature variations at six key locations on the model. Locations on both the bar and the end ring are shown. Points C and D on the ring top surface as well as points E and F on the inner surface showed parallel temperature profiles and only one location on each surface is plotted in the figure.

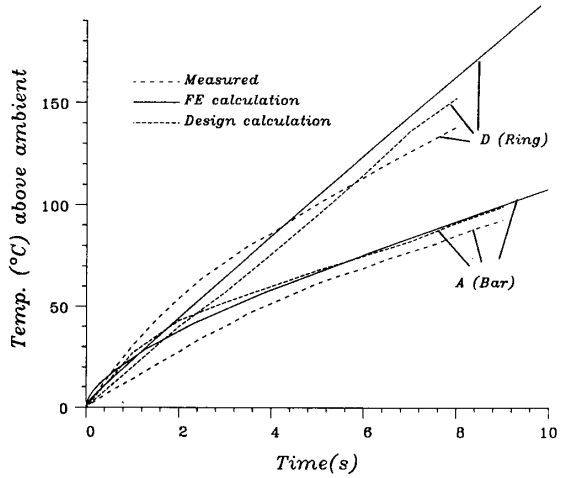

Fig.7. Calculated and measured temperature transient during stall. Locations A and D are identified in figure 1.

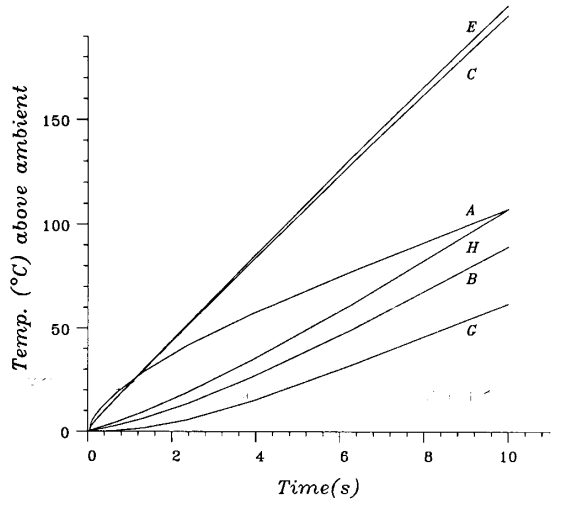

Fig.8. Calculated temperature variation during stall at 6 selected locations. Locations A-H are shown in figure 1.

The calculated and measured temperatures for the ring agree within 10°C during the first 3-second

period. The discrepancy during the latter part of the transient may be partly caused by increased convective heat transfer from the surface at elevated temperatures. The improvement to the difference of 20°C by assigning modest heat transfer coefficients to all free surfaces of the model was about 3°C at 8s.

REDISTRIBUTION AFTER POWER OFF

The rotor thermal profile after the stall condition has been removed by de-energization, is largely determined by its geometry and heat transfer from hot areas to the rotor steel and the air gap. The surface temperatures are again of concern in deciding upon the time duration within which a restart of the machine will not be allowed. The FE analysis for the stall period of 10s was continued for a further 10s-period after de-energizing the machine. All other conditions with regard to heat conduction and convection remained unchanged.

The calculated temperature profile on bar mid-plane at 14s and 20s are shown in figure 9. The previous figure 8 showing time variation of temperature at 6 locations is extended to 20s in figure 10.

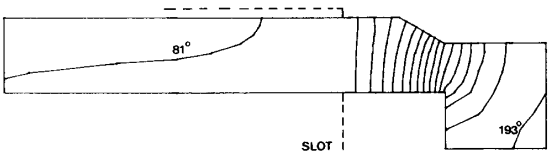

(a) Temperatures at 14s. Contours are 7°C apart.

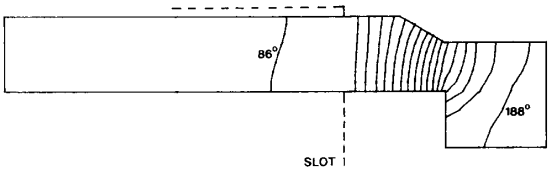

(b) Temperatures at 20s. Contours are 6°C apart.

Fig.9. Temperature distribution on the bar mid-plane after a stall condition of 10s. Times shown are total from the initial cold start.

Effects of heat transfer

The above analyses were done under adiabatic boundary conditions. Modest levels of heat transfer, though small when compared with those at run-up and full speed, can affect the surface temperatures. The retaining ring above the end ring may increase the conductive heat transfer from its upper surface which can be the main contributory factor to the high value of calculated ring temperatures towards the latter part of the transient. The measured temperature profile for the bar and the ring follow similar trends which also indicate that the current distribution on the ring is not uniform but more concentrated at the outer regions. The configuration of the joint to the bar also contributes to the higher current density in the ring upper regions.

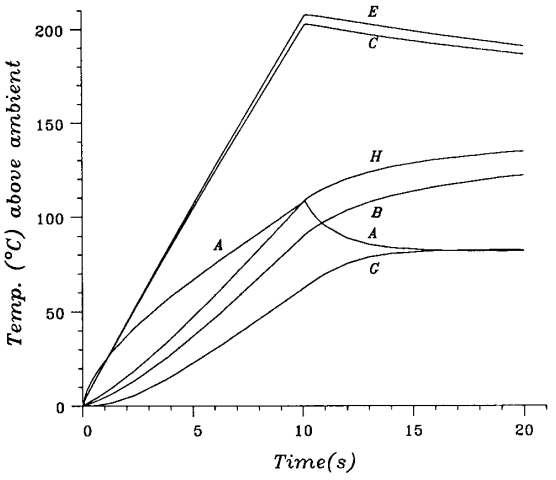

Fig.10. Time variation of temperatures at 6 locations with power off at 10s. Locations A-H are identified in figure 1.

CONCLUSIONS

The 3-dimensional electrical-thermal analysis of rotor bar and end ring during a stall condition is useful in understanding the temperature profile in the bar/end ring joint area of a cage rotor machine designed for operation in hazardous environments. The finite element analysis used in the paper is based on the hyperbolic current distribution in the bar region with uniform distribution in the end ring. The ring resistances are represented by the ac values. The model is capable of predicting the initial temperature profile accurately.

The slotted end ring and geometry of the model indicates large temperature gradients between the ring and the bar region and consequent heat flows from the ring to the bar through the joint. The temperature variation of several locations, which the analysis is able to provide, is useful to determine the possible modifications to the rotor geometry to reduce severe thermal gradients. The variation after de-energizing the machine can be used as a guideline in determining the time to the next restart in order that the specified temperatures are not exceeded. A Rotor electrical-thermal model alone provides sufficient accuracy for the transient calculation during the first few seconds. The incorporation of a magnetic analysis to calculate the currents in bar and ring will be able to reduce the ambiguities in the current assignments used in the present analysis. A further refinement would be to include the retaining ring in the end ring region and the rotor steel in the bar region of the FE model. Both these options will require more computing resources. The 3-dimensional capability of the analysis has enabled the extraction of ring surface temperatures around the joint region. The transient thermal characteristics of a given machine are determined by the geometry of the bar and the ring and a complete understanding of the temperature profile helps to improve design methods and cooling techniques.

ACKNOWLEDGEMENT

This paper is published with the permission of the Directors of Laurence, Scott and Electromotors Ltd., U.K.

REFERENCES

[1] W. T. Martiny, R. M. McCoy and H. B. Margolis, "Thermal relationships in an induction motor under normal and abnormal operation", AIEE Transactions on Power Apparatus and Systems, Vol.PAS-80, pp.66-78, April 1961.

[2] G. M. Rosenberry, "The transient stalled temperature rise of cast-aluminium squirrel-cage rotors for induction motors", AIEE Transactions on Power Apparatus and Systems, Vol.PAS-74, pp.819-824, October 1955.

[3] A.F. Armor, " Transient, Three-dimensional, Finite-element Analysis of Heat Flow in Turbine Generator Rotors", IEEE Transactions on Power Apparatus and Systems, Vol. PAS-99, NO.3, pp.934-946, May/June 1980.

[4] J. W. Griffith, R. M. McCoy and D. K. Sharma, "Induction motor squirrel cage rotor winding thermal analysis", IEEE Transactions on Energy Conversion, Vol.EC-1, pp.22-25, September 1986.

[5] E.Levi, Polyphase Induction Motors, John Wiley and Sons, New York, 1984, pp.211-232.

[6] P.L. Alger, The nature of polyphase induction machines, Chapman and Hall, London, 1951, pp.241-246.

[7] S. Williamson and M.R. Lloyd, 'Cage rotor heating at standstill', To be published in IEE Proceedings 1987.

APPENDIX

Specifications of the experimental machine:-

Rated output	1600 kW
Rated voltage	6.6 kV
Frequency	50 Hz
No. of poles	2
Speed	2960 r/min
Stator connection	Star

Rotor

Bar and ring material	Chrome-copper alloy
Resistivity of bar and ring material	2.51×10^{-8} Ohm m
Temperature coefficient of resistivity	3.5×10^{-3} K^{-1}

Bar cross section	rectangular	40mm x 12.5mm
Ring cross section	rectangular	56mm x 54mm
Rotor stack length		740mm
RMS currents during stall		
	Bar	8808 A
	Ring	72 888 A
Stator phase current during stall		869 A

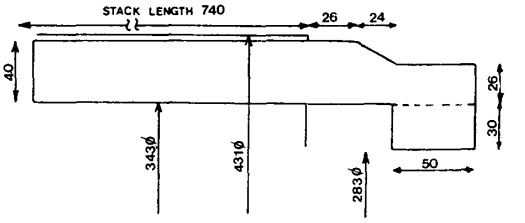

Fig.11- The bar/end ring joint area.(Dimensions in mm)

D.J.Tilak Siyambalapitiya (S'85) was born in Sri Lanka in 1960. He received the B.Sc(Eng.) degree in Electrical Engineering from the University of Moratuwa, Sri Lanka, in 1982.

From 1982 to 1984 he was with the Energy Coordinating Team, Ministry of Power and Energy, Sri Lanka, working on National Energy Planning, Management and Conservation programmes. He is presently on leave from the Sri Lanka Electricity Board, reading for his Ph.D. at University of Cambridge, U. K. His present research interests include measurement of rotor parameters and condition monitoring of Electrical Machines.

Peter G. McLaren (M'78) was born in Perth, Scotland in 1936. He received his B. Sc. with 1st class honours in Electrical Engineering from the University of St. Andrews in 1958.

He was employed by A.E.I. in their Power Systems Development department until late 1961 when he returned to the University of St. Andrews as a lecturer specialising in power systems and machines. During this period at St. Andrews he was also a part time research student and completed his Ph. D. in the subject of sampling techniques applied to power system protection. In 1967, he moved to Heriot-Watt University in Edinburgh for 1 year before joining the staff of the University Engineering Laboratory at Cambridge, U.K. His research interests are in electrical machines, superconductors and signal processing problems arising in power system protection. He is the author of a recent text-book entitled "Elementary electric power and machines" published by Wiley.

On sabbatical leaves, he has spent 3 months at the Technion Institute of Technology in Haifa, Israel, 14 months with the System Studies Section of Ontario Hydro Research Division, 5 months with the Canadian Maglev project at Queens University, Ontario and 9 months on a joint Royal Society/NSERC visiting fellowship at the University of Calgary, Canada.

Peter J. Tavner was born in Erith, England in 1946. He studied at Fitzwilliam College, Cambridge where he graduated with upper second class honours in Engineering in 1969. He took his Ph.D. in Electrical Machines at the University of Southampton, U.K. in 1978.

After serving as an engineer officer in the Royal Navy, he joined the Scientific Services Department of the CEGB and led the Electrical Power Section responsible for investigating service problems in turbo-alternators, electrical machines and high voltage plant. In 1985, he joined Laurence, Scott and Electromotors Ltd. of Norwich, U.K., where he is the Chief Electrical Engineer. His interests are in large and special electrical machines.

He is the author of a number of papers on elctromagnetic problems, particularly associated with the stator cores of large machines. He has also published a book on "Condition Monitoring of Electrical Drives".

Monitoring generators and large motors

P.J. Tavner, M.A., Ph. D., C.Eng., M.I.E.E., B.G. Gaydon, B.Sc., Ph.D., C.Eng., M.I.E.E., C.Phys., M.Inst.P., and D.M. Ward, B.A., Ph.D., C.Phys., M.Inst.P.

Indexing terms: *Generators, Motors*

Abstract: The paper describes how techniques for monitoring the condition of generators and large motors have been used and developed in one region of the UK Central Electricity Generating Board. Many parameters need to be monitored on a generator, so that a comprehensive and clear picture of any degradation can be built up for use in planning shutdowns and maintenance. Only a few parameters are needed for motors. The criteria for successful monitoring are considered, and examples are given of experiences with selected monitoring techniques.

1 Introduction

The Central Electricity Generating Board (CEGB), in its power stations, operates many large electrical machines, ranging from pump motors of a few tens of kW up to main generators of 660 MW. To obtain the maximum benefit from the capital investment in generation plant, it is necessary to maintain high plant availability. This is mainly achieved by good plant design and a high standard of maintenance but there is a need for operators to monitor the plant to detect any deterioration of performance, to give early warning of plant failure and to guide the maintenance work.

Electrical plant has traditionally had a high reliability. This is principally because the complex problems of electrical design have led to machines being generously designed for their rating. Protective relays have also reduced the extent of damage when faults do occur. These relays provide protection by sensing gross disturbances in the currents flowing within the machine. When these disturbances are detected the relays operate to interrupt the electrical supply and they have proved, over the years, to be effective and reliable. For a relay to operate, however, a fault current must normally flow and this can cause extensive melting and burning, requiring substantial repairs to the machine.

Modern rotating electrical machines are now designed to tighter margins. A large turbogenerator is restricted in size, because of weight limitations on its stator, and has the highest mechanical, electrical and magnetic loadings achievable with present materials. Large motors are also designed more accurately to a rating to reduce manufacturing costs. Furthermore, in the CEGB, we have reached a stage where even the oldest generating plant on the system has a relatively good thermal efficiency, so that there is a strong economic incentive to continue running plant up to and beyond its original design lifetime. In this environment, therefore, it is not surprising that modern electrical machines will experience a small but still significant number of defects, leading to failures which cause losses of availability. CEGB experience in this area has been described by Barker and Hodge [1].

It is always best to carry out repairs at a time which incurs the minimum overall cost. So there is an economic incentive to detect plant defects before they became failures and to continue running the plant until the optimum time for repair occurs. This can be achieved by careful plant monitoring. The strategic importance of generators and large motors in power stations and the present level of defects means that condition monitoring of this plant is worth pursuing within the CEGB.

This paper is about monitoring experience in one region of the CEGB and confines itself mainly to the newer techniques applied online to generators and large motors already in service. The work incorporates contributions from a number of the authors' colleagues, within the South Eastern Region, which are gratefully acknowledged. The paper describes those techniques with which we have particular experience but puts these in context alongside the many other developments in electrical machine monitoring being made by colleagues elsewhere in the CEGB and other industries.

2 Benefits of monitoring

The flow of fault current, detected by a protective relay, is the final part of an electrical machine failure, and involves consequential damage. Earlier warning of a failure could be provided by making relays especially sensitive so that they give an alarm. This is often done, for example, in the rotor earth fault relay of a generator, but the warning is relatively short. Damage must precede the flow of a fault current, so for monitoring to improve on relays it must detect this damage, as directly as possible, and give a clear indication that it has occurred. If warning is given early and the information is presented clearly enough, the machine can be removed from service for repair or a repair can be scheduled at a more convenient time.

The benefits which condition monitoring can bring to a particular machine depend upon the following:

(*a*) the amount of warning monitoring can give of an impending failure

(*b*) the value of the machine itself

(*c*) the total cost incurred if the machine fails, which depends upon:

(i) the direct cost of the repair or replacement

(ii) the time to repair or replace the machine

(iii) the replacement generation costs per day for the generating unit in which the machine is operating

(iv) whether standby capacity or a spare for the machine is available

(d) the cost and reliability of the monitoring scheme itself.

As an example, taking these points into account, if reliable monitoring of a high value, strategic machine can detect a fault only 1 s before the protective relays would operate, the monitoring is hardly likely to be any benefit. On the other hand, if monitoring can reliably give 1 h or more warning on this same machine, that is likely to be of considerable value and if days or months of warning can be

Dr. Gaydon and Dr. Ward are, and Dr. Tavner was formerly, with the Central Electricity Generating Board, South Eastern Region, Scientific Services Department, Canal Road, Gravesend, Kent DA12 2RS, United Kingdom. Dr. Tauner is now with Laurence Scott and Electromotors Ltd., PO Box 25, Kerrison Road, Norwich NR1 1JD, United Kingdom

given on machines of less value, that can be beneficial in planning maintenance.

To summarise, condition monitoring of an electrical machine will yield benefits if a reliable monitoring system exists, which can provide sufficient warning of a typical failure mechanism, so that the machine can be taken out of service and repaired at a cost which is substantially less than if fault currents flowed. The net benefit will be positive if the cost of the monitoring system is less than the likely saving in cost of repairs following faults.

At the moment, condition monitoring on electrical machines is in its infancy, largely because of the inherent reliability of electrical plant. Larger motors and generators are already fitted with a number of traditional monitoring sensors. However, a number of new monitoring techniques have been devised, and with the availability of cheap computing power, measurements from these and traditional techniques can now be processed and acted upon in a way that makes condition monitoring viable for large, strategically important machines. But effective condition monitoring must consist of all three of the following parts:

(*a*) measuring selected parameters to give early indication of damage

(*b*) processing and assessing the significance of these measurements

(*c*) taking action upon these measurements.

This paper is primarily concerned with (*a*), giving, in the following Sections, our experience of the development and use of a number of new techniques. But, in the later Sections, we give an indication of how, in the future, (*b*) and (*c*) can be satisfied to complete an effective condition-monitoring package.

3 Monitoring techniques for motors

The vast majority of motors used in power stations are induction machines and in this Section only the detection of faults in these machines is considered. The two principal fates for an induction motor are that it can stall or suffer a flashover. Many of the defects leading to these fates are identifiable at an early stage. Fig. 1 sets out the common defects of electrical machines and we will show how some of them, relevant to motors, can be detected by monitoring. Developments in monitoring techniques have progressed rapidly in the last few years; some of them were reviewed, for smaller machines by Ashen *et al.* [2] and some of the techniques are not yet available commercially. Many of these techniques enable a motor to be run with a slowly developing, known defect until the most economic opportunity for repair occurs.

3.1 Electrical and magnetic techniques

3.1.1 Magnetic flux: Under ideal conditions the induction motor has an airgap magnetic field which varies sinusoidally in space and time. Many rotor or stator defects will cause a distortion of this sinusoidal waveform. Rotor defects can be detected by a search coil fixed to the stator but few industrial motors have such search coils, because there is a natural reluctance to fit a sensor if it could conceivably hazard the machine or personnel. There seems little doubt that suitable search coils could be fitted to new motors, as the hazards can be made negligible and search coils are now becoming common on large alternators (see Section 4.1). The technique was used experimentally on induction motors by Kamerbeek [3].

Any distortion in the airgap flux density due to defects on either rotor or stator will also set up an axial homopolar flux in the shaft which can be detected by a search coil fitted around the shaft. An early proprietary version of such a device is described by Rickson [4] but CEGB experience in detecting faults on the unused winding of two-winding two-speed motors was disappointing. Recent work by Penman *et al.* [5] has developed this idea and shown that a range of both stator and rotor defects can be deduced from the spectrum of the axial flux obtained by carrying out a Fourier transform on the search coil waveform. For rotor defects, the technique provides similar information to the stator current spectrum analysis and speed fluctuation measurement techniques described in the following paragraphs. The technique is applicable to a wide range of motors but there is a possibility that, on some designs, the enclosure may attenuate the amplitude of the axial flux detected by a search coil mounted outside it. This makes the quantitative estimate of the extent of damage difficult without fingerprinting of individual motors.

3.1.2 Stator current: The current drawn by an ideal motor should have a single component at the supply frequency. Changes in load will modulate the amplitude of the current to produce sidebands. Defects in the rotor circuit will generate a sideband below the supply frequency

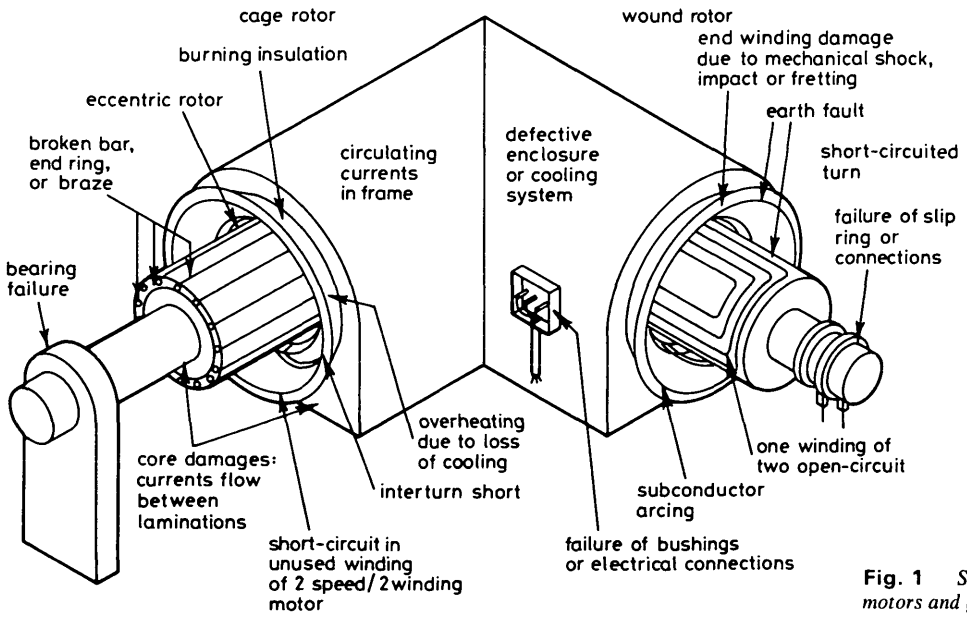

Fig. 1 *Schematic diagram of failure mechanisms in large motors and generators*

and displaced from it by twice the slip frequency. This sideband will be apparent on the machine ammeter as a slow fluctuation in the current supplied to the motor. The ratio of the sideband amplitude to the main supply frequency component gives a straightforward indication of the extent of rotor damage (see Reference 6).

Hargis [7] has shown that a proprietary spectrum analyser with good frequency resolution, a capability known as zoom, looking at the stator current can clearly distinguish between healthy and defective rotors. All that is required is the spectrum analyser and a clip-on current transformer monitoring the motor current in a central switchroom. The technique can also give warning of load and drive-train defects such as worn gear teeth. To prevent any ambiguity a separate measurement of motor speed may be required, but this has rarely proved necessary on operational motors. An automatic monitor could be devised which uses the frequency of slot-ripple currents to provide the motor speed reference. Steele *et al.* [8] have used this technique on small motors.

3.1.3 Rotor current: The rotor circuit of a wound rotor motor is poorly protected in most installations, and one of the reasons for developing the method of Reference 4 was to protect against this type of fault. Defects in brazed joints and slip-ring connections have often caused severe damage because they have not been detected promptly. Overheating of the rotor can also be caused by current imbalance in the external resistors connected to the slip rings. The low frequency of these currents makes measurement with conventional current transformers unsatisfactory.

Recent developments in the NE Region of the CEGB, using air-cored current transducers, or Rogowski coils, have shown promise as the low frequency rotor currents can be measured and an alarm triggered if the currents are unbalanced. Such a monitor has been described by Ellison *et al.* [9]. The Rogowski coils used in the monitor were wound on rigid formers wrapped around the cables to the external resistors from the slip rings. The high accuracy required in the measurement tends to make the cost of this instrument attractive only for the largest motors.

3.1.4 Partial discharges: Warning of incipient electrical breakdown in a motor could be obtained by the online measurement of partial discharge activity. Gradual degradation of stator insulation will lead to increased partial discharge activity, but a quantitative relationship between that activity and the remaining life of the insulation, which is needed for condition monitoring, has not yet been established and may prove difficult to demonstrate. Even under laboratory conditions, the prediction of remanent life for electrically stressed specimens does not have the accuracy needed. Within the CEGB there have been proposals to monitor partial discharge activity on motor windings (see Reference 10). Its success can only be established if motors fail in service after increases in partial discharge activity have been observed. Discharge monitoring techniques, however, have been much more widely applied to generators where damaging discharge activity is a more common precursor of major faults and the financial benefits of obtaining this warning are greater. The technique is described in more detail in Section 4.1.

3.2 Mechanical techniques

3.2.1 Vibration: Motor bearing vibrations are sometimes monitored continuously, and a comprehensive facility with spectral analysis facilities is in use at some power stations. More often, measurements are made as an infrequent routine or when a problem is suspected. The measurements are made using either accelerometers or velocity transducers bolted, or fixed using magnetic clamps, to bearing pedestal caps. The amplitude of the vibration is used as a guide to bearing wear and misalignment, or balancing problems. Displacement probes are also used for monitoring shaft movement directly. Misalignment between bearing centres, which results in a nonuniform airgap may cause twice supply frequency vibration, whereas mechanical imbalance will cause vibration at rotational frequency, both depending on the mechanical response at that frequency. Misalignment between the motor and the driven load will result in a vibration at twice rotational speed. Modulation of the vibration at twice slip frequency can be indicative of rotor damage; both amplitude and frequency modulation can occur as Kamash has described [7]. Many vibration specialists are unaware of how easy it is to measure slip frequency; a mains synchronous stroboscope aimed at a motor shaft will show any mark reappearing at the illuminated location at slip frequency, independent of the number of pole pairs.

Shock pulse measurement (SPM) is also a valuable technique for both plain and rolling element bearings. Rolling element bearings are used on some motors in the CEGB, particularly those driving boiler coal mills, but we do not have any experience of the SPM technique.

3.2.2 Speed fluctuations: The speed of an induction motor driving an ideal load should be constant. Perturbations in load and defects within the rotor circuit of the machine will cause the speed to fluctuate. If the rotor is defective, the speed fluctuation will occur at twice slip frequency. This is because the normal, torque producing, slip frequency currents that flow in the rotor are unable to flow through the defective part. Gaydon *et al.* [7, 11, 12] have measured these fluctuations directly with an instrument that uses a signal averaging technique locked to the slip frequency of the motor. A once-per-revolution pulse is required from the motor shaft, using either an optical or magnetic sensor. This enables the rotational period of the

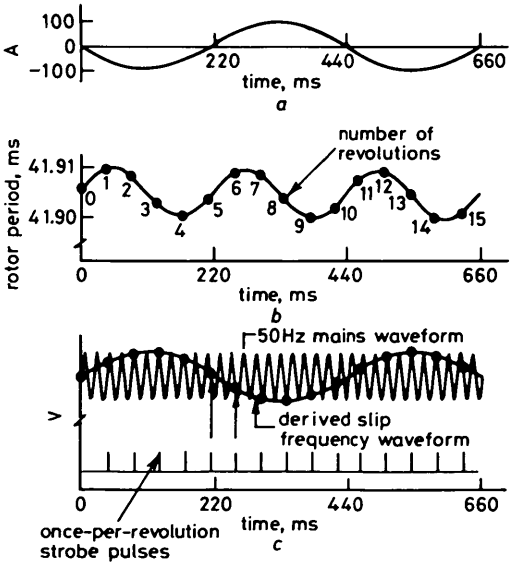

Fig. 2 *Motor speed fluctuation waveforms*

a The current in a healthy rotor bar flows at slip frequency but is normally unmeasurable

b The shaft period is measured; the shaft speeds up and slows down at twice the slip frequency

c The 50 Hz supply frequency is strobed by the once-per-revolution shaft pulses to produce a slip frequency waveform for use as a reference signal

shaft to be measured to a precision of 1 μs. Fig. 2 shows how the rotational period will be perturbed by a typical defect in a rotor. The small changes in shaft period are converted by the instrument to the normalised quantity 'fractional change in slip', and this is directly related to the amount of rotor damage to be expected. For effective signal averaging, a reference signal at slip frequency is obtained by strobing the supply frequency with the once-per-revolution pulse, as shown in the lower part of Fig. 2. This is a rare example of 'aliasing' being used to advantage. The technique has similar capabilities for detecting rotor defects to the stator current and flux analysis techniques described in Section 3.1. Arguably, the speed fluctuation method, as currently implemented, gives a clearer indication of rotor circuit damage, but has less scope for detecting defects in the load or other parts of the machine. Hundreds of motors have been surveyed using this technique and many with defects have been identified and repaired, avoiding costly in-service breakdowns. An automatic installation is also in service monitoring gas circulator motors online and has proved reliable.

A recent development has been to produce an instrument that can communicate over an IEEE-488 bus; the instrument rapidly measures the motor speed fluctuations and passes the data to a proprietary portable computer. For permanent installations, a scanner can be added to the bus so that every large motor on a site can be checked for rotor defects automatically several times each day. The prototype of this instrument (named Rotach) has been produced at the Central Electricity Research Laboratories in collaboration with one of the autors, and commercial exploitation should commence shortly.

3.2.3 Temperature: Bearing temperatures are often surveyed on a routine basis, like vibration levels, and give a useful warning of tribological problems. Coolant bulk outlet temperatures are also valuable for indicating cooling problems and for monitoring when it is proposed to operate a machine beyond its rating. Winding temperatures would be very valuable for determining the limit to which a motor can be loaded and for estimating the remanent life of the winding insulation. They are rarely measured because of the problems of obtaining electrical isolation from high-voltage conductors, although temperature detectors are sometimes embedded in the insulation close to the hottest point of the conductor but this does impair the insulation integrity. There is therefore a need for a rugged temperature sensor which can be mounted on the winding copper or embedded in the insulation which is electrically isolated from its instrumentation. The Vapotherm technique [13] with a vapour pressure capsule has been used with some success for monitoring winding temperatures in transformers. In its present form, it is not considered to be sufficiently rugged for use in motors.

3.3 Chemical techniques

3.3.1 Gas analysis: Most motors are cooled by air, often in a closed circuit arrangement with a water-cooled heat exchanger. Degradation of electrical insulation within the motor produces carbon monoxide gas which passes into the cooling air circuit and can be detected by an infra-red absorption technique. A monitoring system has been developed in the CEGB which scans eight wound rotor motors sequentially and can raise an alarm if the carbon monoxide concentration exceeds 5 parts in 10^6 by volume (vpm). Fig. 3 shows the arrangement that is used in which a plastic tube collects samples from the cooling air circuit of each motor. Air is drawn from the motor through the

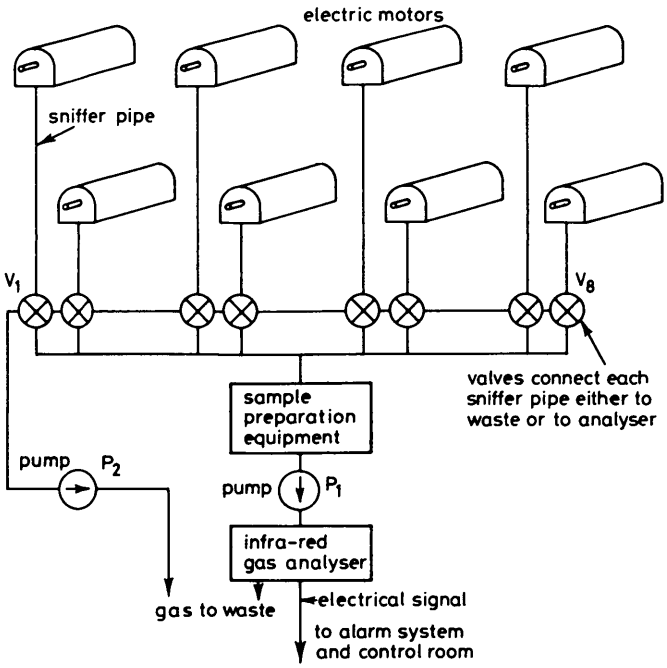

Fig. 3 *Chemical methods of detecting faults in motors*

tube to the infra-red detector by an auxiliary pump. Only motors in service are sampled and the air from each motor is analysed for 2 minutes. If four motors are running, the maximum time to respond to an increase in carbon monoxide concentration is therefore 8 minutes. Within a sealed motor enclosure, the air should recirculate with a long residence time but, because of gaps in a practical machine enclosure, a substantial proportion of the total volume of air is exchanged with the environment every minute. Even so, the gas analyser has been shown to have sufficient sensitivity to detect localised overheating of motor windings.

3.3.2 Oil analysis: The oil from bearings can be routinely analysed, and action taken if degradation products are present. For most motors, the benefits rarely justify the costs of analysis. Continuous monitoring of bearing oil for debris has been employed and proprietary debris monitors are now available but have not been used for our region of the CEGB.

4 Monitoring techniques for generators

A generator in a power station is a much bigger, higher cost, more strategically important item of plant than even the largest motor. When a serious fault occurs, large phase-to-phase or phase-to-earth currents will flow and the generator protection system will trip the unit. However, even if a unit is tripped instantaneously, a substantial amount of damage could be done because of the stored energy and the finite time taken to de-excite the machine. Fig. 4 shows an example of this damage. It is desirable to monitor the possible modes of deterioration long before such a trip occurs so that repairs can be effected at a convenient time and more serious damage prevented. The basic failure mechanisms are the same as for motors, as set out in Fig. 1, although there are additional complexities because large turbogenerators are hydrogen-cooled with water-cooled stator windings. A generator is normally fitted with a wide range of conventional instrumentation as Hodge *et al.* [14] have described,

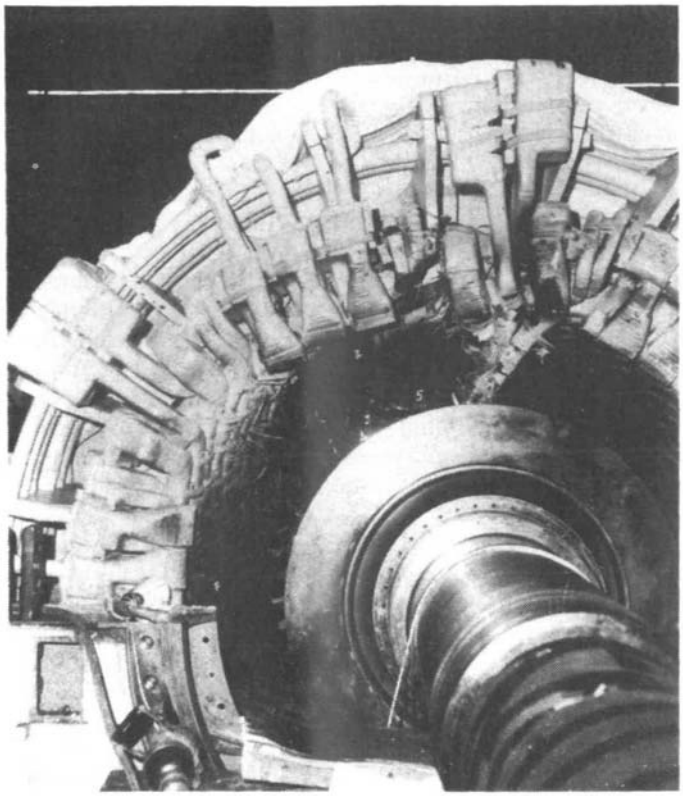

Fig. 4 *Example of damage after an alternator trip*

but a number of new techniques are being developed. The following paragraphs describe some of these new techniques in more detail and set out our experience with them on two-pole, turbine-type, hydrogen cooled generators rated at 350 MW and above.

4.1 Electrical techniques

4.1.1 Partial discharges: Many of the defects shown in Fig. 1 are preceded or accompanied by electrical discharge activity as discussed in Section 3.1. A variety of detection techniques have been tried on generators, both within the CEGB and abroad. The energy propagated through the winding from the discharge contains components at less than 5 MHz which can be detected by a high-frequency current transformer wrapped around the neutral connection as described by Wilson *et al.* [10], Emery *et al.* [15] and Timperley [16]. A variant to this technique is to detect the voltage pulses developed at the terminals of the machine across a blocking capacitor, as described by Kurtz *et al.* [17]. Laboratory tests by our colleagues have shown, however, that the discharge pulses due to breakdown have a frequency spectrum extending to beyond 1 GHz, whereas that for corona discharges extends to only 350 MHz, so that there are signal-to-noise advantages in detecting between these frequencies. The energy in this frequency band is radiated from a discharge site through the cooling gas, rather than along the winding, and can be detected by a radio-frequency (RF) aerial mounted inside the generator casing, or outside close to an aperture in it. This technique has been used by us and is described by Malik *et al.* [18].

Our experience with discharge detection techniques on generators is that they provide valuable information about discharge activity, but their indications are not sufficiently precise for operator action to be taken upon them. The indications should, however, be considered alongside those from other monitors.

4.1.2 Rotor faults: A single earth leakage fault on a generator rotor winding is not of itself serious, because it does not cause any damage. However, if two well-separated earth faults occur, large currents could flow, leading to significant damage to the rotor forging. The normal procedure for detecting earth faults in large generators is to apply a DC bias voltage to the rotor winding and to test the current flowing to earth via an alarm relay (see Reference 19). If such an alarm occurs, it is usually considered that the fault should be thoroughly investigated, but if because of operational pressures it is necessary to continue running the unit, the next step is to monitor the earth leakage current and trip the unit if there is any further increase, indicative of a second earth fault. Methods for doing this are under development and described by Hargis *et al.* [20].

Turn-to-turn faults may lead to local overheating, which then eventually leads to rotor earth faults. In addition, short-circuiting of turns causes unequal heating of the rotor, leading to bending and an unbalanced magnetic pull on the rotor, which together cause increased vibrations as described by Rosenberg [21]. One way of detecting such short-circuited turns using an airgap search coil was first described by Albright [22]. The search coil, of diameter less than the tooth-width of the rotor, is fixed to the stator and suitably positioned in the air gap. Its output voltage waveform is dominated by the rotor tooth-ripple. When there are short-circuited turns in the rotor winding, the height of the corresponding peaks and troughs in the ripple will change so that the output voltage waveform will no longer be symmetrical about zero. In principle, these changes enable the number and location of short-circuited turns to be found. Such search coils have now been installed in a large number of generators in the CEGB. In his original paper, Albright measured the peak heights of the ripple in the waveform from oscilloscope photographs. Byars [23] describes an alternative method whereby the output voltage waveform from the search coil is added to a delayed version of itself, where the delay is half a cycle, thus nulling all the signal except that component which is asymmetric. An instrument to do this is commercially available and can be used to monitor short-circuited turns with the generator on load. Other more sophisticated ways of analysing and interpreting the signals from the search coil, using a digital storage oscilloscope and computer processing, are described by Conolly *et al.* [24] who show how these techniques have been used reliably for interpreting rotor winding faults on a large number of generators.

Computer simulations by one of the authors, and the practical experience of others, suggest that the magnitude of the asymmetric component of the output waveform from the airgap search coil depends on the load as well as the location and number of short-circuited turns. In the absence of magnetic saturation, the magnitude of this asymmetric component would be expected to be proportional to rotor current. However, magnetic saturation local to the short-circuited turn has a significant effect, so that for some loads and locations of short-circuited turn, the magnitude of the asymmetry actually decreases with increasing rotor current. Research is continuing on the best ways to allow for this effect.

An alternative way of monitoring for short-circuited rotor turns, which is still under development, uses the stator winding itself as the search coil. The principle of this technique, first suggested by Khryukin [25], has been developed and fitted to a number of generators in the CEGB (see Muhlhaus *et al.* [26]). This technique makes

use of the fact that in large two-pole generators, each phase of the stator winding consists of two half-phase windings in parallel. The presence of short-circuited turns on the rotor is detected by measuring the even harmonic currents circulating round these parallel windings. A diagram of such a monitor is shown in Fig. 5. An advantage of this new technique, when compared to the airgap search coil, is that the current transducers can be installed without the need to remove the rotor from the generator. A disadvantage is that it does not readily give information on the location of a short-circuited turn.

4.1.3 Shaft voltages: Some utilities, including our own, have attempted to monitor the voltages induced along the shaft of a generator in the hope that these may be a useful general indicator of stator core or winding degradation. Verma *et al.* [27] have given a very full report on the mechanisms for the production of shaft voltage and the faults they may indicate. Experience in the CEGB has included monitoring the shaft voltage online and evaluating the harmonics of the waveform. Shaft voltage has not proved to be a useful parameter for continuous monitoring, because it is difficult to measure reliably and also because it has been shown that any damage to the core or winding would need to be substantial before a significant variation in shaft voltage occurred. This should not detract, however, from the normal procedure of measuring shaft voltages at bearing pedestals, from time-to-time, to check the pedestal insulation.

4.2 Mechanical techniques

4.2.1 Vibration: As mentioned in Section 4.1, short-circuited turns in the rotor winding will lead to a change in the vibration of the rotor. In particular, short-circuited turns will give rise to a component of vibration at a frequency equal to the rotor speed, whose amplitude increases as the square of rotor current. However, if some of the cooling gas ducts in the rotor are partially obstructed, this could also lead to an asymmetric temperature distribution in the rotor body and a component of vibration, at a frequency equal to the rotational speed, the amplitude of which increases as the square of rotor current. An intermittent short-circuited turn in the rotor winding could give rise to sudden changes in vibration, but so too could a shifting end-bell, or stick-slip movement of the rotor windings. For these reasons, analysis of the bearing vibration is not able to identify generator electrical problems unambiguously. So it is better to use devices such as the airgap search coil as the primary indicator of such faults.

The analysis of vibration data from bearings along the whole of a turbine and generator shaft train to diagnose shaft problems has now reached a high degree of sophistication, as described by Mayes *et al.* [28]. We have experience of such methods in the SE Region (see Reference 29), which have been used to identify shaft misalignments and rotor cracking.

Some older turbogenerators have experienced damage due to cracking of stator conductors as a result of end winding vibration. So machines have been instrumented with accelerometers on the end winding structure to give early warning of any excessive movement. We have had experience of this technique but, in general, it is used for occasional survey purposes to determine when end winding tightening needs to take place.

4.2.2 Gas leakage: In older designs of stator windings, arcing can occur between subconductors in the conductor bars. The water carrying subconductors can then be punctured, leading to an increase in the leakage of hydrogen into the stator cooling water. Generators are normally fitted with gas release chambers of known volume and an indication of gas leakage is given from such chambers by an indication with which a chamber is vented. This is satisfactory during normal operation. Experience has shown that on machines where gas leakage has occurred it is very desirable to be able to continuously monitor that leakage with some accuracy. There are difficulties in measuring a small leakage rate of such a low density gas as hydrogen, but we have had some success using a thermal mass flowmeter and relating that leak rate to indications from other new monitoring techniques such as the core monitor and RF discharge monitor (see Reference 30)

4.3 Chemical techniques

4.3.1 Particulate monitors: Overheating of insulation is a common precursor to major damage. This activity will produce gases and pyrolysed particulate matter, which will circulate in the cooling hydrogen and can be detected. One device which detects particulate matter has been installed in a large number of machines in the UK and overseas; it is known variously as a 'core monitor' or 'condition monitor' and is essentially a smoke detector. The principle of operation was described some years ago by Skala [31] and such devices are available commercially from several manufacturers. The device consists of one or more ion

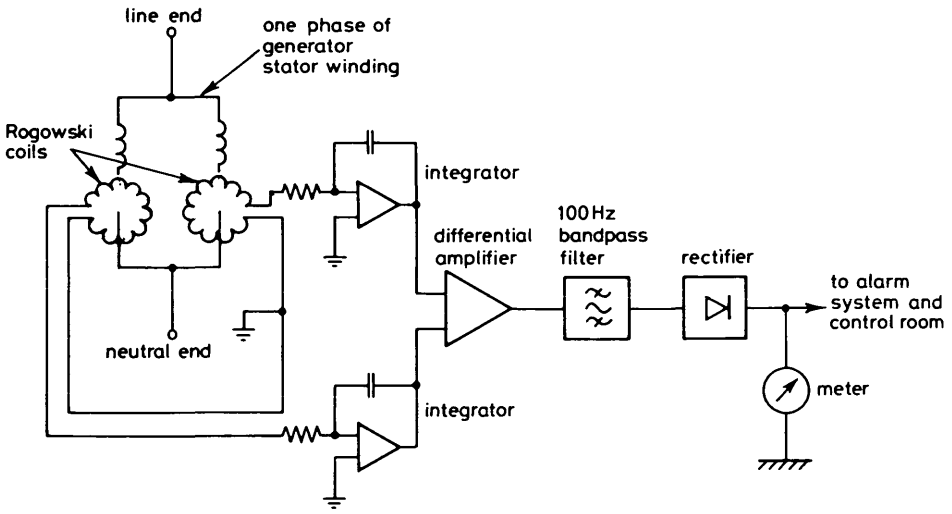

Fig. 5 *Diagram of a monitor to detect short-circuited rotor turns on a generator by measuring stator circulating currents*

chambers, through which hydrogen from the generator casing passes. The ion chambers contain a radioactive source, an ion collector and a sensitive current amplifier. The ion current will remain constant if the hydrogen flow

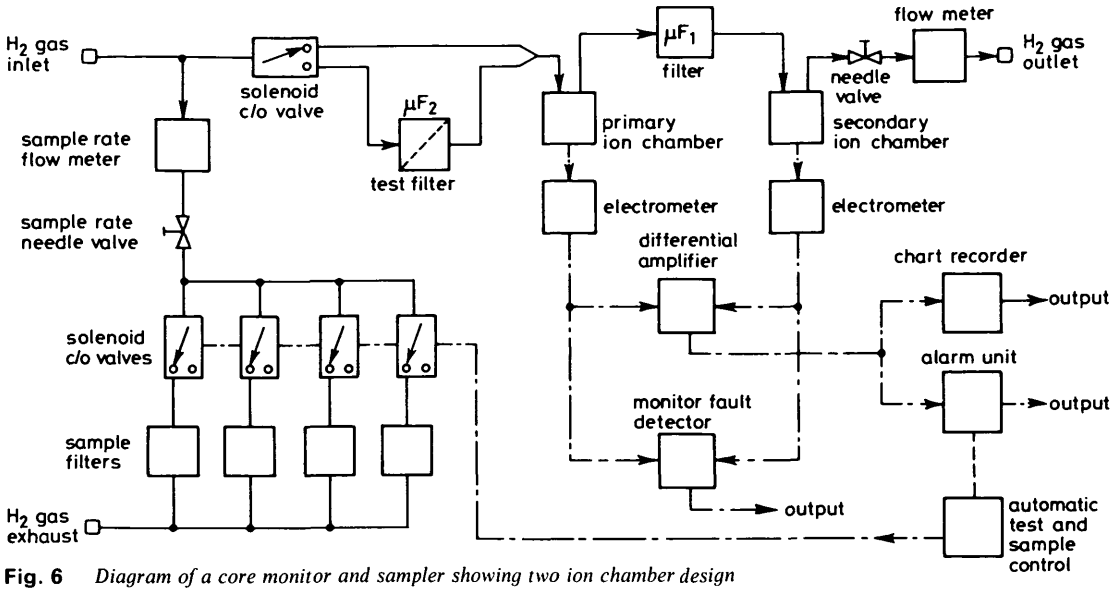

Fig. 6 *Diagram of a core monitor and sampler showing two ion chamber design*
Reproduced from Reference 32

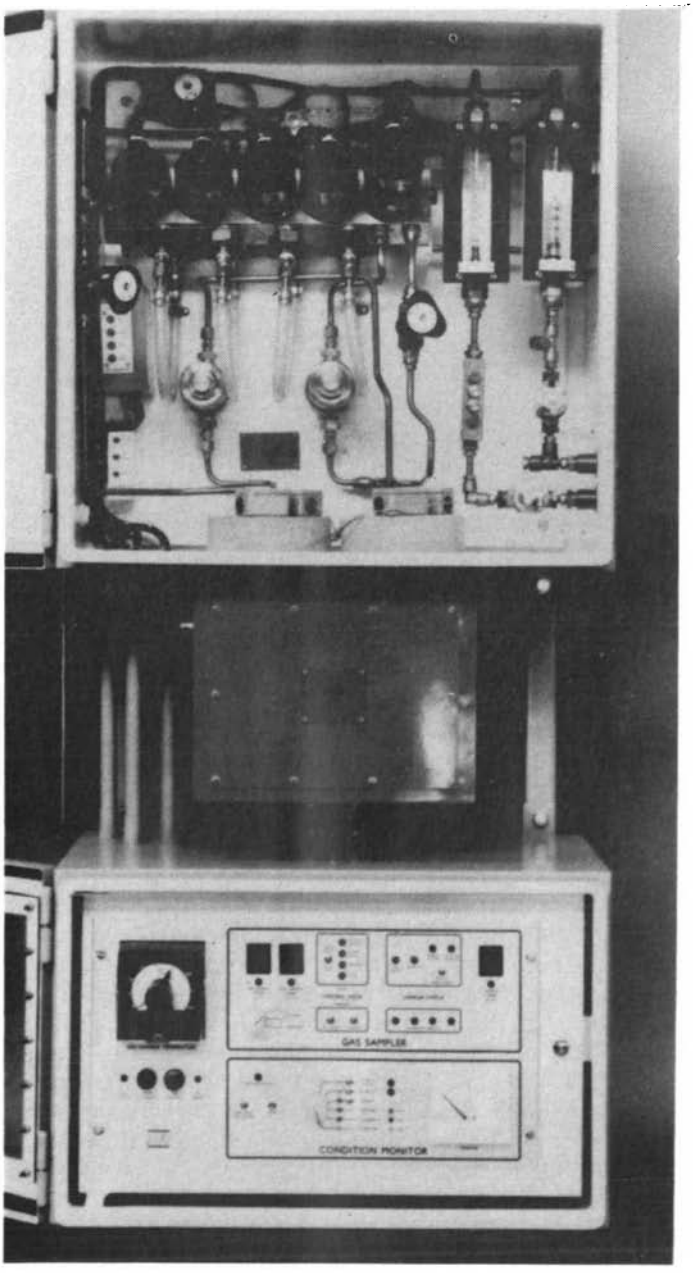

Fig. 7 *Core monitor*

is steady and free from particles, but will fall if particles are present. The lifetime in the generator hydrogen of pyrolysed particles seems to be of the order of 15–30 minutes, so a single instance of insulation overheating leads to a reduction of the ion current for a period of this order.

The practical devices have some difficulties. The ion current, in the absence of particles, is not absolutely steady because it varies with hydrogen gas pressure, gas flow rate, and temperature. For these reasons one design of monitor, reported by Wood *et al.* [32], uses two identical ion chambers in series with an intermediate particulate filter, and it displays the difference between the ion currents in the two chambers. A diagram of this core monitor with its associated sampler is shown in Fig. 6. A core monitor will also show changes in the chamber ion current if there is an oil mist present in the hydrogen. This sensitivity to oil mist will be reduced if the ion chamber of the core monitor is kept at an elevated temperature. Lodge [33] has suggested that an oil mist is only produced by overheating, so that its detection may be useful. For this reason, he advises against the use of heated ion chambers. However, the amount of oil in a generator casing varies widely and can be particularly high in older machines. In this case, we have found there can be frequent core monitor alarms even if there is no other evidence of burning, so the use of a heated ion chamber gives a significant advantage by preventing spurious alarms. The monitor described in Reference 32 also incorporates ion chambers which can be heated. The authors' experience with this monitor, which is shown in Fig. 7, has been that it does give a very steady output even on generators where hydrogen pressure is not closely controlled, it performs satisfactorily in the presence of background oil mist and yet is proven to be capable of detecting pyrolysed insulation. The added complications of this design may not be necessary in those generators where hydrogen pressure is closely controlled or where oil mist is not a problem, but the increased confidence of having a monitor which can deal with these difficulties has proved to be valuable.

Our experience with core monitors on generators is that they provide valuable information about overheating but their indications need to be considered alongside those of other monitoring devices. In particular, the core monitor

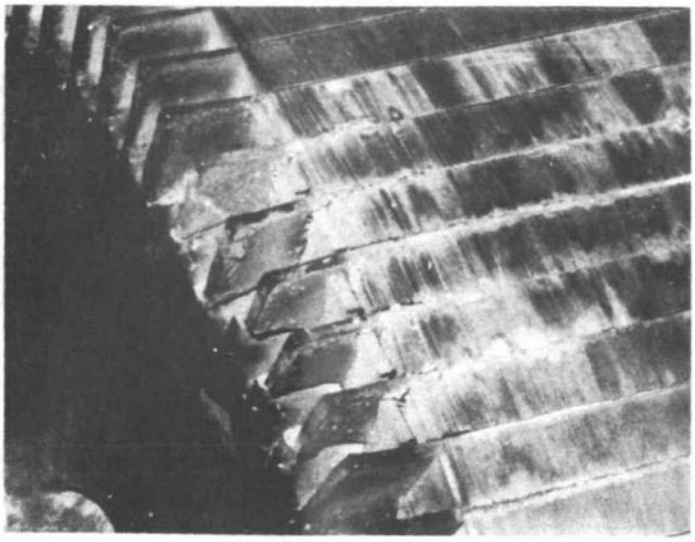

Fig. 9 *Damage to the squirrel cage of a large induction motor detected by rotor speed monitoring*

monitoring then enabled the motors to be repaired in the most sensible sequence and it proved unnecessary to have outages for investigation. No other rotors have been unrepairable.

At another older power station the wound rotors of MW-sized induction motors driving start/standby boiler feed pumps have given trouble. Continuous carbon monoxide monitoring has been fitted to these motors and a number of defects have been detected. In particular, Fig. 10

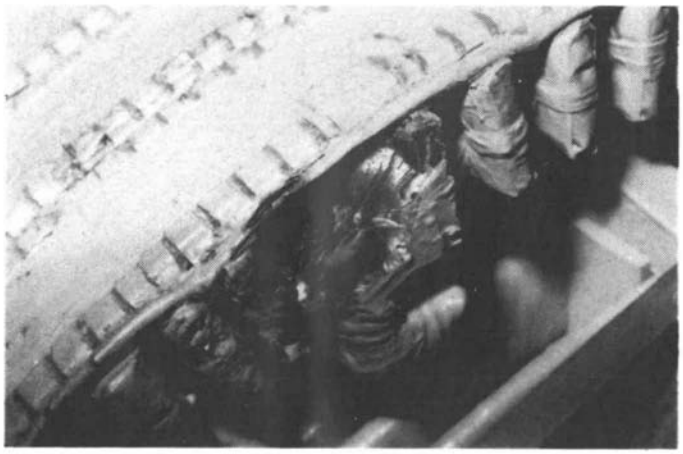

Fig. 10 *Damage to the wound rotor of a 4.8 MW induction motor detected by gas monitoring*

shows damage to a knuckle of a rotor winding which was detected by the monitor one hour before the smell of burning insulation was noticed. The motor was taken out of service and the rotor removed for a repair to the winding and no other damage was done to the machine. In this case, the fault was detected relatively early, but the time taken for the fault to develop from 'undetectable' to 'serious' was a matter of hours rather than months. This is a situation where continuous monitoring is necessary and the indication should be given directly to the power station operating staff so that prompt action can be taken when an alarm occurs.

These experiences have shown the importance of testing laboratory-proven techniques on a variety of operational machines. This produces many practical problems which need to be surmounted if monitoring is to be relied upon by operating staff.

5.2 Generators

We have applied many of the techniques described in Section 4 to a variety of large turbogenerators and on a number of occasions individual techniques such as rotor short-circuited turn indications or gas leakage monitoring have provided information which has been useful to power station staff for maintenance purposes. However, only on relatively few machines have we been able to apply sufficient techniques to give the multiparameter capability which we now believe is necessary for continuous monitoring of large generators. The following describes our experiences at two power stations.

At one power station, the 350 MW generators which are of an old design were experiencing faults in their stator windings which caused arcing between subconductors leading to perforation of water-cooled subconductors, overheating of the insulation and eventually a phase-to-phase or earth fault. Fig. 4 shows the ultimate outcome of one such incident. To provide earlier warning of this activity, core monitors, RF discharge monitors and gas leakage meters were fitted to the generators considered to be most at risk. The indications from these monitors were scanned by a logger and displayed alongside data about the temperatures and terminal conditions in the machines. The system was not incorporated into control room displays because the faults were found to develop slowly over many weeks and it was found adequate to make routine inspections of the logger indications. The results of this exercise were reported by Miller *et al.* [30] and show that on two separate machines the development of the subconductor arcing faults could be traced over a number of weeks. The machines were then removed from service for repair at a time which coincided with other repair work, enabling the overall outage time to be minimised. In these instances, the system provided additional information to the power station maintenance engineers and management, to help them in their decisions about the scheduling of repair work, rather than to provide online operational information.

At another power station we have applied a more advanced monitoring system incorporating core monitors, RF discharge monitors, gas leakage meters, and additional thermocouples on an aging 500 MW generator which has a similar subconductor arcing problem but where, because of the winding design, the fault develops much more rapidly. The system incorporates features to take account of some of the lessons learnt in the earlier exercise. First, a proprietary data-logger with its own computer was used; this allowed simple programming and enabled processing and assessment tasks to be undertaken. Secondly, a simple graphical output of important monitored quantities was provided and the data stored so that they could be analysed in more detail when problems arose. Thirdly, simple alarm information was presented to the power station operating staff so that prompt action could be taken when a fault developed. In this case, the system has operated satisfactorily although no fault has occurred on the generator concerned, but the indications have given confidence that no deterioration is taking place. More modern large alternators in the UK do not incorporate stator winding designs which suffer from subconductor arcing, but monitoring systems can still be of benefit in providing early warning of incipient defects.

In both these cases, the experience has shown the need for ensuring the reliability of both the primary monitoring instrumentation and the logging system. This is particularly important if the output from the system is to be used by operating staff. Considerable experience needs to be

built up using such systems before they will be widely believed and relied upon, so that when an alarm is given it is acted upon.

6 Strategy for monitoring and the future

The preceding Sections make it clear that there are benefits in applying monitoring to large electrical machines, although the benefits depend upon the particular machine concerned. It should also be clear that effective monitoring techniques are available but continuous monitoring techniques must be tailored to detect the particular faults which a machine experiences. In general, for monitoring large motors it is only necessary to apply one or two techniques, but on generators our experience is that a number of techniques should be applied and the results drawn together in an intelligent monitoring system. However, there will be many cases where monitoring is unnecessary or unlikely to succeed. Indeed, we have found that monitoring is no substitute for the regular and thorough inspection of plant by trained personnel and it should be done to complement this activity.

Provided that monitoring is possible and likely to succeed, the economic criteria are probably the most influential in determining whether monitoring should be undertaken. In generating utilities and many other process industries, if a plant failure occurs, the cost of the loss of production, caused by the failure, is usually much greater than the cost of repairing the failure. To give an example of these factors Fig. 11 shows the cost of repair work for an ailing machine as a function of the time when the repair is carried out. At the start of the graph the machine has a defect which is slowly worsening and is detectable. If the machine were repaired at the instant the fault could be detected then costs would be high because other plant

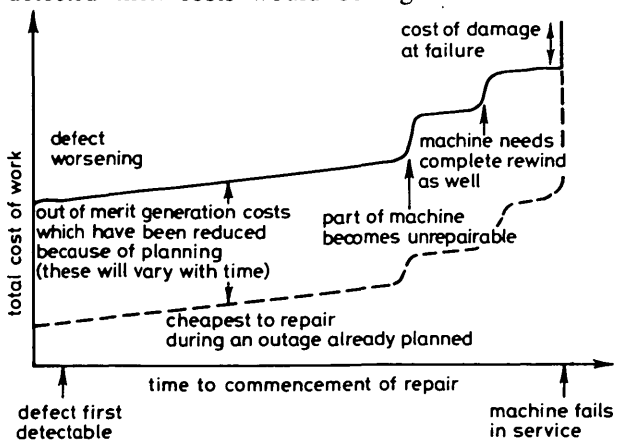

Fig. 11 *Typical pattern of time dependence of total costs for repairing a large electrical machine with a slowly developing fault*

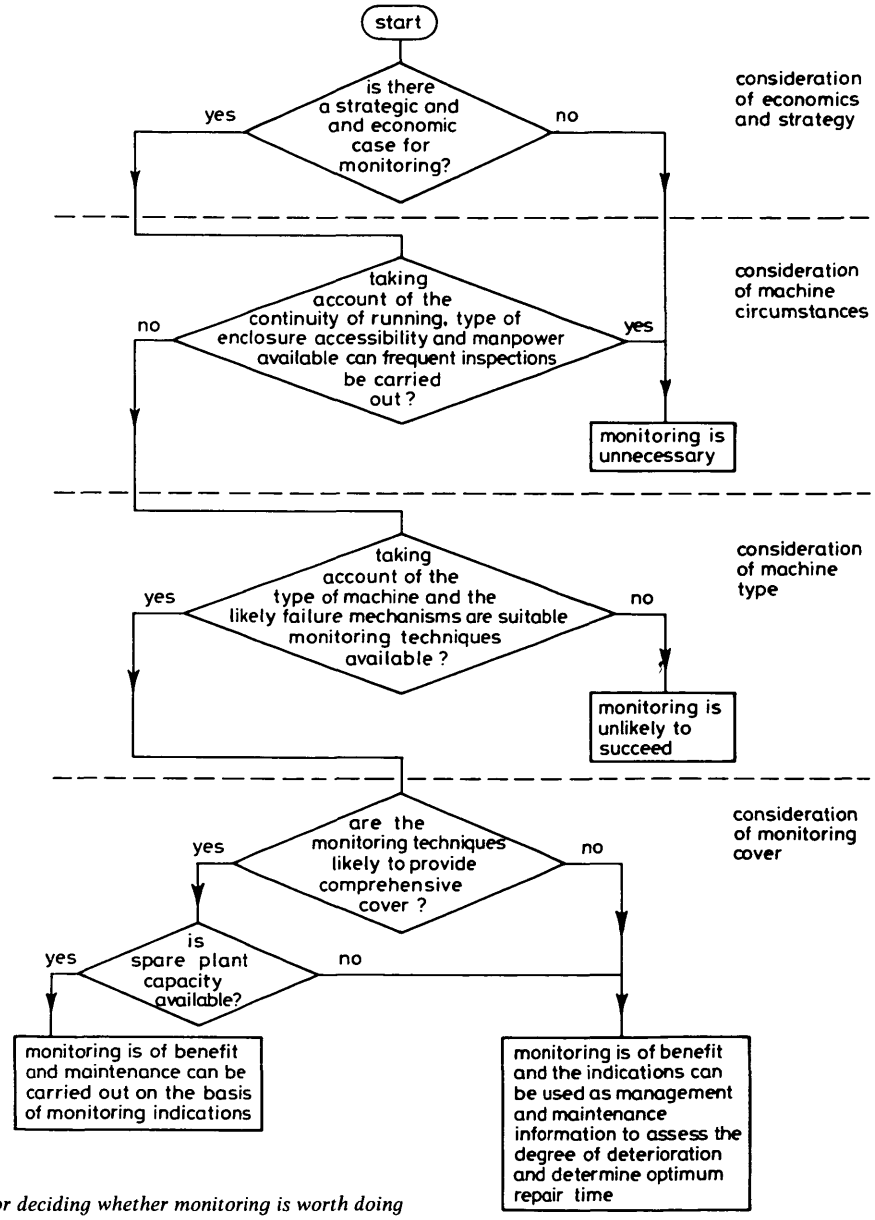

Fig. 12 *Decision tree for deciding whether monitoring is worth doing*

needs to be complemented by an offline technique to chemically analyse filters which sample the particulates from the hydrogen when the core monitor indicates their presence. Work is also going on to develop chemical tagging compounds to identify overheated regions.

4.3.2 Gas monitors: An alternative chemical method of detecting thermally degraded insulation is to analyse the hydrogen for the hydrocarbon gases produced by pyrolysis. This offline method, which has received attention in the CEGB, uses a gas chromatograph and flame ionization detector to measure hydrocarbons in samples of the hydrogen see Dear *et al.* [34]). An online monitor has been developed in the SW Region of the CEGB which uses a flame ionisation detector to measure the total hydrocarbon content in the hydrogen. However, the authors have had no direct experience of this technique.

It is worth noting that there are some significant differences between the behaviour of hydrocarbon gases and pyrolysed particulate material in generator hydrogen. First, whereas pyrolysed particles have a typical lifetime of 15–30 minutes in generator hydrogen, the hydrocarbon gases will have a lifetime of many days, depending mainly on the hydrogen leakage and make-up rate for the generator concerned. Secondly, whereas the concentration of pyrolysed particulate matter in the generator hydrogen will be essentially zero in the absence of burning insulation, there will always be a small and possibly variable concentration of hydrocarbon gases in the hydrogen used for make-up, and this will effectively determine the threshold for detection of burning by this technique. The gas analysis technique is probably less sensitive than the core monitor to burning at the surface of insulation but some experience has suggested that it is more sensitive to deep-seated burning within the winding insulation.

4.4 Multiparameter monitoring

In applying some of the techniques described above in Section 4 we have found that, because of the size and importance of generator plant, no single monitoring signal will be relied upon to give an unequivocal indication of an incipient generator fault. To provide a reliable and convincing warning of damage it is necessary to combine a number of indications together into a monitoring system. Generator monitoring systems have already been used within the CEGB and other utilities (see Hodge *et al.* [14] and Scherer *et al.* [35]). The systems we have used have tended to concentrate on the data logging aspects of condition monitoring. They all incorporated specially programmed computer controlled loggers. Some work has been done on processing and assessing online, the data these systems collect, as was suggested in Section 2, and proposals have been made to apply artificial intelligence techniques to the interpretation and diagnosis of faults [36]. Such systems have been called integrated surveillance schemes.

Our experience with conventional generator monitoring systems has been disappointing for a number of reasons:

(i) The reliability of monitoring instrumentation has to be very high to meet the needs of continuous monitoring

(ii) Overstatement of the capability of some monitoring techniques

(iii) Unreliability of the data logging hardware and difficulties with the development of the software

(iv) Lack of a sufficiently comprehensive set of monitoring signals.

Despite this lack of early success, the work has shown that comprehensive monitoring increases the credibility of the signals which are monitored. Furthermore, it has shown that if a reliable logger monitors reliable primary instrumentation this will form a sound generator condition monitoring scheme, even though the monitoring techniques do not give comprehensive cover of the machine. A full condition monitoring capability, however, is feasible only if the logger is in turn supervised by a computer or itself has sufficient intelligence to be capable of processing and assessing the monitored data and diagnosing fault symptoms from it. Fig. 8 outlines such a scheme which

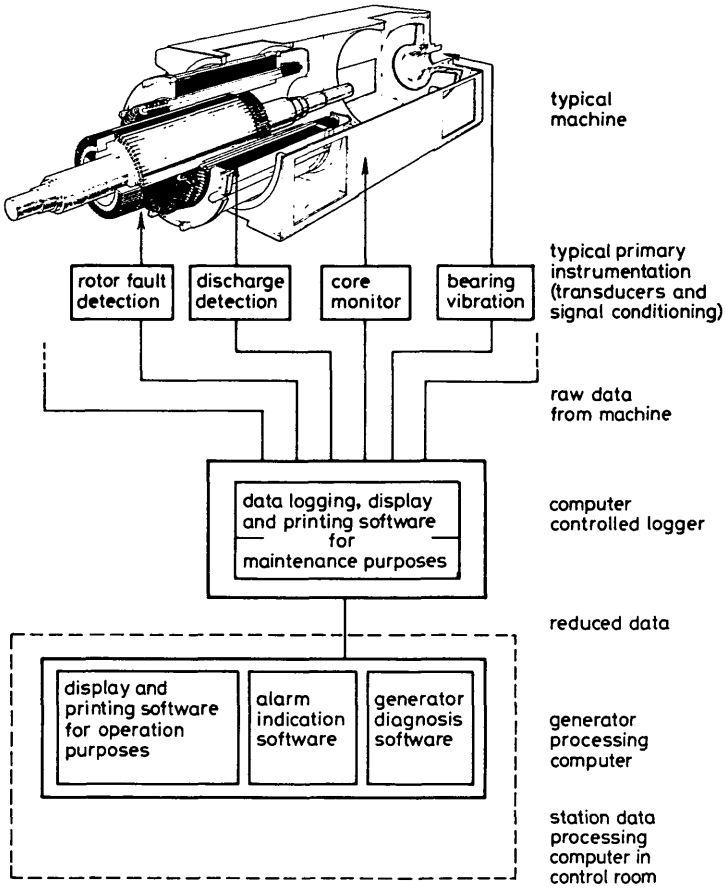

Fig. 8 *Comprehensive monitoring scheme for a typical electrical machine*
Reproduced from Reference 37

requires diagnostic software operating in the supervising computer. Ultimately, such a system should be incorporated into the power station data processing system.

5 Successes with monitoring

5.1 Motors

A most convincing demonstration of the value of motor monitoring occurred recently at a large power station. A MW-sized squirrel-cage induction motor was running rough and vibrated excessively when starting. The speed fluctuation monitoring technique was used and established that the rotor was defective. Inspection subsequently revealed that the starting cage end ring was cracked and that several of the starting cage bars had melted. Damage of this sort on another machine is shown in Fig. 9. The running winding also had major damage, and the rotor was unrepairable. Secondary damage to the stator was sufficiently minor that a rewind was unnecessary. If no monitoring technique had been available, the motor would have continued in service until failure and a stator rewind would have been required. Other motors at the same location were then tested and found to be developing similar defects, which were at a less advanced stage. Routine

would need to be run as a replacement. If the fault is undetected and is allowed to deteriorate then the costs incurred when failure and repair finally take place will escalate. If the repair were delayed until a planned repair period the costs would be lower as is shown in the graph. This shows that monitoring can bring considerable savings when it is used to detect slowly worsening faults.

To decide whether monitoring will be of benefit to a particular piece of plant, an overall strategy is needed, and from our experience we have developed the simple decision tree, shown in Fig. 12. Further work needs to be done to understand the implications of these decisions for typical machine installations and in particular the contribution which monitoring indications could make to the maintenance of plant.

For the future, as instrumentation techniques develop and the costs of electronic systems fall, it is inevitable that monitoring schemes will provide a greater benefit. Problem areas which require further work are:

(*a*) rugged and reliable primary instrumentation which is proved on operational plant

(*b*) combining and interpreting the warnings from separate monitors

(*c*) providing digestible information to plant operators.

The rapid increase in the ratings of motors and alternators that became necessary in the 1960s and early 1970s has now passed, and further development in machines is likely to be slow compared to the growth of instrumentation designed to protect the investment in heavy plant. More needs to be done to quantify the most cost-effective strategy for monitoring individual types of electrical machines. In addition, manufacturers and users need to give consideration to monitoring requirements during the specification and design stages of a new machine, see [14]. For example, provision should be made for tapping points, accelerometers, search coil locations and so on, so that monitoring can be provided if the decision tree shows that it is likely to be beneficial. Furthermore, consideration should be given to the interpretations which operating staff put upon monitoring indications.

7 Conclusions

This paper has described our experience in using monitoring techniques on a wide variety of electrical machines in one region of the CEGB and sets our experience in context alongside the work of others. A number of proven and reliable monitoring techniques exist and new techniques are being developed. The pressing need for those developing new techniques is to demonstrate their performance on operational plant and for those responsible for operating plant to encourage that testing. In addition, more work needs to be done on combining and interpreting indications from different monitoring techniques and presenting the information clearly to plant operating staff. There is also a need to take monitoring into account during the specification and design stage for a machine and the control room from which it is operated. Finally, when consideration is being given to applying monitoring to electrical machines it is essential to assess the benefits which would accrue from the installation and to quantify the savings which would arise.

8 Acknowledgments

The authors would like to acknowledge the work in this field by their colleagues elsewhere in the CEGB as listed in the References. In particular, they would like to acknowledge the contributions of their co-workers in the South Eastern Region; P.J. Burton, who developed the motor gas analysis technique, Dr. A.K. Malik, R. Shead and Dr. R.F. Cook who developed and worked upon the RF discharge detection technique and Dr. B.J. Pink who has worked on core monitors. They would also like to thank their colleague R.D. Rennie for his comments.

The core monitor described in Section 4.3 is manufactured by NEI Electronics Ltd., Gateshead, Tyne and Wear, UK.

This paper is published with the permission of the Director General of the South Eastern Region of the Central Electricity Generating Board.

9 References

1 BARKER, B., and HODGE, J.M.: 'A decade of experience with generator and large motor reliability'. CIGRE, Paris, France, 1st–9th September 1982, Paper 11-07

2 ASHEN, R.A., and STEELE, M.E. 'Motor condition monitoring methods'. Proceedings of Conference on Drives, motors and controls, Harrogate, North Yorkshire, UK, October 1983, pp. 163–171

3 KAMERBEEK, E.M.H.: 'Torque measurements on induction motors using Hall generators or measuring windings', *Philips Tech. Rev.* 1974, **34,** (7), pp. 152–162

4 RICKSON, C.D.: 'Protecting motors from overload due to asymmetrical fault conditions', *Electr. Rev.* 7th December 1983, pp. 777–780

5 PENMAN, J., DEY, M.N., and SMITH, J.R.: 'A new approach to the protection of industrial drives'. IEEE–IAS Annual meeting, San Francisco, CA, USA, September 1982, Paper AI582–44B, pp. 1226–1270

6 JUFER, M., and ABDULAZIZ, M.: 'Influence d'une rupture de barre ou d'un anneau sur les characteristiques externes d'un moteur asynchrone à cage', *Bull. Assoc. Suisse Electr.*, 1978, **69,** (17), pp. 921–925

7 HARGIS, C., GAYDON, B.G., and KAMASH, K.: 'The detection of rotor defects in induction motors'. *IEE Conf. Publ. 213*, 1982, pp. 216–220

8 STEELE, M. E., ASHEN, R.A., and KNIGHT, L.G.: 'An electrical method of monitoring motors'. *ibid.*, 1982, pp. 231–235

9 ELLISON, D.H., EXON, J.L.T., and WARD, D.A.: Protection of slip ring induction motors. *IEE Conf. Publ. 185*, 1980, pp. 49–53

10 WILSON, A., NYE, A.E.T. and HOPGOOD, D.J. 'Discharges in HV plant'. Proceedings of 4th BEAMA International Electrical Insulation Conference, Brighton, Sussex, UK, May 1982, pp. 233–239

11 GAYDON, B.G.: 'An instrument to detect induction motor rotor circuit defects by speed fluctuation measurements'. *IEE Conf. Publ. 174*, 1979, pp. 5–8

12 GAYDON, B.G., and HOPGOOD, D.J.: 'Faltering pulse can reveal an ailing motor', *Electr. Rev.* 1979, **205,** (14), pp. 37–38

13 HAMPTON, B.F., MEDHURST, D.R., ROGERS, A.J., WOOLARD, M.E., and STINTON, C.C.: 'The measurement of transformer winding temperature'. CIGRE, Paris, France, 1st–9th September 1982, Paper 12–02

14 HODGE, J.M., MILLER, T., ROBERTS, A., and STEEL, J.G.: 'Generator monitoring systems in the United Kingdom'. CIGRE, Paris, France, 1st–9th September 1982, Paper 11–08

15 EMERY, F.T., LENDERKING, B.N. and COUCH, R.D: 'Turbine-generator online diagnostics using RF monitoring', *IEEE Trans.*, 1981, **PAS–100,** (12), pp. 4974–4982

16 TIMPERLEY, J.E.: 'Incipient fault identification through neutral RF monitoring of large rotating machines', *ibid.*, 1983, **PAS–102,** (3), pp.693–698

17 KURTZ, M., STONE, G.C., FREEMAN, D., MULHALL, V.R., and LONSETH, P.: 'Diagnostic testing of generator insulation without service interruption'. CIGRE, Paris, France, 1980, Paper 11-09

18 MALIK, A.K., COOK, R.F. and TAVNER, P.J.: 'The detection of discharges in alternators using wide-band radio-frequency techniques'. *IEE Conf. Publ. 254*, 1985, pp. 121–125

19 WARRINGTON, A.R. van C.: 'Protective relays, their theory and practice, Vol 1' (Chapman & Hall Ltd. London, 1968)

20 HARGIS, C., MUHLHAUS, J., ROBERTS, I.A., and SUTTON, J.: 'Turbogenerator rotor earth fault monitoring and protection'. *IEE Conf. Publ. 254*, 1985, pp. 6–10

21 ROSENBERG, L.T.: 'Influence of shorted turns on thermal unbalance in large generators'. IEEE–PES Summer meeting, Los Angeles, CA, USA, July 1978, Paper A78, pp. 587–588

22 ALBRIGHT, D.R.: 'Inter-turn short-circuit detector for turbine generator rotor windings', *IEEE Trans.*, 1971, **PAS–90,** pp. 478–483

23 BYARS, M.: 'Detection of alternator rotor winding faults using an

online magnetic field search coil monitoring unit'. Proceedings of 17th Universities Power Engineering Conference, Manchester, UK, 30th March–1st April 1982.
24 CONOLLY, H.M., JACKSON, R.J., LODGE, I., and ROBERTS, I.A.: 'Detection of shorted turns in generator rotor windings using airgap search coils'. *IEE Conf. Publ. 254*, 1985, pp. 11–15
25 KHRYUKIN, S.S.: 'A new principle for synchronous machine protection from rotor winding inter-turn and double earth faults', *Elect. Technol. USSR*, 1972, **2**, pp. 47–59
26 MUHLHAUS, J. WARD, D.M., and LODGE, I.: 'The detection of shorted turns in generator rotor windings by measurement of circulating stator currents'. *IEE Conf. Publ. 254*, 1985, pp. 100–103
27 VERMA, S.P., and GIRGIS, R.S.: 'Shaft potentials and currents in large turbogenerators'. Report for the Canadian Electrical Association, Report 78–69, May 1981.
28 MAYES, I.W., STEER, A.G., and THOMAS, G.B.: 'The application of vibration monitoring for fault diagnosis in large turbogenerators'. 6th Thermal Generation Specialists Meeting, Madrid, Spain, 5th–6th May 1981
29 HERBERT, R.G.: 'Computer techniques applied to the routine analysis of rundown vibration data for condition monitoring of turbine-alternators'. Proceedings of International Conference on Condition Monitoring, University College, Swansea, UK, 10th–13th April 1984, pp. 229–242
30 MILLER, T. and MALIK, A.K.: 'Monitoring techniques to improve the availability of 350 MW and 500 MW alternators'. IEE Colloquium Digest 1981/25, 1981
31 SKALA, G.F. 'The generator condition monitor and its application to the hydrogen cooled generator'. 41st International Conference of Doble Clients, Boston, USA, 25th April 1974
32 WOOD, J.W., RYAN, M.J., GALLAGHER, P., and GUNTON, D.: 'Condition monitoring of turbogenerators'. *IEE Conf. Publ. 213*, 1982, pp. 131–135
33 LODGE, I.: 'Prevention of catastrophic failure of large generators by early detection of overheating'. *ibid.*, 1982, pp. 123–130
34 DEAR, D.J.A., DILLON, A.F., and FREEDMAN, A.N.: 'Determination of organic compounds in the hydrogen used for cooling large electricity generators', *J. Chromatog.*, 1977, **137**, pp. 315–322
35 SCHERER, H.N., HAJNY, M.R., PROVANANZA, J.H., and WHITE, T.E.: 'Monitoring of large generators on the American Electric Power System'. CIGRE, Paris, France, 1st–9th September 1982, Paper 11–01
36 GONZALES, A.J., OSBORNE, R.S., KEMPER, C.T., and LOWERFELD, S.: 'Online diagnosis of turbine generators using artificial intelligence'. IEEE–PES Winter Meeting, New York, USA, February 1985, Paper 85 WM 105/2
37 BONE, J.C.H., and SCHWARZ, K.K.: 'Large AC motors', *Proc. IEE*, 1973, **120**, (10R), p. 1111

Currents flowing in the stator-core frames of large electrical machines

P.J. Tavner, M.A., Ph.D., C.Eng., M.I.E.E., and J. Penman, B.Sc., Ph.D., C.Eng., M.I.E.E.

Indexing terms: *Turbogenerators, Eddy currents, Leakage flux*

Abstract: The stator cores of large electrical machines are supported in a steel frame in which electrical currents are circulated by leakage flux from the core. These currents can cause serious overheating. The paper gives a qualitative review of the electromagnetic factors which affect the flow of these frame currents. The work shows that the effects of frame currents may be reduced if the frame members are connected electrically in a way which more effectively suppresses core-end leakage flux.

1 Introduction

The stators of large electrical machines, and alternators in particular, are fabricated using an inner frame and building bars to carry the great mass of the laminated stator core, as shown in Fig. 1. The inner frame is then carried within an outer frame and cooling gas casing. The inner steel frame and building bars form an effective squirrel cage outside the core and they lie in the time-varying magnetic leakage field of the stator core back. As a consequence, the building bars and frame members have currents induced in them, and it is known that the magnitudes of these currents can be substantial—a matter of some concern to designers. The currents flowing axially along the building bars must necessarily close circumferentially at either end of their axial extent.

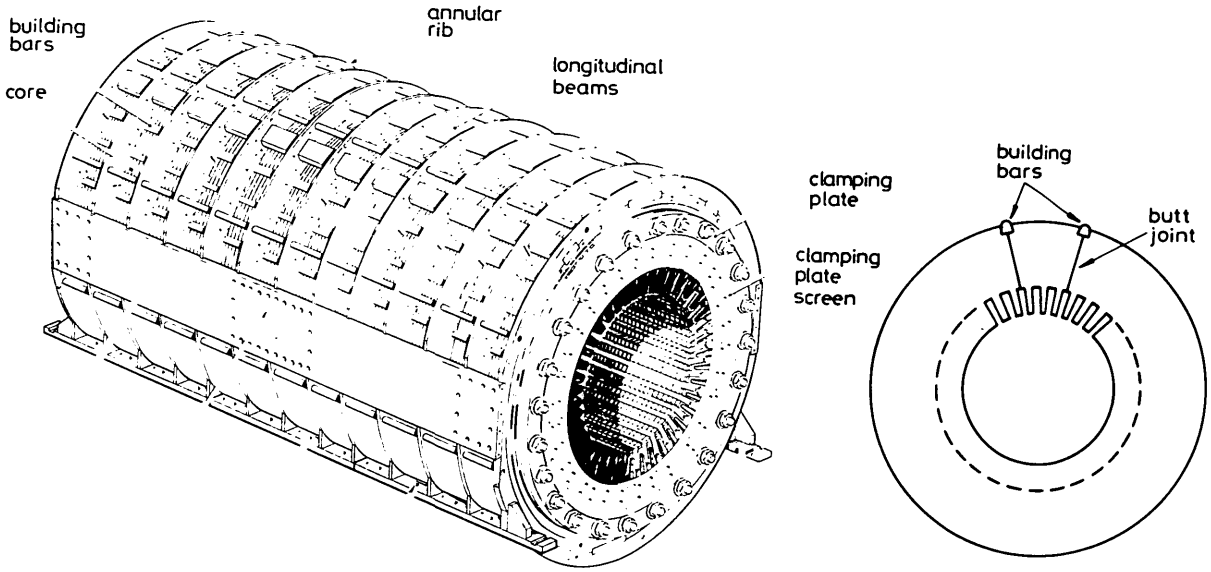

Fig. 1 *Arrangement of typical 660 MW alternator stator core showing inner frame and building bars and construction of segmented core*

At the core end, the building bars are electrically connected together by the stator-core clamping structure and the building bar currents will naturally flow through that structure, where they may cause overheating. The axial frame members are also connected together by successive annular steel ribs throughout the core length.

The building bars may also be in electrical contact with the laminations of the stator core, depending on the core design. It is important to ensure that the building bar currents do not close in the stator core because there they may cause overheating and damage to the core plate.

In this paper, the authors describe qualitatively the electromagnetic and engineering factors which influence the magnitudes and paths of these frame currents.

2 Electromagnetic considerations

Eddy currents are induced in a direction such that they act to reduce the magnetic flux which is inducing them, and they flow in a path where they have maximum effect in reducing that flux. This is implicit in the Maxwell equation $\nabla \times E = -\partial B/\partial t$. Taking account of the complete current circuit, eddy currents, in effect, flow to embrace the maximum inducing flux and, in so doing, they maximise the kinetic energy ($\frac{1}{2}Li^2$), and therefore the inductance, of the induced circuit. It is also implicit in the induction equation that axial currents are induced into a conductor which links radial or circumferential fluxes, while radial and circumferential currents, such as flow at the closure of axial currents, will be driven by axial components of flux. In an alternator stator the paths for induced currents in the building bars are constrained to be axial; in the frame they can be axial in the longitudinal members or circumferential in the annular ribs; while in the core itself the paths can be radial or circumferential, because of the laminated construction.

The leakage flux from an alternator stator core is primarily determined by gross geometrical factors, such as the core length and diameter, stator and rotor-end-winding design and end-region arrangement. An induced current would need to be very large to overpower these geometrical effects. So while the currents induced into the stator

Paper 2768C (P1), first received 30th March and in revised form 12th July 1983

Dr. Tavner is with the Scientific Services Department, CEGB, South Eastern Region, Canal Road, Gravesend, Kent DA12 2RJ, England, and Dr. Penman is with the Department of Engineering, University of Aberdeen, Marischal College, Aberdeen AB9 1AS, Scotland

frame have a local effect on the leakage flux, they probably do not significantly alter the net leakage flux unless they have a very low-resistance path. In effect, the 'reaction field' of frame eddy currents is likely to be small compared with the 'applied field' of the leakage flux.

The path of an induced current depends both on the flux being embraced (i.e. the inductance of the path) and on the resistivity of the path. If the path is constrained along particular members, as it is in the frame of an alternator, then only the resistance of those members can affect the magnitude of the current. However, if the current path is unconstrained, as it is at the core end or inside the core of an alternator, then the inductance of the possible path plays an important part in determining which path is followed.

3 Leakage flux and frame currents

3.1 General

It is clear from Section 2 that, to determine the flow of current in a stator frame, one must understand the pattern of leakage flux around the core. This has never been determined on a full-size machine, but has been investigated experimentally on a slotless model, with a length/diameter ratio similar to a turbogenerator [1]. A diagram of the measured leakage flux around the model, excited on open-circuit, with a low core flux density, is shown in Fig. 2. The

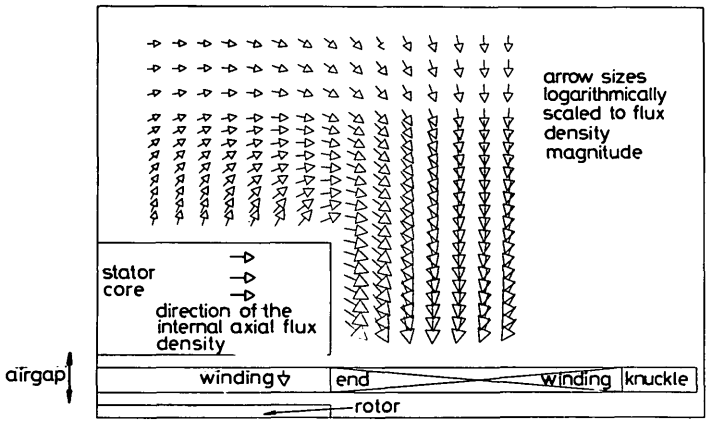

Fig. 2 *Typical leakage flux measurements around end of stator core of a turboalternator model, plotted on open circuit excitation*

diagram shows the magnitude and direction of the leakage flux at the point in time when the air-gap flux was set at a maximum directed in the plane of the paper. The important points to notice are the directions of the core-end and core-back leakage fluxes relative to the air-gap flux. A schematic of the leakage flux plot for a whole turbogenerator, on open-circuit, based on Fig. 2, is shown in Fig. 3. Fig. 3 is drawn on the same basis as Fig. 2.

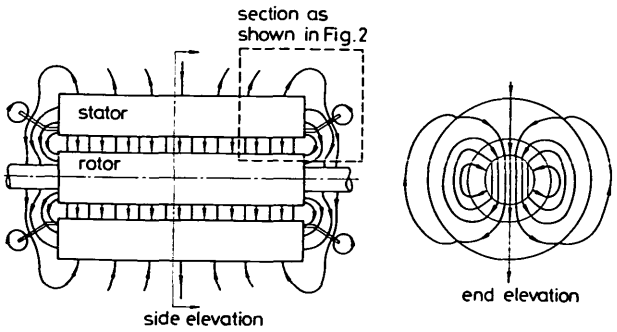

Fig. 3 *Schematic of leakage flux around a turboalternator on open circuit, energised from the stator, based on Reference 1, cf. Fig. 2*

3.2 Influence of the clamping plates

The clamping plates, which hold the core together, see Fig. 1, carry currents induced by the axial leakage flux impinging on the core end, and these currents can severely overheat the clamping plate itself. It is, therefore, common practice to fit a low-resistivity screen to the surface of the clamping plate. The majority of the flux-suppressing currents are then induced into material of lower resistivity. The electrical losses and, consequently, the temperature rises in the clamping plate and screen are therefore lower.

Similarly, both the longitudinal and annular ribs of the frame containing the laminated core carry currents induced is them by the leakage flux from the core back. The problem here is not to prevent the frame as a whole overheating, but to ensure that the frame currents follow a path in which overheating, at electrical contacts or in high-resistivity material, is avoided.

The system of induced currents in the clamping-plate screen and frame members are clearly linked by the pattern of leakage flux shown in Fig. 3. If the building bars were in intimate electrical contact with the clamping-plate screen, then the bar currents would close by flowing into the screen as shown in Fig. 4. There is experimental evi-

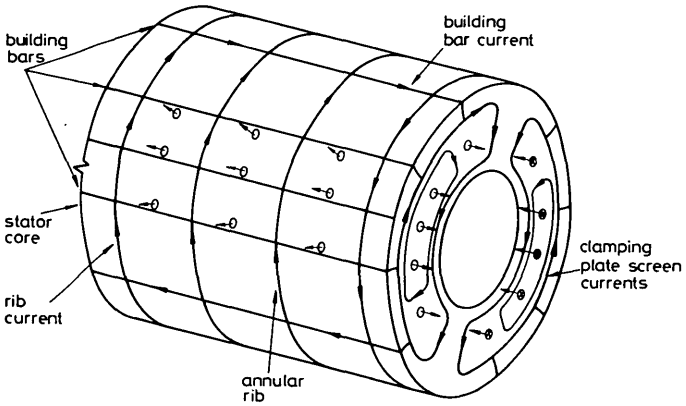

Fig. 4 *Coupling of building bar and clamping plate screen currents due to pattern of leakage flux shown in Fig. 2*

dence on operational alternators that this is what happens. The comments on Section 2 suggest that, in such a case, the building-bar currents would be larger than if they were kept electrically separated from the screen currents, and this leads to an undesirable increase in stray losses.

3.3 Core-end against core-back leakage

In Fig. 2 the sizes of the arrows drawn at each location are related to the magnitude of the flux density at that point. Now, in fact, around the core end the flux density varies by at least an order of magnitude. On the core back its magnitude is very small and on the core end, near the air gap, it is very large and approaching the air-gap flux density. The arrows in Fig. 2 have, therefore, been scaled logarithmically to make the flux-density directions clear, but it can be seen that the time-varying flux is largely centred around the core end, and the net flux leakage from the core back is unlikely to be significant compared with the core-end leakage flux.

Large frame currents are therefore likely to be associated with this flux concentration, and they will flow between the frame and the core-end clamping plate and in the annular ribs some distance from the core end. In that case, it is unlikely that the frame currents will flow for the full length of the inner frame, as in the squirrel cage of an induction motor, but rather they will be concentrated at the core end as shown in Fig. 4.

The theoretical work described in Reference 1 suggested that, at the axial centre of a long stator core, the magnetic leakage flux from the core back at a particular circumferential location should be in the same direction as the flux in the air gap at that location. That is, where the magnetic flux is crossing from the rotor to the stator, in the air gap, the radial leakage flux will be in the same direction, leaving the stator core back. This is shown in the end elevation of Fig. 3.

The experimental results, typified by Fig. 2, however, showed that, at the core end of that model, the core-back leakage flux acted in the opposite direction to that in the air gap. When compared with the results of Reference 1, this implies that, if measurements were made of the radial leakage flux density at points along the core back, there should be a phase reversal some distance in from the core end, as shown in the side elevation of Fig. 3. This further suggested that there may be two opposing sources contributing to the core-back magnetic leakage flux. The first is associated with leakage from the cylindrical body of the core itself and is operative at the axial centre of the core. The second is associated with the leakge from the core ends. Further measurements on the core back of the model of Fig. 2, however, showed that there is no such phase reversal of radial leakage flux density towards the core centre. This suggests that, on a full-sized turbogenerator, the core-back flux is controlled primarily by leakage from the core ends, which confirms the discussion in the preceding text that frame currents are largely associated with core-end effects.

3.4 *Influence of internal axial flux*

Given a current path which is defined, the electrical loss induced by the flux linking that path depends on the AC resistance of that path, which is a combination of the resistivity and permeability of the material of the path, as described in Section 2. That is, the loss is dependent on the skin depth of the material at a particular frequency. If the skin depth is very large or very small then the loss will be small, but there are intermediate values of skin depth for which the loss in the current path becomes large, as described by Hammond [2]. Now this can occur if the building bar currents transfer to the stator when large losses may be expected in the high-resistivity steel-core plate.

Close to the end of a stator core, there is a substantial axial component of flux due to end-region effects. This leads to increased core losses and has been investigated by many workers, including the authors [3].

The direction of internal axial flux in the turbogenerator model of Fig. 2 has been measured and is shown schematically in the Figure. If the building bars are in electrical contact with the core, it might be expected that the building-bar currents would transfer to the core and flow by the shortest route between the bars. This would mean the currents hugging the core back, constrained to flow in the shallow core-plate-skin depth. But the currents must flow to embrace the largest possible inducing flux. They would, therefore, rather continue to the end of the building bar than close on a short path at some intermediate position. A more favoured intermediate route, however, would be to transfer to the core and flow down to the tooth roots, thereby linking a substantial amount of the core internal axial flux, as shown in Fig. 5. This behaviour has been described by Jackson [4] and is similar to the propensity of the building-bar currents to flow into the clamping-plate screen, if the frame construction permits it, as described in Section 3.

When the building bars make contact with the core it is not simply that the core then provides a lower resistance path, for closure of the building-bar currents, but that it provides a higher inductance path, because by threading the core the induced currents can embrace the internal core axial flux.

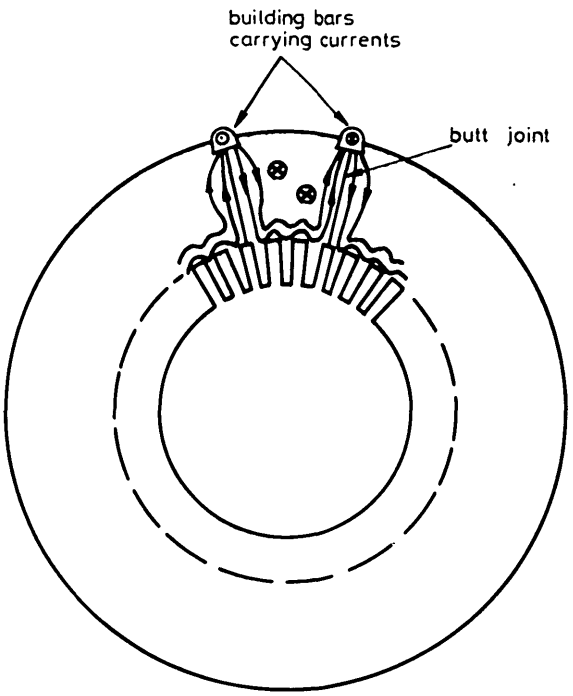

Fig. 5 *Possible current route between building bars*

Many experimentalists, including the authors [3, 5], have noted that the net axial flux threading a stator core, which is a function of surface leakage, increases to a large value some distance in from the core end. A typical isometric plot of experimental axial flux amplitudes is shown in Fig. 6. This suggests that, if the building bars do make uniform electrical contact with the core back, then the highest inductance path for the building bar currents may not be at the core end at all, but some distance in from the end, where these peaks in axial flux can be linked.

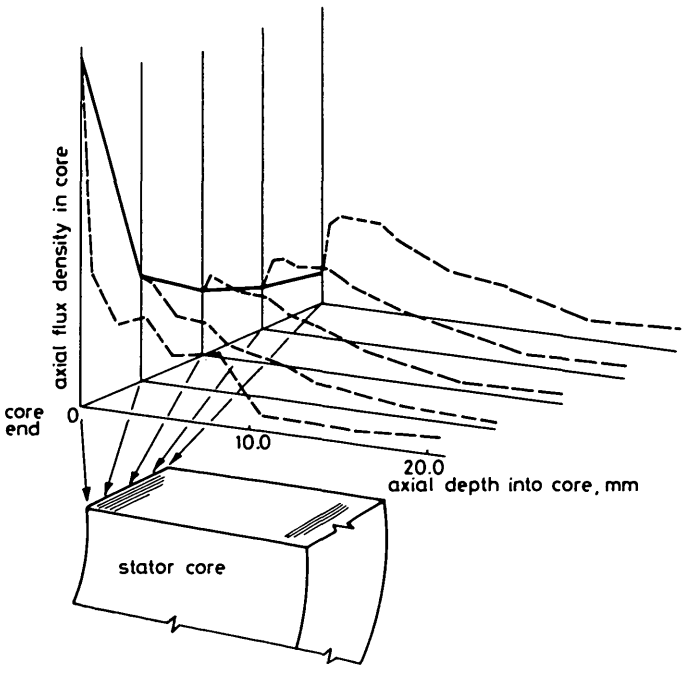

Fig. 6 *Isometric plot of axial-flux-density amplitude inside stator of a turboalternator model (same model as Fig. 2)*

Therefore, whether a building bar current flows to the frame end or transfers into the core, closing as shown in Fig. 5, depends on which of these paths embraces the most flux. This, in turn, depends on the surface leakage flux pattern of the stator core and, at the moment, this cannot be determined by inspection.

In a practical core the core plate is segmented, as shown in Fig. 1, therefore the current from one building bar cannot flow through the core plate to any of the others, but is restricted to flowing only to the bars close to it, as shown in Fig. 5. This current constraint gives rise to substantial interlaminar potentials, as described by Jackson [4], which may break down the interlamination insulation and lead to bridging of the laminations and a removal of the current constraint. This can then cause significant heating and melting of the lamination steel and, hence, growth of the damaged area. The prospective pattern of current flow is shown in Fig. 7 which was developed from Reference 4.

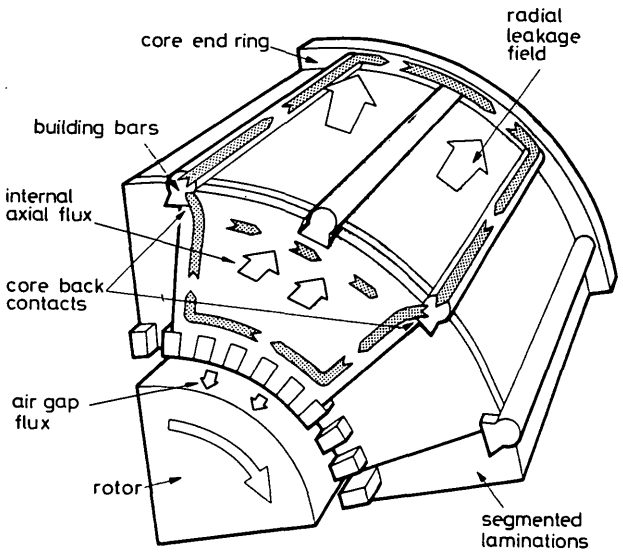

Fig. 7 *Pattern of building bars to core, to core end currents proposed by Jackson [4]*
Flux directions compatible with Fig. 2

4 Experience on full-size machines

In recent years, there has been evidence that damage has been caused by frame currents to the inner frames, building bars, laminated cores and clamping plates of some large turbogenerators. Measurements have been made by other workers of the frame currents on working turbogenerators using Rogowski coil detectors, similar to that described by Stoll in Reference 6. On a 660 MW machine such results have shown that the building-bar currents can be of the order of 1500 A RMS, and circumferential currents, flowing in annular ribs and circumferential connections, of the order of 3500 A RMS.* On a 500 MW machine the currents flowing from the building bars to the clamping plate were measured to be of the order of 4000 A RMS at full load.†

The measurements have shown that frame currents are linearly dependent on the stator winding current and vary nonlinearly with the terminal voltage. Raising the terminal voltage increases the main flux in the machine, and thereby the saturation in the stator core. Hammond has shown, in Reference 7, that the magnetic flux leaking from the surface of an iron body depends on the proximity of the surface to the exciting current sources and on the permeability μ_r of the iron. The permeability is generally large, but reduces towards unity with the onset of magnetic saturation of the iron. Reference 9 showed that the magnetic leakage flux from an iron body, close to the exciting current source, is controlled by the factor $(\mu_r - 1)/\mu_r$, which will be independent of μ_r for all but the smallest values of permeability. This will be the case on the core end of a turbogenerator near to the stator-end windings, and so, although the core-end leakage flux will be large, it will, in general, be independent of saturation. Reference 9 shows, however, that, remote from the exciting current source, the leakage flux is dependent on the factor $1/\mu_r$. The leakage flux will then increase with core saturation; and this will be the case on the core back, where the surface is screened from the exciting current by the mass of stator steel. This explains why the frame currents increase nonlinearly with terminal voltage. On the core end, however, the leakage flux is very much dependent on the magnitude of the current in the stator-end winding. Since the discussion of Section 3 has shown that frame currents are principally dependent on the core-end flux, it is not surprising that they are, in turn, linearly dependent on the stator winding current in the machine.

The dependence of frame currents on stator current has also been confirmed by temperature measurements made on a full-size machine.* Temperature sensors were fitted to the building bars of the machine at various points near the core end to determine the heating effects of frame currents. The measurements showed that, with the alternator on open-circuit, the temperature rise, and therefore the frame current, was moderate, but on short-circuit the temperature rise increased dramatically, confirming that the frame currents are most significantly affected by the stator winding current and, therefore, core-end leakage flux, rather than the core main flux and core-back leakage.

There has also been visual evidence in full-size machines that frame currents flow from the building bars into the laminated stator core, and that this occurs some distance in from the core end. When this happens, they cause overheating at the core-back contact with the building bars and they flow to the tooth roots and slot bottoms of the core plate, causing further local overheating. Core laminations may then become welded together, as described by Jackson [4] and Oberretl [8]. This confirms the proposal in Section 3.4 that, when frame currents flow into the stator core, they are controlled by the internal axial flux of the core, and the consequential current path can lead to overheating.

5 Conclusions

The authors have presented a qualitative description of the factors affecting the flow of frame currents in large electrical machines. It is clear that the frame currents flow most strongly near the stator-core ends, and it appears that the frame currents are driven principally by the large core-end leakage flux rather than the weak stator-core-back leakage. This is confirmed by the fact that the frame currents are linearly dependent on the current flowing in the stator winding and by temperature measurements on the building bars of a full-sized machine.

This qualitative description should be interpreted in the light of more detailed frame current measurements. It has also been shown that frame currents can transfer from the building bars into the stator core, close to the core end, even when highly conductive circumferential paths are

* Ward, D.A., private communication
† Smith, J.W.R., private communication

* Williamson, A.C., private communication

provided between the bars. This transfer of current occurs as a result of the internal core axial flux distribution caused by the core and leakage flux.

It can be seen that the effects of frame currents may be reduced if the frame members are connected electrically, in a way which more effectively suppresses core-end leakage flux. The only completely effective method of preventing overheating due to frame currents is to provide clearly defined circuits of high conductivity. This may be achieved at the core end by ensuring good electrical contact between the frame members, building bars and the core clamping plate and screen. On the core back, current transfer can only be prevented by electrically isolating the building bars from the core, and this practice is now widely adopted. It should, however, only be done if the structural support provided by the building bars is unimpaired.

6 Acknowledgments

This paper is published with the permission of the Director-General, South Eastern Region, Central Electricity Generating Board. The authors would like to acknowledge the work of colleagues in the CEGB, particularly in the North Eastern, North Western and Midlands Regions, for their work on the measurement of frame and building bar currents.

7 References

1 HAMMOND, P., and MARIOTONI, C.A.: 'External flux leakage of synchronous machines'. Proceedings of the international conference on electrical machines, Athens, Greece, Paper GP1/10, September 1980
2 HAMMOND, P.: 'Applied electromagnetism' (Pergamon Press, 1971), p. 219
3 TAVNER, P.J., HAMMOND, P., and PENMAN, J.: 'Contribution to the study of leakage fields at the ends of rotating electrical machines', *Proc. IEE*, 1978, **125**, (12), pp. 1339–1349
4 JACKSON, R.J.: 'Interlamination voltages in large turbogenerators', *ibid.*, 1978, **125**, (11), pp. 1232–1238
5 TAVNER, P.J.: 'Measurements of the influence of core geometry, eddy currents and permeability on the axial flux distribution in laminated steel cores', *IEE Proc. B, Electr. Power Appl.*, 1980, **127**, (2), pp. 57–67
6 STOLL, R.L.: 'Method of measuring alternating currents without disturbing the conducting circuit', *Proc. IEE*, 1975, **122**, (10), pp. 1166–1167
7 HAMMOND, P.: 'Leakage flux and surface polarity in iron ring stampings', *ibid.*, 1955, **102C**, pp. 138–147
8 OBERETL, K.: 'Leakage fields, eddy current losses, temperature rise, forces and parasitic sheet fusion in the end-zone of turbogenerators', *Elecktrotech u Maschinenbau*, 1963, **80**, pp. 539–550

Influence of winding design on the axial flux in laminated-stator cores

P.J. Tavner, M.A., C.Eng., M.I.E.E., J. Penman, B.Sc., Ph.D., R.L. Stoll, D.F.H., Ph.D., A.F.I.M.A., C.Eng., M.I.E.E., and H.O. Lorch, C.Eng., M.I.E.E.

Indexing terms: Machine windings, Stators, Magnetic flux, Laminations, Magnetic cores, Eddy currents

Abstract

The magnetic field of an isolated winding of helical form is obtained both theoretically and by measurement on a small model. The axial and radial fields of that winding are compared with those of straight windings with conventional ends, both when the windings are in air, and inside a slotless, laminated core. It is found that a knowledge of the field in air of a winding is not of itself helpful in predicting the axial-field distribution when the winding is placed inside a laminated core. Experimental results of the axial-flux distribution inside the core are also presented. They demonstrate that axial flux is reduced when the winding radius and overhang are reduced. The axial flux continues to decrease even when the endwinding ceases to project from the core end.

List of symbols

H = magnetic field intensity
I = winding-phase current
I_0, I_1, I_2 = modified Bessel functions of the first kind (zero, first and second order)
I_1' = derivative of I_1
J = current density vector
K_0, K_1, K_2 = modified Bessel functions of the second kind (zero, first and second order)
K_1' = derivative of K_1
N = number of winding turns per phase
R_t = core-bore radius
R_W = winding radius
a_k, c_k = Fourier coefficients describing axial and circumferential current sheets
b = core annular depth
d = end-winding halflength
g = periodic interval of current-sheet system
h = core mean pole pitch
j_z, j_θ = instantaneous values of axial and circumferential line current density
j_z' = axial line current density referred to core bore
k_d = winding fundamental distribution factor
l_w = winding halflength to mid point of end region
p = $\sqrt{2h/\pi\delta_r}$, skin-effect factor
α = helix angle of winding
γ = stacking factor of laminated core
δ_r = skin depth of axial flux
μ = chording angle of winding
μ_z = homogenised relative axial permeability $= (1-\gamma)^{-1}$
ω = angular frequency of excitation
ρ = resistivity of core plate

1 Introduction

A study of the axial flux in the laminated stator cores of large generators is important for three reasons. First, the additional I^2R loss due to eddy currents circulating in the plane of the laminations reduces the efficiency of the machine. Secondly, the associated heating, especially if this produces any local hot spots, causes gradual deterioration of the interlaminar insulation. Thirdly, where the insulation has been damaged or the edges of the laminations burred, both circumferential and axial components of flux can cause electrical breakdown between laminations that may lead to core failure if circulating currents of large magnitude are established.

These problems will become even more severe in a turbogenerator with a superconducting rotor-field winding,[1] in which the conventional slotted-stator core is replaced by a smooth annular screen surrounding the stator-winding cylinder. The main purpose of the screen is to shield the environment from the strong superconducting dipole field, although its presence will also enhance the radial flux density at the stator winding. The centre of the rotor will not contain any ferromagnetic material, and the rotor winding will have a relatively small diameter (less than half that of the stator-screen bore). The superconducting machine will therefore be essentially air-cored and produce a very high rotor m.m.f. The stator screen is therefore likely to have a very large fringing field, and it will be even more important to design the end geometry and the stator and rotor windings to minimise the axial field and associated losses.

For conventional slotted, slotless[2] and superconducting machines, important dimensions associated with the axial field are the radial and axial distances between the ends of the windings and the inner edge of the stator core. In a conventional machine, both windings overhang the end of the core, but in the superconducting machine the rotor winding, at least, will underhang the core end in order to achieve adequate screening. The type of winding is also important; invariably, the rotor winding has a concentric form, and the stator winding varies

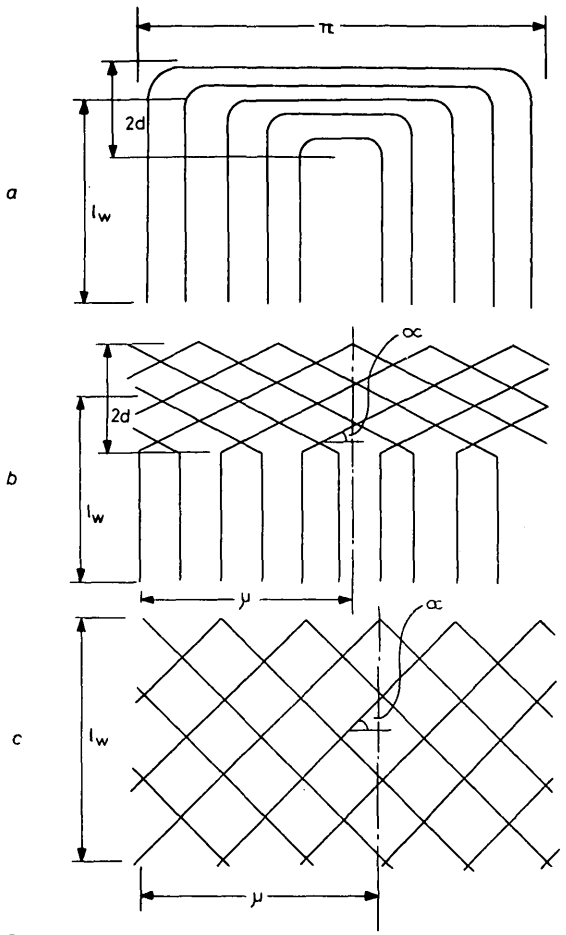

Fig. 1
Developed schematics of windings investigated

The number of conductors shown does not necessarily correspond to that on the practical winding
a Concentric winding
b Diamond winding
c Helical winding
helix angle = α; chording angle = μ

Paper 8186 P, first received 2nd December 1977 and in revised form 30th May 1978

Dr. Stoll and Mr. Lorch are, and Mr. Tavner and Dr. Penman were formerly, with the Department of Electrical Engineering, University of Southampton, Southampton SO9 5NH, England. Mr. Tavner is now with Engineering & Power Developments & Consultants, Marlowe, Station Road, Sidcup, Kent, England, and Dr. Penman is now with the Department of Electrical Engineering, University of Manchester Institute of Science & Technology, Manchester M60 1QD, England

0020-3270/78/100948 + 09 $01.50/0

from the common 2-layer straight winding with diamond ends and a cone angle of about 30°, to the 2-layer helical winding, proposed for the superconducting machine,[1] in which the end windings are effectively absorbed into the active portion of the winding. Thus, the core problem needs to be examined for various types of winding and position. Axial-flux flow in laminated cores is not completely understood. Possible mechanisms are being studied by the authors at the present time, and it is hoped to report shortly on the first stage of a method of calculating the axial-field distribution. This paper, however, concentrates on the results of some fairly extensive measurements on a small core excited in turn by windings of three types, namely a straight winding with concentric ends, a straight winding with diamond ends, and a helical winding, as shown in Fig. 1. Both overhang length and the frequency of excitation have been varied. The latter is important because frequency is the only free parameter with which to attempt to scale the eddy-current phenomenon.

It is often thought that the field of a winding in air gives a good indication of the axial flux that will occur when the winding is inserted in the core. Measurements on the model windings in air, which agree well with the calculated field, are therefore compared with the measurements inside and outside the core. It is found that the presence of the core has a very marked effect on the resultant field.

2 Magnetic fields of various windings in air

Analytical expressions for the magnetic field of windings in air have been devised by various authors.[3-6] The method used here is that of Hammond and Ashworth,[3,4] in which the winding is reduced to a set of current sheets of simple geometrical shape. The field of a concentric winding has been derived in Reference 3, and that of a 2-layer diamond winding in Reference 4. The method is described briefly in Section 8, and has been extended to include the helical winding. The radial and axial field components, which are the two of primary interest, are given in eqns. 1 and 3 for the three windings. The validity of the results for the concentric and diamond windings has already been established experimentally,[4] but this has not been done for the helical winding. Measurements of the radial and axial flux density produced by a model helical winding, the dimensions of which are given in Table 1, are compared with calculated values in Figs. 2 and 3. The results, which show the variation of the field with axial position on three different radii (greater than the winding radius), have been normalised in accordance with the procedure given in Section 4, and demonstrate reasonable agreement between measured and theoretical values, within the limits of experimental accuracy. The form of the field of the helical winding is of interest when compared with that for more conventional windings; not only does the radial field fall off almost cosinusoidally with axial distance from the centre of the winding, but there is significant axial field present everywhere except on the plane of symmetry.

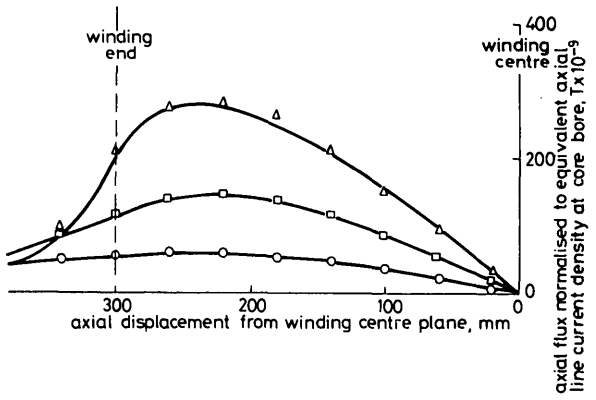

Fig. 2
Comparison between measured and calculated values of axial flux density at various radii from the helical winding

calculated ——
measured △ at 1·24 R_w
□ at 2·95 R_w
○ at 4·34 R_w

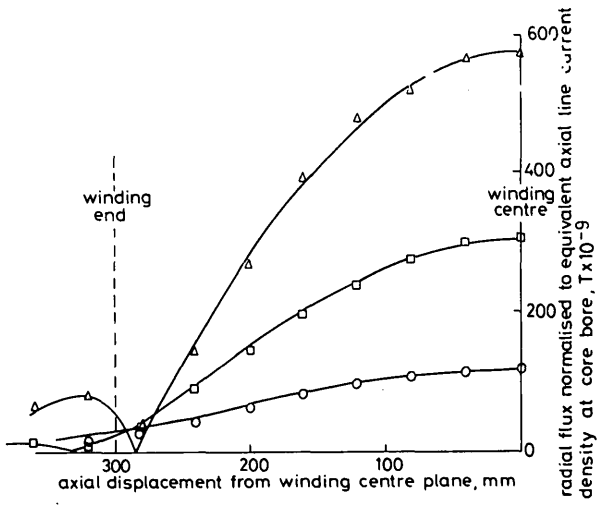

Fig. 3
Comparison between measured and calculated values of radial flux density at various radii from the helical winding

calculated ——
measured △ at 1·24 R_w
□ at 2·95 R_w
○ at 4·34 R_w

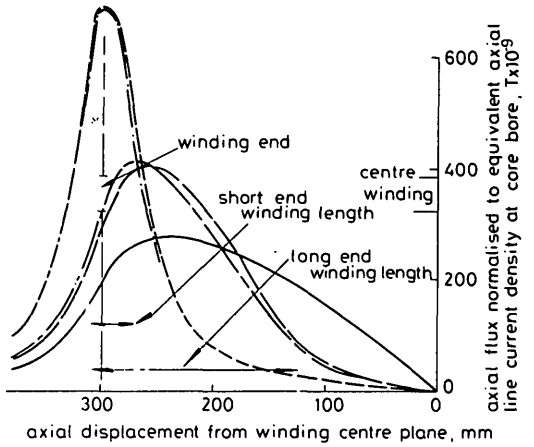

Fig. 4
Comparison between calculated values of axial flux density for three types of winding with various lengths of end winding

—— helical winding
—·— concentric winding — long end winding
— — diamond winding — $d = 0{\cdot}41\, l_w$
—·—·— concentric winding — short end winding
– – – – diamond winding — $d = 0{\cdot}06\, l_w$

Table 1
WINDINGS CONSTRUCTED FOR THE VARIOUS EXPERIMENTS

Denoted by	Winding description	Winding radius	Overall length	End-winding length	Number of turns per phase	Phase spread	Distribution factor
		mm	mm	mm		degrees	
A	Straight winding with diamond ends (simulates a conventional stator winding)	160	1030	165	16	60	0·955
B	Helical winding (simulates a helical stator winding)	143	615	–	16	120	0·827
C	Concentric winding (simulates a small radius rotor)	60	575	55	12	120	0·827
D	Concentric winding (simulates a large radius rotor)	100	550	35	16	120	0·827

The calculated radial and axial field distributions at one radius outside the three types of winding are shown in Figs. 4 and 5, where the length and radius of each winding are the same as for the experimental helical winding. It is clear that the fields developed by the concentric and diamond windings, especially the axial field, depend crucially on the length of the end region. A shorter end winding gives a higher value of axial field spread over a shorter axial span. The results for the concentric and diamond windings are shown with two different values of end-winding length equal to 0·06 and 0·41 times the winding length, respectively. In each case the overall length of the winding remains the same. As the end winding is shortened, the fields of the concentric and diamond windings become indistinguishable, as one would intuitively expect. Conversely, as the end winding is lengthened, the field of the diamond winding tends to that of the helical winding, again as one would expect from their construction.

At first sight these curves might be taken to indicate that a helical winding, or a conventional winding with long ends, will develop large axial fluxes in a laminated core that completely envelopes the winding. From such a hypothesis has developed the belief that the length of the end portion of a conventional winding should be minimised, and that it should overhang from the core so that the laminations do not lie in a region of high applied axial field. This has led to a reluctance to adopt the helical winding in new machine designs, and a resistance to the idea of permitting core length to be increased to cover the end windings.

The measurements presented in the second half of this paper demonstrate that these principles are erroneous, primarily because of the important influence on the axial flux in a laminated core of both the core-end geometry and the eddy currents flowing in the laminations.

However, the calculated winding fields in air are a useful tool if they are considered in conjunction with the contributions due to the core surfaces, and this is the subject of further work by two of the authors.

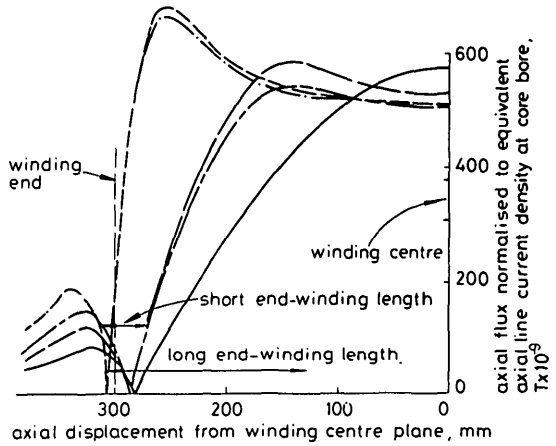

Fig. 5
Comparison between the calculated values of radial flux density for three types of winding with various lengths of end winding

Nomenclature as in Fig. 4

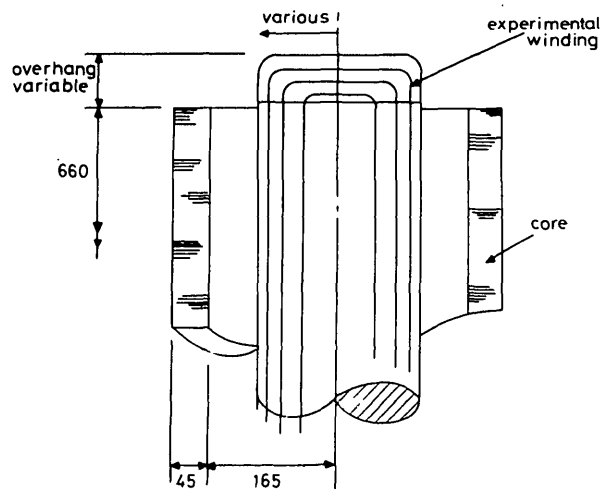

Fig. 6
Experimental model

3 Model core and windings

The experimental results presented in this paper were obtained on a small laminated core enclosing 3-phase windings of various types, as shown in Fig. 6. Because the apparatus was not designed to take a rotating winding, stationary 3-phase concentric windings were used to simulate the conventional concentric d.c. rotor winding. The core was mounted vertically, and the winding under test could be suspended at a wide range of heights with respect to the core. Details of the windings are given in Table 1.

The laminated core was constructed from 0·5 mm thick coreplate, and laminations were randomly arranged within the stack with respect to their rolling directions. The stacking factor of the core was approximately 89%. Measurements were made at various axial positions within the screen. At each site, three axial search coils were fitted across the annulus, as shown in Fig. 7. Each search coil consisted of a single turn of 46 s.w.g., forming a square of 10 x 10 mm, varnished direct to the lamination. The interlaminar gap at the coil sites was increased to 0·125 mm uniformly around the lamination by using a spacer, and the gap between laminations not carrying coils was approximately 0·05 mm. Five multiturn axial search coils were also fitted across the annulus at the end of the core to give detailed end measurements, again as shown in Fig. 7. Measurements of the radial flux density at the bore and at the back of the screen were also made, although they are not presented in this paper.

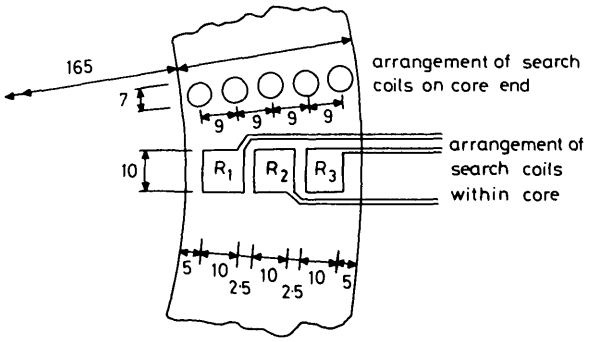

Fig. 7
Layout of axial search coils on core end and within the core

3.1 Scaling of model core

The important property to be scaled is the distribution of axial flux in the core, and this requires that the excitation frequency, which is the only free parameter, should be selected according to scaling principles. Although precise scaling is almost impossible, the most appropriate criterion for the full-scale axial flux phenomenon to be reproduced in the model is that the ratio

$$\frac{\text{core annular depth}}{2 \times \text{skin depth of axial flux}}$$

should be approximately the same for both the model and a fullsize machine of feasible geometry.

The classical expression for the skin depth of the axial-flux distribution is

$$\delta_r = \sqrt{\left(\frac{2\rho}{\omega\mu_0\mu_z}\right)}$$

The scaling suggested will apply subject to the following conditions:

(i) The radial depth of the core is a small proportion of the mean radius, and so that the effect of curvature can be neglected.
(ii) The core has a linear-axial magnetisation characteristic. This condition is satisfied because the axial permeability is dominated by the interlaminar airgaps.
(iii) The pole pitch is sufficiently large compared with the radial depth of the core for the skin effect to be fully developed at the core periphery.

The last condition is satisfied, according to Stoll and Hammond,[7] when $p^2 \gg 1$, where the nondimensional parameter $p = \sqrt{2}\,h/\pi\delta_r$, where h is the pole pitch.

The parameters of typical cores of full-size machines and the model are given in Table 2, and they show that the condition for a fully developed skin effect has been met. It can be seen that an excitation

frequency on the model of 2000 Hz will satisfy our scaling criterion at the lower end of the range of machine sizes. As the use of a higher frequency on the model accentuates the problems of pick up with our instrumentation, the frequency of 2000 Hz has been used. Readings have also been taken at 50 Hz to provide a comparison that demonstrates the influence of the eddy currents in the core.

Table 2
MACHINE PARAMETERS

	Range for full-size machine	Model
Core annular depth b, m	0·4–0·8	0·045
Core mean pole pitch h, m	5–6	0·59
Core plate resistivity ρ, Ωm	55×10^{-8}	55×10^{-8}
Core stacking factor γ, %	75–92	89
Axial permeability μ_z	4–12	9·1
Frequency of excitation f, Hz	50	2000
Classical skin depth δ_r, mm	15–27	2·8
p^2	7000–32000	9000
$b/2\delta_r$	7–27	8

4 Measurements of axial flux in core

The axial flux has been measured inside and on the core end face for each of the windings summarised in Table 1. Only single-winding excitation has been considered, and, as is inevitable in a small-scale air-cored model without special cooling facilities, it has not been possible to saturate the core. The problems introduced by magnetic saturation will be considered when a model with a superconducting rotor has been built and tested. Therefore, in the present model, only the r.m.s. magnitude and phase of each of the search coil outputs have been recorded, and harmonics have not been considered.

In order to compare the axial flux produced by windings of different radii and conductor arrangements, the measured densities are normalised to a convenient datum, namely the r.m.s. value of the fundamental component of axial line current density, referred to the stator-bore radius R_t and given (for a 3-phase 2-pole winding) by

$$j'_z = \frac{3}{\pi} \frac{N\hat{I}}{R_t} k_d \, Am^{-1}$$

In other words, the axial-flux-density measurements are normalised to the equivalent electric loading that the winding in question would produce at the core bore.

All axial and radial dimensions are normalised to the stator-bore radius R_t.

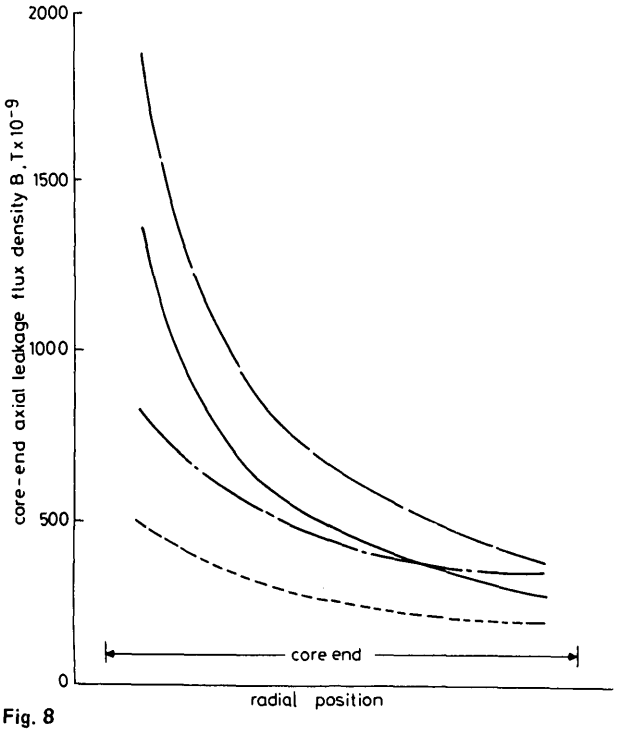

Fig. 8
Core end axial leakage flux density for four different windings

Flux readings have been normalised to the electric loading of the winding referred to the core-bore radius

		radius	overhang
— —	diamond winding	$0{\cdot}97 R_t$	$1{\cdot}11 R_t$
———	helical winding	$0{\cdot}87 R_t$	$1{\cdot}11 R_t$
—·—	concentric winding	$0{\cdot}61 R_t$	$1{\cdot}27 R_t$
– – – –	concentric winding	$0{\cdot}36 R_t$	$1{\cdot}27 R_t$

4.1 Core-end measurements

The first results presented are comparisons of the axial flux on the core end for the various windings with appproximately equal overhangs. These measurements were all taken at 50 Hz and are shown in Fig. 8. Measurements at 2000 Hz are of the same form but are reduced slightly in magnitude; the reason for this is discussed in Section 4.2.

Although the different windings all produce the same electric loading at the core bore, it is clear that the smaller the winding radius, the less the axial flux on the core end. The comparison between the helical winding and conventional diamond winding is particularly interesting as the helical winding produces markedly less core-end leakage. Most proposals for the helical winding have suggested that its length should be equal to that of the core. However, an overhang may be necessary for constructional reasons. The conventional diamond winding used in the experiment had cylindrical end windings with no cone angle. The influence of cone angle on core-end leakage has been investigated elsewhere,[4, 5] but, in general, the core-end flux increases as the cone angle increases. It may therefore be concluded that an overhanging helical winding will have a better core-end leakage performance than a conventional winding of similar dimensions and loading, whether or not that winding is coned.

The length of the overhang will clearly affect the core-end leakage, and Fig. 9 shows this for the 100 mm radius ($0{\cdot}61 R_t$) concentric winding. Core-end axial flux is reduced as the overhang decreases, and this result is also found with the other windings.

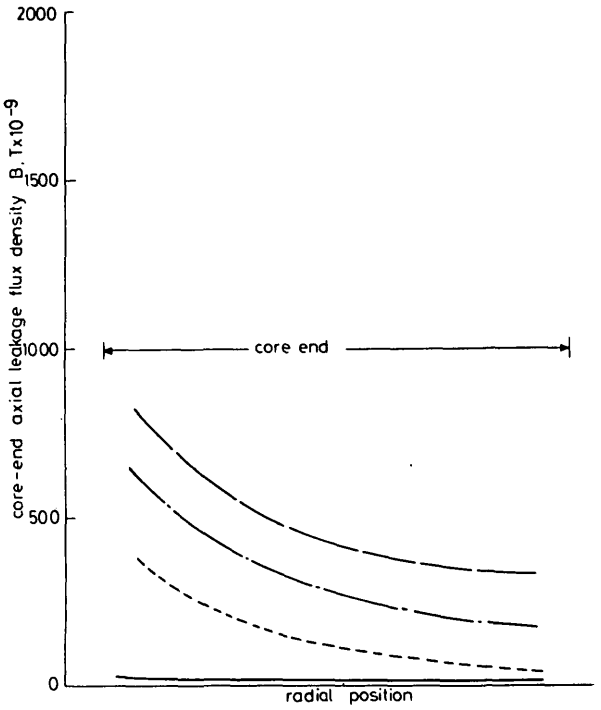

Fig. 9
Core end axial leakage flux density for the concentric winding, radius $0{\cdot}61 R_t$ in four overhang positions

Flux readings have been normalised to the electric loading of the winding referred to the core-bore radius

	overhang
— —	$1{\cdot}27 R_t$
—·—	$0{\cdot}64 R_t$
– – –	$0{\cdot}32 R_t$
———	$0 R_t$

4.2 Internal core amplitude measurements

These measurements were made with the core excited first at 50 Hz and then at 2000 Hz to demonstrate the effect of eddy currents on axial flux. The results are presented in isometric form to show clearly the variation of each of the three search-coil results at different depths and frequencies.

The internal core measurements are presented for comparison in Figs. 10 to 19. Figs. 10 to 13 are for the four windings of Table 1, each with a finite overhang as indicated. Figs. 14 to 16 are for the movable windings B, C, and D (Table 1), with their winding ends level with the core end (i.e. with zero overhang). Figs. 17–19 are for the same windings underhung by the amount indicated. It should be noted that the ordinate scales of the graphs are not equal.

The first important comparison is between the straight and helical windings with equal overhangs (Figs. 10 and 11). These windings had

markedly different axial field distributions in air, as explained in Section 2, and yet it is clear from the Figures that the internal core-flux distributions are of the same form at both frequencies. The helical winding, which produced the lower core-end leakage (Fig. 8), also produces, at 50 Hz, proportionally lower internal axial flux. At 2000 Hz, however, the axial flux distributions for the two windings are indistinguishable.

Figs. 12 and 13 show that the overhung concentric windings produced results of similar form, with their internal-flux magnitudes reduced in proportion to the reduction in their core-end leakage, although the decay of axial flux into the core is rather slower for the small-radius winding.

Figs. 14 to 16 show how the internal axial flux produced by the helical and concentric windings is reduced when the overhang is reduced to zero. In Figs. 17 to 19, the flux is reduced still further as the windings are drawn in beneath the core end, the values of internal axial-flux density being less than 100 units (very small compared with the 1000 units occurring when the windings overhang by a significant amount).

As mentioned in Section 2, these results demonstrate that the axial field of a winding in air may not, on its own, be useful in predicting the likely distribution of axial flux in a surrounding laminated core.

The results further demonstrate that axial flux diminishes as the winding overhang is reduced, even when the winding is drawn in beneath the core end.

The results at 2000 Hz show the important effect of eddy current in redistributing axial flux within the core to such an extent that there is very little penetration deeper than 20 laminations from the core end. The core-end leakage, however, suffers only a slight reduction in magnitude. This implies that the core eddy currents, even at 2000 Hz, are not significantly altering the axial field in air, and this is confirmed by results presented by two of the authors in another paper.[8]

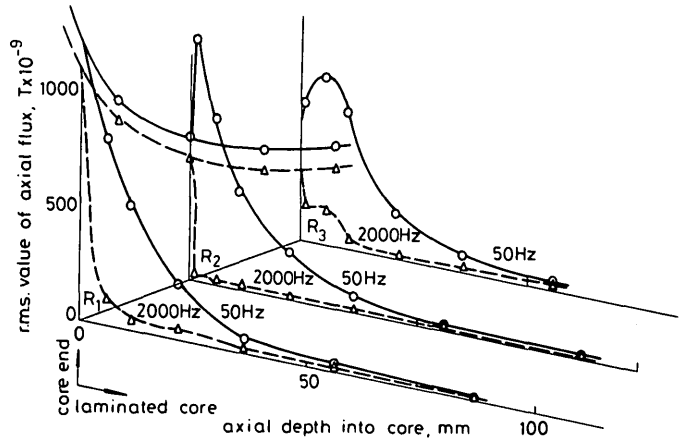

Fig. 10
Axial-flux distribution in laminated stator core

Diamond winding; radius = 0·97 R_t (160 mm);
overhang = 1·11 R_t (183 mm)

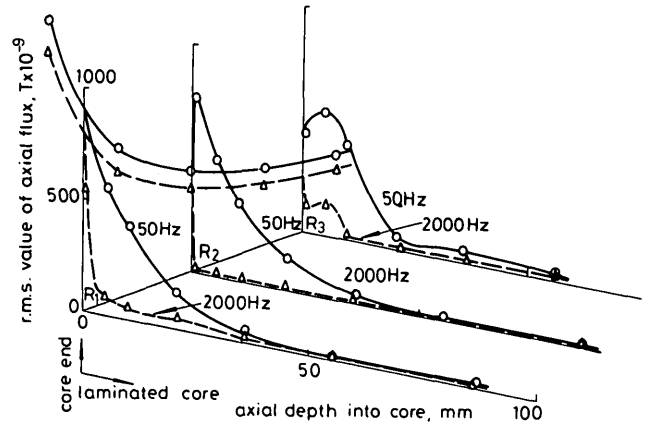

Fig. 11
Axial-flux distribution in laminated stator core

Helical winding; radius = 0·87 R_t (143 mm);
overhang = 1·11 R_t (183 mm)

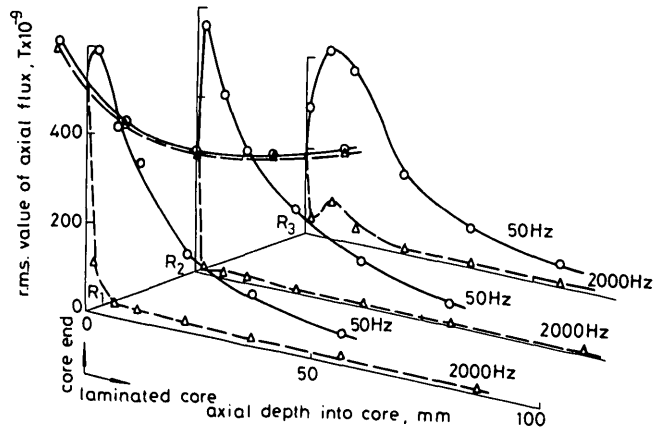

Fig. 12
Axial-flux distribtuion in laminated stator core

Concentric winding; radius = 0·61 R_t (100 mm);
overhang = 0·64 R_t (105 mm)

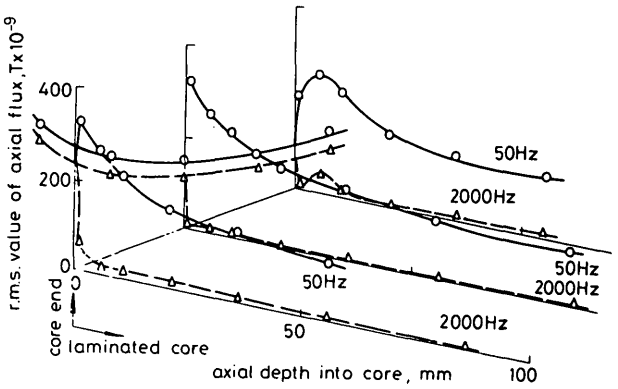

Fig. 13
Axial-flux distribution in laminated stator core

Concentric winding; radius = 0·36 R_t (60 mm);
overhang = 0·64 R_t (105 mm)

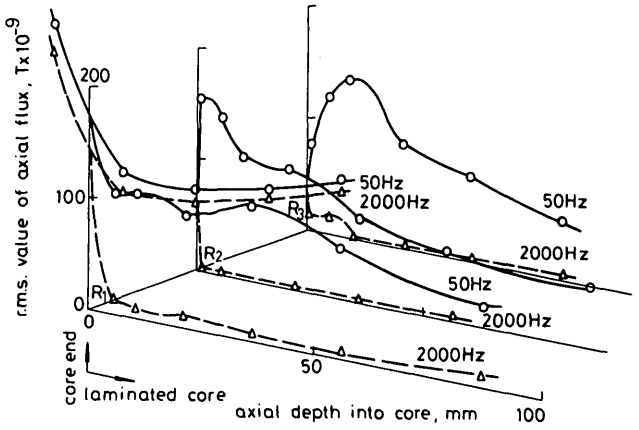

Fig. 14
Axial-flux distribution in laminated stator core

Helical winding; radius = 0·87 R_t (143 mm);
overhang = 0 (0 mm)

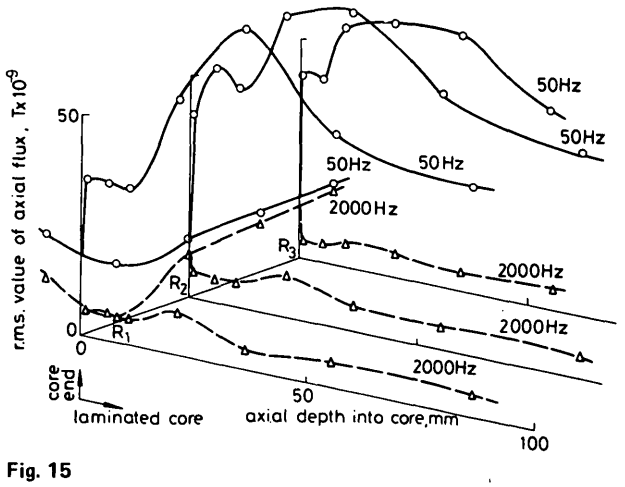

Fig. 15
Axial-flux distribution in laminated stator core

Concentric winding; radius = 0·61 R_t (100 mm);
overhang = 0 (0 mm)

4.3 Internal core phase measurements

There is some difficulty in presenting the phase information in an understandable way. The variation of magnitude and phase of axial flux in the core is of interest in two cases:

(i) the variation with radial position at a given axial distance from the end of the core
(ii) the variation with axial position at a given radius.

The axial search coils used in these experiments were of considerable radial width and were placed at relatively close radial intervals, so that the polar plots of variation (i) are inconclusive.

However, variation (ii) may be investigated, and is of most interest on an axial line at the mean radius of the core. A polar plot may be constructed from the axial search coil readings on this line. Such plots are shown in Figs. 20 and 21 at frequencies of 50 and 2000 Hz, respectively, the core being excited by various windings with overhangs greater than $0{\cdot}5R_t$. The amplitude and phase of each measurement have been normalised with respect to the value on the core end.

At both frequencies, the results from a given search coil are clustered together, regardless of the type of winding or its overhang, provided that the latter is greater than $0{\cdot}5R_t$. In other words, the decrement of axial flux is not significantly influenced by the winding geometry, but only by the structure of the core and the eddy-current flow.

It has been noted, however, that a polar plot is influenced by the winding radius if the overhang length is near zero.

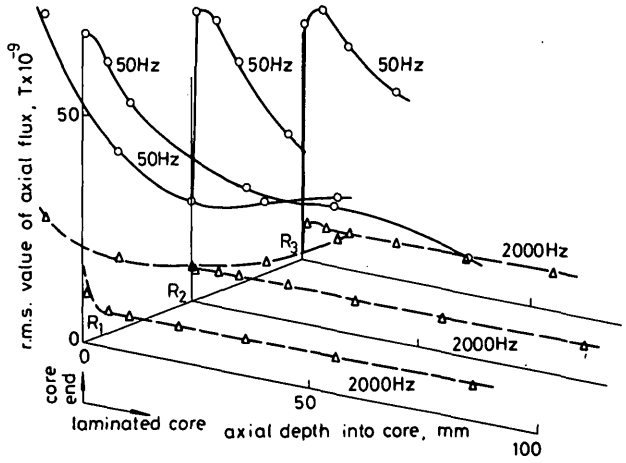

Fig. 16
Axial-flux distribution in laminated stator core

Concentric winding; radius = $0{\cdot}36\,R_t$ (60 mm); overhang = 0 (0 mm)

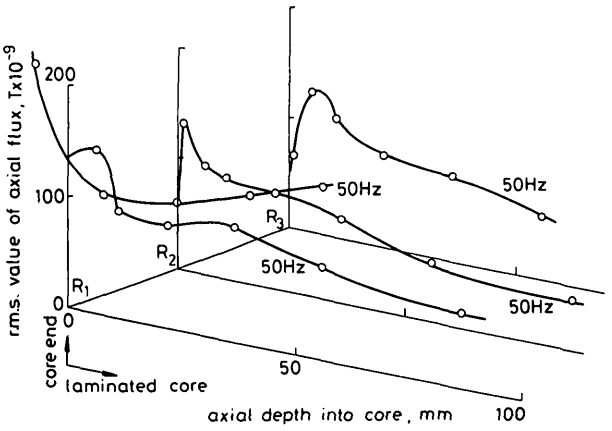

Fig. 17
Axial-flux distribution in laminated stator core

Helical winding; radius = $0{\cdot}87\,R_t$ (143 mm); overhang = $-0{\cdot}06\,R_t$ (− 10 mm)

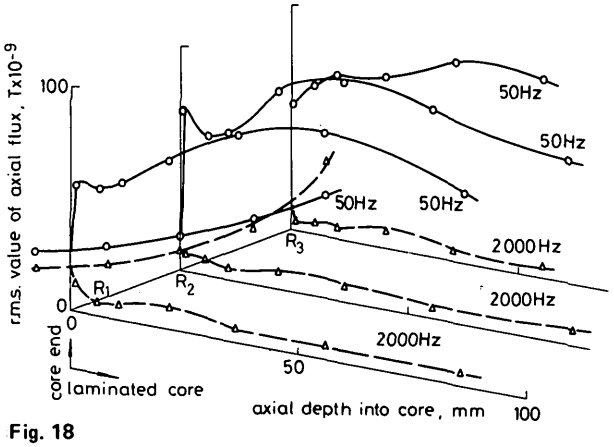

Fig. 18
Axial-flux distribution in laminated stator core

Concentric winding; radius = $0{\cdot}61\,R_t$ (100 mm); overhang = $-0{\cdot}19\,R_t$ (− 31 mm)

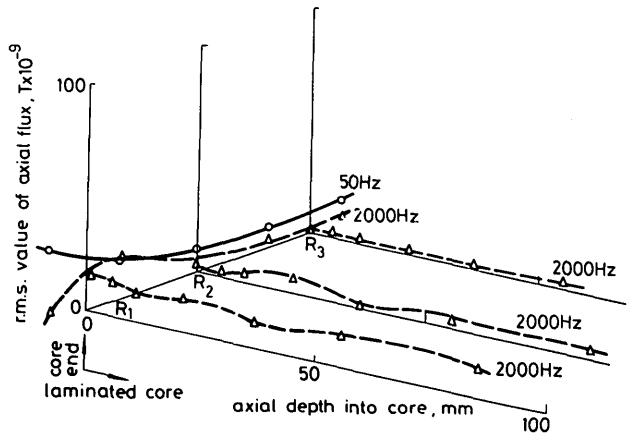

Fig. 19
Axial-flux distribution in laminated stator core

Concentric winding; radius = $0{\cdot}36\,R_t$ (60 mm); overhang = $-0{\cdot}19\,R_t$ (− 31 mm)

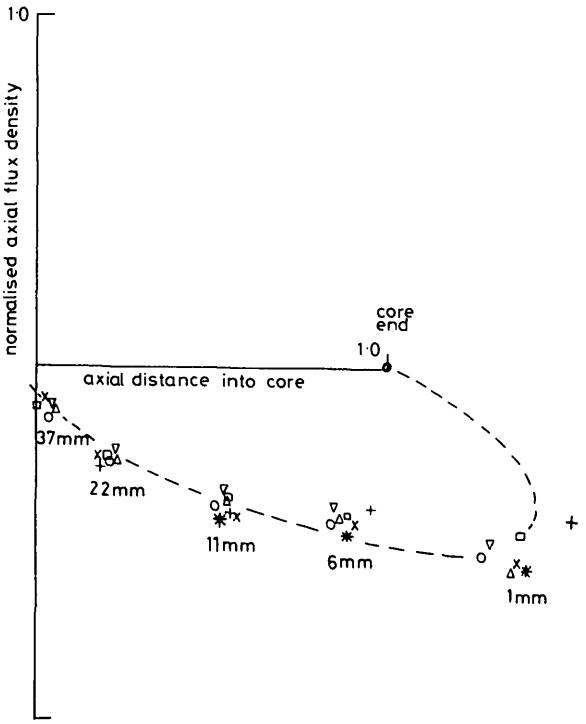

Fig. 20
Polar plot of decrement of axial flux density against axial distance into laminated core excited by various windings at 50 Hz

The axial depths at which measurements were taken are shown on the plot. Each symbol denotes the appropriate search-coil result for a specific winding and overhang

	Overhang	
	$1{\cdot}11\,R_t$	$0{\cdot}55\,R_t$
Diamond winding	△	
Helical winding	□	+
Concentric winding	▽	×
Concentric winding	○	*
Locus of results	----------	

5 Conclusion

The fields in air of concentric, diamond and helical windings have been calculated; first to discover the magnetic behaviour of the helical winding, and secondly to establish the usefulness or otherwise of calculated air fields as a means of predicting the axial flux developed in a core. The results obtained show that the axial field of a helical winding in air does not reach the high peak values of a winding with conventional end connections, but is substantially larger over a greater proportion of the length of the winding.

Measurements have been made, on an experimental model, of the amplitude and phase of axial-flux densities within a laminated core excited by various windings of different designs and at different overhangs. These measurements show that the axial flux impinging on the core end falls as the winding overhang is reduced, or as the winding radius is reduced, irrespective of the winding design. The results also demonstrate that an overhanging helical winding will produce less core-end leakage than a conventional diamond winding of similar size and loading, even if the latter has zero cone angle.

The internal measurements confirm the results on the core end, in that reduced winding overhang and radius produce less axial flux within the core. This is true for the helical winding despite its distributed axial field in air. The polar plots of axial decrement of axial flux within the core confirm that internal distribution of axial flux is independent of winding geometry and design for overhangs greater than $0{\cdot}5\,R_t$, but the distribution is dependent on winding radius for overhangs less than this. The final important conclusion from the internal measurements is that the internal axial flux produced by a winding, whose end does not project beyond the core end, is always less than if the winding were overhanging, again regardless of the windings design. This implies that the proposal to extend the screen in a superconducting generator beyond the end of the stator and rotor windings will not result in large axial-flux densities in the core.

These conclusions all demonstrate that the practice of inferring the axial-flux performance of a winding inside a core, from its calculated axial field in air is erroneous. This practice has led to a pessimistic estimate of the behaviour of the helical winding, and an unnecessary caution in retaining rotor and stator windings of greater length than the core.

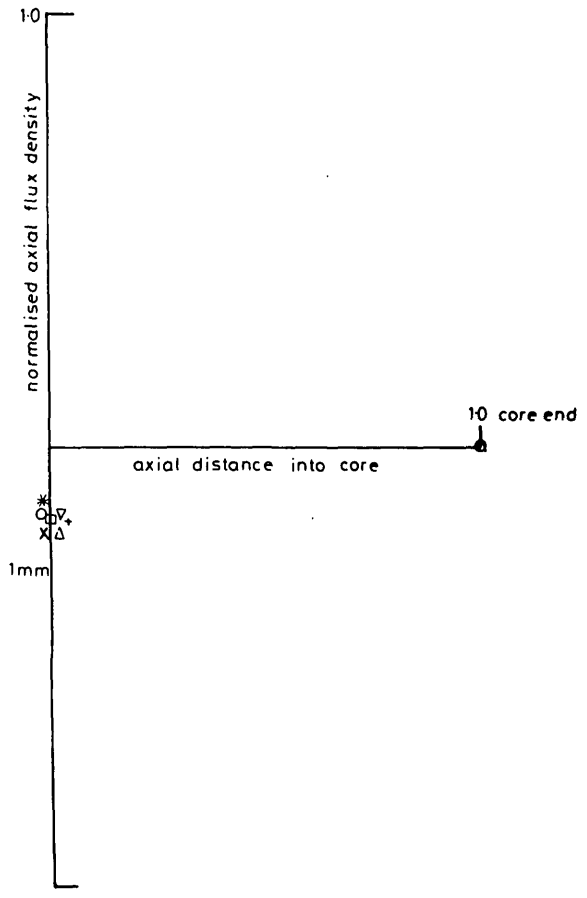

Fig. 21
Polar plot of decrement of axial flux density against axial distance into laminated core excited by various windings at 2000 Hz

Nomenclature as for Fig. 20

6 Acknowledgments

We are indebted to J. Kirwan who constructed the model and windings with great care, and who performed many of the field measurements. We would also like to thank the UK Science Research Council for funding this work, which forms part of a programme of research on electromagnetic problems in large electrical machines.

7 References

1 ROSS, J.S.H.: 'The engineering design of large superconducting a.c. generators'. Proceedings of the International Conference on Electrical Machines, University of Technology, Vienna, 1976, Paper G1
2 SPOONER, E.: 'Fully slotless turbogenerators', *Proc. IEE*, 1973, **120**, (12), pp. 1507–1518
3 HAMMOND, P.: 'The calculation of the magnetic field of rotating machines. Pt. 1 – The field of a tubular current', *ibid.*, 1959, **106C**, pp. 158–164
4 ASHWORTH, D.S., and HAMMOND, P.: 'The calculation of the magnetic field of rotating machines. Pt. 2 – The field of turbogenerator end-windings', *ibid.*, 1961, **108A**, pp. 527–538
5 LAWRENSON, P.J.: 'The magnetic field of end-windings of turbogenerators', *ibid.*, 1961, **108A**, pp. 538–549
6 TEGOPOULOS, J.A.: 'Current sheets equivalent to endwinding currents of turbine-generator stator and rotor', *AIEE Trans.*, 1963, **81**, Part 3, pp. 695–700
7 STOLL, R.L., and HAMMOND, P.: 'Calculation of the magnetic field of rotating machines: Pt. 4 – Approximate determination of the field and the losses associated with eddy currents in conducting surfaces', *Proc. IEE*, 1965, **112**, (11), pp. 2083–2094
8 TAVNER, P.J., HAMMOND, P., and PENMAN, J.: 'A contribution to the calculation of leakage fields at the ends of rotating electrical machines', *Proc. IEE*, 1978, **125**, to be published

8 Appendix

The magnetic field of a cylindrical winding in air can be calculated by representing the winding as a set of axial and circumferential current sheets.[3,4] Windings with conical ends require radial current sheets in addition.[4] The distribution of each component of surface current density, as a function of axial displacement z, can be conveniently represented as a Fourier series by assuming an infinite succession of current sheets (Fig. 22). Each current sheet is separated by an interval g, which is large enough for there to be negligible interference between the fields of adjacent windings. A suitable value for g has been found to be $4(l_w + R_W)$.[3] Provided that the origin is placed as shown in Fig. 22, the axial surface current density will always be formed by an even system

$$j_z(z,t,\theta) = \cos(\omega t - \theta) \sum_{k=1,3,5\ldots}^{\infty} a_k \cos\frac{k\pi z}{g}$$

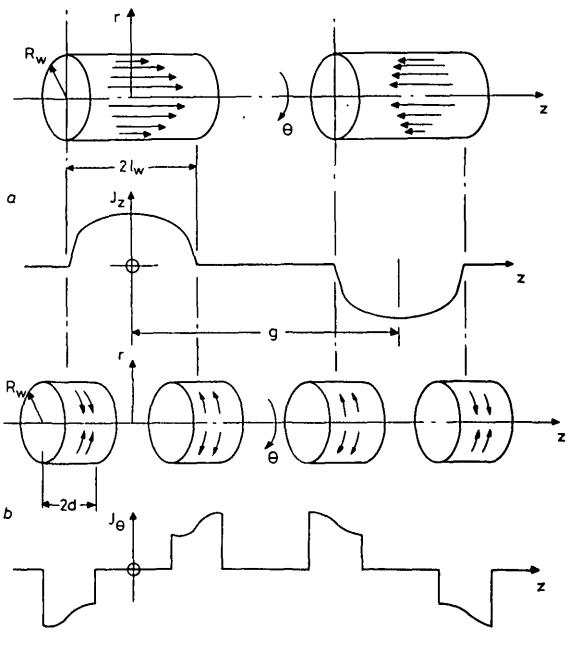

Fig. 22
Form of current sheets required to represent practical winding

a Axial current sheet
b Circumferential current sheet
The form shown does not represent a particular practical winding

Table 3
FORMS OF WINDING CURRENTS AND THEIR FOURIER COEFFICIENTS

Winding type	Current sheet pattern	Expressions for a_k and c_k
Straight winding with concentric ends $\hat{j}_\theta = \hat{j}_z \frac{R_w}{d}$	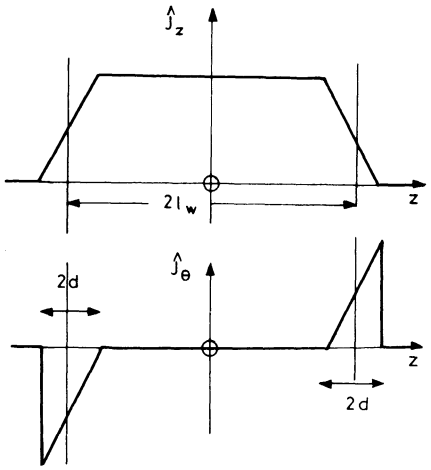	$a_k = \hat{j}_z \frac{2}{k\pi d}\left\{\cos\frac{k\pi}{g}(l_w-d)-\cos\frac{k\pi}{g}(l_w+d)\right\}\Big/\left(\frac{k\pi}{g}\right)$ $c_k = \hat{j}_z \frac{4R_w}{k\pi d}\left\{\cos\frac{k\pi}{g}(l_w+d)\right.$ $\left.-\frac{1}{2d(k\pi/g)}\left(\sin\frac{k\pi}{g}(l_w+d)-\sin\frac{k\pi}{g}(l_w-d)\right)\right\}$
Straight winding with diamond ends (α is the helix angle of the conductors in the end region) $\hat{j}_\theta = \hat{j}_z \cot\alpha$	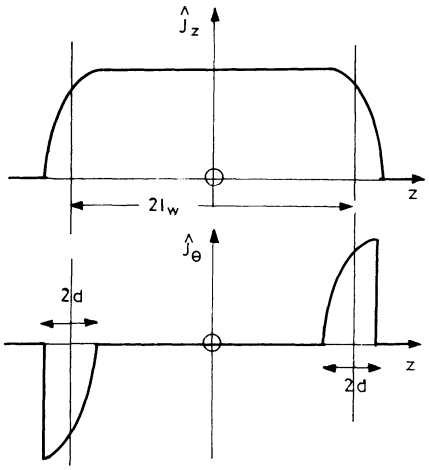	$a_k = \hat{j}_z \frac{2}{g}\left\{\frac{2}{(k\pi/g)}\sin\frac{k\pi}{g}(l_w-d)\right.$ $+\left[\sin\frac{\mu}{2d}(l_w+d)\left\{\frac{\sin\left(\frac{k\pi}{g}-\frac{\mu}{2d}\right)z}{\left(\frac{k\pi}{g}-\frac{\mu}{2d}\right)}+\frac{\sin\left(\frac{k\pi}{g}+\frac{\mu}{2d}\right)z}{\left(\frac{k\pi}{g}+\frac{\mu}{2d}\right)}\right\}\right.$ $\left.\left.-\cos\frac{\mu}{2d}(l_w+d)\left\{\frac{\cos\left(\frac{k\pi}{g}-\frac{\mu}{2d}\right)z}{\left(\frac{k\pi}{g}-\frac{\mu}{2d}\right)}-\frac{\cos\left(\frac{k\pi}{g}+\frac{\mu}{2d}\right)z}{\left(\frac{k\pi}{g}+\frac{\mu}{2d}\right)}\right\}\right]_{l_w-d}^{l_w+d}$ $c_k = \hat{j}_z \cot\alpha \frac{2}{g} \times$ $\left[\sin\mu\frac{(l_w+d)}{2d}\left\{\frac{\sin\left(\frac{k\pi}{g}-\frac{\mu}{2d}\right)z}{\left(\frac{k\pi}{g}-\frac{\mu}{2d}\right)}-\frac{\sin\left(\frac{k\pi}{g}+\frac{\mu}{2d}\right)z}{\left(\frac{k\pi}{g}+\frac{\mu}{2d}\right)}\right\}\right.$ $\left.-\cos\mu\frac{(l_w+d)}{2d}\left\{\frac{\cos\left(\frac{k\pi}{g}-\frac{\mu}{2d}\right)z}{\left(\frac{k\pi}{g}-\frac{\mu}{2d}\right)}+\frac{\cos\left(\frac{k\pi}{g}+\frac{\mu}{2d}\right)z}{\left(\frac{k\pi}{g}+\frac{\mu}{2d}\right)}\right\}\right]_{l_w-d}^{l_w+d}$
Helical winding $\hat{j}_\theta = \hat{j}_z \cot\alpha$	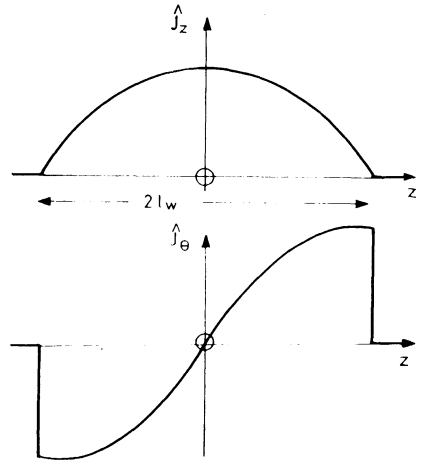	$a_k = \hat{j}_z \frac{2}{g}\left\{\frac{\sin\left(\frac{k}{g}-\frac{1}{2l_w}\right)\pi l_w}{\left(\frac{k}{g}-\frac{1}{2l_w}\right)\pi}+\frac{\sin\left(\frac{k}{g}+\frac{1}{2l_w}\right)\pi l_w}{\left(\frac{k}{g}+\frac{1}{2l_w}\right)\pi}\right\}$ $c_k = \hat{j}_z \cot\alpha \frac{2}{g}\left\{\frac{\sin\left(\frac{k}{g}-\frac{1}{2l_w}\right)\pi l_w}{\left(\frac{k}{g}-\frac{1}{2l_w}\right)\pi}-\frac{\sin\left(\frac{k}{g}+\frac{1}{2l_w}\right)\pi l_w}{\left(\frac{k}{g}+\frac{1}{2l_w}\right)\pi}\right\}$

and the circumferential surface current density will always be formed by an odd system

$$j_\theta(z, t, \theta) = \cos(\omega t - \theta - \tfrac{1}{2}\pi) \sum_{k=1,3,5\ldots}^{\infty} c_k \sin\frac{k\pi z}{g}$$

The symmetrical form of the infinite succession of current sheets ensures that the series contain only odd harmonics, and the circumferential current sheet must lag $\pi/2$ in time pulses from the axial sheet.

The current-density distributions depend on the winding design, and distributions for the windings of interest are shown in Table 3. The coefficients a_k and c_k determine the form of the distributions, and these are found by evaluating the expressions

$$a_k = \frac{4}{g}\int_0^{g/2} j_z(z)\cos\frac{k\pi z}{g}\,dz$$

$$c_k = \frac{4}{g}\int_0^{g/2} j_\theta(z)\sin\frac{k\pi z}{g}\,dz$$

for odd values of k only. The peak axial line current density j_z is given by

$$\hat{j}_z = \frac{3NI}{\pi R_w} k_d$$

and $\hat{j}_\theta$ may be related to it by continuity as shown in Table 3. The expressions for j_z and j_θ must then satisfy the continuity condition $\nabla \cdot J = 0$.

The representation of a winding by current sheets is to some extent an approximation, but it has been shown[3,4] that accurate results can be obtained for concentric and diamond windings with the forms shown in Table 3. The form of the helical winding current sheets can be found from the method for the diamond winding[4] by extending the end region throughout its halflength, and this can be seen in Table 3.

General expressions for the magnetic field of periodic current sheets can be found from their magnetic vector potential. These expressions have been derived in the references, but are presented here in generalised form in terms of the Fourier coefficients a_k and c_k:

$$H_r = \frac{R_w}{2r}\cos(\omega t - \theta) \sum_{k=1,3,5}^{\infty} \left[2K_1\left(\frac{k\pi r}{g}\right) I_1\left(\frac{k\pi R_w}{g}\right) a_k + \frac{k\pi r}{g}\left\{K_0\left(\frac{k\pi r}{g}\right) I_0\left(\frac{k\pi R_w}{g}\right) + K_2\left(\frac{k\pi r}{g}\right) I_2\left(\frac{k\pi R_w}{g}\right)\right\} c_k\right] \cos\frac{k\pi z}{g} \quad (1)$$

$$H_\theta = -\frac{R_w}{2r}\cos\left(\omega t - \theta - \frac{\pi}{2}\right) \sum_{k=1,3,5}^{\infty} \frac{k\pi r}{g}\left[\left\{K_0\left(\frac{k\pi r}{g}\right) I_0\left(\frac{k\pi R_w}{g}\right) - K_2\left(\frac{k\pi r}{g}\right) I_2\left(\frac{k\pi R_w}{g}\right)\right\} c_k + 2K_1'\left(\frac{k\pi r}{g}\right) I_1\left(\frac{k\pi R_w}{g}\right) a_k\right] \cos\frac{k\pi z}{g} \quad (2)$$

$$H_z = \frac{R_w}{2r}\cos(\omega t - \theta) \sum_{k=1,3,5}^{\infty} 2\frac{k\pi r}{g} K_1\left(\frac{k\pi r}{g}\right) I_1'\left(\frac{k\pi R_w}{g}\right) c_k \sin\frac{k\pi z}{g} \quad (3)$$

These expressions must themselves satisfy the condition $\nabla \cdot H = 0$. It can be seen that the radial and circumferential expressions are even in z, while the axial expression is odd, in agreement with our intuitive understanding of the winding fields.

PROCEEDINGS

OF THE INSTITUTION OF ELECTRICAL ENGINEERS

Power

Contribution to the study of leakage fields at the ends of rotating electrical machines

P.J. Tavner, M.A., C.Eng., M.I.E.E, P. Hammond, M.A., C.Eng., M.I.Mech.E., F.I.E.E., and J. Penman, B.Sc., Ph.D.

Indexing terms: *Stators, Electric machines, Magnetic leakage*

Abstract

A method is described for calculating the axial leakage field of the end regions of rotating electrical machines. The method subdivides the problem into the component fields of the magnetic sources that contribute to the axial field. The total field is then found by superposing these component fields. The method is compared with the traditional approach of analysing the magnetic field of electrical machines in terms of magnetic circuits. Measurements are presented of the field in air outside the laminated core of a slotless, cylindrical model. These measurements are in good agreement with the predictions of the method. The method is then used to consider qualitatively the behaviour of the field inside a laminated core. Conclusions are also drawn about the way in which the leakage field will alter with changes in the dimensions and operating conditions of the core.

List of symbols

$\mathbf{B}$ = magnetic flux density
$\mathbf{H}$ = magnetic field strength
I = winding phase current
I_0, I_1, I_2 = modified Bessel functions of the first kind (zero, first and second order)
I_1' = derivative of I_1
$\mathbf{J}$ = current density
J_1, J_2 = Bessel functions of the first kind (first and second order)
J_1' = derivative of J_1
K_0, K_1, K_2 = modified Bessel functions of the second kind (zero, first and second order)
K_1' = derivative of K_1
N = number of winding turns per phase
R_g = periodic interval of annular polarity system
R_1 = inner radius of annulus
R_2 = outer radius of annulus
R_t = radius of core bore
R_w = radius of winding
V^*, V_1^*, V_2^* = magnetic scalar potential
a_k, c_k = Fourier coefficients describing axial and circumferential current sheets
b = core annular depth
d = end winding halflength
d_k = Fourier-Bessel coefficients describing annular surface polarity
g = periodic interval of current sheet and tubular surface polarity systems
j_z, j_θ = instantaneous values of axial and circumferential line current density
j_z' = instantaneous value of axial line current density referred to core-bore radius
k_d = winding distribution factor
l_w = winding halflength to midpoint of end region
l_t = core-bore halflength
p = magnetic surface polarity
$p_t(z)$ = magnetic surface polarity on core bore, as a function of z.
$p_a(r)$ = magnetic surface polarity on annulus, as a function of r.
t_k = Fourier coefficients describing core-bore surface polarity.
α_k = kth zero of Bessel function J_1
γ = core stacking factor
δ_r = skin depth of axial flux
μ = permeability
μ_0 = primary magnetic constant
μ_r = relative permeability
μ_z = homogenised axial permeability
θ = circumferential angular position
ω = angular frequency
ρ = resistivity of core plate

1 Introduction

The distribution of the magnetic field in and around rotating electrical machines can be calculated with the help of modern digital computers. This has been done for the main body of the machine[1] and for the end region[2] using finite-element and finite-difference methods, respectively. The geometry of electrical machines is complicated and as saturation makes the relationship between the magnetic field strength and the flux density nonlinear, the problem of calculation is formidable, so these successes represent a remarkable achievement. What was felt by the earliest workers[3] to require an impossibly powerful and laborious analysis has been accomplished, and future work is likely to involve the improvement and refinement of these computer methods.

Nevertheless, there are other pressing unfinished tasks in the study of the magnetic field of rotating machines. These tasks are concerned with synthesis rather than analysis, and with the design process rather than the testing and operation of completed machines. The solutions that are now available give the field of a complete design, but they do not lay bare the separate effects of the different parts. They give little guidance as to what would happen if the geometry were to be altered or if the magnetic and conducting parts were to be rearranged. Of course it is possible to recalculate the entire problem for a variety of speculative designs, but because the computation is long and intricate, this process is cumbersome and may be unsuited to the design office. A method is required in which each part of the machine is considered as a source of the magnetic field. It is then important to know which of these sources are dominant and which are less important. A generation ago designers relied on relatively simple procedures for calculating the field in a machine. Manipulation of the calculation then

Paper 8233 P, first received 23rd March and in revised form 12th September 1978

Prof. Hammond is, and Mr. Tavner and Dr. Penman were formerly, with the Department of Electrical Engineering, University of Southampton, Southampton SO9 5NH, England. Mr. Tavner is now with Engineering and Power Development Consultants, Sidcup, Kent, England, and Dr. Penman is with the Department of Electrical Engineering, University of Aberdeen, Scotland

0020–3270/78/121339 + 11 $01·50/0

depended on a considerable intuitive understanding of machine magnetic circuits. Nowadays, the digital computer provides such powerful possibilities of numerical calculation that the intuitive part of the design process is in danger of being submerged, with a consequent loss of understanding and control in the design process. In this paper we describe a method of synthesis of the component parts of the core leakage field that should enable the designer to regain control.

The motivation for computer aided analysis of the end-region field, and also for our method of synthesis stems largely from the need to evaluate the loss in the end region. This loss is difficult to predict, not only because of the complexity of the mathematics, but also because the physical behaviour of the axial flux in the core is not fully understood.

In the new slotless and superconducting machine designs the end-region geometries are not yet finalised. There may be considerable scope for reducing the end-region losses in these machines if a new, geometrically dependent approach is adopted for the design of their end regions. It is suggested that the method presented in this paper may be helpful in this task.

2 Historical review

To appreciate the advantages of the proposed method, it is instructive to consider how other methods of end-region analysis have developed from the traditional design procedures.

The scientific design of electrical machines starts with the work of Hopkinson[3] a century ago. Hopkinson was familiar with Maxwell's field theories and he was well aware, from experiment, of the complicated distribution of the magnetic field in and around his machines. He resorted to approximations. Noting that the flux density in the iron was much stronger than that in the surrounding air, he first neglected the leakage flux and assumed that a constant amount of flux threaded the complete iron circuit of his machine, including the airgaps which were relatively short. He knew the flux density required in the airgaps and could therefore estimate the total flux in the machine. Knowing the sizes of the machine components, the flux density in each part of the circuit could be estimated and the ampère-turns required could be found from the magnetising characteristic of the component. By leaving the ampère-turns as the dependent variable, Hopkinson avoided the difficulties cause by magnetic saturation. In short, his method introduced the idea of a magnetic circuit, that was then subdivided into clear physical regions, such as the yoke and the airgap, that were analysed separately. The design of the machine rested on the analysis of its individual components.

This procedure presupposes a knowledge of the magnetic circuit that relies on a clear conceptual picture of the flux pattern of the machine, in which the leakage is a small proportion of the total flux. Designers have used this method successfully to make their calculations on the central plane of machines, where a 2-dimensional flux plot can be drawn. The complex 3-dimensional structure of the field towards the end of the machine has been acknowledged, but the answers obtained from the 2-dimensional central region were sufficiently accurate for most designs. The method has been developed over the years and has led to the compilation of comprehensive sets of formulas and results relating to each part of typical machine magnetic circuits.

The calculation of end-region losses, however, requires a knowledge of the complete end field. When tubes of flux have a significant axial component, a clear picture of their paths is no longer possible, particularly where they enter the core. There is no clearly defined magnetic circuit for the leakage flux, so that the traditional analysis becomes difficult. 2-dimensional flux plots in the end region may give an impression of the leakage flux paths, but they must be treated with caution because their flux lines are no longer continuous. In other words the principle of following tubes of flux, that has been so successful in analysing the magnetic circuit of the central region of machines, is unhelpful in the end region.

Some workers, however, have attempted to apply this flux dominated approach to the airpart of the end region. In particular Winchester's work[4] drew attention to stray losses in the end region, and gave experimental results that he supported with calculations, based on assumptions about the leakage-flux paths. This approach is widely used by machine designers to visualise the field in the airpart of the end region and is further typified by the paper of Walker.[5]

The problem of the end field within the core, however, still remains. This difficulty has led to a different, more ponderous approach to the analysis of the end region. Almost all the methods proposed, subsequent to Winchester, involve some sort of complete solution to the field in the end region and a study of them is instructive. Smith[6] used the end winding current as his primary quantity, and regarded the iron merely as a boundary of the region. He thus treated the field in the end region as a mathematical boundary-value problem, and solved the differential equations. Ashworth and Hammond[7,8] deliberately confined their attention to the field in air of an end winding, subdivided into cylindrical current sheets, to isolate the effect of the winding. Lawrenson[9] calculated the field of end windings by subdividing them into current elements that followed the real winding exactly. He allowed for the stator end surface by the method of images, based on the work of Carpenter[10] and Tegopoulos.[11] and provided a solution for the complete end region, making allowance for all boundaries including the end cover and the rotor surface. He thus reverted to the boundary-value problem of Smith and set the course for most of the subsequent work. Reece and Pramanik[12] refined the treatment of the core surface and the representation of the windings. Okuda[13] used a finite-difference method for the end region and its boundaries. More recently, Myerscough[14] used a Green's function expansion for the magnetic field of end windings completely enclosed in a region bounded by material of infinite permeability. He states that in this method an allowance can be made, by pertubation methods, for additional magnetic and conducting parts within the region.

It will have been noticed that this development has diverged from Hopkinson's simple design method, based on magnetic circuits, to a study of distributed fields by means of differential equations. The solutions are sought in terms of a complete machine structure and are thus, as explained in the introduction, less suited to the design process. The boundary conditions are frequently restricted to either infinite or zero permeability, neither of which assumption gives much insight into the actual field close to the boundaries. This is not to decry a powerful method but to point out some limitations inherent in it.

3 Sources of magnetic field

Hopkinson's traditional method is useful to the designer because it subdivides the machine into clearly defined regions, and it works because it is firmly grounded on the principles of continuity of flux and Ampère's circuital law. The method does not work for leakage flux because its magnetic circuit in the core is not clearly defined. An alternative must be found that is soundly based, and yet incorporates the building-block approach needed by the designer.

An important property of the end region is that both the core and the air have linear axial-magnetisation characteristics, which in the core is due to the presence of the interlaminar airgaps. The principle of superposition may therefore be applied, and this suggests that at each point in the air, or the core, we may sum the component axial fields due to the different parts of the machine. In other words, we are suggesting that a form of integral approach, based on the sources of the magnetic field, may be useful in the analysis of axial leakage fields.

There are two types of source; electric currents in conducting materials and magnetic sources in iron. Mathematically we have three relationships curl $\mathbf{H} = \mathbf{J}$, div $\mathbf{B} = 0$ and $\mathbf{B} = \mu\mathbf{H}$. The first is the statement that the magnetomotive force is equal to the ampère-turns, the second states that magnetic flux is continuous and the third links the magnetising force to the flux density. Mathematically, any vector field is uniquely defined if its curl and divergence sources are specified. We note that the relationship $\mathbf{B} = \mu\mathbf{H}$ can therefore be taken either as a statement about the divergence of $\mathbf{H}$ or about the curl of $\mathbf{B}$, that determines the type of sources needed to represent the iron. It is important to our argument to regard the permeability μ as a specification of magnetic sources rather than as a property of matter. Because it is easier both to envisage divergence sources and also to handle them mathematically, we choose to regard the permeability as a specification of divergence sources of $\mathbf{H}$, that are given the name magnetic polarity. The two types of sources are, therefore, conduction currents and magnetic polarities, and the field under consideration is the $\mathbf{H}$ field.

Both types of sources may be either explicit or implicit. Explicit current sources are the assigned currents in the machine windings and implicit current sources are eddy currents induced in conducting parts. Explicit polarity can be a useful concept for permanent magnets but the polarity of soft magnetic materials has to be treated as an implicit source. This distinction between hard and soft magnetic materials is of course somewhat arbitrary, but it affords a useful simplification.

The magnetic field depends on both the strength and location of the sources. There is no difficulty about the explicit current sources in the windings, because both their strength and position are determined. The problem of eddy currents is more difficult. However, because the energy associated with eddy currents has to diffuse into

the material from the surface, the currents will be strongest near the surface and may, under certain circumstances, be regarded as current sheets. Moreover, in laminated cores, the dominant eddy currents flow in the plane of the laminations.

Magnetic polarity in iron arises from a dipole distribution throughout the volume. The divergence of this dipole distribution determines the pole distribution.[15] Inside the material, a divergence of the dipole distribution arises from a spatial variation of the permeability. If the permeability is constant there can be no volume pole strength and all the polarity will occur on the surfaces. Even if saturation effects cause the permeability to vary, this variation will be small compared with the sharp variation at an iron/air interface. It is therefore a close approximation to assume that the polarity sources are confined to the surface of the iron. Laminated cores, that contain successive surfaces, will exhibit considerable surface pole strength within the core and this may be represented as a distributed volume pole strength. Similarly polarity will be associated with ducts and holes in the material, but these effects are localised and can be treated in isolation.

The various types of sources can be subdivided at will. Thus the currents in the windings can be subdivided into current elements,[9] and the surface polarity can be subdivided into infinitesimal elements of area. The total effect is then obtained by integration that can conveniently be carried out by a computer. This is the approach adopted by Simkin and Trowbridge[16] in the GFUN computer programs. But such a scheme does not provide the large building blocks that the designer may need, and it may again be difficult to separate the effects of different parts of the geometry. The individual sources are too small and there are too many of them. It is better to subdivide the sources into fewer, more recognisable pieces. As far as the windings are concerned it is convenient to use axial, circumferential and radial current sheets.[7,8] This subdivision gives immediate insight into the effect of winding geometry. The polarity sources, that we have considered as confined to surfaces, can be conveniently divided into cylindrical tubes and annular discs. The tubes represent the cylindrical rotor surface and the inner and outer surfaces of the stator. The discs represent the stator end surfaces. If required, eddy-current sources can also be represented by such discs as magnetic shells.

In this subdivision of the sources the designer can retain control of the design process. The chief difficulty is caused by interaction, particularly since the implicit sources depend not only on the explicit sources but also on each other. Nevertheless, this difficulty can be overcome. It is important to remember that the effect of a magnetic source falls off with distance. There is an inverse square law for current elements and small areas of polarity. The decrease will be less for larger sources, but it is still true that strong local fields require local sources. For example, fields will be strong near the edges of a source distribution, but this effect is likely to leave the field elsewhere relatively undisturbed. This is a matter where experience is the best guide, and it will be shown that starting with the explicit sources, it is possible to calculate the approximate size of the major implicit sources.

In this discussion some of the boundaries, which in the literature reviewed in Section 2 appear as mathematical constraints on the magnetic scalar or vector potential, are identified as sources in their own right. For example, the effect of the end surface of a stator core may be more important than the effect of the winding overhang, a problem that has been studied by two of the authors in an investigation on the influence of winding design on core axial flux.[17] Moreover, the surface polarity at an iron/air interface is proportional to the normal magnetic field in the ratio $(\mu_r - 1)/(\mu_r + 1)$.[18] This ratio is insensitive to changes in μ_r and makes polarity a particularly important parameter. Therefore, the method of sources is not limited to the assumption of infinite permeability.

On the other hand, the method has unsatisfactory features. A mathematical boundary-value problem can be solved to any degree of accuracy provided the boundaries are correctly represented. The method of sources, however, will always contain inaccuracies because interaction effects may have been neglected. The use of the method is to give general guidance to the designer about the effect of the various parts of the machine. Once he has arrived at a suitable design he may well have recourse to one of the large computer programs to examine the fine structure of the end-region field.

4 Axial field at the end of a model stator core

To demonstrate the use of the method of sources we examine a relatively simple part of the end-region problem, namely the axial field in the air close to the core end of a slotless air-cored machine. From this we draw conclusions about the behaviour of the axial field within the core, and outline the additions to the method that will be needed to predict the field accurately in that region in a practical machine.

4.1 Model arrangement and its principal sources

Our model, which is shown in Fig. 1, consists of a parallel-sided winding surrounded by a slotless, laminated, iron core, and may represent the winding and environmental screen of a slotless superconducting generator. The sources that make a contribution to the axial field are listed here as follows:

(*a*) the circumferential components of the winding currents
(*b*) the polarities on the core bore and core back surfaces of the machine
(*c*) the polarities on the annular surfaces of the machine
(*d*) eddy currents within the core
(*e*) volume polarities within the core.

The core is excited by only one winding; load conditions are therefore not discussed in this paper. There is, however, no inherent difficulty in adding another winding.

The leakage flux from the back of the core is controlled partly by the magnetostatic flux-carrying capacity of the core and partly by the eddy currents flowing in the planes of the laminations. For a core of practicable radial depth, the core-back leakage-flux density will be small and the surface polarity will be weak. For this reason it has been neglected in this paper as a source of axial flux. However, the surface area of the core-back is large and so there will be appreciable leakage flux. It is this flux which sets up large circulating currents in the supporting frames of large cores. These currents may cause subsidiary electromagnetic effects.

The contribution of the core eddy currents has also been omitted because one intuitively expects their effect in the air region to be

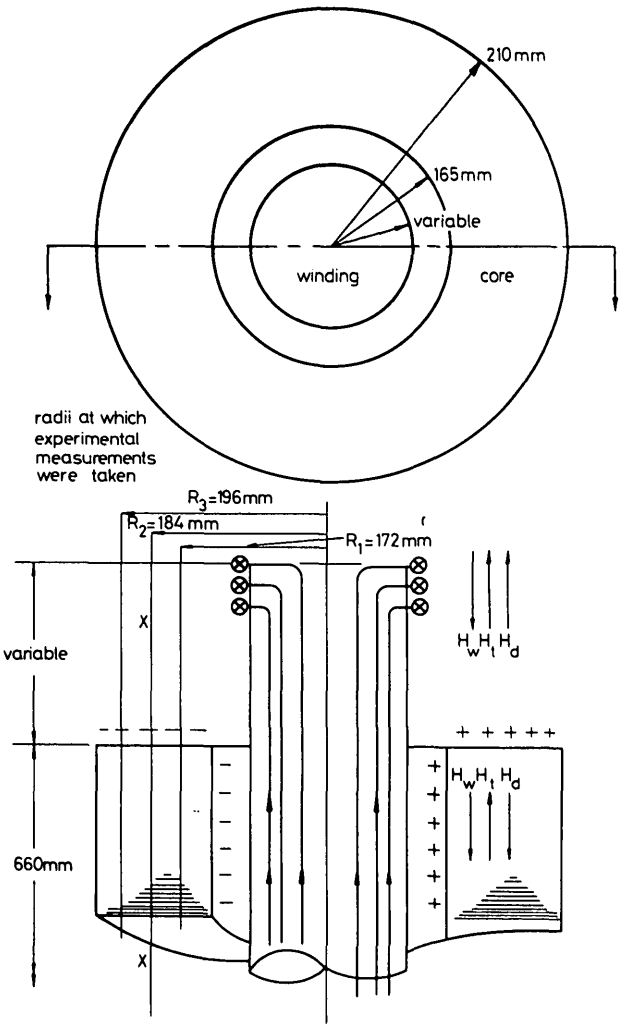

Fig. 1
Experimental model showing relative direction of axial fields due to important sources

H_ω axial field due to winding
H_t axial field due to tube of polarity
H_d axial field due to disc of polarity

small, and this has been confirmed by experiment.[17] This does not mean that the field of the eddy currents inside the core will be neglected. Indeed, the determination of the eddy currents will be an important future goal of the method, but their incorporation presents particular problems that are discussed later.

The principal sources of axial field at the core end for this model have thus been reduced to the circumferential currents of the winding, the polarity on the core bore and the polarity on the core annular end surface. Each of these sources may be represented physically by the method originally used by Hammond[7] for machine windings. This has been extended to deal with tubular and annular surface polarities by one of the authors[19] and is summarised in Appendix 11. The variation of axial field with distance from these sources depends on their geometry, and this is shown in the following Sections.

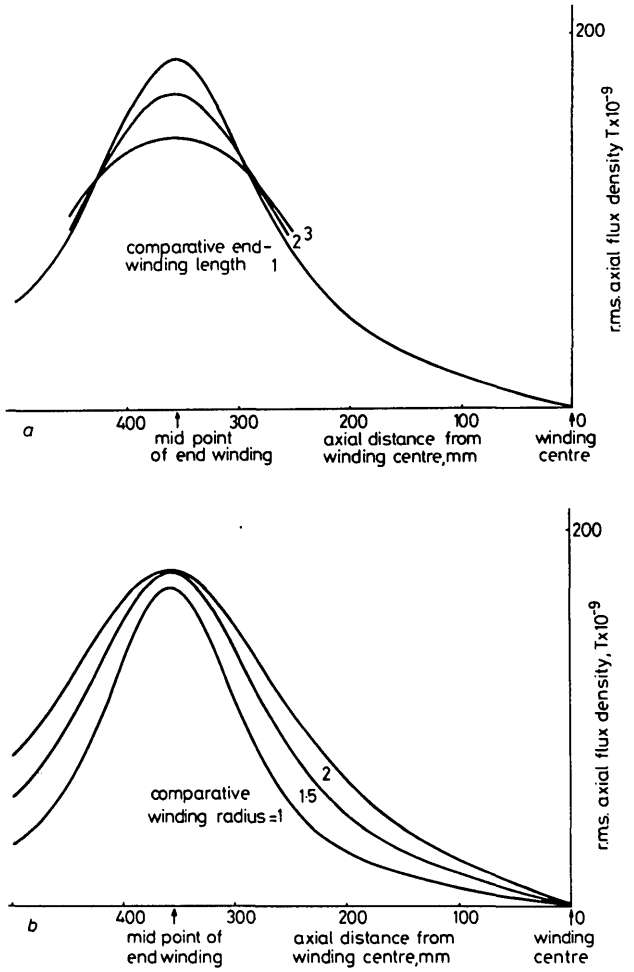

Fig. 2
Axial field due to concentric winding

Field calculated at a radius = 1·65 X winding radius
a Varying end-winding length
b Varying radius

4.2 Machine windings

The machine winding is represented by periodic current sheets of the form given in References 7 and 17. The analytical expressions for the field of this source are given in Appendix 11. The axial field of such a winding depends solely on the distribution of circumferential current density and this is borne out by these expressions. Fig. 2 shows the variation of axial field with axial distance, on a line parallel to the winding axis, at a radius greater than that of the winding. The sharpness of the peak in axial field depends partly on the end-winding length but also on the radius of the winding. Fig. 2*a* shows that reducing the end-winding length increases the magnitude of the peak of axial field, although the field will be correspondingly reduced some distance from the winding. In Fig. 2*b* it can be seen that reducing the winding radius also sharpens the peak of axial field.

4.3 Tubular surface polarity

The tubular surface polarity is represented by a periodic system shown in Fig. 3, for which the field is given in Section 11. The existence of an axial field component from this source may at first seem unexpected, but the finite length of the tube ensures a fringing field, in the axial direction, towards the end of the tube. Fig. 4 shows how this field varies on a line parallel to the tube axis. The peak of axial field naturally occurs adjacent to the end of the tube, and the sharpness of the peak is accentuated as the radius of the tube is reduced.

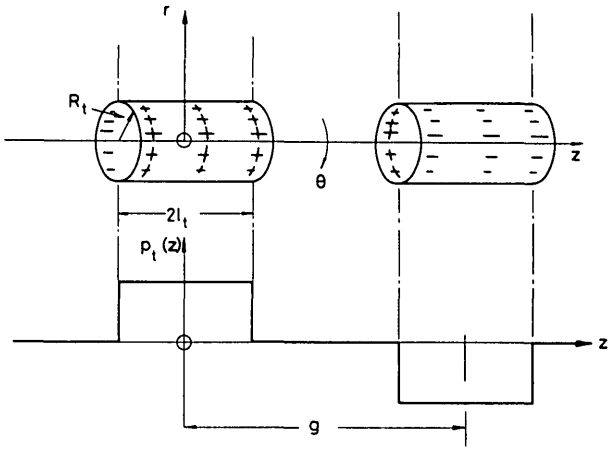

Fig. 3
Form of tubular surface polarities

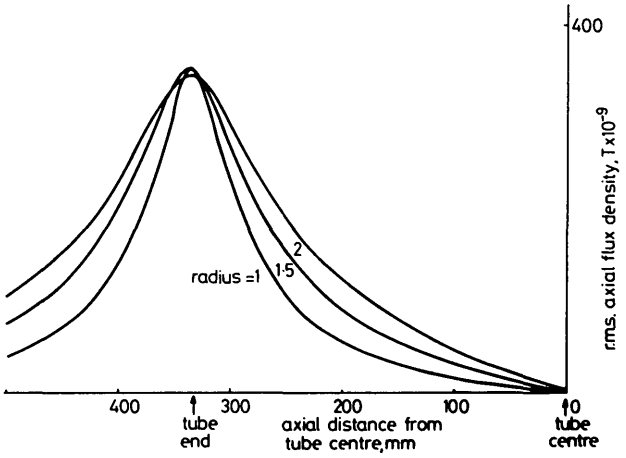

Fig. 4
Axial field due to tube of polarity of varying radius

Field calculated at a radius = 1·65 X tube radius

4.4 Annular surface polarity

This source may be represented by a system of annuli, periodic in r, as shown in Fig. 5, for which the field is given in Section 11. The decay of axial field with distance from the annulus depends on the annular width and Fig. 6 shows that the wider the annulus the more slowly the field decays.

4.5 Superposition of axial fields

The total axial field in the end region is the superposition of the fields of these three sources. Care must be taken that they are summed in the correct sense and Fig. 1 shows the relative signs of the sources for a given excitation. It can be seen from the diagram that outside the winding radius R_w, the end winding produces an axial field that opposes the fields due to the end annulus and core bore. In addition, the field of the end annulus must reverse sign inside the core. It should be remembered at this point that the model is singly excited and core eddy currents are ignored, so the phase angles of the component fields are permitted to be only 0 or π. The superposition of the axial fields of the three sources is shown in Fig. 7. The form of this total field therefore depends crucially on the geometries of the sources and on their position relative to one another. A number of important points emerge from this procedure and these are now discussed.

At the core end the axial field is principally due to the effect of the annulus and core bore, with the end winding making only a small contribution. This contribution, however, would increase if the

overhang of the winding were reduced causing the net axial flux impinging on the core end to be diminished. The discontinuity in the axial field at the core end is equal to the surface polarity at that point. Within the core, for the winding overhang shown, the axial field is controlled by the relative magnitudes of the annulus and bore fields that are now in opposition. Close to the end surface, where the field of the annulus is strong, the resultant field is small. Further into the core the field of the annulus falls rapidly, because the annular width is small, while the bore field decays more slowly. The result is therefore an increase in axial field as we move into the core, which is a natural result of the given source geometry. Thus the increases of axial flux within machine stator cores, which have been reported by one of the authors,[20] appear to be due to the magnetic interaction of the surfaces of the machine rather than the effects of saturation, as has been suggested. The influence of eddy currents and other internal sources have not been included, but their distributed nature makes it unlikely that they will radically alter the effect, except to attenuate it. Experimental results presented elsewhere[17] confirm this, and the problem is discussed in greater detail in Section 6.

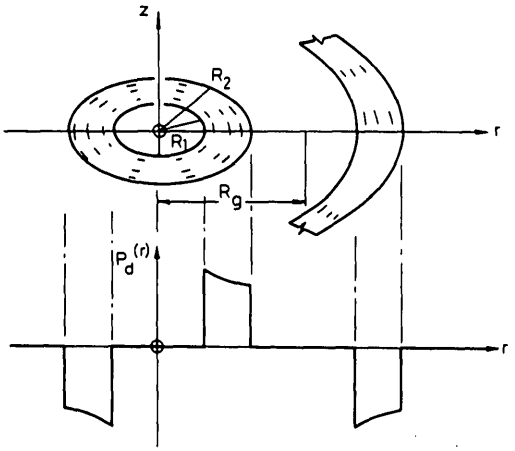

Fig. 5
Form of annular surface polarities

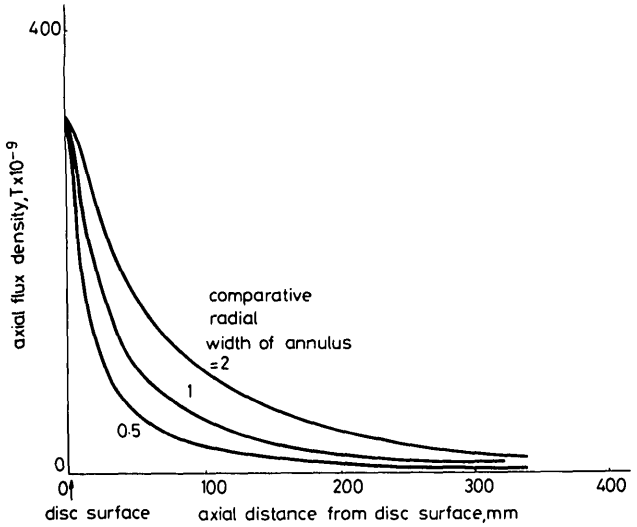

Fig. 6
Axial field due to disc of polarity of varying radial width

4.6 Calculating the magnitude of the sources

This superposition procedure has been carried out assuming that the magnitudes of the three sources are known. The calculation of these magnitudes is straightforward, requiring only a knowledge of the excitation current and the dimensions of the machine and its winding.

A designer will start his magnetic calculations on the 2-dimensional central plane of the machine and our approach will do the same. With a knowledge of the existing winding design, the flux density at the core bore can be predicted, for a given current, from simple calculations.[21] For a 2-pole machine with a core of reasonably high permeability it can be shown from this reference that

$$B_r \simeq \mu_0 j_z \left(\frac{R_t}{R_w}\right)^2$$

where j_z is the axial line current density at the winding, given by

$$j_z = \frac{3NIk_d}{\pi R_w}$$

The surface polarity p_t at the bore is related to the radial flux density B_r by the expression $p_t = B_r(\mu_r - 1)/\mu_r$.[18] Thus if the permeability is greater than 100, $p_t \simeq B_r$. Our method then assumes that the tubular surface of the bore carries this polarity uniformly throughout its length, an assumption which is within 10% of measurement.

The first two sources of axial field, namely the winding currents and the bore polarity are now known, and by the use of the field expressions from Appendix 11 the total axial magnetising force at the core end H_t can be found by summing these two components. The annular surface polarity is related to this magnetising force H_t by the expression $p_d = 2\mu_0 H(\mu_z - 1)/(\mu_z + 1)$ where μ_z is the homogenised axial permeability. Hence the magnitude of this final source may be found.

4.7 Interaction of sources

The procedure in the previous Section is a first attempt at finding the magnitude of the surface polarity sources, which, as we have explained in Section 3, must interact with one another. In spite of the interaction it is found that this process brings us surprisingly close to the final answer, provided sufficient terms are taken in the field expressions, to form the field to a reasonable degree of accuracy. Using the periodic intervals and number of terms suggested in Appendix 11 we have investigated this interaction for a number of iterations. The results show that both the bore and end-surface polarities are altered by less that 10% by the iterative process and this effect is confined to the corner. In physical terms this means that there is very little interation between these two orthogonal surfaces and, as a first approximation, we may neglect it.

We are then left with three magnetic sources, exhibiting negligible interaction, that control the axial field in the air beyond the core end. In the next section we compare the predictions of the method with measurements on our model.

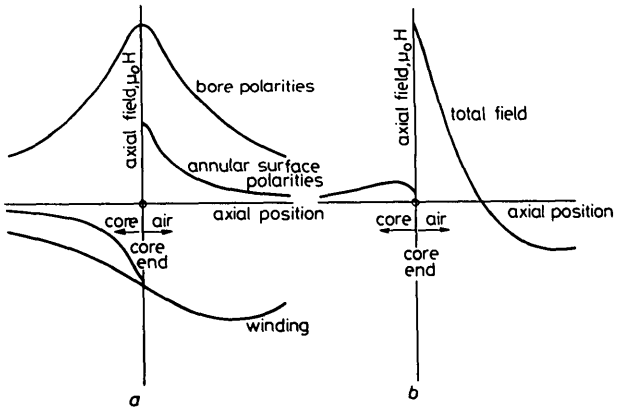

Fig. 7
Superposition of component fields due to the sources

a Components of axial field
b Superposition of those components

5 Discussion of results

Various windings may be inserted into the model (Fig. 1) and for the purposes of demonstrating the method of sources, results for windings of two different radii are presented. We only consider the case where these windings are overhung, as the core bore will then be approximately uniformly magnetised. This ensures that the Fourier coefficients of the field expressions are simple to calculate (Appendix 11). The model was excited by a rotating magnetic field, and results are presented at both 40 Hz and 2000 Hz, to demonstrate the effect of eddy currents on the axial field. The measured values of axial flux have been normalised to the axial line current density j_z', of the appropriate winding, referred to the core bore, where

$$j_z' = \frac{3NIk_d}{\pi R_t}$$

In this way results from the two windings may be compared directly and this is discussed further in Section 7.1.

Fig. 8 shows in isometric form the measured values of axial flux at three radii (marked on Fig. 1) at the two frequencies for a winding of radius 60 mm in two overhang positions. The axial field calculated by the sources method is also shown and agreement is close. Fig. 9 compares results for a winding of radius 100 mm, at the same overhang positions, and agreement is again close. The axial field on the core end has also been predicted with good accuracy and Fig. 10 demonstrates this for the winding of radius 100 mm in three different overhang positions.

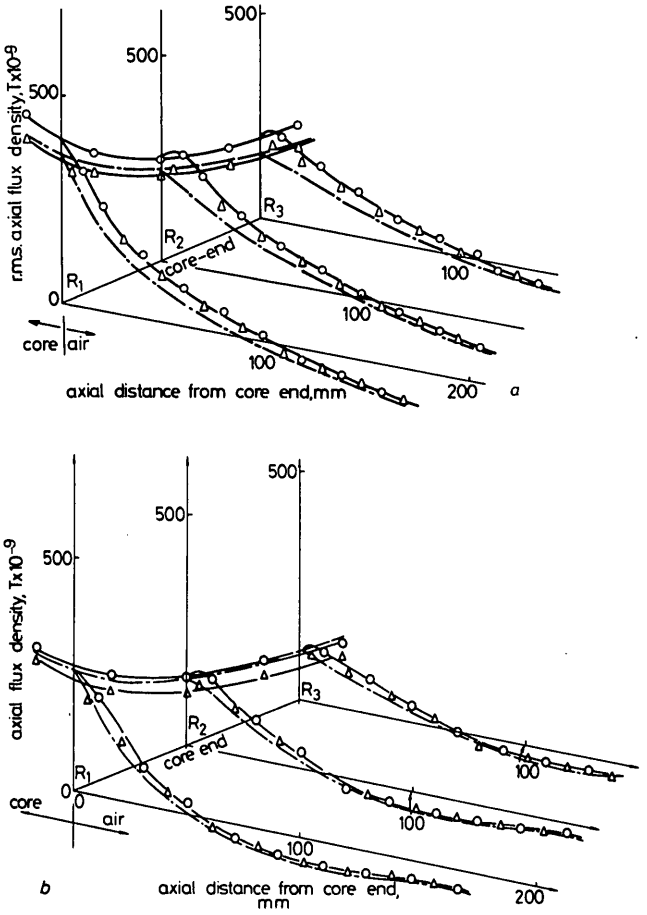

Fig. 8

Measured and predicted values of axial flux density at three radial positions with core excited by winding of 60 mm radius

o measured results at 40 Hz
Δ measured results at 2000 Hz
— · — results predicted by method of sources
a Winding overhang = 210 mm
b Winding overhang = 105 mm

It is interesting to note that there is very little change in the measured values of this field when the frequency is altered. It has been suggested that this implies that the eddy currents in the laminations beneath the core end are therefore resistance-limited. Internal axial flux measurements, which are presented in Reference 17, show that this is not the case. What the core-end results do demonstrate, however, is that the lamination eddy currents are having only a small effect on the leakage flux in the air. This is similar to the problem of tooth-ripple flux in the airgap of induction machines which has been shown[22] to be insensitive to changes in the tooth-ripple frequency. A physical explanation for this has been offered[23] that suggests that in magnetic circuits with a short aspect ratio, where the airgap is large compared with the iron length, the total eddy-current reaction is insufficient to affect the field in the air. This is the situation for core end-leakage flux which has a large part of its path in air outside the core end.

6 Qualitative assessment of sources within a practical core

We have shown that the axial field outside a slotless laminated core can be predicted by considering the sources of axial field. A full treatment of the distribution of axial flux within a practical core is beyond the scope of this paper, but it is desirable to show how the method of sources may be adapted to deal with real machine cores. We therefore consider the qualitative behaviour of the internal sources.

The presence of axial flux on the core-end surface demands the presence of axial flux within the core, because the end lamination is unlikely to be able to carry the total leakage flux by itself. Consideration of symmetry shows that this axial flux must be zero at the centre of the machine and will in general diminish from the core ends, although there may be local increases due to inhomogeneities in the magnetic circuit, caused by such features as ventilating ducts. The exact variation of axial field in the core will depend partly on the sources of Section 4, but also on volume polarities and eddy currents present in the core. We have already discussed the effect of the sources of Section 4 inside the core, and now we must consider the influence of these additional internal sources. Fig. 11 shows the axial flux in the core of our model (on the line X X, Fig. 1) predicted by neglecting the internal sources. Additional curves show the measured values of axial flux at various frequencies. There is good agreement outside the core, as explained in Section 5, but inside the core it is clear that internal sources must be taken into account.

6.1 Volume polarities within the core

The behaviour of volume polarities is particularly interesting. We have explained in Section 3 that the laminated construction of cores permits the establishment of pole strengths on the lamination surfaces that, when the core is viewed as a whole, may be represented as distributed volume polarities. The purpose of laminating the core is to reduce the eddy-current loss caused by the core flux. The laminations also provide a preferential direction for the flux because the axial permeability is much lower than the permeability in the plane of the lamination, that is the transverse direction. The axial leakage flux is therefore deflected into the path of the main flux. From the point of view of sources this deflection is achieved by polarity on the surfaces of the laminations (Fig. 12). These polarities on successive surfaces do not cancel one another, as shown in Fig. 12*a*, because of the transverse flux flowing between the laminations. They can therefore be thought of as a net volume polarity. Consider the problem in

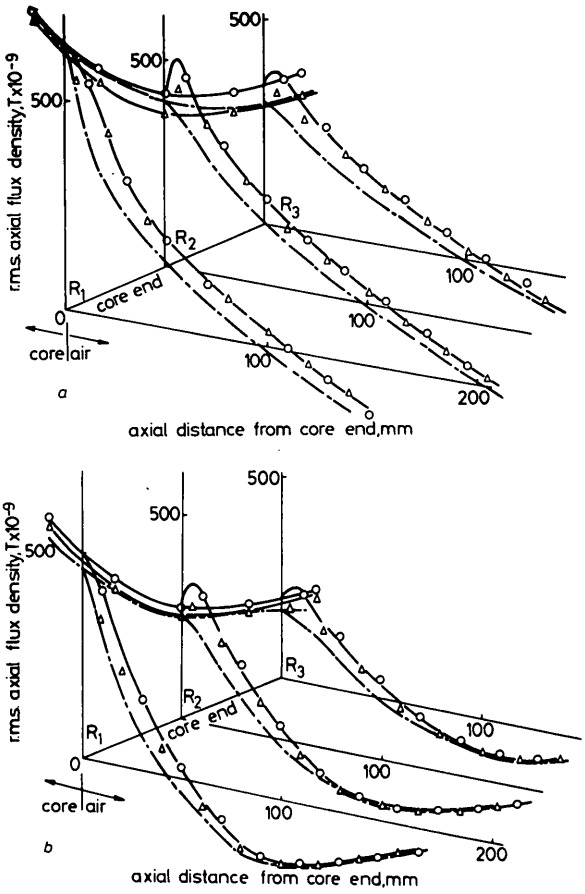

Fig. 9

Measured and predicted values of axial flux density at three radial positions with core excited by winding of 100 mm radius

o measured results at 40 Hz
Δ measured results at 2000 Hz
— · — results predicted by method of sources
a Winding overhang = 210 mm
b Winding overhang = 105 mm

terms of permeability, which implies that the core is treated as a homogeneous, anisotropic magnetic structure. When axial flux turns into the transverse direction it encounters a large increase in permeability. Mathematically this means that the distribution of permeability has a $\nabla\mu$ component, and this implies the existence of volume polarity which is shown in Fig. 12*b* and 12*c*. It will be seen that this volume polarity is associated with a significant amount of transverse interlaminar flux. The amount of transverse interlaminar flux and hence of volume polarity depends on the stacking factor of the core. The higher the stacking factor the smaller is the resultant volume polarity. Inside the coreplate the polarities on the lamination surfaces reduce the field in the axial direction and increase it in the plane of the lamination. This has the effect of turning any axial components of flux into the laminar plane, consistent with the anisotropic structure of the core.

The mechanism of transverse interlaminar flux, whereby the volume polarities are supplied, is extremely sensitive to the permeability, and therefore the state of saturation, of the coreplate. This is confirmed by experience with large machines in which axial flux penetration is increased as the degree of saturation increases. When the coreplate is unsaturated, the end laminations can absorb a large proportion of the axial leakage flux with only minor adjustments in the radial and circumferential field strength. At high saturation these laminations can absorb a much smaller proportion of the leakage flux, which must therefore penetrate deeper into the core before being turned into the plane of the laminations. In terms of sources this means that the laminations will carry matching surface polarities deeper into the core, and there will be very little transverse interlaminar flux near the core end. The resultant volume polarity distribution will therefore be less dense and extend further into the core, permitting the rise in axial field which drives the increased axial flux (Fig. 13).

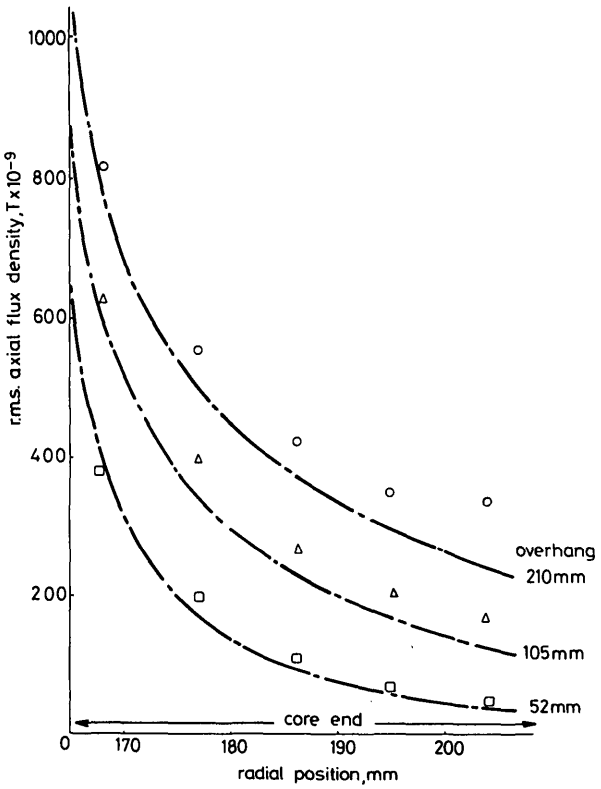

Fig. 10
Measured and predicted values of axial flux density on the core end with core excited by winding of 100 mm radius (measurement results at 40 Hz) and various overhangs

— · — results predicted by method of sources
o measured results at 210 mm overhang
△ measured results at 105 mm overhang
□ measured results at 52 mm overhang

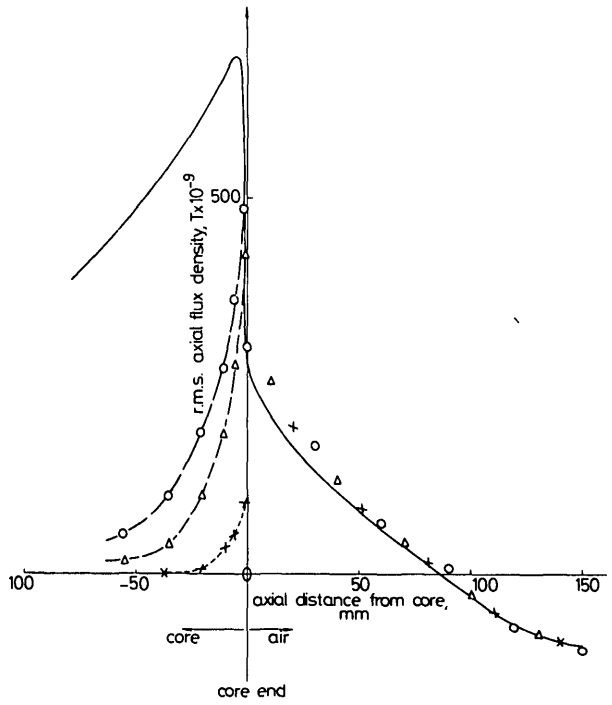

Fig. 11
Measured axial flux density both outside and within the core at various frequencies, also showing prediction from method of sources

o measured results at 5 Hz
△ measured results at 50 Hz
\+ measured results at 500 Hz
—— results predicted by method of sources

6.2 Eddy currents within the core

The action of the eddy currents flowing in the core is to suppress the penetration of the axial flux, and in this they assist the volume polarities. They also force the axial flux to the edges of the

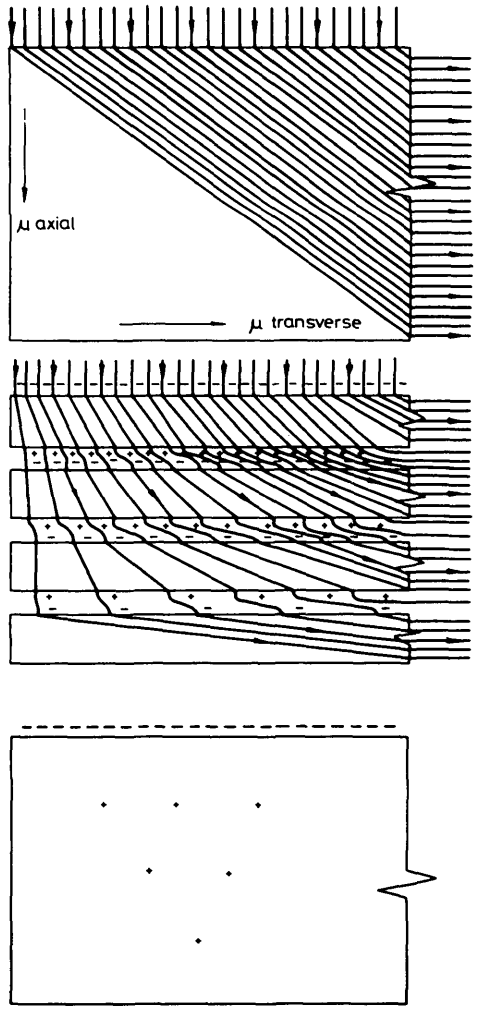

Fig. 12
Section of core at core end showing existence of volume polarities within core as a result of its laminar construction

a Equivalent homogenised core, $\mu_{transverse}$ μ_{axial}
b Laminar core showing surface polarities on successive laminations
c Resultant surface and volume polarities on such a core

core. Both these effects are enhanced with increasing frequency and are dependent on the effective axial permeability and coreplate resistivity.

The flow of eddy currents is confined to the plane of the laminations and, by continuity, the circumferential current close to the bore must be equal to that flowing at the core back. Thus the strength of axial field due to the eddy currents at those two sites must be nearly equal. The eddy currents also redistribute the surface polarities on the laminations, thereby altering the volume pole strength as illustrated in Fig. 14. As the frequency is increased so the strength of the eddy currents increases and the volume polarities are weakened. The axial field within the core is then controlled more exclusively by the eddy currents, and the distribution of axial flux becomes more nearly symmetrical across the radial depth of the core.

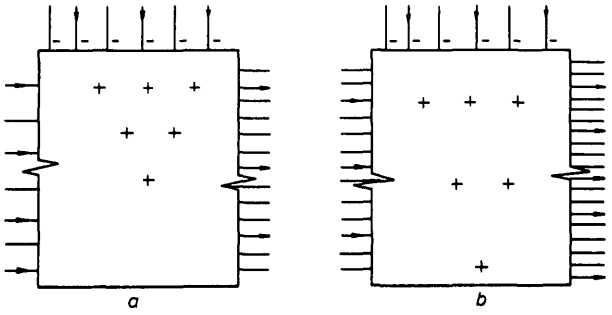

Fig. 13
Section of core at the core end showing influence of core saturation on volume polarities within core

a Core with low transverse saturation showing volume polarities to a shallow depth
b Core with higher transverse saturation showing volume polarities to a greater depth

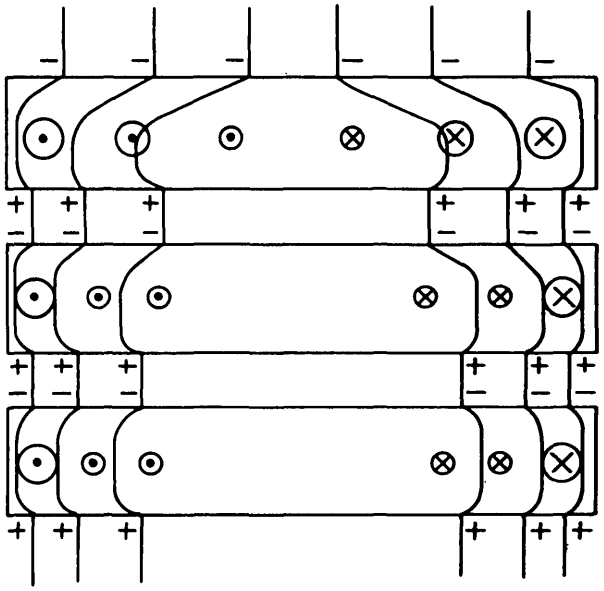

Fig. 14
Redistribution of surface polarities on laminations as a result of eddy currents flowing within laminations

6.3 The effects of practical core construction

The cores of present day machines are deeply slotted and contain radial and axial ventilation ducts, while the laminations will almost certainly by segmented. All these discontinuities establish additional sources of axial field which have not been considered in Sections 4 and 5. Although these additional sources are important many of their effects are localised. They are unlikely therefore to have an overwhelming effect on the axial field in the unslotted region of the core where the principal sources already discussed hold sway. Thus their effects may often legitimately be considered in isolation.

Perhaps the most important problem is that due to surface polarities on slots. It is unlikely that these will alter the total polarity on the cylindrical surfaces and so the field in the coreback region will remain substantially as described in Section 4. If necessary the field expressions of Appendix 11.2 can be adapted to deal with slotting by incorporating higher circumferential harmonics. Within the teeth the effect of slot polarities on the axial field is, however, going to be marked. But, because this is a local effect, it can be dealt with by 2-dimensional methods of the type described by Howe and Hammond.[20]

The segmented construction of practical cores causes a number of interesting effects. The surface polarities on the butt joints between segments gives rise to an increase in the circumferential reluctance of the core and they act as a source of axial field. Again these are local effects that cause only minor perturbations to the axial field in the core-back region and have been successfully analysed, in isolation, by Stoll.[24] The principal effect of butt joints is the disturbance they cause to the eddy-current patterns in the laminations. The flow of laminar eddy currents in the core of Sections 4 and 5 was unimpeded, but in a segmented core current is forced to complete its circuit at the butt joints and this must reduce the effectiveness of the eddy currents in suppressing axial flux. One may therefore expect that axial flux penetration will increase in a segmented core and this has been observed by other workers. This is a difficult phenomenon to analyse, but it could be incorporated in a calculation based on sources by attenuating the effect of the eddy-current sources.

7 Influence of size, frequency and saturation on the field of magnetic sources

One of the great difficulties in electromagnetic problems is to explain how particular field effects alter with dimensions and operating conditions. An important advantage of the method of sources is that in separating the component causes of the axial field we can scale the sources individually. This enables the designer to separate the variables of the problem.

Table 1 sets out the sources influencing the distribution of axial flux and lists the factors which control their strength. In this paper, comparison has been made between experimental results and prediction due to sources of group 1, while sources of groups 2 and 3 are described qualitatively in Section 6. We now consider how each of these sources may be scaled so that their behaviour under changed conditions can be predicted and so that measurements on small-scale models can be related to the behaviour of fullsize machines.

7.1 Scaling of winding and surface-polarity sources

The magnetic field of a winding in air is invariant with frequency, and is linearly dependent on the winding current. The field due to iron surface polarities is insensitive to μ_r, as stated in Section 3, and hence varies little with the state of saturation of the core. There is also evidence[17] that external surface polarities are only slightly affected by eddy currents flowing in the material beneath them and are thus invariant with frequency. The fields due to group 1 sources may therefore be considered by normalising their magnitude to the winding current, and scaled by simply scaling their dimensions.

7.2 Scaling of volume polarity sources

Volume polarity sources of group 2 have been shown in Section 6 to be dependent on the state of saturation of the core, its stacking factor and the annular depth of the core. The field of these

Table 1
INFLUENCE OF SCALING ON SOURCES OF AXIAL FIELD

Sources influencing axial flux in a laminated core	Controlling factors	Scaling criteria
1 Magnetostatic sources due to		
machine windings	winding radius, design and end-winding length	Linear scaling of dimensions and winding current
magnetisation of iron surfaces of the machine	core radius and annular depth	
2 Magnetostatic sources due to		
volume polarities within the core	core annular depth core stacking factor core saturation	Linear scaling of core depth Comparable values of core flux density
3 Eddy currents within the core.	core annular depth, core stacking factor, coreplate resistivity, frequency	Scaling of the ratio $b/2\delta_r$

sources may therefore be represented by scaling the annular depth of a core and working it at a similar flux density to that used in a fullsize machine, provided the core stacking factor is representative. The scaling of dimensions is straightforward but establishing high flux densities in small experimental cores presents practical cooling problems.

7.3 Scaling of eddy-current sources

Eddy-current sources of group 3 may be represented if the ratio between the skin depth to axial flux and the annular depth of the core is the same in the model core as in a fullsize machine. The most appropriate criterion for scaling has been shown to be[17]

$$\frac{\text{core annular depth}}{2 \times \text{skin depth of axial flux}} = \frac{b}{2\delta_r}$$

Where the classical expression for the skin depth of axial flux is

$$\delta_r = \left(\frac{2\rho}{\omega\mu_0\mu_z}\right)^{1/2}.$$

Once the dimensions of the core have been decided by the scaling criteria of group 1 and 2 sources, the ratio $b/2\delta_\gamma$ may be set by adjusting the frequency of excitation of the core.

8 Conclusions

A method has been described for calculating the core-end leakage field for a slotless machine, that synthesises the axial fields due to the principal magnetic sources of the machine. The method does not involve an assumption of infinite permeability in the core material. Expressions for the fields due to the sources described are presented, and results from them are compared with measurements made on a simple model. These results show that the method gives a reasonable prediction of the axial flux incident on the core end and for the axial field further from the core, around the end winding of the machine. They also confirm the assumption that the effect of the core eddy currents on the air field is small. The implications of a sources approach to the internal distribution of flux within the core have also been discussed. As a result of this method of synthesis, it has been possible to take a fresh look at the changes in axial flux distribution due to changes in the dimensions and operating conditions of machines.

It is suggested that the method may be useful to the designer during the early stages of machine design, as it allows him to investigate the effect on the axial field of the geometrical arrangement of the machine.

9 Acknowledgments

The authors are indebted to Mr. J. Kirwan who constructed the model and windings with great care, and who performed many of the field measurements. They are also indebted to Dr. R. L. Stoll for helpful discussion. They would also like to thank the UK Science Research Council for funding this work which forms part of a programme of research into flux distributions in laminated cores.

10 References

1 CHARI, M.U.K., and SILVESTER, P.: 'Analysis of turboalternator magnetic fields by finite elements', *IEEE Trans.*, 1971, **PAS-90**, pp. 454–459
2 JACOBS, D.A.H., MINORS, R.H., MYERSCOUGH, C.J., ROLLASON, M.L.J., and STEEL, J.G.: 'Calculation of losses in the end region of turbogenerators', *Proc. IEE*, 1977, **124**, (4), pp. 356–361
3 HOPKINSON, J.: 'Dynamo-electric machinery', *Philos. Trans. R. Soc.*, Part 1, 1886
4 WINCHESTER, R.L.: 'Stray losses in the armature end iron of large turbine generators', *Trans. Amer. Inst. Elect. Engs.*, 1955, **74**, pp. 381–391
5 WALKER, J.H.: 'End leakage flux of machine cores', *Proc. IEE/IERE, India*, 1971, **9**, (2), pp. 42–47
6 SMITH, R.T.: 'End component of armature leakage reactance of round rotor generators', *Trans. Amer. Inst. Elect. Engs.*, 1958, **77**, pp. 636–647
7 HAMMOND, P.: 'The calculation of the magnetic field of rotating machines. Pt. 1. – The field of a tubular current', *Proc. IEE*, Monograph 333, 1959, **106C**, pp. 158
8 ASHWORTH, D.S., and HAMMOND, P.: 'The calculation of the magnetic field of rotating machines. Pt. 2. – The field of turbo-generator end-windings', *Proc. IEE*, 1961, **108A**, pp. 527–538
9 LAWRENSON, P.J.: 'The magnetic field of the end-windings of turbo-generators', *ibid.*, 1961, **108A**, pp. 538-548
10 CARPENTER, C.J.: 'The application of the method of images to machine end-winding fields', *ibid.*, 1960, **107A**, pp. 487–500
11 TEGOPOULOS, J.A.: 'Determination of the magnetic field in the end zone of turbine generators', *Trans. Amer. Inst. Elect. Engs.*, 1963, **82**, pp. 562–572
12 REECE, A.B.J., and PRAMANIK, A.: 'Calculation of the end region field of a.c. machines', *Proc. IEE*, 1965, **112**, (7), pp. 1355–1368
13 OKUDA, H.: 'Calculation of magnetic field distribution in the end zone of generator winding', *Elecr. Eng. Jpn.*, 1969, **89**, pp. 27–33
14 MYERSCOUGH, C.J.: 'Calculation of magnetic fields in the end regions of turbogenerators', *Proc. IEE*, 1974, **121**, pp. 653–656
15 PANOFSKY, W.K.H., and PHILLIPS, D.M.: 'Classical electricity and magnetism' (Addison-Wesley, 1956), pp. 17–21
16 SIMKIN, J., and TROWBRIDGE, C.W.: 'Magnetostatic fields computed using an integral equation derived from Green's theorems'. Proceedings of the conference on the computation of magnetic fields, Oxford, 1976, pp. 5–14
17 TAVNER, P.J., PENMAN, J., STOLL, R.L., and LORCH, H.O.: 'The influence of winding design on the axial flux in laminated stator cores', *Proc. IEE*, 1978, **125**, (10), pp. 948–956
18 HAMMOND, P.: 'Leakage flux and surface polarity in iron ring stampings', *Proc. IEE*. Monograph 116, 1955, **102C**, pp. 138–147
19 TAVNER, P.J.: 'Axial flux distribution in laminated steel cores'. Ph.D. thesis, University of Southampton, 1978
20 HOWE, D., and HAMMOND, P.: 'Examination of the axial flux in stator cores with particular reference to turbogenerators', *Proc. IEE*, 1974, **121**, (12), pp. 1536–1541
21 HUGHES, A., and MILLER, T.J.E.: 'Analysis of fields and inductance in air-cored and iron-cored synchronous machines', *ibid.*, 1977, **124**, (2), pp. 121–126
22 GREIG, J., and MUKHERJI, K.C.: 'An experimental investigation of tooth-ripple flux pulsations in smooth laminated pole shoes', *Proc. IEE*, Monograph 2235, 1957
23 GREIG, J., and THOMPSON, D.S.: 'A tooth-ripple phenomenon – a physical explanation'. Proceedings of the international conference on electrical machines, Vienna, 1976, paper G.13
24 STOLL, R.L.: 'The effects of butt joints in large a.c. machine cores'. Proceedings of the international conference on electrical machines, Vienna, 1976, paper G.9
25 MOON, P., and SPENCER, D.E.: 'Field theory for engineers' (Van Nonstrand, 1961), p. 161

11 Appendix
Sources of simple geometry and their resultant fields

11.1 Tubular windings

The windings of machines are represented by a system of current sheets which are periodic in z, a method which has been fully described in References 7 and 8. The important principles are summarised here.

The winding considered in the paper is parallel-sided and can therefore be represented by an axial and a circumferential current-sheet system. Radial current sheets may also be employed for coned end windings[8] but these are not considered here. The current sheets are represented by a Fourier series on the z axis (Fig. 2) with the axial current sheet forming an even system as follows:

$$j_z(z, t, \theta) = \cos(\omega t - \theta) \sum_{k=1,3,5\ldots}^{\infty} a_k \cos\frac{k\pi z}{g}$$

and the circumferential current sheet forming an odd system as follows:

$$j_\theta(z, t, \theta) = \cos(\omega t - \theta\tfrac{1}{2}\pi) \sum_{k=1,3,5\ldots}^{\infty} c_k \sin\frac{k\pi z}{g}$$

The coefficients a_k and c_k prescribe the form of the current sheets and may be calculated by integration of the formulas for orthogonal functions.[25]

The forms shown in Fig. 2 are for the concentric winding used in this paper, when

$$a_k = \frac{4}{k\pi}\hat{j}_z \sin\frac{k\pi l_w}{g}$$

$$c_k = \frac{8}{k\pi}\hat{j}_\theta \sin\frac{k\pi l_w}{g} \sin\frac{k\pi d}{g}$$

where

$$\hat{j}_\theta = \hat{j}_z \frac{R_w}{2d} \qquad \text{by continuity.}$$

There are however a number of patterns describing other windings and these are given in Reference 17. It should be noted that all these forms must satisfy the condition $\nabla \cdot \mathbf{J} = 0$.

The components of $\mathbf{H}$ for the region $r > R_w$ can be found from the vector potential and are given here without proof as follows:

$$H_r = \frac{R_w}{2r}\cos(\omega t - \theta) \sum_{k=1,3,5\ldots}^{\infty} \left\{ 2K_1\left(\frac{k\pi r}{g}\right) I_1\left(\frac{k\pi R_w}{g}\right) a_k \right.$$

$$+\frac{k\pi r}{g}\left\{K_0\left(\frac{k\pi r}{g}\right)I_0\left(\frac{k\pi R_w}{g}\right)+K_2\left(\frac{k\pi r}{g}\right)I_2\left(\frac{k\pi R_w}{g}\right)\right\}c_k\Bigg\}\cos\frac{k\pi z}{g} \quad (1)$$

$$H_\theta = -\frac{R_w}{2r}\cos(\omega t-\theta-\tfrac{1}{2}\pi)\sum_{k=1,3,5\ldots}^{\infty}\frac{k\pi r}{g}\left\{\left\{K_0\left(\frac{k\pi r}{g}\right)I_0\left(\frac{k\pi R_w}{g}\right)-K_2\left(\frac{k\pi r}{g}\right)I_2\left(\frac{k\pi R_w}{g}\right)\right\}C_k+2K_1'\left(\frac{k\pi r}{g}\right)I_1\left(\frac{k\pi R_w}{g}\right)a_k\right\}\cos\frac{k\pi z}{g} \quad (2)$$

$$H_z = \frac{R_w}{r}\cos(\omega t-\theta)\sum_{k=1,3,5\ldots}^{\infty}\frac{k\pi r}{g}K_1\left(\frac{k\pi r}{g}\right)I_1'\left(\frac{k\pi R_w}{g}\right)c_k\sin\frac{k\pi z}{g} \quad (3)$$

These expressions, in turn, must satisfy the necessary condition $\nabla\cdot\mathbf{H}=0$. The radial and circumferential expressions are even on the z axis while the axial expression is odd and this agrees with our intuitive picture of the winding field. The effect of the different current sheets on each field component can be noted by identifying where the coefficients a_k and c_k occur, and by observing the behaviour of the associated Bessel expressions.

A value of $g=4(R_w+l_w)$ was used as suggested in Reference 7. Sufficient terms were summed to ensure that the field had converged to within 1% of its final value.

11.2 Tubular surface polarities

The magnetisation of tubular surfaces of the machine is represented by a system of tubes of surface polarity which are periodic in z. A Fourier series in z forms the polarity distribution

$$p_t(z,t,\theta) = \cos(\omega t-\theta)\sum_{k=1,3,5\ldots}^{\infty}t_k\cos\frac{k\pi z}{g}$$

The form shown in Fig. 3 is for the uniform radial magnetisation of a tubular surface by a rotating field varying sinusoidally with θ. The expression for t_k for a general variation of magnetisation, $\hat{p}_t(z)\cos(\omega t-\theta)$, can be obtained from the theory of orthogonal functions[25] and will be

$$t_k = \frac{4}{g}\int_0^{g/2}\hat{p}_t(z)\cos\frac{k\pi z}{g}\,dz$$

For the particular case of uniform magnetisation, shown in Fig. 3, this becomes

$$t_k = \frac{4\hat{p}_t}{k\pi}\sin\frac{k\pi l_t}{g}$$

The field due to such a source does not seem to have been derived before. From separation of the variables the magnetic scalar potential for the system is given by

$$V_1^* = \cos(\omega t-\theta)\sum_{k=1,3,5\ldots}^{\infty}A_kI_1\left(\frac{k\pi r}{g}\right)\cos\frac{k\pi z}{g} \quad \text{when } r<R_t$$

$$V_2^* = \cos(\omega t-\theta)\sum_{k=1,3,5\ldots}^{\infty}B_kK_1\left(\frac{k\pi r}{g}\right)\cos\frac{k\pi z}{g} \quad \text{when } r>R_t$$

where A_k and B_k are constants

At the surface of the tube

$$H_{r_2}-H_{r_1} = \frac{\hat{p}_t(z)}{\mu_0}\cos(\omega t-\theta)$$

$$H_{\theta_2} = H_{\theta_1}$$

Therefore

$$\left(\frac{\partial V_2^*}{\partial r}\right)_{r=R_t}-\left(\frac{\partial V_1^*}{\partial r}\right)_{r=R_t} = \frac{\hat{p}_t(z)}{\mu_0}\cos(\omega t-\theta)$$

$$\frac{1}{r}\left(\frac{\partial V_2^*}{\partial\theta}\right)_{r=R_t} = \frac{1}{r}\left(\frac{\partial V_1^*}{\partial\theta}\right)_{r=R_t}$$

From these equations it can be shown that

$$V_1^* = \frac{1}{\mu_0}\cos(\omega t-\theta)\sum_{k=1,3,5\ldots}^{\infty}R_tI_1\left(\frac{k\pi R_t}{g}\right)K_1\left(\frac{k\pi r}{g}\right)t_k\cos\frac{k\pi z}{g} \text{ when } r>R_t$$

$$V_2^* = \frac{1}{\mu_0}\cos(\omega t-\theta)\sum_{k=1,3,5\ldots}^{\infty}R_tK_1\left(\frac{k\pi R_t}{g}\right)I_1\left(\frac{k\pi r}{g}\right)t_k\cos\frac{k\pi z}{g} \text{ when } r<R_t$$

where the Fourier coefficients t_k depend on the magnetisation, as described above.

The components of $\mathbf{H}$ can now be found, and for the field in the region $r>R_t$ they are given by

$$H_r = \frac{\partial V_2^*}{\partial r} = -\frac{1}{\mu_0}\cos(\omega t-\theta)\sum_{k=1,3,5\ldots}\frac{k\pi R_t}{g}I_1\left(\frac{k\pi R_t}{g}\right)K_1'\left(\frac{k\pi r}{g}\right)t_k\cos\frac{k\pi z}{g} \quad (4)$$

$$H_\theta = -\frac{1}{r}\frac{\partial V^*}{\partial\theta} = -\frac{1}{\mu_0}\cos(\omega t-\theta-\tfrac{1}{2}\pi)\sum_{k=1,3,5\ldots}^{\infty}\frac{R_t}{r}I_1\left(\frac{k\pi R_t}{g}\right)K_1\left(\frac{k\pi r}{g}\right)t_k\cos\frac{k\pi z}{g} \quad (5)$$

$$H_z = -\frac{\partial V_2^*}{\partial z} = \frac{1}{\mu_0}\cos(\omega t-\theta)\sum_{k=1,3,5\ldots}^{\infty}\frac{k\pi R_t}{g}I_1\left(\frac{k\pi R_t}{g}\right)K_1\left(\frac{k\pi r}{g}\right)t_k\sin\frac{k\pi z}{g} \quad (6)$$

These expressions satisfy the necessary condition $\nabla\cdot\mathbf{H}=0$. The value of $g=4(R_t+l_t)$ was used and sufficient terms were summed to ensure accuracy within 1%.

11.3 Annular surface polarities

The magnetised annular surfaces of the machine are represented in a similar manner to the tubular surfaces, except that the geometry prescribes simple rather than modified Bessel functions and the system of surfaces is periodic in r, (Fig. 5).

The polarity distribution is formed as a Fourier-Bessel series

$$P_d(r,t,\theta) = \cos(\omega t-\theta)\sum_{\text{all}\,\alpha_k}^{\infty}d_kJ_1\left(\frac{\alpha_k r}{R_g}\right)$$

where α_k is the kth zero of J_1. The magnetisation of the end surfaces of the machine will be derived from the magnetising field acting at that surface due to the other sources, as described in Section 4. So the surface polarity will be of an arbitrary form and from the theory of orthogonal functions,[25] the coefficients d_k can be shown to be

$$d_k = \frac{\int_{R_1}^{R_2}\hat{p}_d(r)rJ_1\left(\frac{\alpha_k r}{R_g}\right)dr}{\frac{1}{2}R_g^2J_2^2(\alpha_k)}$$

Again the field due to such a source does not seem to have been derived before. From separation of the variables the magnetic scalar potential will have the form

$$V^* = \cos(\omega t - \theta) \sum_{\text{all}\,\alpha_k} A_k \exp\left(\frac{-\alpha_k z}{R_g}\right) J_1\left(\frac{\alpha_k r}{R_g}\right)$$

where A_k is a constant. At the surface of the annulus over the range $R_1 < r < R_2$

$$H_z(r) = \frac{\hat{p}_d(r)}{2\mu_0} \cos(\omega t - \theta)$$

and from this it can be shown that

$$V^* = \frac{1}{2\mu_0} \cos(\omega t - \theta) \sum_{\text{all}\,\alpha_k} d_k \frac{R_g}{\alpha_k} \exp\left(\frac{-\alpha_k z}{R_g}\right) J_1\left(\frac{\alpha_k r}{R_g}\right)$$

where the coefficients d_k depend on the magnetisation and can be found from the expression above.

Thus the components of **H** can be found and in the region $R_1 < r < R_2$ they are given by

$$H_r = -\frac{\partial V^*}{\partial r}$$

$$= -\frac{1}{2\mu_0} \cos(\omega t - \theta) \sum_{\text{all}\,\alpha_k} d_k \exp\left(\frac{-\alpha_k z}{R_g}\right) J_1'\left(\frac{\alpha_k r}{R_g}\right) \quad (7)$$

$$H_\theta = -\frac{1}{r}\frac{\partial V^*}{\partial \theta} = -\frac{1}{2\mu_0} \cos(\omega t - \theta - \tfrac{1}{2}\pi)$$

$$\sum_{\text{all}\,\alpha_k} d_k \left(\frac{R_g}{\alpha_k r}\right) \exp\left(\frac{-\alpha_k z}{R_g}\right) J_1\left(\frac{\alpha_k r}{R_g}\right) \quad (8)$$

$$H_z = -\frac{\partial V^*}{\partial z}$$

$$= \frac{1}{2\mu_0} \cos(\omega t - \theta) \sum_{\text{all}\,\alpha_k} d_k \exp\left(\frac{-\alpha_k z}{R_g}\right) J_1\left(\frac{\alpha_k r}{R_g}\right) \quad (9)$$

These expressions again satisfy the necessary conditions $\nabla \cdot \mathbf{H} = 0$.

The field expression were summed using $R_g = 2R_2$ and sufficient terms were taken to ensure accuracy within 1%.